The Colloid Chemistry of Silica

ADVANCES IN CHEMISTRY SERIES 234

The Colloid Chemistry of Silica

Horacio E. Bergna, EDITOR
DuPont

Developed from a symposium sponsored
by the Division of Colloid and Surface Chemistry,
at the 200th National Meeting of the
American Chemical Society,
Washington, DC,
August 26–31, 1990

American Chemical Society, Washington, DC 1994

The Colloid chemistry of silica

Library of Congress Cataloging-in-Publication Data

The Colloid chemistry of silica: developed from a symposium sponsored by the Division of Colloid and Surface Chemistry at the 200th National Meeting of the American Chemical Society, Washington, DC, August 26–31, 1990 / Horacio E. Bergna, editor.

p. cm.—(Advances in chemistry series, ISSN 0065–2393; 234)

Papers from the Ralph K. Iler Memorial Symposium.

Includes bibliographical references and indexes.

ISBN 0–8412–2103–0

1. Colloids—Congresses. 2. Silica—Congresses. I. Bergna, Horacio E., 1924– . II. American Chemical Society. Division of Colloid and Surface Chemistry. III. American Chemical Society. Meeting (200th: 1990: Washington, D.C.) IV. Ralph K. Iler Memorial Symposium (1990: Washington, D.C.) V. Series.

QD1.A355 no. 234
[QD549]
540 s—dc20
[546'.683] 93–11456
CIP

The paper used in this publication meets the minimum requirements of American National Standard for Information Sciences—Permanence of Paper for Printed Library Materials, ANSI Z39.48–1984. ∞

1994 Advisory Board

Advances in Chemistry Series

M. Joan Comstock, ***Series Editor***

FOREWORD

The ADVANCES IN CHEMISTRY SERIES was founded in 1949 by the American Chemical Society as an outlet for symposia and collections of data in special areas of topical interest that could not be accommodated in the Society's journals. It provides a medium for symposia that would otherwise be fragmented because their papers would be distributed among several journals or not published at all.

Papers are reviewed critically according to ACS editorial standards and receive the careful attention and processing characteristic of ACS publications. Volumes in the ADVANCES IN CHEMISTRY SERIES maintain the integrity of the symposia on which they are based; however, verbatim reproductions of previously published papers are not accepted. Papers may include reports of research as well as reviews, because symposia may embrace both types of presentation.

ABOUT THE EDITOR

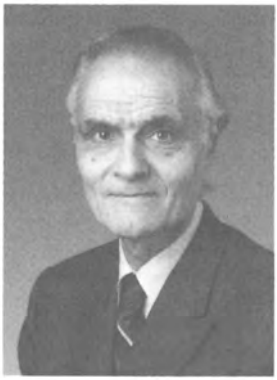

HORACIO E. BERGNA is a Senior Research Associate at the DuPont Experimental Station. He first joined DuPont in 1956 as part of Ralph K. Iler's research group.

Bergna received his Licenciado and doctorate in chemistry at the National University of La Plata in Argentina and worked on his doctoral thesis (Honors) on clay electrokinetics under Marcos Tschapek at the National Institute of Soils in Buenos Aires, Argentina. Bergna taught at the School of Chemistry in La Plata and worked at L.E.M.I.T. (Technological Research Laboratory of the Province of Buenos Aires). He did post-doctoral work at the Sorbonne in Paris and the Massachusetts Institute of Technology, where he worked with E. A. Hauser as a Guest of the Department of Chemical Engineering and as a Research Staff Member of the Division of Industrial Cooperation with J. Th. Overbeek, A. Gaudin, and P. de Bruyn. He studied humanities at the City of London College and Columbia University. Bergna is the author of 30 papers and holds 31 U.S. patents and more than 200 foreign corresponding patents in subjects such as colloidal silica synthesis; silica; alumina; aluminosilicates; zeolites; vanadyl phosphate catalysts; submicron grained products for metallurgy; coated particulates for ceramics, electronics, chromatography, and polymers; and binders for foundry sands.

In 1989 he was appointed Chevalier of the Ordre Des Palmes Academiques by the French government. Bergna is a retired president of the Alliance Française de Wilmington, Delaware, and a founder and chairman of the board of the Fondation Internationale de Delaware.

In 1990 he organized and chaired the Ralph K. Iler International Symposium on the Colloid Chemistry of Silica held at the 200th ACS National Meeting. Bergna co-authored the Colloidal Silica Section of the 1993 edition of the *Ullmann Encyclopedia of Chemistry* and guest edited two special issues of the Elsevier international journal *Colloids and Surfaces*.

ASSOCIATE EDITORS

PREFACE

INDUSTRIAL USE OF COLLOIDAL SILICAS is growing steadily in both traditional areas and an ever-increasing number of novel areas. Colloidal silicas are found in fields as diverse as catalysis, metallurgy, electronics, glass, ceramics, paper and pulp technology, optics, elastomers, food, health care, and industrial chromatography. However, in spite of the apparent simplicity of silica's composition and structure, fundamental questions remain about the formation, constitution, and behavior of colloidal silica systems. As a result, a broad and fascinating area of study is open to scientists interested in fundamental aspects of silica chemistry and physics and to technologists looking for new uses of silica and for answers to practical problems.

The work presented here includes both theoretical and experimental aspects of some of the most significant areas of colloidal silica science and technology. This book constitutes an update in the field since Ralph K. Iler, the distinguished silica scientist, published the definitive book on silica chemistry in 1979. This new book includes the 11 plenary lectures presented at an international symposium honoring Iler and 22 related research papers.

To solve the lack of coherence typical of some publications emerging from scientific gatherings, the symposium organizers selected nine fundamental topics in the area of colloidal silica chemistry and then extended an open invitation to the world's most prominent silica scientists, asking for either an overview of the current state of knowledge in their field or an original paper representing current trends of research. More than 190 overview lectures and research papers were presented by some of the most outstanding silica scientists from the former Soviet Union, Europe, China, Japan, Australia, and New Zealand as well as Canada and the United States. Renowned authorities in the areas discussed at the symposium edited selected papers for publication in this book or in two special issues of Elsevier's international journal *Colloids and Interfaces*.

This book offers a clear introduction to the science and technology of colloidal silica and will increase the reader's understanding of the most important problems in this area of science.

Acknowledgments

The Ralph K. Iler Memorial Symposium organizing committee is most grateful to the people and organizations that made the symposium and the publication of this book possible, especially the keynote speakers, the authors of papers presented at the symposium, the session chairpersons, the officers of the Division of Colloid and Surface Chemistry, and the staff of the American Chemical Society.

The committee also thanks the Cabot Corporation, DuPont, Degussa Corporation, Imperial Chemical Industries, Nalco Chemical Company, PQ Corporation, Sandia National Laboratory, and the former Soviet Academy of Sciences for their contributions to the symposium.

I and the editors of the nine sections of this book wish to thank Janet S. Dodd, Cheryl Shanks, Cathy Buzzell-Martin, and Steven Powell of the ACS Books Department for their help and patience during the writing and editing of the manuscripts. We also appreciate the assistance of William B. Hambleton Jr., Donald Nickerson, and Carol Little of DuPont in various stages of the project. We give special thanks to Amelia V. Kahn, Executive Secretary, for her many contributions to the development of the symposium and the subsequent preparation of the papers for publication in this book.

A special tribute goes to my good friend George Scherer for his kind support in the development of this book.

HORACIO E. BERGNA
DuPont
Wilmington, DE 19880–0262

March 6, 1993

DEDICATION

RALPH K. ILER DEVOTED MOST OF HIS CAREER to exploratory and industrial research in the chemistry of colloidal materials. He is recognized worldwide for his unique contributions to a unified understanding of the colloidal chemistry of silica and silicates. His book *The Chemistry of Silica*, published in 1979, is the definitive book on silica chemistry and remains a primary source of reference in the field.

Perhaps more than anybody else, Iler helped advance the chemistry of colloidal silica from an art to a science; through the imagery he created to explain his ideas, he elevated this science to a fine art. Today his graphics are universally used to illustrate colloidal silica structure and behavior. Through his lectures, more than 30 papers, 101 U.S. patents, and more than 500 foreign counterparts, he has deeply influenced the thinking of silica chemists all over the world.

At the end of World War II, when "colloidal silicic acid" was used on a very large scale in industry for water purification and as catalyst support, there was widespread disagreement as to its true chemical nature, the mechanism of its polymerization, its surface chemistry, and what determined its stabilization. Sols and gels were made by recipes and varied by empirical methods. Stability toward gelation was generally unpredictable because mechanisms were only speculative. In a series of investigations, publications, and patents, beginning in the early 1940s and continuing until his death, Iler, his co-workers, and people working under his direction did much to clarify these uncertainties. They made significant contributions toward the development of a clear and coherent picture of the polymerization, growth, aggregation, stabilization, physical properties, surface chemistry, kinetics, and uses of silica sols and gels.

This work was summarized and combined with an extensive and critical review of the literature in the lectures Iler gave at Cornell University as George Fischer Baker Lecturer in chemistry. These series of lectures formed the basis for his first book, *The Colloid Chemistry of Silica and Silicates*, published by Cornell Press in 1955. Iler's ideas were also expressed in chapters he wrote for other books and in the proceedings of conferences he attended as Alexander Memorial Lecturer at the Fourth Australian Conference on Colloids and Surfaces (1984) and as Keynote Awardee of the Second International Conference on Ultrastructure Processing of Ceramics, Glasses, and Composites held in Florida in 1985. Iler's Keynote Award was given for a lifetime's contribution to

Adapted with permission from *Colloids Surf.* **1992**, *63*, ix.

Ralph K. Iler

inorganic chemistry and for his pioneering work in the study of silica polymerization and colloidal chemistry.

The work of Iler and his co-workers led to the creation of new materials and industries. His studies of the surface chemistry of silica led to the invention of unique organophilic and hydrophobic silica products termed "estersils". Virtually a new industry was created when he rendered titania pigment particles in organic films and finishes photochemically inert by coating them with silica.

In another area of surface chemistry, his discoveries of chromium complexes capable of forming a permanent and water-resistant bond between polyester resins and fiberglass was of great importance in establishing the current fiberglass-reinforced plastics industry. His recognition of the importance of having a bireactive molecule forming a permanent chemical bond with both surfaces to be joined, as exemplified by these chromium complexes, provided the model for many coupling agents that have subsequently been developed.

He also discovered a water-soluble chromium composition, stearato chromic chloride, and demonstrated its use as a water repellent when applied to a surface and dried. This composition was used first in the paper industry, but applications have widened. Today stearato chromic chloride and related compo-

sitions are used in many industries as water repellents, grease repellents, insolubilizing agents, and dispersing aids. Stearato chromic chloride is also used as a surface treatment to improve the finish and handling of the glass fibers going into textile uses.

In an entirely different area of colloid chemistry, Iler directed a research effort that led to the discovery and development of fibrillar colloidal alumina. He participated personally in this research program and also carried out studies of the sintering and transformation of phases in this colloidal alumina at high temperature, making observations on the mechanism of its conversion to alpha alumina.

After 1952, as Manager of Exploratory Research at DuPont, Iler led the way in applying colloid chemistry to the field of metallurgy. This work led directly to the development of TD Nickel, recognized as one of the outstanding developments of metallurgy. This new composition consists of a colloidal dispersion of thoria in nickel. It is many times stronger than nickel and retains useful strengths over longer periods at higher temperatures than the superalloys previously available. This development in metallurgy is equally considered an outstanding achievement in the field of colloids.

Applying basic colloid techniques to the manufacture of microcrystalline refractory solids, Iler led a research group in the invention and development of several new compositions exhibiting a combination of strength and hardness previously unattained. The performance of Baxtron in cutting and forming tools for the metal-working industries was outstanding. A 1973 article in *American Machinist*, the 115-year-old magazine of manufacturing technology, said that Baxtron was a material that "cutting tools experts would include near the top of any list of significant developments of recent years".

One of Iler's accomplishments was the development of a new structure consisting of porous silica beads built up from colloidal silica particles. Use of this structure in liquid phase chromatography greatly increased speed of operation and provided a first-order advance in the state of the art.

Iler was a member of the Chemistry Advisory Committee, Air Force Office of Scientific Research, from 1953 to 1955. He was on the advisory board of *Journal of Colloid and Interface Science*.

Iler died on November 9, 1985. To all of those who had the privilege of knowing him and working with him, he will remain foremost an inspired teacher of unbounded generosity in sharing new observations and discoveries. His memory will remain with us as an example of unparalleled ethical standards and driving energy in the exploration and harnessing of nature to improve the quality of our lives.

In May 1990, DuPont's Lavoisier Academy awarded the Lavoisier Medal for Technical Achievement to Iler posthumously, and in September 1990, the DuPont Company opened a new research center in New Johnsonville, Tennessee, and named it after Ralph K. Iler.

1

Colloid Chemistry of Silica

An Overview

Horacio E. Bergna, DuPont, Wilmington, DE 19880–0228

Silicon dioxide is the main component of the crust of the earth. Combined with the oxides of magnesium, aluminum, calcium, and iron, it forms the silicate minerals in our rocks and soil.

Over millions of years silicon dioxide, or silica, has been separated from the original silicate rocks by the action of water to appear as quartz. In a few places it was deposited in the amorphous form as opal.

Our English word silica has a very broad connotation: it includes silicon dioxide in all its crystalline, amorphous, soluble, or chemically combined forms in which the silicon atom is surrounded by four or six oxygen atoms. This definitely excludes all the organosilicon compounds made by man in which carbon atoms have been linked directly to silicon atoms—commonly referred to as "silicones", which do not occur in nature. Silica is soluble enough in water to play important roles in many forms of life. It forms the skeletons of diatoms, the earliest form of life that absorbed sunlight and began to release oxygen into the atmosphere. Many plants use silica to stiffen stems and form needles on the surface for protection.

As animals developed, the role of silica became less obvious. But each one of us contains about half a gram of silica, without which our bones could not have been formed, and probably also not our brains.

Silica has played a key role since the beginning of civilization, first in flint for tools and weapons and in clay and sand for pottery. The high strength and durability of Roman cement 2000 years ago is now known to be due to the use of a special volcanic ash that is an almost pure form of amorphous colloidal silica. Today there is active research on the use of the somewhat similar silica fume from electric furnaces to make a super-strong Portland cement.

Our present technology would be very different without the silica for the catalysts of our oil refineries, for the molds for casting the superalloys in our jet engines, for modern glass and ceramics, electronic microcircuits, quartz crystals, and fiber optics.

0065–2393/94/0234–0001$12.86/0

— Ralph K. Iler, Alexander Memorial Lecture, Australia, 1989. Reprinted with permission from *Chemistry in Australia* (October 1986, p 355).

SILICON DIOXIDE, *SILICA*, CAN BE NATURAL OR SYNTHETIC, crystalline or amorphous. This book is concerned mostly with synthetic amorphous silica in the colloidal state.

The building block of silica and the silicate structures is the SiO_4 tetrahedron, four oxygen atoms at the corners of a regular tetrahedron with a silicon ion at the center cavity or centroid (Figure 1). The oxygen ion is so much larger than the Si^{4+} ion that the four oxygens of a SiO_4 unit are in mutual contact and the silicon ion is said to be in a *tetrahedral hole* (*1*). Natural silicas can be crystalline, as in quartz, cristobalite, tridymite, coesite, and stishovite, or amorphous, as in opal. Crystalline silica polymorphs are divided according to their framework density (SiO_2 groups per 1000 $Å^3$) into pyknosils and porosils, and the latter are further divided into clathrasils and zeosils depending on whether the pores are closed or open, that is, accessible to adsorption (*see* Chapter 8).

Familiarity with the structure of crystalline silica is helpful in understanding the bulk and surface structure of amorphous silica. All forms of silica contain the Si–O bond, which is the most stable of all Si–X element bonds. The Si–O bond length is about 0.162 nm, which is considerably smaller than the sum of the covalent radii of silicon and oxygen atoms (0.191 nm) (*2*). The short bond length largely accounts for the partial ionic character of the single bond and is responsible for the relatively high stability of the siloxane bond. Although in most silicas and silicates the silicon atom is surrounded by four oxygen atoms, forming the tetrahedral unit $[SiO_4]^{4-}$, a sixfold octahedral coordination of the silicon atom has also been observed in stishovite and coesite (*3*). The arrangements of $[SiO_4]^{4-}$ and $[SiO_6]^{8-}$ and the tendency of these units to form a three-dimensional framework structure are fundamental to silica crystal chemistry.

The silicates are built up in a manner analogous to that of the polyborates and the polyphosphates by sharing of oxygen atoms. In practice, two different SiO_4 groups may share only one oxygen atom, but any or all of the four of the oxygen atoms on a SiO_4 group may be shared with adjacent groups. Sharing of two oxygen atoms per unit yields a *chain*, three oxygen atoms a *sheet*, and four oxygen atoms a *three-dimensional network* (*1*). The crystalline silicas quartz, tridymite, and cristobalite are in truth network silicates, each silicon being bound to four oxygens and each oxygen being bound to two silicons. Quartz is the stable form of crystalline silica below 870 °C, tridymite below 1470 °C, and cristobalite below 1710 °C, but either of the two high-temperature forms can exist for long periods

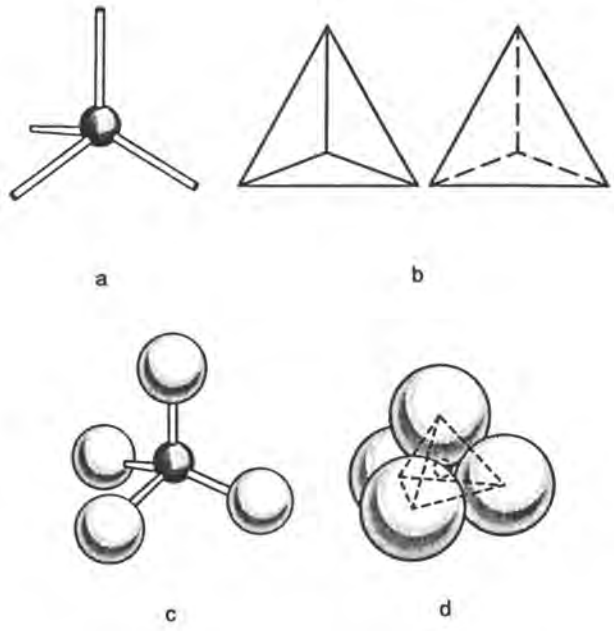

Figure 1. Methods of representing the tetrahedral coordination of oxygen ions with silicon: (a) ball and stick model, (b) solid tetrahedron, (c) skeletal tetrahedron, and (d) space-filling model based on packed spheres. (Reproduced with permission from reference 95. Copyright 1974.)

of time at room temperature and atmospheric pressure without turning to quartz (2).

The polymorphism of silicas is based on different linkages of the tetrahedral $[SiO_4]^{4-}$ units (2). Quartz has the densest structure, and tridymite and cristobalite have a much more open structure. All three forms exist in α- and β-forms, which correspond to low- and high-temperature modifications, respectively. The α- and β-modifications differ only slightly in the relative positions of the tetrahedral arrangements. This similarity is evident from the fact that the conversion $\alpha \rightleftharpoons \beta$ is a rapid displacing transformation that occurs at relatively low temperatures. Quartz is the most stable modification at room temperature; all other forms are considered to be metastable at this temperature (2).

In amorphous silica the bulk structure is determined, as opposed to the crystalline silicas, by a random packing of $[SiO_4]^{4-}$ units, which results in a nonperiodic structure (Figure 2). As a result of the structural differences the various silica forms have different densities (Table I).

The structure, Si–O bond length, and Si–O–Si bond angle in crystalline and amorphous silicas have been studied by X-ray, electron, and neutron diffraction and by infrared spectroscopy. Three strong absorption

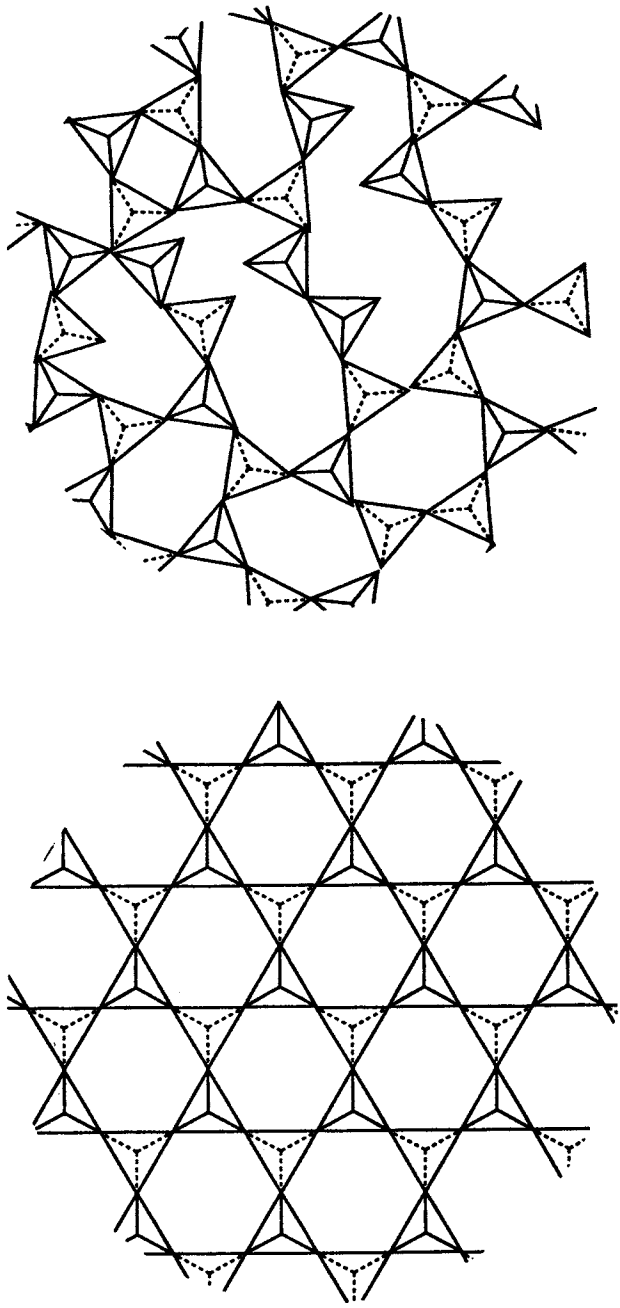

Figure 2. Two-dimensional representation of random versus regular packing of $(Si–O_4)^{4-}$ tetrahedra: amorphous (top) and crystalline silica. (Crystalline diagram reproduced with permission from reference 96. Copyright 1960.)

Table I. Density (*d*) of Crystalline and Amorphous Silicas

Silica	*Density (g/mL at 273 K)*
Coesite	3.01
α-Quartz	2.65
β-Quartz	2.53
β-Tridymite	2.26
β-Cristobalite	2.21
Amorphous silica	2.20

SOURCE: Reproduced with permission from reference 2. Copyright 1979 Elsevier Science Publishing Co., Inc.

bands at 800, 1100, and 1250 cm^{-1} measured by infrared transmission techniques are attributed to fundamental Si–O vibrations and do not differ greatly in the various silica modifications, whereas in the high-frequency region (2800–4000 cm^{-1}) certain distinct differences are observed (2). Figure 3 is a schematic representation of adjacent SiO_4 tetrahedra that shows the Si–O–Si bond angle (4). Diffraction measurements have shown a difference between the Si–O–Si bond angle of quartz (142°), cristobalite (150°), and fused quartz (143°).

Silicate glasses are conventionally regarded as silicate frameworks in which cations are distributed at random. However, Gaskell et al. (5), using neutron scattering with isotopic substitutions of Ca in a calcium silicate

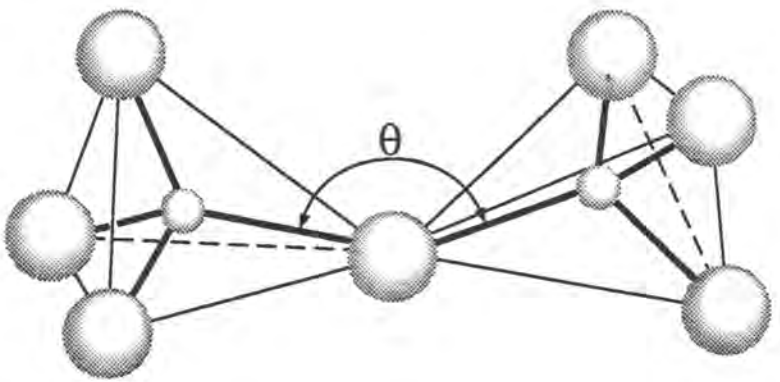

Figure 3. Schematic representation of adjacent SiO_4 tetrahedra that shows the Si–O–Si bond angle. Small circle, Si; large circle, O. (Reproduced with permission from reference 97. Copyright 1976 John Wiley & Sons, Inc.)

glass, revealed a high degree of ordering in the immediate environment of Ca over distances approaching 1 nm. The technique was later extended to obtain a direct measurement of the Ca–Ca distribution and provided what they considered strong evidence that such glasses and possibly other amorphous oxides are more extensively ordered than previously seemed possible. These findings on silicate glasses made some researchers review the largely discredited notion, originally based on the observation of broad X-ray diffraction peaks centered in the range of the crystalline silica's strong peaks, that amorphous silica may also have limited domains with a high degree of ordering.

Colloidal Dispersions and Colloid Science

As previously pointed out, this book deals mostly with *colloidal silicas*, that is, disperse systems in which the disperse phase is silica in the colloidal state of subdivision. The colloidal state of subdivision comprises particles with a size sufficiently small (≤ 1 μm) not to be affected by gravitational forces but sufficiently large (>1 nm) to show marked deviations from the properties of true solutions. In this particle size range, 1 nm (10 Å) to 1 μm (1000 nm), the interactions are dominated by short-range forces, such as van der Waals attraction and surface forces. On this basis the International Union of Pure and Applied Chemistry (IUPAC) suggested that a colloidal dispersion should be defined as a system in which particles of colloidal size (1–1000 nm) of any nature (solid, liquid, or gas) are dispersed in a continuous phase of a different composition or state (*6*). If the particles are solid they may be crystalline or amorphous. The disperse phase may also be small droplets of liquids, as in the case of emulsions, or gases, as for example in foams.

By way of comparison, the diameters of atoms and molecules of classical chemistry are below 0.5 nm. On the other end of the colloidal range, at about 1000 nm, the region of suspensions begins. Thus, colloid science, concerned with the intermediate range, is generally understood to be the study of systems containing kinetic units that are large in comparison with atomic dimensions (*7*). Such systems may be those in which the particles are free to move in all directions, or they may be derived systems, as a coagulum or a gel (discussed later), in which the particles have lost their mobility either partially or entirely, but have maintained their individuality.

All three dimensions need not be in the colloidal range: fibers or needle-shaped particles in which only two dimensions are in this range and thin films or disk-shaped particles in which only one dimension is in this range may also be treated as colloidal (*7*). Nor must the units of a colloidal

system be discrete: continuous-network structures, the basic units of which are of colloidal dimensions, also fall in this class, for example, porous solids and foams in addition to gels.

A more modern approach to colloidal dispersions is based on fractal geometry. The fractal approach, as explained later, provides a new basis for the definition and characterization of colloidal systems.

Sols, Gels, and Powders

A stable dispersion of solid colloidal particles in a liquid is called a *sol.* Stable in this case means that the solid particles do not settle or agglomerate at a significant rate. If the liquid is water, the dispersion is known as an *aquasol* or *hydrosol.* If the liquid is an organic solvent, the dispersion is called an *organosol.* The term *gel* is applied to systems made of a continuous solid skeleton made of colloidal particles or polymers enclosing a continuous liquid phase. Drying a gel by evaporation under normal conditions results in a dried gel called a *xerogel.* Xerogels obtained in this manner are often reduced in volume by a factor of 5 to 10 compared to the original wet gel as a result of stresses exerted by capillary tension in the liquid.

An *aerogel* is a special type of xerogel from which the liquid has been removed in such a way as to prevent any collapse or change in the structure as liquid is removed (*8*). This is done by drying a wet gel in an autoclave above the critical point of the liquid so that there is no capillary pressure and therefore relatively little shrinkage. The product is mostly air, having volume fractions of solid as low as about 0.1% (*8*), hence the term aerogel.

An *aerosol* is a colloidal dispersion of particles in gas. *Fumed* or *pyrogenic* oxides, also known in the case of silica as *aerosils,* are powders made by condensing a precursor from a vapor phase at elevated temperatures. (Usage has converted Aerosil, the trademark of Degussa's pyrogenic silica, into a generic term that includes other pyrogenic silicas, such as the Cabot Corporation's Cab-O-Sil.) Dried gels obtained by dispersing aerosils in water and then drying are called by some authors *aerosilogels.* Powders obtained by freeze-drying a sol are known as *cryogels.*

Commercial colloidal silicas are commonly available in the form of sols or powders. The powders can be xerogels, dry precipitates, aerogels, aerosils, or dried and calcined coacervates. The ultimate unit for all of them is a *silica particle,* the size of which determines the specific surface area of the product.

Figure 4 shows the formation of silica sols, gels, and powders—a genealogical tree of colloidal silicas.

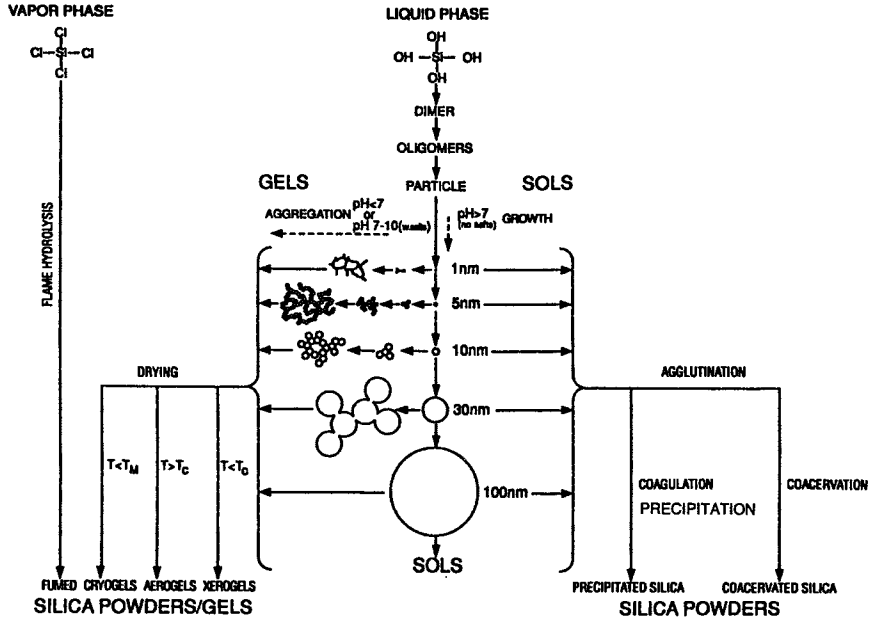

Figure 4. Formation of silica sols, gels, and powders by silica monomer condensation–polymerization followed by aggregation or agglutination and drying. Growth of nascent colloidal particles with a decrease in numbers occurs in basic solutions in the absence of salts. In acid solutions or in the presence of flocculating sols the colloidal silica particles form gels by aggregation into three-dimensional networks. The diagram is an expansion of Iler's classic Figure 3.1 (3) and constitutes a genealogical tree of colloidal silicas. (Reproduced with permission from reference 3. Copyright 1979.)

Colloidal Silica—Stability and Aggregation

Figure 5 is a diagram representing a particle of silica, the unit of all colloidal silicas. In a restricted sense the term "colloidal silica" is often used to refer to concentrated stable dispersions or "sols" made of discrete, dense particles of amorphous silicas of uniform particle size from about 5 to about 1500 nm and especially from about 5 to 100 nm. In a broad sense, silica gels and powders are also colloidal silicas because they consist of silica particles of colloidal size that range from 1 to 1000 nm in diameter. Because colloidal silica is composed of discrete particles, the difference with silica glass (also referred to as fused silica or, inappropriately, quartz glass) is that although both are amorphous, the structure of the glass is macroscopically continuous.

Silica fibers show some colloidal properties and are often included in the studies of colloidal silica. Figure 6 is an electron micrograph of synthetic silica fibers with a specific surface area of 400 m^2/g (9).

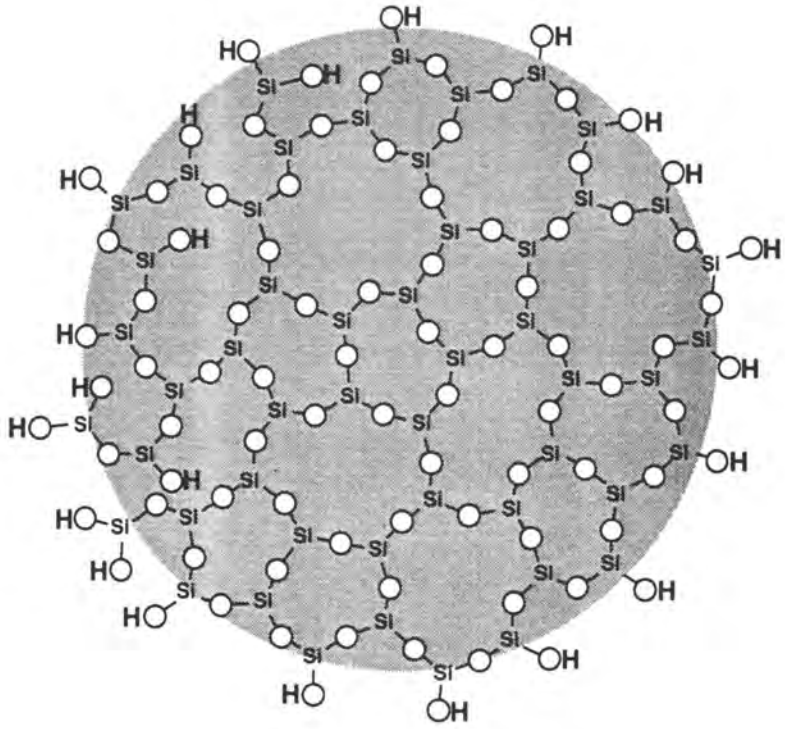

Figure 5. Schematic representation in two dimensions of a dehydrated but fully hydroxylated colloidal silica particle. The fourth oxygen coordinated with Si is above or below the plane of the paper. The figure is only a diagram, not a model. In an amorphous silica model the Si–O–Si bond angle may vary, but the Si–O distances are constant; each oxygen ion is linked to not more than two cations; the coordination number of oxygen ions about the control cation is 4 or less; oxygen tetrahedra share corners, not edges or faces; and at least two corners of each tetrahedron are shared.

Silica aquasols with particle size in the 5-nm to about the 60–100-nm range may remain for very prolonged periods of time without significant settling or loss of stability. *Stability* in colloid science is used not only in the thermodynamic sense but also in a strictly colloidal sense. "Colloidally stable" means that the colloidal particles do not settle and do not aggregate at a significant rate (*6*). An *aggregate* in colloid science is a group of particles held together in any possible way. The term aggregate is used to describe the structure formed by the cohesion of colloidal particles.

Silica sols lose their stability by aggregation of the colloidal particles. Colloidal silica particles can be linked together or aggregate by *gelation*, *coagulation* or *flocculation*, or *coacervation*.

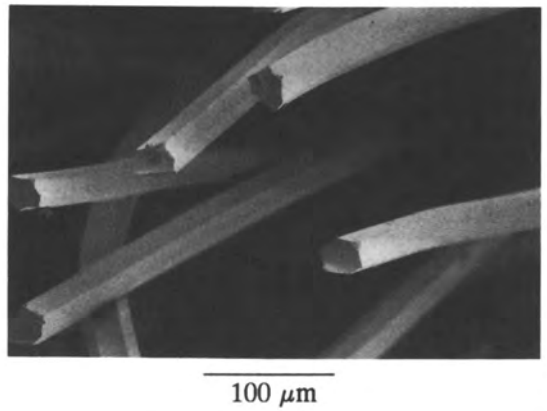

Figure 6. Porous silica fiber synthesized by W. Mahler. Details of preparation are given in reference 9. Scanning electron micrograph by M. L. Van Kavelaar. (Reproduced from reference 14. Copyright 1989.)

Gelation, Coagulation, Flocculation, and Coacervation

There is a basic difference between gelling or gelation and coagulation or flocculation. Both involve colloidal particles or polymers linking together and forming three-dimensional networks. But when a sol is gelled, it first becomes viscous and then develops rigidity and fills the volume originally occupied by the sol. On the other hand, when a sol is coagulated or flocculated, a precipitate is formed. In a concentrated sol the precipitate may be too voluminous to separate and will remain as a thixotropic mass, but in a dilute sol the precipitate will settle out. The difference between a sol, a gel, and a precipitate is illustrated in Figure 7 (*3*).

The terms coagulation (from the Latin "to drive together") and flocculation are commonly used interchangeably, but some authors prefer to introduce a distinction between coagulation—implying the formation of compact aggregates leading to the macroscopic separation of a *coagulum*—and flocculation—implying the formation of a loose or open network, a *floc*, that may or may not separate macroscopically (*10*).

Iler (*3*) distinguished the way in which colloidal particles aggregate or link together in the following manner:

1. Gelling, where the particles are linked together in branched chains that fill the whole volume of sol so that there is no increase in the concentration of silica in any macroscopic region in the medium. Instead, the overall medium becomes viscous and then is solidified by a coherent network of particles that, by capillary action, retains the liquid.

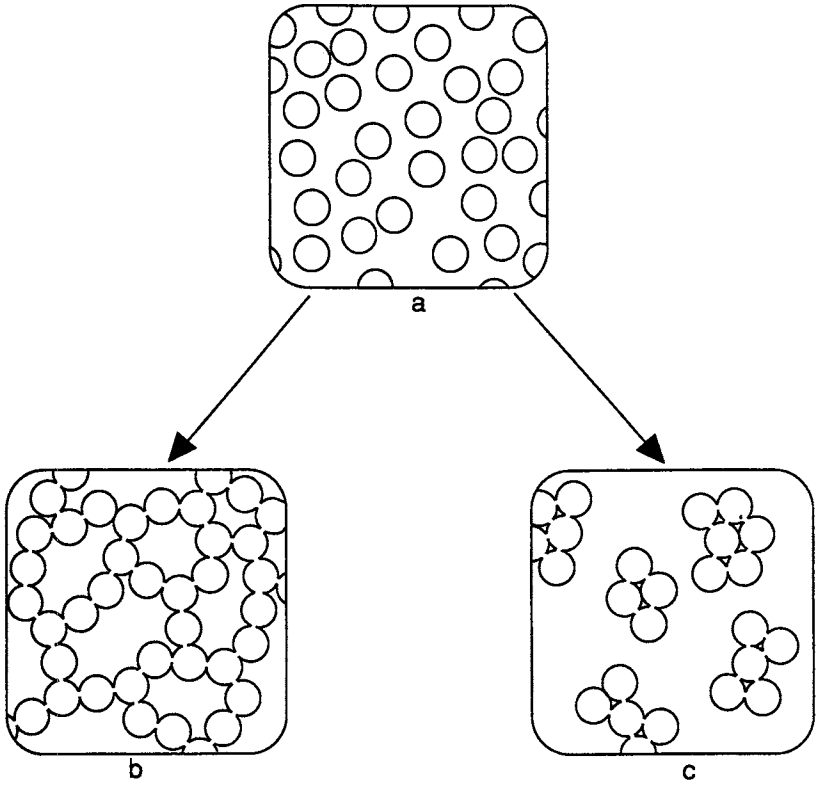

Figure 7. Silica gel versus precipitate: (a) sol, (b) gel, and (c) flocculation and precipitation. (Reproduced with permission from reference 3. Copyright 1979.)

2. Coagulation, where the particles come together into relatively close-packed clumps in which the silica is more concentrated than in the original sol so the coagulum settles as a relatively dense precipitate. Industrial precipitated silicas are powders formed when the ultimate silica particles are coagulated as loose aggregates in the aqueous medium, recovered, washed, and dried. A simple way to differentiate between a precipitate and a gel is that a precipitate encloses only part of the liquid in which it is formed.

3. Flocculation, where the particles are linked together by bridges of the flocculating agent that are sufficiently long so that the aggregated structure remains open and voluminous. It is apparent that these differences will be noted mainly in dilute sols containing only a few percent of silica. In

concentrated mixtures one can distinguish a gel, which is rigid, but not between a coagulate and a flocculate.

4. Coacervation, a fourth type of aggregation, in which the silica particles are surrounded by an adsorbed layer of material that makes the particles less hydrophilic, but does not form bridges between particles. The particles aggregate as a concentrated liquid phase immiscible with the aqueous phase.

Fractal Approach to Colloid Systems

One of the most exciting developments of the past decade in the study of colloidal silica is the application of the fractal approach to the study of sols and gels. Fractals are disordered systems for which disorder can be described in terms of nonintegral dimension. The concept of fractal geometry, developed by Mandelbrot (*11*) in the early 1980s, provides a means of quantitatively describing the average structure of certain random objects. The *fractal dimension* of an object of mass M and radius r is defined by the relation

$$M \propto r^{D_f}$$

where D_f is named the *mass fractal dimension* of the object. For Euclidean (nonfractal) objects, D_f equals the dimension of space D. In three dimensions the mass of a sphere scales as the radius cubed, that is, $D \propto r^3$. Fractals are objects for which D_f is less than the dimension of space: $D_f < 3$. Because D_f has many of the properties of a dimension but is often fractional, it is called fractal dimension (*12*).

Fractal geometry also describes *surface fractals*, in which the surface area S is related to the radius by a fractional power:

$$S \propto r^{D_s}$$

where D_s is called the surface fractal dimension and is smaller than D but larger than $D - 1$.

In sum, objects with $D_f < D$ are referred to as mass fractals, and objects with $D_f = D$ and $D > D_s > D - 1$ have very rough surfaces and are referred to as surface fractals (*12*). Brinker and Scherer (*8*) give a tree as an example of a mass fractal, because its branches become wispier as they move away from the trunk, so the mass of the tree increases more slowly than the cube of its height. On the other hand, they think of a piece of paper crumpled into a ball as a surface fractal because the area increases as the radius of the ball cubed ($D_s = 3$), but it is not a mass fractal because its mass also increases as r^3. Rarity (*12*) notes that a two-dimensional projection of a

tree's root system looks very much like an overhead view of a river delta. Both are random fractals, and the similarities arise from similar large-scale rules of growth that seem not to be influenced by their detailed constituents.

For Rarity the attraction of fractal theories of nature is that the application of large-scale geometrical rules can lead to simple universal properties in many important and complex random-growth processes such as colloidal aggregation (*12*). The fractal dimensions of objects with radii on the order of 10^2–10^4 Å may be measured in a small-angle X-ray scattering (SAXS) or static light-scattering experiment (*13*).

Application of scaling concepts has resulted in a much deeper understanding of the structure of colloidal aggregates and the kinetics of their formation (*14*). Two distinct, limiting regimes of irreversible colloid aggregation have been identified: diffusion-limited (DL) and reaction-limited (RL) cluster aggregation. Lin et al. (*14*) compared electron micrographs of aggregates of colloidal silica with colloidal gold and polystyrene and showed compelling visual evidence for universalities in their reactions (Figure 8). Scaling analysis of light-scattering data used to compare the behavior of the three systems under both DL and RL aggregation conditions provided convincing experimental evidence to the authors that the two regimes of aggregation are indeed universal. They used static light scattering to measure the fractal structure of the aggregates and quasielastic light scattering (QELS) to measure the aggregation kinetics and to probe the shape of the cluster mass distributions.

On the basis of experimental observations of aggregation, including electron microscopy and QELS, Matsushita (*15*) concluded that at least some colloidal aggregates can be well described in terms of fractal geometry and that the size distribution of aggregates and the kinetics of their aggregation can also be related to their fractal structure.

Aubert and Cannell (*16*) showed that silica spheres about 22 nm in diameter in an aquasol (Ludox AS-40) can form aggregates through addition of salt to the sol, that is, salting out, with fractal dimensions of 1.75 ± 0.05 and 2.08 ± 0.05. Slow aggregation (RL) always yielded clusters with $D = 2.08 \pm 0.05$, whereas fast aggregation (DL) produced clusters with either $D = 1.75 \pm 0.05$ or $D = 2.08 \pm 0.05$, depending on the pH and silica concentration. Moreover, aggregates with $D = 1.75$ were observed to restructure to those with $D = 2.08$.

Legrand et al. (*17*) applied the concept of fractal dimensionality to describe texture and porosity, giving a better description of the process underlying the tiling of the surface of silica powders. Taking fractality into consideration, they were able to interpret consistently different experimental results (isotherms and SAXS) and to reveal clearly significant differences between pyrogenic silica and samples of silicas prepared in an

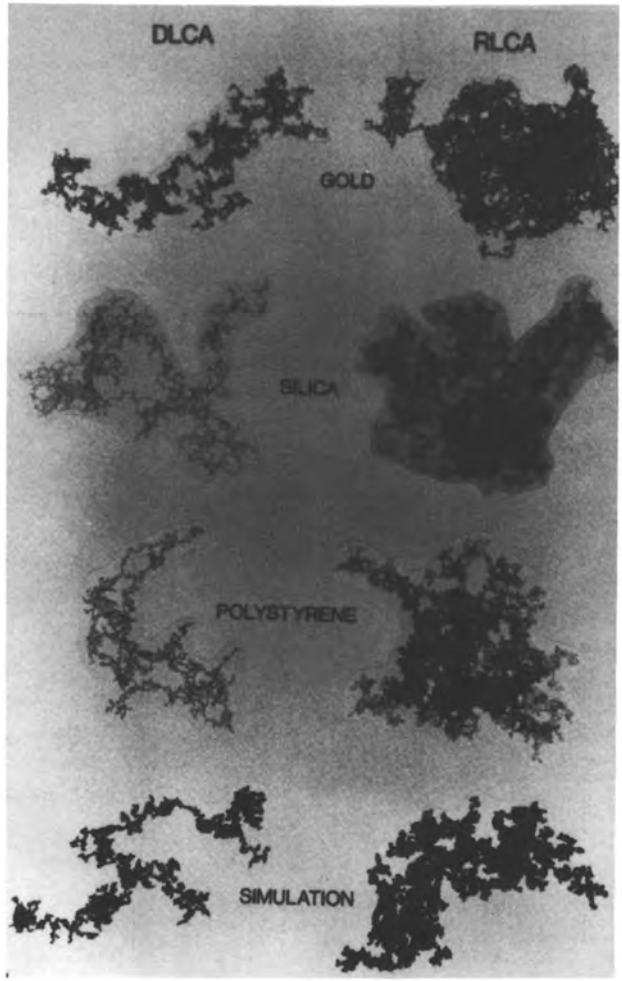

Figure 8. Transmission electron micrographs of typical clusters of gold, silica, and polystyrene colloids, prepared by both diffusion-limited and reaction-limited cluster aggregation and by computer simulation. There is a striking similarity in the structure of the clusters of different colloids in each regime. (Reproduced with permission from reference 14. Copyright 1989.)

aqueous medium. They found a difference in fractal dimensionality between pyrogenic and precipitated silicas of about 0.3; the pyrogenic silica was characterized by a smaller dimensionality. Suggested reading about the fractal approach to colloid science includes the letter to *Nature* by Mandelbrot and Evertsz (*18*) in addition to all the references cited in this section.

Colloid Chemistry of Silica—State of the Art

The state of the art of silica colloid chemistry in the late 1970s is extensively covered by Iler's classic book *The Chemistry of Silica* (*3*), Unger's *Porous Silica* (*2*), and in the specific case of silica powders by Barby's monograph (*19*).

Since the publication of these books, colloidal silica research has been driven forward not only by new applications in the conventional glass and ceramic industries and in metallurgy but also by the development of new and more sophisticated needs, for example, in the areas of electronic materials, catalysis, chromatographic substrates, and paper and pulp processes.

The fabrication of the super alloys of today and those of the future requires improved molds, cores, and binders. Chemical processes and oil refining require catalysts with improved activity, selectivity, and mechanical properties. Classic ceramics and the new ceramics for electronic microcircuits (microelectronics) require purer and more reliable precursors and processes. Chromatographic processes require substrates with improved physical, mechanical, and surface properties. And there is an ever-increasing need of better absorbents, binders, and pigments.

The next sections of this chapter constitute an overview linking the state of the art—as of the year of publication of Iler's definitive book (1979)—with current trends based on work done until 1990, the year of the R. K. Iler Memorial Symposium in Washington, DC, at the American Chemical Society's 200th National Meeting.

The symposium was exceptional because it gathered together for the first time many of the world's outstanding silica scientists, who presented close to 200 selected papers. Forty of the most prominent silica researchers from the former Soviet republics, who could not attend the symposium, sent papers to be discussed at the meeting. On this basis Iler's book and the symposium can be considered landmarks in the history of exchange of information on colloidal silica systems. A most valuable source of information published before the symposium was the excellent textbook by Brinker and Scherer printed in 1990 (*8*).

This book includes the plenary lectures and selected research papers presented at the symposium. Selected research papers are included in two special issues of *Colloids and Surfaces* (*20*).

The following fundamental aspects of the colloid chemistry of silica are briefly reviewed in this chapter: nucleation, polymerization, and preparation; stability of sols; surface structure; characterization methods; sol–gel science; gels and powders; and uses of silica sols and powders. Silica in biology is not within the scope of this book. Scientists working in this area should soon put together a protocol covering progress done since the publication of Iler's book.

The nascent field of biomimetic processing as applied to siliceous materials is not within the scope of this book either. A starting point in the search for information in this area is the article by Donald D. Ulrich in *Chemical and Engineering News* (*21*).

Silica Nucleation, Polymerization, and Growth: Preparation of Monodisperse Silica Sols

The possibility of producing uniform and reproducible ceramic microstructures through sol–gel techniques requires a better understanding of the processes of silica nucleation, growth, and polymerization. In other areas of technology, monodisperse silica sols of large and uniform particle size are required, and the field of colloidal silica synthesis is being broadened and extended from the classic aquasols of 5- to about 100-nm particle diameter to sizes up to 1 and 2 μm in the form of aquasols, organosols, and powders.

The classic silica aquasols 5–100 nm in particle diameter are prepared by nucleation, polymerization, and growth in aqueous systems. The particle size range can be extended to at least 300 nm by autoclaving. Silica organosols can be obtained by transferring the aquasols to an organic solvent.

Monodisperse silica sols of particle size up to about 2–3 μm in diameter were first obtained by Stober in an alcohol–ammonia system with enough water to hydrolyze a silane precursor (*22*).

The general theory of nucleation and polymerization in aqueous systems, in which silica shows some solubility, is discussed in detail in Iler's book (*3*). However, very little was known at the time the book was published (1979) about the polymerization of silica when $Si(OH)_4$ is formed in nonaqueous systems. Progress made up to 1990 in the understanding of the hydrolysis and condensation of silicon alkoxides that leads to silica gels or to silica sols of large particle diameter are lucidly discussed by Brinker and Scherer (*8*). Brinker's chapter in this book (Chapter 18) includes a clear explanation of the difference between hydrolysis and condensation of aqueous silicates and silicon alkoxides.

B. A. Keiser's contribution to this book (the introduction to the section "Preparation and Stability of Sols") constitutes an excellent introduction to silica nucleation, polymerization, and growth in both aqueous and alcoholic systems for the preparation of silica sols. Yoshida's chapter (Chapter 2) focuses on industrial development in the preparation of monodisperse sols from sodium silicate and predicts further progress in the development of silica sols that have shapes other than spherical, such as elongated, fibrous, and platelet. Colloidal silica particles with these shapes show novel properties and open the possibility of new industrial applications.

Although they are not discussed in Yoshida's chapter, new silica aquasols, organosols, and powders with particle diameters from 100 to about 2000 or 3000 nm (2–3 μm) are already being produced on industrial or semiindustrial scale in Japan for special uses.

Van Blaaderen and Vrij's chapter (Chapter 4) constitutes an excellent contribution to the understanding of the mechanisms of nucleation and growth of silica spheres in the alcohol–ammonia–water system to achieve particle sizes much larger than those of the classic silica sols synthesized in water. Kozuka and Sakka (Chapter 6) provide detailed conditions and the mechanism of formation of micrometer-sized particles of gels synthesized in highly acidic solutions of tetramethoxysilane (TMOS).

Using ultracentrifugation and a series of advanced experimental techniques such as small-angle neutron scattering (SANS), photon correlation spectroscopy (PCS), and ^{29}Si NMR, Ramsay et al. (Chapter 3) were able to study in detail the oxide–water interface of silica aquasols ~7 to 30 nm in particle diameter and found that all the sols investigated contained a significant proportion of oligomeric silicate species that could be associated with the core particle surface. This fact may not only explain the high charge density and exceptional stability of silica sols, but it may also affect the surface and pore structure of gels obtained by dehydrating these sols. Legrand et al. (*17*) also found evidence of polysilicic acid on the surface of silica aquasols as residues of the synthesis process that may be responsible in some cases for high counts of surface silanols.

In addition to these chapters, a picture of the state of the art as of 1991 in the synthesis of silica by hydrolysis and condensation of alkoxides is given in this book by Coltrain and Kelts (Chapter 19) and by Schmidt and Bottner (Chapter 20) and in the open literature by Minihan and Messing (*23*) and Bailey and Mecartney (*24*).

In sum, using as a landmark the 1979 book by Iler, in which he states that little is known about the polymerization of silica when $Si(OH)_4$ is formed in nonaqueous systems, one can say today that not only the knowledge of the theory of nucleation and polymerization of silica in aqueous systems is being fairly well consolidated, but also that significant progress is being made in the understanding of the hydrolysis and condensation of silicon alkoxides leading to silica gels and large-particle-size silica sols.

Stability of Silica Sols

Derjaguin (*25*) distinguished three types of stability of colloidal systems.

1. *Phase stability*, analogous to the phase stability of ordinary solutions.

2. Stability of *disperse composition*, that is, stability with respect to change in dispersity (particle size distribution).

3. *Aggregative stability*, the most characteristic for colloidal systems. *Colloidally stable* means that the particles do not aggregate at a significant rate (6). As explained earlier, *aggregate* is used to describe the structure formed by the cohesion of colloidal particles.

On the basis of work done in the years just before World War II, Derjaguin and Landau (26) were able to explain in 1941 many of the complex phenomena involved in aggregative stability on the basis of forces of interaction between colloidal particles, namely the van der Waals–London forces of attraction and the electrostatic forces of repulsion. In the meantime, as a result of theoretical investigations and calculations performed in the years 1940–1944 and without the benefit of much of the literature that appeared during the war years, Verwey and Overbeek (7) formulated a theory of stability of lyophobic colloids and published it as a book in 1948. Because their ideas were virtually identical to those of Derjaguin and Landau, the theory became known as the DLVO theory, and it appeared to allow the science of colloids to enter a new stage, less empirical, in which the experimental study of better defined objects could be guided by more quantitative ideas rather than by qualitative rules or working hypotheses. For example, the DLVO theory provided an explanation and a quantitative refinement of the empirical, qualitative Schulze–Hardy rule. It also predicted correctly the small influence of the co-ion for electrolytes of the 1–2 and 2–1 types and provided a basis for the calculation of the potential energy–distance relationship of colloidal particles.

The enunciation of the theory of stability of colloids stimulated an enormous volume of literature, most of which involved use of the theory in experimental and applied work. On this basis, Derjaguin wrote in 1989 a new monograph setting forth the present state of the theory of colloid stability (25).

The advent of concentrated monodisperse silica sols in the 1950s appeared to offer an ideal model to test the DLVO theory: a stable system of solid spheres with a particle diameter that could be varied in a broad range from about 5 to 100 or 300 nm. However, it soon became quite evident to many researchers, both in Iler's laboratories and elsewhere, that silica sols do not conform to the DLVO theory as originally formulated (27–32). As an example, Figure 9 illustrates the problem, showing an area in the stability–pH curve of experimentally proven relative stability (metastability) of silica sols at around the zero point of charge where the theory predicts minimum stability. In addition, the plot of experimental

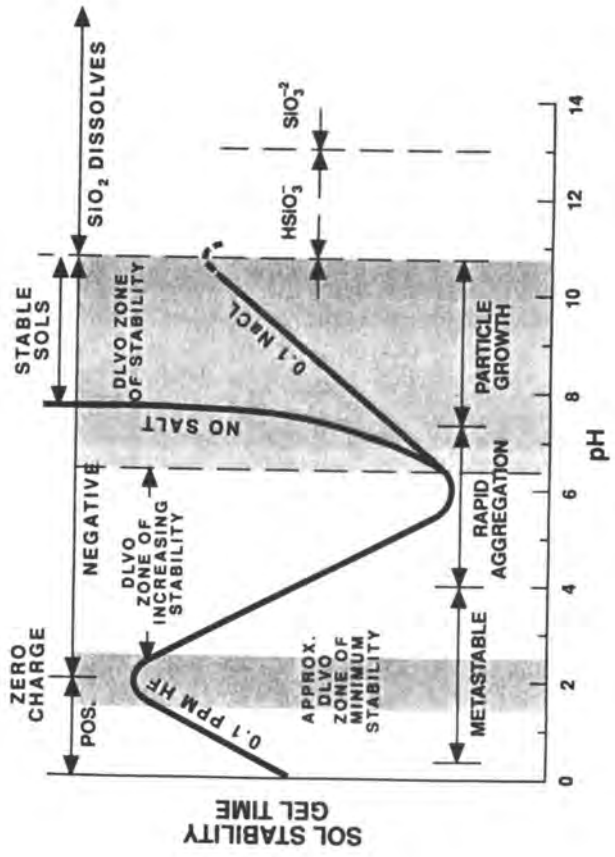

Figure 9. Effect of pH on the stability (gel time) of the colloidal silica–water system. Thick solid lines represent experimental results (3). Shaded areas and white area in between are approximate zones corresponding to behavior predicted by the DLVO theory (7, 26), some in contrast with experimental results: minimum stability predicted at pH around 2–3, increasing stability predicted at pH between 3 and 6–8, and maximum stability predicted at pH higher than 8. (Reproduced with permission from reference 3. Copyright 1979 John Wiley & Sons, Inc.)

values shows an unexpected minimum in what ought to be, according to the theory, a gradual rise from pH 2 to maximum stability at higher pH values. Another example is constituted by Horn's measurements (*33*). Horn made direct studies of the forces between amorphous silica surfaces and found them to be repulsive in nature down to a few angstroms of separation. Horn did not observe in the case of silica what Dumont considers the "undeniable existence of overwhelming positive forces of attraction", a key factor in the DLVO theory (*see* the introduction to the section "Surface Chemistry of Silica").

Two possibilities are open: amend the DLVO theory or design a new theory based on typical properties of colloidal silica. Lyklema (*34*) believes the first approach is promising if features such as solvation layers, hydrophobic bonding, and surface charge fluctuations are incorporated into the DLVO theory.

Healy (Chapter 7) and Dumont also prefer the first approach. Healy sets down a model based on the control of coagulation by surface steric barriers of polysilicate plus bound cations. Healy's electrosteric barrier model is designed to stimulate new experimental initiatives in the study of silica sol particles and their surface structure. Dumont believes that many particular aspects of the stability of silica hydrosols could be explained not only by the low value of the Hamaker constant but also by the relative importance of the static term of the Hamaker equation.

Yates (*35*) pointed out that if an approach such as the DLVO theory is to be generally applicable, it should be extended at least to include solvent effects and adsorption. It should also allow for substantial chemical activation energies for the formation of surface chemical bonds in irreversible coagulations and particle growth. However, Yates believes that a better approach might be to attempt a thermodynamic rather than a kinetic analysis of changes in the free energy of the system as a whole, attendant upon coagulation and separation into a more dilute suspension and a coagulated phase. Yates pointed out that Langmuir (*36*) suggested such an approach many years ago that was further extended by Iler (*3*), and although the mathematical treatment Langmuir attempted may not be applicable, the basic idea retains merit.

What Derjaguin considers the central issue of colloidal solutions remains largely unresolved for silica sols. This book mentions the ideas of the proponents of both the kinetic and the thermodynamic approach to the problem of stability of silica sols and is intended to stimulate the continuation of the healthy controversy started at the R. K. Iler Memorial Symposium. In this manner a consensus should eventually be reached that will allow the establishment of common quantitative parameters in the treatment of stability of silica sols and other disperse phase materials composed of polyvalent atoms linked by strong covalent bonds and the explanation of their experimentally observed behavior.

Silica Surface

Many of the adsorption, adhesion, chemical, and catalytic properties of silicas depend on the chemistry and geometry of their surfaces. Because of the importance of these properties in determining the practical applications of silica, its surface chemistry is a subject of intensive studies. Considerable progress was made in the 1960s and 1970s in determining the silica surface structure by the combination of thermogravimetry and IR spectroscopy with chemical surface reactions and deuterium-exchange methods. The state of the art in that general period is covered by classic textbooks and monographs by Hair (*37*), Kiselev and Lygin (*38*), and Little (*39*). Information on the silica surface structure obtained specifically by transmission IR spectroscopy before 1980 has been summarized by Hair (*40*).

More demanding needs for materials for the new technologies of the 1980s required further understanding of the silica surface. Significant advances in computer instrumentation and the development of new techniques for surface analysis are now allowing significant progress in the elucidation of the structure of silica surfaces.

Discussions of old and new techniques used to study the surface of silica, including diffuse reflectance Fourier transform (DRIFT) infrared spectroscopy, ^{29}Si cross polarization magic-angle nuclear magnetic resonance (CP MAS NMR) spectroscopy, as pioneered by Maciel and Sindorf (*41*) and others, and deuterium-exchange methods, may be found in review essays by Unger (Chapter 8) and in articles by Legrand et al. (*17*) and Kohler et al. (*42*). The use of computational chemistry and computational vibration spectroscopy vis à vis experimental spectra of inelastic neutron scattering is discussed in monographs by Chuiko et al. (*43*) and Khavryutchenko et al. (*44*).

Brinker and Scherer (*8*) pointed out that the area of a surface is defined largely by the method of surface area measurement. Many of the measurements of surface areas in work reported before the 1980s were based on the method of determining monolayer capacity of an adsorbent molecule of known cross-sectional area. In the Brunauer–Emmett–Teller (BET) method (*45*) the apparent surface area is determined from nitrogen adsorption. However, because the nitrogen molecule surface area is 16.2 $Å^2$, this definition of the surface excludes microporosity that is accessible, for example, to water molecules.

For materials such as porous gels, the monolayer capacity of water should be a more accurate definition of the surface. Belyakova et al. (*46*) reviewed the adsorption behavior of water on porous silicates as revealed by water adsorption isotherms. Another method for surface area measure-

ment that uses water as a structural probe is based on proton nuclear magnetic resonance techniques. Application of the NMR method to porous gels is discussed by Gallegos et al. (*47*).

The most modern methods of dealing with irregular, rough surfaces are based on fractal geometry. Examples of the application of the fractal approach to the analysis of silica surfaces are included in the Legrand et al. monograph (*17*) and in Brinker and Scherer's textbook (*8*).

In 1934 Hofman (*48*) postulated the existence of silanol groups (≡Si–OH) on the silica surface. Various analytical techniques allowed silica scientists to confirm and expand the view of the silica surface in terms of silanol groups, siloxane bridges, and hydrogen-bonded water. It is now generally accepted that surface silicon atoms tend to have a complete tetrahedral configuration and that in an aqueous medium their free valence becomes saturated with hydroxyl groups, forming silanol groups. Silanol groups in turn may condense to form, under proper conditions, siloxane bridges: ≡Si–O–Si≡.

Silanol Groups, Siloxane Bridges, and Physically Adsorbed Water. Most of the following postulated groups involving Si–O bonds either as silanols or as siloxanes have been identified on the surface or in the internal structure of amorphous silica (Figures 10 and 11).

- single silanol groups, also known as free or isolated silanols
- silanediol groups, also called geminal silanols
- silanetriols; postulated but real existence not yet generally accepted
- hydrogen-bonded vicinal silanols (single or geminal), including terminal groups
- internal silanol groups involving OH groups, sometimes classified as structurally bound water
- strained and stable siloxane bridges and rings
- physically adsorbed H_2O hydrogen-bonded to all types of surface silanol groups

Silanol groups are formed on the silica surface in the course of its synthesis during the condensation–polymerization of $Si(OH)_4$ or as a result of rehydroxylation of thermally dehydroxylated silica when treated with water or aqueous solutions (Scheme I). The silanol groups on the silica surface may be classified according to their nature, multiplicity of sites, and type of association (*17*).

An *isolated* silanol includes an OH group located at a distance sufficiently far from neighboring hydroxyl groups to prevent hydrogen bonding. A silicon site of this kind is designated as Q^3 in NMR Q^n

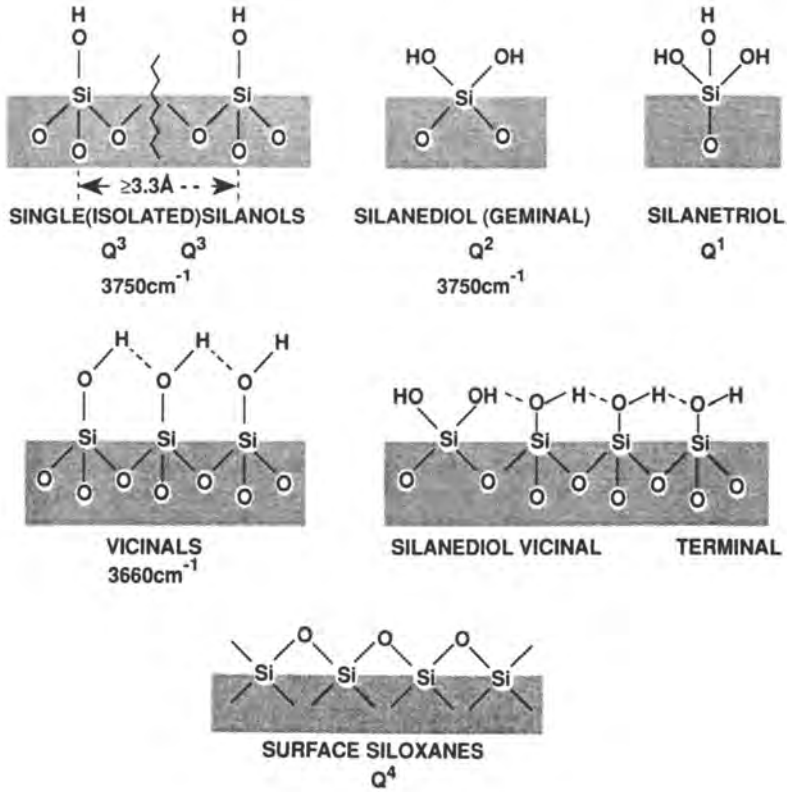

Figure 10. Silanol groups and siloxane bridges on the surface of colloidal silicas. Characteristic infrared bands at 3750 and 3660 cm^{-1} are shown for single and vicinal groups. Q^n terminology is used in NMR; n *indicates the number of bridging oxygens (–O–Si) bonded to the central silicon* (n = 0–4).

terminology, where *n* equals the number of bridging oxygens (SiO–) bonded to the central silicon. The isolated silanol shows a sharp band at around 3750 cm^{-1} in the infrared spectrum.

Geminal silanols are silanediols groups located in Q^2 silicon sites (**1**). Their existence was postulated by Peri and Hensley (*49*) but not confirmed experimentally until the advent of solid state ^{29}Si CP MAS NMR spectroscopy. On the basis of this technique, Fyfe et al. (*50*) determined in the particular case of a commercial silica gel that the ratio of $Q^4/Q^3/Q^2$ silicon sites was 8.8/5.7/1.

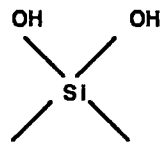

1

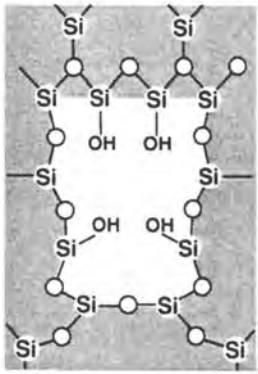

Figure 11. Left diagram: internal silanol groups. The fourth oxygen is above or below the plane of the paper. Right diagrams: two basic types of orientation of the water molecule with respect to the silanol group on the SiO_2 surface (53). Type A, Oxygen atom in the H_2O molecule bonded to the hydrogen atom of the ≡Si–OH group. Type B, Hydrogen atom in the H_2O molecule bonded to the oxygen atom of the ≡Si–OH group.

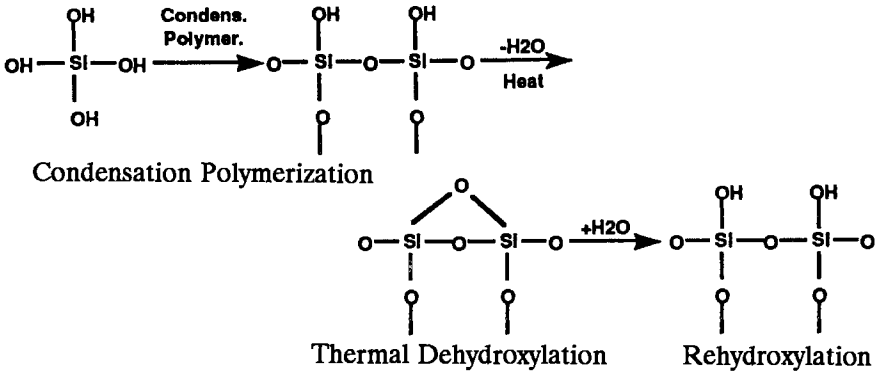

Scheme I.

Vicinal or H-bonded or associated silanols are Si–OH groups located on neighboring Q^3 sites in which the OH to O distance is sufficiently small that hydrogen bonding occurs. Hydrogen bonding causes a reduction in the O–H stretching frequency, the magnitude of which depends on the strength of the hydrogen bond, and thus on the O–H to O distance (*8*). The characteristic band of vicinal groups in the IR spectrum occurs at about 3660 cm^{-1} (*40*).

Geminal Q^2 silanol sites bonded to a neighboring Q^3 silicon through a single siloxane bridge also result in a hydrogen-bonded pair. The remain-

ing OH experiences very weak hydrogen bonding. The identification of various configurations of surface silanol species by high-resolution IR spectroscopy is discussed by Hoffman and Knozinger (*51*).

Silanol groups may be found not only on the surface but also within the structure of the colloidal particles. These groups are designated *internal* silanols and in some cases are considered *structurally bound water*. Internal silanol groups are present within colloidal silica particles at various concentration levels depending on the synthesis temperature and other variables. According to Rupprecht (*52*), as much as 20% of the silanols present in hydrogels after surface dehydration may be internal. It is estimated that at about 600–800 °C, and sometimes at lower temperatures, the internal silanols begin to condense. Complete evolution of internal silanols occurs at higher temperatures.

Surface and internal silanol groups may condense to form *siloxane* bridges. *Strained siloxane* bridges are formed on the hydroxylated silica surface by thermally induced condensation of hydroxyl groups up to about 500 °C. At higher temperatures, the strained siloxane groups are converted into *stable siloxane* groups (*2*) (Scheme II).

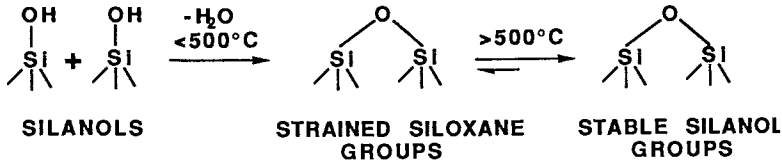

Scheme II.

Strained siloxane bridges completely rehydroxylate upon exposure to water. Stable siloxane bridges also rehydroxylate but at a slower rate. For example, a wide-pore silica sample of 340 m^2/g calcined in air at 900 °C took 5 years of contact with water at room temperature to rehydroxylate completely (*53*).

The silica surface OH groups are the main centers of adsorption of water molecules (*53*). Water can be associated by hydrogen bonds to any type of surface silanols and sometimes to internal silanol groups. On the basis of thermograms obtained with various kinds of pure amorphous silicas, Zhuravlev (*53*) suggested that there may be two types of physically adsorbed water (physisorbed water) on the silica surface at a low degree of surface coverage, one with activation energies of desorption in the range of 6–8 kcal/mol and another one with activation energies in the range of 8–10 kcal/mol (Figure 11).

Impurities, such as Na, K, or Al, are sometimes picked up during the synthesis of aquasols in alkaline medium and may be occluded inside the

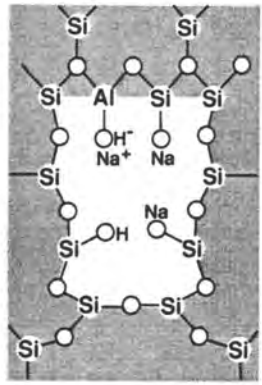

Figure 12. Occluded Na impurity and internal hydroxyl and Al impurities that form an isomorphic tetrahedron by substitution of Si. The fourth oxygen coordinated with Si is above or below the plane of the paper.

colloidal particles, taking the place of the silanol protons (as with sodium or potassium) or forming isomorphic tetrahedra with an extra negative valence on the surface or inside the particles (as with aluminum) (Figure 12).

Surface silanol groups of silica aquasols stabilized in an alkaline medium exchange protons for the alkaline ion such as Na^+, K^+, or NH_4^+ (Figure 13). The surface silanol groups can be esterified, as in silica organosols, or silanized (silylated) (Figure 14). Derivatization of the silica surface is the basis for the use of silica in analytical and process chromatography.

Sindorf and Maciel (*41, 54–60*) first used CP MAS NMR spectroscopy as a valuable surface-selective strategy to observe local silicon environments on the silica surface and to study the effects of dehydration and rehydration or derivatization on colloidal silicas in general. From a more recent work involving a combination of NMR techniques referred to as CRAMPS (combined rotation and multiple-pulse spectroscopy) emerges the picture of a possible silica surface structure of large hydrogen-bonded clusters of SiOH groups in complex arrays of hydrogen-bonding patterns and $Si(OH)_2$ islands isolated spatially from the $(SiOH)_n$ clusters. (*See* Figure 5 in Chapter 14.)

A description of surface heterogeneity dependent on the mode of preparation for both amorphous and crystalline silicas was attained by Vidal and Papirer (Chapter 12) by calculation of the distribution of the energy of adsorption of alkane probes on the solid surfaces. The experimental data were obtained after the changes of the silica surfaces upon chemical treatment or heat treatments by inverse gas chromatography (IGC).

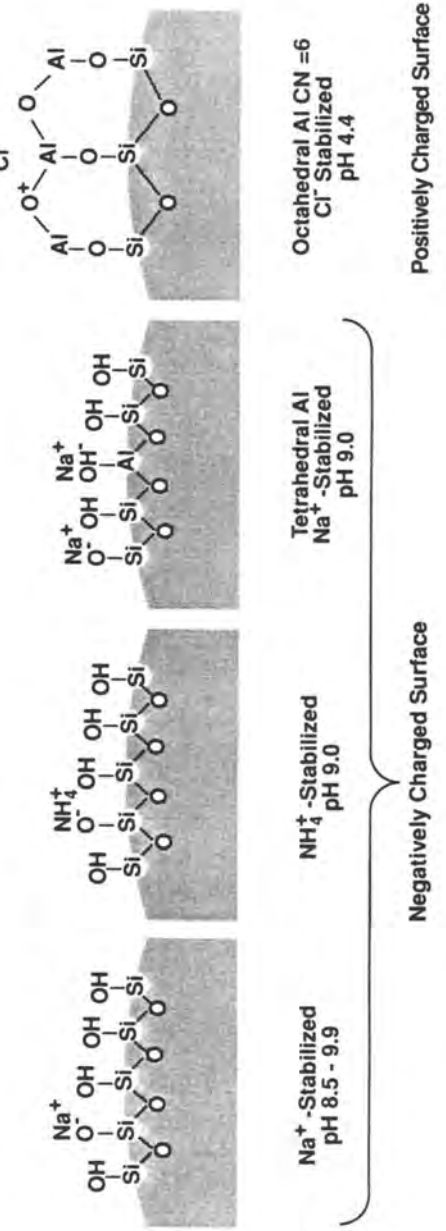

Figure 13. Sodium- and ammonium-stabilized and aluminum-modified surfaces of colloidal silicas.

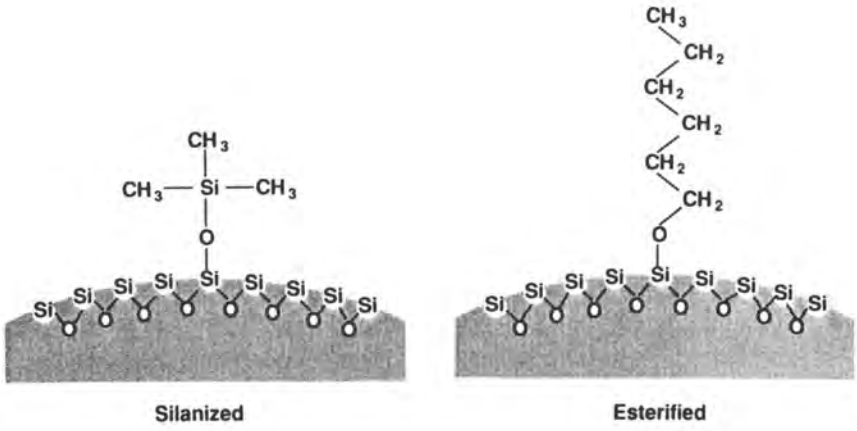

Figure 14. Silanized (silylated) and esterified surfaces of colloidal silica.

The concentration of hydroxyl groups and the dehydration, dehydroxylation, and rehydroxylation of the silica surface, as well as the nature of the structurally bound water inside amorphous silica particles, have been studied in detail by the Russian school of Kiselev, Zhuravlev, and colleagues. Two sections that follow (Dehydroxylation of the Silica Surface and Hydroxylation of the Silica Surface) are annotated excerpts from an overview monograph presented by Zhuravlev at the R. K. Iler Memorial Symposium (*53*). By comparing the views expressed here with the concepts advanced by authors such as Unger (Chapter 8), Legrand et al. (*17*), Maciel et al. (Chapter 14), Burneau et al. (Chapter 10), Morrow et al. (Chapter 9), Krasnansky and Thomas (Chapter 11), Vidal and Papirer (Chapter 12), Kohler et al. (*42*), Brinker et al. (*61*, *62*), and others whose work is more readily available in the West, and the views expressed in the work in Ukraine of Chuiko (*63*), Chuiko et al. (*43*), and Khavryutchenko et al. (*44*), the reader will have an understanding of the status of silica surface structure at the beginning of this decade. On this basis researchers can be prepared to follow the new insights that are developing in the 1990s, with the promising advent of relatively new and potentially very powerful techniques such as computational chemistry and the fractal approach, in addition to not yet developed novel methods for surface analysis.

Concentration of Hydroxyl Groups on the Silica Surface. The concentration of silanol groups on the silica surface expressed in number of OH groups per square nanometers, α_{OH}, is often called the *silanol number*. Zhdanov and Kiselev (*64*) first suggested that the silanol number of dehydrated but *fully hydroxylated* amorphous silica is a physicochemical constant independent of origin and structural characteristics of the silica.

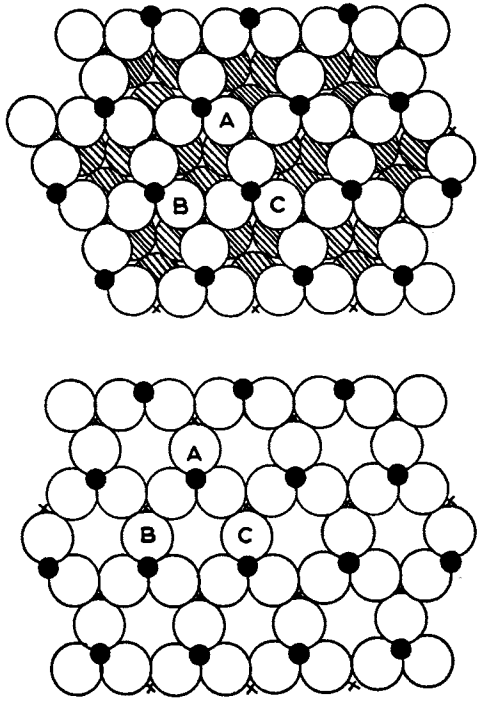

Figure 15. Top: Octahedral face of β-cristobalite. Bottom: Rhombohedral face of β-tridymite. The large open circles represent surface oxygen atoms. The small black circles represent surface silicon atoms, each of which carries one hydroxyl group when the surface is fully hydrated. The small crosses represent second-layer silicon atoms. The second-layer oxygen atoms are not shown, being directly under the second-layer silicon atoms. The partly visible third-layer oxygen atoms of β-cristobalite are shown as shaded circles. The third-layer oxygen atoms of β-tridymite are hidden because they are directly under the first-layer oxygen atoms. (Reproduced with permission from reference 65. Copyright 1961.)

The numerical value Zhuravlev obtained for this constant is $\alpha_{OH} = 4.6$ OH groups per square nanometer (discussed later). This value is fairly close to the α_{OH} values obtained by other authors and is in good agreement with the surface concentration of silicon atoms on the octahedral face of β-cristobalite ($\alpha_{Si} = 4.55$ Si atoms per square nanometer) and on the rhombohedral face of β-tridymite represented in Figure 15 (*65*). These two crystalline silicas are selected as references because they have densities and refractive indices close to those of amorphous silica.

Legrand et al. (*17*), on the basis of results obtained by chemical, thermogravimetric, and spectroscopic methods, showed how the structure of silica surfaces *as synthesized* (before rehydration) is strongly dependent

on the method of preparation. For example, pyrogenic silicas as synthesized were found to have isolated OH statistically distributed in the order of 3 OH molecules per square nanometer, whereas precipitated silicas as synthesized showed a concentration of surface OH from 8 to 15 depending on the measuring technique. However, Legrand et al. attributed these high values to the presence of internal silanols and to a complex surface structure involving a very heterogeneous distribution of hydroxyls due to the presence of polysilicic acid.

Morrow and McFarlan (Chapter 9), using IR and vacuum microbalance techniques to study the accessibility of the silanol groups on silica surfaces to chemical and hydrogen–deuterium exchange probes, also found that the silanol number is larger in precipitated silicas ($\alpha_{OH} = 6.8$) than in pyrogenic silica *as synthesized* ($\alpha_{OH} = 3$), but the fraction of SiOH groups that exchange with a given probe is the same on both silicas, and this fraction decreases as the size of the exchange molecule increases. They observed that the reaction with H-bonded silanols on both silicas stopped well before that of the isolated silanols; this observation illustrates the blocking effect of the adjacent derivatized vicinal silanols, which prevents further reaction whatever the size of the reactant.

The Kiselev–Zhuravlev constant α_{OH} value of 4.6 was obtained with a deuterium-exchange method that distinguished between surface and bulk OH and with a mass spectrometric thermal analysis (MTA) method in conjunction with temperature-programmed desorption (TPD) (*66*).

One hundred fully hydroxylated silica samples prepared by different processes and having different structural characteristics such as specific surface area, type or size distribution of the pores, particle packing density, and structure of the underlying silica skeleton were analyzed two or more times each. Eighty-five percent of the 231 measurements were from samples with a specific surface area less than 400 m^2/g. The OH groups in ultramicropores, into which only water molecules can penetrate, were not classified as surface silanol groups but as structurally bound water.

The silanol numbers obtained for the 100 samples are plotted versus specific surface area in Figure 16 (*66*). The average silanol number of the 231 independent measurements is 4.9 OH groups per square nanometer. Calculations by the least-squares method gave 4.6 OH groups per square nanometer as an average silanol number.

Dehydration of the Silica Surface. Dehydration of the silica surface, that is, removal of physisorbed water, occurs at relatively low temperatures. The threshold temperature corresponding to the completion of dehydration and the beginning of dehydroxylation by condensation of surface OH groups is estimated to be 190 ± 10 °C (*53*).

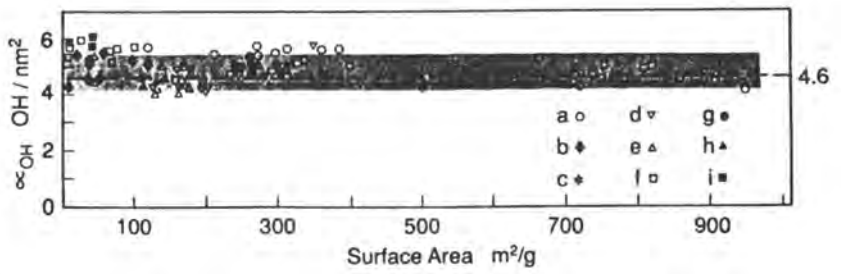

Figure 16. Concentration of the surface hydroxyl groups (the silanol number) α_{OH} for silicas having different specific surface areas S *when the surface has been hydroxylated to a maximum degree. The letters a through i represent different types of amorphous silica (see text). The shaded area is a range of experimental data (100 samples of SiO_2 with different specific surface area, from 9.5 to 950 m^2/g). The average value of α_{OH} is 4.6 OH groups per square nanometer (least-squares method). (Reproduced with permission from reference 53. Copyright 1993.)*

In Zhuravlev's model (53) of adsorbed water the activation energy of water desorption increases from 6 to 10 kcal/mol as the fraction Θ of silica surface covered with physically adsorbed water decreases from $\Theta = 1$ to $\Theta = 0$.

Dehydroxylation of the Silica Surface.* The concentration of OH groups on the surface decreases monotonically with increasing temperature when silicas are heated under vacuum. Most of the physisorbed water is removed at about 150 °C. At 200 °C all the water from the surface is gone so that the surface is made of single, geminal, vicinal, and terminal silanol groups and siloxane bridges. By about 450–500 °C all the vicinal groups condense, yielding water vapor, and only single, geminal, and terminal silanol groups and strained siloxane bridges remain. The estimated ratio of single to geminal silanol groups on the surface is about 85/15 [a value close to the one reported by Fyfe et al. (50)] and is believed not to change with temperature, at least to about 800 °C. Internal silanols begin to condense at about 600–800 °C and in some cases at lower temperatures. At higher temperatures, up to about 1000–1100 °C, only isolated (single) silanol groups remain on the silica surface.

*This and the following section are annotated excerpts from the paper "Surface Characterization of Amorphous Silica", presented by L. T. Zhuravlev at the 1990 symposium and now published in *Colloids and Surfaces* (53).

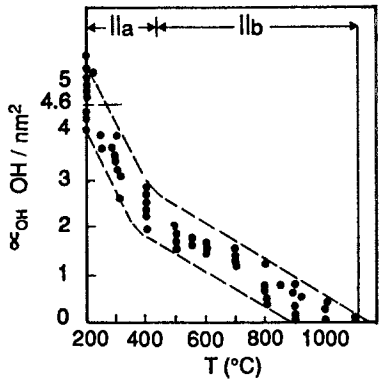

Figure 17. Silanol number as a function of the temperature of pretreatment in vacuo for different samples of SiO_2. The dashed lines indicate the area range of experimental data (16 samples with different specific surface areas from 11 to 905 m^2/g). Subregions of dehydroxylation: IIa, from 200 to ~450 °C; and IIb, from 450 to ~1100 °C. (Reproduced with permission from reference 53. Copyright 1993.)

At a sufficient surface concentration the OH groups make the silica surface hydrophilic. On the other hand, predominance of siloxane bridges on the silica surface makes the surface hydrophobic.*

In Figure 17 the concentration of surface hydroxyl groups α_{OH} is plotted versus the temperature of thermal treatment in vacuum up to 1100 °C. The α_{OH} experimental values were obtained by analyzing, via the deuterium-exchange method, 16 different samples with specific surface areas ranging between 11 and 905 m^2/g. Porosity also varied within a wide range. For comparison, Figure 18 includes the values reported in 1966 by Kiselev and Lygin (*38*), obtained by analyzing 11 samples of aerogels, xerogels, and pyrogenic silica and a more recent measurement obtained via proton NMR analysis of Zorbax PSM 60 (a coacervated fully hydroxylated porous silica of about 400-m^2/g specific surface area) treated in vacuum at temperatures ranging between 200 and 900 °C (*67*). Despite the differences between samples, the value of α_{OH} at a given temperature of treatment and the decrease in α_{OH} as a function of temperature is similar in all cases. The most probable values of α_{OH} averaged from the plot of Figure 17 and the degree of surface coverage by hydroxyl groups Θ_{OH} are shown in Table II (*53*).

* Derjaguin (25) pointed out that the term "lyophilic colloids" is not really accurate, suggesting that it is better to speak of a "lyophilic state of colloids", because various types of lyophobic colloids, regardless of their material composition, can be brought into the lyophilic state by adsorption of surface-active substances or, in the case of silica, by rehydroxylation.

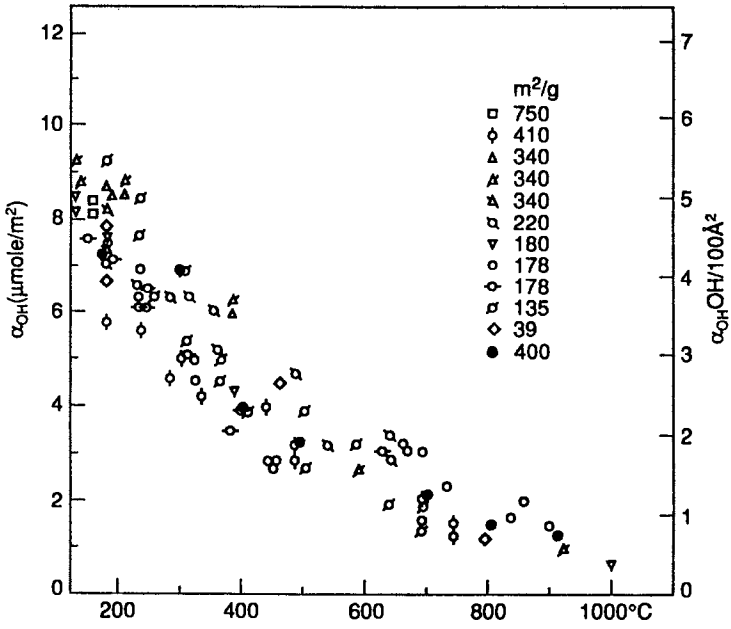

Figure 18. Concentration of surface hydroxyls on Zorbax PSM 60 by proton NMR (67) and on various samples of silica gel, aerogel, and pyrogenic silica by analytical methods other than NMR as a function of temperature. (Reproduced with permission from reference 98. Copyright 1966.)

Table II. Temperature Dependence of α_{OH} and Θ_{OH}

Temperature of Vacuum Treatment (°C)	α_{OH}	Θ_{OH}
180–200	4.60	1.00
300	3.55	0.77
400	2.35	0.50
500	1.80	0.40
600	1.50	0.33
700	1.15	0.25
800	0.70	0.15
900	0.40	0.09
1000	0.25	0.05
1100	<0.15	<0.03

NOTE: Values for α_{OH} are reported as OH groups per square nanometer.
SOURCE: Reproduced from reference 40. Copyright 1980 American Chemical Society.

Infrared analysis of the silica samples involved in this study showed no bound hydroxyls, only free hydroxyl groups, in the samples calcined in vacuum at temperatures 400 °C and higher. On the basis of the infrared quantitative analysis of free hydroxyl groups, $\alpha_{OH\ free}$, and the total α_{OH} values obtained from Figure 17, the concentration of bound OH groups, $\alpha_{OH\ bound}$, throughout the temperature range 200–400 °C and the concentration of siloxane bridges, $\alpha_{Si\text{-}O\text{-}Si}$, throughout the range 200–1100 °C, can be calculated. In the lower part of Figure 19 the plots showing the monotonic decrease with temperature of silanol groups on the silica surface have been combined with plots of the corresponding increase of surface siloxane bridges with the estimated temperature limits for the presence of physisorbed water and geminal, vicinal, and isolated silanol groups on the silica surface.

Rehydroxylation of the Silica Surface. Rehydroxylation occurs and silanol groups are formed when the dehydroxylated silica surface reacts with water in a vapor or liquid state. Complete rehydroxylation was once thought possible only in samples that had been subjected to preliminary treatments at temperatures below 400 °C. Rehydroxylation of silica samples activated at temperatures in the range of 400 °C to 1000–1100 °C is now known to be completely restored to the maximum hydroxylated state (α_{OH} = 4.6 OH groups per square nanometer) by treatment with water at room temperature. For samples subjected to extensive dehydroxylation, more time is required for complete rehydroxylation. Thus, in the example given before, a starting wide-pore silica sample of specific surface area $S = 340$ m²/g that had been calcined in air at 900 °C (α_{OH} = 0.66 OH groups per square nanometer), about 5 years was required, during which time the sample was in contact with water at room temperature, before the complete rehydroxylation of its surface was achieved (α_{OH} = 5.30 OH groups per square nanometer). Accelerated rehydroxylation can be achieved by subjecting dehydroxylated silica samples to a hydrothermal treatment at 100 °C. For example, an aerosilogel ($S = 168$ m²/g) was calcined in vacuo at 1100 °C for 10 h. After this treatment its silanol number was α_{OH} = 0.06 OH groups per square nanometer. The sample was then boiled in water for 60 h. The specific surface area was now 108 m²/g and the silanol number α_{OH} = 4.60 OH groups per square nanometer.

The rehydroxylation of a wide-pore silica gel sample calcined in air at 850 °C and held in water at 100 °C for periods covering 1 to 100 h was found to take 5–10 h for complete rehydroxylation. These and other results indicate that rehydroxylation of dehydroxylated silica (calcined at >400 °C) in the presence of water requires considerable energy to activate the process of dissociative adsorption, E_d. Chemisorption of water appears to take place, resulting in the formation of hydroxyl groups bound through

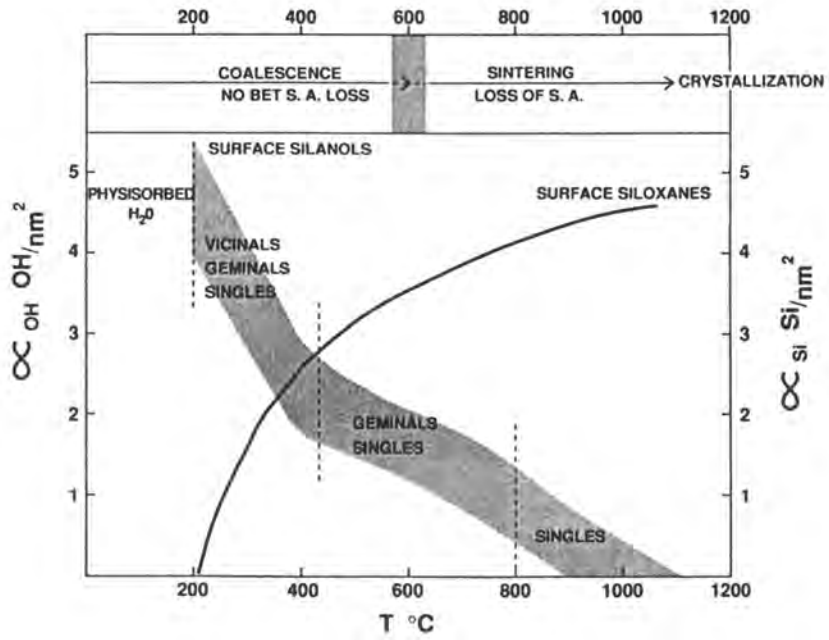

Figure 19. Different types of surface groups as a function of pretreatment of silica in vacuo (shaded area); average concentration of all OH groups is given. Broken vertical lines mark temperature limits for various types of silanol groups. Water may be physisorbed below 190 °C. Hydroxyl groups bound through hydrogen bonds (vicinal silanols) may be present on the silica surface up to about 450 °C, geminal silanols up to around 800 °C, and free or isolated silanol groups up to around 1000 °C. The curve represents the concentration of the surface Si atoms that are part of siloxane bridges. The upper part of the figure illustrates the effect of heat on silica powders obtained by drying silica aquasols synthesized in alkaline medium. (Reproduced with permission from reference 38. Copyright 1993.)

valence bonds to the SiO_2 surface. The reaction that takes place on the surface, which involves the breaking of the surface siloxane bonds, is the opposite of the condensation reaction.

Thus, the rehydroxylation of silica can be considered a process taking place in two subregions, below and above the temperature of the preliminary treatment at 400 °C. This view agrees with the two subregions, IIa and IIb, observed in the hydroxylation process (Figure 20).

In subregion IIb the silica surface is occupied only by free hydroxyl groups and siloxane bridges. In subregion IIa, on the other hand, there are also OH groups bound together by hydrogen bonds (Figure 20).

For strongly dehydroxylated silica the surface concentration of siloxane groups is high (Figure 19). Because of the shift in the electronic

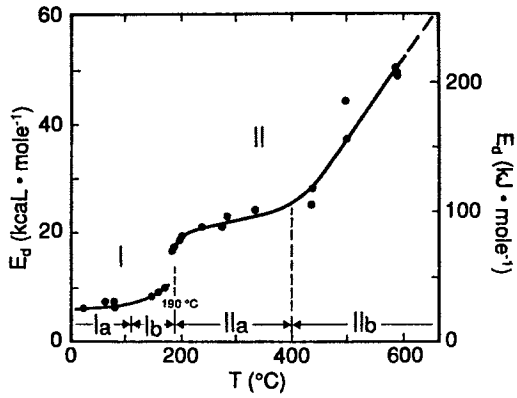

Figure 20. Activation energy of water desorption, E_d, as a function of temperature of the preliminary treatment of silica in vacuo. Ia, Ib—subregions of region I; IIa, IIb—subregions of region II. (Reproduced with permission from reference 53. Copyright 1993.)

density in going from O atom to Si atom, the formation of a hydrogen bond between the oxygen on the surface of the sample and water molecules is not favored. Thus, the siloxane surface is hydrophobic.

The hydroxylated surface with a predominance of silanol groups is hydrophilic. In the terminal ≡Si–O–H group, the electronic density is believed to become delocalized from the O–H bond to the neighboring Si–O bond. This delocalization permits the silanol groups to form strong hydrogen bonds with water molecules.

The data in Figures 19 and 20 appear to show that the high rate of rehydroxylation of silica subjected to preliminary activation at 200–400 °C (subregion IIa) is apparently due to the fact that the concentration of the siloxane bridges is still low and each ≡Si–O–Si≡ bridge is surrounded by OH groups. Such a location of the surface groups weakens the Si–O bond in the siloxane bridge itself. During the rehydroxylation, additionally introduced water molecules first become adsorbed on silanol groups and have a direct effect on the neighboring weakened siloxane groups. This situation results in the splitting of the groups and the formation of new OH groups on the surface of silica.

Upon a preliminary activation of SiO_2 at >400 °C (subregion IIb), the concentration of the siloxane bridges increases sharply. These bridges form whole hydrophobic regions on the surface, whereas the concentration of OH groups drops with an increase in temperature (Figure 19). But even under the condition of maximum activation (1000–1100 °C) free OH groups still exist (Table II), but at a large distance from one another. These OH groups act as the centers of adsorption when an additional amount of

water is introduced, and rehydroxylation takes place first in the vicinity of the silanol groups. The localized areas of hydroxylated spots gradually expand. Rehydroxylation may be thought as proceeding along the boundary separating the hydrophilic and hydrophobic sections. Such rehydroxylation of the surface requires a considerable energy of activation of adsorption, E_a. Thus, rehydroxylation due to dissociative adsorption (chemisorption) of H_2O, with the splitting of siloxane bridges and the formation of new OH groups, proceeds according to a different mechanism, depending on the coverage of the surface with OH groups, Θ_{OH}.

At $1 \geq \Theta_{OH} > 0.5$ (subregion IIa, Figure 21) the activation energy of chemisorption, E_a, is close to zero. At $\Theta_{OH} < 0.5$ (subregion IIb, Figure 21) chemisorption proceeds very slowly at room temperature, but the rate of reaction increases sharply with an increase in the reaction temperature to 100 °C. The physical adsorption of water on silanol groups precedes chemisorption, which requires a much higher energy of activation: $E_a >>$ O.

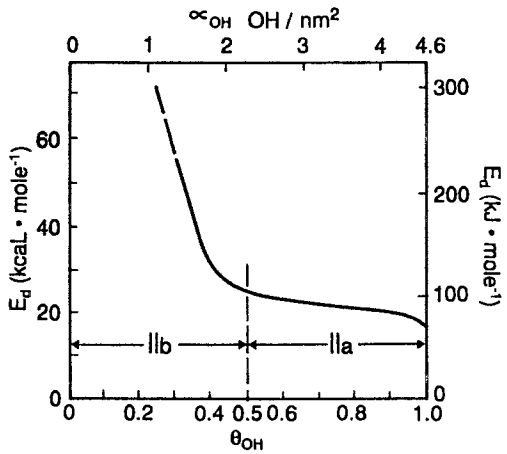

Figure 21. Activation energy of water desorption, E_d in region II, as a function of the surface concentration of OH groups, α_{OH}, or as a function of the surface coverage of SiO_2 with OH groups, Θ_{OH}. (Reproduced with permission from reference 53. Copyright 1993.)

A novel approach to the study of the hydroxylation and dehydroxylation of fumed and precipitated silicas is given in the study by Burneau et al. (Chapter 10), which was based on FTIR and Raman spectroscopy techniques.

Structurally Bound Water in Silica Particles. Deuterium-exchange measurements have shown that various types of amorphous

dispersed silica contain not only surface hydroxyl groups but also structurally bound water inside the silica skeleton and fine ultramicropores. According to infrared spectral measurements (53), such bound water consists of silanol groups inside the silica sample (the absorption band of stretching vibrations is about 3650 cm^{-1}). The distribution of OH groups between the surface and the bulk of the sample depends on a number of factors, but mainly on the method of preparation of the silica sample and its subsequent treatment.

Coalescence and Sintering. In the process of drying and heating, the particles of colloidal silica first coalesce extensively, but the area of contact between particles is not large enough to allow the loss of surface area to be detected by nitrogen sorption methods. The degree of coalescence is estimated by measuring the coalescence factor.* For silica powders made by drying an aquasol synthesized in an alkaline medium such as Ludox, the coalescence factor can be as high as 29 or 30, depending on particle size, even when the sol is freeze-dried or spray-dried at low temperatures. At this high range of coalescence the powders cannot be redispersed to the original level of discreteness by simply slurrying in water, although the diameter of the necks formed in between particles is not large enough to result in a loss of specific surface area as measured by nitrogen sorption. This range of coalescence is referred to as the range of incipient sintering. Beginning at about 600 °C, again depending on particle size and degree of purity, coalescence may be so extensive that significant loss of BET surface area takes place. This is the onset of extensive sintering. Depending on the purity of the powder, especially Na content, pressed colloidal silica powders may sinter to theoretical density at about 1000 to 1100 °C. Higher temperatures mark the onset of crystallization, generally with transition of amorphous silica to cristobalite. Figure 19 illustrates the overall effects of heat on the surface and bulk of colloidal silica.

Particle Size and Characterization Techniques

The behavior of colloidal silica is based on its morphology and structure and on the chemistry of its surface. To fully characterize colloidal silicas one must measure not only the particle size, particle size distribution, surface area, and degree of aggregation, but also the structural and surface properties.

*The coalescence factor is the percent silica that has to be dissolved to restore the light transmission under standard conditions of a silica powder redispersed in water (68).

Methods of characterization utilized before the 1980s were discussed by Iler (3). Significant advances in instrumentation have made possible the optimization of the classical techniques and the development of new ones.

One of the most important developments in the 1980s in the search for novel concepts to characterize colloidal systems such as silica sols and gels was the advent of the fractal approach. Another very important development in the past 10 years was the application of ^{29}Si CP MAS NMR methods to the study of the silica surface. This technique made it possible, for example, to identify without ambiguity the presence of silanediol groups on the silica surface (55).

A survey of the physical and chemical techniques to characterize the surface structure of amorphous and crystalline silica is presented by Unger in this book (Chapter 8). Methods to measure particle size and particle size distribution and surface area are discussed by Kirkland (Chapter 18) and by Allen and Davies (69). The use of some of these techniques by Morrow et al. (Chapter 9), Burneau et al. (Chapter 10), Vidal and Papier (Chapter 12), Kohler et al. (*42*), and Legrand et al. (*17*) to provide new insights into the silica surface structure was already mentioned in the section "Silica Surface" in this chapter.

Also discussed in that section was the information obtained by Zhuravlev, who used mainly classic methods, such as differential thermogravimetry combined with mass spectroscopy and deuterium-exchange. A novel and modern approach for the study of silica surfaces is based on the combined use of computational chemistry and inelastic neutron scattering spectroscopy (*43*, *44*).

As already mentioned in the discussion of fractals, small-angle X-ray scattering (SAXS) and static light-scattering techniques may be used to measure the fractal dimension of objects with radii on the order of 10^2–10^4 Å (*12*).

The use of one experimental method alone is usually not sufficient to obtain a complete picture to characterize the features of the various types of silica under study. The authors mentioned in the preceding text used complementary techniques to obtain a balanced view of the silica characteristics. The same approach was applied by Bergna, Firment, and Swartzfager (Chapter 28) to study amorphous silica coatings on the hydroxylated surface of a particulate alumina. In this case, transmission electron microscopy, BET nitrogen sorption, particle size measurements via Sedigraph and Coulter counter, zeta potential measurement, X-ray photoelectron spectroscopy (ESCA), high-resolution electron microscopy, diffuse reflectance infrared Fourier transform (DRIFT) spectroscopy, and secondary ion mass spectroscopy (SIMS) were used to characterize the silica coatings and to postulate a possible mechanism for the deposition of silica on hydroxylated surfaces.

The use of complementary techniques is well illustrated by Minihan et al. (Chapter 17) for measurements of pore size and pore size distribution of silica powders. Mercury intrusion and nitrogen sorption techniques are commonly used in the structural characterization of porous solids, often independently, despite the fact that very often the pore size distributions obtained by the two techniques fail to agree. For silicas Minihan et al. were able to demonstrate that mercury intrusion can lead to compression of silica structures and that this compression can account for differences in pore size distribution as measured by nitrogen sorption and may lead to misconceptions regarding the structure of the material under investigation.

Sol–Gel Science and Technology

The growing and more sophisticated needs of modern technology have attracted the attention of scientists from diverse disciplines to the study of formation and properties of colloidal silica. A good example of the development and growth of an important area of the chemistry and physics of colloidal silica in the past decade by an interdisciplinary effort is provided by the extraordinary increase in the volume and the quality of published work on the so-called sol–gel science and technology. The term *sol–gel science* was coined in the 1950s to refer to the art of manufacturing materials by preparation of a sol, gelation of the sol, and removal of the solvent. In the field of ceramics and glass the term *sol–gel* applies not only to processes in which sols are gelled, but also to processes in which it is never clear whether *discrete* colloidal particles may at some time exist. If there is no evidence of a sol, Johnson (*70*) suggested that the use of the term sol–gel can better be thought of as an abbreviation of *solution–gelation*.

The sol–gel techniques have been practiced willingly and unwillingly since the first encounters with colloidal materials. One can imagine the frustration of the early Chinese and Egyptians laboring to find a suitable protective agent such as gelatin or gum arabic to manufacture ink before finally succeeding in avoiding gelation, or of the alchemists trying to prevent the gelation of their "aurum potabile", or of T. Bergman before finding in 1779 a way to stabilize what Hauser described as a "colloidal silicic acid" (*71*). It is to the credit of contemporary material scientists to have converted a source of frustration into an art, then into a technology, and now into a science. At the time the term sol–gel became common, many colloid scientists felt like Molière's Monsieur Jourdan, who discovered at a very late age that, unknowingly, he had spoken prose all his life. In the same manner, some colloid scientists realized at one point that unknowingly and often unwillingly, they had been practitioners of sol–gel technologies.

What is now called sol–gel technology was originally developed by mineralogists for the preparations of homogeneous powders for use in studies of phase equilibria (*72–74*), by chemists for manufacturing nuclear fuel pellets (*75, 76*), and by ceramists for the preparation of advanced ceramic materials (*77, 78*).

The explosion of literature in the field of sol–gel science in the past decade made it difficult for newcomers to catch up to the state of the art and overwhelmed researchers already involved in the subject. The book by Brinker and Scherer (*8*) and the chapter by Brinker (Chapter 18) fill the need for a coherent account of the principles of sol–gel processing. Additional detailed discussions on this subject are included in the section on sol–gel technology in this book, in the collection of articles edited by Klein (*72*), and in the *Proceedings of the Materials Research Society* (*79–81*) and the *Ultrastructure Processing* meetings (*82–84*).

The development of sol–gel science and related colloidal techniques is contributing significantly to the development of the advanced materials required by the high technologies. For example, a crucial issue in the manufacture of ceramics for electronics is reliability. Improved processes are required to produce improved products, to minimize the number of rejects, and to achieve the high quality required for electronic parts. Product reliability (reproducible performance) comes with microstructure control, which requires process reproducibility, which in turn requires materials reproducibility. In this respect Turner (*85*) points out that the sol–gel process exhibits a number of advantages over conventional ceramic processing. The first advantage is increased chemical homogeneity in multicomponent systems. A second advantage of the sol–gel process is the high surface area of the gels or powders produced, which leads to relatively low sintering temperatures. A third advantage is that relatively high chemical purity can be maintained because of the absence of grinding and pressing steps. Finally, a fourth advantage of the sol–gel process according to Turner (*85*) is that a range of products in the form of fibers, powders, coatings, and spheres can be prepared with relative ease from simple solutions. Suggested reading on sol–gel science and its applications include the book by Brinker and Scherer (*8*) and references 72 through 85.

Gels and Powders

Silica powders in the form of precipitated silica, pyrogenic or fumed silicas (aerosils), and silica gels are the largest volume specialty silicas. "Silica gel" is the term commonly used to refer to the xerogels obtained by drying silica hydrosols.

According to the *Chemical Economics Handbook* (*86*), the value of the precipitated silicas used annually in the United States is in the order of $100 million. For fumed silicas and silica gels these values are about $85

million and $65 million, respectively. In comparison, the value for silica aquasols ("colloidal silica") is in the order of $50 million.

The introduction to the section "Silica Gels and Powders" by W. Welsh constitutes an introduction to the study of silica powders. Detailed accounts of the synthetic processes and applications of fumed silicas, silica gels, and precipitated silicas are given by Ferch (Chapter 24) and Patterson (Chapter 32). For scientists, silica powders are of special interest because they offer the opportunity of working with very pure systems with well-controlled ultimate particle size and specific surface area. One of the most important aspects of silica powders is their adsorptive properties. These properties are the subject of the work by Kenny and Sing (Chapter 25), which includes the crystalline zeolitic silica known as silicalite.

In contrast to organic gels, gels prepared from an aqueous precursor solution consist of a broad spectrum of structurally different silicate species. Chapter 26 (Wijnen et al.) describes the use of modern spectroscopic techniques in the study of the formation of aqueous silica gels. Silicon-29 NMR was used to study the oligomerization process of monomeric silicic acid, showing how the steady increase in monomer concentration induced dimerization at a critical monomer concentration followed by preferential formation of cyclic as opposed to linear trimeric silicate species at high pH values. SAXS was used to follow the aggregation of primary silica particles of molecular size (<1 nm), revealing reaction-limited aggregation as the process of gel formation at pH 4 in all systems studied. NMR and SAXS were combined with physical sorption techniques to follow the aging of the as-synthesized gel structures and thus allowed the proposal of a new model for the aging process. The Wijnen et al. model suggests that monomeric silicic acid is transported via the solution from the periphery of the aggregate into the core of the solution, as such contributing to a lower value for the observed fractal dimensionality of the aged silica gel.

Silica gels constitute one of the oldest silica commercial products in the colloidal state of dispersion, and yet much has to be learned about them. A deeper understanding of their structure, mode of formation, and properties should increase their relatively small rate of growth [now projected as about 1.5–2% for the next several years (*86*)] as a commercial product by consolidating current uses and expanding the range of applications.

Uses of Silica—From the Caves of Altamira and Cro-Magnon to Silicon Valley and Outer Space

When asked, "Where has colloidal silica been used?" Charles C. Payne answers that a more pertinent question is, "Where hasn't it been used?" (Chapter 29). This question applies also to silica in general. From the caves

of Cro-Magnon and Altamira, where flint was used to make early tools and weapons, to Silicon Valley, where colloidal silica is used to polish sophisticated microcircuit parts, and to outer space, where silica has been used to help in the safe reentry of space vehicles, silica has played a role in the development of Western, and for that matter, world civilization.

In the modern world, colloidal silica powders and sols have different fields of application, with a few overlapping areas. As modern technology develops, new opportunities for silica proliferate, and new uses are constantly replacing the classic applications soon to become overshadowed by even newer uses.

Ferch, Payne, Patterson, and Falcone (Chapters 24, 29, 32, and 30, respectively) cover the history of applications of fumed silicas, silica gels and sols, and silicates. To this list the use of silica coacervates in analytical and process chromatography should be added. Furlong (Chapter 27) discusses the field of silica coatings; Ralph K. Iler was a pioneer in this area, and it is still dominated by his inventions. The starting point for uses of silica sols in modern technology is marked by the advent of monodisperse, concentrated, stable aquasols made of discrete particles (*87–89*). For fumed and coacervated silicas, the starting point is constituted by the inventions of Kloepfer (*90*) and Iler (*91*), respectively, and by Iler again for silica-coated particulates (*92*).

At the risk of the list soon becoming obsolete, the current major applications of colloidal silica powders and sols can be summarized as follows (*93*):

- colloidal silica: investment casting, silicon wafer polishing, and fibrous ceramics
- fumed silica: silicone rubber, unsaturated polyester, and specialty coatings
- precipitated silica: rubber, food, health care, battery separators, pesticides, and catalysts
- silica gel: food, health care, and industrial coatings

New challenges should open in the future for colloidal silicas and silicates. Opportunities exist, for example, in microelectronics, a $500 billion industry worldwide, spanning from consumer products such as compact disc players to supercomputers (*94*). As Tummala said (*94*):

> Microelectronics involve a broad spectrum of technologies, including semiconductors, packaging for processing information, magnetic and optical media for storing information, cathode ray tubes and liquid crystals with thin-film transistors for displaying information, electrophotography for displaying information, and optical fibers for transferring information. Computers in the 1990s are expected

> to perform functions not even dreamed in the 1970s. Microelectronic packaging is one of the key technologies that will make all the advances possible.

In fact, packaging has been identified recently as one of the 10 critical technologies for the advancement of mankind in the 1990s. Sol–gel technology—based on a better understanding of the formation and properties of sols and gels—and the coating of ceramic particles should represent the key for the invention of vastly improved ceramics and glass ceramics. Imagination is the only limit to the range of uses that scientists will find for old and new forms of colloidal silica to contribute to the quality of life of people around the world.

Acknowledgment

This book, written by some of the most talented silica scientists in the world, is dedicated to Ralph K. Iler. Not only did he make outstanding contributions to science and industry, but he was an individual sensitive to the beauty of nature and the works of humanity. I would like to finish this overview by paying special homage to the creator of some of the most beautiful forms of silica, yesterday and today: the diatom (Figure 22). May the diatom continue oeuvres of art and science for many more millions of years without the impediment of our foolishness, but instead with the admiration of humanity.

Figure 22. The diatom.

References

1. Gould, E. S. *Inorganic Reactions & Structures*; Henry Holt & Company: New York, 1957.
2. Unger, K. D. *Porous Silica*; J. Chromatogr. Library; Elsevier: Amsterdam, Netherlands, 1979, p 16.
3. Iler, R. K. *The Chemistry of Silica*; Wiley: New York, 1979.
4. Kingery, W. D.; Bowen, H. K.; Uhlmann, D. R. *Introduction to Ceramics*, 2nd ed.; Wiley: New York, 1976.
5. Gaskell, P. H.; Eckersley, M. C.; Barnes, A. C.; Chieux, P. *Nature* **1991**, *350*, 675–677.
6. Everett, D. H. *Symbols and Terminology for Physiocochemical Quantities and Units*; International Union of Pure and Applied Chemistry; Butterworths: London, 1971.
7. Verwey, E. J. W.; Overbeek, J. Th. *Theory of the Stability of Lyophobic Colloids*; Elsevier: New York, 1949.
8. Brinker, C. J.; Scherer, G. W. *Sol–Gel Science*; Academic: San Diego, CA, 1990.
9. Mahler, W.; Bechtold, M. F. *Nature* **1980**, *285*, 27–28.
10. La Mer, V. K.; Healy, T. H. *Pure Appl. Chem.* **1963**, *13*, 112–133.
11. Mandelbrot, H. H. In *A Fractional Approach to Heterogeneous Chemistry*; Avnir, D., Ed.; Wiley: New York, 1989.
12. Rarity, J.; *Nature* **1989**, *339*, 340–341.
13. Keefer, K. *Science of Ceramic Chemical Processing*; Hench, L. L.; Ulrich, D. R., Eds.; Wiley: New York, 1986.
14. Lin, M. Y.; Lindsay, H. M.; Weitz, D. A.; Ball, R. C.; Klein, R.; Meakin, P. *Nature* **1989**, *339*, 360–362.
15. Matsushita, M. In *The Fractal Approach to Heterogeneous Chemistry*; Avnir, D., Ed.; Wiley: Chichester, United Kingdom, 1989.
16. Aubert, C.; Cannel, D. S. *Phys. Rev. Lett.* **1986**, *56*(7), 738–741.
17. Legrand, A. P. et al. *Adv. Colloid Interface Sci.* **1990**, *33*, 91–330.
18. Mandelbrot, B. B.; Evertsz, C. J. G. *Nature* **1990**, *348*, 143–145.
19. Barby, D. In *Characterization of Powder Surfaces*; Parfitt, G. D.; Sing, K. S. W., Eds.; Academic: New York, 1976.
20. *Colloids Surf.* **1992**, *63*, (1/2); **1993**, *74*, 1.
21. Ulrich, D. D. *Chem. Eng. News* **1991**, *69*, 32.
22. Stober, W.; Fink, A. *J. Colloid Interface Sci.* **1968**, *26*, 62.
23. Minehan, W. T.; Messing, G. L. *Colloids Surfaces* **1992**, 63, 181–187.
24. Bailey, J. K.; Mecartney, M. L. *Colloids Surfaces* **1992**, *63*, 151–161.
25. Derjaguin, B. V. *Theory of Stability of Colloids and Thin Films*; Consultants Bureau: New York, 1989.
26. Derjaguin, B. V.; Landau, L. *Acta Physiochim.* **1941**, *14*, 633.
27. Allen, L. H.; Matijevic, E. *J. Colloid Interface Sci.* **1970**, *33*, 420.
28. Matijevic, E.; Allen, L. H. *Environ. Sci. Technol.* **1969**, *3*, 264.
29. Allen, L. H.; Matijevic, E. *J. Colloid Interface Sci.* **1969**, *31*, 287.
30. Allen, L. H.; Matijevic, E. *J. Colloid Interface Sci.* **1971**, *35*, 66.
31. Matijevic, E.; Allen, L. H. *J. Colloid Interface Sci.* **1973**, *43*, 217.
32. Milonjic, S. K. *Colloids Surfaces*, **1992**, *63*, 113–119.
33. Horn, R. G. *Abstracts of Papers, 200th ACS National Meeting*; American Chemical Society: Washington, DC, 1990; Division of Colloids and Surfaces, paper no. 41.
34. Lyklema, J. *Croatica Chemica Acta* **1977**, *50*(*1–4*), 77–82.

35. Yates, P. C. *Abstracts of Papers, 200th ACS National Meeting*; American Chemical Society: Washington, DC, 1990; Division of Colloids and Surfaces, paper no. 235.
36. Langmuir, I. *J. Chem. Phys.* **1938**, *6*, 893.
37. Hair, M. L. *Infrared Spectroscopy in Surface Chemistry*; Dekker: New York, 1967.
38. Kiselev, A. V.; Lygin, V. I. In *Infrared Spectra of Surface Compounds*; Wiley: New York, 1975.
39. Little, L. H. *Infrared Spectra of Adsorbed Species*; Academic: New York, 1966.
40. Hair, M. L. In *Vibrational Spectroscopies for Adsorbed Species*; Bell, A. T.; Hair, M. L., Eds.; ACS Symposium Series 137; American Chemical Society: Washington, DC, 1980.
41. Maciel, G. E.; Sindorf, D. W. *J. Am. Chem. Soc.* **1980**, *102*, 7606–7607.
42. Kohler, J.; Chase, D. B.; Farlee, R. D.; Vega, A. J.; Kirkland, J. J. *J. Chromatogr.* **1986**, *352*, 275–305.
43. Chuiko, A. A.; Khavryutchenko, P.; Nechitajlov, P. *Abstracts of Papers, 200th ACS National Meeting*; American Chemical Society: Washington, DC, 1990; Division of Colloids and Surfaces, paper no. 87.
44. Khavryutchenko, V.; Ogenko, V.; Nechitajlov, P.; Sheha, E.; Musychka, A.; Natkaniec, I. *Abstracts of Papers, 200th ACS National Meeting*; American Chemical Society: Washington, DC, 1990; Division of Colloids and Surfaces, paper no. 100.
45. Brunauer, S.; Emmett, P. H.; Teller, E. *J. Am. Chem. Soc.* **1938**, *60*, 309.
46. Belyakova, L. D.; Dzhigit, O. M.; Kiselev, A. V.; Muttik, G. G.; Shcherbakova, K. D. *Russ. J. Phys. Chem.* (Engl. transl.) **1959**, *33*, 551.
47. Gallegos, D. P.; Smith, D. M.; Brinker, C. J. *J. Colloid Interface Sci.* **1988**, *124*, 186–198.
48. Hofman, V.; Endell, K.; Wilm, D. *Angewan. Chem.* **1934**, *30*, 539–558.
49. Peri, J. B.; Hensley, A. L., Jr. *J. Phys. Chem.* **1968**, *72:8*, 2926–2933.
50. Fyfe, C. A. et al. *J. Phys. Chem.* **1985**, *89*, 227–281.
51. Hoffman, P.; Knozinger, E. *Surf. Sci.* **1987**, *188*, 181.
52. Rupprecht, H. *Mitt. Dtsch. Pharm. Ges.* **1970**, *40*, 3–24.
53. Zhuravlev, L. T. *Colloids Surf.* **1993**, *74(1)*, 71.
54. Maciel, G. E. *Science* **1984**, *226*, 282–287.
55. Maciel, G. E.; Sindorf, D. W.; Batuska, V. J. *J. Chromatogr.* **1981**, *205*, 438–443.
56. Sindorf, D. W.; Maciel, G. E. *J. Am. Chem. Soc.* **1981**, *103*, 4263–4265.
57. Sindorf, D. W.; Maciel, G. E. *J. Phys. Chem.* **1983**, *87*, 5516–5521.
58. Sindorf, D. W.; Maciel, G. E. *J. Am. Chem. Soc.* **1982**, *86*, 5208–5219.
59. Sindorf, D. W.; Maciel, G. E. *J. Am. Chem. Soc.* **1983**, *105*, 1487–1493.
60. Sindorf, D. W.; Maciel, G. E. *J. Am. Chem. Soc.* **1983**, *105*, 3767–3776.
61. Brinker, C. J.; Kirkpatrick, R. J.; Tallant, D. R.; Bunker, B. C.; Montez, B. *J. Non-Crystalline Solids* **1988**, *99*, 418–428.
62. Brinker, C. J.; Brow, R. K.; Tallant, D. R. *J. Non-Crystalline Solids* **1990**, *120*, 26–33.
63. Chuiko, A. A. *Abstracts of Papers, 200th ACS National Meeting*; American Chemical Society: Washington, DC, 1990; Division of Colloids and Surfaces, paper no. 177.
64. Zhdanov, S. P.; Kiselev, A. W. *Zhur. Fiz. Khim.* **1957**, *31*, 2213.
65. Hockey, J. A.; Pethica, B. A. *Trans. Faraday Soc.* **1961**, *57*, 2247–2262.
66. Zhuravlev, L. T. *Langmuir* **1987**, *3(3)*, 316–318.
67. Bergna, H. E.; Letter to J. J. DeStefano, June 8, 1982.

68. Bergna, H. E.; Simko, F. A., Jr., U.S. Patent 3,301,635, 1967.
69. Allen, T.; Davies, R. *Abstracts of Papers, 200th ACS National Meeting*; American Chemical Society: Washington, DC, 1990; Division of Colloids and Surfaces, paper no. 37.
70. Johnson, D. W. *Ceramic Bulletin* **1985**, *64*, 1597.
71. Hauser, E. A. *Colloidal Phenomena*; McGraw-Hill: New York, 1939.
72. Roy, D. M.; Roy, R. *Am. Mineralogist* **1955**, *40*, 147.
73. Ewell, R. H.; Insley, H. *J. Res.* NBS **1935**, *15*, 173–186.
74. Barrer, R.; Hinds, L. *Nature* **1950**, *166*, 562.
75. Dell, R. M.; In *Reactivity of Solids*; Anderson, J. S.; Roberts, M. W.; Stone, F. S., Eds.; Chapman and Hall: New York, 1972; pp 553–566.
76. Woodwead, J. L.; *Silic. Ind.* **1972**, *37*, 191–194.
77. Roy, R. *J. Am. Ceram.* **1956**, *39*(4), 145–146.
78. Roy, R. *J. Am. Ceram.* **1969**, *52*(6), 344.
79. *Better Ceramics Through Chemistry*; Brinker, C. J.; Clark, D. E.; Ulrich, D. R., Eds.; Materials Research Society: Pittsburgh, PA, 1984.
80. *Better Ceramics Through Chemistry*; Brinker, C. J.; Clark, D. E.; Ulrich, D. R., Eds.; Materials Research Society: Pittsburgh, PA, 1986.
81. *Better Ceramics Through Chemistry*; Brinker, C. J.; Clark, D. E.; Ulrich, D. R., Eds.; Materials Research Society: Pittsburgh, PA, 1988.
82. *Ultrastructure Processing of Ceramics, Glasses, and Composites*; Hench, L. L.; Ulrich, D. R., Eds.; Wiley: New York, 1984.
83. *Science of Ceramic Chemical Processing*; Hench, L. L.; Ulrich, D. R., Eds.; Wiley: New York, 1986.
84. *Ultrastructure Processing of Advanced Ceramics*; Mackenzie, J. D.; Ulrich, D. R., Eds.; Wiley: New York, 1980.
85. Turner, C. W. *Ceramic Bull.* **1991**, *70*, 1487–1490.
86. *Chemical Economics Handbook, Silicates and Silicas Report*; SRI International: Palo Alto, CA, 1990.
87. Bird, P. G., U.S. Patent 2,244,325, 1945.
88. Bechtold, M. F.; Snyder, O. E., U.S. Patent 2,574,902, 1951.
89. Rule, J. M., U.S. Patents 2,577,484 and 2,577,485, 1951.
90. Kloepfer, H. German Patent 7,62,723, 1942.
91. Iler, R. K.; McQueston, H. J., U.S. Patent 3,855,172, 1971.
92. Iler, R. K., U.S. Patent 2,885,336, 1959.
93. *Opportunities in Special Silicas*; Kline & Co.: Fairfield, NJ, 1992.
94. Tummala, R. R. *J. Am. Ceram. Soc.* **1991**, *74*, 895–908.
95. Breck, D. W. *Zeolite Molecular Sieves*; Wiley: New York, 1974, p 32.
96. Pauling, L. *The Nature of the Chemical Bond*, 3rd ed.; Cornell University Press: Ithaca, NY, 1960; p 556.
97. Kingery, W. D.; Borren, H. K.; Uhlman, D. R. *Introduction to Ceramics*, 2nd ed.; Wiley: New York, 1976.
98. Kiselev, A. V.; Lygin, V. I. In *Infrared Spectra of Adsorbed Species*; Little, L. H., Ed.; Academic: London, 1966; p 275.

RECEIVED for review March 23, 1992. ACCEPTED revised manuscript July 24, 1992.

2

Silica Nucleation, Polymerization, and Growth Preparation of Monodispersed Sols

Akitoshi Yoshida

Central Research Institute, Nissan Chemical Industries, Ltd., 722-1, Tsuboi-cho, Funabashi-shi, Chiba 274, Japan

The industrial development of silica sol manufacturing methods is reviewed. Primary attention is focused on the preparation of monodispersed sols from water glass by the ion-exchange method. Details are given for variations of manufacturing process and for the characteristics of both the processes and sols obtained. Furthermore, the following surface modifications of particles are demonstrated: silica sols stabilized with ammonia, amine, and quaternary ammonium hydroxide; aluminum-modified or cation-coated silica sol; and lithium silicate. Finally, future trends in silica sol manufacturing are discussed from the viewpoint of not only raw materials and improvement of the procedures but also the function of the silica sols and their particle shape.

MONODISPERSED SOL IS COMMONLY REFERRED TO as silica sol or colloidal silica. The term "colloidal silica" here refers to a stable dispersion of discrete, amorphous silica particles.

The industrial development of silica sols first began with the initial research by Graham (*1*) in 1861 involving the addition of hydrochloric acid to an aqueous solution of sodium silicate followed by dialysis to obtain dilute silica sol. In 1933, silica sol containing 10% SiO_2 was first marketed. This step was followed in 1941 by the announcement of an ion-exchange process (*2*), including procedures for stabilization and for concentration of the sol by heating, that used an ion-exchange resin to remove sodium ions

0065–2393/94/0234–0051$08.00/0

from the dilute aqueous solution of sodium silicate. This sodium removal process is the most common today. In 1951, a process (*3*) for creating colloidal silica particles of uniform and controlled size was announced for the first time. In 1956, a method (*4*) was established for making stable sols consisting of microscopic particles having a diameter of only 8 nm yet containing more than 30% of silica. The history of the development of silica sols and a description of the fundamental and application research up to and throughout the 1950s was summarized in detail by Iler (*5*).

Various raw materials can be used in the manufacturing of monodispersed sol. Examples of these materials include silicon metals (*6*), silicon tetrachloride (*7*), ethyl silicate (*8*), water glass (*2*), and silica powder (*9*). In this chapter, I focus attention on the preparation of monodispersed sols from water glass, a raw material that is presently used in large amounts industrially for the inexpensive production of silica sols.

The manufacturing processes of silica sols can be broadly divided into the following three steps:

1. formation of active silicic acid by removal of alkali ions from a dilute aqueous solution of water glass
2. formation of a dilute silica sol by nucleation from the active silicic acid and growth of discrete silica particles by polymerization
3. concentration of the dilute silica sol

In addition, I will discuss modification of the surfaces of silica particles.

Manufacturing Methods of Silica Sols and Their Characteristics

History of Silica Sol Manufacturing Methods. Although numerous techniques have been proposed for manufacturing of silica sols, including dialysis (*10*), electrodialysis (*11*), peptization (*12*), acid neutralization (*13*), and ion exchange (*3*, *14*), the last three methods have come to be used most commonly. At present, the ion-exchange method is considered the most prominent technique.

Although the dialysis method, which involves the reaction of dilute water glass with an acid followed by dialytic removal of the sodium salt as the formed electrolyte, was proposed in 1861, it was never applied on an industrial basis. Furthermore, the electrodialysis method was attempted in various ways as a method for electrically removing sodium salt from water glass. But, unlike the last three methods mentioned, it did not reach the level of practical application.

Peptization Method. As shown in Figure 1, an acid such as sulfuric or hydrochloric is added to a dilute aqueous solution of water glass while stirring, or while heating as necessary, to neutralize and obtain a silica gel containing salt. Next, the crude silica gel is washed with water to remove the salt and obtain a silica wet gel. Then, water and an aqueous sodium hydroxide solution are added to the gel so that the pH of the resulting solution is 8.5–10 and a silica gel slurry is formed. The slurry is then heated for several hours in an autoclave at 120–150 °C to allow the gel to peptize and form a sol. Thus, a silica sol is prepared. For example, the resulting silica sol contains 30 wt% SiO_2, has a pH of 10, has a molar ratio of SiO_2:Na_2O of about 100, and consists of irregular particles having a diameter of 10–20 nm. However, it is difficult to obtain silica sols having a desired particle size or high purity with this method.

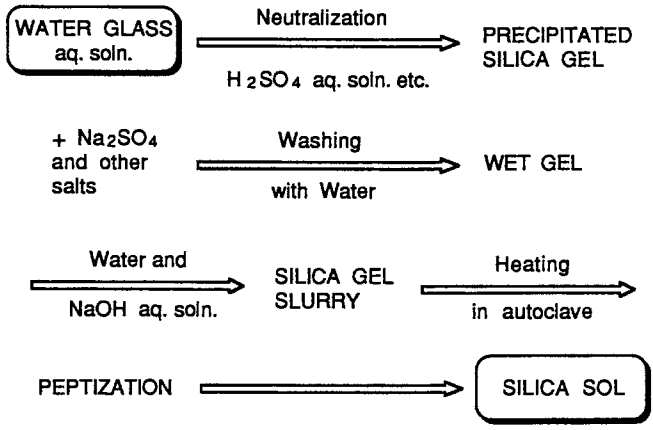

Figure 1. Flow chart of peptization method for manufacturing silica sols.

Acid-Neutralization Method. As is indicated in Figure 2, an acid, such as sulfuric or hydrochloric, is added to a dilute aqueous solution of water glass while heating and stirring. This addition results in silica sol nucleation and particle growth to obtain a dilute silica sol containing salt. The salt is removed by either dialysis or electrodialysis, and the solution is concentrated to obtain a silica sol. In recent years, as the removal of salt has been made easier through the use of ultrafiltration membranes, this method has come to be considered as having potential for the future.

Ion-Exchange Method. Sophisticated ion-exchange resins have been developed to efficiently remove sodium ions at the industrial application level. This method is currently the primary means of manufacturing silica sols. The following section provides a detailed description of this method.

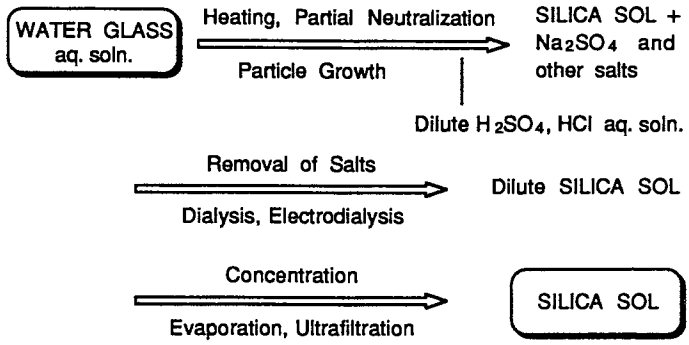

Figure 2. Flow chart of acid-neutralization method for manufacturing silica sols.

Silica Sol Manufacturing Using the Ion-Exchange Method. The silica sol manufacturing method using ion-exchange is as shown in the basic flow chart of Figure 3.

Ion Exchange. An aqueous water-glass solution as the raw material in this process can have a SiO_2 content of 30%, a Na_2O content of 10%, a molar ratio of SiO_2:Na_2O of 3.1, a specific gravity of 1.2, and a pH of 12–13. Water is added to this aqueous water-glass solution while stirring to obtain a dilute aqueous water-glass solution containing 2–6% SiO_2. In this state the silica takes the form of polysilicate anion. Next, this dilute aqueous water-glass solution is passed through a bed of cation-exchange resin in a column for which hydrogen ions have been regenerated in advance to allow the sodium ions to be adsorbed onto the resin bed and leave an aqueous solution of active silicic acid. This liquid is a microscopic colloidal solution with a pH of 2–4 containing 2–6% SiO_2 comprising particles with a diameter of 2 nm or less. The colloidal solution is also in an unstable state and easily gels upon standing because the degree of polymerization is several tens to several hundreds.

Particle Growth. Nucleation (*3*), polymerization (*15*), and particle growth (*16, 17*) are performed on this active silicic acid in the presence of alkali at a temperature of at least 60 °C, a pH of 8–10.5, and a molar ratio of SiO_2:Na_2O of about 20–500, and thus a dilute silica sol is formed. The process of particle growth is discussed in more detail in the next section. The formed dilute silica sol generally consists of spherical particles having a diameter of 4–100 nm, a pH of 8–10.5 and a SiO_2 content of 2–6%. This silica sol is a colloidal liquid in a stable state, and therefore it causes no gelling. As illustrated in the flow sheet, the dilute aqueous water-glass solution is in the form of polysilicate anion. In contrast to this ionic state,

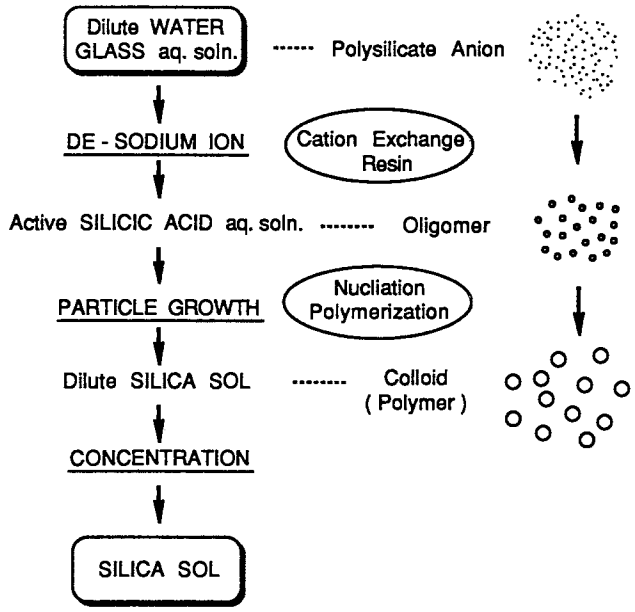

Figure 3. Flow chart of ion-exchange method for manufacturing silica sols.

the active silicic acid is in the form of an oligomer, that is, a colloid of microscopic particles. The dilute silica sol is a polymer in the colloidal state.

Concentration. Next, this dilute silica sol is concentrated so that the SiO_2 content is increased to 15–60%. The concentration is needed not only to ensure efficient transport of a small volume of sol but also for use in silica sol applications, for example, as a binder, a catalyst carrier, and a gelation agent. Because the concentration process of the dilute silica sol efficiently removes the dispersion medium of water, the most common way (*3*, *14*) of accomplishing this step in the past was by using steam under reduced pressure or normal pressure. However, more recently, use of the ultrafiltration membrane (*18–20*), originally intended for the separation of colloidal size particles, has been evaluated for ion removal; this approach is energy saving. It is actually employed in some applications.

Finished products are obtained after the concentration, pH, and conductivity of the concentrated sol are adjusted to maintain their stability. In actuality, several types of manufacturing methods are used, depending on the particular combination of particle growth and concentration.

Mechanism of Particle Growth. As shown in Scheme I, the silicic acid undergoes dehydrating condensation polymerization in the presence of alkali. The higher the temperature and the pH and the longer the reaction time, the faster the polymerization proceeds. As a result of polymerization, Na^+OH^- that was adsorbed onto the active silicic acid is released and increases the pH.

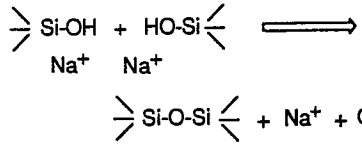

Scheme I. Polymerization of silicic acid by dehydrating condensation.

As shown in Schemes II and III, active silicic acid is polymerized by heating in the presence of alkali and first forms nuclei. Active silicic acid then polymerizes around the nuclei, and thus particles are formed. This process is often referred to as "buildup". In actuality, nucleation and particle growth take place simultaneously. When the temperature is high (such as in autoclave heating) or when the concentration of silicic acid is high during particle growth, particles grow through bonding between nuclear particles or between larger particles, respectively. During nucleation and particle growth as well, Na^+ and OH^- ions are released, and thus the pH of the reaction system is increased. The higher the pH is, the faster the particles grow. However, dissolution occurs if the pH is too high, so pH control is considered to be the most important factor.

In addition, when the pH of this liquid exceeds 10.5, the formed particles undergo dissolution and hydrolysis and then precipitate, and such dissolution and precipitation take part in the particle growth. The main factors that dominate particle growth are amount of alkali such as Na_2O, silica concentration, SiO_2:Na_2O molar ratio, temperature, time, and method of addition.

Variations of Silica Sol Manufacturing Process. As shown in Figure 4, the four methods, A-1, A-2, B-1, and B-2, use different technical combinations of nucleation, particle growth, and concentration. In any of these methods the raw material aqueous water-glass solution is diluted, and sodium is removed with a cation-exchange resin to obtain an active silicic acid. The characteristics of these four processes are shown in Table I.

Methods A-1 and A-2. In Methods A-1 and A-2, a small amount of an aqueous NaOH solution is added, while stirring, to the acidic active silicic

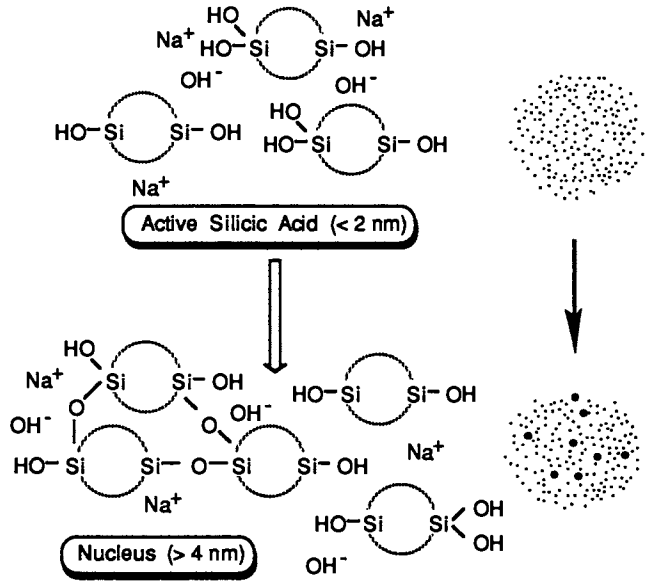

Scheme II. Polymerization of active silicic acid to form nuclei.

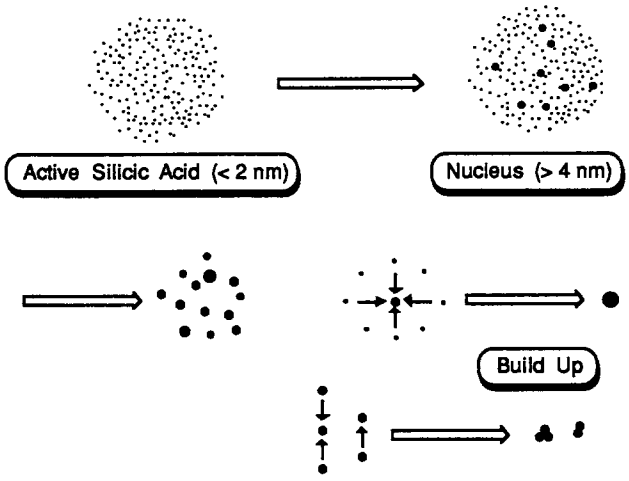

Scheme III. Polymerization of active silicic acid around nuclei to form particles.

acid having a SiO_2:Na_2O molar ratio of 500–1000 until the SiO_2:Na_2O molar ratio is, for example, 80–100 and the solution is stable.

In Method A-1, a fixed amount of this liquid is first charged in an evaporator that is heated from the outside with steam. Simultaneous to the beginning of solution concentration under reduced or normal pressure,

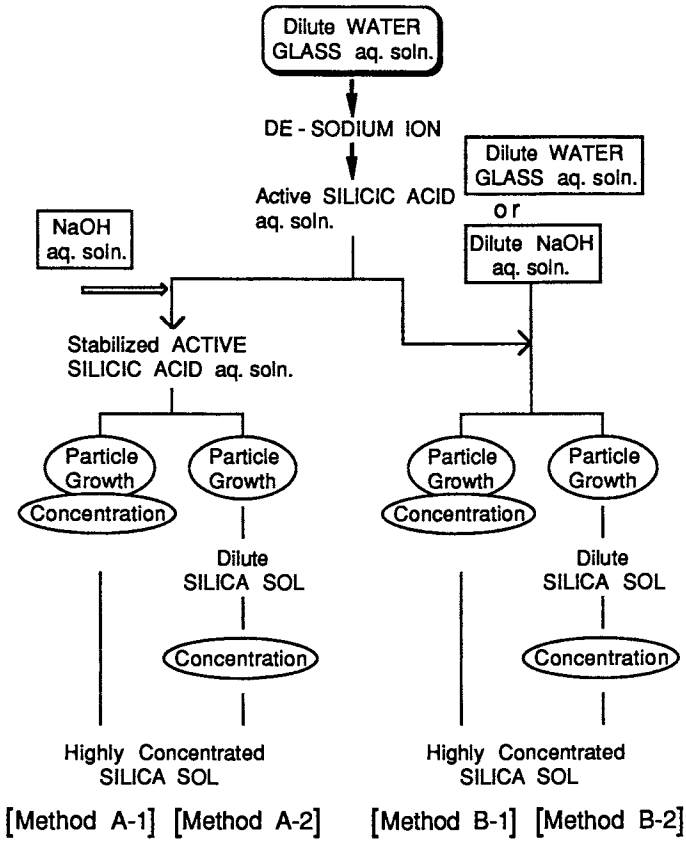

Figure 4. Four methods of silica sol manufacturing.

aqueous active silicic acid solution is continuously metered into the evaporator to carry out particle growth and concentration at the same time.

On the other hand, in Method A-2, particle growth and concentration are carried out separately. In the particle-growth step, a fixed amount of the stable aqueous active silicic acid solution is charged into a heating–aging tank and heated. Continuous charging of the aqueous silicic acid solution then follows to carry out buildup of particles. Alternatively, in another method the stable aqueous active silicic acid solution that was initially charged in the heating–aging tank is simply heated to carry out particle growth. A temperature of 60–150 °C is commonly used for the aging under heating. The dilute silica sol prepared in this manner has a SiO_2 content of 2–6%, a pH of 9–10.5, and a particle size of 4–20 nm. Next, this sol is passed on to the concentration step. Because the silica

Table I. Characteristics of Silica Sol Manufacturing Methods

Characteristics	*Method A-1*	*Method A-2*	*Method B-1*	*Method B-2*
Intermediate material	dilute silica sol		silicic acid and water glass	
Particle growth and concentration	simultaneous	separate	simultaneous	separate
Change in pH during particle growth	7 → 9–10.5		11.5 → 9–10.5	
Particle growth rate	slow		fast	
Size of nuclei	small		small–large	
Nucleation mechanism	polymerization of particles		initial: hydrolysis of water glass; intermediate to final: polymerization of particle	
Manufacturing of large-particle sols	difficult (normal pressure) possible (with pressurization)		possible	
Ease of buildup	more difficult than in Process B		easy	
Control of particle size	possible for microscopic- to medium-sized particles		possible for microscopic- to large-sized particles	
Control of particle size distribution	impossible or difficult	possible	impossible or difficult	possible
Manufacturing time	long (longer than in B-1)	short (longer than in B-2)	long	short

particles have already grown and are in a stable state, concentration can be performed in an arbitrary manner, for example, through evaporation or using an ultrafiltration membrane. The pH, concentration, and conductivity of the highly concentrated sol are then adjusted to obtain a finished sol product.

Methods B-1 and B-2. Characteristically in Methods B-1 and B-2, the aqueous solution of active silicic acid is continuously charged into either a dilute aqueous water-glass solution or dilute aqueous NaOH solution that has preliminarily been heated, and stirred if necessary, to effect particle growth. In Method B-1, concentration and particle growth are carried out simultaneously under conditions similar to those of Method A-1. In Method B-2, particle growth and concentration are carried out separately, and in this regard it is essentially the same as Method A-2. However, in Method B-1 or B-2, larger diameter silica sol particles, 4–100 nm, can be formed. On the other hand, Methods A-1 or A-2 allows production only up to medium-sized silica particles having a diameter of 4–20 nm.

Manufacturing of Large-Particle Silica Sols. A method for manufacturing silica sols consisting of large-diameter particles of 50–200

nm is as follows. The buildup method is used because the growth of particles is difficult in Method A-1 or A-2 even when medium-diameter silica sols are manufactured.

As indicated in Scheme IV, stable dilute sol is nucleated to obtain sols having a particle size of, for example, 20 nm, which is used as a heel. Then, in the next step, an active silicic acid or stable dilute sol is continuously charged onto the heel to allow the silica particles to grow to a diameter of 50 nm. Thus, the process consists of two separate steps. In either Method B nucleation is carried out in the initial stage of the process, and buildup occurs from the intermediate to the final stages. However, this method is not clearly separated into two steps.

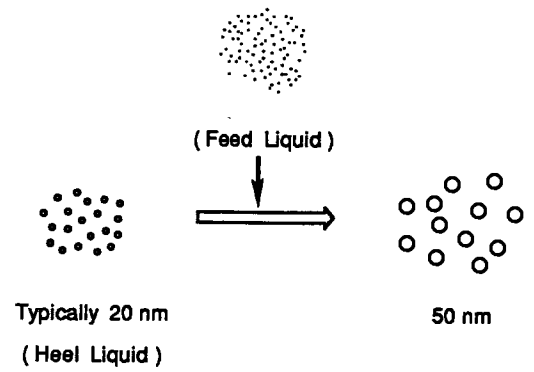

Scheme IV. Preparation of silica particles from stable dilute sol using the buildup method.

Figure 5 illustrates the production of large-particle silica sols. In Process A, silica sol consisting of microscopic- to medium-sized particles is heated in an autoclave at 120–130 °C for several hours, and the hydrothermal treated silica sol is concentrated to obtain a highly concentrated large-particle silica sol. In Process B, medium- to large-particle-size sols, which serve as nuclei, are added to an aqueous water-glass solution or a dilute aqueous NaOH solution. The mixture is then heated to carry out aging while stirring, and in this state active silicic acid is charged to allow buildup of particles. Factors that dominate particle growth are the size and concentration of the silica particles that serve as the nuclei, the amount of active silicic acid to be added, the aging temperature, aging time, pH behavior, and others. Method B characteristically facilitates formation of sols with large particle sizes showing a uniform particle size distribution ranging up to about 200 nm.

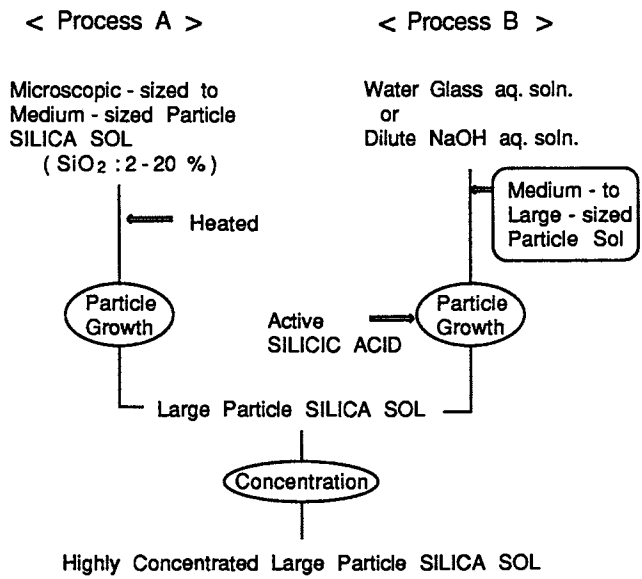

Figure 5. Flow chart of production of large-particle silica sols.

Characteristics of Silica Sols Produced by the Four Methods. The characteristics of the sols manufactured according to Methods A and B are shown in Table II.

Table II. Characteristics of Sols Formed by the Different Methods

Characteristics	*Method A-1*	*Method A-2*	*Method B-1*	*Method B-2*
Particle size distribution	broad	narrow	broad	narrow
Particle shape	irregular	spherical	spherical	spherical
Degree of silica particle distribution	low	high	high	high
Illustrations of particle shape	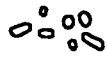			

Manufacturing Methods of Surface-Modified Silica Sols

The silica sols described in the manufacturing methods are all generally stabilized with NaOH, and the majority of the silanol groups on the surface of the silica sol are covered with Na^+ ions, as indicated in Scheme V. Na^+ ions are strongly adsorbed onto the silanol group, and this condition sometimes is expressed as Si–ONa.

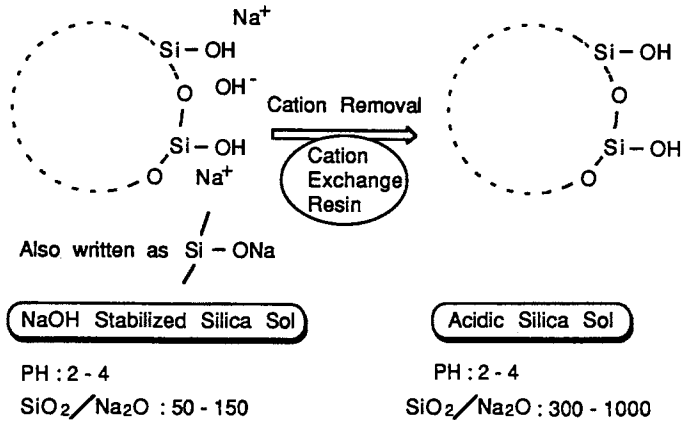

Scheme V. Removal of cations from stable silica sol to form acidic silica sol.

For manufacturing a surface-modified silica sol, an acidic silica sol (*20*) from which these Na^+ ions have been removed is used in most cases. As shown in Scheme V, silica particles are brought into contact with a cation-exchange resin, and if necessary, with an anion-exchange resin, to obtain an acidic silica sols of pH 2–4. This acidic sol is stable because it is negatively charged even at pH 2–4, according to zeta-potential measurements. Starting from such acidic silica sol, surface-modified silica sols are manufactured.

Silica Sols Stabilized with Ammonia, Amine, and Quaternary Ammonium Hydroxide. As shown in Figure 6, ammonia (*21*), amine (*22*), or quaternary ammonium hydroxide (*22*) is added to the acidic silica sol while stirring, and if necessary the mixture is aged with heating to obtain a correspondingly stabilized silica sol. Such sols have a SiO_2 content of 20–50% and a pH of 8–12. This type of sol fits new applications because the sols remain mixed for a fixed period with strongly alkaline water glass, CaO, and MgO, with which ordinary silica sols can hardly be mixed because of gelling.

Aluminum-Modified Silica Sol. As shown in Figure 6, an aluminum-modified silica sol (*23*) can also be formed by adding an aqueous sodium aluminate solution to the acidic silica sol while stirring at room temperature so that the SiO_2:Al_2O_3 molar ratio is approximately 350 and aging the mixture with heating at 100 °C. This modified silica sol has a SiO_2 content of 20–40%, and a pH of 8–10, and the surfaces of the silica particles are negatively charged. A major characteristic of this type of sol is that it does not gel and is stable in the neutral pH region. Ordinary silica

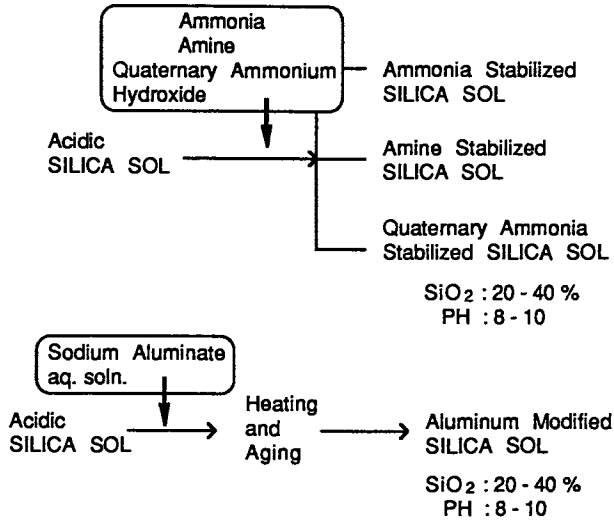

Figure 6. Flow chart of production of silica sols stabilized with ammonia, amine, or quaternary ammonium hydroxide.

sols cannot be used in this neutral region because they undergo gelation but the aluminum-modified sol has enabled various new applications. The aluminum-modified silica sol is the first surface-modified silica sol that has considerable industrial value.

Cation-Coated Silica Sol. As shown in Figure 7, an aqueous solution of basic aluminum chloride is added to an acidic or alkaline silica sol while stirring, and then a dilute aqueous NaOH solution is added until the PH of the mixture is 4–6. The mixture is then aged by heating to 80–100 °C to form a cation-coated silica sol (*24*). This silica sol is used in applications where the pH is in the acidic region and where it is used as a mixture with a cationic aqueous solution. Moreover, the cation-coated silica sol can be mixed easily with water-soluble organic solvents. Besides aluminum salt, other basic salts such as of Zr and Ti and cationic surface-active agents (*25*) can also be used for cation coating.

Lithium Silicate. In this chapter, the term lithium silicate means very small silica sol particles whose surfaces are coated with lithium hydroxide. As shown in Figure 8, this lithium silicate (*26*) can be prepared by adding an aqueous solution of lithium hydroxide to the acidic silica sol while stirring, and then heating the mixture to a temperature of 60 °C or less for an extended period of time, for example, a half day to several days. This lithium silicate typically has a SiO_2 content of 10–25%, a SiO_2:Li_2O molar ratio of 3–9, and a pH of about 11. Lithium silicate is a kind of water

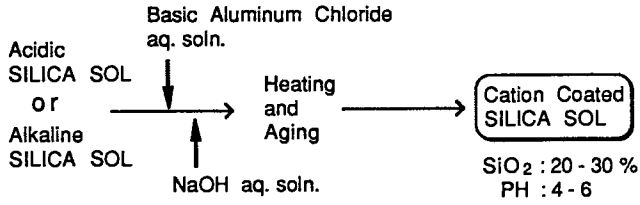

Figure 7. Flow chart of production of cation-coated silica sol.

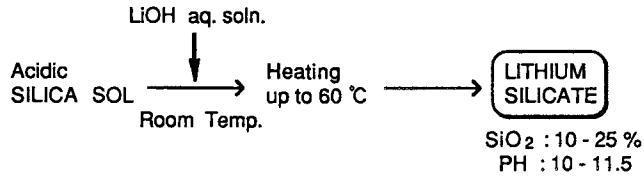

Figure 8. Flow chart of production of lithium silicate.

glass like sodium silicate and potassium silicate, but it is used as a binder because it has particularly high levels of water resistance and heat resistance.

Future Trend in Silica Sol Manufacturing

Silica sols will be required to have more unique and sophisticated characteristics in the future to meet the needs of various application fields (27). Therefore, raw materials will no longer be limited to the aqueous water-glass solutions, but a variety of raw materials will be used corresponding to the specific properties required for the desired silica sol. For example, large- to very large-sized silica sols that are of high purity and as truly spherical as possible are required in electronics applications. Ethyl silicate will most likely be used as a raw material for this purpose. In addition, organosilica sols dispersed in organic solvents, such as methanol silica sol (28) and dioctyl phthalate sol (29), are beginning to be used in the field of plastics modification.

Furthermore, in an effort to discover unknown characteristics of silica sols, further progress will occur in the development of silica sols (30) having shapes other than spherical, such as elongated, fibrous, and platelet. We are currently working on the development of elongated silica sols. Compared with the spherical silica sols, the elongated silica sols have high film-forming properties and demonstrate unique properties as a binder or coating agent for the formation or surface treatment of inorganic fibers. As shown in the transmission electron microscope photographs of

Figure 9, this new silica sol is elongated. For example, the particles have a diameter of about 10 nm and a length of 50–100 nm. To prepare such elongated silica sols, a calcium salt and an aqueous sodium hydroxide solution are added to an active silicic acid or an acidic silica sol, and the mixture is heated in an autoclave at 100–150 °C for several hours. Thus, particle polymerization takes place in nonuniform directions, and an elongated silica sol (*31*) can be formed.

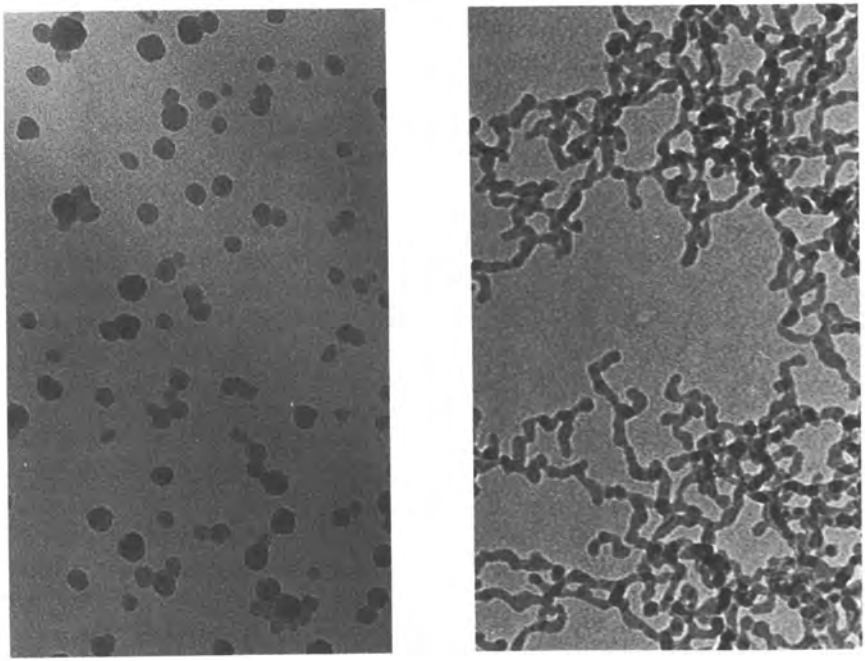

Figure 9. Silica sols with spherical (left) and elongated (right) particles.

Besides varying the shapes of silica sols, the functions of silica sols will be varied in the future. Examples include a sol that gives a film with a high refractive index made up of a composite of silica and titanium oxide; a conductive silica sol whose surface is covered with an electrically conductive oxide or metal; and a porous silica sol that is made from ethyl silicate as the raw material.

On the other hand, in terms of manufacturing processes, the procedures employed will have to be improved continually, to improve the efficiency of the cation-exchange procedure, to manufacture silica sols continuously, and to enhance the efficiency of the concentration processes.

Concluding Remarks

From the 1940s to the 1960s, the fundamental technology for manufacturing silica sols was fully established, and wide variety of silica sol products was developed, mainly owing to the achievements of Iler. From the 1970s to the 1980s, mass production processes were developed to achieve cost reduction to meet large-scale applications. And now, the manufacturing of silica sols is entering a new era. Even in this new era, we will surely continue to formulate our ideas and thoughts on the basis of the valuable research results achieved by Ralph Iler.

References

1. Griessbach, R. *Chem. Ztg.* **1933,** *57,* 253–274.
2. Bird, P. G. U.S. Patent 2,244,325, 1941.
3. Bechtold, M. F.; Snyder, O. E. U.S. Patent 2,574,902, 1951.
4. Alexander, G. B. U.S. Patent 2,750,345, 1956.
5. Iler, R. K. *Colloid Chemistry of Silica and Silicates;* Cornell University Press: Ithaca, NY, 1955.
6. Balthis, J. H. U.S. Patent 2,614,994–5, 1952.
7. Radczewski, O. E.; Richter, H. *Kolloid-Z.* **1941,** *96,* 1.
8. Stöber, W.; Fink, A. *J. Colloid Interface Sci.* **1968,** *26,* 62.
9. Loftman, K. A.; Thereault, J. R. U.S. Patent 2,984,629, 1961.
10. Graham, T. *J. Chem. Soc. London* **1864,** *17,* 318.
11. Sanchez, M. G. Canadian Patent 586,261, 1959.
12. White, J. F. U.S. Patent 2,375, 1945.
13. Alexander, G. B.; Iler, R. K. U.S. Patent 2,601,235, 1952.
14. Bird, P. G. U.S. Patent 2,244,325, 1941.
15. Alexander, G. B. *J. Am. Chem. Soc.* **1954,** *76,* 2094.
16. Alexander, G. B.; Mcwhorter, J. R. U.S. Patent 2,833,724, 1958.
17. Broge, E. C.; Iler, R. K. U.S. Patent 2,680,721, 1954.
18. Chiton, H. T. J. British Patent 1,148,950, 1969.
19. Iler, R. K. U.S. Patent 3,969,266, 1976.
20. Mindick, M.; Reven, L. E. U.S. Patent 3,342,747, 1967.
21. Akabayashi, H.; Syoji, H. Japanese Patent 288,231, 1961.
22. Iler, R. K. U.S. Patent 2,692,863, 1954.
23. Alexander, G. B. U.S. Patent 2,892,797, 1959.
24. Alexander, G. B.; Bolt, G. H. U.S. Patent 3,007,878, 1961.
25. Akabayashi, H.; Yoshida, A. Japanese Patent 447,161, 1965.
26. Iler, R. K. U.S. Patent 2,668,149, 1952.
27. Yoshida, A. *Chem. Econ. (Jpn)* **1988,** *6,* 22.
28. Akabayashi, H.; Yoshida, A. *Kogyo Kagaku Zasshi* **1966,** *68,* 429.
29. Akabayashi, H.; Yoshida, A. *Kogyo Kagaku Zasshi* **1966,** *69,* 1832.
30. Broge, E. C. U.S. Patent 2,680,721, 1954.
31. Watanabe, Y.; Ando, M. European Patent Appl. Publication No. A2,0335195, 1989.

RECEIVED for review December 17, 1990. ACCEPTED revised manuscript December 30, 1991.

3

The Formation and Interfacial Structure of Silica Sols

John D. F. Ramsay[1], Stephen W. Swanton, Akihiko Matsumoto[2], and Dhanesh G. C. Goberdhan[3]

Atomic Energy Authority Technology, Harwell Laboratory, Oxfordshire, OX11, United Kingdom

Several techniques, including small-angle neutron scattering (SANS), ultracentrifugation, photon correlation spectroscopy, and ^{29}Si NMR spectroscopy, were used to investigate the nature of the oxide–water interface of silica sols and its significance in the formation and growth of colloidal particles in aqueous solution. These studies were performed with a range of commercial silica sols of different diameters in the range ≈7–30 nm. When the diameter is small the sols contain a significant proportion of oligomeric silicate species that may be associated at the surface of the particles. For sols of the largest diameter, the relative proportion of oligomers is much smaller. In all the sols the core of the particles has a highly condensed Si–O–Si structure.

THE CLASSIC DESCRIPTION of the structure and mechanisms of formation of silica sols by the hydrolysis and condensation of silicates in aqueous media was given by Iler in 1979 (*1*). According to Iler, polymerization may occur in essentially three stages: (1) the polymerization of monomers to oligomers and then to primary particles, (2) growth of particles, and (3) particle aggregation to form networks that eventually give rise to a gel

[1]Corresponding author. Current address: Centre National de la Recherche Scientifique, Institut de Recherches sur la Catalyse, 2 Avenue Albert Einstein, 69626 Villeurbanne, France.
[2]On assignment from Department of Chemistry, Faculty of Science, Chiba University, Yayoi, Chiba 260, Japan.
[3]Present address: Esso Chemical Research Centre, Abingdon, Oxon, United Kingdom.

0065–2393/94/0234–0067$08.00/0

structure extending throughout the liquid medium. Stages 2 and 3 depend on the pH and salt concentration, as discussed by Iler. These general processes have subsequently been confirmed by many workers using a range of microscopic techniques (2) such as ^{29}Si NMR and IR spectroscopy, light scattering, small-angle X-ray scattering (SAXS), and small-angle neutron scattering (SANS), although less attention has been given to stage 2.

Considerable advances in understanding stage 1 have been obtained from ^{29}Si NMR investigations (3–5) and stage 3 from scattering measurements (light, X-rays, and neutrons) (6, 7). Stage 1 has been shown to give rise to a range of complex polysilicic acid structures. In general extensive condensation takes place in which monomers form ring structures that associate and condense further, eventually to form the core of silica particles containing few silanol groups. In stage 3 the present understanding of the double-layer interaction between particles and the mechanisms of aggregation to give gel formation is extensive and has been advanced by descriptions based on fractal theory (8).

In this chapter we will describe some recent investigations of the formation and interfacial structure of a series of commercially produced silica sols (Nalco, Dupont, and Ludox) with different diameters in the range ≈ 7–30 nm. This type of sol, which has wide industrial applications, has been used as a model system in numerous studies of colloidal silica, although in general, the nature of the silica–water interface has received little attention. The interfacial structure may well explain some of the unusual properties of silica sols, such as the high surface charge and exceptional colloidal stability together with the enhanced capacity for sorption and complexation of ionic species in solution. Indeed in the past these features have been ascribed to a surface "gel layer" resulting from extensive hydroxylation within a few ångstroms at the surface (9), although definitive evidence of this gel layer is still lacking. Here we have applied several techniques (photon correlation spectroscopy (PCS), SANS, analytical ultracentrifugation, and ^{29}Si NMR spectroscopy) to explore the properties of these silica sols. Particular interest attaches to the sol of smallest diameter because here we anticipate that any effects due to incomplete condensation of oligomeric components will be relatively more marked, especially in the diffusion behavior and effective diameter of the spherical particles.

Experimental Details

Silica Sols. Concentrated (ca. 15 to ca. 40% w/w) silica sols of different particles size (S1 to S4) were obtained commercially from designated sample batches, viz., S1 is Nalcoag 1115 from Nalco Chemical; and S2, S3, and S4 are Ludox SM, HS, and TM respectively, from DuPont. These sols are prepared by

hydrothermal treatment of sodium silicate solutions (*1*) and contain Na^+ as the counterion. These sols have already been studied extensively (*6, 10, 11*). The mean diameters of the sol particles, as previously determined from transmission electron microscopy (*10*) together with the effective particle radius as derived from the specific surface areas, S_{BET}, of the outgassed gels (*10*) are given with other properties in Table I. Measurements were made with sols of different concentration by diluting the stock samples with demineralized water. The stock sol, S1, was also dialyzed repeatedly against water (denoted $S1^D$) and used in further studies.

Table I. Properties of Silica Sols

Sol	*Stock Concentration (w/v)*	*Particle Diameter (nm)*[a]	*Surface Area of Gel, S_{BET} (m^2/g)*	*Particle Radius (nm)*[b]	*Na^+ Content (mg/mL)*	*pH*
S1	16.1	8	410	3.3	5.6	10.5
S2	32.8	12	260	5.2	6.0	10.1
S3	40.3	16	210	6.5	4.9	9.8
S4	47.2	30	130	10.5	3.2	9.0

[a]From electron microscopy.
[b]From S_{BET}, assuming silica density of 2.2 g/mL.

Small-Angle Neutron Scattering. Measurements were made as described previously (*10, 11*) using a multidetector instrument installed in the PLUTO reactor at Harwell and also with the D11 instrument at the Institut Laue-Langevin, Grenoble, France.

Photon Correlation Spectroscopy. Measurements were made with a commercial 96-channel photon correlator (Malvern K7023) using a helium–cadmium laser and with a 256-channel correlator (Malvern K7032) using a helium–neon laser with a standard spectrometer system (Malvern 4700), adopting procedures as described previously (*12*).

Analytical Ultracentrifugation. Sedimentation coefficients were determined with an ultracentrifuge (Beckman L8–70M) fitted with a schlieren analytical attachment. Photographic images of schlieren (refractive index gradient) profiles were analyzed with a profile projector (Nikon, model V10) using standard procedures (*13*).

^{29}Si NMR Spectroscopy. ^{29}Si NMR spectra of the stock sols contained in 1-mL plastic vials were recorded at a field strength of 39 MHz using a commercial instrument (Bruker-Physics CXP200) at a 10-s pulse repetition rate.

Results and Discussion

Small-Angle Neutron Scattering. The intensity of small-angle scattering, $I(\mathbf{Q})$, for a concentrated colloidal dispersion of identical particles is given by (*14*)

$$I(\mathbf{Q}) = K\,(\rho_p - \rho_s)^2 V_p^2 n_p P(\mathbf{Q}) S(\mathbf{Q}) \qquad (1)$$

where **Q** is the scattering vector, defined as

$$|\mathbf{Q}| = 4\pi \sin \Theta/\lambda$$

for a scattering angle 2Θ and wavelength λ; ρ_p and ρ_s are, respectively, the mean scattering length densities of the particles and solvent; V_p is the volume of each particle; n_p is the particle number density; K is an experimental constant; and $P(\mathbf{Q})$ is the particle form factor, which for spheres of radius R is given by

$$P(\mathbf{Q}) = \left[\frac{3[\sin(QR) - QR\cos(QR)]}{\mathbf{Q}^3R^3}\right]^2 \tag{2}$$

The structure factor, $S(\mathbf{Q})$, is determined by the nature of the particle interaction potential (*7*); for noninteracting systems $S(\mathbf{Q}) = 1$ (viz., for systems in the limit of very low concentration where electrical double-layer interactions are negligible).

Extensive SANS investigations have been performed previously with silica sols of the present type (*6, 10, 11*). The scattering behavior of the sols can be closely described on the basis of the foregoing theoretical treatment for monodispersed spherical particles. Furthermore, detailed analysis of the form of the scattering curves (relative intensity $I(\mathbf{Q})$ vs. $\mathbf{Q}$) for sols of different concentration has provided information on the size of particles and the nature of the interaction potential. Typical values of R, derived from experimental fits of extensive scattering data (*11*) to equation 1, are ~5 nm for S1, ~7 nm for S2, ~9 nm for S3, and ~15 nm for S4. These values confirm that R, although slightly larger, is in satisfactory accord with that determined from transmission electron microscopy (TEM). There is more discrepancy with the sol of smallest particle size. The possible explanation for this discrepancy will be discussed subsequently.

The structure and composition of the particles themselves are determined during the formation process. Information on the nature and composition of the particles can be obtained from contrast variation studies, as described previously (*7, 14*). Thus for the simple case of a uniform and homogeneous particle, the scattering length density, ρ_p, can be derived from variations of the solvent scattering length, ρ_s. This derivation is readily achieved with water using H_2O–D_2O mixtures (*see* Table II). ρ_p is derived from the solvent composition of zero contrast (i.e., $\rho_p = \rho_s$). This fact is illustrated by the scattering of sol S2 in different H_2O–D_2O mixtures (Figure 1), in which scattering is negligible for a composition of ~65% (v/v) D_2O. A precise determination of ρ_p is obtained from the linear relationship of $I(\mathbf{Q})^{1/2}$ vs. %v/v D_2O (cf. equation 1) as illustrated in Figure 2. The experimentally determined value of ρ_p ($3.6 \times$

10^{-10} cm^{-2}) is in close accord with that calculated for amorphous silica (3.47×10^{10} cm^{-2}) assuming a framework density of 2.2 g/mL (*see* Table II). This agreement indicates that the sols have a dense silica core and that any surface-hydroxylated species are readily exchangeable with D_2O. The form of the scattering curves in Figure 1, which show a maximum at $Q \approx 3 \times 10^{-2}$ and a decrease in intensity at lower Q, is due to the maximum in the structure factor S(Q) (cf. equation 1). This feature becomes progressively pronounced as the sol concentration is increased and indicates that appreciable interaction occurs between the sol particles at the concentration (0.15 g/cm^{-3}) here.

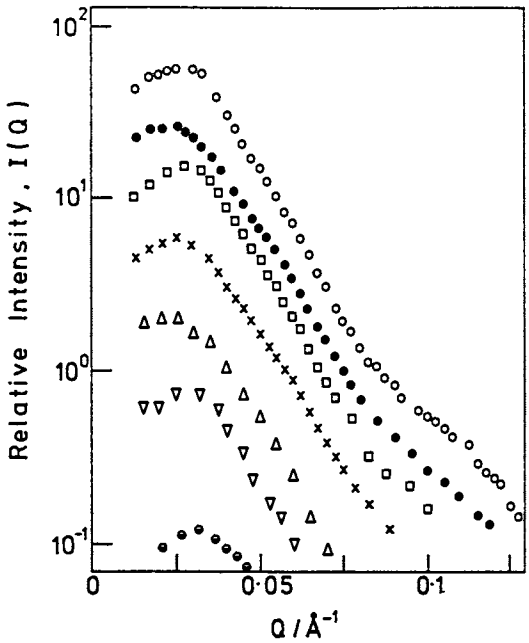

Figure 1. SANS results for silica sol S2 (0.15 g/cm³) in different D_2O–H_2O mixtures. Key (% v/v D_2O): ○, 0; □, 30, △, 50; ▽, 55; ◒, 65; ×, 80; and ●, 100. (Reproduced with permission from reference 18. Copyright 1991 Academic Press.)

Ultracentrifugation Studies. On ultracentrifugation the silica dispersions show a single solute boundary separating from the meniscus, which is observed as a peak in the schlieren (refractive index gradient) profile of the cell. Schlieren photographs recorded for a dilute dispersion of S4 are shown in Figure 3 and are typical of those observed for all the silicas. With increasing sedimentation time the boundary broadens as a

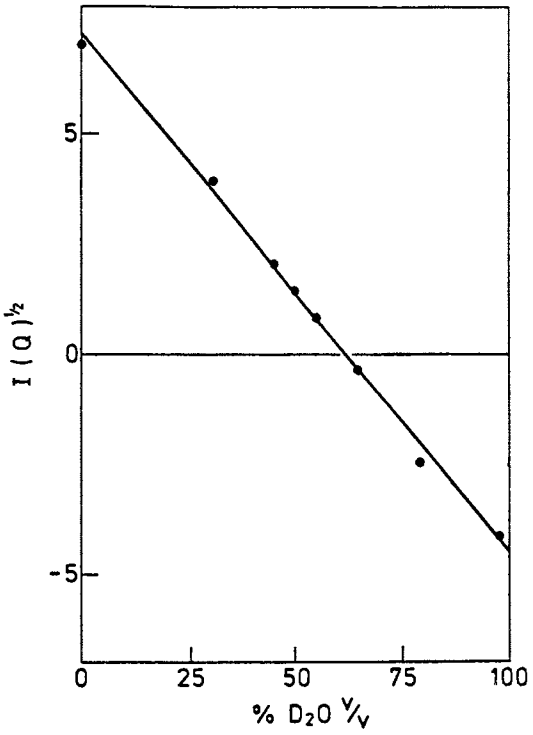

Figure 2. SANS contrast variation results for silica sol S2 in D_2O–H_2O mixtures. Intensity corresponds to Q ($Å^{-1}$) of 2.5×10^{-2}.

Table II. Molecular Scattering Lengths, $\Sigma_i b_i$, and Corresponding Coherent Scattering-Length Densities, ρ, for Neutrons for Silica and Water of Mass Densities, δ

Compound	$\Sigma_i b_i$ *(10^{-12}/cm)*	δ *(g/cm²)*	ρ *(10^{10}/cm^{-2})*
H_2O	−0.168	1.00	−0.56
D_2O	1.914	1.10	6.36
SiO_2	1.575	2.20	3.47
SiO_{2exp}[a]			3.6

[a]Experimentally determined value.

result of diffusion and the centrifugal separation of particles of slightly different size. The observed boundary shapes indicate that the dispersions are reasonably monodisperse but with some increase in polydispersity for the smaller sized sols S1 and S2.

The effect of sol concentration on the sedimentation coefficients, s^{25}, of all four sols is illustrated in Figure 4. The values of s^{25} decrease as the

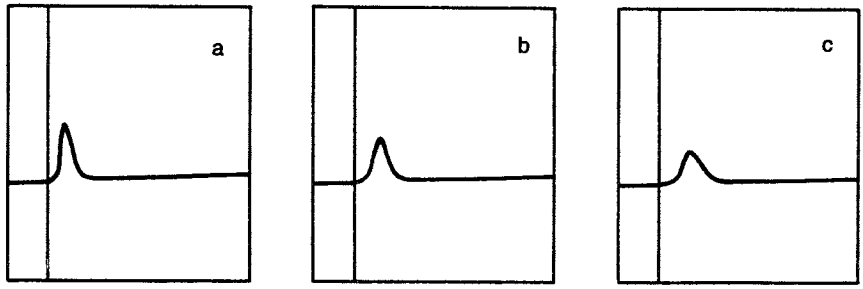

Figure 3. Schlieren photographs of silica sol S4 taken during ultracentrifugation at 1100 rpm after (a) 3.5 min, (b) 5.5 min, and (c) 7.5 min. The vertical lines toward the left side of the photographs indicate the air–solution meniscus; sedimentation is from left to right.

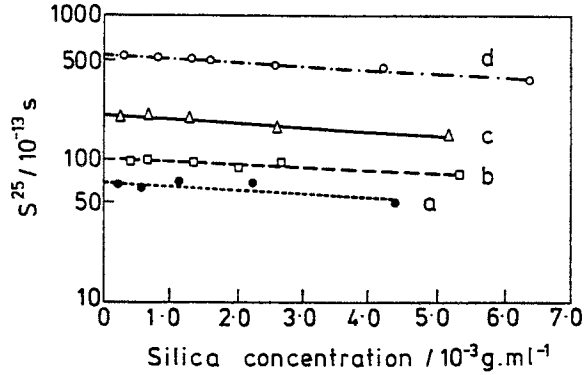

Figure 4. Variation of the sedimentation coefficient, s^{25}, with concentration for diluted silica sols as determined by analytical ultracentrifugation for (a) S1, (b) S2, (c) S3, and (d) S4.

size of the sol particle becomes smaller, as would be expected, and furthermore s^{25} is relatively insensitive to concentration in the range studied ($\sim 2 \times 10^{-3}$ to 6×10^{-2} g/mL). From the values of s_0^{25}, in Table III an effective radius, r_s can be derived by applying the Svedberg equation

$$M = \frac{RTs_0}{D(1 - \nu\delta_w)} \tag{3}$$

where M is the particle "molecular weight", R is the gas constant, T is absolute temperature, D is the diffusion coefficient, ν is the volume per unit mass ($= \delta_s^{-1}$) of the particles, and δ_w is the density of water. For anhydrous, spherical particles

Table III. Sedimentation Coefficients, s_0^{25} of Silica Sols

Sol	$10^{13}s_0^{25}$ *(s)*	*Effective Radius* r_s *(nm)*[a]
S1	68	4.8
S2	98	5.7
S3	198	8.1
S4	518	13.1
S1[D]	52	4.1

[a]Corresponds to sol radius assuming particle density, δ_s, of 2.2 g/mL.

$$r_s = \left(\frac{9}{2}\,\frac{\eta s_0 v}{1 - v\delta_w}\right)^{1/2} \tag{4}$$

where η is the viscosity of water.

The values of r_s for sols S2, S3, and S4 are all in reasonable accord with the sizes derived from SANS and TEM. That for S1 is considerably larger than that determined by TEM (~3.5 nm). However on extensive dialysis of the S1 sol a significant reduction occurs (Table III). Furthermore, the change in the shape of the schlieren peaks that occurs after dialysis is marked as illustrated in Figure 5. The significance of these changes will be discussed in more detail later. After dialysis there appears to be a much smaller component that sediments considerably more slowly than the original sol particle. The areas under the two schlieren peaks after corresponding times of sedimentation are almost identical (Figure 5), a result showing that the mass of silica species is virtually unchanged. However, the skewing of the peak shape close to the meniscus can be ascribed, on semiquantitative examination of the peaks, to a smaller species that contributes up to ~20% of the total silica in the system. Furthermore, after dialysis the major component (measured in terms of the maximum ordinate of the peak) sediments more slowly, an observation indicating that it is reduced in effective size. Such effects can be tentatively ascribed to a change in the structure of the sol after dialysis. Thus in the initial sol the particles may be composed of a dense core surrounded by adsorbed oligomeric species. On dialysis and reduction of the ionic strength, a large proportion of these oligomeric species may be released into solution as a freely sedimenting fraction. Further support for such a process will be given later.

PCS Studies. Translational diffusion coefficients, D_T, as a function of sol concentration were determined from PCS measurements. Measure-

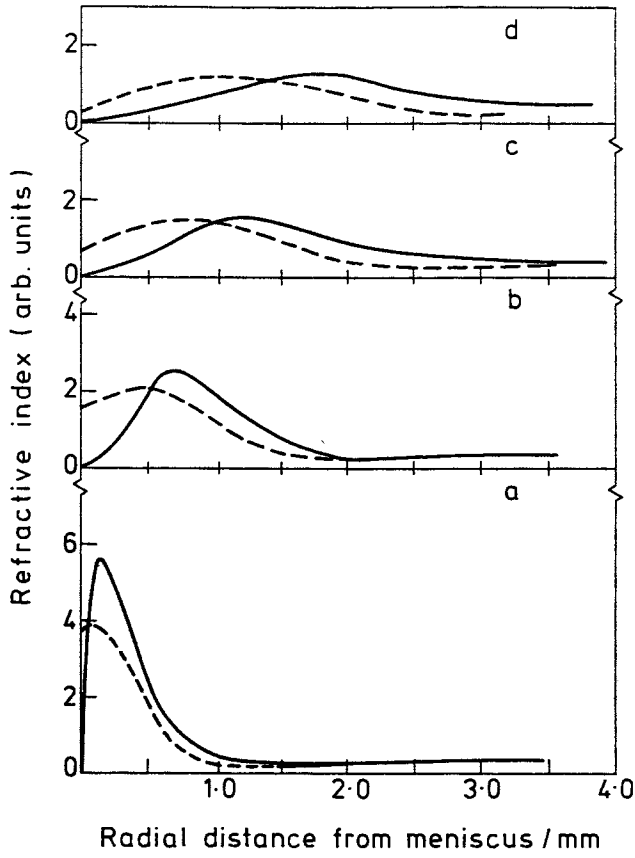

Figure 5. A comparison of the profiles of schlieren images for dilute (2.2×10^{-3} g/cm^3) samples of the dialyzed (- - -) and undialyzed (—) silica sol S1 after equivalent sedimentation times at 22,000 rpm. Time (min): a, 2; b, 6; c, 10; and d, 14.

ments were made at different scattering angles ($2\Theta = 45°$, 90°, and 135°), and D_T was determined from initial slopes of the autocorrelation functions.

Typical autocorrelation functions, $g(\tau) - 1$, for dilute (<5 mg/mL) S3 and S4 sols (Figure 6) showed good fits to a single exponential decay, over a wide range of $Q^2\tau$, a result indicating little polydispersity and particle interaction. ($Q = 4\pi \sin \Theta\tilde{n}/\lambda$, where $\tilde{n}$ is the refractive index of the medium and τ corresponds to a delay time). For sols S1 and S2 single exponential fits were less satisfactory, a condition suggesting greater polydispersity. On the basis of a more detailed cumulants analysis of the form of $g(\tau)$, polydispersity indices for S3 and S4 were shown to be in the range ~0.13–0.2, whereas for S1 and S2 the index was considerably

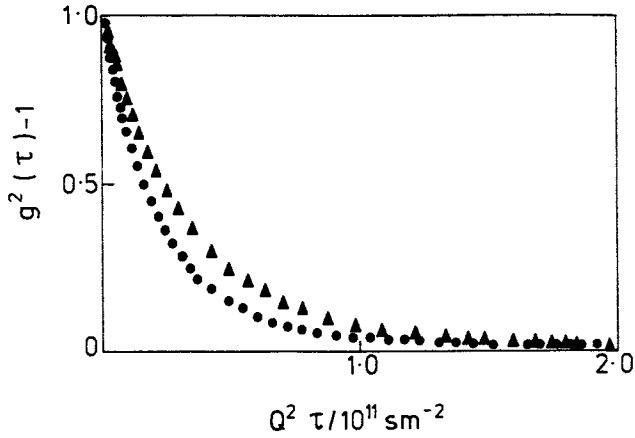

Figure 6. A comparison of normalized autocorrelation functions determined by PCS for diluted samples (1×10^{-3} g/cm³) of silica S3 (●) and S4 (▲).

greater (0.25–0.4). Also, both light scattering and SANS give a Z-average size, and in consequence this size will be larger than that derived from TEM for polydispersed samples.

The variation of D_T with concentration for diluted stock sols S1, S2, S3, and S4 is shown in Figures 7 and 8. In the range of concentration here a slight increase in D_T occurs with concentration. Although it is not appropriate to discuss in detail here, this effect can be ascribed (*15*) to the effects of electrical double-layer interactions. Values of D_T obtained on extrapolation to zero concentration and the corresponding hydrodynamic radii, R_H, are given in Table IV. For S4 R_H is slightly greater, although in reasonable accord with the radius derived from scattering and ultracentrifuge measurements. This difference becomes more significant for S3. However, for sols S2 and S1, R_H is considerably greater. A possible explanation may arise from an extension of the shear plane from the particle surface due to adsorbed or associated oligomeric silicate species, as discussed earlier. Such an explanation is consistent with the changes in D_T that occur on dialyzing the S1 sol (cf. Figure 8): Dialysis results in a marked increase in D_T and a corresponding reduction in R_H (Table V), presumably due to the release of oligomeric species to the aqueous solution.

A reduction in scattered light intensity (by ~65%) for sols of the same SiO_2 concentration after dialysis is also consistent with a reduction in the effective size of the particles. Any free oligomeric species will not make any significant contribution to the total scattered intensity because of their much smaller size. In this respect light scattering differs from ultracentrifugation in being sensitive only to the larger colloidal component.

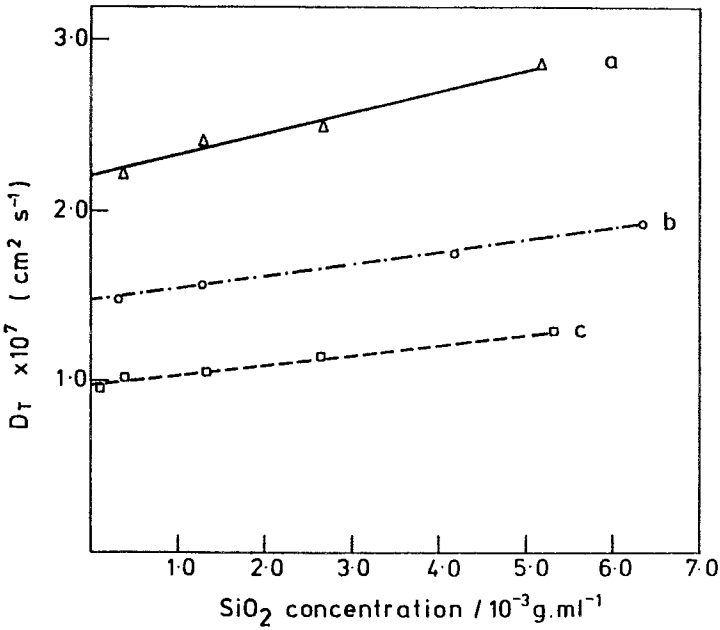

Figure 7. Translational diffusion coefficients determined by PCS as a function of concentration for dilute sols S3 (a), S4 (b), and S2 (c).

Measurements of D_T on sols of higher concentration show the effects of hydrodynamic interactions that lead to marked reductions in D_T (Figure 9). However, the onset of interaction sets in at considerably higher concentration for sol S4 (~0.15 g/mL) compared with sols of smaller particle size (~0.05 g/mL for S2). This feature may reflect a more extended range of hydrodynamic interactions in the sols of smaller particle size because of oligomers associated with the sol particles.

^{29}Si NMR Spectroscopy of Colloidal Silica. ^{29}Si NMR spectroscopy has been used extensively to study aqueous solutions of silicates and has provided detailed information on the types of polymeric species in solution (*3–5*). However, despite the power of the technique it has not been exploited previously to investigate colloidal silica. The usefulness of the technique arises from the successive shift of the ^{29}Si resonance to high field on replacement of Si–OH bonds in silicate species with siloxy bonds, Si–O–Si. Thus monomeric species are observed furthest downfield (Q^0) and other resonances are observed at intervals of ~10 ppm for end units (Q^1), middle units (Q^2), branching units (Q^3), and tetrafunctional units (Q^4). (Q refers to four possible coordination bonds; the superscript refers to the actual number.) From the relative intensities of the different

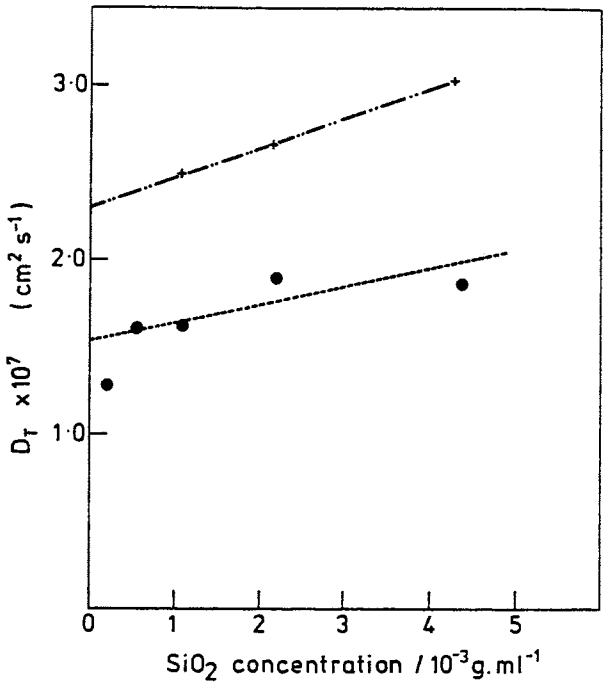

Figure 8. The variation of translational diffusion coefficients, D_T, measured by PCS with different sol concentrations for dilute samples of the dialyzed (+) and undialyzed (●) silica sol S1.

Table IV. Translational Diffusion Coefficients, D_T, and Hydrodynamic Radii, R_H, of Silica Sols at Infinite Dilution

Sol	$10^7 D_T$ (cm^2/s)	R_H (*nm*)
S1	1.5	16.5
S2	0.96	25.5
S3	2.2	11
S4	1.5	16.5
$S1^D$	2.3	9

resonances the relative proportions of the various structural entities can be derived.

^{29}Si NMR spectra of the four sols of different particle size (Figure 10) show three resonance peaks. The main intense resonance at −107 ppm can be assigned (*16*) to Q^4 units corresponding to four siloxy bridges. Those at −96 and −85 ppm are assigned to Q^3 and Q^4 (corresponding to silicon with respectively three and two siloxy bridges) units, respectively. As the

Table V. Proportions of Q^4, Q^3, and Q^2 Species in Silica Sols

Sol	*Concentration (% w/w)*	Q^4	Q^3	Q^2
S1	15	68	23	9
S2	15	76	20	4
S3	40	78	17	5
S4	50	86	13	1

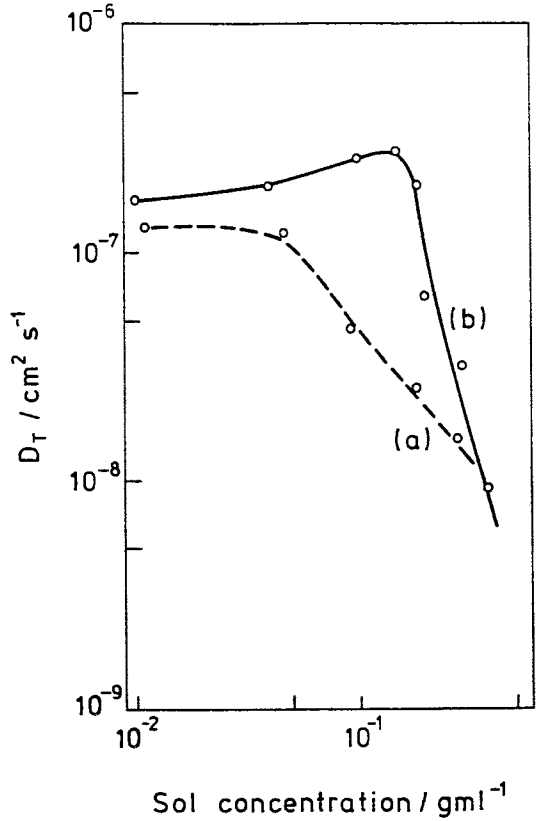

Figure 9. The effect of sol concentration on translational diffusion coefficients, D_T, determined by PCS for silica sols S2 (a) and S4 (b).

particle size decreases, the intensities of the two lower field peaks (−85 and −96 ppm) increase relative to the more prominent upfield resonance (−107 ppm). The relative proportions of these species can be derived form Gaussian fits to the peak profiles, and the results of such an analysis are given in Table V. More detailed interpretation and further details of these

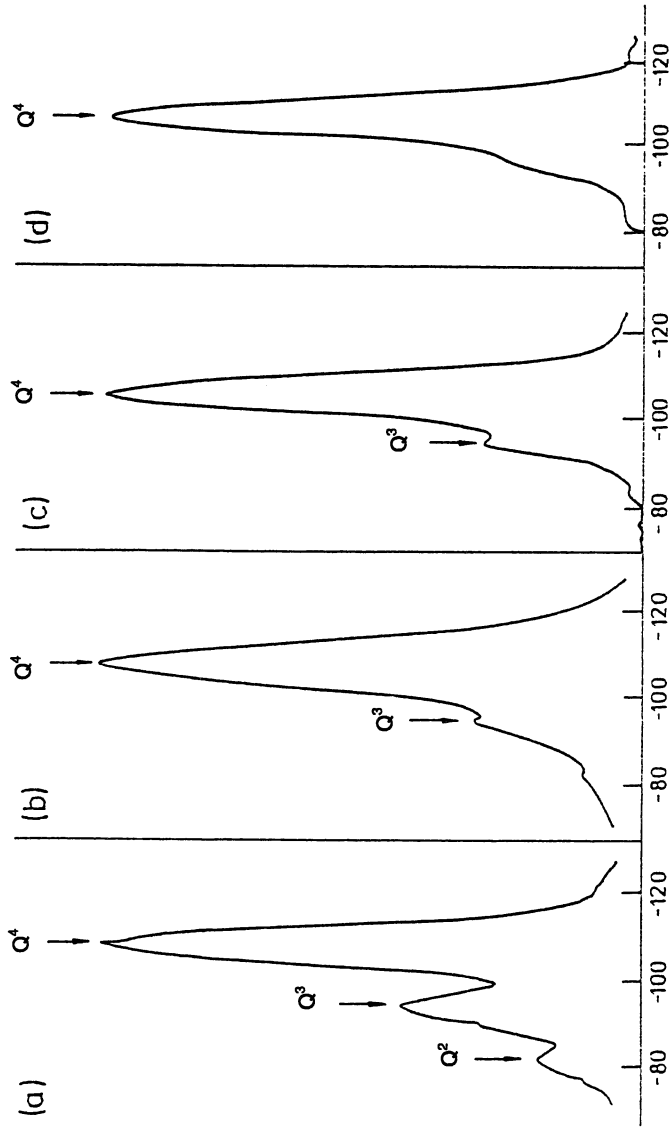

Figure 10. High-resolution ^{29}Si NMR spectra of silica colloids in water: (a) S1, (b) S2, (c) S3, (d) S4. The different chemical shifts (measured as parts per million with respect to $Si(CH_3)_4$) correspond to Si atoms in different environments: Q^4 to SiO_4^{4-} tetrahedra in a three-dimensional structure; Q^3 and Q^2 to Si atoms that are coordinated to one and two hydroxyl groups, respectively.

investigations will be reported elsewhere (*17*). However, the Q^4 resonance corresponds to the silica core of the sol particles, and the Q^3 and Q^2 components to polyhydroxy units, either bound to the silica surface or as free oligomers in solution. For the smallest particle size sol, S1, the high proportion (32%) of these hydroxylated species is far in excess of that corresponding to a simple hydroxylated plane surface. Thus these results are consistent with the association of oligomers at the sol surface, as indicated from PCS and ultracentrifuge investigations.

Conclusion

The experimental investigations reported here provided further insight into the mechanisms of formation and growth of silica sols in aqueous solution. For sols of very small particle size (~7 nm), colloidal particles coexist with a high proportion (>20%) of oligomeric species. These species are predominantly associated with the colloidal particle surface. After dialysis, however, these species may be partially released into solution. This process probably results from the reduction of ionic strength and the consequent increase in electrostatic repulsion between the negatively charged surface and the anionic oligomers. The relative proportion of oligomeric silica decreases as the size of the sol particles is increased. Particle growth may thus arise from the condensation of monomers and oligomers at the particle surface in accord with the mechanism proposed by Iler (*1*).

Furthermore, the particle core has a density consistent with amorphous silica. The adsorption of oligomers around the core of the particles has implications that may explain the high charge density and exceptional stability of silica sols (*9*). Enhanced stability may also arise from solvation forces. Such an interfacial structure has important consequences in both determining the mechanism and enhancing the capacity for sorption of other ionic species from solution.

Finally, the surface and pore structure of gels obtained after dehydrating sols may be affected by the presence of oligomeric silica. This effect will be particularly evident with sols of small particle size in which partial particle coalescence may occur, together with the generation of small micropores (<2 nm), as has been previously observed (*18*).

Acknowledgements

The work described was undertaken as part of the Underlying and Corporate Research Programme of the UKAEA. We acknowledge the access to neutron scattering facilities, provided at the ILL, Grenoble, France.

References

1. Iler, R. K. *The Chemistry of Silica;* Wiley: New York, 1979.
2. *See,* e.g., Brinker, C. J.; Scherer, G. W. *Sol–Gel Science;* Academic Press: New York, 1990.
3. Harris, R. K.; Knight, C. T. G.; Smith, D. N. *J. Chem. Soc. Chem. Commun.* **1980,** 726.
4. Arkakai, I.; Bradley, M.; Zerda, T. W.; Jones, J. *J. Phys. Chem.* **1985,** *89,* 4399.
5. Oriel, G.; Hench L. L. *J. Non-Cryst. Sol.* **1986,** *79,* 177.
6. Ramsay, J. D. F.; Avery, R. G.; Benest, L. *Faraday Discuss. Chem. Soc.* **1983,** *76,* 53.
7. Ramsay, J. D. F. *Chem. Soc. Rev.* **1986,** *15,* 335.
8. Schaefer, D. W.; Martin, J. E.; Wiltzius, P.; Cannell, D. S. *Phys. Rev. Lett.* **1984,** *52,* 2371.
9. Lyklema, J. *Croat. Chem. Acta* **1971,** *43,* 249.
10. Ramsay, J. D. F.; Booth, B. O. *J. Chem. Soc. Faraday Trans. I* **1983,** *79,* 173.
11. Penfold, J.; Ramsay, J. D. F. *J. Chem. Soc. Faraday Trans. I* **1985,** *81,* 117; Bunce, J.; Ramsay, J. D. F.; Penfold, J. *J. Chem. Soc. Faraday Trans. I* **1985,** *81,* 2845.
12. Avery, R. G.; Ramsay, J. D. F. *J. Colloid Interface Sci.* **1986,** *109,* 448.
13. Swanton, S. W., Ph.D. Thesis, Bristol University, Bristol, England, 1989.
14. Jacrot, B. *Rep. Prog. Phys.* **1976,** *39,* 911.
15. Klein, R; Hess, W. *Faraday Discuss. Chem. Soc.* **1983,** *76,* 137.
16. Sindorf, D. W.; Maciel, G. E. *J. Am. Chem. Soc.* **1980,** *102,* 7606.
17. Dobson, C. J.; Goberdhan, G. C.; Ramsay, J. D. F. unpublished.
18. Ramsay, J. D. F.; Wing, G. *J. Colloid Interface Sci.* **1991,** *141,* 475.

RECEIVED for review December 17, 1990. ACCEPTED revised manuscript February 25, 1992.

4

Synthesis and Characterization of Colloidal Model Particles Made from Organoalkoxysilanes

A. van Blaaderen and A. Vrij

Van't Hoff Laboratory, University of Utrecht, Padualaan 8, 3584 CH Utrecht, The Netherlands

Monodisperse colloidal silica spheres were prepared by hydrolysis and condensation of tetraethoxysilane (TES) in a mixture of water, ammonia, and a lower alcohol. These silica spheres were coated with the coupling agent 3-aminopropyltriethoxysilane (APS) in the reaction medium. A new colloidal model system that was prepared consisted of a stable dispersion of monodisperse, hybrid, organic–inorganic "silica" spheres. Particles were characterized by ^{13}C and ^{29}Si NMR spectroscopy, elemental analysis, transmission electron microscopy, and static and dynamic light scattering. The particles made from TES alone (with radii between 15 and 100 nm) consisted of partially condensed siloxane structures, which were approximately the same for all particle sizes. Thus, the siloxane structure did not reflect differences in the particle shape and surface roughness. The percentage of silicon atoms not bonded to four other silicons, but bonded to one hydroxyl or ethoxy group, was close to 30%. A few percent of silicons had only two siloxane bonds, and at least a few percent of the ethoxy groups were present in the core of the particles, having never been hydrolyzed. Thus, hydrolysis probably is the rate-determining step in base-catalyzed particle growth. Further, the particle radius could be altered only by addition of $LiNO_3$, if the salt was added to the reaction mixture at the start of the reaction. Thus, the ionic strength provides a new parameter to study the reaction mechanism. Its influence confirms that the particles form through a controlled aggregation process of homogeneously precipitating nuclei early in the reaction. Monodispersity and a smooth particle surface are achieved through subsequent monomer addition. The new parti-

0065–2393/94/0234–0083$09.62/0

cles prepared from a mixture of APS and TES contained, on a silicon basis, as much as 26% APS distributed through the particle interior.

MONODISPERSE COLLOIDAL SILICA SPHERES with various surface coatings are of considerable interest to many fields, such as ceramics, colloids, catalysis, chromatography, and glass preparation. We are interested in these particles for their use as a model colloid. Previous work (*1–9*) has shown that by using scattering techniques, much insight can be gained in the interparticle structure and dynamics of concentrated dispersions. To avoid, for example, multiple scattering, it is important to determine and change the chemical microstructure of the (single) colloidal particles. The surface coating determines the solvents in which the colloids can be dispersed and the kind of interactions between colloidal spheres. An understanding of the mechanisms responsible for particle formation and the coating of its surface is very important to tailor the scattering properties and particle interactions.

Through the hydrolysis and condensation of tetraalkoxysilanes in mixtures of ammonia, water, and alcohols, (uncoated) silica particles are easily prepared by using a method developed by Stöber et al. (*1*). The experimental procedure is very simple, but the mechanisms responsible for the formation and growth of the charge-stabilized silica spheres are not. A generally accepted scheme has not yet been presented. A tentative mechanism for the nucleation and growth is described in this chapter, based on an analysis of the final particle morphology and chemical microstructure. A description is also given of the use of the silane coupling agent 3-aminopropyltriethoxysilane (APS) to prepare model colloids.

APS is known for its stability in basic solutions (*10*). The amine functionality facilitates the coupling of other desired molecules to a particle. For these reasons, this alkoxide was chosen to coat the surface of the Stöber silica spheres. A simple procedure was followed, first described by Philipse and Vrij (*4*), who used other coupling agents. Badley et al. (*11*) also described the coupling of APS and other organosilanes to silica.

APS and tetraethoxysilane (TES) were also used in the synthesis of a new kind of monodisperse colloidal system. Spherical particles were made by starting from a mixture of the organoalkoxysilanes TES and APS. This procedure will probably be applicable to other mixtures of organoalkoxysilanes as well.

The microstructure and particle morphology (size, shape, and surface roughness) of the colloids were studied with ^{13}C and ^{29}Si NMR spectroscopy, elemental analysis, transmission electron microscopy, and static and dynamic light scattering.

To facilitate the interpretation and to place the proposed mechanism into perspective, a literature survey is presented. Relevant details concerning the base-catalyzed chemistry and characterization of alkoxysilanes by NMR spectroscopy and some of the proposed particle formation and growth theories are given.

Theory and Earlier Work

Reactions and Chemical Mechanisms. Alkoxysilanes in a mixture of water, ammonia, and a lower alcohol may undergo many different reactions. Reactions between the different silane intermediates can be represented as follows:

$$-\overset{|}{\underset{|}{\text{Si}}}\text{OR} + \text{HOR}' \rightleftharpoons -\overset{|}{\underset{|}{\text{Si}}}\text{OR}' + \text{HOR} \qquad (1)$$

$$-\overset{|}{\underset{|}{\text{Si}}}\text{OR} + \text{HO}\overset{|}{\underset{|}{\text{Si}}} \rightleftharpoons -\overset{|}{\underset{|}{\text{Si}}}\text{O}\overset{|}{\underset{|}{\text{Si}}}- + \text{HOR} \qquad (2)$$

Here R and R′ stand for a hydrogen atom or an alkoxy group (methoxy, ethoxy, or propoxy). The other atoms bonded to silicon that are not depicted can either be carbon (in the organoalkoxides), or oxygen (belonging to a silanol and alkoxy group or a siloxane bond). The breaking of a C–Si bond and direct ester exchange between the alkoxides are not considered possible (*12*). We will discuss only base-catalyzed reactions.

The reactions in equation 1 constitute ester exchange, hydrolysis, and their reversals. In the base-catalyzed case these reactions proceed through a nucleophilic attack on the silicon atom, resulting in a pentacoordinate transition state (*12–15*).

We first consider the hydrolysis and the influence on its rate by some reaction conditions. OH^- is acting as the nucleophile; an increase in the concentration of this catalyst will increase the reaction rate. OH^- is produced by reaction of NH_3 with H_2O. The rate increases almost linearly with $[NH_3]$ (*16*). As expected, the hydrolysis appears to be first order in TES (*16, 17*). The dependence of the rate constant on $[H_2O]$ is even higher, according to Harris et al. (*18*), than the dependence on $[NH_3]$: $[H_2O]^{1.5}$. The effect on the reaction rate of changing the solvent alcohol is quite complex, and further experimental work and a theoretical explanation are needed (*15–18*).

The influence of a substituent on the silicon atom can be derived from its ability to withdraw electrons or its steric hindrance to an attacking nucleophile. For these reasons, the lower alkoxides are hydrolyzed faster than the higher and branched alcohol derivatives. Hydrolysis of a given alkoxide proceeds in successive steps. Because the alkoxy group is less

electron-withdrawing and more bulky than a hydroxy group, each successive loss of an alkoxy group is accompanied by an increase in the rate of loss of the next.

The base-catalyzed condensation reactions in equation 2 also take place through a base-catalyzed nucleophilic attack on silicon resulting in a pentavalent transition complex (*12, 15, 19, 20*). The influence of [H_2O] and [NH_3] on the reaction rate and the type of alcohol used is almost the same as for the hydrolysis (*12, 18*).

An important question to be explained by the chemical mechanism is why base catalysis often leads to condensed structures. In 1950, Aelion et al. (*13*) pointed out that the condensation reaction in base-catalyzed systems was faster than with acid catalysis and that the microstructure of the final product was different. Many of these facts are due to the opposite effects of, for example, substituents, on silicon on the stabilization of the transition state in base- and acid-catalyzed reactions (*15*). For the base-catalyzed condensation reaction to take place, a silicon atom has to be attacked by a deprotonated silanol oxygen: the nucleophile. The acidity of the silanol proton increases as the basicity of the other groups bonded to the silicon decreases. This feature implies that polysilicic acid is a stronger acid than $Si(OH)_4$ (*20*). Therefore, monomers react preferentially with higher polymerized species.

Under certain conditions (for instance, high [TES] or low water concentrations), the reaction between not fully hydrolyzed species must also be considered. In this case the condensation and hydrolysis reactions can occur in one step: After attack of a silanolate ion, the transition state can subsequently lose an alkoxy group. Alkoxy groups that end up on a highly condensed unit are then much more difficult to hydrolyze because of steric constraints.

The replacement of an alkoxy group causes an inductive effect. Binding of an organofunctional group through a C–Si bond decreases both the hydrolysis rate and the condensation rate through the same mechanism. The less electronegative carbon makes a nucleophilic attack on silicon more difficult.

This reasoning also applies to APS: Compared to TES, base-catalyzed hydrolysis and condensation are slower for APS. However, in some respects this molecule does not behave like other silane coupling agents. Solutions of APS in water are quite stable at basic pH values, whereas solutions of other coupling agents rapidly form insoluble precipitates under the same conditions (*21*). This difference in behavior is explained by Plueddemann (*21*) by assuming that the hydrolyzed APS forms a six- or five-membered chelate ring. The six-membered ring is thought to form by binding of the amine with a silanolate ion and the pentacoordinate complex by binding between nitrogen and silicon. No direct evidence has been found for one of these structures. Most likely, one of them exists, because

compounds with one CH_2 group more or less in the aliphatic chain do not display the increased stability of APS and rapidly form precipitates in water. Moreover, these precipitates remained insoluble after they were acidified, a result indicating that the insolubility is not caused by the amine portion (*15*).

Nucleation and Growth: Results from the Literature. Before discussing different mechanisms of nucleation and growth that have appeared in the literature, we first present some general observations about the hundreds of silica sols that have been described (*1*, *2*, *4–7*, *16–18*, *22–28*) and synthesized according to Stöber.

Most of the work was done with the alkoxide TES and the alcohol ethanol as solvent. Lowering the temperature always results in larger particles. Sometimes the radius can become 4 times larger by lowering the temperature 30 °C (*26*). In the range of TES concentrations in which particles seem to be stable, larger particles generally tend to be more monodisperse. Standard deviations in particle size of only 2% have been observed.

Mostly, particles are larger when synthesized from higher concentrations of TES, although the increase in radius is quite small, and sometimes the opposite trend is described (*2*). After the reactants are mixed, the turbidity of the solution suddenly rises after a certain induction time and then slowly increases to its final value. The induction time is closely related to the total time of the particle growth. If the particles reach their final radius in a short time, the induction period is also short.

Increasing [H_2O] and [NH_3] results in faster reactions and initially, at low concentrations, in larger radii. However, both H_2O and NH_3 show a concentration for which a maximum radius is achieved. Increasing the concentration any further still gives shorter reaction times, but the radius decreases. Near these maxima the sols sometimes flocculate and are not so monodisperse. This instability is also found in the limits of high TES or high NH_3 concentrations. Under some conditions, particles with a grainy surface are observed.

Increasing the length of the solvent *n*-alcohol results in larger particles (*1*, *16–18*, *22*). Densities of the resulting homogeneous particles were reported in the range 1.9–2.1 g/mL, and the refractive index was found close to 1.45 (*2*, *3*, *26*).

Matsoukas and Gulari (*17*) convincingly showed that the particle mass grows exponentially with the same time constant that describes the first-order hydrolysis of TES. They used the plasma lines in a Raman spectroscopy experiment to observe not only the intensities of the Si–O–Et and Et–OH bands, but at the same time used the light scattering of the particles to follow their growth. The induction period found in the scattering experiments was not found for the hydrolysis reaction.

Subsequently, Matsoukas and Gulari (22) worked out a model describing the nucleation and growth in more detail. In a purely kinetic theory, they formulated a monomer addition model in the presence of a rate-determining first-order initiation step and investigated the effect of different particle growth models upon the final particle size and polydispersity. In their model the dynamic competition between nucleation and growth is controlled by the hydrolysis that releases the active monomer. This monomer is produced in a slow hydrolysis reaction that inhibits nucleation and, therefore, promotes growth of large particles.

In the model, two limits are considered: a reaction-limited growth, which is characterized by a strong size dependence of the growth rate, and diffusion-limited growth, with much weaker size dependence. These limits refer only to the bonding between a particle and a monomer; the overall rate is still governed by the hydrolysis.

The actual rate equations are based on a succession of irreversible steps. Hydrolysis is modeled as first order in TES and produces the active monomer. These monomers can react with another monomer forming the (second-order) nucleation step, or can react with an already higher condensed species. All the subsequent addition steps are considered elementary and are described with different rate constants k_i (with i the number of monomers that formed the particle). Generally, k_i depends on the radius (R) of the particle. The limit that k_i is independent of the particle size was assumed to represent a reaction-limited growth (the correct dependence is $k_i \sim R$), and k_i proportional to the particle volume (R^3) was assumed to represent diffusion-limited growth (the correct dependence is $k_i \sim R^2$). Under these assumptions, Matsoukas and Gulari (22) derived for the final particle radius (R) the following expressions:

$$R \sim (k_p c/k_h)^{1/9} \qquad \text{diffusion-limited growth} \qquad (3)$$

$$R \sim (k_p c/k_h)^{1/6} \qquad \text{reaction-limited growth} \qquad (4)$$

where k_p and k_h are the polymerization and hydrolysis rate constants, respectively, and c is the starting TES concentration.

Using the correct dependencies of the rate constants k_i on the particle size, they also obtained expressions relating the final polydispersity to the final mean particle radius $<R>$:

$$\sigma^2 \sim <R>^{-3} \qquad \text{diffusion-limited growth} \qquad (5)$$

$$\sigma^2 \sim <R>^{-2} \qquad \text{reaction-limited growth} \qquad (6)$$

In the experimental part the relations between equations 3 and 6 were tested; the data were best described with a reaction-limited growth (in the presence of a rate-limiting hydrolysis of the monomers). The increase in

particle size with increasing ammonia concentration was rationalized by stating that, although this effect resulted in an increase in k_h, k_p would have to increase even further.

Bogush and co-workers (*24*, *26*, *27*) investigated the Stöber synthesis using electron microscopy, conductivity measurements, and the (small) change in reaction medium volume. They concluded that all the TES hydrolyzes completely in the first few minutes and that the Stöber silica particles are formed through a size-dependent, controlled, coagulative nucleation and growth mechanism. They argued that nucleation from the extremely supersaturated solutions continued almost to the point at which the particles reached their final size. In the beginning of the reaction, small unstable particles aggregate until a critical size is reached at which the probability of two particles of equal size sticking together becomes negligible. Homogeneous nucleation still continues, and the freshly formed small particles are taken up by the large stable particles that now remain constant in number. Classical nucleation expressions were used to estimate nucleation rates per unit volume (*29*, *30*). Their proposed size-dependent nucleation–aggregation mechanism is analogous to a similar model developed to explain the emulsion polymerization of styrene (*31*).

Philipse (*5*) also assumed that fast hydrolysis created an active monomer bulk. He studied the growth of silica nuclei, already synthesized, after extra addition of different amounts of TES with static light scattering. To explain his growth curves (radius versus time), he used a diffusion-controlled particle growth in a finite bulk of monomers or subparticles. The model contained equations from classical flocculation theories. It takes into account the exhaustion of the monomer bulk and the retarding influence of an (unscreened) electrostatic repulsion between growing spheres and monomers.

Harris and co-workers (*16*, *18*) concluded that the Stöber system obeyed La Mer's homogeneous nucleation and growth model (*32*). In this scheme the slow hydrolysis of TES builds up the critical concentration of silicic acid required to form nuclei. The short nucleation phase then lowers the concentration of silicic acid below its critical value, followed by growth of monodisperse silica particles. Monodispersity is always achieved if the nucleation phase is short enough, whether the growth process is diffusion- or reaction-controlled (*33*). They found that under conditions where the amount of silicic acid remained relatively high (that is, a few times the equilibrium value) during an important part of the reaction, the resulting sol was polydisperse.

Schaefer and Keefer (*14*, *19*, *34*, *35*) used a model developed by Eden to describe the growth of cell colonies to explain their X-ray scattering experiments. They used this simple model of nucleation and chemical limited growth to mimic the growth of silica structures in TES solutions (1

M) with a relatively low water concentration (1–4 M) and with very little catalyst, 0.01 M NH_3.

In their version of the Eden model, one starts with a seed, that is, one site on a two-dimensional lattice, and randomly chooses and occupies one of the four neighboring sites. The next growth site is picked from the resulting six neighboring sites, etc. This method results in spherical particles with uniform interiors and smooth surfaces relative to their radii.

The fact that the interior becomes uniform seems an artifact, because growth is even allowed in free places inside a particle. The formation of such regions in three-dimensional growth is very unlikely, so allowing this kind of growth inside a particle in the two-dimensional model makes comparison with three-dimensional studies more realistic.

The effects on the particle shape of particle formation from partially hydrolyzed monomers were also investigated. By choosing certain mixtures of monomers, Schaefer and Keefer generated all kinds of particle morphologies, from porous clusters to surface and mass fractals.

Silicon Environments and Solid-State NMR Spectroscopy. Magic-angle spinning (MAS) and high-power proton decoupling (HPD) make it possible in solid-state NMR spectroscopy to obtain high-resolution ^{13}C and ^{29}Si spectra. These techniques average the chemical-shift anisotropy and dipolar interactions that otherwise would cause very broad lines. In a liquid this averaging is accomplished by the rapid thermal motions of the molecules in the magnetic field.

The NMR solid-state technique of cross-polarization (CP) consists of a transfer of magnetization from ^{1}H nuclei to ^{13}C or ^{29}Si nuclei through dipolar interactions. In this way, selective detection of only those ^{13}C and ^{29}Si nuclei that are near protons becomes possible. For silica consisting mainly of SiO_2, this technique entails a selective detection of only those nuclei close to the surface where OH groups and other proton-containing species are present. In addition to this selectivity, CP enhances the sensitivity of the NMR experiment and shortens the necessary delay between acquisitions of successive transitions to a few seconds. For the ^{29}Si nucleus that can have spin-lattice relaxation times (T_1) of minutes, this enhanced sensitivity can be important.

Through siloxane bonds, a silicon atom can be bonded to a maximum of four other silicon nuclei. If a ^{29}Si nucleus is bonded to four other silicon atoms, the chemical shift of this so-called Q^4 species lies around −110 ppm. The Q^4 representation comes from the old siliconen-chemistry (*12*); the Q stands for quaternary (that is, having the possibility of forming four siloxane bonds). The number 4 gives the actual number of siloxane bonds in which the nucleus is participating (Figure 1). For every siloxane bond less, a shift of about 10 ppm occurs. Therefore, Q^2 has a chemical shift around $-110 + 2 \times 10 = -90$ ppm.

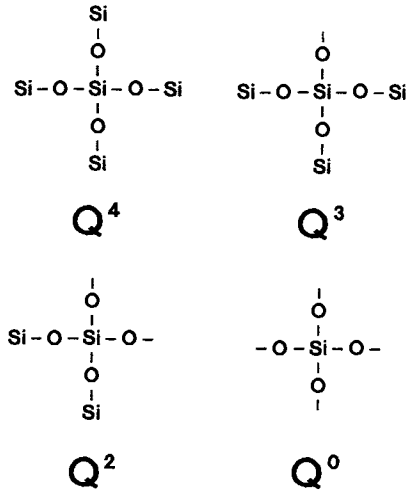

Figure 1. Silicon environments. Groups not depicted are alkoxy or silanol.

The exchange of one Si–O bond with a Si–C bond makes a significant difference in chemical shift. For APS this exchange results in a shift +40 ppm. The organosilane is now designated T^0 to T^3 (T from ternary).

Clearly these features make silicon NMR spectroscopy a valuable technique in examining the microstructure of silica and its derivatives (*36–40*). However, almost no difference in chemical shift is seen between a silicon atom that has an alkoxy and one that has a hydroxy group bonded to it. Carbon solid-state NMR spectroscopy is useful to determine the presence of alkoxy groups and to detect the carbon atoms of a coupling agent if present.

Experimental Details

Materials and Particle Preparation. Methanol (Baker), ethanol (Merck), and 1-propanol (Baker) were of analytic reagent quality. Absolute technical grade ethanol (Nedalco) was used only for the large-scale (9 L) synthesis of A1. Solvents, tetraethoxysilane (Fluka, purum grade) and γ-aminopropyltriethoxysilane (Janssen) were freshly distilled before each synthesis. Ammonium hydroxide (Merck, 25%) was of analytical reagent quality and contained 14.0 mol/L NH_3 as indicated by titration. The silicas Ludox AS40 and Compol were kindly provided by DuPont and Fujimi.

Alcosols, silica particles dispersed in the reaction medium, were synthesized at 20 °C according to the method of Stöber et al. (*1*) and the detailed description given by Van Helden et al. (*2*). Glassware was cleaned with 6% hydrogen fluoride and rinsed with deionized water and absolute ethanol. Ammonium hydroxide, ethanol, and, if necessary, deionized water were mixed in a reaction vessel and placed in a constant-temperature bath. After allowing the temperature to come to equilibrium, the TES was added under vigorous stirring. After a few minutes the

reaction was continued using a slow stirring speed. The total amount of alcosol varied between 0.4 and 9 L. Concentrations of reactants used are given in Table I; in their calculation, volume contraction was assumed to be absent.

Table I. Reactant Concentrations

System	*[TES] (M)*	*[APS] (M)*	*[H_2O] (M)*	*[NH_3] (M)*	*Solvent*
A1	0.155		0.855	0.318	ethanol
A1APS[a]		0.477	0.855	0.318	ethanol
A2	0.0119		5.51	0.682	ethanol
A3	0.17		1.65	0.68	ethanol
A4	0.167		1.58	0.512	ethanol
A5[b]	0.159		3.01	1.12	ethanol
A5APS[a]		0.205	3.01	1.12	ethanol
A6	0.160		2.65	0.986	ethanol
A7[c]	0.160		2.65	0.986	eth–$LiNO_3$
A8[c]	0.160		2.65	0.986	eth–$LiNO_3$
Mix1	0.0809	0.0774	2.34	0.870	ethanol
M1	0.161		2.50	0.928	methanol
P1	0.178		1.03	0.383	propanol

[a]Alcosol taken as reaction medium for the coating reaction.
[b]Reaction temperature was 25 °C; all other reactions were at 20 °C.
[c][$LiNO_3$] = 1.0 mM. For A8 the $LiNO_3$ was added before TES, and A7 was added 15 min after TES.

For the coating reactions with APS (Table I), a procedure similar to that described by Philipse and Vrij (*4*) was applied. Philipse and Vrij used the coupling agent 3-methacryloxypropyltrimethoxysilane to coat colloidal silica. Because an alcosol was used, the actual concentrations of water as listed in Table I have to be corrected for the (not exactly known) amount consumed in the hydrolysis–condensation reactions. After addition of the APS to 400 mL of alcosol, the solution was stirred slowly for an hour. After 2 h of refluxing, 250 mL was distilled slowly for an hour. The remaining unreacted APS was removed in four centrifugation redispersion steps. The ultracentrifuge used was from Beckmann (L5-50B), and the sediment was redispersed each time in absolute ethanol.

Silica spheres with APS distributed in the particle interior were prepared by adding APS (Table I) first to the reaction mixture. Subsequently an equal volume of TES was added within 1 min. Free APS was again separated from the particles by centrifugation and redispersing in ethanol. Particle densities were measured by drying, under dry nitrogen for 24 h at 100 °C, a known volume of a concentrated dispersion in absolute ethanol and weighing the residue.

Alcosols are referred to in this chapter as A*x*, with *x* being a numeral. The A is replaced by a P or a M if the alcohol used was not ethanol but 1-propanol or methanol, respectively (Table I). Coated particles are designated A*x*APS and A*x*S; the last code stands for a coating with stearyl alcohol according to the procedure developed by Van Helden et al. (*2*). *Mix* denotes particles prepared from a mixture of the alkoxides TES and APS. Some of these systems have been used in earlier work with different names, so some translation is necessary. A3S is designated in several investigations as SJ9 (*9*). SM2, known here as A1, is described by Penders and Vrij (*41*). The Ludox and Compol systems are described elsewhere by Duits et al. (*42*).

Light Scattering. Light-scattering measurements were made at 25 ± 0.1 °C on dust-free, very dilute dispersions in ethanol. The dispersions were made by adding one drop of alcosol to 25 mL of ethanol followed by filtration through Millipore filters (the pore was typically several particle diameters). Cuvets with a diameter of 2 cm were cleaned by continuously rinsing with freshly distilled acetone.

Static light scattering (SLS) was performed with a Fica-50 photometer using vertically polarized light (λ = 436 and 546 nm). A correction was made for scattering of the solvent. The Rayleigh–Gans–Debye approximation could be used, and the particles were assumed to be spherical and to have a homogeneous refractive index. Under these assumptions, the particle radius (R_0) was obtained from a fit of the calculated form factor to the scattered intensity as a function of the scattering angle θ ($20° \leq \theta \leq 150°$). Intensities at low angles are sensitive to dust or clustered particles (*2*); no irregularities were found, a result indicating monodisperse, nonclustered sols.

Dynamic light scattering (DLS) results were obtained with an argon ion laser (Spectra Physics Series 2000) operating at 488.0 and 514.5 nm. Autocorrelation functions were measured with a Malvern Multibit K7025 128-point correlator. Diffusion coefficients were obtained from a second-order cumulant fit (*43*, *44*) by using autocorrelation functions obtained from six scattering angles between 35° and 145°. From the diffusion coefficient, a hydrodynamic radius R_h was calculated by using the Stokes–Einstein relation. Except for dispersion A1, the normalized second cumulant yielded values smaller than ~0.05; the value for A1 was around 0.12. More information can be found elsewhere about the procedures and equipment of SLS (*3*, *6*) and DLS (*45*, *46*).

Elemental Analysis. Elemental analysis was carried out by Elemental Microanalysis Limited (Devon, U.K.). Prior to shipping, the samples were dried for 24 h at 100 °C under nitrogen; before the measurements were made, they were dried again for 3 h under the same conditions.

Electron Microscopy. Transmission electron micrographs were made by dipping copper 400-mesh carrier grids in a dilute dispersion. The grids were covered with carbon-coated Formvar films, and the photographs were made of particles on the film. Philips EM301 and Philips CM10 transmission electron microscopes were used, with the magnification calibrated with a diffraction grating.

Some of the particles were studied after supercritical point drying. The particles were dispersed in acetone by several centrifugation steps (45,000 × *g*). In a critical point dryer (Balzers Union, CPD 020), the carbon-coated grids and the dispersion in acetone were placed. Under pressure, the acetone was exchanged against liquid CO_2; after increasing the temperature and passing the critical point, the particles adsorbed on the film were supercritically dried.

Particle radii of 500–2000 particles were measured with an interactive image analysis system (IBAS). From these data, a number-averaged particle radius $\langle R \rangle$ and a standard deviation σ defined by:

$$\sigma = \left[\frac{\langle R^2 \rangle - \langle R \rangle^2}{\langle R \rangle^2} \right]^{1/2} \tag{7}$$

were determined.

NMR Spectroscopy. High-resolution solid-state NMR spectra were measured at room temperature on a Bruker AM 500 spectrometer (silicon frequency 99.4 MHz and carbon, 125.7 MHz) equipped with a Bruker solid-state accessory. Spectra were obtained with a broad-band probehead with a 7-mm double air-bearing magic-angle spinning (MAS) assembly. Spinning speeds around 4000 Hz were employed. The 90° pulse lengths for the nuclei ^{13}C, ^{29}Si, and ^{1}H were around 5.5 μs. The spectra that were obtained with cross-polarization had contact times between 0.5 and 2 ms for carbon and between 0.5 and 6 ms for silicon; pulse sequences were repeated after 4s. The number of accumulated free induction decays (FIDs) per spectrum ranged between 200 and 4000, depending on the system being investigated.

Quantitative silicon spectra were obtained by using 90° ^{29}Si pulses; it was not necessary to use high-power proton decoupling. Even at the high magnetic field used, the relatively small chemical-shift anisotropy and dipolar coupling with protons could be removed completely by MAS alone. Because, for some samples, the Q^4 silicon atoms had spin–lattice relaxation times of about 90 s, the time delay between 90° pulses was chosen as long as 400 s. Typically, 200 FIDs were accumulated. Deconvolution of the spectra was performed by manually adjusting the height, width, and frequency of the Gaussian line shapes to obtain the best visual fit.

The samples used for NMR spectroscopy were freeze-dried to prevent any reaction during the drying process. Adamantane and the trimethylsilyl ester of double four-ring octameric silicate, Q^8M^8 were used to optimize experimental parameters and as external secondary (relative to TMS) chemical-shift references for ^{13}C and ^{29}Si, respectively. Both the T_1 measurements and a discussion on the use of ^{29}Si NMR spectroscopy for quantitative measurements will be described elsewhere (*47*).

Results and Discussion

In this section, experimental results obtained with several different experimental techniques and measured on several different colloidal silica dispersions are described and discussed. The ultimate goal of the investigations is the ability to synthesize stable, monodisperse colloidal model spheres from organoalkoxysilanes with different chemical compositions and surface properties (*47–52*).

The first step was the synthesis of several colloidal systems with different radii from TES alone (A1–A6), and comparison of these particles with commercially available systems that were prepared in a different way, such as Ludox and Compol (*20*). The stabilities of the sol and the radii were probed with static and dynamic light scattering (SLS and DLS, respectively) because these techniques are sensitive to particle clustering. The polydispersity in the particle size, particle shape, and surface roughness (all these particle properties are further referred to as the particle morphology) were investigated with transmission electron microscopy (TEM). The chemical microstructure of the particles or, more precisely, the siloxane structure of the final particles and the presence of alkoxy groups were investigated with solid-state silicon and carbon NMR,

combined with elemental analysis. To obtain more information on the particle formation mechanism, two colloidal systems were made by using a different alcohol as solvent (M1 and P1), and two systems were made after addition of $LiNO_3$ to change the ionic strength (A7 and A8).

The second step consisted of the coating of several "Stöber" silica particles with APS and the synthesis of a new kind of particles from a mixture of APS and TES. The colloidal dispersions obtained were also characterized by the techniques just mentioned.

Particle Morphology (SLS, DLS, and TEM). In this section the results of the "Stöber" silica particles are presented, followed by the Ludox and Compol particles, and finally the particles made with APS. Then, the results relevant to a tentative formation and growth model are discussed.

All the synthesized alcosols except M1 remained stable for months, as indicated by light scattering. M1 flocculated 2 weeks after the synthesis but did not show any sign of instability directly after the reaction.

The general trends on the dependence of the final particle radius on the concentrations of NH_3 and water, on the alcohol used as solvent, and on the temperature can be found in Tables I and II. Increasing the concentrations of NH_3 and water results in larger radii (compare for example, A1, A4, and A5). This effect is no longer true for very high concentrations of water (A2). Increasing the temperature decreased the radius (compare A5 and A6). Going from methanol to propanol increases the radius (compare M1, A1, and P1).

An interesting new result is the strong dependence of the radius on the ionic strength if this is increased *before* the addition of TES (A6, A7, and A8, Tables I and II). $LiNO_3$ was chosen to change the ionic strength because it dissociates completely in this concentration range (*53*). The flocculation concentration of the sol A6 was 5 mM of $LiNO_3$.

The radii R_o and R_h as obtained with SLS and DLS, respectively, show reasonable-to-good agreement (Table II). The small differences and the small corrections that can be made if the polydispersity is taken into account are discussed in more detail elsewhere (*9*, *49*). The differences between the light-scattering radii and the radii as obtained with TEM are not negligible and cannot be explained by the differences in the averages that are determined with the different experimental techniques (*2*, *9*). As was suggested by Van Helden et al. (*2*) we attribute these differences to radiation damage that causes the particles to shrink somewhat. (The drying process does not influence the radius determined with TEM, because no differences were observed between normally and supercritically dried samples.)

Despite the fact that the absolute radii are probably too small, the polydispersities determined with TEM are correct. As is known from the

Table II. Radii According to Transmission Electron Microscopy and Static and Dynamic Light Scattering

System	TEM[a] (nm)	SLS (nm)	DLS (nm)
A1	9.01 (20%)		9 ± 2
A1APS	9.15 (20%)		14 ± 3
A2	50.2 (150%)		
A3S	30.9 (13%)	39.6 ± 0.5	38.5 ± 0.5
A4	31.2 (13%)	40.2 ± 0.5	36.6 ± 1.6
A5	62.4 (11%)	71.5 ± 0.4	72.1 ± 1.2
A5APS	66.1 (11%)	73.6 ± 0.5	80 ± 3
A6	89.4 (6%)	107.2 ± 0.3	108.1 ± 0.7
A7	93.2 (8%)	109.4 ± 0.4	
A8	154.3 (8%)	179.3 ± 0.4	
Mix1	92.2 (11%)	128 ± 2	118 ± 3
M1	18.2 (16%)	26.1 ± 0.9	30 ± 2
P1	24.2 (12%)	33.1 ± 0.5	35.1 ± 1.3
Ludox	11.1 (20%)	17.5 ± 0.3	20.8 ± 0.5
Compol	50.5 (16%)		

[a]The number in parentheses is the relative standard deviation.

literature (*1*, *2*, *26*), the polydispersities decrease as the mean radius increases. The only exception is A2, but this system was made from a very low concentration of TES (Table I).

The appearance of "Stöber" silica particles may depend strongly on the conditions under which they were made (*2*, *4–7*, *24–27*). Particles have been described as being irregular, roughly spherical, spherical, and large, flocculated, and fused structures (*28*). All the different types of morphology can be seen in the electron micrographs of the various alcosols shown in Figure 2, except for the flocculated structures. The irregularly shaped particles were not deformed in any way by capillary forces (*20*), because some samples (A1 and A4) were supercritically dried, a condition that eliminates the effects of the surface tension. Probably because of the high speed of centrifugation needed to settle these small particles, a fraction of them appeared to be clustered after redispersing in acetone. However, the amount of separately laying particles (Figure 2a) was sufficient to clearly demonstrate that both the form and radius were the same when compared with a sample of A1 that was not supercritically dried. Figure 2e shows another highly magnified supercritically dried particle (A4). The particle shown in Figure 2e had the characteristics of particles that are smaller than ~70-nm radius and are synthesized from concentrations of TES around 0.17 M. These smaller "Stöber" particles are only roughly spherical and possess a grainy irregular surface (Figure 2d). However, the particles A2 prepared from a low concentration of TES and a high concentration of

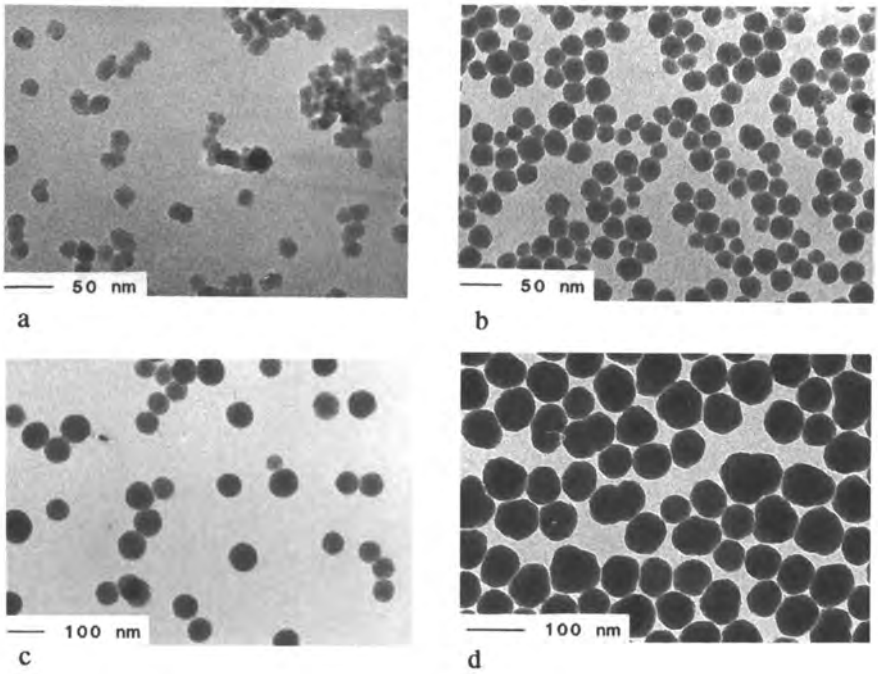

Figure 2. Transmission electron micrographs. Part a: A1, <R> = 9.01 nm (20%), supercritically dried. Part b: Ludox, <R> = 11.1 nm (20%). Part c: A2, <R> = 50.2 nm (150%). Part d: A3S, <R> = 30.9 nm (13%). *Continued on next page.*

water (Table I) are small, but almost perfect spheres with very smooth surfaces. Only the polydispersity is very high.

In Figure 2g a typical larger Stöber particle (A6) is shown. These particles are smooth and almost perfect spheres. Comparing the shape of the Ludox particles (Figure 2b) and the Compol particles (Figure 2f) with the Stöber particles of about the same size (Figure 2a and 2d) shows only small differences. The particles not synthesized from TES are slightly more spherical, and the surfaces are somewhat less rough.

The micrographs of the APS-coated particles were not different from the uncoated spheres and are therefore not shown. In Figure 2h the particles Mix1 are shown. Considering the amount of APS that is part of these particles, it is amazing how spherical and monodisperse these particles are. Clearly, all the organic groups (disrupting the siloxane structure) inside the particles do not influence the final particle shape. When compared with A6, they appear only slightly rougher. The difference in density between these two systems is considerable and is visible in the micrographs. The density of Mix1 is 1.51 g/mL, and that of A6 is 2.08 g/mL (*50*).

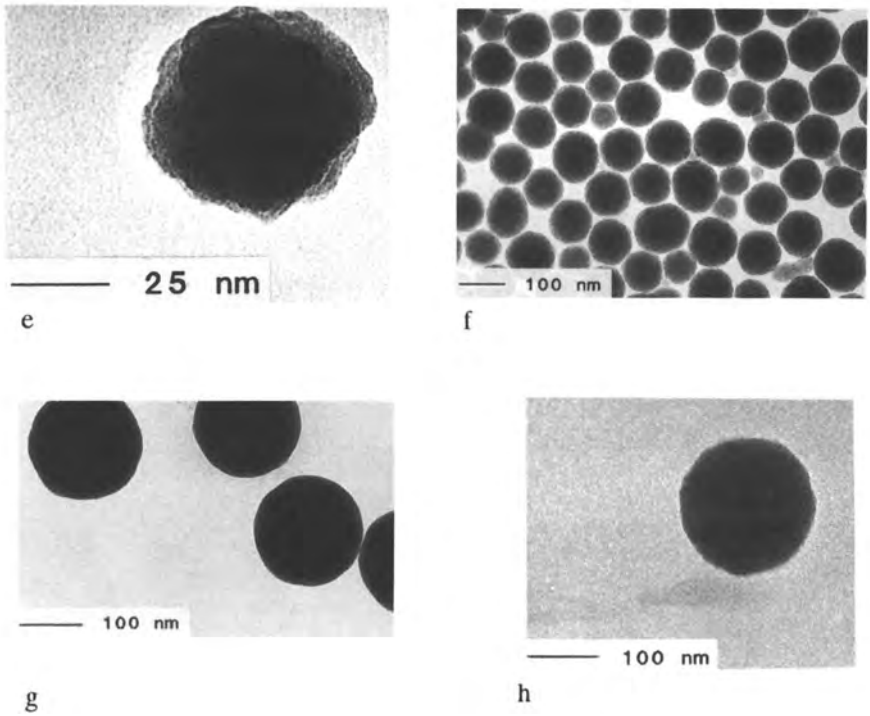

Figure 2.—Continued. Transmission electron micrographs. Part g: A6, <R> = 89.4 nm (7%). Part h: Mix 1, <R> = 92.2 nm (11%).

Particle Microstructure (NMR Spectroscopy and Elemental Analysis). The ^{29}Si CP NMR spectra were much easier to obtain than the direct excitation spectra, because of the long spin–lattice relaxation time of the silicon nuclei. Nevertheless, direct excitation was used to obtain the quantitative results of the siloxane structure, because not all Q^4 nuclei were detected with CP (Figure 3 and Table III) (*47*).

Surprisingly, all the quantitative spectra of the alcosol particles looked similar. As is also demonstrated in Table III, the siloxane structure of all the Stöber silica spheres is more or less constant and independent of the particle size and thus the reaction conditions. Even the coated stearylsilica particle A3S is no exception, despite the 3 h at 200 °C necessary for the coating. Thus, the differences mentioned in the previous section in the particle morphology are not correlated with the siloxane structure.

The colloidal particles Ludox and Compol consist of a more condensed silica structure (Table III). As mentioned, CP detects only those nuclei that have dipolar interactions with protons. Because of the condensed structure, a significant number of Q^4 silicon nuclei is too far away from protons and is not detected in a CP experiment (contrary to Q^4 nuclei in the alcosol

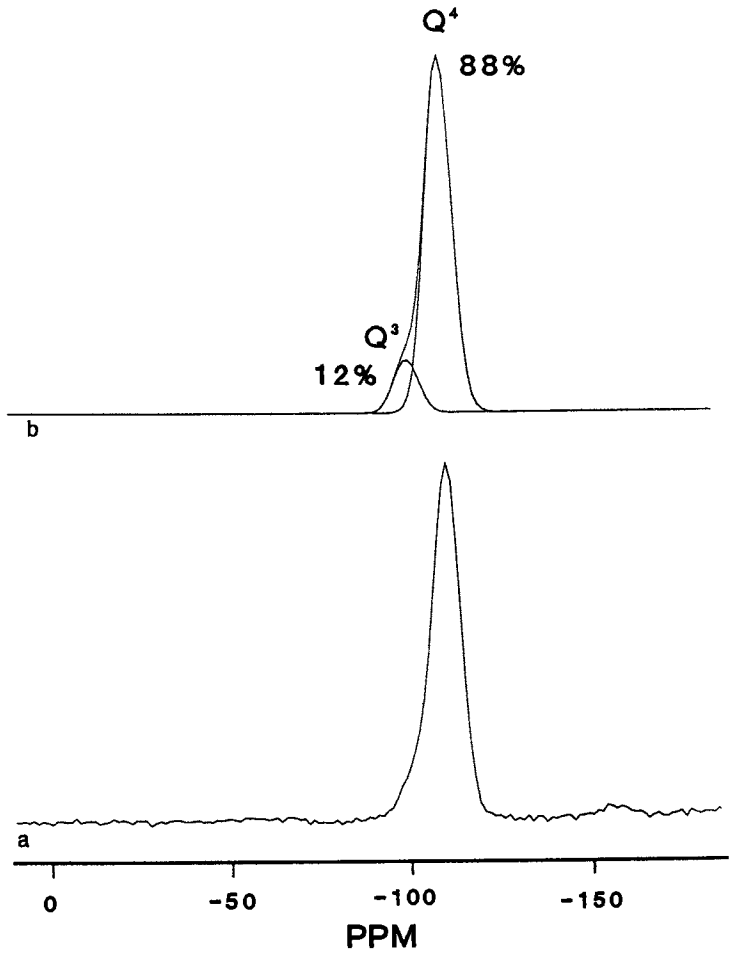

Figure 3. ^{29}Si NMR spectra of Compol. Part a: Direct polarization MAS, 300 accumulations, and repetition time of 400 s. Part b: Deconvoluted spectrum using Gaussian line shape. Continued on next page.

particles). An example of this effect can be seen in Figure 3a and 3c of the Compol particles. The spectrum in Figure 3a was obtained by using direct polarization through 90° pulses, MAS, and repetition times of 400 s. CP–MAS was used for Figure 3c. The CP spectrum, Figure 3c, contains more Q^3 signal than Q^4, whereas the quantitative spectrum, Figure 3a, shows no detectable amount of Q^2, and only 12% of Q^3 against 88% Q^4.

The Ludox silica structure can be calculated to be more or less fully condensed. The surface and volume of a Ludox sphere are calculated from the radius (e.g., 11 nm, Table II). Assuming 4.5 OH groups per square nanometer (*20*), the expected number of silanol groups as a percentage of

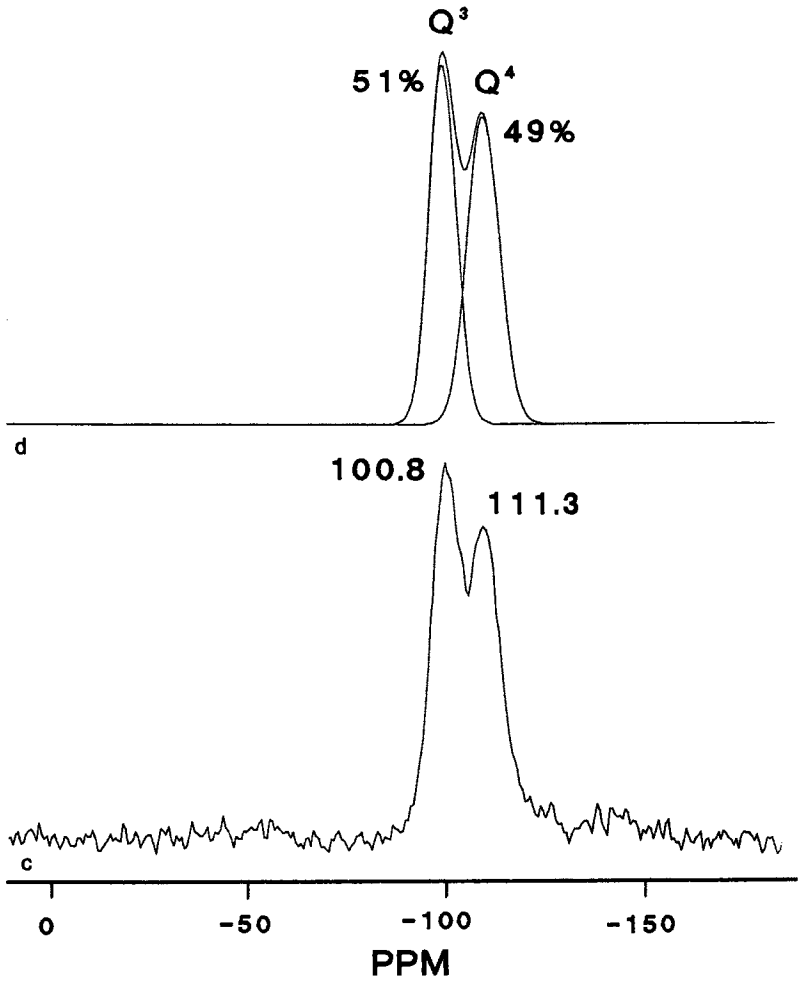

Figure 3.—Continued. ^{29}Si *NMR spectra of Compol. Part c: CP–MAS, 2000 accumulations, repetition time of 4 s, and contact time of 4 ms. Part d: Deconvoluted spectrum using Gaussian line shape.*

the number of silicon atoms per particle can be determined. The number of silicon atoms in the particle can be obtained from the density [2.2 g/mL (*20*)] and the molecular weight, which is, taking 15% Q^3 into account, 61.43 g/mol. These calculations result in a percentage of silanol groups of 5.7%. This amount is small compared to the experimental number of 15% as obtained by NMR spectroscopy. It may be clear, however, that some surface roughness, as was observed by TEM, will increase the surface area. Because the siloxane structure of the Compol particles is close to that of

Table III. Relative Intensities of the Different Types of Silicon Environments

System	Q^4	Q^3	Q^2	T^3	T^2
A1[a]	73[b]	26	1.7		
A1APS	67	21	—	7.2	4.4
A2	69	32	—		
A3S	65	31	4.1		
A5[a]	64	31	5.5		
A5APS	65	30	4.0	—	—
A6	66	30	4.2		
Mix1	40	31	3.8	19	7.2
M1	64	30	6.5		
P1	66	28	5.6		
Ludox	85	15	—		
Compol	88	12	—		

NOTE: Data are reported as percentages. Blank cells indicate that the nuclei could not be present in the sample. Dashes indicate that the numbers were too small to be determined.
[a]The same reaction procedures as for the coating were followed, except for the addition of APS.
[b]Estimated errors for Q^4 and Q^3 were ±2%; for the other species, ±1%.

Ludox, and the radius is about 5 times larger, it is also clear that even the Compol particles are not fully condensed SiO_2 with only silanol groups at the particle surface.

^{13}C CP–MAS NMR spectroscopy showed the presence of ethoxy groups for all the alcosols prepared in ethanol, in accordance with elemental analysis (Table IV). The carbon next to oxygen was found close to 60 ppm, and the methyl group was at around 17 ppm (Figure 4a). The stearyl-coated A3S was no exception: an important part of the carbon signals originated from ethoxy groups. The carbon content of the larger particles, A5 and A6, is even higher than that of the particles A1. This result seems to indicate that for the larger particles most of the ethoxy groups are trapped inside the particles. This hypothesis is corroborated by a washing procedure of A6 (Table IV), which did not remove much of the carbon content. For the particles with a (much) higher surface area, the effect of washing with water (P1 in Table IV) or the refluxing of the particles A1 was visible in a significant change in carbon content. The almost complete removal of the carbon content for P1 after washing seems to suggest that the particles are microporous.

The chemical shifts of a carbon next to an OH group or next to O–Si are very close together. If only one O–C carbon is found, it is difficult to distinguish between ethoxy groups chemically bound and ethanol molecules bonded through hydrogen bonds with silanol groups. Another

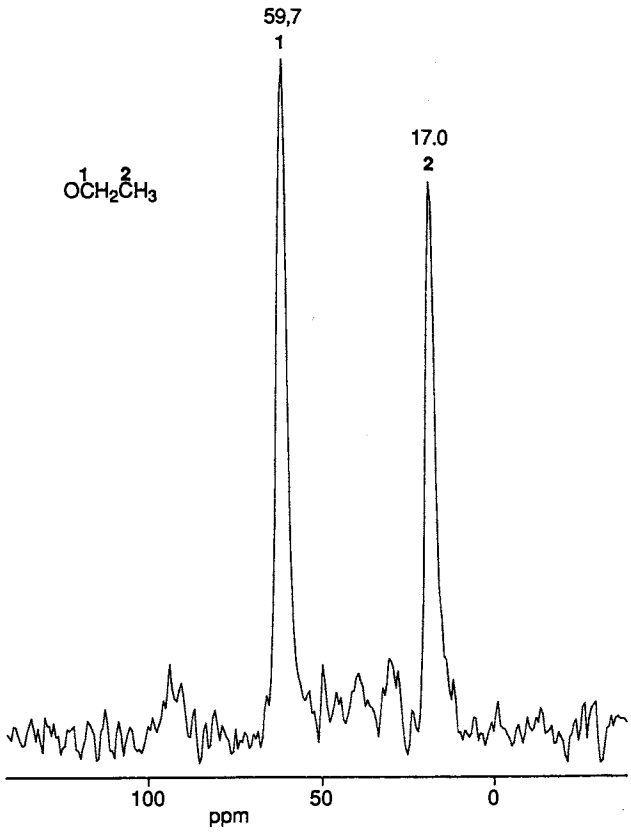

Figure 4. ^{13}C CP–MAS NMR spectra of alkoxy groups in silica; contact time of 2 ms. Part a: A1, 1000 accumulations.

possibility for the origin of the ethoxy signals in the ^{13}C alcosol spectra is reesterification of hydrolyzed silanol groups.

To resolve the questions raised in the previous paragraph, particles were synthesized in methanol and 1-propanol. Complete hydrolysis and reesterification in these solvents would result in the appearance of only methoxy and propoxy groups. The ^{13}C CP–MAS spectra of A1, P1, and M1 are shown in Figure 4. Ethoxy groups can still be seen in both particles prepared in methanol and propanol. No reesterification of ethoxy groups is possible in these solvents; thus the detected groups must never have left the TES molecule. Although care must be taken in using CP spectra quantitatively, it is probably safe to conclude from Figure 4 and Table IV that between 10% and 30% of the detected carbon in the elemental analysis belongs to ethoxy groups from TES. The amount of silicon atoms with ethoxy groups bonded to them that have never left the original TES

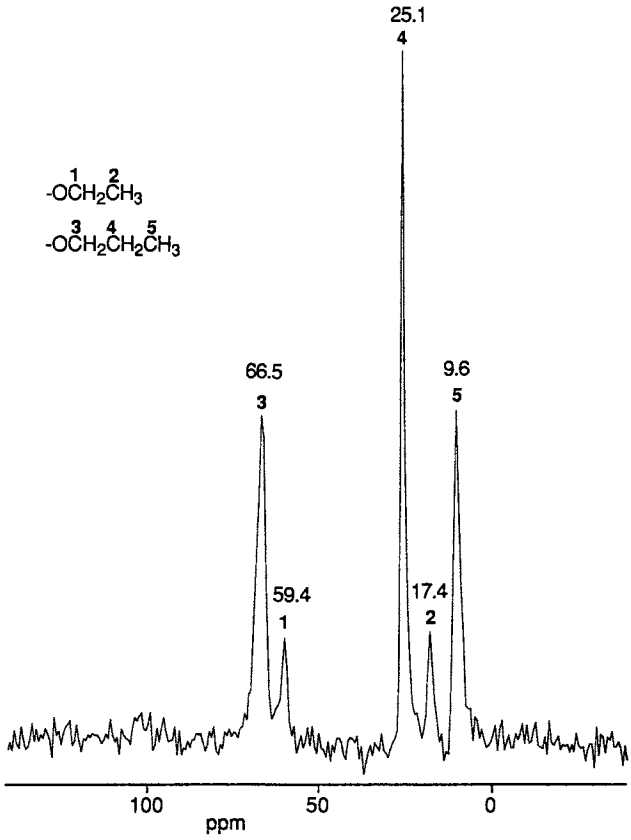

Figure 4.—Continued. Part b: P1, 500 accumulations. Continued on next page.

molecule is at least a few percent, whereas some reesterification or ester exchange seems to take place as well.

If the carbon and proton weight percentages are subtracted from 1 g of particles (Table IV), the remainder of the weight can be equalized to $n\mathrm{SiO}_x$, where x can be determined from the relative intensities of **Q** species as determined by NMR spectroscopy (Table III). The carbon content can be used to calculate the number of ethoxy groups. The number of silicon atoms with bonded ethoxy groups ranges from almost zero (for the particles A2 made in a relatively high concentration of water) to 14% for sample A5.

For the sample A3S, the amount of silicon was determined: 39.0% (elemental analysis described in reference *4*). Subtracting C and H and using the siloxane structures from NMR as before, yields 38.94% Si, in perfect agreement with the measured value. Apparently, the amount of

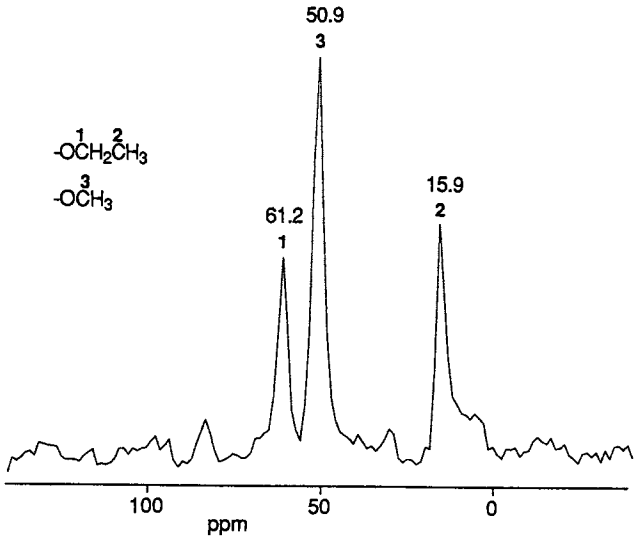

Figure 4.—Continued. Part c: M1, 3000 accumulations.

Table IV. Elemental Analysis (Weight Percentages)

System	*C (%)*	*H (%)*	*N (%)*
A1[a]	1.68 ± 0.01[b]	0.97 ± 0.08	
A1	1.11 ± 0.02	0.99 ± 0.08	
A1APS	7.29 ± 0.01	2.20 ± 0.03	2.18 ± 0.02
A2	0.59 ± 0.01	0.85 ± 0.02	
A3S	9.7	2.7	
A5[a]	5.07 ± 0.12	1.66 ± 0.07	
A5APS	6.03 ± 0.05	2.05 ± 0.04	0.32 ± 0.01
A6	3.95 ± 0.04	1.55 ± 0.08	
A6[c]	3.54 ± 0.03	1.45 ± 0.08	
Mix1	12.95 ± 0.02	3.97 ± 0.07	4.49 ± 0.05
P1	3.84 ± 0.02	1.55 ± 0.04	
P1[c]	0.27 ± 0.04	1.34 ± 0.10	
Compol	0.1 ± 0.01	0.23 ± 0.02	

[a]Samples underwent the coating conditions.
[b]Errors indicate differences in duplicate results.
[c]Samples were washed for 3 h with water before drying.

physically absorbed water can be neglected in this case. This is not so strange, considering the heating to 190 °C for 3 h during esterification. Jansen, et al. (*8*) stated that 5% H_2O was present inside the particles, but this error was made because it was assumed that only Q^4 was present.

Figure 5 shows all the possible silicon signals that can be obtained from reactions between TES and APS. Carbon assignments will be described in more detail elsewhere (*50*). The chemical shifts compare well

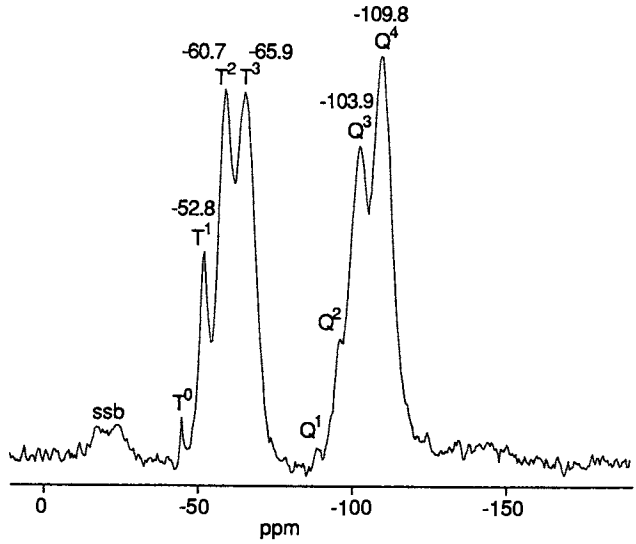

Figure 5. ^{29}Si *CP–MAS NMR spectra of a mixture of TES–APS hydrolyzed by atmospheric water; 2000 accumulations and contact time of 4 ms.*

with literature data (*36–40, 54–56*). This test sample was made by mixing equal amounts of TES and APS and letting the mixture hydrolyze by atmospheric water. The white powder thus obtained (no colloidal spheres) was crushed and placed in a spinner. The quantitative silicon spectra obtained from A1APS and Mix1 did not contain signals from T^1, but were similar.

For the APS-coated A1APS, the silicon nuclei of APS could be determined quantitatively with NMR spectroscopy (Table III). For 1 g of A1APS, as explained before, one calculates 1.68 mmol of APS. Using the N percentages gives 1.56 mmol of APS. The difference, 0.12 mmol, can be explained by assuming that a few percent physically adsorbed water was also present. The number of Q^3 and Q^2 becoming Q^4 because of the coating reaction is clearly lower than the number of T species formed (Table III). This result shows that APS did not form all its siloxane bonds with Q species.

Unfortunately, the coating of A5 contained too few APS to be determined with NMR spectroscopy. Comparing the surface-to-volume ratio of A1 and A5 using the TEM radius gives a value of 6.9; the ratio of the N percentages is 6.8. Probably, the amount of coating scales with the surface available and the reaction stops if the silanols belonging to Q species are not available anymore. For A5 this means that only 1.1% of the available APS actually ended up on the particle surface. Without the silica particles, the APS does not form any structure that scatters light (*50*).

These surface coverages are somewhat less than the coating with methacryloxypropyltrimethoxysilane as described by Philipse and Vrij (*4*). He calculates ~10 groups per square nanometer. Using the values of A5 one finds ~2 APS molecules per square nanometer. Badley, et al. (*11*) found for particles of radius 58.1 nm with elemental analysis 0.90% N. The difference with this work was that the concentration of APS was approximately 10 times smaller and no refluxing or distillation was used, but the reaction was continued for 20 h. The methoxy derivative of APS also was used, probably resulting in faster hydrolysis. Apparently, APS reacts very slowly with silica.

The results obtained for Mix1 are amazing: 36.3% of the APS used ended up inside the particles (Table IV). This value contrasts sharply with the small amount found in the coating reaction, even though the concentrations used there were higher. The APS did not end up as a surface coating, as is indicated by the very low amount of Q^4. This result can only be explained if the APS is distributed through a large portion of the colloid.

As before, calculating the amount of APS per gram using SiO_x gives 3.28 mmol and, from the percent N one gets 3.19 mmol. The small difference is again probably due to a few percent H_2O. The amount of carbon also indicates that 5% of the Si atoms can still be bonded to an ethoxy group.

Nucleation and Growth Mechanism. In the following sections, we will test some of our findings with predictions and assumptions of the proposed mechanisms in the literature.

The finding that a few percent of ethoxy groups never leave the TES molecule is in accordance with the findings of Harris and co-workers (*16*, *18*) and Matsoukas and Gulari (*17*, *22*) that the growth rate of the silica particles is limited by the hydrolysis of TES. Under these conditions, some monomers may polymerize before the hydrolysis of all the groups on the silicon atom is complete. Were the hydrolysis complete in the first few minutes, it would indeed seem strange to find ethoxy groups in the methanosol and propanosol. This kind of reasoning can also be used to explain the large amount of APS that was build inside the Mix1 Particles. Here, hydrolyzed TES molecules could have reacted with the slower hydrolyzing APS molecules.

We find a contradiction with the assumptions made by Bogush and co-workers (*24–27*) that in the first few minutes all TES hydrolyzes and that during the whole particle growth the nucleation continues. If growth continued through aggregation of subparticles during the whole process, the surfaces of the spheres that can be seen in Figure 2c and 2g could not have been as smooth.

In our work and from the literature (*1*, 2, *24–27*), it can be seen that particles with a radius of 15 nm to about 400 nm can be made with a single concentration of TES by changing only the amount of ammonia. This is a 25-fold increase in radius. Using equations 3 and 4 derived by Matsoukas and Gulari in their kinetic model yields for the ratio of hydrolysis and polymerization rate constants 2.4×10^8 and 3.8×10^{12} for the diffusion and reaction-limited cases, respectively. Both the hydrolysis and polymerization are caused by a nucleophilic reaction mechanism; hence, such an increase of one over the other is very unlikely. The factor 2.4×10^8 is also very far from the differences in reaction rates that have been determined experimentally by Harris and co-workers (*16*, *18*). Therefore, although the model of Matsoukas and Gulari (22) seems to explain the polydispersity and growth of a particle distribution, it fails to predict the final size. This deficiency is because their kinetic model is also used to describe the particle nucleation process.

However, if we use the expressions for the classical nucleation rate, we also do not find the large increase in radius that is possible. Furthermore, Weres et al. (*57*) state that addition of NaCl to a homogeneous nucleating solution of silicic acid in water has only a moderate effect if the concentrations are below 1 M. Addition of salt to the reaction mixture of the Stöber process has, however, very large effects. Clearly, classical nucleation cannot explain all the features of the Stöber synthesis either.

One possible solution is to assume that the number of nuclei that have been formed through homogeneous nucleation decreases early in the reaction by a controlled aggregation process. After, and perhaps during, the short aggregation period, monodispersity is reached by the addition of monomers or small oligomers. The assumption that small silica particles are not stable against aggregation can be made plausible as follows: The silica particles in an alcosol derive their stability from the negative surface charge originating from dissociated silanol groups. Preliminary conductivity and electrophoretic measurements on the A6 particles in the reaction mixture indicate a surface potential of about 50 mV, a low, reasonable value. This value has also been reported by Bogush et al. (*24*) but it is very difficult to make an accurate interpretation of the measurements. Many of the important physical properties of the alcosol mixture are not exactly known. A better indication of the stability of the particles comes from the observation of the flocculation concentration of 5 mM $LiNO_3$. At a concentration of 1 mM, the sol remains stable, but the final particle radius is almost doubled (A6–A8, Tables I, II) *only* if the salt is added before the first particles are visible! When a concentration of 2 mM was added, the sol flocculated during its formation.

The Derjaguin–Landau–Verwey–Overbeek (DLVO) theory of charged colloids (*58*) predicts a substantial decrease in stability against flocculation with decreasing particle radius. Most likely the newly formed

nuclei are not yet stabilized, and stability sets in only after a certain radius is obtained. After this size is reached, particles grow through monomer addition either reaction- or diffusion-limited, but with an overall rate still depending on the hydrolysis.

The finding that particles increase in size by using more ammonia (Table I), in spite of the fact that this increases the surface charge, probably involves an increase in ionic strength that compresses the double layer. As reported by Bogush (*27*), during the first minutes of the reaction, there is a sharp increase in solution conductivity that decreases slowly during the remainder of the reaction. The production of silicic acid, partly dissociated by NH_3, causes this increase. When the particles grow, the number of available silanol groups slowly decreases, and so does the conductivity. This sudden increase in ionic strength is probably higher for higher concentrations of ammonia and results in larger particles. Clearly, these predictions have to be verified experimentally (*49*).

Eventually, the effect on the surface charge of the increase in $[NH_3]$ and $[H_2O]$ overcomes the increase in ionic strength, and the decrease in the number of nuclei is less, so that the particle radius decreases.

The model as proposed can also explain why solvents with a higher dielectric constant produce smaller particles and why, under conditions where the largest particles are formed, the sols sometimes flocculate.

Finally, the particle morphology must be explained in terms of the nucleation or growth mechanism. We tentatively assume that the irregular shape of some particles (for instance, A3 and A1) is caused by the proposed controlled aggregation mechanism early in the formation of the particles. For these systems the monomer growth was not yet able to create a smooth surface, as present on the larger spheres like A6. A2 also has very spherical and smooth particles, but here the low TES and high water concentration stabilized the aggregating particles at a small radius before most of the TES was used and a smooth particle surface could be achieved.

Conclusions

We conclude that hydrolysis is the rate-limiting step in growth because a few percent of the ethoxy groups of TES are not hydrolyzed fully before they polymerize and these groups are also included in the interior of the larger particles. This conclusion can also be drawn from more direct measurements presented in the literature (*16–18*, *22*).

We propose that silica particles synthesized according to the method of Stöber are formed through a controlled aggregation of nuclei formed through homogeneous nucleation, followed by growth through monomer addition. The ionic strength is an important parameter in the determination of the final particle size, and it is easily changed by addition of salt (*49*).

Silica particles can be coated by the silane coupling agent APS in the reaction medium to obtain stable colloids. These systems can be used to further bind relevant groups to the particle surface (*48, 51, 52*). Quantitative ^{29}Si NMR spectroscopy appears to be a valuable tool in characterizing a new kind of stable colloidal particles synthesized from a mixture of the alkoxides APS and TES. These monodisperse, spherical particles can already be prepared with a low polydispersity and contain APS molecules distributed through an important part of the bulk of the particle. It would be interesting to see whether this method is also applicable to other mixtures of alkoxides. More work concerning the characterization of these new systems has to be done (*50*).

Acknowledgments

We thank G. Nachtegaal and Dr. A.P.M. Kentgens for their help with the NMR measurements at the SON-NWO HF-NMR facility (Nijmegen, the Netherlands). We also thank J. Suurmond and J. Pieters for performing the electron microscopy, and A. Philipse for his comments.

This work was supported by the Netherlands Foundation for Chemical Research (SON) with financial aid from the Netherlands Organization for Scientific Research (NWO).

References

1. Stöber, W.; Fink, A.; Bohn, E. *J. Colloid Interface Sci.* **1968,** *26*(1), 62–69.
2. Van Helden, A. K.; Jansen, J. W.; Vrij, A. *Colloid Interface Sci.* **1981,** *81*(2), 354–368.
3. Van Helden, A.K.; Vrij, A.J. *Colloid Interface Sci.* **1980,** *78*(2), 312–329.
4. Philipse, A. P.; Vrij, A. *J. Colloid Interface Sci.* **1989,** *128*(1), 121–136.
5. Philipse, A. P. *Colloid Polym. Sci.* **1988,** *266*(12), 1174–1180.
6. Philipse, A. P.; Smits, C.; Vrij, A. *J. Colloid Interface Sci.* **1989,** *129*(2), 335–352.
7. Philipse, A. P.; Vrij, A. *J. Chem. Phys.* **1987,** *87*(10), 5634–5643.
8. Jansen, J. W.; De Kruif, C. G.; Vrij, A. *J. Colloid Interface Sci.* **1986,** *114*(2), 481–491.
9. Moonen, J.; Pathmamanoharan, C.; Vrij, A. *J. Colloid Interface Sci.* **1989,** *131*(2), 349–365.
10. Plueddemann, E. P. *Silane Coupling Agents*; Plenum: New York, 1982.
11. Badley, R. D.; Ford, W. T.; McEnroe, F. J.; Assink, R. A. *Langmuir* **1990,** *6*, 792–801.
12. Noll, W. *Chemie und Technologie der Silicone*; 2nd ed.; Verlag Chemie GmbH: Weinheim, Germany 1968.
13. Aelion, B. R.; Loebel, A.; Eirich, F. *J. Am. Chem. Soc.* **1950,** *72*, 5705–5712.
14. Keefer K. D. *Mater. Res. Soc. Symp. Proc.* **1984,** *32*, 15–24.
15. Brinker, C. J.; Scherer, G. W. *Sol–Gel Science*; 1st ed.; Academic Press: Boston, MA, 1990.
16. Byers, C. H.; Harris, M. T.; Williams, D. F. *Ind. Eng. Chem. Res.* **1987,** *26*(9), 1916–1923.

17. Matsoukas, T.; Gulari, E. *J. Colloid Interface Sci.* **1988,** *124*(1), 252–261.
18. Harris, M. T.; Brunson, R. R.; Byers, C. H. *J. Non-Cryst. Solids* **1990,** *121*, 307–403.
19. Schaefer, D. W.; Keefer, K. D. *Phys. Rev. Lett.* **1984,** *53*(14), 1383–1386.
20. Iler, R. K. *The Chemistry of Silica*; Wiley & Sons: New York, 1979.
21. Plueddemann, E. P. In *Silylated Surfaces*; Leyden, D. E.; Collins, W. T., Eds.; Gordon & Breach: New York, 1980; pp 31–53.
22. Matsoukas, T.; Gulari, E. *J. Colloid Interface Sci.* **1989,** *132*(1), 13–21.
23. Coenen, S.; De Kruif, C. G. *J. Colloid Interface Sci.* **1988,** *124*(1), 104–110.
24. Bogush, G.; Zukoski, C. *The Colloid Chemistry of Graving Silica Spheres*; Ceramic Microstructures 1986; Plenum Press: New York, 1987; pp 475–483.
25. Brinker, C. J.; Scherer, G. W. *Sol-Gel Science*; 1st ed.; Academic Press: Boston, MA, 1990; pp 199–203.
26. Bogush, G. H.; Tracy, M. A.; Zukoski, C. F., IV *J. Non-Cryst. Solids* **1988,** *104*, 95–106.
27. Bogush, G. H.; Dickstein, G. L.; Lee, P.; Zukoski, C. F., IV *Mater. Res. Soc. Symp. Proc.* **1988,** *121*, 57.
28. Adams, J.; Baird, T.; Braterman, P. S.; Cairns, J. A.; Segal, D. L. *Mater. Res. Soc. Symp. Proc.* **1988,** *121*, 361–371.
29. Makrides, A. C.; Turner, M.; Slaughter, J. *J. Colloid Interface Sci.* **1973,** *73*(2), 345–367.
30. Nielsen, A. E. *Kinetics of Precipitation*; Pergamon Press: Oxford, England, 1964.
31. Feeney, P. J.; Napper, D. H.; Gilbert, R. G. *Macromolecules* **1984,** *17*, 2520–2529.
32. La Mer, V. K.; Dinegar, R. H. *J. Am. Chem. Soc.* **1950,** *72*, 4847.
33. Overbeek, J. Th. G. *Adv. Colloid Interface Sci.* **1982,** *15*, 251–277.
34. Keefer, K. D. In *A Model for the Growth of Fractal Silica Polymers*; Hench, L. L.; Ulrich, D. R., Eds.; Science of Ceramic Chemical Processing; Wiley & Sons: New York, 1986; pp 131–139.
35. Schaefer, D. W.; Keefer, K. D. *Mater. Res. Soc. Symp. Proc.* **1986,** *72*, 277–287.
36. Sindorf, D. W.; Maciel, G. E. *J. Am. Chem. Soc.* **1981,** *103*, 4263–4265.
37. Sindorf, D. W.; Maciel, G. E. *J. Am. Chem. Soc.* **1983,** *105*(12), 3767–3776.
38. Sindorf, D. W.; Maciel, G. E. *J. Phys. Chem.* **1982,** *86*(26), 5208–5219.
39. Fyfe, C. A.; Gobbi, G. C.; Kennedy, G. J. *J. Phys. Chem.* **1985,** *89*(2), 277–281.
40. Fyfe, C. *Solid State NMR for Chemists*; CFC Press: Ontario, Canada, 1983.
41. Penders, M. H. G. M.; Vrij, A. *Colloid Polym Sci,* **1991,** *286*, 823–831.
42. Duits, M. H. G.; May, R. P.; Vrij, A.; De Kruif, C. G. *J. Chem. Phys.* **1991,** *94*, 4521–4531.
43. Koppel, D. E. *J. Chem. Phys.* **1972,** *57*(11), 4814.
44. *Dynamic Light Scattering: Applications of Photon Correlation Spectroscopy*; Pecora, R., Ed.; Plenum: New York, 1985.
45. Kops-Werkhoven, M. M.; Fijnaut, H. M. *J. Chem. Phys.* **1981,** *74*(3), 1618–1625.
46. Van Veluwen, A.; Lekkerkerker, H. N. W.; De Kruif, C. G.; Vrij, A. *J. Chem. Phys.* **1988,** *89*(5), 2810–2815.
47. Van Blaaderen, A.; Van Geest, J.; Vrij, A. *J. Colloid Interface Sci.* **1992,** *154*(2), 481–501.
48. Van Blaaderen, A.; Vrij, A. *Langmuir* **1992,** *8*, 2921–2931.
49. Van Blaaderen, A.; Kentgens, A. P. M. *J. Non-Cryst. Solids* **1992,** *149*, 161–178.

50. Van Blaaderen, A. Vrij, A. *J. Colloid Interface Sci.* **1993,** *156,* 1–18.
51. Van Blaaderen, A.; Peetermans, J; Maret, G.; Dhont, J. K. G. *J. Chem. Phys.* **1992,** *96*(6), 4591–4603.
52. Van Blaaderen, A. *Adv. Mater.* **1993,** *5*(*1*), 52–54.
53. De Rooy, N. Ph.D. Dissertation, University of Utrecht, Utrecht, Netherlands, 1979.
54. Chiang, C. H.; Liu, N. I.; Koenig, J. L. *J. Colloid Interface Sci.* **1982,** *86*(1), 26–34.
55. Vankan, J. M. J.; Ponjee, J. J.; De Haan, J. W.; Van de Ven, L. J. M. *J. Colloid Interface Sci.* **1988,** *126*(2), 604–609.
56. De Haan, J. W.; Van den Bogaert, H. M.; Ponjee, J. J.; Van de Ven, L. J. M. *J. Colloid Interface Sci.* **1986,** *110*(2), 591–600.
57. Weres, O.; Yee, A.; Tsao, L. *J. Colloid Interface Sci.* **1980,** *84*(2), 379–402.
58. Verwey, E. J. W.; Overbeek, J. Th. G. *Theory of the Stability of Lyophobic Colloids*; Elsevier: New York, 1948.

RECEIVED for review December 17, 1990. ACCEPTED revised manuscript March 30, 1992.

5

Synthesis of Nanometer-Sized Silica by Controlled Hydrolysis in Reverse Micellar Systems

F. J. Arriagada and K. Osseo-Asare

Department of Materials Science and Engineering and The Particulate Materials Center, The Pennsylvania State University, University Park, PA 16802

The synthesis of nanometer-sized silica particles by the base-catalyzed, controlled hydrolysis of tetraethoxysilane (TEOS) in a nonionic reverse micellar system is described. Spectrofluorometric techniques were used to characterize the reverse micellar solutions. Particle characterization was conducted by transmission electron microscopy. The effect of the water-to-surfactant molar ratio (R) on particle size and size distribution was investigated over a wide range of R values (0.50 to 3.54). Stable dispersions of amorphous silica with mean particle diameters in the range of 46 to 68 nm were produced. Small (46 nm) and extremely monodisperse particles (polydispersity below 4%) were obtained at intermediate R values (1.4), whereas both particle size and polydispersity increased at lower and higher R values. The effects of R on particle size and size distribution are discussed in terms of water "reactivity" (i.e., proportion of bound to free water), concentration of reverse surfactant aggregates, distribution of hydrolyzed TEOS molecules among aggregates, and dynamics of intermicellar matter exchange. A mechanistic model for particle nucleation and growth in these systems is proposed.

THE SYNTHESIS OF UNCOATED AND SURFACE-MODIFIED silica particles via the hydrolysis of tetraethoxysilane (TEOS) in a homogeneous alcoholic solution of water and ammonia is well documented in the literature (*1–7*). TEOS and other metal alkoxides (including those of titanium and iron) can

0065–2393/94/0234–0113$08.00/0

be hydrolyzed in reverse microemulsion systems for the production of gels or metal oxide particles (*8–16*). Systems incorporating surfactant aggregates have also been exploited in the synthesis of a number of other ultrafine particulate materials (*13, 15, 17–20*).

Yanagi et al. (*9*) reported that silica particles could be produced by the base-catalyzed hydrolysis of TEOS in a nonionic reverse micellar system. Yamauchi et al. (*12*), on the other hand, focused on the characterization of the product particles synthesized in an anionic system. Nitrogen adsorption and IR spectral data showed that the silica nanoparticles were highly porous; this result suggested a mechanism of formation involving primary particle aggregation (*12*). The importance of microemulsion structural and dynamic factors in the nucleation and growth of silica particles in reverse micellar systems was recently discussed (*14, 15*). It was demonstrated (*14*) that the nanometer-sized particles produced had an extremely narrow size distribution that had not been achieved before in the conventional technique of TEOS hydrolysis in homogeneous ethanolic media. Emphasis was also given to the connection between microemulsion properties and silica particle size in an attempt to further understand the detailed mechanisms of particle formation. In the limited range of water-to-surfactant molar ratio (R) that was investigated (0.55 to 1.7), it was found that both particle size and size distribution decreased as R increased. Furthermore, particle formation statistics (calculated on the basis of micellar concentration and terminal particle size) indicated that the solute contents of about 10^5 aggregates were involved in the formation of each particle. Under the experimental conditions used, each aggregate was considered to contain enough solute (hydrolyzed TEOS) to form a stable nucleus. Thus, it was suggested that the nuclei initially formed aggregated during intermicellar collisions; this aggregation dramatically reduced the particle number densities to those found in the final stages of growth (*14*).

In this chapter, the results obtained in the synthesis of silica over a wide range of R are presented. As illustrated by these new results, particle size and size distribution are complex functions of the initial microemulsion formulation (essentially defined by R and the initial TEOS content).

Experimental Details

Materials. The nonionic surfactant Igepal CO-520 (GAF Chemicals Corporation) is a polydisperse preparation of polyoxyethylene nonylphenyl ether with an average of five oxyethylene groups per molecule (hereafter NP-5). The material as received contained ca. 0.2% water, as determined by Karl Fisher titration. Water and low-boiling impurities (such as free alcohols) were removed by treatment at 60–70 °C under vacuum for 26 h. Reagent-grade cyclohexane (Aldrich) was used after storage under molecular sieves. Ammonium hydroxide (Baker, 29.5 wt % NH_3), TEOS (Alfa, 99 wt %), and the fluorescent probe rutheniumtris(bipyridyl) chloride (Aldrich) [hereafter $Ru(Bpy)_3^{2+}$] were used without further purification.

Preparation and Characterization of Particles. The synthesis experiments were conducted at 23 °C. As in previous work (*14*), R was the main variable studied. Different R values in the range of 0.5 to 3.5 were obtained by changing the concentration of the surfactant (in the range of 0.056 to 0.277 M) in the micellar system. The overall TEOS concentration and the water-to-TEOS molar ratio (h) were kept constant at 0.023 M and 7.8, respectively. A microemulsion plus second reactant synthesis route (*15*) was used; that is, TEOS was added to the NP-5–cyclohexane–ammonium hydroxide microemulsion to initiate the synthesis. Dispersion samples were extracted at different reaction times and deposited on transmission electron microscope (TEM) grids. Number-average and weight-average particle diameters and size distributions were determined on enlarged TEM micrographs with a ZIDAS image analysis system (Zeiss). Several hundred particles were measured for each sample.

Microemulsion Characterization. Fluorescence spectra were measured on a Shimadzu RF-5000 spectrofluorometer. Samples with R values in the range of 0.50 to 4.80 were prepared in a manner similar to that used for the samples in the synthesis experiments, that is, by using a fixed amount of aqueous phase and different surfactant concentrations. The probe $Ru(Bpy)_3^{2+}$ concentration was 9×10^{-6} M. The excitation wavelength was 460 nm.

Results

Particle Characteristics. Under the experimental conditions investigated, particle growth was essentially completed after 160 h. The dispersions exhibited a bluish opalescence and remained stable for weeks after preparation. The TEMS in Figure 1 show that the resulting silica particles are essentially monodisperse and spherical in shape. The particles obtained after 21 and 160 h of reaction time at low (0.50), intermediate (1.35), and high (3.54) R values are shown in Figures 1a to 1c and 1d to 1f, respectively. The presence of the surfactant allows the formation of an ordered particle arrangement upon volatilization of cyclohexane. Similar filmlike aggregates formed in the presence of surfactant molecules were described by Alexander and Iler (*21*) and by Aksay (*22*).

The number-average particle diameter (d_n) at different R values obtained after 21 and 160 h of reaction time are shown in Figure 2. As R increases in this range, the terminal particle size decreases sharply, reaches a minimum at R values of about 1.4, and then increases again. A similar trend is observed for the particle size at earlier reaction times. Thus, at up to 21 h of reaction time, particle growth is much faster at the lower R range. Particles produced at low R values (below about 1.3) have achieved about 80% of their final size in this time, whereas the percentage decreases to 75, 70, and 65% for R values of 1.73, 2.43, and 3.54, respectively.

The size distribution of the particles, expressed as the standard deviation over the number-average diameter (polydispersity parameter in percentage), is shown in Figure 3. The size distribution is narrower at

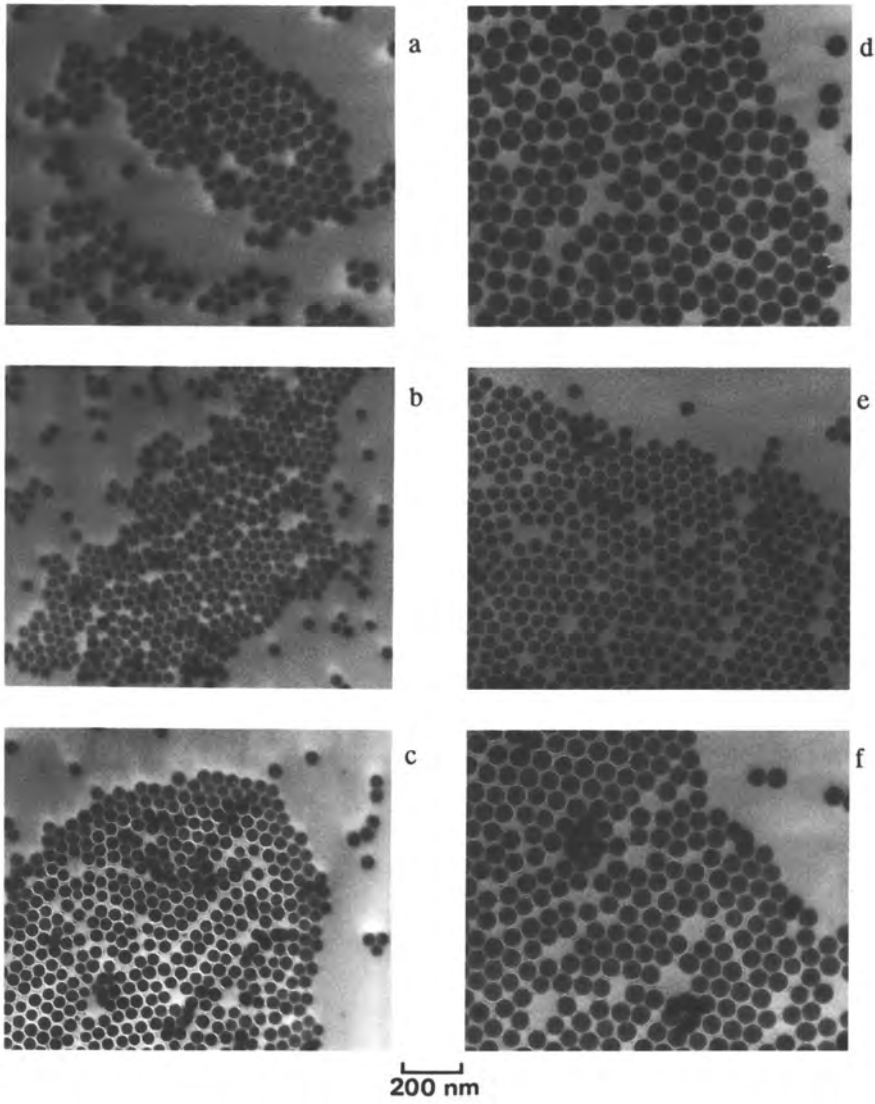

Figure 1. TEM micrographs of silica particles obtained by hydrolysis of TEOS in reverse NP-5–cyclohexane–NH_4OH microemulsions. Temperature was 23 °C with t = 2 *h for* R = *(a) 0.50, (b) 1.35, and (c) 3.54; and* t = 160 *h for* R = *(d) 0.50, (e) 1.35, and (f) 3.54.*

intermediate *R* values, and furthermore it decreases as time proceeds. This latter effect seems more pronounced in the higher *R* range. In the complete *R* range, however, the size distributions are significantly narrower than those typically obtained in the alcoholic hydrolysis of TEOS (*3*, *5*) for particles in this size range. For example, the polydispersity

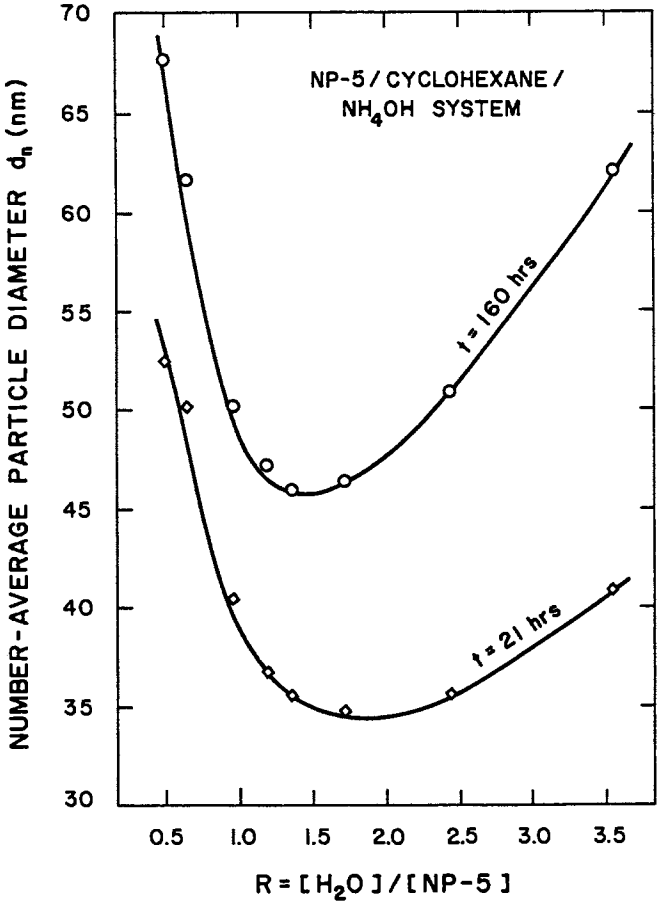

Figure 2. Effect of R *on* d_n *for silica particles at 21 and 160 h;* T = 23 °C, h = *7.8, and [TEOS] = 0.023 M.*

parameter for 46.3-nm (d_n) particles obtained at R of 1.73 is only 3.8% (Figure 3). The calculated weight-average particle diameter (d_w) for this sample is 46.5 nm, so the uniformity factor (d_w/d_n) is only 1.005. These results compare favorably with the higher uniformity factor of 1.033 for 57.7-nm (d_n) particles reported by Badley et al. (*3*) and underscore the potential of reverse microemulsion systems to produce colloidal particles of extremely narrow size distribution.

Microemulsion Characterization. The effects of R on the aggregation number N (i.e., the number of surfactant molecules per micelle) and on the nature of the solubilized water (i.e., bound or free) for this microemulsion system were reported (*14*). As R increases, dipole–dipole

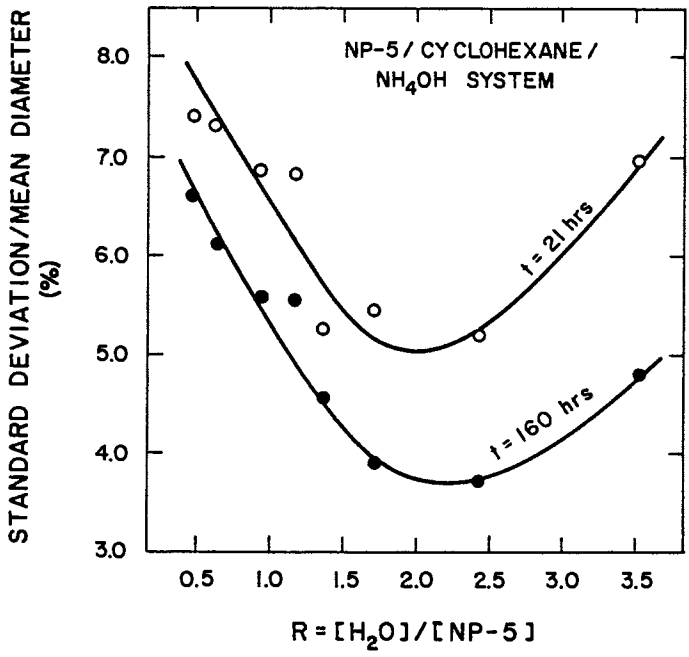

Figure 3. Effect of R *on the size distribution of silica particles at 21 and 160 h;* T = 23 °C *and,* h = *7.8. [TEOS] = 0.023 M.*

interactions between hydrated oxyethylene groups of the surfactant molecule provide the driving force for aggregation (*23*). Within the *R* range of interest, the aggregation number *N* of NP-5 molecules increases linearly from 23 at *R* of 0.5 to 135 at *R* of 3.54 (*14, 24*). By combining these aggregation numbers with the concentration of NP-5 used in each sample, the number of aggregates (N_a) in the total microemulsion volume (5.06 mL) can be calculated. Furthermore, the average number of TEOS molecules per aggregate (N_t) can be calculated from the total TEOS content and the value of N_a at each *R* value. The results are presented in Figure 4. The number of aggregates decreases about 30-fold when *R* increases from 0.5 to 3.54. Thus, as *R* increases, fewer (but larger) surfactant aggregates are present in the system. As a result, N_t increases from 2 to about 60 as *R* increases.

Not only is aggregation favored as *R* increases, but there is also a change in the nature of the solubilized water. Initially, water is tightly hydrogen-bonded to the oxyethylene groups of the nonionic surfactant. Further water addition induces aggregation (dipole–dipole interactions), and a point is reached where unbound or "free" water molecules are present in the hydrophilic (polar) domain. The state of water in the polar

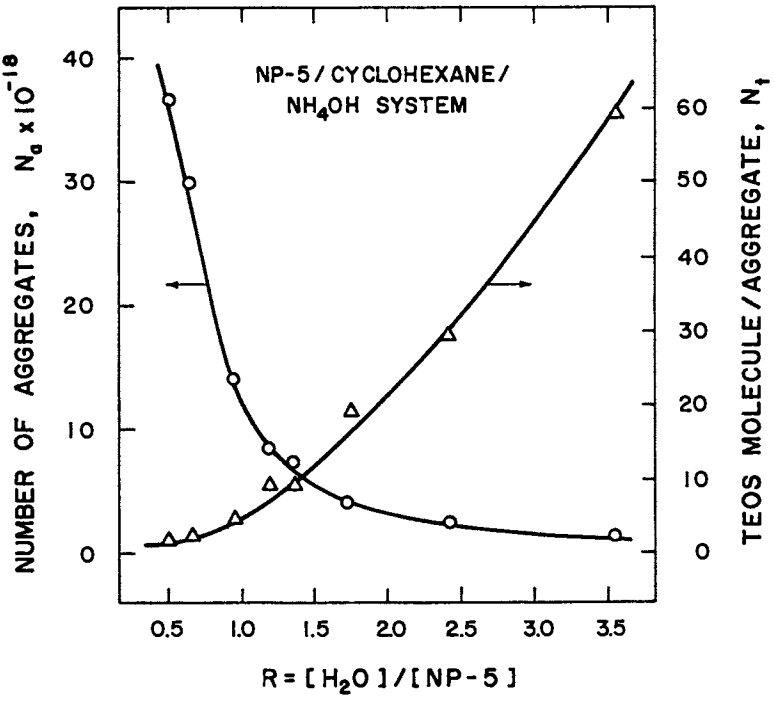

Figure 4. Effect of R *on* N_a *and* N_t; T = 23 °C, h = 7.8, *and [TEOS] = 0.023 M.*

domain is relevant to the formation of particles, because the initial hydrolysis of TEOS in the reverse micelle is expected to be favored as more "free" water molecules are available. Such an effect is expected because the hydrolysis of titanium alkoxides (naturally more reactive than TEOS toward water) is strongly inhibited in reverse microemulsions formulated with nonionic or anionic surfactants at low *R* values (*10, 16*).

The fluorescence emission spectra of hydrophilic probes solubilized in the polar domains of reverse micelles provide a convenient means of ascertaining the nature of the solubilized water (25) and thus the expected reactivity of TEOS with these water molecules. For example, the emission spectra of $Ru(Bpy)_3^{2+}$ is blue-shifted with respect to water in media of reduced polarity (26). Figure 5 shows the spectra of $Ru(Bpy)_3^{2+}$ obtained at different *R* values. At low *R* values (below about 0.9) the emission spectra have a maximum intensity at about 575 nm with a red shoulder at 615 nm. As the water content increases, the intensity at 615 nm increases and the emission at 575 nm decreases. For *R* values above 1, the spectra resemble that of the probe in water (26). These results agree very well with previous results (*14*) for the fluorescence of $Ru(Bpy)_3^{2+}$ in NP-5–cyclohexane microemulsion samples of constant surfactant concentration. In addition,

replacement of water by ammonium hydroxide results in spectral changes very similar to those of Figure 5 (*14*). As suggested by Handa et al. (*26*), the probe is located close to the oxyethylene groups at low *R* values. As *R* increases, $Ru(Bpy)_3^{2+}$ is partitioned to the hydrophilic "pool" and behaves as in bulk water.

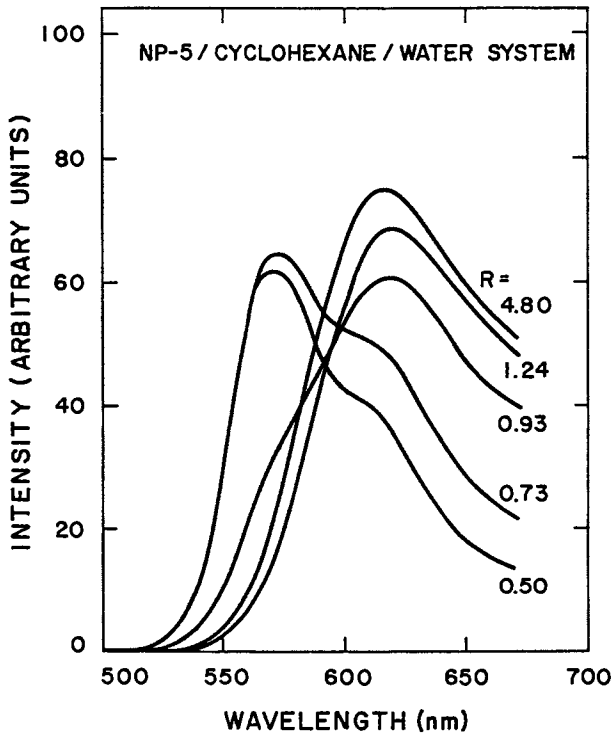

Figure 5. Fluorescence spectra of $Ru(Bpy)_3$ solubilized in the NP-5–cyclohexane–water reverse micellar system at different R *values; $\lambda_{ex} = 460$ nm, $[Ru(Bpy)_3] = 9 \times 10^{-6}$ M, and* T = 23 °C.

Discussion

TEOS–Microemulsion System. In these experiments the overall concentrations of water, ammonia, and TEOS were kept constant. The water-to-surfactant molar ratio *R* was varied by changing the total surfactant concentration. Thus, the observed effect of *R* on particle size and size distribution is due to the presence of surfactant aggregates, which result in the localization of reagents in well-defined polar (hydrophilic) and nonpolar (hydrophobic) domains. The NP-5–cyclohexane–NH_4OH system

is visualized as consisting of small reverse micelles before TEOS addition. As R increases within the range investigated, larger but fewer aggregates are present (*14*, *24*), and a larger number of TEOS molecules will on average interact with each micelle (Figure 4). In addition, as R increases, a larger proportion of the water molecules is free within the micellar core (Figure 5). To interpret the effect of R on particle size and size distribution shown previously, the following basic assumptions have been made.

Amphiphilic Nature of Hydrolyzed TEOS. The TEOS molecules, readily solubilized in the external oil phase, interact with the water molecules present within the aggregates to produce hydrolyzed species. It is assumed that the products of hydrolysis, once formed, remain bound to the micellar aggregates (i.e., solubilized within the surfactant film or the aqueous core or both) because of their enhanced amphiphilic character (brought about by the formation of silanol groups). The exact locale for the solubilization of hydrolyzed TEOS molecules in a reverse micelle is expected to be dependent on the degree of hydrolysis; for example, the most polar species [$Si(OH)_4$] would be expected to reside within the aqueous core. Once the hydrolyzed TEOS becomes solubilized, all further reactions (further hydrolysis and condensation) are restricted to the locale of the surfactant aggregates.

Locale of Evolving Solid Particles. The adsorption of polyoxyethylene nonylphenyl ethers (such as NP-5) on silica surfaces is dependent on pH. In relatively alkaline medium, the silica surface is deprotonated and highly negatively charged, and adsorption of the oxyethylene groups is inhibited (*27–30*). Accordingly, because alkaline conditions prevail in these synthesis experiments, stabilization of the particles in cyclohexane (the external microemulsion phase) by direct attachment of NP-5 molecules to the particles is unlikely. The hydrophilic silica surface is thus suggested to be surrounded by a thin film of water molecules as well as polar reaction products (such as ethanol); this film is then stabilized by NP-5 molecules. Under these conditions, the micellar system can be viewed as containing two different populations of aggregates, that is, particle-filled aggregates and empty micelles. This situation has been well documented in studies of the solubilization of enzymes and proteins in reverse microemulsion systems (*31–33*) by "segregation" or "water shell" models.

Distribution of Surfactant Molecules. As a first approximation, the reverse micellar aggregates present in the solution are assumed not to be significantly affected by the addition of TEOS molecules nor by the subsequent reactions, and in particular the aggregation numbers (hence the micellar concentration) are assumed to remain unchanged. Consideration of the total number of particles produced (N_p) indicates that only a

minor fraction of the total surfactant present would be associated with the growing particles.

Model of Particle Formation. In the reverse micellar system, the nucleation process will in principle be governed by the ease with which (1) TEOS molecules are hydrolyzed to form silanol groups and (2) silanol groups interact to form Si–O–Si bonds. Interaction of TEOS molecules with the micellar aggregates, hydrolysis with formation of silanol groups, and attachment of the partially hydrolyzed molecules to the micelles are illustrated in Figure 6a for low and high R values. Consideration of the effect of R on the proportion of free ("reactive") water in the micellar aggregates (Figure 5) indicates that hydrolysis of TEOS to form silanol groups is not favored at low R values, because water is mostly bound to the surfactant molecules. Furthermore, there are few silanol groups per aggregate (given the low values of N_t), so nucleation through intermicellar interactions is expected to predominate. In addition, the concentration of aggregates under these conditions is higher, and therefore the rate of intermicellar collisions is higher (*34*). At high R values, on the other hand, the number of silanol groups per micelle is higher (based on the larger value of N_t at high R). Under these conditions, the probability of interactions between neighboring silanol groups in a given micelle to form Si–O–Si bonds (a nucleus) is higher, and therefore intramicellar nucleation would be favored. The essential features of the nucleation process at both low and high R values are shown in Figure 6b.

According to these ideas, the formation of a high number of nuclei is favored at high R values. Thus, the final particle size should decrease continuously as R increases, but as shown in Figure 2 this theory does not conform with the experimental data. To explain the minimum particle size observed at intermediate R values, the effect of R on both the number of aggregates and the distribution of hydrolyzed TEOS molecules among aggregates needs to be considered. On the one hand, the number of nuclei formed is expected to be proportional to the number of aggregates in the microemulsion volume, which as shown in Figure 4 decreases significantly as R increases. On the other hand, only a fraction of the total number of aggregates may contain sufficient hydrolyzed TEOS molecules to form a stable nucleus. This fraction can be quantified as a function of R if the average number of TEOS molecules per micelle (N_t), the number of hydrolyzed TEOS molecules required to form a stable nucleus (i_c), and the probability distribution of TEOS molecules per micelle are known. A Poisson statistical law can be assumed; this law has been shown (*35, 36*) to satisfactorily describe the distribution of solute species among micelles in reverse microemulsions.

The probability (P_k) of having k hydrolyzed TEOS molecules per aggregate provided that the average value is N_t is therefore given by

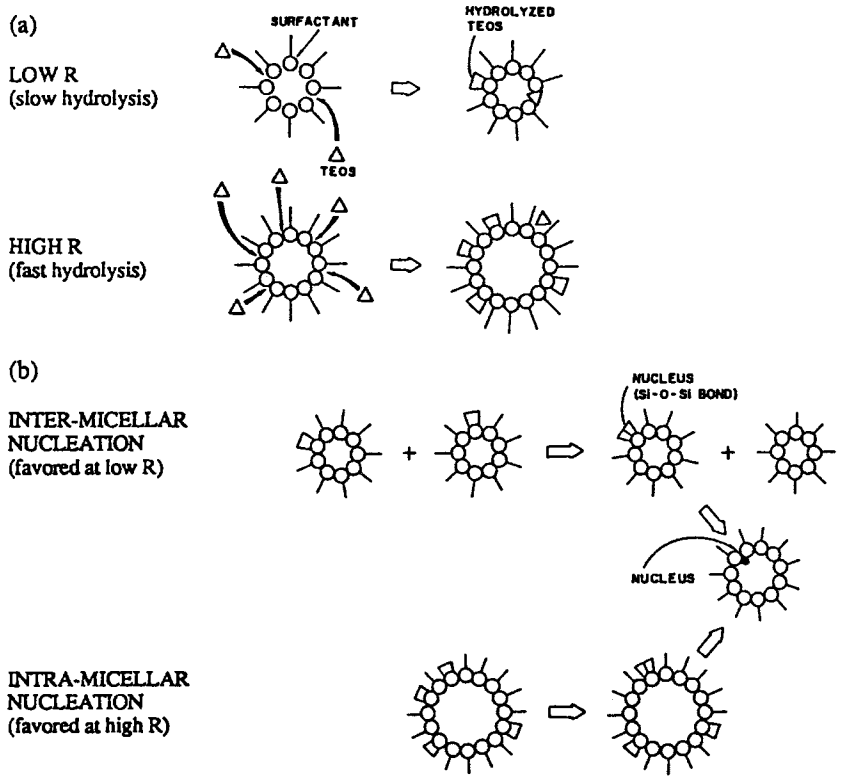

Figure 6. Formation of silica nuclei by hydrolysis of TEOS in reverse micellar systems: a, partial hydrolysis of TEOS and association to reverse micelles; and b, inter- and intramicellar nucleation.

$$P_k = \frac{N_t{}^k \; e^{-N_t}}{k!} \tag{1}$$

If the minimum number of hydrolyzed TEOS molecules per micelle required to form a stable nucleus is i_c, then the number of nuclei (N_n) formed at each R value can be calculated from

$$N_n = N_a \sum_{k=i_c}^{\infty} P_k \tag{2}$$

where N_a is the number of aggregates present at the given R value and ΣP_k ($k = i_c$ to infinity) is the probability that an aggregate contains i_c or more hydrolyzed TEOS molecules. The value of N_n was evaluated as a function of R for different i_c values, which were chosen to be in a reasonable range

(37). The results obtained are shown in Figure 7. The number of nuclei formed displays a maximum at intermediate R values; this maximum furthermore decreases and shifts toward higher R values as the value of i_c increases. Although no quantitative assessment on a unique value for i_c can be offered at this time, the trends shown by these results may explain the minimum in particle size obtained at intermediate R values; that is, the minimum in particle size is the result of a maximum in the production of nuclei.

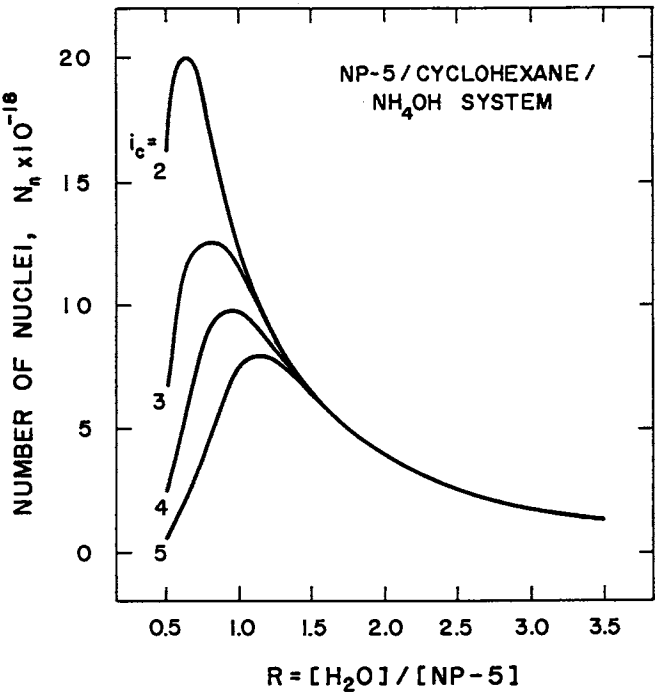

Figure 7. Effect of R *on* N_n *at different* i_c *values; [TEOS] = 0.023 M.*

Particle Growth. A comparison of the relative number of nuclei formed and particles produced at each R value suggests a significant role of nuclei aggregation in the particle formation process. If a single (limited time) nucleation event occurred upon addition of TEOS to the micellar system, and if particle growth occurs only by addition of monomers (hydrolyzed TEOS) to condensed species, then the number of particles produced should correspond to the number of nuclei formed, which may be assumed to be of the order of magnitude given in Figure 7. Calculation of the population of particles (on the basis of their terminal diameter and

assuming complete TEOS conversion), however, indicates that there are about 5 orders of magnitude fewer particles than nuclei. Forming only one stable nucleus out of 10^5 aggregates that are potentially capable of nucleation seems too low a probability. Therefore, it is proposed that a large number of nuclei is initially formed and that aggregation of nuclei during intermicellar collisions reduces dramatically the particle number density. Similar processes of particle growth via aggregative mechanisms have been suggested by Towey et al. (*38*) for CdS colloids growing in an anionic reverse microemulsion system and by Bogush and Zukoski (*39*) in the alcoholic hydrolysis of TEOS.

This particle aggregation process may occur only during a limited period of time, after which a constant particle number density of the growing particles is achieved. In a manner similar to the nucleation process, the aggregation may be governed by the number of micelles and the probabilistic fraction of aggregates containing a nucleus. In addition, it will strongly depend on the rate of intermicellar exchanges. After this process is completed, particle growth occurs by addition of monomers to existing particles, which then involves the interaction between particle-filled aggregates and empty micelles (containing hydrolyzed TEOS). Such a mechanism of growth is believed to be predominant at 21 h and longer times, as suggested by the narrow size distributions obtained (Figure 3).

Assessment of Particle Formation Mechanisms. The mechanisms of particle nucleation and growth in the nonionic micellar system discussed may in principle explain the observed particle size data. However, this is most likely a simplified model of the underlying processes that may be operative during the course of the synthesis reactions. The aggregation number of the surfactant molecules in the bulk oil phase (i.e., the population of empty micelles) may be affected by the presence of guest molecules, such as hydrolyzed TEOS, ethanol product, or both. The amphiphilic partially hydrolyzed TEOS (silanol groups as polar head) may also act as a cosurfactant, affecting the rigidity of the surfactant-stabilized oil–water interface and therefore the dynamics of intermicellar interactions (*34*, *35*). On the other hand, the ethanol molecules produced are expected to remain within the polar domain because of their hydrophilic nature. Under these conditions, the aqueous phase is being enriched in ethanol as time proceeds (in fact, it may contain a significant fraction of ethanol under the conditions of these experiments). At the same time, water is being progressively consumed. Such significant changes in the nature of the solubilized aqueous phase (including an effective decrease in R) may dramatically affect the aggregation behavior.

Thus, the situation is much more complex if the characteristics of the reverse micellar system (e.g., aggregation, micellar concentration, and dynamic behavior) are functions of time. In light of the available results, no

definitive explanation can be offered at this time to account for the remarkable monodispersity obtained at intermediate R values, at which maximum number of nuclei is formed. Quantitative evaluation of the main features of the proposed model must await further experimental data. Of particular interest in this connection are the development of a quantitative description of the nucleiaggregation process and the determination of surfactant aggregation numbers with water–ethanol mixtures as aqueous solubilizate.

Conclusions

Further work is clearly needed to unravel the detailed mechanisms of the hydrolysis and polymerization reactions in these micellar systems. Of particular interest is a better description of the initial stages of growth, which are believed to be responsible for the narrow monodispersity of the particles obtained within the entire R range. Other issues of interest are the location of hydrolysis products and other intermediates, changes in the aggregation number of surfactant molecules due to changes in the nature of the solubilized aqueous phase, and a quantitative description of the particle-filled and empty reverse micelle populations.

The potential capabilities of microemulsion synthesis of colloidal silica and related materials are yet to be realized. For example, the compartmentalization of reagents at the molecular level in these media may allow close control of chemical homogeneity in the synthesis of glass (e.g., Si–Al) particles. In situ synthesis of silica-supported catalysts and synthesis protocols involving seeding techniques, coating techniques, or infiltration are also possible.

Acknowledgments

This work was supported in part by the The Ben Franklin Partnership Program, Advanced Technology Center of Central and Northern Pennsylvania, Inc., and the Cooperative Program in Metals Science and Engineering, The Pennsylvania State University.

References

1. Stober, W.; Fink, A.; Bohn, E. *J. Colloid Interface Sci.* **1968**, *26*, 62.
2. Van Helden, A. K.; Jansen, J. W.; Vrij, A. *J. Colloid Interface Sci.* **1981**, *81*, 354.
3. Badley, R. D.; Ford, W. T.; McEnroe, F. J.; Assink, R. A. *Langmuir* **1990**, *6*, 792.
4. Matsoukas, T.; Gulari, E. *J. Colloid Interface Sci.* **1989**, *132*, 13.
5. Bogush, G. H.; Zukoski IV, C. F. In *Ultrastructure Processing of Advanced Ceramics*; Mackenzie, J. D.; Ulrich, D. R., Eds.; Wiley: New York, 1988; p 477.

6. Byers, C. H.; Harris, M. T.; Williams, D. F. *Ind. Eng. Chem. Res.* **1987**, *26*, 1916.
7. Brinker, C. J.; Scherer, G. W. *J. Non-Cryst. Solids* **1985**, *70*, 301.
8. Tricot, Y. M.; Rafaeloff, R.; Emeren, A.; Fendler, J. H. In *Organic Phototransformations in Nonhomogeneous Media*; Fox, M. A., Ed.; ACS Symposium Series 278; American Chemical Society: Washington, DC, 1985; p 99.
9. Yanagi, M.; Asano, Y.; Kandori, K.; Kon-no, K. *Abs. 39th Symp. Div. Colloid Interface Chem.*; Chemical Society of Japan: Tokyo, Japan, 1986; p 386.
10. Guizard, C.; Stitou, M.; Larbot, A.; Cot, L.; Rouviere, J. In *Better Ceramics Through Chemistry III*; Brinker, C. J.; Clark, D. E.; Ulrich, D. R., Eds.; *Mat. Res. Soc. Symp. Proc.* Vol. 121; Materials Research Society: Pittsburgh, PA, 1988; p 115.
11. Friberg, S. E.; Yang, C. C. In *Innovations in Materials Processing Using Aqueous, Colloid and Surface Chemistry*; Doyle, F. M.; Raghavan, S.; Somasundaran, P.; Warren, G. W., Eds.; Minerals, Metals, and Materials Society: Warrendale, PA, 1988; p 181.
12. Yamauchi, H.; Ishikawa, T.; Kondo, S. *Colloids Surf.* **1989**, *37*, 71.
13. Ward, A. J. I.; Friberg, S. E. *MRS Bull.* **1989** (December), 41.
14. Osseo-Asare, K.; Arriagada, F. J. *Colloids Surf.* **1990**, *50*, 321.
15. Osseo-Asare, K.; Arriagada, F. J. In *Ceramic Powder Science III*; Messing, G. L.; Hirano, S.; Hausner, H., Eds.; American Ceramic Society: Westerville, OH, 1990; p 3.
16. Arriagada, F. J.; Osseo-Asare, K. In *Refractory Metals: Extraction, Processing and Applications*; Liddell, K. C.; Sadoway, D. R.; Bautista, R. G., Eds.; Minerals, Metals and Materials Society: Warrendale, PA, 1991; pp 259–269.
17. Fendler, J. H. *Chem. Rev.* **1987**, *87*, 877.
18. Sugimoto, T. *Adv. Colloid Interface Sci.* **1987**, *28*, 65.
19. Leung, R.; Hou, M. J.; Shah, D.O. In *Surfactants in Chemical/Process Engineering*; Wasan, D. T.; Ginn, M. E.; Shah, D. O., Eds.; Surfactant Science Series Vol. 28; Dekker: New York, 1988; p 315.
20. Robinson, B. H.; Khan-Lodhi, A. N.; Towey, T. In *Structure and Reactivity in Reverse Micelles*; Pileni, M. P., Ed.; Studies in Physical and Theoretical Chemistry Vol. 65; Elsevier: Amsterdam, Netherlands, 1989; p 198.
21. Alexander, G. B.; Iler, R. K., U.S. Patent 2,801,902, 1957.
22. Aksay, I. L. In *Ceramic Powder Science R*; Messing, G. L.; Fuller, E. R.; Hausner, H., Eds.; American Ceramic Society: Westerville, OH, 1988; Vol. 1, p 663.
23. Ravey, J.C.; Buzier, M.; Picot, C. *J. Colloid Interface Sci.* **1984**, *97*, 9.
24. Kitahara, A. *J. Phys. Chem.* **1965**, *69*, 2788.
25. *Surfactant Solutions: New Methods of Investigation*; Zana, R., Ed.; Surfactant Science Series Vol. 22; Dekker: New York, 1987.
26. Handa, T.; Sakai, M.; Nakagaki, M. *J. Phys. Chem.* **1986**, *90*, 3377.
27. Iler, R. K. *The Chemistry of Silica*; Wiley: New York, 1979.
28. Partyka, S.; Zaini, S.; Lindheimer, M.; Brun, B. *Colloids Surf.* **1984**, *12*, 255.
29. Van den Boomgaard, Th.; Tadros, Th. F.; Lyklema, J. *J. Colloid Interface Sci.* **1987**, *116*, 8.
30. Travalloni Louvisse, A. M.; Gonzalez, G. In *Surfactant-Based Mobility Control*; Smith, D. H., Ed.; ACS Symposium Series 373; American Chemical Society: Washington, DC, 1988; p 220.
31. Luisi, P. L. *Angew. Chem. Int. Ed. Engl.* **1985**, *24*, 439.
32. Brochette, P.; Petit, C.; Pileni, M. P. *J. Phys. Chem.* **1988**, *92*, 3504.

33. *Structure and Reactivity in Reverse Micelles*; Pileni, M. P., Ed.; Studies in Physical and Theoretical Chemistry Vol. 65; Elsevier: Amsterdam, Netherlands, 1989.
34. Fletcher, P. D.; Howe, A. M.; Robinson, B. H. *J. Chem. Soc. Faraday Trans. I* **1987,** *83*, 985.
35. Atik, S. S.; Thomas, J. K. *J. Am. Chem. Soc.* **1981,** *103*, 3543.
36. Nagy, J. B. *Colloids Surf.* **1989,** *35*, 201.
37. Nielsen, A. E. *Kinetics of Precipitation*; International Series of Monographs on Analytical Chemistry Vol. 18; Pergamon: New York, 1964.
38. Towey, T. F.; Khan-Lodhi, A.; Robinson, B. H. *J. Chem. Soc. Faraday Trans.* **1990,** *86*, 3757.
39. Bogush, G. H.; Zukoski, C. F. *J. Colloid Interface Sci.* **1991,** *142*, 19.

RECEIVED for review December 17, 1990. ACCEPTED revised manuscript June 29, 1992.

6

Formation of Silica Gels Composed of Micrometer-Sized Particles by the Sol–Gel Method

Hiromitsu Kozuka and Sumio Sakka

Institute for Chemical Research, Kyoto University, Uji, Kyoto-Fu 611, Japan

Formation of silica gels composed of micrometer-sized particles from highly acidic solutions of tetramethoxysilane (TMOS) is described. In this method a limited amount of H_2O and a large amount of HCl are used in hydrolyzing TMOS. Detailed conditions and the mechanism of the formation of micrometer-sized particles in the solutions are discussed. Applications of the gels are also described.

SILICA GELS WITH CONTINUOUS LARGE PORES are ideal as precursors for bulk silica glasses. Low-temperature synthesis of bulk silica glasses by the sol–gel method consists of hydrolysis and polycondensation of silicon alkoxide in a solution, gelation of the alkoxide solution, drying of the wet gel to remove residual liquid components, and heat treatment of the dried gel to remove the organic substances and for sintering. Because large, continuous pores reduce the capillary pressure on the gel framework during drying, synthesis of silica gel monoliths with large pores is desirable for the sol–gel process for the production of bulk glasses (*1–5*).

Acid or base is used as a catalyst for the hydrolysis of silicon alkoxide. Acid or base with a mole ratio to alkoxide as low as 0.01 or less is usually enough for the catalytic effect. On the other hand, water with a mole ratio to alkoxide as high as 10 or more is used for the complete hydrolysis of alkoxide. We have found, however, that monolithic opaque gels composed of micrometer-sized silica particles can be prepared from tetramethoxysilane (TMOS) when a limited amount of water and a large amount of

0065–2393/94/0234–0129$08.00/0

hydrochloric acid are used for the hydrolysis (*6*, *7*). Because of the large particle size and the accordingly large pore size, the gels can be dried without cracking.

The Stöber route (*8*) is a well-known method for providing submicrometer- or micrometer-sized silica particles by hydrolysis and condensation of silicon alkoxide; an excess of base and water is used in the reaction. Compared with this method, ours has quite different reaction conditions, namely, the use of a limited amount of water and a large amount of acid. In contrast to the reaction of silicon alkoxide with a large amount of water in basic conditions, Sakka and Kamiya (*9*) noticed from the measurement of the intrinsic viscosity of silica sols that linear particles or polymers, not round particles, are formed with acidic conditions and the addition of a small amount of water. Therefore, the reaction conditions for this method for producing round micrometer-sized particles is new, and the mechanism of formation of round particles is of interest.

In this chapter, detailed conditions for the formation of silica gels composed of micrometer-sized particles from highly acidic TMOS solutions are described, and the mechanism of the sol–gel reaction is discussed. Application of the gels is also discussed.

Conditions for the Formation of Micrometer-Sized Particles

Process for Making Gels. Figure 1 shows the flow diagram for the sol–gel process for making gels. TMOS, methanol, 36% hydrochloric acid,

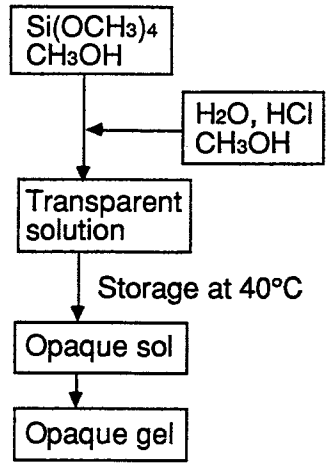

Figure 1. Flow diagram of the sol–gel process for making silica gel monoliths composed of micrometer-sized particles.

and ion-exchanged water are used as the starting materials. Silicon alkoxide solutions of the desired mole ratios are prepared by mixing the reagents under vigorous stirring at room temperature. Fifty milliliters of the alkoxide solution is kept at 40 °C until gelation. The quantity of acid reported refers to hydrogen chloride (HCl), and that of water includes water from the hydrochloric acid solution.

Effect of H_2O and HCl Content of the Starting Solutions. In the studies of gelation of TMOS solutions having mole ratios TMOS:H_2O:HCl:CH_3OH of 1:1.44–2.00:0.01–0.40:2, gels composed of larger particles were formed from the solutions with higher HCl content and lower H_2O content (*6*). Figure 2 shows the scanning electron micrographs (SEMs) of the fracture surface of the dried gels. In the series of gels formed from the solutions with the same H_2O content at H_2O/TMOS = 1.53, larger particles in the gel skeleton are visible in the gels from the solutions with greater HCl concentrations. In the gel formed from the solution with HCl/TMOS = 0.40, particles 5 μm in diameter and connected at the neck are visible. Dependence of the particle size on the HCl content of the starting solution is shown in Figure 3. As the particle size increases, the transparency of the resultant dried gel is lost, and as shown in Figure 3, the bulk density of the gels decreases. Greater concentrations of H_2O, however, decrease the particle size, as shown in Figure 2d.

Effect of the Concentration of the Solutions. The structure of the gel also depends on the concentration of the solutions, that is, the amount of alcohol in the solutions. Figure 4 shows the SEMs of the fracture surface of the dried gels derived from various solutions. Micrometer-sized particles are visible in the gel formed from the solution with CH_3OH/TMOS = 3 (Fig. 4b) as well as that from the solution with CH_3OH/TMOS = 2 (Fig. 2c). Solutions with smaller (CH_3OH/TMOS = 0.5) and larger (CH_3OH/TMOS = 5) CH_3OH concentrations, however, resulted in gels composed of fine particles (Fig. 4a and 4c).

Effect of the Kind of Alkoxides, Acids, and Alcohols. In the experiments on the gelation of solutions of tetramethoxysilane, tetraethoxysilane, tetraisopropoxysilane, and tetra-*n*-butoxysilane, in which solutions with H_2O/alkoxide = 1.5, HCl/alkoxide = 0.40, and [alkoxide] = 2 mol/L with CH_3OH as solvent were kept at 40 °C in air-sealed flasks, an opaque gel formed only from the TMOS solution, whereas no gelation took place in the solutions of the other alkoxides (*7*).

Substitution of methanol by isopropyl or *n*-butyl alcohol also prevented formation of opaque monolithic gels composed of micrometer-sized particles (*7*). TMOS solutions with mole ratios TMOS:H_2O:HCl:alcohol of

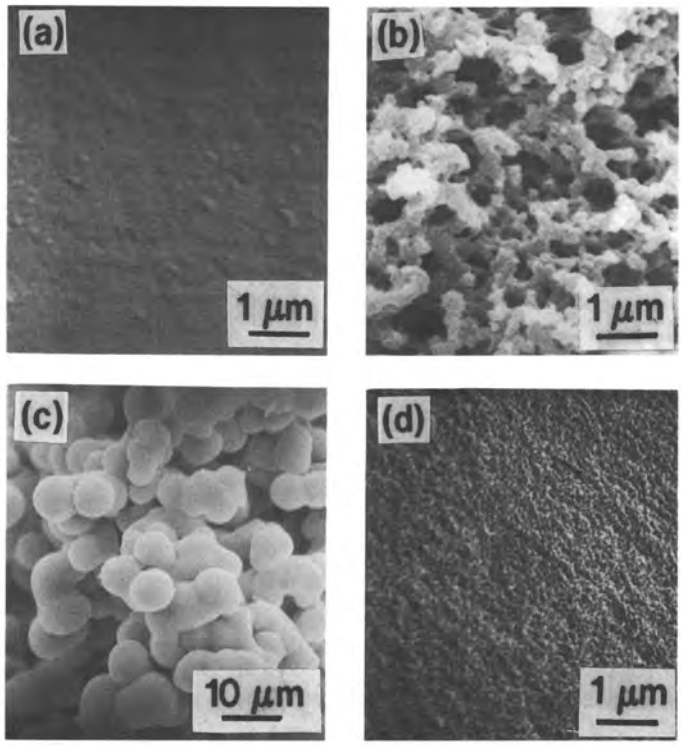

Figure 2. SEMs of dried gels formed from solutions with mole ratios TMOS:H_2O:HCl:CH_3OH of 1:1.53 or 2.00:0.01–0.40:2. Mole ratios were as follows: a, HCl/TMOS = 0.01 and H_2O/TMOS = 1.53; b, HCl/TMOS = 0.25 and H_2O/TMOS = 1.53; c, HCl/TMOS = 0.40 and H_2O/TMOS = 1.53; and d, HCl/TMOS = 0.40 and H_2O/TMOS = 2.00.

1:1.53:0.40:2 converted to opaque gel monoliths when methanol was used, whereas slightly opalescent gel fragments formed when isopropyl or *n*-butyl alcohol was used.

Mechanism of the Formation of Micrometer-Sized Particles

^{29}Si NMR Spectra of the Gels. Molecular structure of the polymerized species is compared for three kinds of materials: the opaque gel composed of micrometer-sized particles formed from a highly acidic TMOS solution with mole ratios TMOS:H_2O:HCl:CH_3OH of 1:1.53:0.40:2, the transparent gel derived from a weakly acidic TMOS solution with mole ratios TMOS:H_2O:HCl:CH_3OH of 1:1.53:0.01:2, and the silica particles formed from a solution with mole ratios TMOS:H_2O:NH_3:CH_3OH of 1:30:5:171. The first and second gels corre-

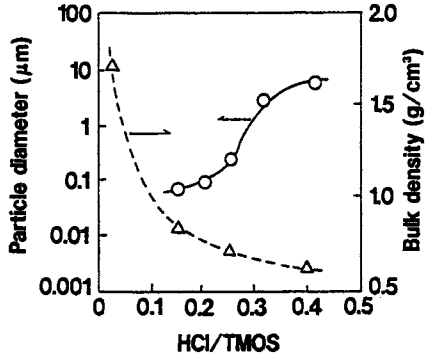

Figure 3. Dependence of particle size and gel bulk density on HCl/TMOS mole ratios. TMOS: H_2O: HCl: CH_3OH is 1:1.53:0.01–0.40:2.

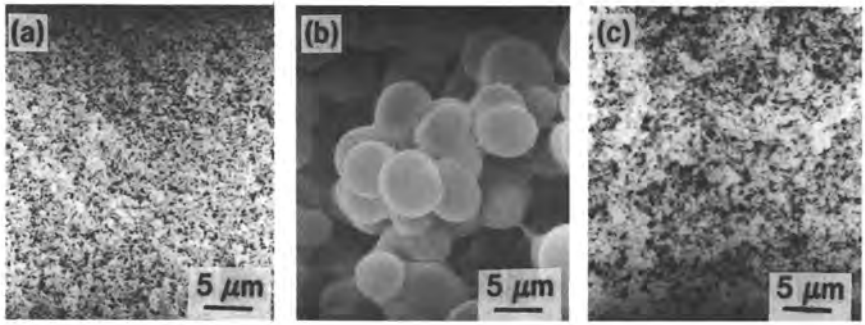

Figure 4. SEMs of the dried gels prepared from the solutions with mole ratios TMOS: H_2O: HCl: CH_3OH of 1:1.53:0.40:x, where x = 0.5 (a), 3 (b), and 5 (c).

spond to those shown in Figure 2c and 2a, respectively. The third one is made through a method similar to that of Stöber.

Figure 5 shows the ^{29}Si NMR spectra of these materials. There is less cross-linking in the gel from the highly acidic solution with a limited amount of water than in the silica particles from the highly basic solution with an excess of water; fewer Q^4 species, Si atoms having four bridging oxygens, and more Q^2 species, Si atoms having two bridging oxygens, are present in the gels from the acidic solutions. The extent of cross-linking of the polymerized species is totally different, although gels from both highly acidic and highly basic solutions have micrometer- or submicrometer-sized particles that can be seen microscopically.

In contrast, the gels from the highly acidic and weakly acidic solutions have similar NMR spectra. This similarity indicates that the extent of cross-linking of the silica polymers from the highly acidic solution is as low as

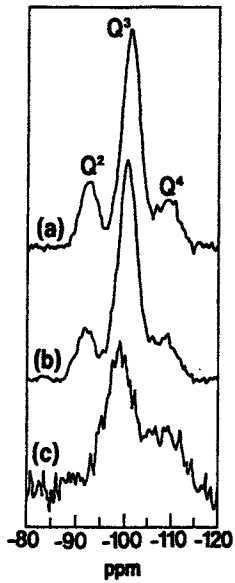

Figure 5. Silicon-29 NMR spectra of (a) a silica gel derived from a solution with molar composition TMOS:H_2O:HCl:CH_3OH of 1:1.53:0.4:2, (b) a silica gel derived from a solution with molar composition TMOS:H_2O:HCl:CH_3OH of 1:1.53:0.01:2, and (c) silica particles derived from the solution with molar composition TMOS:H_2O:NH_3:CH_3OH of 1:30:5:171.

that from the weakly acidic solution. It would be possible to assume that the round particles formed from the highly acidic solution consist of linear polymers or particles, which have been proposed to be polymerized species in the weakly acidic solutions with a limited amount of water (9). The sol from the weakly acidic solution has spinnability, that is, gel fibers can be drawn from the sol, and the resultant gel shows no particulate microstructure, whereas the sol from the highly acidic solution has no spinnability (6) and has particulate structure. It is plausible to think that these differences in the microstructure of the gels and the rheological properties of the sols do not arise from different polymer structures but from different aggregation states of the polymerized species.

The gels derived from the solutions with various CH_3OH concentrations, which have different microstructures, as mentioned in the section "Effect of the Kind of Alkoxides, Acids, and Alcohols", have almost the same ^{29}Si NMR spectra as those in Figure 6. This similarity indicates that the different microstructures observed for the gels from the solutions with different CH_3OH concentrations do not result from different structures of the polymers but rather from differences in the aggregation states of the polymers.

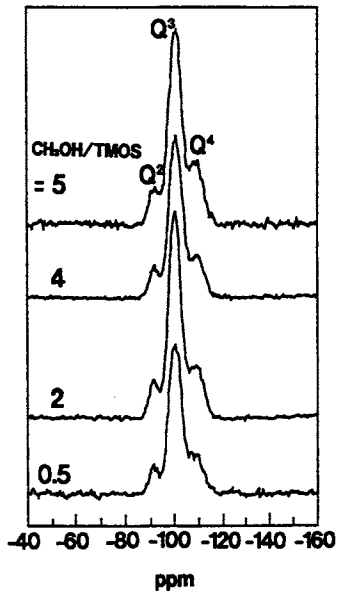

Figure 6. Silicon-29 NMR spectra of gels prepared from solutions with mole ratios TMOS: H_2O: HCl: CH_3OH of 1:1.53:0.40:x, where x = 0.5, 2, 4, and 5.

Instability of Particles in Organic Liquids. Sol particles formed in the TMOS solutions with excess HCl and a limited amount of H_2O are not stable in nonpolar organic solvents; a translucent sol derived from a solution with mole ratios TMOS: H_2O: HCl: CH_3OH of 1:1.53:0.40:2 becomes transparent when benzene is added. Thus, the particles, which are the source of the translucence of the sol, are composed of polymers or primary particles soluble in nonpolar organic solvents. Figure 7 shows SEMs of dried gels derived from the sols in which nonpolar benzene was added and polar methanol was added after the occurrence of translucence. Much finer microstructure is evident in the gel from the benzene-added sol, whereas micrometer-sized particles are seen in the gel from the methanol-added sol.

Instability of Particles under Centrifugation. The sol particles, the source of the translucence of the sols, are not stable against centrifugation. Figure 8 shows the dried gel obtained by centrifuging a sol with mole ratios TMOS: H_2O: HCl: CH_3OH of 1:1.53:0.40:2 before the occurrence of opalescence. Round, closed pores are visible instead of particulate structure; this observation suggests that the micrometer-sized, round particles formed in the reaction are not stable against mechanical forces and may consist of weakly cross-linked, flexible polymers.

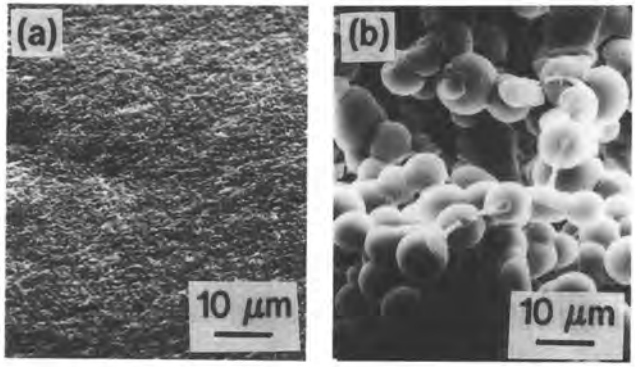

Figure 7. SEMS of the fracture surface of dried gels derived from solutions to which benzene was added (a) and methanol was added (b) after the occurrence of opalescence.

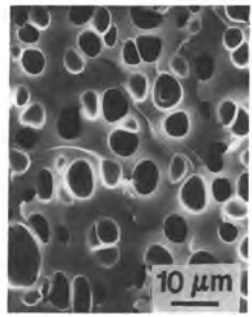

Figure 8. SEM of dried gel obtained with centrifugation.

Mechanism of the Formation of Round Particles. Because of the small amount of water used in the hydrolysis reaction in the starting solutions that give large particles, a large number of unhydrolyzed alkoxy groups are left on the polymerized species. These alkoxy groups give rise to the lipophilic nature of the polymerized species. A larger portion of methanol may be protonated and the ionic nature of the solvent may increase when a larger amount of HCl or an acid with a larger dissociation constant is used; these conditions result in a decrease in the solubility of the polymerized species in the solutions.

In the starting solutions with a large amount of water, the polymerized species would be soluble in the solvent because of the larger number of hydroxyl groups. Acids with lower dissociation constants were assumed to decrease the number of protonated alcohols, which reduce the ionic nature of the solvent. Alkoxides with longer hydrocarbon chains than

methanol—which will release the alkoxy groups in the hydrolysis reaction to generate alcohols with longer chains than methanol—and alcohols other than methanol would increase the solubility of the polymerized species in the solvent.

The amount of methanol in the solution will change the state of the aggregation of the polymerized species. The aggregation of the lipophilic polymerized species discussed here is also regarded as phase separation of the sol, in which oil-like polymerized species are separated from the solutions. The change of the ratio of the solvent to the polymers is expected to change the degree of phase separation.

Because of the lipophilic nature of the primary particles, translucent sols become transparent as a result of dissolution of the primary particles in the solvent when nonpolar organic solvents are added. Flexibility of the primary particles results in instability of the secondary particle, as seen in the centrifugation experiment. Changes in the gel structure by addition of organic compounds and by centrifugation and the formation of round particles are illustrated in Figure 9.

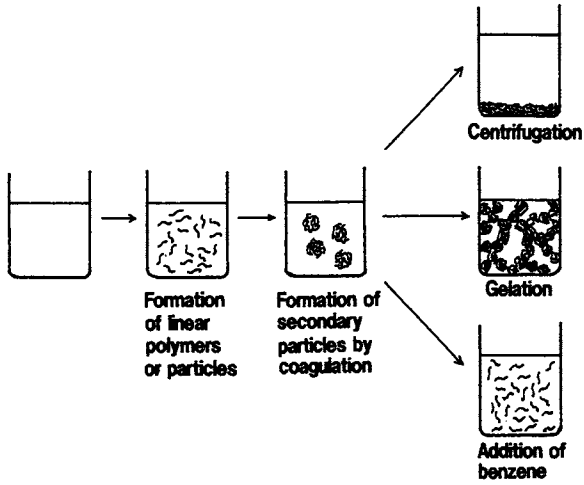

Figure 9. Illustration of the changes in the gel structure caused by the addition of organic compounds and by centrifugation.

Surface Changes in the Ambient Atmosphere. Large numbers of unhydrolyzed methoxy groups in the particles cause instability of the surface structure of the gel particles. Figure 10 shows SEMs of gels obtained from a TMOS solution and kept at 40 °C in the ambient atmosphere for various times after gelation. Because the round particles are secondary particles, gels kept at this temperature for 2 days have rough

surfaces. The surfaces of the particles, however, become more smooth with time. Reaction of the unhydrolyzed methoxy groups with the vapor in the atmosphere takes place after gelation, and polycondensation at the hydrolyzed sites may lead to the smoothing of the particle surface.

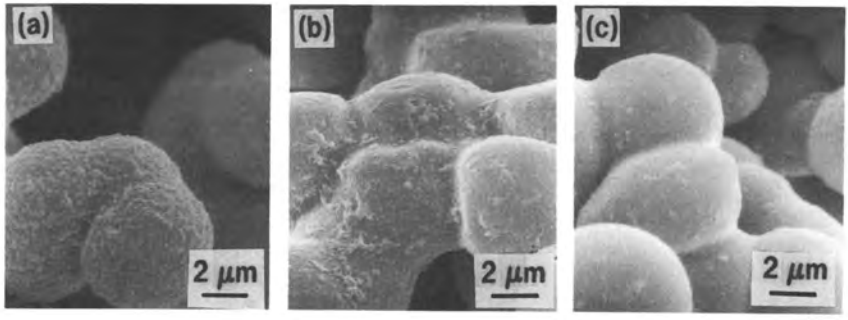

Figure 10. SEMS of dried gels prepared from solutions with mole ratios TMOS: H_2O: HCl: CH_3OH of 1:1.53:0.40:2 kept at 40 °C in the ambient atmosphere for (a) 2 days, (b) 5 days, and (c) 13 days after gelation.

Figure 11 shows the change of the specific surface area of the gel with time after gelation. Specific surface area is measured by the Brunauer–Emmet–Teller (BET) method by using N_2 gas as the adsorptive agent. The surface area decreases with time; this observation corresponds to Figure 10, in which a rough particle surface turned smooth.

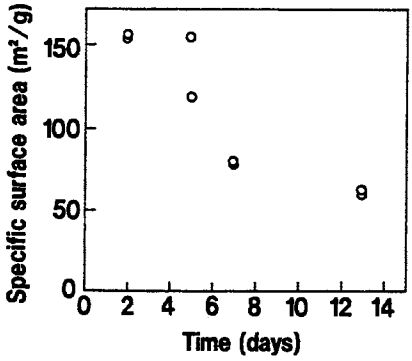

Figure 11. Change of the specific surface area of a gel with time after gelation. The gel was obtained from a solution with molar ratios TMOS: H_2O: HCl: CH_3OH of 1:1.53:0.40:2.

Applications

As mentioned in the introduction, the most serious problem encountered in sol–gel process for making bulk silica glasses is the fracture of gels during drying. At the interface between the residual liquids and the pore walls, large capillary forces are generated, which cause cracking of the gel body. Preparation of gels having large pores is effective in preventing fracture, because the capillary force decreases as the pore radius increases. The method described in this chapter can produce such gels easily, as shown in Figure 12, where a crack-free gel plate of 21 cm × 17 cm × 0.9 cm prepared from a solution with mole ratios TMOS:H_2O:HCl:CH_3OH of 1:1.53:0.25:2 and dried at 40 °C for about 1 month is shown.

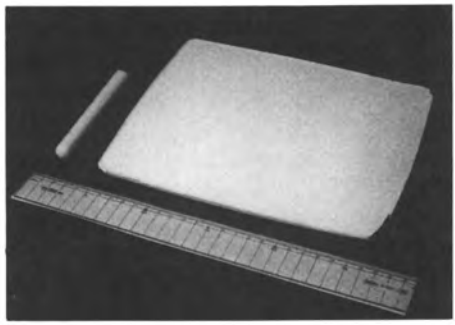

Figure 12. A gel plate and a rod obtained from a solution with mole ratios TMOS:H_2O:HCl:CH_3OH of 1:1.53:0.25:2 and dried at 40 °C for about 1 month.

These gels can be used as the precursor for porous silica glass bodies as well as for pore-free bulk silica glasses. Conventionally, porous silica glasses have been made by preparing sodium borosilicate glasses by the melt–quench method, heating the resultant glasses for phase separation, and leaching the Na_2O- and B_2O_3-rich phase out of the phase-separated glasses (*10*). High-purity porous silica glasses should be produced by a simple method, however, if silica gels are used as the precursor. Figure 13 shows a bulk porous silica glass made by the sol–gel method and an SEM of the fracture surface. The gel was prepared from a solution with mole ratios TMOS:H_2O:HCl:CH_3OH of 1:1.53:0.40:2 and dried at 40 °C for a few months. The dried gel was then heated at a rate of 0.5 °C/min to 1300 °C and kept at that temperature for 3 h. A crack-free porous glass was successfully obtained, and continuous pores more than 10 μm in diameter are visible.

The pore characteristics can be controlled not only by changing the composition of the starting solution but also by changing the heat

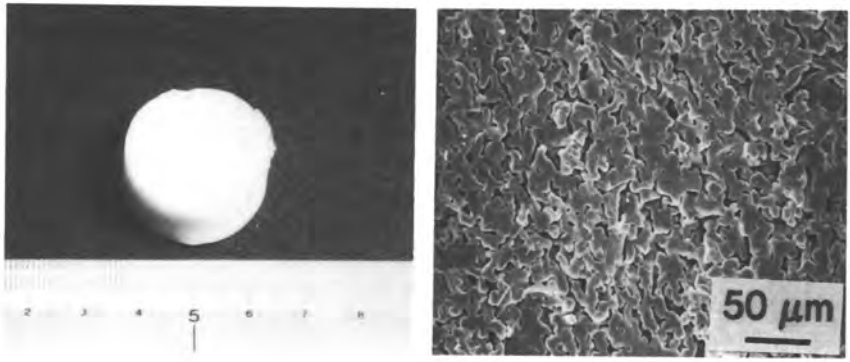

Figure 13. Appearance (left) and SEM of the fracture surface (right) of a porous silica glass prepared by the sol–gel method.

treatment conditions of the gels. Figure 14 shows pore-size distributions of a gel and its derivatives made with differing heat treatments. Because measurement was possible only at pressures higher than 1 atm (101 kPa), measurement of the pore-size distribution could not be made for pores larger than 7.5 μm in radius. However, pores larger than 7.5 μm in radius are present in the gel, and the pore volume decreases and the pore-size

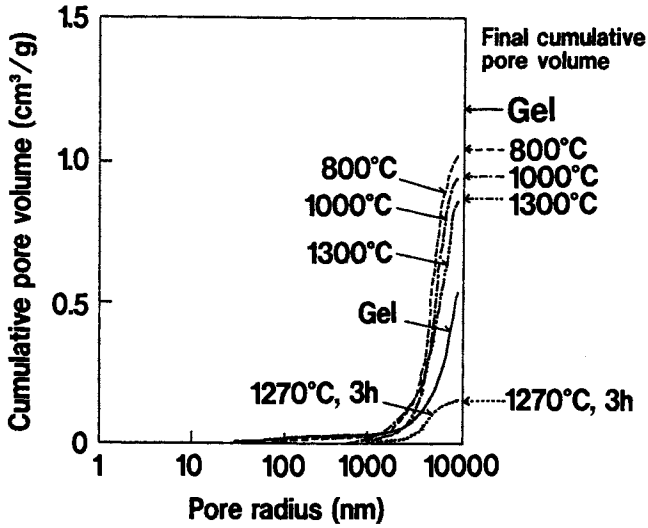

Figure 14. Pore-size distribution curves of silica gel and gel-derived porous silica glasses. The gel was obtained from a solution with mole ratios TMOS:H_2O:HCl:CH_3OH of 1:1.53:0.40:2. The gel was dried at 40 °C for 7 days and heated at a rate of 0.5 °C/min to various temperatures.

distribution shifts to smaller radius when the upper heat treatment temperature is increased.

Such porous silica glasses of micrometer-sized pores can serve as filters and enzyme and microbe supports. If the small pores on the particle surface or the roughness of the particle surface are designed to be retained after heat treatment, the resultant porous glasses can be used as filters that function as catalyst supports.

References

1. Rabinovich, E. M.; Johnson, D. W., Jr.; MacChesney, J. B.; Vogel, E. M. *J. Am. Ceram. Soc.* **1983,** *66,* 683.
2. Rabinovich, E. M. *J. Mater. Sci.* **1985,** *20,* 4295.
3. Scherer, G. W.; Luong, J. C. *J. Non-Cryst. Solids* **1984,** *63,* 163.
4. Prassas, M.; Phalippou, J.; Zarzycki, J. *J. Mater. Sci.* **1984,** *19,* 1656.
5. Toki, M.; Miyashita, S.; Takeuchi, T.; Kanbe, S. *J. Non-Cryst. Solids* **1988,** *100,* 479.
6. Kozuka, H.; Sakka, S. *Chem. Mater.* **1989,** *1,* 398.
7. Kozuka, H.; Yamaguchi, J.; Sakka, S. In *Proceedings of the XVth International Congress on Glass*; Mazurin, O. V., Ed.; Nauka: Leningrad, U.S.S.R., 1989; Vol. 2a, p 32.
8. Stöber, W.; Fink, A.; Bohm, E. *J. Colloid Interface Sci.* **1968,** *26,* 62.
9. Sakka S.; Kamiya, K. *J. Non-Cryst. Solids* **1982,** *48,* 31.
10. Nordberg, M. E. *J. Am. Ceram. Soc.* **1944,** *27,* 299.

RECEIVED for review December 19, 1990. ACCEPTED revised manuscript January 3, 1992.

7

Stability of Aqueous Silica Sols

Thomas W. Healy

School of Chemistry, The University of Melbourne, Parkville, VIC., 3052, Australia

The control of silica sol coagulation by pH and by addition of simple electrolytes is said to be "anomalous" in that it is not simply predicted by conventional Derjaguin–Landau–Verwey–Overbeck (DLVO) theory. This chapter describes a model based on the control of coagulation by surface steric barriers of polysilicate and bound cations. The model suggests new experimental directions.

THE COAGULATION–DISPERSION BEHAVIOR of aqueous silica sols is central to almost all processes requiring their unique adsorption, dispersion, gelation, and sol–gel properties. Aqueous silica sols are of particular interest in colloid science because their coagulation–dispersion behavior is said to be "anomalous", that is, their stability in terms of electrolyte–pH control does not follow the pattern followed by almost all other oxide and latex colloidal materials. This chapter examines aqueous silica sol coagulation effects in light of studies of macroscopic silica–water interfaces and in particular the electrical double layer at such interfaces.

It is difficult to define precisely the term "aqueous silica sols" and thereby contrast them with other forms of silica (colloidal silica, colloidal quartz, pyrogenic silica, and so forth). Bulk chemical distinctions are not very useful. The definition chosen here follows Iler's terminology (*1*). Aqueous silica sols are characteristically composed of spherical particles nucleated and grown by alkaline hydrolysis of sodium silicate solutions. They are often monodisperse systems and have particle diameters in the range 1–100 nm (density, ~2.2 g/cm^3) that lead to sols that vary from optically transparent to opalescent.

The colloidal behavior referred to in the preceding text as "anomalous" helps to further define the term "aqueous silica sols". Iler (*2*) noted,

0065–2393/94/0234–0147$08.00/0

in a second major monograph, that such silica sols were colloidally stable at their isoelectric point pH (pH_{iep}). Iler also noted their remarkable stability in high salt concentration at near-neutral pH.

The first definitive study of the "anomalous" coagulation behavior of silica sols was by Allen and Matijévic (*3*) in 1969. They focused on the measurement of the "critical coagulation concentration" of Ludox AM & HS sols 15 nm in diameter [210 m^2/g Brunauer–Emmett–Teller (BET) surface area], as determined by standard Rayleigh ratio light-scattering measurements. Figure 1 is a summary of the key results of Allen and Matijévic (*3*). In particular, when Na^+ and Li^+ were the coagulating cations, the critical coagulation concentration decreased with increasing pH. Further, the silica sols were colloidally stable below the pH limit of Figure 1 and stable at the observed pH_{iep} of about pH 2–3. For K^+ and Cs^+ the silica sols were stable from pH 2–3 to pH 6, and these ions showed an irregular series effect in the pH 6–11 range, as shown schematically in Figure 1.

Depasse and Watillon (*4*) in a similar study in 1970 observed the same "anomalous" coagulation trends, again using standard light-scattering techniques with 50-nm-diameter silica sol particles prepared in a way similar to the technique of Allen and Matijévic (*3*). Figure 2 is a summary of the Na^+ and Li^+ coagulation data of Depasse and Watillon (*4*) for an addition of electrolyte of 1.5 M.

The simplest way of focusing on the "anomalous" character of these results is to present the variation of the electrokinetic or zeta potential of the silica sols as a function of pH and added salt. The general form of the electrokinetic results obtained for a vitreous silica (*5*) and for all silica sols is shown schematically in Figure 3.

The silica sols, and indeed all oxide sols, show an increasing negative zeta potential with increasing pH as the pH is raised above the pH_{iep}. The magnitude of the zeta potential decreases uniformly at each pH as the salt concentration is increased. There are subtle effects in the electrokinetics as the counterion is varied from Li^+ to Cs^+, but these effects are minor compared with the general reduction in zeta potential as the pH is moved toward the isoelectric point or as 1:1 electrolyte is added at any pH.

The usual result of such variation in the zeta potential with pH and 1:1 electrolyte concentration is that the critical coagulation concentration normally varies with pH as shown schematically by the theory line in Figure 4. The critical coagulation concentration increases as the pH is increased above the isoelectric point and peaks at high values as shown. Many examples of these trends are confirmed for oxide and latex colloids for which H^+ and OH^- are potential-determining ions (*6, 7*). The inset of Figure 4 illustrates this normal or theoretical variation with pH expected of the critical coagulation concentration, together with the form of the observed results for silica sols. In this inset the high-PH critical coagulation

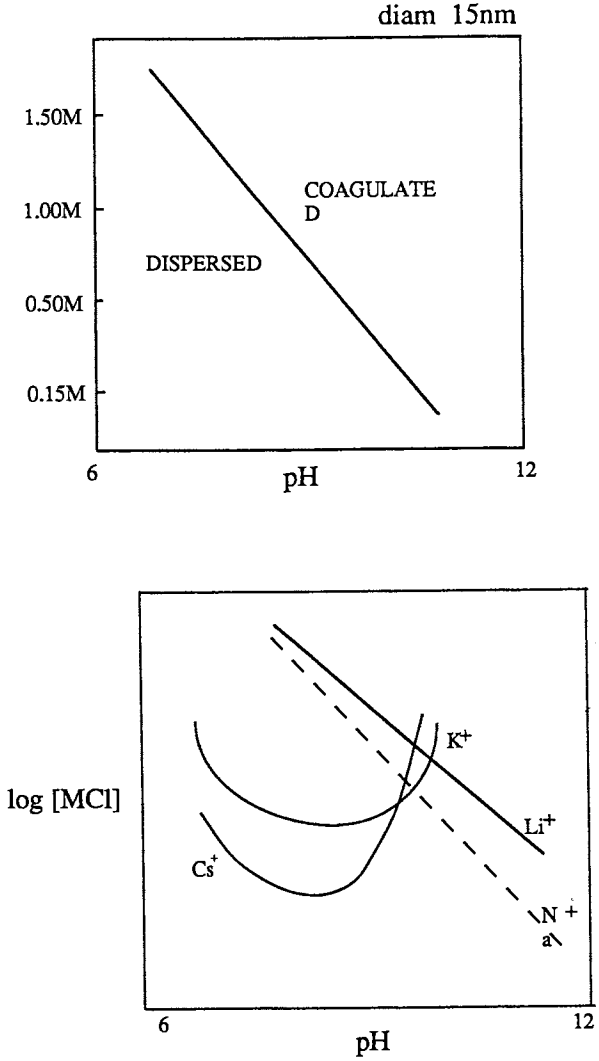

Figure 1. Schematic view of the coagulation domains of Ludox silica sols observed by Allen and Matijević. (Adapted from reference 3.)

concentration values, for both theory and experiment, are shown coinciding for reasons to be highlighted subsequently. The challenge for researchers is to seek an understanding in terms of classic Derjaguin–Landau–Verwey–Overbeek (DLVO) theory, and more recent formulations of stability theory of the increased stability with decreasing pH and the observed stability at the pH_{iep}.

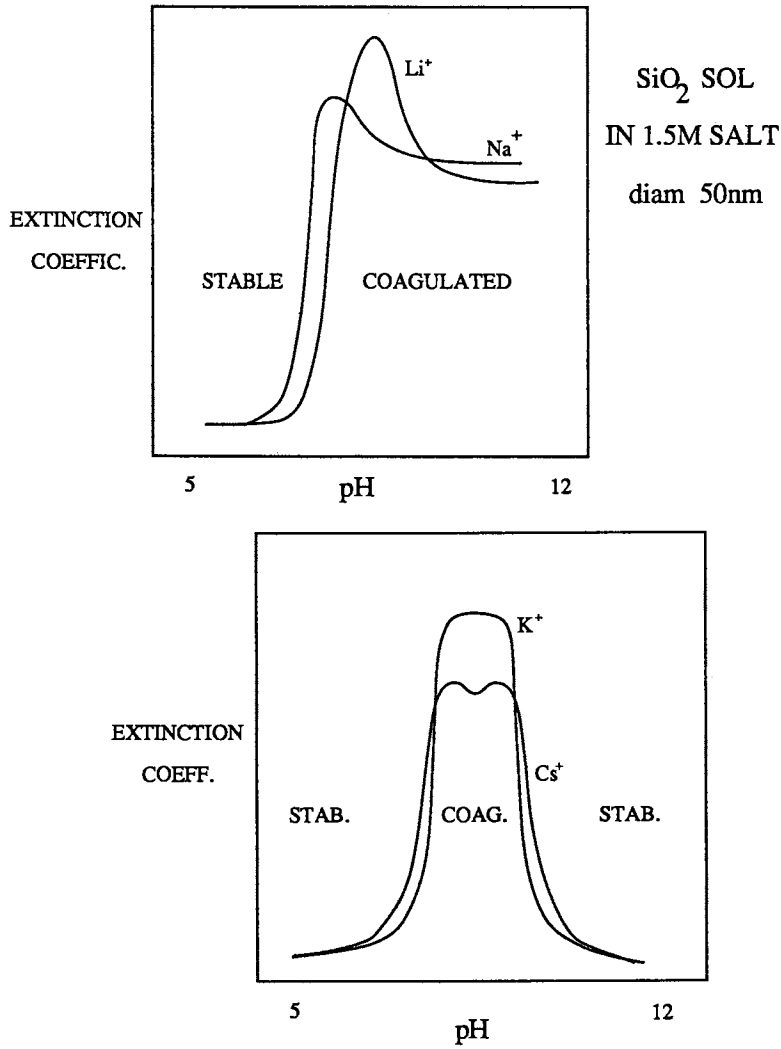

Figure 2. Schematic view of the coagulation domains of SiO_2 sols as determined by Depasse and Watillon. (Adapted from reference 4.)

Origins of Colloid Stability

The intention in this section is to define key concepts and terms; detailed descriptions of the forces between colloidal particles are in standards texts (*8*, *9*).

Electrostatic Repulsion. The electrostatic energy of repulsion (V_R) between like charge surfaces arises from the overlap of the electrical double layers on the two particles. The range of interaction is of the order

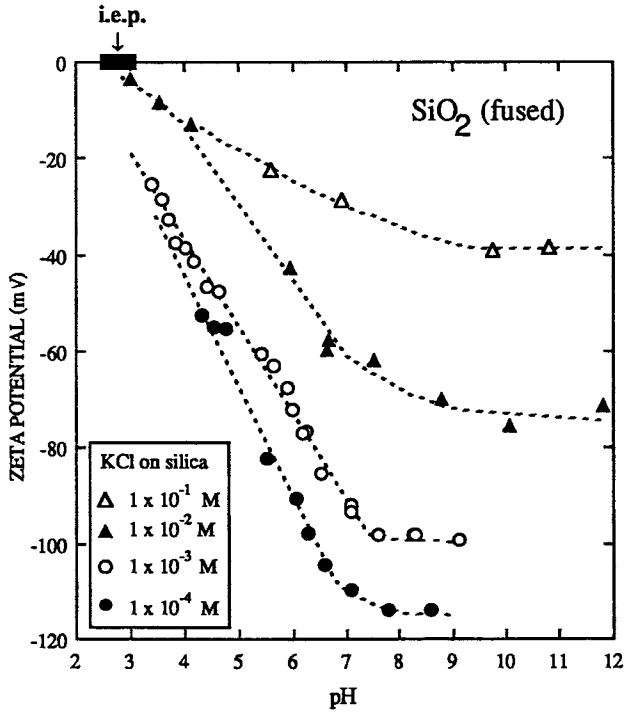

Figure 3. Plot of the zeta potential of a fused silica capillary versus pH in aqueous solutions of KCl as determined by the flat-plate streaming potential technique. (Adapted from reference 5.)

of the Debye–Hückel reciprocal length (κ^{-1}). For 1:1 electrolytes the value of κ^{-1} is approximately 10, 3, and 1.0 nm for concentrations of 10^{-3}, 10^{-2}, and 10^{-1} M, respectively. The magnitude of V_R at any given value of separation between two particle surfaces at given values of particle size, electrolyte concentration, and temperature is proportional to the surface potential (ψ_o) on each particle. A measure of ψ_o and hence the repulsive energy of interaction can be obtained from the experimentally accessible, measured electrokinetic or zeta potential (ζ) by equating ζ to ψ_d, the diffuse-layer potential.

The link between the surface charge and the potentials ψ_o, ψ_d, and ζ is not trivial in the case of the silica–water interface (*10*). Unlike other oxides, the SiO_2 pH–charge relationship shows a characteristically small charge at small values of ΔpH for pH values exceeding pH_{iep} (*11, 12*). According to Healy and White (*13*), this relationship means that ψ_d ($\equiv\zeta$), within 2–3 units of the isoelectric point, will be expected to be smaller than that of oxides such as TiO_2, Al_2O_3, and Fe_2O_3. Such a relatively slow increase in potential is seen in some studies of the ζ–pH relationship of

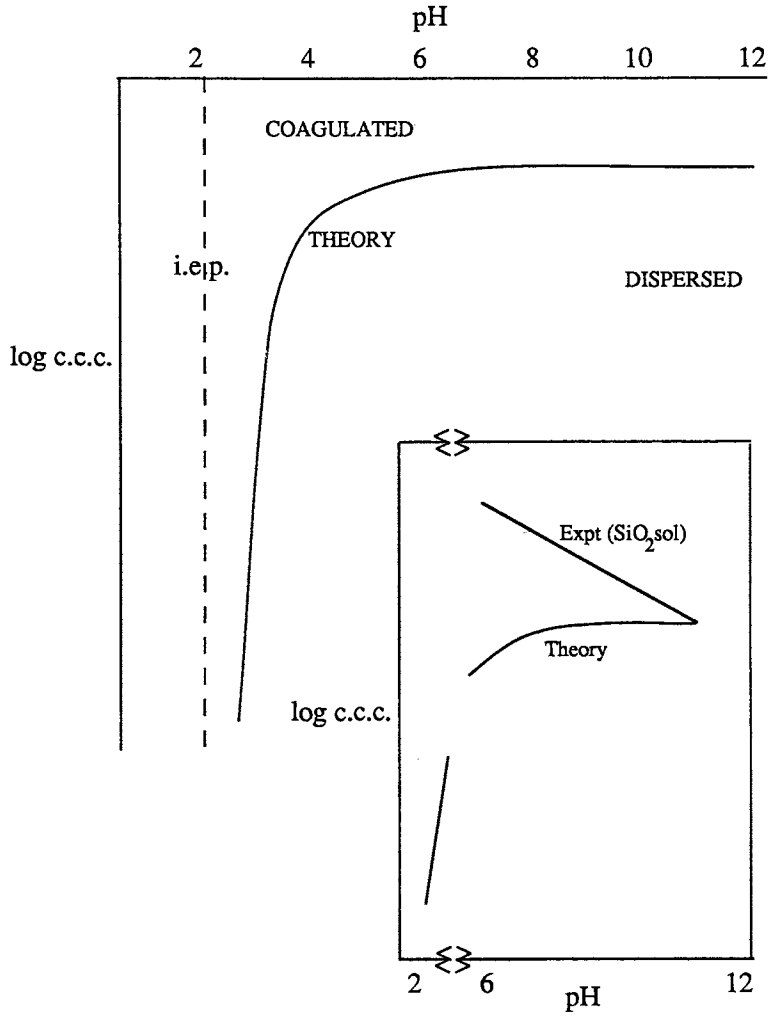

Figure 4. Schematic variation of the DLVO theoretical stability domain for a $pH_{i.e.p.}$ colloid of pH 2 (critical coagulation concentration, c.c.c.; isoelectric point, i.e.p.). The insert shows this theoretical prediction compared to that observed for silica sols.

silica sols (*3*) but is less evident in studies of the zeta potential of macroscopic vitreous silica or quartz surfaces (*5*, *14*).

Again, silica, unlike other oxides, will not regulate charge during the approach of two surfaces (*15*) and may demonstrate a subtly different V_R–separation curve. Recent computations (*16*) suggest such charge-regu-

lation effects will be small, but will be seen most especially around pH_{iep}, at which point the SiO_2 surface charge is low.

Consideration of the stability of silica sols, that is, the so-called "anomalous" stability, will, in later sections of this chapter, focus on 1:1 electrolyte concentrations of 0.1 M and greater. At this salt concentration, the range of the repulsive electrostatic forces between particles is small, and any subtle differences in the electrostatics between silica and other oxide sols in itself cannot provide the necessary repulsion to stabilize silica sols at such high electrolyte levels.

van der Waals Attraction. The attractive van der Waals energy of interaction (V_A) for spheres in the 10- to 100-nm size range for silica sols discussed here varies as the inverse of the separation distance, and at any separation V_A is directly proportional to particle size. The Hamaker constant (A), which controls the magnitude of the variation of van der Waals attraction with particle radius (a) and separation (H_o) between surfaces, is for silica–water–silica not a large number. Further, the known hydration–polysilicic acid formation at silica–water interfaces will further reduce the overall Hamaker constant in the silica sol–water–silica sol system.

The simple attractive van der Waals term (V_A) and the simple electrostatic (double-layer) repulsive interaction energy (V_R) are now summed. Silica sol particles in the 10–100 nm radius size range, for salt concentrations of 0.1 M and greater and for pH values of 5 or more above the pH_{iep} of silica are now considered. The isoelectric point is taken as pH 2–3. Thus for 25-nm-radius particles the variation of total energy V_T ($= V_A + V_R$) with particle separation is attractive at all separations, and the sols are therefore expected to be unstable over this entire pH range above 5 as shown by the theory line in Figure 4 and in the inset in Figure 4.

It is important to dispel any hope that adjustment of the electrostatic or van der Waals term will bring theory into line with experiment for silica sols. At about 0.1 M 1:1 electrolyte, reductions in the Hamaker constant to values near that of water itself or potentials of near −100 mV at, for example, pH 9–10 would be required. The experimental evidence (*17*) clearly points to a value more like −20 mV. Furthermore, several successful fits of double-layer theory to the observed charge and potential behavior of silicas are illustrated by the results (points) and theory (solid lines) in Figure 5, taken from the work of James (*17*) for a well-studied pyrogenic silica. James (*17*) invoked site dissociation, that is,

$$-SiOH \longrightarrow -SiO^- + H^+$$

and counterion binding, for example,

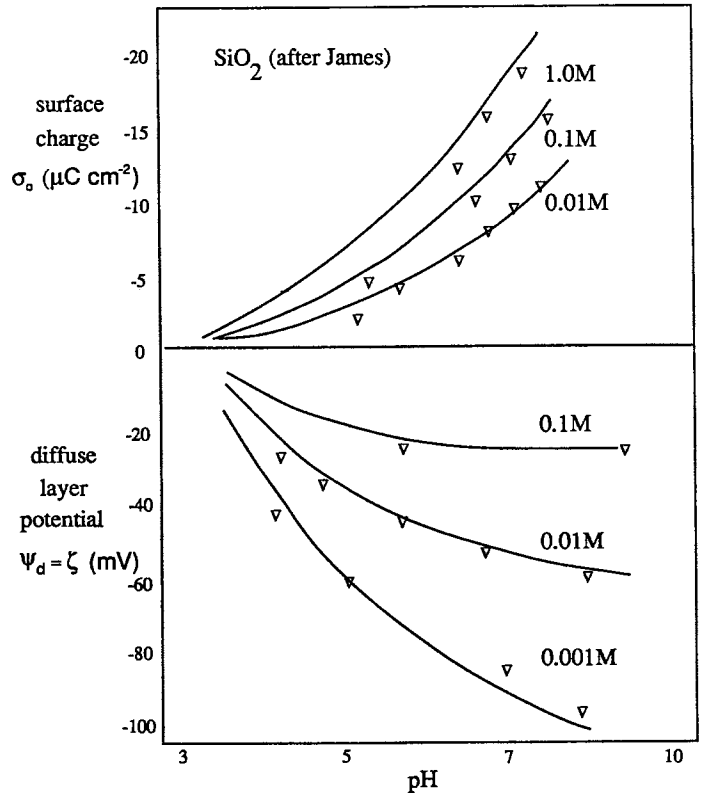

Figure 5. Comparison of theory and experiment in the variation of surface charge and electrokinetic potential for a pyrogenic silica. (Adapted from reference 17.)

$$-SiO^- + Na^+ \longrightarrow -SiO^-Na^+$$

and fitted simultaneously (as shown in Figure 5) the observed charge and potential data. Similar fits to observed charge and potential data for many forms of silica, including silica sols, have been made, and only minor adjustment of the (sodium) ion binding constants are required.

Steric Stabilization and "Anomalous" Stability. An explanation of the "anomalous" stability of Iler's silica sols in terms of steric stabilization effects requires that oligomeric or polymeric silicate species are present at the silica–water interface and that steric repulsion results during overlap of such layers. This mechanism is appealing in that soluble silicates, usually sodium silicates, are universal dispersants of many

electrostatic colloids. Again, well-hydrated silicas (*2*) and other colloids exposed to aqueous silicate (*18*) acquire high adsorption densities of aqueous silica.

To construct a model for "anomalous" stability, observations of silica sols at pH 11 are used. Allen and Matijévic (*19*) observed a critical coagulation concentration of approximately 0.15 M for Na^+ at pH 11.0. If they take this pH 11 sol to, for example, pH 8.0, it remains stable in salt concentrations much greater than 0.15 M, and the critical coagulation concentration increases even further as the pH is reduced from pH 8 to pH 6.

At pH 11.0, if the silica sol is treated as a "normal" 30-nm-diameter silica (without adsorbed silicate layers), DLVO calculation generates a coagulation condition ($V_{Tmax} = 0$) at just under 2-nm surface separation. The electrostatic repulsion is inside this separation and cannot overcome the van der Waals attraction.

A key element of this postulate is that the silica sol is "normal" at pH 11.0; that is, it has no protective (steric) layer of silicate. Iler (*2*) and more recently Furlong et al. (*18*) noted the desorption (or lack of adsorption) of oligomeric and polymeric aqueous silica at pH values above 10.5. Conversely, these workers observed adsorption of oligomeric and polymeric aqueous silica below pH 10.5.

Thus, as the pH is changed from 11 to 8 in 0.15 M salt, silicate steric layers are generated. For these layers to stabilize the sol under these conditions, they must extend farther than the $V_{Tmax} = 0$ condition of 2 nm. The hypothesis is therefore that a 2-nm steric silicate oligomer–polymer barrier protects a silica sol at pH 8.0 in 0.15 M salt.

To explore this very simple picture further, the ion-exchange behavior of silica sols must be considered. In their 1970 paper Allen and Matijévic (*19*) linked the observed coagulation behavior to the observed ion exchange. In this elegant study they introduced the concept of a "critical exchange curve", namely, the increase in exchange capacity with increasing pH at the critical coagulation concentration condition at each pH. These ion-exchange results can be used to consider what happens as salt is added to the pH 8, 0.15 M salt case that we have proposed is stabilized by a steric silicate polymer layer.

The stabilizing adsorbed polysilicate layer is the actual exchange volume or layer, and addition of salt above 0.15 M must lead to further binding of Na^+ to the stabilizing layer. It is therefore important to view the barrier at the surface as a M^+–polysilicic acid coating, which will increase in thickness as the pH is decreased because of decreased –SiOH ionization; conversely, it will decrease in thickness as the amount of bound cation increases (i.e., it will "exchange") in the language of Allen and Matijévic.

Indeed, the presence of increasing amounts of bound Na^+ must switch off the electrosteric contribution of the adsorbed polysilicate layer, and,

for the pH 8.0 sol at its critical coagulation concentration, which is greater than 0.15 M, a secondary minimum well of $>2kT$ must open up as a result of the compression of the thickness and screening length of the adsorbed layer (k, Boltzmann constant; T, temperature).

Similar effects will operate at pH 6.0, initially at 0.15 M salt, where again the sol is electrosterically stabilized. As salt is added at pH 6, again the thickness and range of the electrosteric coating will eventually decrease to yield a $>2kT$ secondary minimum at the critical coagulation concentration, which is very much greater than 0.15 M. These effects are summarized schematically in energy–distance curves in Figure 6.

The sequence is as follows:

1. pH 11; 0.15 M NaCl—unstable "normal" sol behavior
2. pH 8.0; 0.15 M NaCl—stable because of electrosteric coating
3. pH 8.0; >0.15 M NaCl—secondary minimum coagulation
4. pH 6.0; 0.15 M NaCl—stable; electrosteric barrier
5. pH 6.0; >>0.15 M NaCl—secondary minimum coagulation

The proposed mechanism has several interlocking postulates that will need experimental testing. They are as follows:

- At pH 11, oligomeric–polymeric silicate is absent from the sol particle surface.
- At pH <10.5, oligomeric–polymeric silicate coatings appear.
- These oligomeric–polymeric coatings are electrosteric stabilization barriers.
- The range of steric thickness plus electrostatic screening increases as the pH is reduced from 11 to 6 and decreases as the layers bind more Na^+ as the total coagulating salt concentration is increased above 0.15 M.

The final application of the hypothesis concerns the behavior of silica sols at, say, 0.15 M salt as the pH is reduced from 11 to 2. The energy–distance curves for such cases are shown schematically in Figure 7. The top starting curve illustrates the case of a sol initially at pH 11 but now at pH 2. The $V_{T\max} = 0$ condition is maintained, and at pH 2 such a sol should be coagulated. Coating by oligomeric–polymeric silica generates a thick (low degree of ionization) coating at pH 2 that gives significant steric, rather than electrosteric, protection. Addition of salt fails to diminish this coating thickness at the low cation-exchange state or low cation-exchange

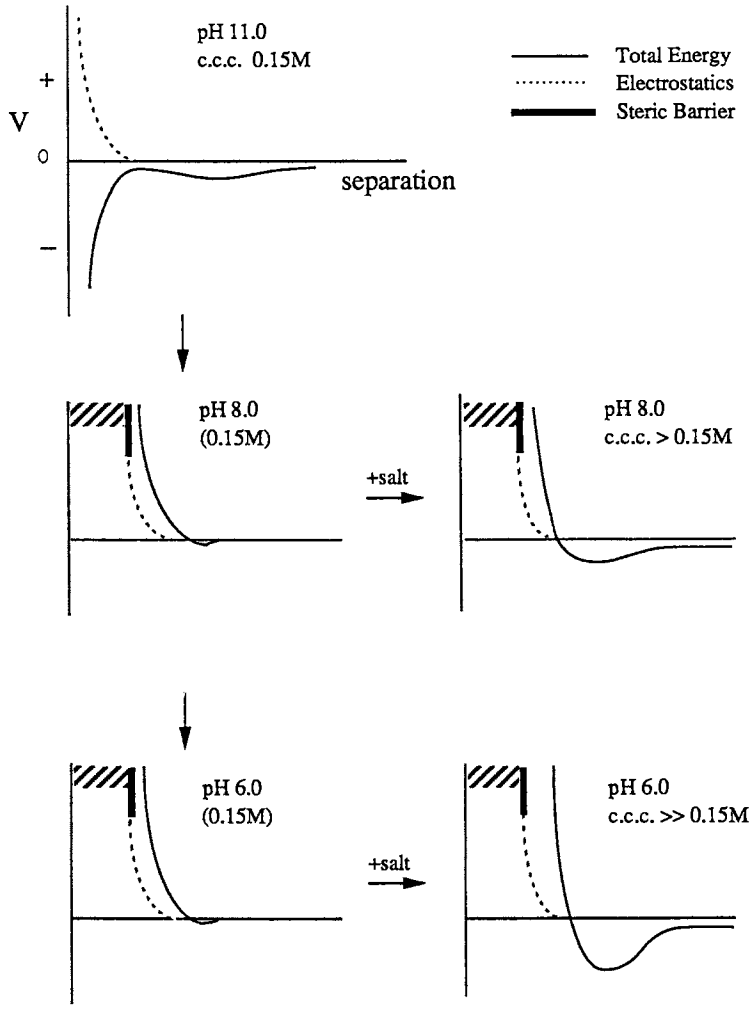

Figure 6. Total energy–distance curves for silica sols initially at pH 11 and 0.15 M 1:1 electrolyte, together with an illustration of the electrosteric barrier effect at pH values of 8.0 and 6.0 and electrolyte concentrations in excess of 0.15 M.

capacity state of pH 2. Secondary minimum effects would be pushed out to unrealistic values of greater than 5 nm.

Hydration Effects. In this discussion of silica sols at pH 11, 8, 6, and 2, the cation effects or critical coagulation concentration effects are focused on Na^+. As indicated in Figures 1 and 2, the silica sol coagulation behavior, with respect to the sequence Cs^+ through Li^+, is not simple. Thus, in general terms, Li^+ behaves in a manner similar to Na^+ in that the critical coagulation concentration increases as the pH moves from 11 to 6;

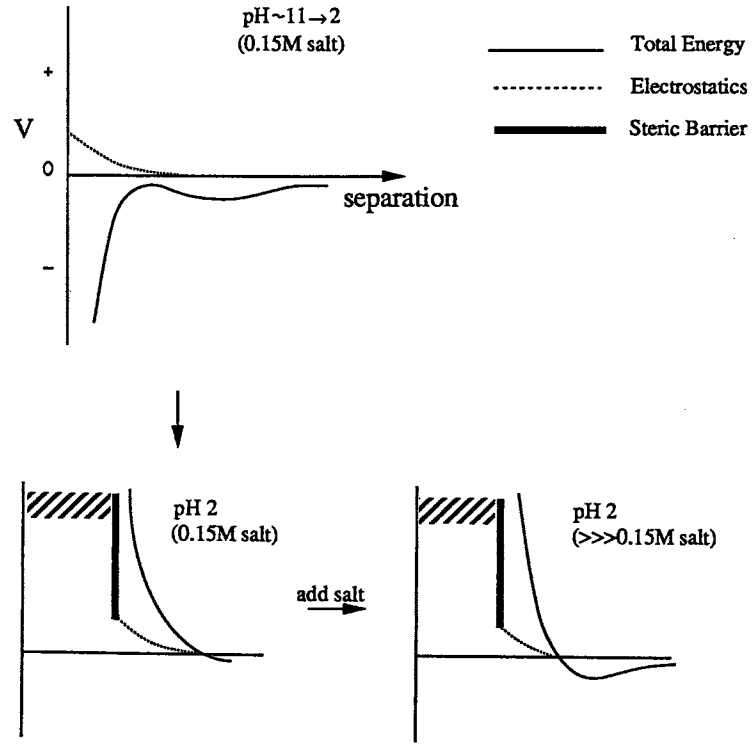

Figure 7. Total energy–distance curves for silica sols initially at pH 11 and 0.15 M 1:1 electrolyte, together with an illustration of the steric barrier effect at pH 2 and electrolyte concentrations very much in excess of 0.15 M.

Li^+ contains sols more "anomalously" stable than those with Na^+ as counterion. The behavior with Cs^+ is "normal"; that is, the critical coagulation concentration decreases slightly as the pH moves from 11 to 8.5, but again increases as the pH moves from 8.5 to 6.0.

Viewed in terms of the electrosteric mechanisms outlined in Figures 6 and 7, the 1:1 electrolyte cation effects indicate that relative to Na^+, Li^+ enhances any stability imposed by the barrier of polysilicate plus bound cation, whereas Cs^+ diminishes such effects. This observation is consistent with a "hydration stabilization" (*6*) mechanism. Thus, the more strongly hydrated the cations in the polysilicate exchange layer,

- the lower the binding energy,
- the lower the extent of exchange,
- the thicker the layer at any given pH and salt molarity, and
- the more effective the electrosteric barrier.

Conclusions

The origin of the coagulation behavior of Iler's "silica sols" is far from understood. The electrosteric barrier model herein proposed is designed to stimulate new experimental initiatives in the study of colloidal silica sol particles and their surface structure. The adsorbed steric layer, impregnated with bound (exchanged) cations, at the surface of 1–100-nm-diameter silica sol particles has the general properties needed to understand the "anomalous" coagulation behavior. The details await experimental and theoretical input.

Acknowledgments

This work was supported by an Australian Research Council Program grant. Participation in the ACS R. K. Iler Memorial Symposium in September 1990 was made possible by a generous grant from the Corporate Colloid Group of ICI (United Kingdom).

References

1. Iler, R. K.; *The Colloid Chemistry of Silica and Silicates;* Cornell University Press: Ithaca, NY, 1955.
2. Iler, R. K.; *The Chemistry of Silica;* Wiley: New York, 1979.
3. Allen, L. H.; Matijévic, E. *J. Colloid Interface Sci.* **1969,** *31,* 287.
4. Depasse, J.; Watillon, A. *J. Colloid Interface Sci.* **1970,** *33,* 430.
5. Scales, P. J.; Grieser, F.; Healy, T. W.; White, T. W.; Chan, D. Y. C. *Langmuir* in press.
6. Healy, T. W.; Homola, A.; James, R. O.; Hunter, R. J. *Faraday Discuss. Chem. Soc.* **1978,** *65,* 156.
7. Wiese, G. R.; Healy, T. W. *J. Colloid Interface Sci.* **1975,** *51,* 427.
8. Hunter, R. J. *Foundations of Colloid Science;* Oxford University Press: New York, 1989; Vol. 1.
9. Russel, W. B.; Saville, D. A.; Schowalter, W. R. *Colloidal Dispersions;* Cambridge University Press: Cambridge, UK, 1990.
10. Yates, D. E.; Levine, S.; Healy, T. W. *J. Chem. Soc. Faraday Trans. 1* **1974,** *70,* 1807.
11. Tadros, Th. F.; Lyklema, J. *J. Electroanal. Chem. Interfacial Electrochem.* **1968,** *17,* 267.
12. Yates, D. E.; Healy, T. W. *J. Colloid Interface Sci.* **1976,** *55,* 9.
13. Healy, T. W.; White, L. R. *Adv. Colloid Interface Sci.* **1978,** *9,* 303.
14. Wiese, G. R.; James, R. O.; Healy, T. W. *Faraday Discuss. Chem. Soc.* **1971,** *52,* 302.
15. Healy, T. W.; Chan, D. Y. C.; White, L. R. *Pure Appl. Chem.* **1980,** *52,* 1207.
16. Metcalfe, I. M.; Healy, T. W. *Faraday Discuss. Chem. Soc.,* in press.
17. James, R. O. *Adv. Ceram.* **1987,** *21,* 349.
18. Furlong, D. N.; Freeman, P. A.; Lau, A. C. M. *J. Colloid Interface Sci.* **1981,** *80,* 21.
19. Allen, L. H.; Matijévic, E. *J. Colloid Interface Sci.* **1970,** *33,* 420.

RECEIVED for review May 2, 1991. ACCEPTED revised manuscript March 25, 1992.

8

Surface Structure of Amorphous and Crystalline Porous Silicas

Status and Prospects

K. K. Unger

Institut für Anorganische Chemie und Analytische Chemie, Johannes Gutenberg-Universität, P.O. Box 3980, D-6500 Mainz, Germany

Substantial progress in the elucidation of the surface structure of crystalline and amorphous silicas has been achieved by means of high-resolution spectroscopic techniques, for example, ^{29}Si cross-polarization magic-angle spinning NMR spectroscopy and Fourier transform IR spectroscopy. The results lead to a better understanding of the acidity, dehydration properties, and adsorption behavior of the surface. These properties are key features in the design of novel advanced silica materials. The current methods of characterization are briefly reviewed and summarized.

THE SURFACE CHEMISTRY OF SILICA was a subject of intensive study in the period between 1960 and 1970 as a consequence of the widespread industrial use of colloidal, pyrogenic, and precipitated silicas, as well as silica hydrogels and xerogels. Chemical surface reactions and IR spectroscopy were the most-applied methods in surface structure elucidation. Significant contributions to the understanding of the silica surface were made by Fripiat (*1*), Kiselev and co-workers (*2*), Hair (*3*), Little (*4*), Peri (*5*), and others. In contrast to this active period, little progress was since made until about 1980. Advances in surface and materials science caused a search for novel materials with controllable properties, and the surface structure of silica regained considerable interest. Three major developments were important: first, the experience gained in silicate chemistry (*6*), particularly in the area of synthetic zeolites (*7*); second, the increasing

0065–2393/94/0234–0165$08.00/0

use of surface-modified silicas as packings in high-performance liquid chromatography (HPLC) (*8*); and third, the progress made in high-resolution spectroscopic techniques applied to surface characterization. This chapter summarizes the most important achievements made in this field and puts the problems involved into perspective.

Structural Aspects in Silica Chemistry

The term silica, as applied to solid forms having the stoichiometric composition of SiO_2, has many meanings. Thus, it is useful to attempt to classify the different solid forms and modifications of silica according to distinct structural characteristics (*9*).

The bulk structures of silicas are classified as crystalline and amorphous polymorphs. More than 35 well-defined crystalline silicas are known, which are well-characterized by the Si–O length, the Si–O–Si bond angle, and the Si–O bond topology and coordination (*10*). Some of the crystalline polymorphs are collected in Table I. Because of the lack of sufficiently precise methods to assess the long-range structural order, amorphous silicas remain poorly characterized. They can be loosely discriminated according to their dispersity, bulk density, and type of pore structure.

The first classifying quantity in the characterization of crystalline silica polymorphs is the framework density d_f, which is expressed as the number of SiO_2 groups per 1000 Å^3 (*10*). Values of d_f range from 17 to 43 SiO_2 groups per 1000 Å^3 (Table I).

According to the value of d_f, crystalline silicas were divided by Liebau (*10*) into pyknosils ($d_f > 21$ SiO_2 groups per 1000 Å^3) and porosils ($d_f < 21$ SiO_2 groups per 1000 Å^3). Pyknosils are defined as "polymorphs with frameworks too dense to enclose guest molecules that are larger than helium and neon" (*10*). Pyknosils are nonporous.

The second quantity is the type of porosity and pore structure. Phases with silica frameworks that have pores wide enough to accommodate larger guest molecules are called porosils, irrespective of whether their pores are filled or empty (*10*). Porosils have a micropore system of pores with widths between 0.4 and 0.8 nm. In contrast to the well-defined microporous crystalline silicas, porous amorphous silicas lack any long-range structural order. The average pore diameter of amorphous silica materials covers the range between a few to several thousand nanometers. Porosils are further divided into clathrasils and zeosils, depending on whether the pores are closed or open, that is, accessible to adsorption. Clathrasils form cagelike pores that are schematically described by polyhedra. A typical representative of the clathrasil family is Dodecasil 1H, the crystals of which are depicted in Figure 1 (*11*). Zeosils can be considered as aluminum-free and zeolites, which are microporous crystal-

Table I. Crystalline Phases That Have Topologically Distinct SiO_2 Frameworks

Name	d_f	*Formula; Unit Cell Content*
Stishovite	43.0	SiO_2
SiO_2(Fe_2N-type)	42.8	SiO_2
Coesite	29.3	SiO_2
Quartz	26.6	SiO_2
Moganite	26.3	SiO_2
Keatite	25.1	SiO_2
Cristobalite	23.2	SiO_2
Tridymite	22.9	SiO_2
Nonasils	19.2	$88SiO_28M^88M^94M^{20}$
Melanophlogites	19.0	$46SiO_22M^{12}6M^{14}$
Dodecasils 3C (Silica ZSM-39)	18.6	$136SiO_216M^{15}8M^{16}$
Dodecasil 1H	18.5	$34SiO_23m^{12}2M^{12}1M^{20}$
SIGMA-2	17.8	$64SiO_28M^94M^{20}$
Silica sodalites	17.4	$12SiO_22M^{14}$
Decadodecasils 3R	17.6	$120SiO_26M^{10}9M^{12}6M^{19}$
Decadodecasils 3H	17.6	$120SiO_26M^{10}9M^{12}1M^{15}4M^{19}\ 1M^{23}$
Silica ZSM-23	20.0	$24SiO_2(CH_3)_2N(CH_2)_7N\ (CH_3)_2$
Silica ZSM-48	19.9	$48SiO_2H_2N(CH_2)_8NH_2$
Silica ZSM-22	19.7	$24SiO_2HN(C_2H_5)_2$
Silica ferrierite	19.3	$36SiO_22H_2N(CH_2)_2NH_2$
Silica ZSM-12	18.5	$28SiO_2N(C_2H_5)_3$
Silica ZSM-50	18.2	$112SiO_2n$-$[(CH_3)_3N(CH_2)\ _6N(CH_3)_3](OH)_2$
Silicalite II (Silica ZSM-11)	17.9	$96SiO_2n$-$[N(C_4H_9)_4]OH$
Silicalite I (Silica ZSM-5)	17.8	$96SiO_24[N(C_3H_7)_4]F$
Fibrous silica	19.6	SiO_2

NOTE: Abbreviations are as follows: d_f, framework density in number of SiO_2 groups per 1000 Å^3; M, guest molecule located in a cage that has $f = m_j$ faces.
SOURCE: Reproduced with permission from reference 10. Copyright 1988.

line-network aluminosilicates (*10*). The end-member of the pentasil ZSM-5 family, for instance, is silicalite-I, with an Si:Al ratio of >1000 (*12*). Silicalite-I exhibits an open bidirectional pore system of straight and zig-zag channels about 0.5–0.6 nm in width (*12*). Silicalite-I can be synthesized with a defined phase composition, with high purity, and as large crystals with a narrow particle size distribution (*13*). Because of these properties and its high thermal stability up to 1200 K, silicalite-I is well-suited as a reference material for crystalline and amorphous porous silicas.

A third classifying quantity relates to the surface structure of silicas, which is characterized by the coordination of surface silicon atoms; the resulting functional groups; their density, topology, and distribution; the degree of hydroxylation; the hydration–dehydration behavior; the acidic

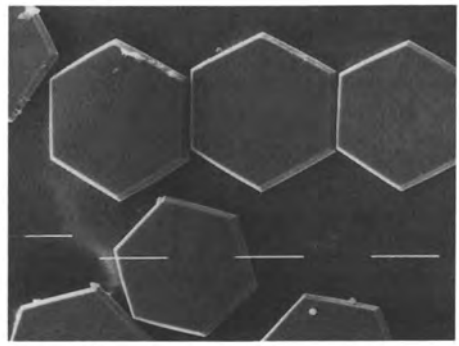

Figure 1. Crystals of Dodecasil 1H, synthesized with 1-amino adamantan. (Reproduced with permission from reference 11. Copyright 1989.)

and basic properties of surface functional groups; and their adsorption behavior and chemical reactivity. The pattern of the surface structure in terms of these properties is discussed in the section "Current View of the Silica Surface". The following section reviews the methods by which reliable information on these properties is obtained.

Survey of Methods for Characterizing the Silica Surface

According to the underlying principle, the methods are grouped into spectroscopic, thermal and calorimetric, adsorption and wetting, isotopic exchange, microscopic, scattering, and chemical reactions techniques (Table II) (*14–29*). This chapter is not a comprehensive treatment of all methods in depth. Results of spectroscopic and adsorption methods are discussed for aspects of content of information, validity, applicability, and limitations.

Spectroscopic Methods. ***Fourier Transform Infrared (FTIR) Spectroscopy.*** FTIR is carried out either in the transmission mode or as diffuse reflectance FTIR (*14*) with pellets, self-supporting sample disks, or loosely packed powders. Spectra are commonly recorded in the frequency range between 400 and 4000 cm^{-1}. Figure 2 (*30, 31*) shows the adsorption bands and band assignments of three different types of silicas: an amorphous highly disperse nonporous silica (Aerosil 200, Degussa), a crystalline nonporous silica (α-quartz), and a microporous crystalline silica (silicalite-I). The band at 3750 cm^{-1} is assigned to the stretching vibration of free hydroxyl groups that occur at the surface of amorphous silicas. This band usually overlaps with the absorption bands originating from hydrogen-bonded hydroxyl groups and from adsorbed water. Adsorbed water on amorphous silica is removed under vacuum at 383 to 473 K. Above 473 K,

Table II. Physical and Chemical Methods for Characterizing the Surface Structure of Silica

Method	*Information*	*Ref.*
Spectroscopic:		
FTIR	Types of hydroxyl groups, acidity	
Diffuse reflectance FTIR adsorption of probe molecules (pyridine, carbon monoxide, and so forth, monitored by FTIR)	Brönsted and Lewis acid sites, adsorption behavior, and chemical reactivity	14
^{29}Si CP–MAS[a] NMR spectroscopy	Short-range structural order of surface silicon atoms, bond	15–18
^{29}Si CP–MAS NMR spectroscopy, ^{1}H MAS NMR spectroscopy	Length, bond angles, acidic properties (protonic sites) of silica, and concentration of protons	19
Secondary ion mass spectrometry (SIMS)	Chemical composition of the surface as a function of the depth	
Extended X-ray absorption fine-structure spectroscopy	Local structural surrounding, nearest neighbor distances, coordination number, and bond lengths	
Electron spectroscopy for chemical analysis (ESCA)	Chemical compositions of the surface	
Photophysical studies of direct energy transfer between excited donor and ground-state acceptor molecules	Pore and surface morphology	20
Thermal and calorimetric:		
Microcalorimetry	Heat of adsorption, phase transitions of adsorbates	
Thermogravimetry	Weight loss as a function of temperature	
Differential thermogravimetry (DTG), differential scanning calorimetry (DSC), and thermoporometry (monitoring liquid–solid phase transitions of a pure liquid capillary condensate in a porous system)	Enthalpic (exothermic or endothermic) changes upon heating surface area, pore size distribution, and average pore diameter	21
Isotopic exchange:		
Heterogeneous isotopic exchange using deuterated (D_2, D_2O, CH_3OD, CF_3COOD, and so forth) and tritiated (HTO) substances, combined with mass spectrometry, IR spectroscopy, and ^{1}H NMR spectroscopy	Total content of surface hydroxyl groups, content of physisorbed water	22–24

Continued on next page.

Table II.—Continued

Method	*Information*	*Ref.*
Adsorption and wetting:		
Adsorption of gases and vapors, combined with IR spectroscopy, microcalorimetry, and so forth	Heats of adsorption, specific surface area, pore size distribution, average pore diameter, and fractal dimension	
Temperature-programmed desorption of absorbed substances (ammonia, pyridine, and so forth, coupled with mass spectrometry and IR spectroscopy	Acidic functional groups, relative acid strength	
Adsorption of bases (*n*-butylamine) in aprotic solvents using Hammett or arylmethanol indicators	Total content of surface acid sites, acidity distribution	25
Wetting with liquids	Surface energy, surface wettability, and contact angle	
Microscopy:		
Transmission and scanning electron microscopy, scanning tunneling microscopy	Texture of silica, geometrical surface structure, pore shape, and pore homogeneity	26
Scattering:		
Small-angle X-ray and neutron scattering	Pore morphology, roughness of pore surface, and pore size distribution	27, 28
Chemical Methods:		
Using chemically reactive substances such as chlorine, metal halides, grignard compounds, and reactive chloro- and alkoxysilanes	Stoichiometry of surface reactions, reactivity of surface hydroxyl groups	29

[a]CP–MAS denotes cross-polarization–magic-angle spinning.

hydrogen-bonded hydroxyl groups condense, and the corresponding absorption band diminishes. Free surface hydroxyl groups still exist after annealing the silica at 1273 K at a low content. Figure 3 (32) shows the IR spectra of a porous silica measured at different pretreatment temperatures. Thus, for IR spectroscopic measurements it is essential to control the pretreatment conditions (vacuum, temperature, and moisture) to achieve reproducible results.

There is still a discussion on the appearance of the absorption band due to geminal groups. Although Camara et al. (33) suggested that the band at 3710 cm^{-1} was specific for geminal groups, Morrow and Gay (34) claimed that they absorb at 3750 cm^{-1}. Discrimination between bulk and surface hydroxyl groups is effected by subjecting the silica to deuteration with D_2O and monitoring the absorption of the corresponding –OD bands (22). Bulk hydroxyls and bulk water do not take part in the isotopic

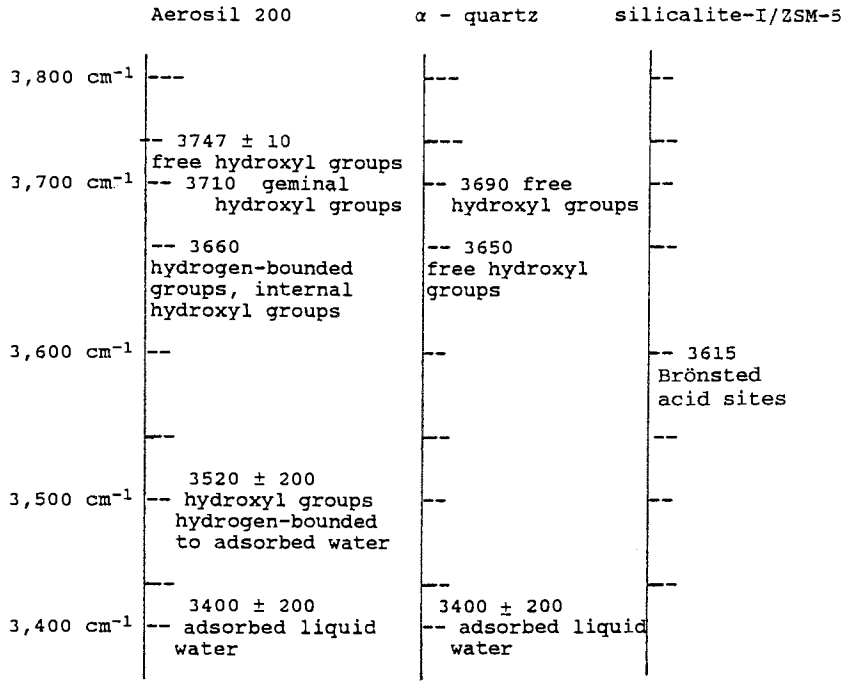

Figure 2. Band assignment of surface silica species in the high-frequency region (2000–4000 cm⁻¹). (Reproduced with permission from reference 30. Copyright 1979.)

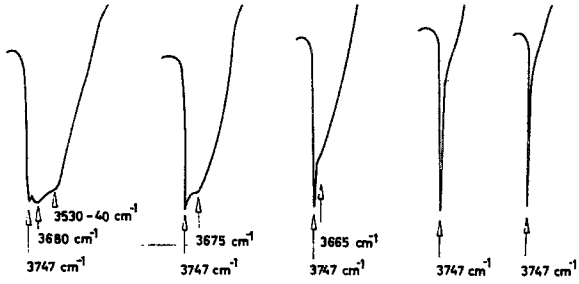

Figure 3. IR spectra of a porous silica (specific surface area a_s = 475 m²/g; average pore diameter p = 7 nm) obtained after evacuation at (left to right) 473, 673, 773, 873, and 973 K. (Reproduced with permission from reference 32. Copyright 1979.)

exchange, and thus their absorption bands remain unaffected. FTIR spectroscopy is a technique to identify surface hydroxyl groups and to follow their adsorption behavior toward selected probe substances. Quantitation is difficult to achieve because of the lack of absorption coefficients.

Several types of cells have been constructed and are commercially available that allow an in situ measurement or have a movable holder to evacuate and heat the sample. With these cells it is also possible to admit gas or vapor to subsequently measure the frequency shift upon adsorption. This technique can reveal additional information about the surface properties of the material. Carbon monoxide, for instance, has been applied as a probe to detect hydroxyl groups at the silica surface. Upon adsorption of CO at 77 K, the band due to free hydroxyl groups shifts to a lower frequency by 78 or 93 cm^{-1} (*35, 36, 37*).

Brønsted and Lewis acid sites are distinguished by the adsorption of pyridine monitored by means of IR spectroscopy (*38*). Pyridine adsorbed on Brønsted sites gives rise to an absorption band at about 1550 cm^{-1}; pyridine adsorbed on Lewis sites generates a band between 1440 and 1460 cm^{-1}, depending on the type of Lewis acid sites.

It is interesting to compare the absorption pattern of the three types of silicas that differ in bulk and surface structure (Figure 2). α-Quartz shows two types of free hydroxyl, with absorption bands at 3690 and 3620 cm^{-1} (*32, 39*). On silicalite-I, a band at 3750 cm^{-1} with low intensity is assigned to free hydroxyl groups at defect sites of the crystals. Increasing the aluminum content, that is, forming ZSM-5 zeolite, leads to an appearance of a band at 3615 cm^{-1}, which is assigned to a Brønsted acid of the following type (*31*):

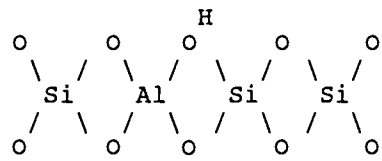

^{29}Si CP–MAS NMR Spectroscopy. This method is very useful for characterizing silica (*15–17*). The main information derived from an NMR spectrum is the chemical shift, the intensity, and the line width. The ^{29}Si chemical shift is determined by the number and type of tetrahedral framework atoms connected to tetrahedral silicon atoms. The spectrum thus allows the detection of the number of structurally inequivalent kinds of silicon atoms of various Si $(O–)_{4-n}(OSi)_n$ units in silicates and as Q^4 (*m* Al) for Si $(OSi)_{4-n}(OAl)_m$ units in framework alumosilicates (Figures 4 and 5) (*40*).

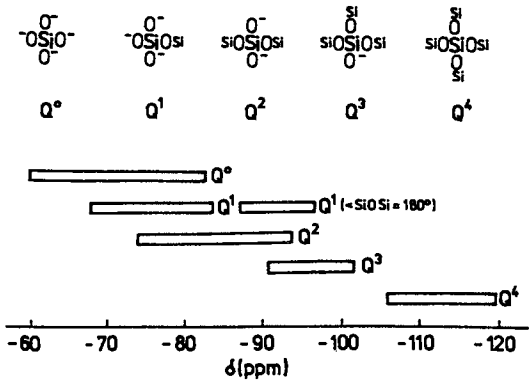

Figure 4. Typical ranges of ^{29}Si chemical shifts of Q^n units in silicates. (Reproduced with permission from reference 40. Copyright 1990.)

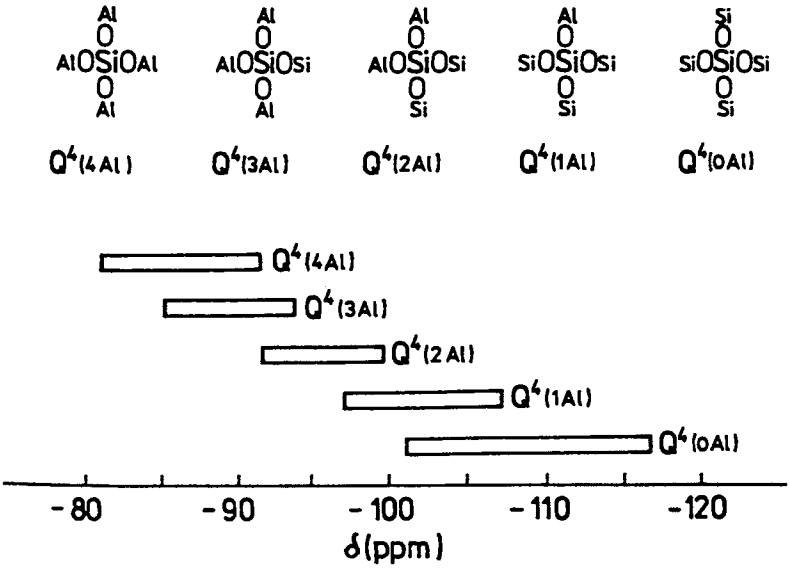

Figure 5. Typical ranges of ^{29}Si chemical shifts of $Q^4(mAl)$ units in aluminosilicates. (Reproduced with permission from reference 40. Copyright 1990.)

A ^{29}Si CP–MAS NMR spectrum of amorphous silica shows three signals, at −91, −100, and −109 ppm, that are assigned to geminal hydroxyl groups (Q_2), free hydroxyl groups (Q_3), and siloxane groups (Q_4) (Figure 6). The amplitude of all three signals is a function of the contact time (*18*). Q_2 and Q_3 show comparable maxima at a contact time of 6 to 8 ms, whereas a broad maximum is observed for Q_4 between 8 and 25 ms (*18*). With

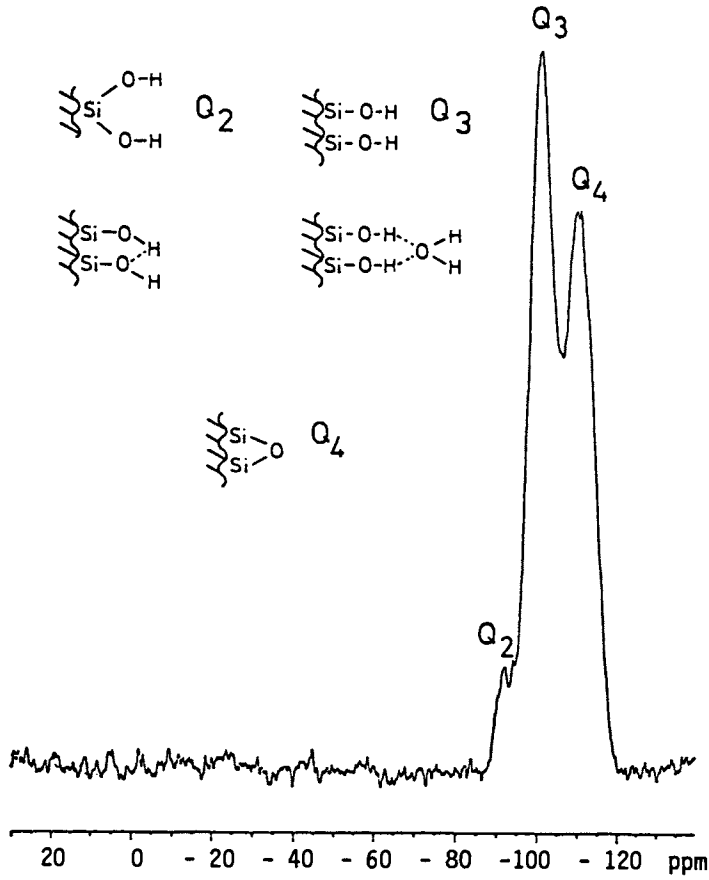

Figure 6. ^{29}Si CP–MAS NMR spectrum of an amorphous porous silica. (Reproduced with permission from reference 18. Copyright 1991.)

known relaxation times, the relative ratios of $Q_2/Q_3/Q_4$ can be assessed (*19*). Dynamic studies have been performed to detect changes in the surface structure after certain treatments. On acid-treated silicas, for example, two types of Q_4 groups appeared with different T_{SiH} and $T_{i\rho H}$ values, where T_{SiH} is the cross-relaxation constant and $T_{i\rho H}$ the proton spin-lattice relaxation time in the rotating frame (*41*). The Q_4 units with low T_{SiH} and $T_{i\rho H}$ values are considered polycrystalline domains at the surface of amorphous silica. By independent neutron diffraction measurements on acid-treated silica samples, a tridymite-like phase could be monitored (*42*). The Q_4 units with high T_{SiH} and $T_{i\rho H}$ values are believed to be of amorphous type (*42*).

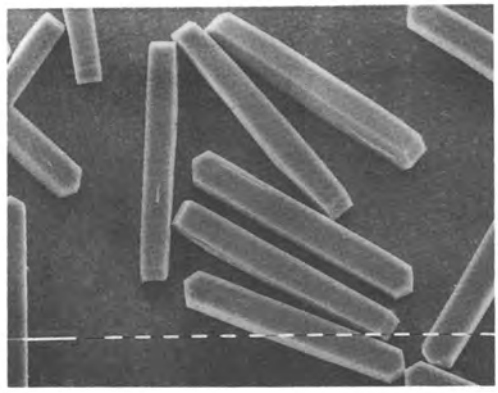

Figure 7. Large crystals of silicalite-I that were synthesized alkaline-free with tetrapropylammonium bromide as template. (Reproduced with permission from reference 46. Copyright 1990.)

Adsorption Methods. Adsorption studies are a classical method of characterizing silicas. A new generation of high-resolution dynamic volumetric adsorption equipment now commercially available allows automatic measuring of several thousand data points of the isotherm down to a relative pressure ratio p/p_0 of about 10^{-5} with high precision (*43*). Adsorption measurements are extremely useful for characterizing silicas, in particular microporous types. The progress achieved is demonstrated by the following examples of microporous crystalline silicas. Sorption experiments were performed with argon and nitrogen at 77 K on large and uniform crystals of silicalite-I (Figure 7) (*44*). The results obtained drastically deviated from the expected data: instead of a Langmuir type of isotherm, an isotherm with distinct steps was obtained (Figure 8) (*45*). These steps are interpreted as a successive filling of the microporous channels where the gas molecules are adsorbed at distinct adsorption sites. The nitrogen isotherm on silicalite-I shows a second peculiar phenomenon: a pronounced hysteresis occurs between the adsorption and desorption branch at p/p_0 of about 0.1–0.15 (Figure 9) (*46*). This additional uptake is probably due to a phase change of the liquid adsorbate into a solidlike one, which is evidenced by concurrent microcalorimetric and in situ neutron diffraction measurements (*47*).

Current View of the Silica Surface

Surface Charge. For a number of applications the surface charge of silica is of eminent interest. The isoelectric point (point of zero charge) can be derived from electrophoretic mobility (zeta potential) measurements on

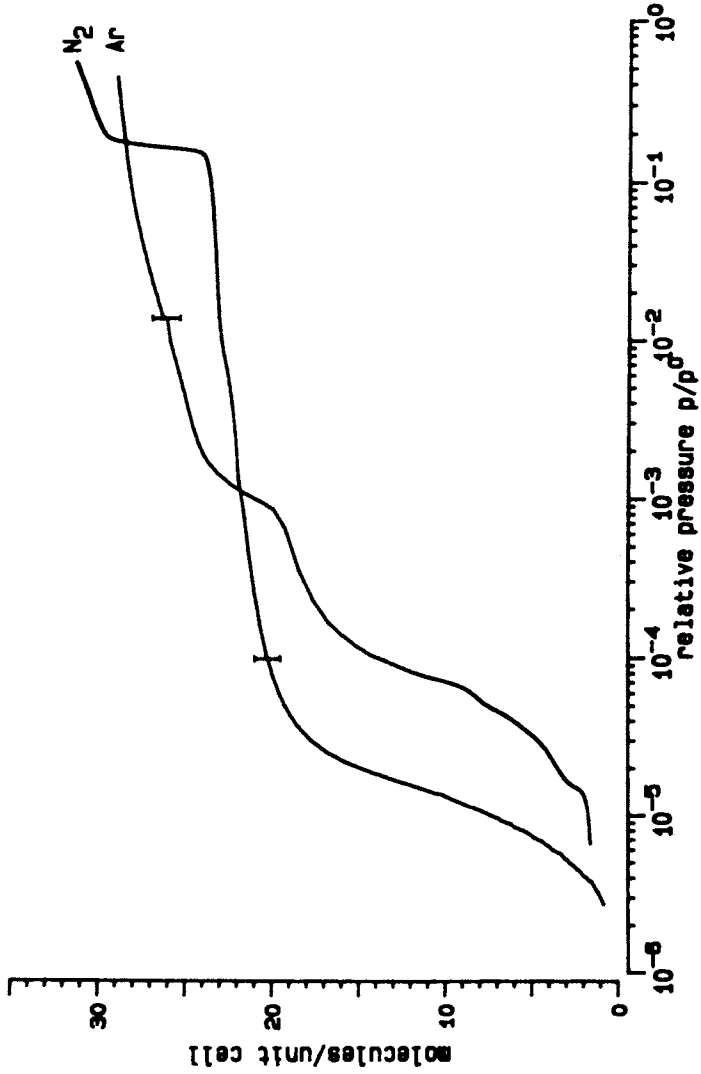

Figure 8. Adsorption isotherms of argon and nitrogen at 77 K on silicalite-I obtained with high-resolution dynamic volumetric sorption equipment. (Reproduced with permission from reference 45. Copyright 1989.)

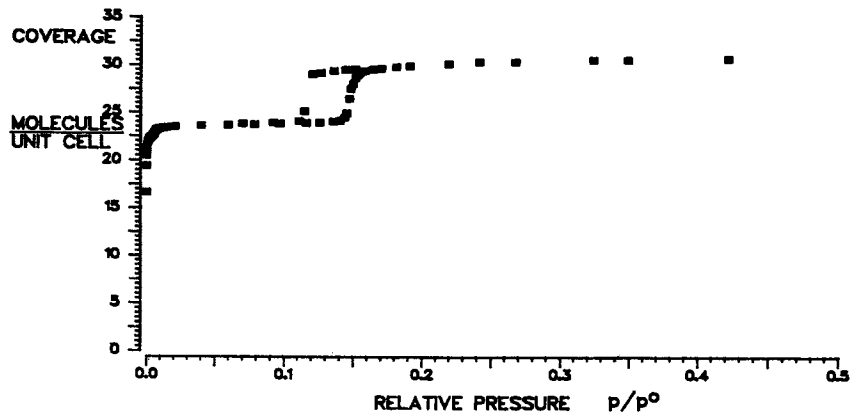

Figure 9. Adsorption isotherm of nitrogen at 77 K on silicalite-I obtained with conventional gravimetric sorption equipment. (Reproduced with permission from reference 46. Copyright 1990.)

silica suspensions of varying pH. The isoelectric point was measured to be between pH 1 and 2 (*48*). Above pH 2 the particles are negatively charged; below pH 1 the particles bear a positive charge. In one study the isoelectric point of silica was reported to be at about pH 5 (*49*). Recently, a chromatographic-grade silica (Zorbax RX) became commercially available, and it exhibits distinct anion-exchange properties at about pH 5 (*50*). The origin of this peculiar behavior is not yet clear.

Surface Functionality. Several groups contribute to Brønsted acidity, as free (isolated), paired (geminal), and hydrogen-bonded (vicinal) hydroxyl groups. Bridging hydroxyl groups in microporous amorphous silicas may also contribute (*51*). They are identified by their absorption bands in the frequency region between 3000 and 4000 cm^{-1} and by ^{29}Si and ^{1}H CP–MAS NMR spectroscopy. Much attention has been paid to geminal hydroxyl groups, which were first postulated by Peri (*5*).

Geminal hydroxyl groups have been shown to exist at the surface of Aerosil 200 even at high thermal pretreatment of 1073 K (*34*). Geminal hydroxyl groups are formed as a result of acid treatment of amorphous porous silicas (*42*). Geminal hydroxyl groups have been found to be more reactive in chemical surface modification of amorphous porous silicas than free hydroxyl groups (*8*).

The relative proportion of the hydroxyl groups heavily depends on the method used for estimation. The relative content varies from silica to silica depending on the manufacturing process and after-treatment conditions.

The total concentration of surface hydroxyl groups at a fully hydroxylated surface has been assessed to be about 5 per square nanometer,

independent of the type of silica (52). The concentration decreases monotonically with increasing temperature when silicas are thermally pretreated under vacuum. Physisorbed water is first removed at temperatures between 380 and 420 K. Simultaneously, hydrogen-bonded hydroxyl groups condense to strained siloxane groups, which act as Lewis sites according to equation 1.

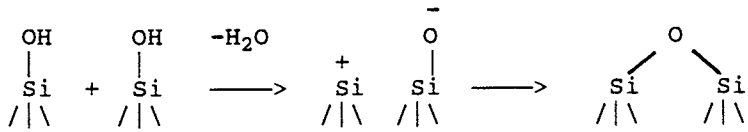

Strained siloxane groups are formed up to about 770 K and then convert into stable siloxane groups (53). Strained siloxane groups completely rehydroxylate upon exposure to water, whereas stable siloxane groups rehydroxylate slowly. With the removal of hydroxyl groups and the formation of siloxane groups, the silica surface loses its hydrophilic character and becomes hydrophobic. The movement of the hydrophilic to hydrophobic character can be followed by measuring the heats of adsorption of water and other polar adsorptives.

The protonic sites at the surface of amorphous silica are weakly acidic compared to the acid centers in crystalline aluminosilicates (e.g., zeolites). On ZSM-5, Brønsted sites are formed by protons adjacent to aluminum atoms in the tetrahedral framework. The concentration of acid sites increases with the aluminum content. The total acidity as well as the acid strength distribution can be determined by using *n*-butylamine and Hammet or arylmethanol indicators (25). Depending on the pK_a of the indicator, a relative scale of the strength distribution is obtained (54). Results for a series of amorphous porous silicas of graduated pore size are shown in Figure 10. The acidity varies between pK_a −1 and +9 and is nearly the same for all silicas studied. The results are specifically valid for this method only and cannot be compared with those derived from other methods.

One of the major factors that determines the acidity values is the accessibility of surface sites, which is a function of the pore size of the silica, the surface morphology, and the size of the amine molecule used for the acidity assessment (54). A great deal of work has been carried out to elucidate the chemical and geometrical heterogeneity of the silica surface. The geometrical heterogeneity can be described by the fractal dimension *D*, which varies between 2 and 3 (55). The surface heterogeneity in terms of thermodynamic aspects can be visualized by the surface energy and the energy distribution (56). Appropriate functions are derived from potential energy equations that aid adsorption measurements. Although an enormous literature exists on the aspects of surface heterogeneity, this

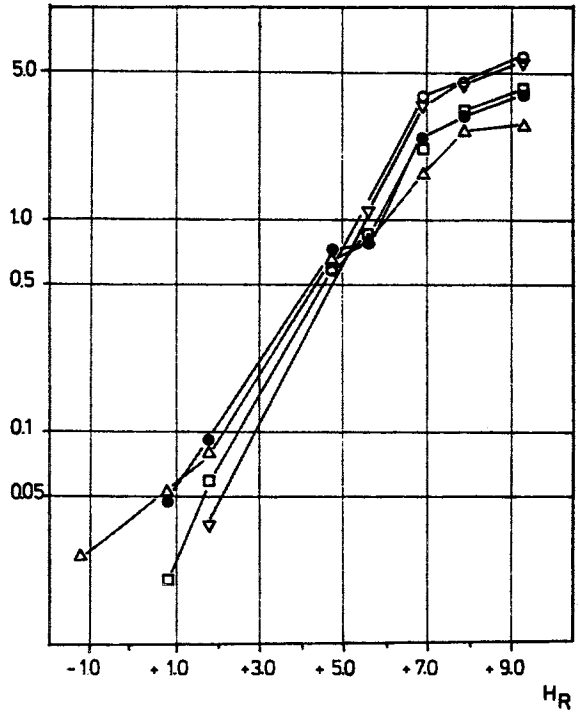

Figure 10. Cumulative acidity in micromoles per square meter on silica-20 (△), silica-40 (□), silica-60 (●), silica-100 (▽), and silica-200 (○) as a function of the acidity strength H_R. *(Reproduced with permission from reference 54. Copyright 1980.)*

approach has so far gained little importance in the evaluation of silicas in practice.

Conclusions

The silica surface represents a dynamic system that undergoes slight to notable changes depending on the conditions of the environment. To assess the dynamic character of the surface, studies are required that enable monitoring of structural changes during silica formation, after-treatment, use, and storage. Spectroscopic methods are the most suitable in this respect. In this context, the use of selected probe molecules embedded, adsorbed, or chemically bonded opens a new dimension in gaining substantial information and is exemplified by photophysical studies. A particular focus will be on in situ measurements to directly monitor subtle structural properties of the surface. The combined applica-

tion of sophisticated, in situ, high-resolution, physicochemical methods will shed much light on the understanding of the silica surface.

References

1. Fripiat, J. J.; Uytterhoeven, J. *J. Phys. Chem.* **1962,** *66,* 800.
2. Kiselev, A. V.; Lygin, V. I. *Infrared Spectroscopy of Surface Compounds*; Wiley Interscience: New York, 1975.
3. Hair, M. L. *Infrared Spectroscopy in Surface Chemistry*; Dekker: New York, 1967.
4. Little, L. H. *Infrared Spectra of Adsorbed Species*; Academic Press: London, 1966.
5. Peri, J. B.; Hensley, A. L., Jr. *J. Phys. Chem.* **1968,** *72,* 2926.
6. Liebau, F. *Structural Chemistry of Silicates*; Springer Verlag: Heidelberg, Germany, 1985.
7. Van Bekkum, H.; Flanigen, E. M.; Jansen, J. C. *Introduction to Zeolite Science and Practice*; Elsevier: Amsterdam, Netherlands, 1991.
8. Unger, K. K. *Porous Silica: Its Properties and Use in Column Liquid Chromatography*; Elsevier: Amsterdam, Netherlands, 1979.
9. Iler, R. K. *The Chemistry of Silica and Silicates*; Wiley Interscience: New York, 1979.
10. Liebau, F. In *Silicone Chemistry;* Correy E. R.; Correy, J. Y.; Gasper, P. P., Eds; Ellis Horwood: Chichester, UK, 1988, pp 309–323.
11. Müller, U.; Reich, A.; Unger, K. K. In *Recent Advances in Zeolite Science*; Klinowski, J.; Barrie, P. J., Eds.; Elsevier: Amsterdam, Netherlands, 1989; pp 241–252.
12. Jacobs, P. A.; Martens, P. A. *Synthesis of High-Silica Aluminosilicate Zeolites*; Elsevier: Amsterdam, Netherlands, 1987.
13. Müller, U.; Unger, K. K. *Zeolites* **1988,** *8,* 154–156.
14. Leyden, D. E.; Murthy, R. S. S. *Trends Anal. Chem.* **1988,** *7,* 164.
15. Maciel, G. E.; Sindorf, D. W. *J. Am. Chem. Soc.* **1980,** *102,* 7607.
16. Sindorf, D. W.; Maciel, G. E. *J. Am. Chem. Soc.* **1983,** *105,* 1487.
17. Engelhardt, G.; Michel, D. *High-Resolution Solid State NMR of Silicates and Zeolites*; Wiley Interscience: New York, 1987.
18. Albert, K.; Bayer, E. *J. Chromatogr.* **1991,** *544,* 345.
19. Köhler, J.; Chase, D. B.; Farlee, R. D.; Veega, A. J.; Kirkland, J. J. *J. Chromatogr.* **1986,** *352,* 275.
20. Zachariasse, K. A. In *Photochemistry on Solid Surfaces*; Matsumo, T.; Anpo, M., Eds.; Elsevier: Amsterdam, Netherlands, in press.
21. Eyraud, C.; Quinson, J. T.; Brun, M. In *Characterization of Porous Solids*; Unger, K. K.; Rouquerol, J.; Sing, K. S. W.; Kral, H., Eds.; Elsevier: Amsterdam, Netherlands, 1988; p 295–316.
22. Zhuravlev, L. T.; Kiselev, A. V.; Nadina, V. P.; Polyakov, A. L. *Russ. J. Phys. Chem.* 1963, *37,* 113, 1216.
23. Holik, M.; Matejkova, B. *J. Chromatogr.* **1981,** *213,* 33.
24. Unger, K. K. *Porous Silica: Its Properties and Use in Column Liquid Chromatography*; Elsevier: Amsterdam, Netherlands, 1979; p 72–76.
25. Tanabe, K. *Solid Acids and Bases*; Academic Press: New York, 1970.
26. Kuk, Y., Silverman, P. J. *Rev. Sci. Instrum.* **1989,** *60,* 165.
27. Schmidt, P. W. In *Characterization of Porous Solids*; Unger, K. K.; Rouquerol, J.; Sing, K. S. W.; Kral, H., Eds.; Elsevier: Amsterdam, Netherlands, 1988; pp 35–48.

28. Ramsay, J. D. F. In *Characterization of Porous Solids*; Unger, K. K.; Rouquerol, J.; Sing, K. S. W.; Kral, H., Eds.; Elsevier: Amsterdam, Netherlands, 1988; pp 23–34.
29. Unger, K. K. *Porous Silica: Its Properties and Use in Column Liquid Chromatography*; Elsevier: Amsterdam, Netherlands, 1979; pp 64–68.
30. Unger, K. K. *Porous Silica: Its Properties and Use in Column Liquid Chromatography*; Elsevier: Amsterdam, Netherlands, 1979; p 10.
31. Tissler, A. Ph.D. Thesis, Johannes Gutenberg-Universität, Mainz, Germany, 1989.
32. Unger, K. K. *Porous Silica: Its Properties and Use in Column Liquid Chromatography*; Elsevier: Amsterdam, Netherlands, 1979; pp 69–70.
33. Camara, B.; Dunken, H.; Fink, P. Z. *Chem.* **1968,** *8,* 155.
34. Morrow, B. A.; Gay, I. D. *J. Phys. Chem.* **1988,** *92,* 5569.
35. Zaki, M. I.; Knoezinger, H. *Mater. Chem. Phys.* **1987,** *17,* 201.
36. Knözinger, H. In *Acid-Base Catalysis*; Tanabe, K.; Hattori, H.; Yamaguchi, T.; Tanaka, T., Eds.; Kodansha Ltd.: Tokyo, Japan, 1989; pp 147–167.
37. Baila, R. M.; Kantner, T. R. *J. Phys. Chem.* **1966,** *70,* 1681.
38. Ward, J. W. *J. Catal.* **1967,** *9,* 225.
39. Gallei, E. *Ber. Bunsenges. Phys. Chem.* **1973,** *77,* 81.
40. Engelhardt, G. *Trends Anal. Chem.* **1989,** *8,* 343–347.
41. Pfleiderer, B.; Albert, K.; Bayer, E.; Van De Ven, L.; De Haan, J.; Cramers, C. *J. Phys. Chem.* **1990,** *94,* 4189–4194.
42. Unger, K. K.; Lork, K. D.; Pfleiderer, B.; Albert, K.; Bayer, E. *J. Chromatogr.* **1991,** *556,* 395–406.
43. Reichert, H.; Unger, K. K. *Trends Anal. Chem.* **1990,** *100,* 44–48.
44. Müller, U.; Brenner, A.; Reich, A.; Unger, K. K. In *Zeolite Synthesis*; Occelli, M. L.; Robson, H. E., Eds.; ACS Symposium Series 398; American Chemical Society: Washington, DC, 1989; pp 346–359.
45. Müller, U.; Reichert, H.; Robens, E.; Unger, K. K.; Grillet, Y.; Rouquerol, F.; Rouquerol, J.; Dongfen Pan, A.; Mersmann, A., Fresenius Z. *Anal. Chem.* **1989,** *333,* 433.
46. Müller, U. Ph.D. Thesis, Johannes Gutenberg-Universität, Mainz, Germany, 1990.
47. Reichert, H.; Müller, U.; Unger, K. K.; Grillet, Y.; Rouquerol, J.; Coulomb, J. P. In *Characterization of Porous Solids*; Rodrigues-Reinoso, F.; Rouquerol, J.; Sing, K. S. W.; Unger, K. K., Eds.; Elsevier: Amsterdam, Netherlands, 1991; pp 535–542.
48. Unger, K. K. *Porous Silica: Its Properties and Use in Column Liquid Chromatography*; Elsevier: Amsterdam, Netherlands, 1979; p 138.
49. Denoyel, R.; Rouquerol, F.; Rouquerol, J. In *Fundamentals of Adsorption*; Liapis, A. I., Ed.; Engineering Foundation: New York, 1987; pp 199–210.
50. Kirkland, J. J. personal communication.
51. Kondo, S. personal communication.
52. Zhuravlev, L. T. *Langmuir* **1987,** *3,* 316.
53. Knözinger, H.; Stählin, W. *Progr. Colloid Polymer Sci.* **1980,** *67,* 33.
54. Kittlemann, U.; Unger, K. K. *Progr. Colloid Polymer Sci.* **1980,** *67,* 19.
55. Avnir, D.; Farin, D.; Pfeifer, P. *New J. Chem.* **1992,** *16,* 439.
56. Oscik, J. *Adsorption*; Ellis Horwood: Chichester, England, 1982.

RECEIVED for review October 31, 1990. ACCEPTED revised manuscript June 2, 1992.

9

Infrared Study of Chemical and H–D Exchange Probes for Silica Surfaces

B. A. Morrow and A. J. McFarlan

Department of Chemistry, University of Ottawa, Ottawa, Ontario K1N 6N5, Canada

The accessibility of surface silanols toward hydrogen-sequestering agents with steric dimensions that increase in the order $ZnMe_2$, BCl_3, $TiCl_4$, $AlMe_3$, and $Me_3SiNHSiMe_3$ (HMDS) were compared spectroscopically and gravimetrically for a fumed and a precipitated silica. The H–D exchange reaction was similarly studied with D_2O, ND_3, and deuterated methanol, isopropyl alcohol, and tert*-butyl alcohol. The surface areas of the two silicas are similar, but the silanol density on the precipitated silica is about twice that on the fumed silica. Approximately equal fractions of the total number of OH groups per square nanometer undergo H–D exchange with a given probe, and this fraction decreases as the size of the molecule increases. The fraction of silanols that can be derivatized by chemisorption is about twofold greater on the fumed silica, but the surface densities of derivatized silanols on the two silicas are nearly equal for the same chemisorption probe. The degree of exchange is much greater than the degree of chemisorption for molecules of similar size because the chemisorbed product on the surface inhibits further reaction.*

THE SURFACE PROPERTIES OF AMORPHOUS SILICAS are largely influenced by the nature of the surface silanol (SiOH) groups (*1–3*). Lewis acid–base sites are absent unless the silica has been activated at very high temperatures, Brønsted acidity at the gas–solid interface is low or nonexistent, and the siloxane bridges are relatively unreactive toward most molecules. This chapter discusses some methods that employ chemical modification and H–D exchange to probe the nature of the surface hydroxyl groups on

0065–2393/94/0234–0183$08.00/0

silica. Infrared spectroscopy is the main technique used, and one objective has been to compare the silanol groups on a fumed silica with those on a precipitated silica.

Experimental Details

This work was carried out with (1) a fumed silica (Cab-O-Sil HS5; designated A-x, where x is the temperature of activation for 1 h in vacuum) having a Brunauer–Emmett–Teller (BET) (N_2) surface area of 325 ± 5 m^2/g and (2) a high-purity (Na 60 ppm, Al <100 ppm, Fe 20 ppm, and Ti <20 ppm) nonporous precipitated silica (designated P-x) from Rhône-Poulenc (France) having a surface area of 285 ± 5 m^2/g. The powder (50 mg total, 10 mg/cm^2) was compacted at 10^7 Pa into thin self-supporting disks for IR transmission studies. The IR cell (*4*) was constructed of quartz, had a volume of about 300 mL, and was connected via a lightly greased ball joint to a Pyrex vacuum line (300 mL in volume) capable of attaining a base pressure of about 10^{-7} torr (1.3×10^{-5} Pa). All reactants were transferred as gases from the main manifold to the reaction cells, and pressures (measured with a capacitance manometer) or doses are indicated in the text. Fourier transform infrared (FTIR) spectra were recorded with a Bomem DA3-02 instrument (mercury cadmium telluride, or MCT, detector) or a Bomem Michelson MB100 instrument at a resolution of 2 cm^{-1}, except for those shown in Figure 7, for which a resolution of 4 cm^{-1} was used. Vacuum microbalance experiments were carried out with a Sartorius model 4433 instrument having a sensitivity of 0.1 μg.

Results

Untreated Silica. Figures 1A through 1C show infrared spectra of fumed silica in the 3800- to 3000-cm^{-1} spectral region after activation in vacuum at 150, 450, and 800 °C, respectively. Figures 2A through 2C show the corresponding spectra for the precipitated silica activated at the same temperatures. Both sets of spectra for all temperatures of activation exhibit the well-known (*1–3, 5–7*) sharp intense band near 3747–3740 cm^{-1} due to isolated noninteracting SiOH groups, this peak being the sole feature after activation at 800 °C.

For 150 °C activation, the peak due to isolated silanols is at 3747 cm^{-1} for A-150 and at 3738 cm^{-1} for P-150, and for both silicas there is a broad band centered near 3520 cm^{-1}. For A-150 (Fig. 1A) there is a shoulder that extends to low wave number of the 3747-cm^{-1} peak near 3720–3715 cm^{-1}, and the 3520- and 3720-cm^{-1} bands have been assigned (*6, 7*) to the H-bonded and free silanol groups of a pair or chain of silanols as follows:

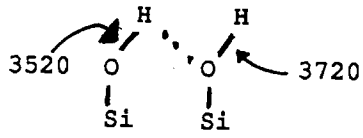

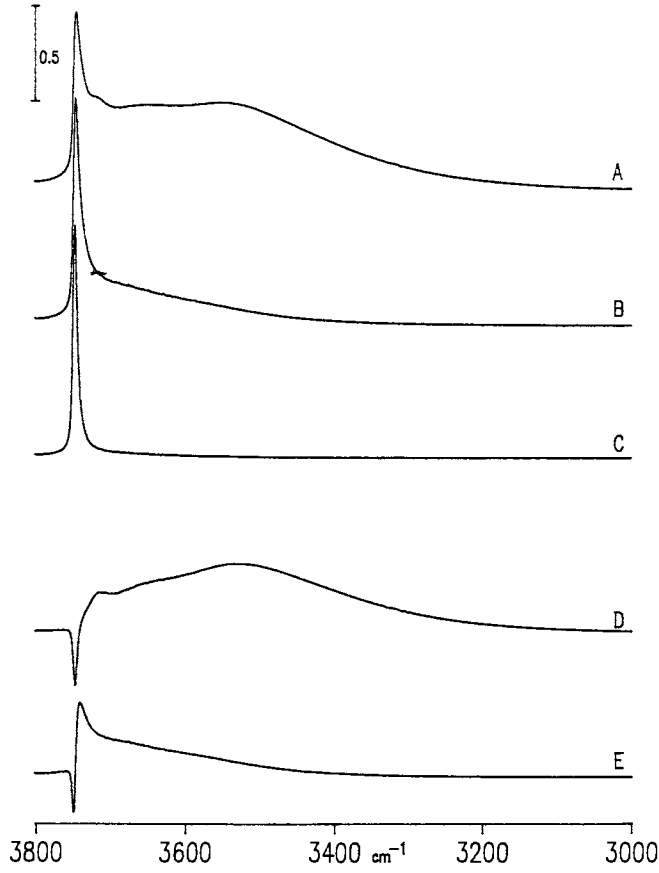

Figure 1. Infrared spectra of fumed silica in the SiOH stretching region after vacuum activation for 1 h at (A) 150, (B) 450, and (C) 800 °C. Curves D and E are the difference spectra A – B and B – C, respectively.

A slight inflection near 3660 cm^{-1} can just be discerned in Figure 1A. This band is due to perturbed or inaccessible internal silanols (*8–10*), the numbers of which increase as the pressure used to prepare self-supporting disks is increased. They are largely inaccessible to many reactant gases, and this topic is discussed in more detail later in the chapter. The 3720- and 3660-cm^{-1} features are not resolved in the spectrum of the precipitated silica (Fig. 2A), which instead exhibits a broad feature near 3695 cm^{-1}.

Activation at 450 °C eliminates most of the intensity due to the H-bonded and inaccessible silanols and leaves an asymmetric peak at 3747 cm^{-1} for A-450 and at 3745 cm^{-1} for P-450; this asymmetry largely disappears following activation at 800 °C, at which point the frequency of both peaks is at 3748 cm^{-1}. The most noticeable difference between the

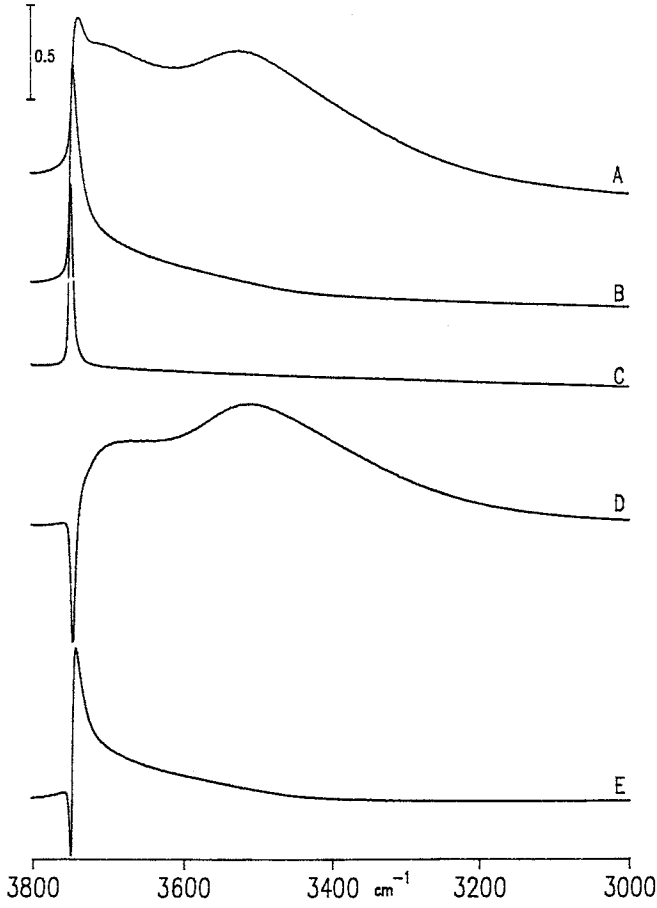

Figure 2. Infrared spectra of precipitated silica in the SiOH stretching region after vacuum activation for 1 h at (A) 150, (B) 450, and (C) 800 °C. Curves D and E are the difference spectra A – B and B – C, respectively.

fumed and precipitated silicas is that for the precipitated silica, and particularly for P-150, the isolated SiOH peak intensity is lower, and that due to H-bonded silanols is higher.

Figures 1D and 2D show the difference spectra upon heating from 150 to 450 °C, that is, curve 1A – 1B and curve 2A – 2B. Peaks going upward indicate bands that have decreased in intensity upon going from 150 to 450 °C, and those going downward indicate bands that have increased in intensity. For both, there is a loss of intensity associated with H-bonded silanols and an increase in the isolated free SiOH intensity with increasing temperature. This loss can be attributed (*6*, *7*) to a condensation process whereby a chain of H-bonded silanols containing an odd number of silanols

(three in the example) condense to liberate water, thereby creating a siloxane bridge site and an isolated silanol:

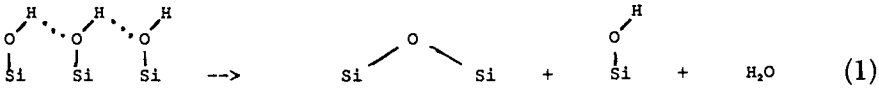

(1)

Such effects have been observed for other silicas (*5*, *11*), and the changes are much more pronounced for the precipitated silica.

Figures 1E and 2E show the corresponding spectral changes upon heating from 450 to 800 °C. The changes here are mainly associated with the disappearance of the asymmetric tail to low wave number of the 3747–3745-cm^{-1} peaks, and the change is again more pronounced for the precipitated silica.

A comparison of the spectra of A-150 and P-150 after 150 °C activation (Figs. 1A and 2A, respectively) shows that the band area of the precipitated silica is apparently greater than that of the fumed silica. In a series of spectra recorded with identical 2-cm^{-1} resolution, the integrated intensities (band areas) were 150 and 292 cm^{-1} for the same quantity (10 mg/cm^2) of fumed or precipitated silica (for convenience the unit cm^{-1} will be omitted in future discussions of integrated intensities). These integrated intensities have no quantitative meaning because the extinction coefficient of an H-bonded OH oscillator varies with wave number (*12*), but they suggest that there are more silanol groups on the precipitated silica under these conditions. As is discussed in more detail in the next section, the number of OH groups per square nanometer is about 3.1 and 6.8 for A-150 and P-150, respectively.

The strong peaks in the spectra of A-450 and P-450 are asymmetric to low wave number, and much of this asymmetry disappears after activation at 800 °C. This asymmetry has been attributed in the past to isolated non-hydrogen-bonded geminal silanol groups (*13*), $Si(OH)_2$, which are expected to exhibit two OH stretching modes. However, theoretical calculations indicate (*14*) that the shift between these modes might be as small as 1 or 2 cm^{-1}. IR spectroscopy has not been able to demonstrate whether geminal species indeed exist on silica, although ^{29}Si NMR spectroscopy evidence has apparently demonstrated that these species can be distinguished, even on vacuum-activated fumed silica up to 1000 °C (*13*, *15*). The fraction of geminal silicon sites is always about 17 ± 3% of total silicon sites bearing hydroxyls, regardless of the method of preparation of the silica or the activation temperature under vacuum (*13*, *15–18*). Thus, this 17% figure seems to be characteristic of all amorphous annealed silicas. In the work discussed here, no distinction is made between isolated and geminal silanols insofar as the 3747–3737-cm^{-1} peak can be assigned to either species.

Chemical and H–D Exchange Probes for 150 °C Activated Silica. The infrared spectrum of fumed silica after vacuum activation at 150 °C for 1 h (A-150) is identical to that observed after simple evacuation for 1 h at ambient temperatures (*6, 19*). Experiments with a vacuum microbalance have confirmed that there was insignificant mass loss upon going from 1-h evacuation at 22 °C to further evacuation at 150 °C for 1 h. Therefore, the spectrum shown in Figure 1A can be considered to be that of an "as received" hydroxylated fumed silica that contains no adsorbed water. The infrared spectrum of P-150 is almost identical to that observed after evacuation at ambient temperature for 1 h, except that there was about a 5% decrease in the intensity of the broad 3520-cm^{-1} feature upon going to 150 °C. The microbalance indicated a small decrease in mass of the sample upon going from 22 °C vacuum treatment to 150 °C (discussed later). After evacuation of either silica for 1 h at 22 °C, there was no indication of an infrared band at 1620 cm^{-1} characteristic of the bending mode of H_2O; thus, the ambient temperature vacuum treatment was sufficient to remove all adsorbed water. Therefore, the loss of mass of P-22 upon heating to 150 °C can probably be attributed to the condensation of pairs of H-bonded silanols, which results in the desorption of water.

One notable difference between A-150 and P-150 was that there was no mass loss with A-150 during prolonged evacuation at 150 °C, whereas with P-150 there was a continuing very slow decrease in mass. Thus, for this precipitated silica the condensation process is a continuous slow process even at 150 °C. This situation poses difficulties in specifying the number of SiOH groups that are present on P-150. Because most of the data described here for both silicas were obtained after a standard 1-h activation at 150 °C, the initial SiOH density was measured under these conditions only, with the understanding that for the precipitated silica these numbers would be slightly lower if longer activation times were used. Before these results are given, the question of the accessibility of surface silanols is first addressed.

Figure 3 shows infrared spectra of A-150 and P-150 before and after complete reaction with excess $TiCl_4$. (A "complete reaction" is considered to have occurred when no further spectral changes are observed; this time was about 1 min for $TiCl_4$. The time evolution of these spectral changes is discussed later.) Curves C and C′ show the difference spectra, illustrating the spectral *change* as a result of the reaction. Curves B and B′ show that not all of the silanols react with $TiCl_4$, because there is a large residual intensity with a maximum near 3660 cm^{-1}. The band at 3660 cm^{-1} has been attributed to perturbed silanols that are at points of interparticle contact and are inaccessible to some reactants (*8–10*). The number of these inaccessible silanols on fumed silica increases with the pressure used to prepare self-supporting disks.

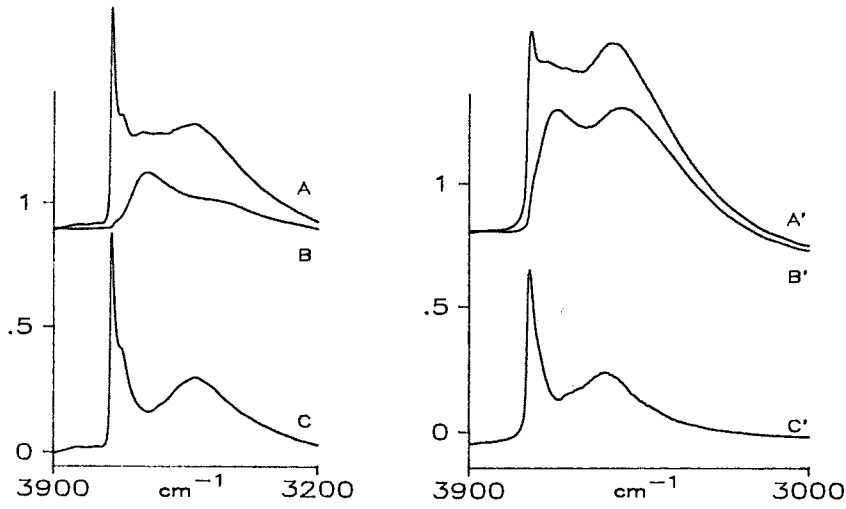

Figure 3. Infrared spectra of A-150 and P-150 before (A and A', respectively) and after (B and B') complete reaction at 22 °C with $TiCl_4$. Curves C and C' show the difference spectra (A – B and A' – B').

In principle, $TiCl_4$ might react with single silanols, vicinal pairs, or geminal pairs of silanols on silica as shown in reaction 2, 3, and 4. Although these reactions are not shown, it is possible that only one or both of the OH groups of a vicinal pair or geminal pair of silanols might react as depicted for an "isolated" silanol.

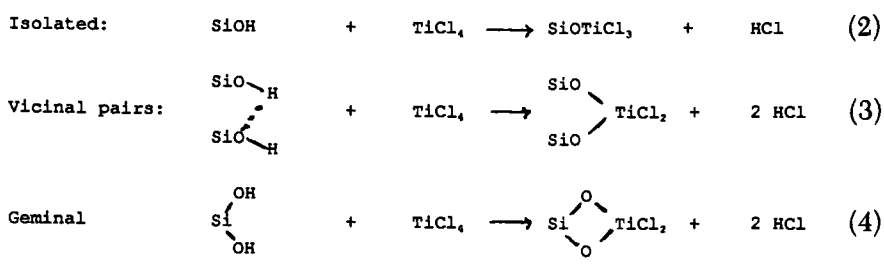

For other reactive hydrogen-sequestering (HS) agents, the extent of reaction would be expected to be different as the size of the reactant changed. Figure 4 shows a series of spectra observed after the complete reaction of A-150 with various HS agents (the exchange reaction with D_2O is included for comparison; in this reaction accessible SiOH is converted to SiOD), and Figure 5 shows the corresponding spectra for P-150. Inspection shows that there is a considerable difference in the numbers of residual or inaccessible silanols according to the nature of the reactant.

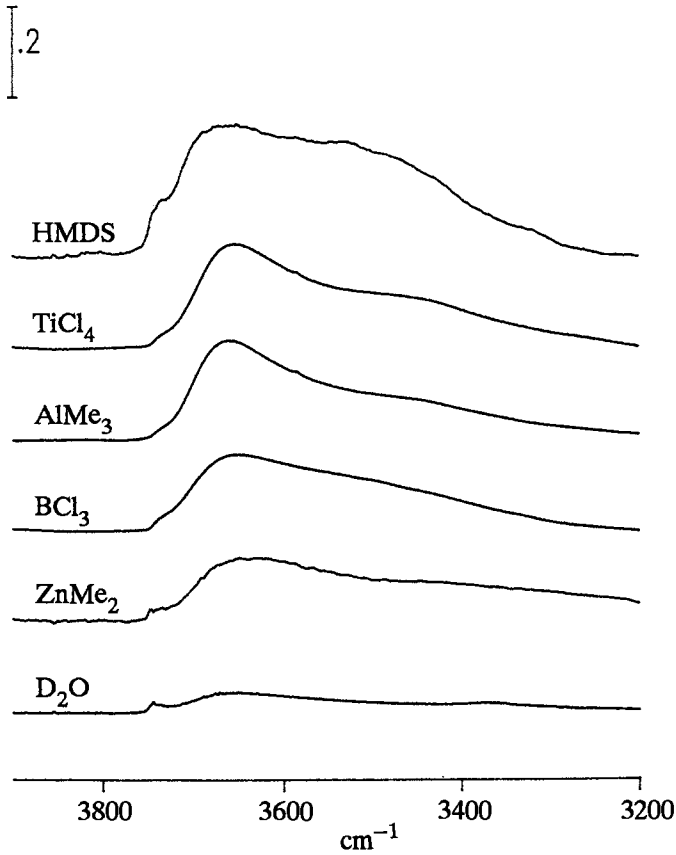

Figure 4. Infrared spectra of fumed silica A-150 after complete reaction at 22 °C with the indicated hydrogen-sequestering agent or after H–D exchange with D_2O. The integrated intensities are shown in Table I.

We have attempted to quantity the effect of the size of the reactant on the number of silanols that react with a given HS agent. Table I shows the cross-sectional area of each reactant, the integrated intensity of the residual silanol band profile after reaction with each HS agent (and D_2O), and the percentage decrease of the initial SiOH band intensity. The reactant area was calculated by using the same method used to calculate BET cross-sectional areas, that is, on the basis of values of the density of the liquid reactant and with the assumption of close-packed spheres. These values are at best approximate; for example, a molecule such as $ZnMe_2$ having a linear C–Zn–C configuration is probably far from spherical in its reactive cross section. The data show that the area of the residual band after reaction with A-150 increases as the size of the reactant increases. However, for P-150 there is little change upon going from $TiCl_4$ to $ZnMe_2$,

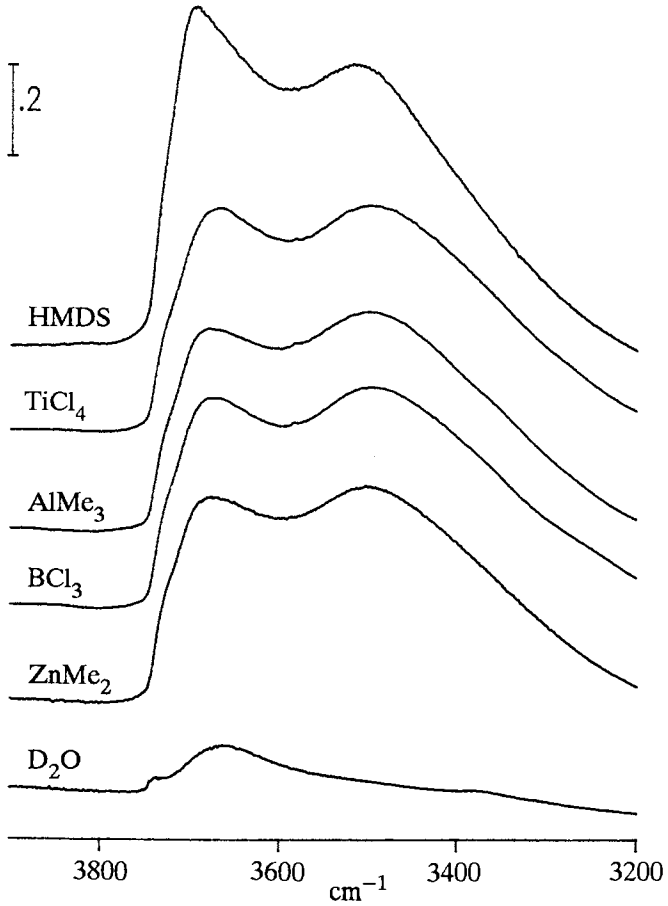

Figure 5. Infrared spectra of precipitated silica P-150 after complete reaction at 22 °C with the indicated hydrogen-sequestering agent or after H–D exchange with D_2O. The integrated intensities are shown in Table I.

and then a very large change upon going from $ZnMe_2$ to exchange with D_2O.

The data shown in Table I were obtained with A-150 or P-150 sample disks that were pressed under identical conditions and that contained the same quantity of silica, 10 mg/cm². The integrated area of P-150 before reaction was about twice that of A-150; this observation suggests that there are a greater number of silanols initially on P-150. As stated earlier, the relative areas before reaction have no quantitative significance because the extinction coefficient of an H-bonded OH oscillator is expected to vary with the strength of the interaction and is generally larger the greater the shift to lower wave number (*12*). Therefore, the silanol density (SiOH

Table I. Chemisorption Data for Reactions on A-150 and P-150

Reactant	Reactant Area (Å²)	A-150 Intensity[a] I_A	A-150 % SiOH Change[b]	P-150 Intensity[c] I_p	P-150 % SiOH Change[b]
HMDS[b]	54.2	100	33	248	15
$TiCl_4$	35.2	54	64	200	32
$AlMe_3$	32.1	45	70	189	35
BCl_3	30.3	47	69	196	33
$ZnMe_2$	25.7	36	76	188	36
D_2O	10.5	12	92	22	92

[a]Integrated intensity I_A after reaction; initial intensity $I_{0A} = 150$.
[b]Percent decrease in the SiOH intensity after reaction, I/I_0 for A-150 and P-150.
[c]Integrated intensity I_p after reaction; initial intensity $I_{0P} = 292$.

groups per square nanometer) was measured for both silicas after 1 h of activation. This attempt immediately poses the problem of whether the accessible silanol density or the total silanol density is wanted; for the accessible silanol density, the "size" of the reactant will obviously influence the results. Therefore, three procedures were used to obtain a measure of this parameter. By using the vacuum microbalance, the mass change was measured, first after exchange with either D_2O or ND_3, these being the "smallest" probe molecules used (as will be discussed, the molecules have similar degrees of exchange and similar cross-sectional areas), and then after complete reaction with HMDS (hexamethyldisilazane), this being the largest probe used. In the third method, the total SiOH density was determined by measuring the mass loss upon heating the silicas from 150 to 450 °C (this heating eliminates most of the H-bonded and perturbed inaccessible silanols as water). Then the remaining free isolated silanols were totally exchanged with D_2O, and the mass change for the conversion of SiOH to SiOD was measured. This third method gives the total silanol density on these silicas. The results are summarized in Table II.

A comment on these silanol densities is necessary. A value of about 4.5–5.0 OH/nm² is generally accepted for "fully hydroxylated" silicas, although there is considerable scatter in the literature data (*1, 2, 20, 21*). Fumed silicas that have not been intentionally rehydrated generally have a density lower than 4.5, as has been found by others (*22, 23*). Precipitated silicas and silica gels can have silanol densities much greater than 5 if polymerization is not complete, or if there is a large number of geminal silanols. The values reported here are well within the ranges expected for both types of silica considered to be "as received" materials. Thus, the most important result of the data in Table II is that the total silanol density of P-150 is about 2.2 times greater than that on A-150, and this factor also

Table II. Silanol Density on A-150 and P-150 Determined by Different Methods

Method	*A-150*	*P-150*
D_2O–ND_3 exchange	2.5 ± 0.1	5.6 ± 0.3
HMDS reaction	1.42 ± 0.02	1.48 ± 0.02
Total SiOH	3.1 ± 0.1	6.8 ± 0.3

NOTE: Densities are reported as SiOH groups per square nanometer.

is reflected in the number accessible to D_2O or ND_3 for exchange. However, *equal numbers of silanols* are capable of reacting with HMDS.

The exchange reaction itself depends on the reactant area. Studies of this dependence have been carried out by using exchange molecules of differing steric dimension (D_2O, ND_3, and OD-containing methanol, isopropyl alcohol, and *tert*-butyl alcohol). After an initial spectrum of A-150 or P-150 was recorded the sample was exposed at 22 °C to 10 torr (1300 Pa) of a given molecule for 10 min, followed by evacuation for 10 min. This process was repeated a total of five times, and after the last exposure the sample temperature was raised to 150 °C while the sample was evacuated, held at 150 °C for 10 min, and cooled to 22 °C before the final spectrum was recorded. There was very little change between the fourth and fifth exposure, and all final spectra for both silicas are shown in Figure 6. Table III shows the area of each exchange molecule, the integrated intensity after exchange, and the percent change in intensity as a result of the exchange. As expected, the degree of exchange increases as the size of the reactant decreases. However, for the same probe molecule, *the percent exchange is virtually identical for each silica.* A comparison of the data in Tables I and III shows that for molecules of comparable size, those that exchange are accessible to many more silanol groups than those that chemisorb. For example, in a comparison of i-PrOD or *t*-BuOD (i-Pr is isopropyl; *t*-Bu is *tert*-butyl) with the series $ZnMe_2$, BCl_3, $AlMe_3$, and $TiCl_4$, the contrast is particularly dramatic for P-150, for which only about 33% of the silanols were accessible to the molecules that chemisorb on silica, whereas about 80% underwent exchange with i-PrOD or *t*-BuOD.

Relative Rates of Reaction of Various Silanol Types. The question of whether there is a difference of reactivity at 22 °C between the H-bonded accessible silanols (3520 cm^{-1}) and free isolated silanols (3748–3738 cm^{-1}) with the most reactive HS agents is now addressed. This question was studied by using the rapid scan facility of a DA3 FTIR spectrometer, in which a single 4-cm^{-1} resolution spectrum can be obtained in 0.25 s. The procedure involves the addition of excess reactant and following the spectral changes as a function of time. The results for

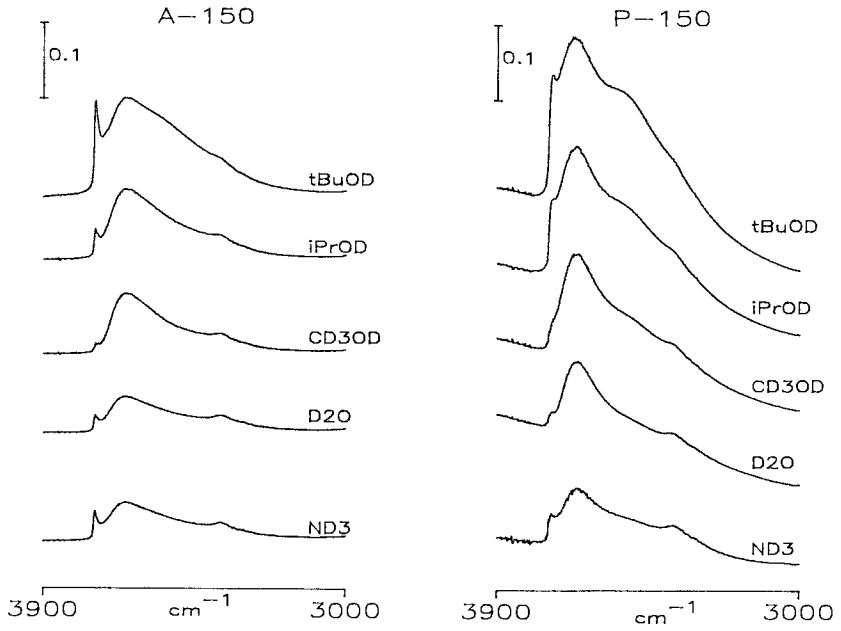

Figure 6. Infrared spectra of A-150 and P-150 after H–D exchange at 22 °C with the indicated molecule. The integrated intensities are shown in Table III.

Table III. Exchange Data for Reactions on A-150 and P-150

		A-150		*P-150*	
Reactant	*Reactant Area (Å²)*	*Intensity*[a] I_A	*% SiOH Change*[b]	*Intensity*[c] I_p	*% SiOH Change*[b]
t-BuOD	31.7	36	76	74	75
i-PrOD	27.6	23	85	54	81
CD_3OD	18.0	17	89	36	88
ND_3	12.9	13	92	21	93
D_2O	10.5	12	92	22	92

[a]Integrated intensity I_A after exchange; initial intensity $I_{0A} = 150$.
[b]Percent decrease in SiOH intensity after exchange, I/I_0 for A-150 and P-150.
[c]Integrated intensity I_p after exchange; initial intensity $I_{0P} = 292$.

$AlMe_3$, BCl_3, and $TiCl_4$ on both silicas are reported here. These reactions are essentially complete after 12, 24, and 60 s, respectively, after a reactant exposure of 4–8 mmol/g of silica (this exposure corresponds to about a three- or four-fold excess of reactant when compared with the number of SiOH groups that react).

The results are presented as difference spectra in Figure 7, which show the spectral *changes* that occurred in a given time interval. The

number of scans and the interval between spectra are shown in Table IV. Only the first three intervals are shown because 50–70% of the silanols had reacted at the end of the third sequence, and the time of each interval was chosen to represent about the same degree of reaction for each reactant. The signal-to-noise level in these spectra is poor, particularly for BCl_3 and $AlMe_3$, for which a single scan was used. However, for the A-150 series an inspection, particularly of the first interval, shows that the broad 3520-cm^{-1} band due to H-bonded silanols has a greater intensity in the order $BCl_3 > TiCl_4 > AlMe_3$. This trend continues for the other intervals. A parameter "*R*", which is the ratio of the peak height of the isolated SiOH peak (≈3745 cm^{-1}) to that at 3520 cm^{-1}, was determined. From the curves shown and other sets of experimental data, the *R* values were estimated to be 5.0 ± 0.3 for $AlMe_3$, 2.7 ± 0.2 for $TiCl_4$, and 1.9 ± 0.1 for BCl_3. A low value of *R* indicates that the H-bonded silanols are initially relatively more reactive than the isolated silanols in the order $BCl_3 > TiCl_4 > AlMe_3$.

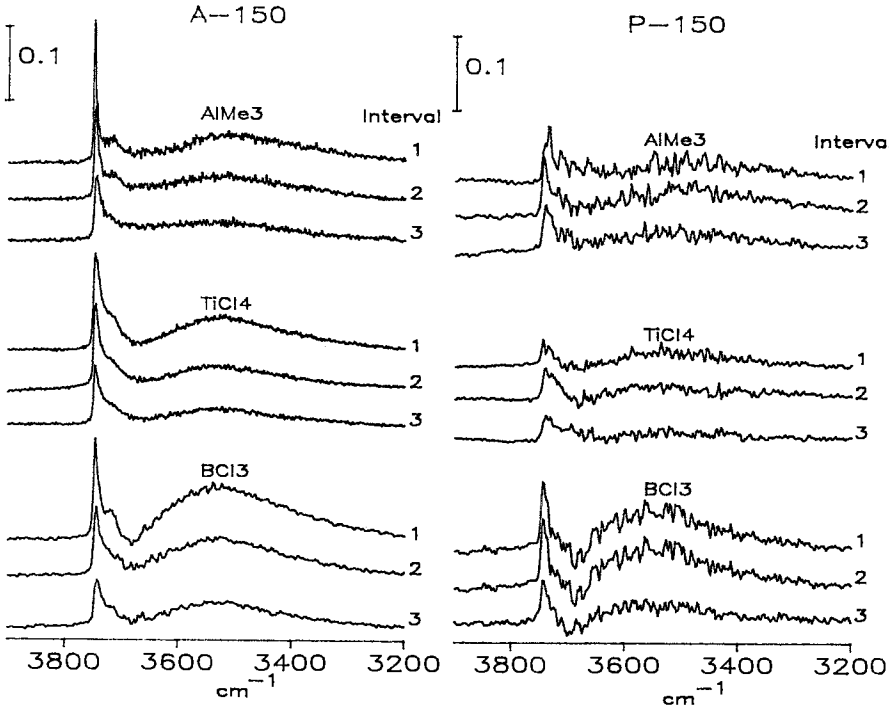

Figure 7. Difference spectra for A-150 and P-150 as a function of time after reaction with the indicated HS agents at 22 °C. The "interval" corresponds to the recording of the first three sets of successive spectra with the time lapse indicated in Table IV (seconds between spectra).

Table IV. Time and Scan Data for Fast-Scan Spectra

	A-150		*P-150*	
Reactant	*Time between Spectra (s)*	*No. of Scans*[a]	*Time between Spectra (s)*	*No. of Scans*[a]
$AlMe_3$	1	1	2	1
BCl_3	2	1	2	1
$TiCl_4$	4	4	4	4

[a]A single scan requires 0.25 s. For multiple scans, one 0.25-s scan can be acquired every 0.5 s.

For the P-150 series, the intensity is low, and there is not such a clear difference in the extent of "disappearance" of the 3520- versus ≈3745-cm^{-1} peaks with any reactant. Qualitatively, the trend follows the same order as for A-150, but because of the very poor signal-to-noise level, characterization via the *R* factor was not attempted.

Although not shown in Figure 7, from about the fifth interval on for any reactant and for either silica, there was very little change in intensity due to H-bonded silanols, whereas the sharp peak at 3745 cm^{-1} continued to "disappear", albeit to a lesser extent than in the earlier intervals. Thus, the reaction with H-bonded silanols ceases before that with isolated silanols. This observation is consistent with the results obtained for the static and exchange reactions.

Discussion

The purpose of this work has been to compare the chemical reactivity and the H–D exchange characteristics of the silanol groups on two hydroxylated "as received" silicas of different origin. The silicas have similar surface areas, and both are essentially nonporous. This discussion addresses only the properties of the A-150 and P-150 materials.

The total SiOH density on P-150 is about twice that on A-150 (Table II; 6.8/3.1 = 2.2). This factor of about 2 occurs frequently. For example, the number of SiOH groups per square nanometer accessible to exchange with D_2O and ND_3 also differs by about two (Table II; 5.6/2.5 = 2.2). For each of the exchange reagents listed in Table III, about the same percent of H–D exchange occurred on each silica, meaning that about 2 times the absolute number of silanols on P-150 were inaccessible to each reagent as on A-150. Finally, for the chemisorption reagents listed in Table I (ignoring the exchange data for D_2O), the "percent SiOH change" for A-150 is about twice that observed for P-150 (*see* columns 4 and 6). However, the absolute number of silanols that reacted with HMDS (Table II) was about equal for both silicas.

The exchange data shows that the texture or porosity of both surfaces is probably similar, because the same fraction of silanols underwent H–D exchange on both silicas when a variety of exchange probes of differing size was used. Moreover, the chemisorption data for the various HS agents show that the reaction with H-bonded and inaccessible silanol groups ceases when about the same total number of silanols have been derivatized, regardless of the silica type. Given the factor of 2 difference in the silanol densities per square nanometer, the absolute number of silanols that "react" with a given HS agent is about the same on both silicas (and this fact was directly verified for HMDS; *see* Table II). That is, when a similar density of chemisorbed product per square nanometer is formed on either silica, then further reaction is essentially inhibited. This point of inhibition presumably occurs when a shroud of chemisorbed product covers the accessible external surface, thereby preventing diffusion of the reactant to other silanols that are normally accessible to the exchange probes. Because the silicas have similar surface areas, this shroud is formed when the same absolute number of silanols have reacted. This observation again suggests that the surface texture of these silicas is similar.

The rate studies showed that there is a difference in the reactivity of H-bonded versus isolated silanols. About 98% of the spectral changes occurred within 12, 24, or 60 s for $AlMe_3$, BCl_3, and $TiCl_4$, respectively. These molecules have comparable sizes (*see* Table I), so differences in the rates of reaction are probably chemical in origin, although diffusion might also play a small role. As has been discussed for A-150 (*6*), the greater ability of the chlorine-containing HS agents to react initially with the H-bonded silanols may be related to the ability of these agents to react bifunctionally with vicinal pairs of silanols (reaction 3). Further, the BET "areas" are probably not a realistic measure of the differences in the reactive cross-sectional areas of these molecules. A methyl group may occupy more space than a Cl atom on the basis of van der Waals dimensions so that, relative to BCl_3 or $TiCl_4$, $AlMe_3$ may have a greater effective cross-sectional area than is suggested by the numbers in Table I. Whatever the interpretation of these results, the reaction with H-bonded silanols on *both* silicas stopped well before that of the isolated silanols; this observation again illustrates that the blocking effect of adjacent derivatized vicinal silanols (reaction 3) is effective in preventing further reaction, whatever the size of the reactant.

Finally, this work has demonstrated the utility of probing the silanol groups on silica by using both chemisorption and H–D exchange. The conclusions reached could not have been arrived at without this combined approach that used probes of differing steric dimensions. The chemisorption probes clearly inhibit reaction by blocking access to other silanols, whereas this inhibition does not occur with the H–D exchange probes. It would be very interesting to extend this study to compare nonporous

silicas with meso- or micropores to assess the possible role of proton migration in the exchange reaction.

Acknowledgement

We are grateful to the Natural Sciences and Engineering Research Council of Canada for financial support.

References

1. Kiselev, A. V.; Lygin V. I. *Infrared Spectra of Surface Compounds*; Wiley: New York, 1975.
2. Iler, R. K. *The Chemistry of Silica*; Wiley: New York, 1979.
3. Hair, M. L. *Infrared Spectroscopy in Surface Chemistry*; Dekker: New York, 1967.
4. Morrow, B. A.; Ramamurthy, P. *J. Phys. Chem.* **1973,** *77,* 3052.
5. Hoffmann, P.; Knozinger, E. *Surface Sci.* **1987,** *188,* 181.
6. Morrow, B. A.; McFarlan, A. J. *J. Non-Cryst. Solids* **1990,** *120,* 61.
7. Morrow, B. A. *Stud. Surf. Sci. Catal.* **1990,** *57A,* A161.
8. Tyler, A. J.; Hambleton, F. H.; Jockey, J. A. *J. Catal.* **1969,** *13,* 35.
9. Armistead, C. G.; Tyler, A. J.; Hambleton, F. H.; Mitchell, S. A.; Hockey, J. A. *J. Phys. Chem.* **1969,** *73,* 3947.
10. Hambleton, F. H.; Hockey, J. A.; Taylor, J. A. G. *Nature (London)* **1965,** *208,* 138, and *Trans. Faraday Soc.* **1966,** *62,* 801.
11. Burneau, A.; Barrès, O.; Gallas, J. P.; Lavalley, J. C. *Langmuir* **1990,** *6,* 1364.
12. Paterson, M. S. *Bull. Minéral.* **1982,** *105,* 20.
13. Morrow, B. A.; Gay, I. D. *J. Phys. Chem.* **1988,** *92,* 5569.
14. Sauer, J.; Schröder, K. P. *Z. Phys. Chem.* **1985,** *266,* 379.
15. Maciel, G. E.; Sindorf, D. W.; *J. Am. Chem. Soc.* **1980,** *102,* 7606.
16. Sindorf, D. W.; Maciel, G. E. *J. Am. Chem. Soc.* **1983,** *105,* 1487.
17. Fyfe, C. A.; Gobbi, G. C.; Kennedy, G. J. *J. Phys. Chem.* **1985,** *89,* 277.
18. Legrand, A. P.; Hommel, H.; Tuel, A.; Vidal, A.; Balard, H.; Papirer, E.; Levitz, P.; Czernichowski, M.; Erre, R.; Van Damme, H.; Gallas, J. P.; Hemidy, J. F.; Lavalley, J. C.; Barrès, O.; Burneau, A.; Grillet, Y. *Adv. Colloid Interface Sci.* **1990,** *33,* 91.
19. Ghiotti, G.; Garrone, E.; Morterra, C.; Boccuzzi, F. *J. Phys. Chem.* **1979,** *83,* 2863.
20. Zhuravlev, L. T. *Langmuir* **1987,** *3,* 316.
21. Tanabe, K.; Misono, M.; Ono, Y.; Hattori, H. *Stud. Surf. Sci. Catal.* **1989,** *51,* 92.
22. Gay, I. D.; McFarlan, A. J.; Morrow, B. A. *J. Phys. Chem.* **1991,** *95,* 1360.
23. Mathias, J.; Wannemacher, G. *J. Coll. Interface Sci.* **1988,** *125,* 61.

RECEIVED for review October 3, 1990. ACCEPTED revised manuscript December 23, 1991.

10

Fourier Transform Infrared and Raman Spectroscopic Study of Silica Surfaces

A. Burneau[1], B. Humbert,[1] O. Barrès,[1] J. P. Gallas,[2] and J. C. Lavalley[2]

[1]Laboratoire de Spectrométrie de Vibrations, Université de Nancy I, B. P. 239, F 54506 Vandoeuvre Lès Nancy Cédex, France
[2]Catalyse et Spectrochimie URA 04.414, Institut des Sciences de la Matière et du Rayonnement–CNRS F 14050 Caen Cédex, France

Infrared and Raman spectra of silica powders differ for fumed and precipitated samples. Site models of the surfaces of fumed silica are proposed. These models involve surfaces resembling faces {111} of β-cristobalite, edges and steps. The site SiOH···Ob(H)SiOaH, located at steps between planes {111}, is related to the absorptions at 3500, 3715, and 3742 cm^{-1}, for the hydroxyl groups from left to right, respectively. Dehydroxylation into SiOSiOH is easy because of the comparatively strong hydrogen bond; this siloxane bridge is a part of two five-fold (–SiO–)$_5$ rings and does not contribute to the Raman band at 607 cm^{-1} (D_2). The single silanols that are closer than about 0.4 nm on faces {111}—and thus are weakly interacting—condense around 400 °C into three-fold (–SiO–)$_3$ rings, the breathing mode of which gives rise to the D_2 Raman band. Most of these siloxane bridges need a high relative humidity to be rehydroxylated. Vicinal single silanols on edges could also condense above 500 °C into very reactive (–SiO–)$_2$ rings.

THE SURFACE REACTIVITY OF SILICA POWDERS depends on the nature, distribution, and accessibility of the surface sites. The definition of such sites on the atomic scale is rather difficult, all the more because it is not independent of the underlying network structure. The silanol groups,

0065–2393/94/0234–0199$08.72/0

either single or geminal, are of particular interest. The infrared transmission spectra of pressed, self-supporting silica disks have been used to study the νOH stretching mode of silanols in the 3200–3800 cm^{-1} region (*1*). The principal results obtained before 1980 have been summarized by Hair (*2*). The broad absorption around 3530 cm^{-1} is due to H-bonded silanols. The amount of bonding is much greater on a silica that is precipitated from solution than on a sample prepared by flame oxidation (*1*). Another component, observed at about 3715 cm^{-1} on fumed silicas, has been assigned to terminal silanols, which are only proton acceptors and have their own proton free for an additional H-bond (*3*). A narrow band at 3747 cm^{-1} remains alone at the end of any thermal treatment. It is assigned to isolated silanols because environment effects are minimized in this configuration. The distance of such an isolated OH group to a first neighbor (fn) has been estimated to be 0.44 nm (*4*). Some silanols are not exchangeable with heavy water. They are called internal and absorb around 3660 cm^{-1}. The surface chemistry also depends on the configuration of the silicon and oxygen atoms building up the surface. These heavy atoms are involved in vibrations at wave numbers much lower than νOH. Before 1980, some of these modes were studied with infrared spectra, despite a strong absorption of the bulk (*5*, *6*).

During the past decade, the main advances in the spectroscopic characterization of silica powders have come from ^{29}Si NMR, Raman diffusion, and Fourier transform infrared (FTIR) studies. NMR studies have given two types of results. First, single and geminal silanols have been quantitatively differentiated as a function of dehydroxylation by thermal treatment and subsequent rehydroxylation by liquid water (*7*). The fraction of geminal silanols

$$f_g = \frac{[Si(OH)_2]}{[SiOH] + [Si(OH)_2]}$$

is about 0.15 on a fully hydroxylated silica surface (*7*). Such a clear characterization had not been previously possible from infrared spectra. Second, surface dehydroxylation induces a diminution of the average of the four Si–O–Si angles around a part of the silicon atoms. In conjunction with results from Raman spectra, this effect has suggested the formation of small planar rings on the surface (*8*, *9*).

The Raman characterization of silica gels is a by-product of researches on the sol–gel process to obtain silica glasses at low temperature from solutions of tetraalkoxysilanes. These spectra have two puzzling features that are also observed in the Raman spectrum of fused, vitreous (v) silica. Two peaks, at 490 cm^{-1} (called D_1) and 604 cm^{-1} (called D_2), are superimposed on the broad band at about 440 cm^{-1}, which is the most intense signal in the spectrum of v-SiO_2. These two peaks are unusually

sharp for a noncrystalline solid and have not been explained with a continuous random network model. Their intensities in v-SiO_2, particularly for the D_2 peak, increase with "fictive" temperature, that is, the temperature (up to 1500 °C) from which the sample has been quenched to room temperature (*10*). The D_2 peak also dramatically increases with neutron irradiation (*11*, *12*). Numerous structural models have been proposed for D_1 and D_2, mainly defects such as a broken Si–O bond, or the breathing modes of planar rings of order $n = 4$ (four-fold) or 3 (three-fold), where n is the number of SiO groups in a ring (*13*).

The Raman spectrum of a gel before any heating displays the D_1 band, but not the D_2 band. The D_2 peak appears only after the gel has been preheated above 200 °C. Its intensity is maximum after a pretreatment around 600 °C. With a gel of high surface area, this intensity is then greater than that with untreated v-SiO_2 and similar to that observed with irradiated v-SiO_2. The D_2 peak decreases above 600 °C and becomes similar to that observed for a fused silica after the gel has been consolidated to dense amorphous silica at 1100 °C (*14–16*). For a preheated gel, the D_2 intensity is reduced by exposure to water vapor (*17*). Exchanges with $H_2{}^{18}O$ have shown that, in a gel, both the D_1 and D_2 modes involve surface sites (*16*). After some controversy, the D_2 band has been convincingly assigned to three-fold rings (*8*, *16*), and a surface model has been proposed on this basis. Brinker et al. have suggested that the precursor structure could be the {111} faces of β-cristobalite. The condensation of two "isolated vicinal" silanols on such a surface would result in equal numbers of three-, five-, and six-membered rings (*9*). The assignment of D_1 to four-fold planar rings is not so straightforward. A very intense band at 490 cm^{-1} has been found in the Raman spectrum of a gel before any drying. With the assumption of two quasi-degenerate features, this band has been called D_0 and assigned to symmetric stretching mode $\nu_s O_3Si(OH)$ (*18*). Such an assignment of a Raman peak near 490 cm^{-1} to single silanols is also supported by NMR results (*19*).

Numerous FTIR studies have become available. FTIR devices have the following advantages:

1. access to extended spectral ranges, from far to near infrared (*20–22*)
2. easier data processing, for example, for differences between successive spectra and quantitative analysis (*23*, *24*)
3. sampling by methods other than transmission, for example, with a diffuse reflectance (DR) attachment (*25*, *26*)

As far as possible, three types of comparisons are made in this chapter:

1. between samples (a fumed silica and silica powders obtained from solutions)
2. between two kinds of infrared spectra (transmission through self-supporting silica disks and also DR of a powder)
3. between infrared and Raman spectra

A summary is given for spectral variations as a function of dehydration in vacuum, dehydroxylation by thermal pretreatment up to 700 °C, rehydroxylation, and grafting. On the basis of recent NMR, X-ray, and Raman results, the infrared spectra are further assigned in terms of surface sites related to the local structure of the underlying SiO network. Emphasis is given to a detailed structure analysis of a fumed silica. Additional features are necessary to describe other types of silicas.

Experimental Details

The experimental details have been described (*22*, *25*, *26*). The silica samples are (1) a fumed (or pyrogenic) silica called A (Aerosil 200, Degussa, specific surface area $A_s = 200$ m^2 g^{-1}, as provided by the supplier), (2) a precipitated silica called P (Zeosil 175 MP, Rhône Poulenc, $A_s = 175$ m^2 g^{-1}, as provided by the supplier), and (3) a silica gel called G (Rhône Poulenc, $A_s = 320$ m^2 g^{-1}, as provided by the supplier). The apparent surface densities deduced from thermogravimetric measurements were 4, 14, and 12 OH groups per square nanometer for silicas A, P, and G, respectively (*26*). From ^{29}Si NMR measurements, the fractions of geminal sites were evaluated to be $f_g = 0.21$, 0.18, and 0.17 for silicas A, P, and G, respectively (*27*). These values correspond, respectively, to 0.35, 0.30, and 0.29 for the fractions of geminal hydroxyl groups

$$x_g = \frac{2[Si(OH)_2]}{[SiOH] + 2[Si(OH)_2]}$$

The preparation of grafted silicas by reaction with methanol under high pressure at 200 °C for 2 h has been described (*28*). These samples are called AC_1, PC_1, and GC_1.

The spectra were obtained with FTIR spectrometers, either by transmission through self-supporting silica disks or from diffuse reflectance of silica powder. Silica disks pressed under 50 MPa could be evacuated with a residual pressure of about 10^{-3} Pa. The spectra are shown in a normalized absorbance scale, according to

$$\text{normalized absorbance} = \text{measured absorbance} \cdot s/(mA_s) \qquad (1)$$

with m the mass in grams of the pellet of hydroxylated silica, and s the pellet area in square centimeters.

Powder DR data were collected with a Harrick DRA-2CI attachment and a HVC-DRP heatable cell, evacuable below 0.1 Pa. To collect spectra below 4000 cm^{-1}, the silica powder was generally mixed with potassium bromide, without any pressure, so that there was no close interaction between KBr and the silica surface.

The measured temperature, called apparent temperature, is that of the stainless steel cup containing the sample; the difference from the real temperature of the sample surface analyzed by infrared radiations has been examined (25). The temperature used in this chapter is the apparent temperature.

Raman spectra of self-supporting disks of silica A were obtained with a spectrometer Coderg T800 and a spectral resolution of 7 cm^{-1}. The 514.5-nm emission line of an Ar^+ laser was used with a power of about 200 mW at the sample.

Results

Water Desorption. The spectral range 5000–5350 cm^{-1} characterizes the combinations of the bending (ν_2) and one of the stretching modes (ν_1 or ν_3) of water molecules. Because this range is fairly isolated from the silica absorptions, it allows the study of physisorbed water. Despite some controversy about this point (29), most of the silicas are readily dehydrated by evacuation at room temperature (5, 22, 23, 30–32). For instance, the DR spectra of pure powder G shows that the $\nu_2 + \nu_3$ water absorption disappears below 0.1 Pa (curve d of Figure 3 in reference 22). Moreover, the $\nu_2 + \nu_3$ band gives some insight into the states of adsorbed water. A shoulder at 5315 cm^{-1} corresponds to water molecules with at least one unbonded OH group on the outer surface (22). This species is the most readily desorbed from silica G. Simultaneously, the νOH absorption of the liberated silanols appears at 3740 cm^{-1} for silicas G and P (Figure 1, curve b – a). A further dehydration eliminates water molecules H-bonded through their two OH groups (22) and causes an increase in silanol absorption between 3730 and 3675 cm^{-1} (Figure 1).

Silica A has an unusual spectrum. The νOH absorption of the silanols that become non-H-bonded to water increases first at 3746 cm^{-1}, which corresponds to isolated silanols, then between 3746 and 3700 cm^{-1}, with a shoulder near 3715 cm^{-1} (Figure 1). In a last stage, the absorption sharply decreases at 3748 cm^{-1}, whereas it goes on increasing around 3742 and 3715 cm^{-1} (curve d – c). Although puzzling, this last stage has been confirmed in various experiments and with different spectrometers, either by diffuse reflectance or by transmission (22). It was concluded that the absorbance diminution at 3748 cm^{-1} at the end of dehydration is not an artifact in spectrum subtraction. This feature is assigned to a real shift of the νOH band to low wave number when vapor pressure becomes smaller than about 10 Pa. Such a shift might itself be related to a temperature increase of the sample due to the strong absorption of infrared radiation below 1300 cm^{-1}.

Silanol Heterogeneity. The νOH absorbance profile of each dehydrated silica is shown in Figure 2. A narrow absorption at 3747 cm^{-1} dominates the spectrum of silica A and characterizes isolated silanols on surfaces that are not completely hydroxylated. This last statement is also

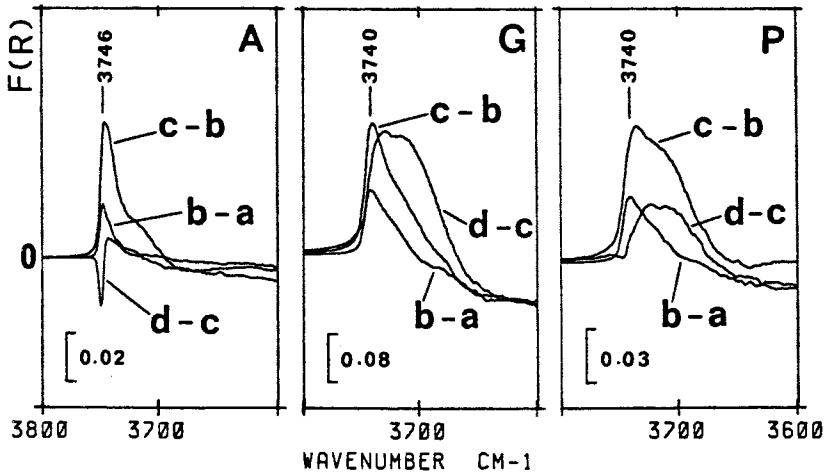

Figure 1. Successive variations of the diffuse reflectance spectra of silicas A, G, and P (mass fraction 0.12 in KBr) by progressive evacuation at 20 °C; a, in air; b, 30 Pa; c, 3 Pa; and d, 0.4 Pa. (Reproduced from reference 22. Copyright 1990 American Chemical Society.)

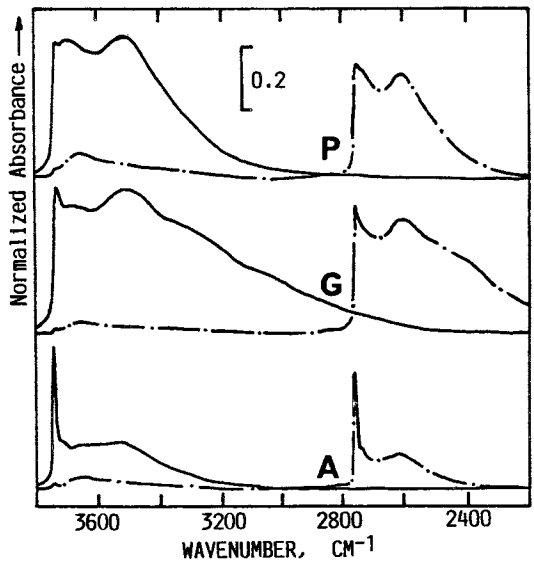

Figure 2. Normalized absorbances of self-supporting silica disks evacuated at room temperature, before (solid line) or after (broken line) D_2O exchange at room temperature. (Reproduced from reference 22. Copyright 1990 American Chemical Society.)

based on the Raman spectrum discussed later. About 9% of the silanols are internal, inaccessible to D_2O molecules at room temperature ($\nu OH \approx 3670$ cm^{-1}; Figure 2). The weakness of the components at 3715 and 3530 cm^{-1} is also characteristic of fumed silicas (*3*).

The spectra of silicas G and P are very different from that of silica A. The absorptions of both the H-bonded and the weakly perturbed silanols are very strong. Because most of the silanols are exchangeable with heavy water (Figure 2), these absorptions cannot be assigned to internal silanols. A body of results suggests the presence of inner silanols on the silicas prepared from solutions before any thermal treatment (22). These inner silanols are not taken into account by nitrogen or argon adsorption, although their protons are exchangeable. They explain the anomalously large apparent surface densities of silanols on silicas G and P. The structure of such inner silanols is not straightforward. According to Yates and Healy (32), the surface of disperse SiO_2 obtained from solutions would be made of a gel layer of incompletely condensed polysilicic acid, which remains permeable to water molecules although more or less compacted. Another model is suggested by X-ray diffraction of silica gels (33). Those silicas would be made of very small primary particles that associate to bigger clusters in the course of gelation or precipitation. Various types of inner silanols could result from this association (*34*). For instance, the primary polyhedron postulated by Himmel et al (33) can build up a surface resembling a {111} face of β-cristobalite, but with some Si atoms lacking. A hole of SiOH corresponds to three single silanols, each being exchangeable and H-bonded as in a cyclic trimer. However, argon or nitrogen adsorption would probe nearly the same area as on a regular surface.

Thermal Treatments. ***Infrared Spectra.*** The successive variations of the νOH absorptions of self-supporting silica disks degassed at 160, 260, 460, 645, and 745 °C have been studied at room temperature (*26*). For every sample, the two main features are as follows:

1. The higher the degassing temperature, the higher is the wave number of the absorbance diminution. This fact corresponds to a preferential dehydroxylation of the silanols that interact the most strongly with neighbors.

2. A concomitant creation of free silanols is observed in the range 3742–3747 cm^{-1}.

More accurately, three silanol distributions are successively evidenced by increasing the activation temperature, even though these distributions are not completely separated.

1. Up to 260 °C, the eliminated silanols are strongly H-bonded. An important difference between the samples exists, however. For silica A, the νOH diminution around 3500 cm^{-1} is observed simultaneously with another component, weaker but well resolved, at 3715 cm^{-1}. Most of the H-bonded silanols on silica A are thus involved in pairs, in agreement with previous studies of fumed silicas (3). In contrast, no component is resolved at 3715 cm^{-1} for silicas G and P. Those spectra are explained by additional clusters of H-bonded silanols larger than pairs, for example, by the hydroxyl triplets mentioned, which correspond to "holes of SiOH".
2. Between 260 and 460 °C, the preceding reaction is completed while a second group of weakly bonded silanols, absorbing between 3620 and 3700 cm^{-1}, are dehydroxylated. At this stage, silica A is again differentiated from other samples, because the absorbance diminution is rather localized at 3620 cm^{-1}.
3. Between 460 and 645 °C, the absorption diminution peaks near 3735 cm^{-1} and is very asymmetrical toward low wave numbers, with a submaximum near 3680 cm^{-1} only for silica A.

Another difference between the silicas concerns the wave number of the absorption augmentation. For silica A, the maximum of the variation is close to 3747 cm^{-1} whatever the pretreatment temperature. For the other two silicas, it shifts from 3742 to 3747 cm^{-1} when the pretreatment temperature is increased.

The same spectral evolutions were observed for the silicas mixed with KBr, pretreated in the DR cell at high temperature, and then cooled down to room temperature. The successive variations of the νOH absorptions are shown in Figure 3 for silicas G and P. An apparent temperature of 500 °C is necessary to eliminate the most strongly H-bonded silanols (curve a). In contrast, the distribution of weakly perturbed silanols is desorbed between 540 and 580 °C (curve c), which corresponds to a rapidly increasing efficiency of the treatment above 540 °C. After a treatment at the apparent temperature of 580 °C, the νOH profiles are similar to those of self-supporting silica disks pretreated at the real temperature of 645 °C. An intermediate distribution of desorbed silanols, with two broad peaks at about 3570 and 3675 cm^{-1}, is also shown in Figure 3 (curve b).

Raman Spectra. The fluorescence of samples G and P prevented the recording of their Raman spectra. Only silica A was successfully studied, in

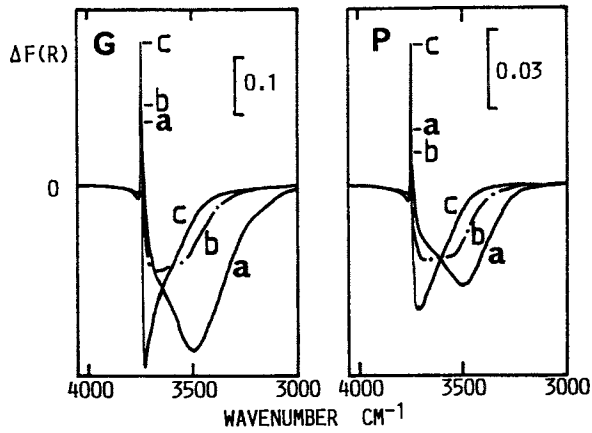

Figure 3. Successive variations of the diffuse reflectance spectra, at room temperature, of silicas G and P (mass fraction 0.12 in KBr), induced by preheating the samples in vacuum below 0.1 Pa. Apparent temperatures of the pretreatment: a, 500–350; b, 540–500; and c, 580–540 °C.

spite of a poor signal-to-noise ratio (Figure 4). As provided by the supplier, its Raman spectrum is quite different from that usually observed for a silica gel before a thermal pretreatment, because it displays a comparatively strong band D_2 at 607 cm^{-1}. A preheating at 400 °C in air induces an augmentation of the D_2 band by a factor 1.5. Simultaneously, the intensity of the D_0 or D_1 peak or both at 490 cm^{-1} is lowered by a factor of about 0.7 (curve b). A further preheating at 580 °C does not increase the D_2 band any more. On the contrary, both the D_0–D_1 and the D_2 components decrease somewhat (curve c). The exposure of the initial silica A to 100% relative humidity (RH) induces a diminution of band D_2 by 50% and an obvious augmentation of the signal at 490 cm^{-1}.

Three conclusions can be drawn.

1. The silica A surface is not fully hydroxylated. About two-thirds of the sites that are precursors of type D_2 siloxane bridges are already dehydroxylated in the initial sample. That observation is consistent with both the high manufacturing temperature of the fumed silica and its low hydroxyl surface density (≈ 3.65 OH groups per square nanometer; Table I) but is not in agreement with Brinker's view that the hydrolysis of three-fold rings D_2 is easy (9). In contrast, the primary hydration of silica A should take place on sites other than faces {111} of β-cristobalite (9), which is further discussed later in the chapter.

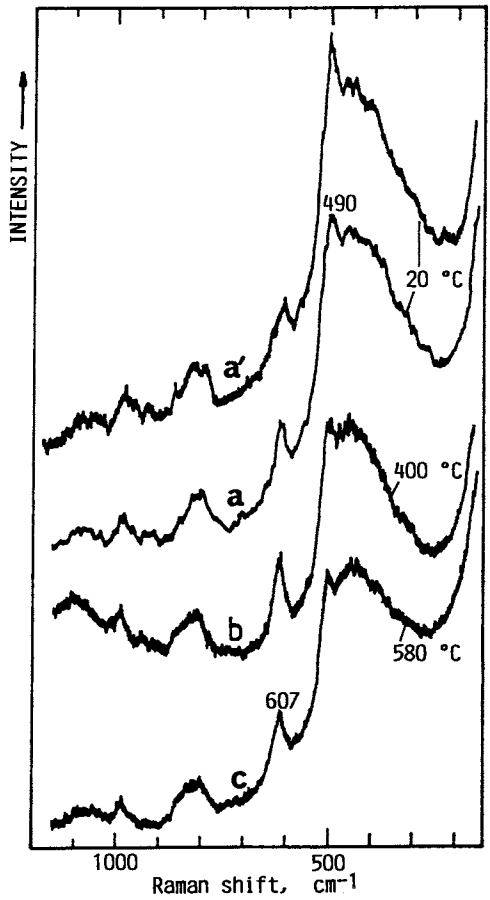

Figure 4. Raman spectra of silica A: a, as received; a', exposed for 120 h to 100% relative humidity; b and c, preheated in air (b) to 400 and (c) to 580 °C.

2. The strong diminution of the Raman scattering at 490 cm^{-1} by heating up to 400 °C is related to dehydroxylation rather than to the opening of four-fold rings. In fact, the spectra a' to b in Figure 4, although not normalized, suggest that the diffusion around 490 cm^{-1} involves vibrations of some silanol sites. Thus, the band at 490 cm^{-1} would be assigned to structure D_0 (*18*).
3. Whereas species D_0 appears as a precursor of D_2 for the hydroxyl condensation observed below 400 °C, it does not do so between 400 and 580 °C. Indeed, the signal at 490 cm^{-1} decreases without the creation of a corresponding

Table I. Hydroxyl and Methoxyl (OMe) Surface Densities on Initial Sites of Silica A

Sample	*Group*	*Total*	$S_m + S_e$	S_p	G_p	G_e	D_2
A	OH	3.65	1.6	0.65	1.3	0.1	
AC_1	OH	1.35		0.65	0.65	0.05	
(Fig. 5, curve a)	OMe	2.9	1.6		0.65	0.05	0.6
AC_1,460 °C	OH	0.7			0.65	0.05	
(Fig. 5, curve b)	OMe	2.25	1.6			0.05	0.6
AC_1,460 °C, MeOH	OH	0.05				0.05	
(Fig. 5, curve c)	OMe (eq 5a)	4.9	1.6		0.65	0.05	2.6
	OMe (eq 5b)	4.9	1.6	0.65	1.3	0.05	1.3

NOTE: Surface densities are per square nanometer. Abbreviations are as follows: S_m, single silanol surrounded by other single silanols, as in the middle of a {111} face of β-cristobalite (Figure 6a); S_e, single silanol on an edge (Figure 6b); S_p, single silanol perturbed by H-bonding with a neighboring hydroxyl of a site G_p at a step between {111}-like faces (Figure 6a); G_p, geminal silanol at a step; G_e, geminal silanol at an edge; and D_2, surface siloxane bridge belonging to an $(SiO–)_3$ ring.

amount of structure D_2. That observation shows that there is a condensation into a structure other than D_2. Some sintering is also possible, which would not be in contradiction with the constant value found for the specific surface area of silica A up to 650 °C (*27*), because A_s should somewhat increase by hydroxyl condensation alone because of the mass diminution at nearly constant surface area.

Methyl Grafts. Infrared spectra show that the reaction of surface silanols with methanol (MeOH) at 200 °C for 2 h under high pressure is incomplete. As previously described (*27*), every silica grafted under these conditions (samples AC_1, GC_1, and PC_1) displays a resolved component between 3737 and 3743 cm^{-1}, in addition to internal and H-bonded silanols. For instance, curve a of Figure 5 shows the spectrum of AC_1 with a density of 2.9 methoxyl groups per square nanometer (Table I) (*28*). Compared with the H-bond band, the component near 3740 cm^{-1} is the most intense for sample AC_1. Such an incomplete reaction is mainly assigned to geminal sites in the particular case of silica A. A site $SiOH\cdots O_b(H)SiO_aH$ (called S_p–G_p) is speculated: it is made of a single silanol (S_p) and two geminal hydroxyls (G_p). On the initial silica A, S_p would be H-bonded (νOH ≈3500 cm^{-1}) to the terminal O_bH group of site G_p (νO_bH ≈3715 cm^{-1}); O_bH would interact somewhat with the second geminal group O_aH (νO_aH ≈3742 cm^{-1}). In this structure, the hydroxyl most reactive toward alcohols is thought to be O_bH, which is the most proton donor group because of the cooperative effect in the $OH\cdots O_b(H)$ bond. The reaction of silica A with methanol displays an absorption

decrease mainly at 3715 and 3747 cm^{-1}, the latter decrease corresponding to the methoxylation of isolated single silanols. The presence of unreacted hydroxyls absorbing at both 3743 and about 3500 cm^{-1} on AC_1 could be due to a partial methoxylation of site S_p–G_p according to

$$SiOH \cdots O(H)SiOH + MeOH \rightarrow SiOH \cdots O(Me)SiOH + H_2O \quad (2)$$

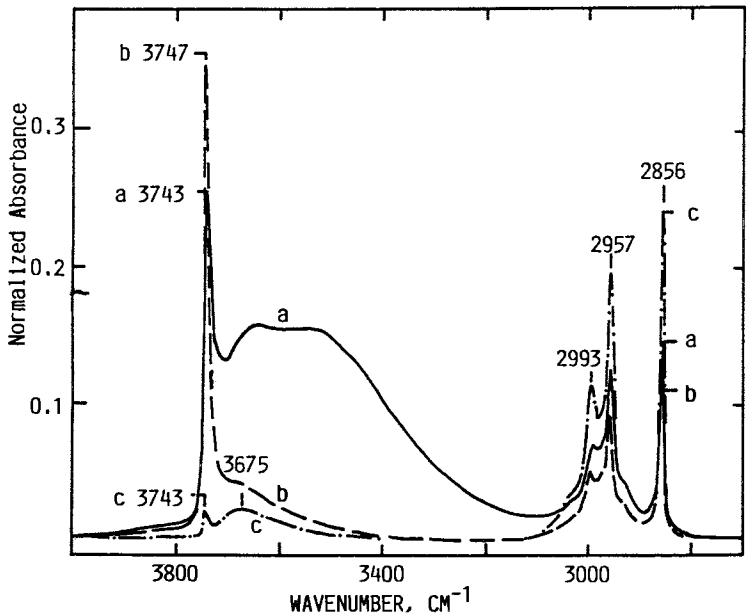

Figure 5. Normalized absorbances of a self-supporting disk of grafted silica AC_1: a, evacuated at room temperature; b, predegassed at 460 °C; and c, after 1 h of contact with 4700-Pa methanol at 460 °C and evacuation.

Curve b of Figure 5 shows the spectrum of AC_1 after degassing at 460 °C. The methoxyl density, deduced from the variation of the CH_3 stretching bands, decreases to 2.25 per square nanometer (Table I). The free silanol νOH wave number shifts from 3743 to 3747 cm^{-1}, whereas the H-bonded hydroxyls disappear and a few internal silanols remain at 3675 cm^{-1}. By using the value $\epsilon = 350$ L mol^{-1} cm^{-1} for the molar decadic absorption coefficient of silanols that have been isolated by thermal pretreatment, the density of these OH groups is found to be close to 0.65 per square nanometer. Whatever the final state of the degassed molecules, the following reaction is in agreement with the spectral changes of AC_1 from curve a to b:

$$\text{SiOH} \cdots \text{O(Me)SiOH} \rightarrow \text{SiOSiOH} + \text{MeOH} \quad (3)$$

Thus, the isolated single silanols on thermally treated sample AC_1 would be located on the ex-G_p sites (Table I). The density of these hydroxyls gives an estimate of the density of sites S_p–G_p on silica A to be about 0.65 per square nanometer. As a consequence, the OH density on initial sample AC_1 would be about 1.3 per square nanometer. The sum of this value and 2.9 (the methoxyl density) gives a total larger than the surface OH density on silica A. Thus when sample AC_1 is prepared, some methanol is added to siloxane bonds according to

$$\text{SiOSi} + 2\ \text{MeOH} \rightarrow 2\ \text{SiOMe} + \text{H}_2\text{O} \quad (4)$$

This conclusion is in agreement with Raman spectra showing that the surface of initial silica A is not fully functionalized: sites D_2 are the most likely location of this addition (Table I).

A further exposure to 4700-Pa MeOH at 460 °C for 1 h gives final densities of 4.9 OMe per square nanometer, 0.05 isolated OH per square nanometer, and a few internal hydroxyls (curve c of Figure 5 and Table I). In this stage, the change of S_p–G_p sites can be schematized in two extreme ways: either the change only induces the methoxylation of the remaining 0.65 OH per square nanometer according to

$$\text{SiOSiOH} + \text{MeOH} \rightarrow \text{SiOSiOMe} + \text{H}_2\text{O} \quad (5a)$$

or every S_p–G_p site is completely methoxylated in spite of steric hindrance according to

$$\text{SiOSiOH} + 3\ \text{MeOH} \rightarrow \text{SiOMe}\ \ \text{MeOSiOMe} + 2\ \text{H}_2\text{O} \quad (5b)$$

This methoxylation would not be observed at 200 °C because of a high activation energy. In both hypotheses, the final density of 4.9 OMe per square nanometer involves the complementary opening of siloxane bridges (Table I).

Discussion

A description of silica surfaces should not be made only in terms of hydroxyl groups without reference to the underlying atoms. Various experimental results suggest some local order on the surface, even though the bulk network is amorphous. The presence of typical sites on the atomic scale is all the more likely because constraints due to disorder should relax on a hydroxylated surface. Therefore, network and surface models based

on crystalline structures are needed to define possible silanol sites and relate them to the spectral features discussed. References to crystalline silicas for studying divided samples have often been made (*7, 9, 31, 35*). The models that follow use a few structures on the scale of some SiO_4 tetrahedra (in a radius of about 0.5 nm) and disorder at longer distances, between 1 nm and the diameter of silica particles, which is about 10 nm for silicas A and P and 5 nm for silica G (*27*). A consequence of this view is that the whole surface can be described with a fractal model, an assumption supported by both small-angle X-ray (*27*) and Raman (*34, 36*) scatterings.

Network Models. With a value increasing from about 2.12 g cm^{-3} at 200 °C up to 2.31 g cm^{-3} at 900 °C, the skeletal (or true) mass per unit volume (or density) of silica gels is consistent with a network structure looking like either tridymite or cristobalite (*37, 38*). X-ray results have suggested for a long time that the structure of silica powders most closely resembles that of cristobalite. Recent results confirm that silica gels are built up of interconnected six-membered rings of [SiO_4] tetrahedra. One polyhedron type, with four rings similar to those in cristobalite, has been found predominant (*33*). By using small-angle X-ray scattering, displacing phase transitions have also been observed around 100 °C for silica gels that were not preheated (*33*). On that basis, adequate models of the structure of silica powders are α-cristobalite at low temperature and β-cristobalite at high temperature. The values of the true density between 200 and 900 °C mentioned are consistent with that of β-cristobalite (2.175 g cm^{-3} at 290 °C) (*38*), provided the surface is taken into account. The augmentation of density with temperature is indeed related to the condensation of the surface silanol layer into siloxane bridges. The effect can be estimated as follows. With a thickness of 0.16 nm and a surface density of 4.5 SiOH per square nanometer, the mass per unit volume of a silanol layer would be $4.5 \times 10^{14} (16 + 1 + 28/2)/(6 \times 10^{23} \times 0.16 \times 10^{-7}) = 1.45$ g cm^{-3}. In contrast, the mass per unit volume of this layer after complete condensation into a siloxane layer 0.06 nm thick would be $2.25 \times 10^{14} (16 + 28)/(6 \times 10^{23} \times 0.06 \times 10^{-7}) = 2.74$ g cm^{-3}. These values show that, when hydroxyl condensation proceeds, the apparent density, corresponding to both the network and the surface layer, increases from a value smaller to a value larger than the network density. Whatever the temperature and the corresponding structure of cristobalite, the cubic unit cell of β-cristobalite is used to discuss surface models, because the α-structure can also be described with a similar pseudo-cube (*38*).

Surface Models. A surface corresponding to the {111} faces of β-cristobalite would bear single silanols on alternate Si atoms (*36*). The O–O distance of two fn silanols is about 0.51 nm in an idealized structure of β-cristobalite with the orientation *Fd*3*m* (*38*). The corresponding surface

density is 4.5 OH per square nanometer. The condensation of two fn silanols would generate a three-fold siloxane ring and a five-fold siloxane ring.

Faces {110} would show parallel rows of vicinal single silanols, with two SiO directions making ideally an angle of 70.5°. The smallest O–O distance between silanols, both inside a row and in two neighboring rows, would ideally be 0.44 nm. The O–O distance between second neighbor (sn) silanols in a row is 0.51 nm. The corresponding surface density is 5.5 OH per square nanometer. The condensation of fn silanols in two neighboring rows would generate nonplanar four-fold siloxane rings (*36*). The condensation of two vicinal silanols in a row would give a very strained two-fold ring. The condensation of sn silanols inside a row would give a three-fold ring as on a plane {111}.

Faces {100} could display geminal silanols with a surface density of 7.8 OH per square nanometer. The $SiO_2(H_2)$ groups are located in parallel planes containing an axis <110> (*36*). In this direction, an idealized O–O distance of 0.25 nm is found for both silanols of a given geminal site and of two fn sites. The distance between rows is 0.51 nm. The most likely condensation is between two strongly H-bonded hydroxyl groups of two neighboring (nonvicinal) sites inside a row. This condensation would generate a couple of nonplanar five-fold siloxane rings.

The adequacy of faces {110} in explaining the experimental results has not been fully investigated, but faces {111} appear, up to now, to be the best model of a uniform surface for silica. With a density of about 135 siloxane bridges per cubic nanometer, a hydroxylated {111}-like surface is indeed likely to be very stable. In opposition to this view, it has been claimed (*7*) that reducing the hydroxyl density below 4.5 per square nanometer appears rather infeasible, because all OH groups would be separated by at least 0.5 nm. Such a description of faces {111} comes in fact from an overidealized cristobalite, in the orientation $Fd3m$. In contrast, the condensation of fn silanols into three-fold siloxane rings appears quite feasible by reference to the real structures of α- or β-cristobalite (orientations $P4_12_1$ or $P2_13$, respectively) (*38*). Furthermore, the formation of such rings is supported by NMR and Raman spectra (*8*, *9*). However, the extension of the faces should not be overestimated, even though *n*-hexadecyl grafts 2 nm long can lie in an ordered structure on such faces (*25*). Edges and steps must be taken into account. Four sites are further defined:

1. S_m is a single silanol, somewhere on the middle of a surface {111} (Figure 6a). The idealized O–O distance with a fn silanol, which is 0.51 nm, only applies to one-fourth of the silanols in a more realistic model of β-cristobalite in the orientation $P2_13$ (*38*). The three other silanols, which are

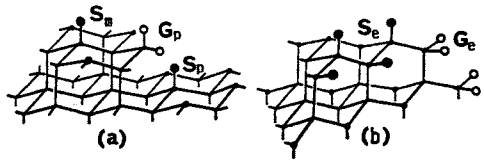

Figure 6. Definition of some silanol sites at steps (a) or at edges (b) between planes {111} of β-cristobalite. The silicon atoms bonded to hydroxyl groups are shown by small dots. Only a few silanols are shown for sake of clarity. Full and open circles denote single and geminal hydroxyls, respectively.

related by a three-fold symmetry axis, are brought closer together, to 0.41 nm (they are displayed by the triplet i-j-k in Figure 7). With the α-cristobalite model in the orientation $P4_12_1$ (*38*), the hydroxyl groups would be rotated towards each other as streetlights on opposite sides of a street. Across this "avenue", the fn O–O distance is 0.40 nm for all silanols (Figure 8). The sn O–O distance is 0.60 nm outside this avenue. With a fn O–O distance of about 0.4 nm, silanols S_m should not be strongly H-bonded, although a further distortion, compared to the cristobalite models, could allow a significant perturbation.

2. S_e is a single silanol on the edge between two faces {111} making a dihedral angle of 109.5° (Figure 6b). The edge is a zig-zag chain of staggered silanols and has the characteristics of a silanol row on a plane {110}. For two vicinal silanols of this row, the O–O distance is calculated between 0.37 and 0.50 nm on the basis of the real structures of α- and β-cristobalite, near the idealized value of 0.44 nm.
3. G_e is a geminal site on the edge between two faces {111} making an angle of 70.5°. The $SiO_2(H_2)$ plane is perpendicular to the edge. The fn O–O distances between the silanols of the edge are similar to those with neighboring silanols S_m, in the range of 0.4–0.5 nm.
4. Geminal sites are also involved in steps between parallel surfaces {111}. Such steps between two successive planes can be built either with one site G_e (Figure 6b) or with one geminal site G_p and one single silanol S_p (Figure 6a). The O(H) atoms of G_e are parallel to the step, whereas they are perpendicular in a site S_p–G_p.

A step of more than one $[SiO_4]$ tetrahedron would involve a portion of {100} plane, with more than one H-bonded G_p site. Sindorf et al. explained

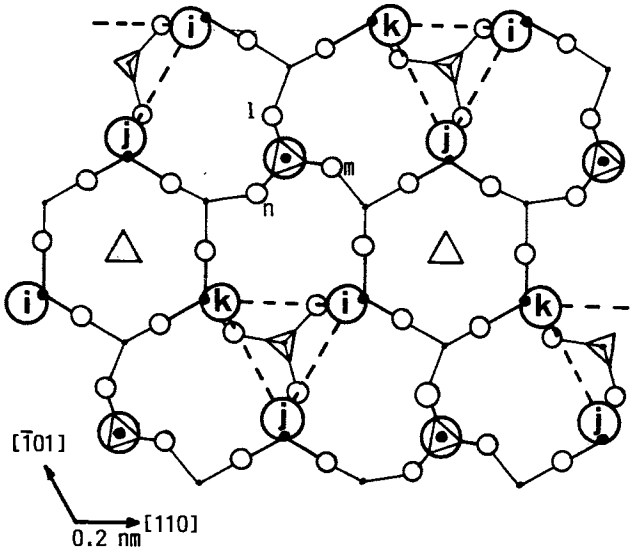

Figure 7. Projection along [1$\bar{1}$1]° of the surface atoms of face (1$\bar{1}$1) of β-cristobalite in the orientation $P2_13$ *(38). Small dot, Si atom at height ≈0; big dot, Si atom at height ≈0.1 nm; small open circle, O atom; large open circle, OH group at height ≈0.26 nm; triangle, three-fold symmetry axis; and dashed line, possible weak H-bond between nearest neighbor OH groups.*

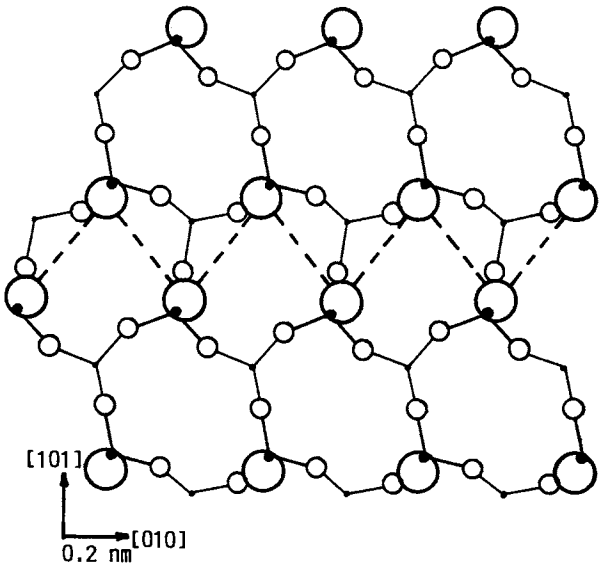

Figure 8. Projection along [$\bar{1}$01]° of the surface atoms of face ($\bar{1}$01) of α-cristobalite in the orientation $P4_12_1$ *(38).*

their NMR results with a model made of both {111} and {100} faces (*see* Figure 12 of reference 7). However, two facts suggest that faces {100} do not participate much on the silica surfaces and that geminal silanols are rather located at short steps between faces {111} on a consolidated silica surface. First, the fraction of geminal sites on a hydroxylated silica is rather low, with a value $f_g \approx 0.15$ (7). Second, no augmentation of a single silanol population was observed (7) by heating around 200 °C, which causes the density of geminal sites to decrease by more than 10%. This result does not agree with the expectation that two neighboring G_p sites should be transformed into two single silanols at the very beginning of dehydroxylation, according to

$$\cdots O(H)SiOH \cdots O(H)SiOH \rightarrow \cdots O(H)SiOSiOH + H_2O \qquad (6)$$

In contrast, the reaction

$$SiOH \cdots O_b(H)SiO_aH \rightarrow SiOSiO_aH + H_2O_b \qquad (7)$$

leaves unchanged the single silanol density, because S_p is replaced by O_aH.

Indeed, the possible arrangements of silanols on a surface are quasi-infinite, even with the hypothesis of a cristobalite-like local structure of the network, and we do not claim to completely describe the surface with these sites. However, strongly H-bonded hydroxyls are not located on the silicon atoms ending one siloxane bridge, according to the structure HO–Si–O–Si–OH: the condensation of these hydroxyls into a two-fold ring would be unlikely at low temperature, in contrast with experiment. The H-bonded hydroxyls are rather bonded to silicon atoms that are brought close together through a siloxane chain [HO–(SiO–)$_4$Si–OH] and condense easily into unstrained (–SiO)$_5$ rings. For silica A, H-bonded hydroxyls are hereafter described as pairs involving geminal silanols of faces {100}, the extension of which is probably limited to steps. Other sites are involved in the larger clusters of H-bonded hydroxyls evidenced on samples G and P through thermal treatment.

Surface of a Fumed Silica. Several results obtained for silica A, as received and after some contact with air, can be rationalized in the following way. The low silanol surface density (about 3.65 OH per square nanometer, internal silanols excluded), the comparatively high fraction of geminal sites ($f_g = 0.21$), and the presence of a rather strong D_2 band in the Raman spectrum indicate an only *partial* and *selective* hydrolysis of the surface after the manufacturing of silica A at high temperature.

From silanol densities measured between 4.2 and 5.7 OH per square nanometer, Zhuravlev (39) found a mean value of 4.9 OH per square nanometer at 180–200 °C under vacuum for 100 samples of different, fully

hydroxylated, amorphous silicas. Thermogravimetry of silica A showed that the silanol density that must be compared to these values, in the same conditions, is about 3.3 OH per square nanometer. As received, silica A is thus not completely hydroxylated. Other results corroborate this conclusion: the D_2 Raman band decreases under a further exposure to water vapor (Figure 4, curve a'), and the methoxyl density of 4.9 per square nanometer observed after reaction with methanol at 460 °C is larger than the initial OH density (Table I).

According to the NMR study of Sindorf et al. (*7*), the f_g value measured for the initial silica A is comparatively high and suggests a preferential hydrolysis of sites that are precursors of geminal silanols. Conversely, the thermal treatment at 260 °C mainly condenses geminal silanols (*7*). Thus, the absorbance diminutions centered at 3500 and 3715 cm^{-1} and the augmentation at 3747 cm^{-1} mainly correspond to reaction 7, even though other contributions are not excluded, particularly contributions of aggregates larger than pairs. This assignment agrees with etherification by methanol leading to the structure $SiOH\cdots O_b(CH_3)SiO_aH$ on sample AC_1. It gives additional support to the structure $SiOH\cdots O_b(H)SiO_aH$ located at steps between planes {111}. Because the first hydration stage of silica A induces the decrease of two bands near 3715 and 3742 cm^{-1}, the most stable adsorption of water should take place at steps S_p–G_p, from which water clusters are growing toward the middle of faces {111}. The formation of water clusters has been shown (*22, 40*). This mechanism is in agreement with the kinetic of deuteration by D_2O (*41*) and with the hydration process previously described (*42*), provided each pair of so-called "vicinal single silanols" is changed into a site S_p–G_p, the silicon atoms of which are not vicinal, *vicinal* meaning bridged by an oxygen atom.

A further pretreatment of silica A at 460 °C eliminates weakly H-bonded groups (νOH ≈ 3620–3680 cm^{-1}). This variation is assigned not only to internal silanols (*26*), but also to silanols S_m (and perhaps S_e) with fn O–O distances around or smaller than 0.4 nm. The simultaneous enhancement of the Raman band D_2 supports the formation of three-fold rings on cristobalite faces {111}, as proposed by Brinker et al (*9*). However, the regular condensation model suggested by Brinker, which could be possible on α-cristobalite, is unlikely because the network rather resembles β-cristobalite at such a temperature. We suggest that $(-SiO-)_3$ rings are first made from triplets i-j-k of nearly equivalent hydroxyls on faces {111} (Figure 7), according to

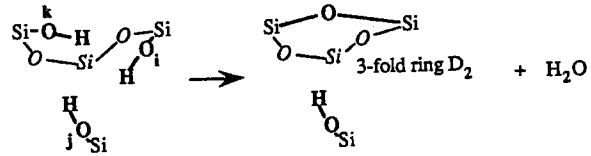

(8)

The following dehydroxylation stage, between 460 and 645 °C, can be interpreted by the condensation of about 0.3 OH per square nanometer absorbing around 3680 cm^{-1} (full width at half height (*fwhh*) ≈180 cm^{-1}), internal silanols excluded, and of nearly the same number with νOH ≈3736 cm^{-1} (*fwhh* ≈20 cm^{-1}) (*26*). Although not firmly proved, a condensation as pairs of weakly proton donor and acceptor hydroxyls is suggested:

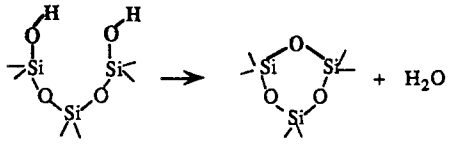

(9)

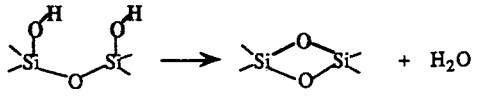

(10)

Reaction 10 would characterize vicinal silanols S_e. It is in agreement both with the Raman spectrum, because band D_2 is not enhanced, and with the infrared components simultaneously observed at 908 and 888 cm^{-1}. The resulting two-fold ring, which would be located at edges, is known to be very reactive (*3*).

A tentative assignment of the main features of the infrared spectrum of silica A is summarized as follows: 3500 cm^{-1}, mainly S_p; 3620 cm^{-1}, closest S_m in triplet sites i-j-k; 3670 cm^{-1}, internal silanols; 3680 cm^{-1}, weak proton donors S_m, S_e, and G_e in pairs; 3715 cm^{-1}, terminal G_p; 3736–3742 cm^{-1}, weakly perturbed G_p, S_m, S_e, and G_e; 3747 cm^{-1}, isolated S_m, S_e, and single silanols ex-G_p and ex-G_e. This assignment gives a possible explanation of the Raman components appearing at about 3685 and 3615 cm^{-1} by rehydroxylation of a silica gel pretreated at 600 °C (*14*).

Sites S_p–G_p achieve a somewhat concave step, accommodating what has been called inner silanols (*22*). The present assignment gives an improved picture of the surface and of the hydration mechanism of a fumed silica. However, the infrared spectrum is intricate, and its assignment is still partly speculative. Whereas the comparison of the infrared and Raman spectra supports the conclusion that the formation of three-fold rings is mainly due to the condensation of weakly perturbed silanols (that absorb above about 3600 cm^{-1}), the reciprocity is not warranted. For instance, the contribution of isolated silanols (νOH = 3750 cm^{-1}), postulated by Brinker et al (*16*), is excluded. In fact, a further analysis of both spectra will be necessary to know their relation to the various sites of a silica.

A rough picture of a fumed silica surface that comes out of the spectroscopic measurements on both initial and grafted silica A is

summarized in Table I. The hydroxyl and methoxyl populations refer to the sites of the initial silica. For instance, the 0.6 OMe per square nanometer located on ex-D_2 sites of sample AC_1 come from reaction 4. This evaluation is based on the assumption that only three-fold rings D_2, mainly precursor of S_m, are not hydroxylated. In fact, some five-fold rings, precursor of S_p–G_p, are not excluded, because the initial sample has been exposed only to low relative humidity. According to equation 5b given for sample AC_1 methoxylated at 460 °C, a completely hydroxylated silica A would accommodate 4.95 OH per square nanometer (3.65 OH per square nanometer + 0.65 siloxane bridge per square nanometer opened on the initial sample), with a fraction of geminal sites $f_g = 0.16$, internal silanols excluded. This evaluation is in agreement with the results of literature for equivalent samples (*7*, *39*), which suggests that steric hindrance at the steps S_p–G_p does not preclude species SiOMeO(Me)SiOMe. A density of about 1.95 OH per square nanometer, including the free O_aH group, would lie at these steps. This value is rather high: it corresponds, in the hypothesis corresponding to equation 5b in Table I, to 40% of the hydroxyls on the fully hydroxylated sample. Such steps are related to the fractal dimensions $D_s = 2.1 \pm 0.05$ in the framework of a fractal model of the surface (*27*). As for the surface reactivity, these sites are involved in intricate mechanisms, because they accommodate the strongest proton donor O_bH, although they show some steric hindrance.

Surface of a Gel or a Precipitated Silica. Samples G and P display a very large apparent silanol density (12–14 OH per square nanometer with Ar or N_2 specific surface area). Most of these hydroxyls can be deuterated and many are engaged in H-bonded aggregates larger than pairs. Thus, for these samples the sites S_p–G_p provide a minor part of the H-bonded silanols: the surface picture of silica A cannot be extensively applied. Without describing here detailed aggregation mechanisms of these samples, which is in progress (*34*), we focus on the site called the "hole of SiOH" earlier. Suppose that on a face {111} of β-cristobalite the missing SiOH is located on a "three-fold axis": the three neighboring O atoms, l-m-n in Figure 7, become a triplet of strongly H-bonded hydroxyls on account of their short distance. The first dehydroxylation stage could mainly condense triplets l-m-n of strongly H-bonded silanols according to

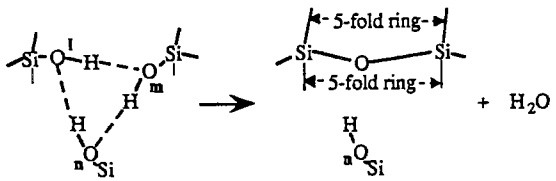

(11)

The new siloxane bridge is part of two five-fold siloxane rings and is not involved in the Raman band at 607 cm^{-1} that characterizes $(-SiO-)_3$. This model is consistent with the fact that the D_2 band only appears for a gel preheated above 200 °C and mainly around 600 °C (*14–16*). Such holes on gel or precipitated silicas add to the steps mentioned to define the roughness of the surface, which is modeled with higher fractal dimensions (D_s = 2.4–2.5) than for a fumed sample (*27*).

Unified Interpretation of the D_0–D_1 and D_2 Raman Bands of Disperse Silicas, Monolithic Gels, and Fused Silicas. There is an apparent discrepancy about the occurrence of these bands. On the one hand, the D_2 peak is maximum in a gel preheated at about 600 °C, whereas the Raman signal is strongly decreased in the range 480–500 cm^{-1} compared to the initial, hydroxylated state. Further heating decreases both signals to the typical intensities of *v*-silica (*15, 16*). On the other hand, these features are enhanced with the fictive temperature of *v*-silica. The hydroxyl content of *v*-silica has been reported (*10*) not to change the defect concentration, but only the dynamic of the structural relaxation. The opposite temperature dependences of the gel and *v*-silica Raman spectra obviously correspond to different mechanisms. However, the similarity of the spectral signatures suggests a similarity of the involved structures.

We assign the 490 cm^{-1} peak to the unstrained sites $(-SiO)_3SiO'$, where O′ is an oxygen atom fully bonded to only one silicon atom. The type of motion involved could be similar to that of the network, giving rise to the strong and broad Raman signal around 440 cm^{-1}, that is, O atom displacements bisecting the SiOSi angles. A particular configuration of such an anchored O_3SiO' tetrahedron about the network would determine a combination of these transverse oxygen displacements that induces a strong polarizability change (*43*). Thus, the 490-cm^{-1} band of a disperse silica would be assigned to some O_3SiO' tetrahedra bearing single silanols (structure D_0), as previously speculated (*18*). The population of the single silanol sites involved in band D_0 and that giving rise to structure D_2 probably are not fully coincident, even for a fumed sample. For instance, silanols S_p can contribute to D_0, whereas they condense with G_p into five-fold rings. Similarly, vicinal silanols S_e could condense into two-fold rings.

We postulate that in *v*-silica a relaxed O_3SiO' structure ensures the particular oxygen arrangement that generates the D_0 band and that D_0 can lead to three-fold rings giving rise to band D_2. This interpretation is supported by the tremendous augmentation of D_2 by neutron irradiation, whereas D_0 is not enhanced much by such irradiation (*12*). This fact suggests that D_0 is an intermediate species between the initial network and three-fold rings D_2. Similarly, D_2 is more favored than D_0 above 1300 °C (*10*). In a first stage, high temperature or neutron irradiation can induce a

relaxed bond $O_3SiO^-{}^+SiO_3$ in a highly strained region of the network. Because six-fold rings are dominant, the most likely mechanism is then

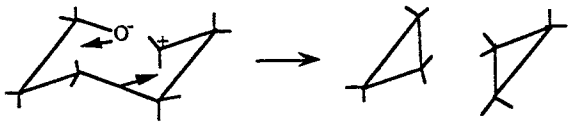

(12)

which gives two three-fold rings from one relaxed bond. This reaction is catalyzed by OH groups because a proton can attack a strained siloxane bridge and, upon completion of reaction 12, it becomes available to diffuse toward another strained site. According to the experimental results of reference 10, the standard enthalpy for reaction 12 is 1.3 eV. The main objection to this interpretation for v-silica is that the band $\nu SiO'$ is not observed in the range 950–1050 cm^{-1} (*12*). A possible explanation is that the scattering activity of pure SiO stretching modes is very weak in the silica network because of a polarizability compensation in the SiO'Si structure (*44*). This effect is not involved when a SiO^- group lies in front of a counterion, for instance, in mixtures of SiO_2 and Na_2O (*43*). Only a weak signal around 850 cm^{-1} can be related to the increase of D_1 in Figure 3 of reference 10. This band could correspond to the breathing mode $\nu_s O_3(SiO')$ previously shown in disperse silicas (*45*).

Acknowledgments

We gratefully acknowledge B. Morrow for helpful discussions and financial help from CNRS (Action de Recherche Coordonnée: "Hydroxyles Superficiels des Silices, Alumines, et Silico-Aluminates").

References

1. McDonald, R. S. *J. Phys. Chem.* **1958**, *62*, 1168.
2. Hair, M. L. In *Vibrational Spectroscopies for Adsorbed Species*; Bell, A. T.; Hair, M. L., Eds.; ACS Symposium Series 137; American Chemical Society: Washington, DC, 1980; pp 1–11.
3. Morrow, B. A.; Cody, I. A.; Lee, L. S. M. *J. Phys. Chem.* **1976**, *80*, 2761.
4. Davydov, V. Ya.; Zhuravlev, L. T.; Kiselev, A. V. *Russ. J. Phys. Chem.* **1964**, *38*, 1108.
5. Hino, M.; Sato, T. *Bull. Chem. Soc. Jpn.* **1971**, *44*, 33.
6. Boccuzzi, F.; Coluccia, S.; Ghiotti, G.; Morterra, C.; Zecchina, A. *J. Phys. Chem.* **1978**, *82*, 1298.
7. Sindorf, D. W.; Maciel, G. E. *J. Am. Chem. Soc.* **1983**, *105*, 1487.
8. Brinker, C. J.; Kirkpatrick, R. J.; Tallant, D. R.; Bunker, B. C.; Montez, B. *J. Non-Cryst. Solids* **1988**, *99*, 418.
9. Brinker, C. J.; Brow, R. K.; Tallant, D. R.; Kirkpatrick, R. J. *J. Non-Cryst. Solids* **1990**, *120*, 26.
10. Galeener, F. L. *J. Non-Cryst. Solids* **1985**, *71*, 373.

11. Stolen, R. H.; Krause, J. T.; Kurkjian, C. R. *Discuss. Faraday Soc.* **1970,** *50,* 103.
12. Bates, J. B.; Hendricks, R. W.; Shaffer, L. B. *J. Chem. Phys.* **1974,** *61,* 4163.
13. Galeener, F. L. *Solid State Commun.* **1982,** *44,* 1037.
14. Gottardi, V.; Guglielmi, M.; Bertoluzza, A.; Fagnano, C.; Morelli, M. A. *J. Non-Cryst. Solids* **1984,** *63,* 71.
15. Bertoluzza, A.; Fagnano, C.; Morelli, M. A.; Gottardi, V.; Guglielmi, M. *J. Non-Cryst. Solids* **1986,** *82,* 127.
16. Brinker, C. J.; Tallant, D. R.; Roth, E. P.; Ashley, C. S. *J. Non-Cryst. Solids* **1986,** *82,* 117.
17. Krol, D. M.; Van Lierop, J. C. *J. Non-Cryst. Solids* **1984,** *68,* 163.
18. Mulder, C. A. M.; Damen, A. A. J. M. *J. Non-Cryst. Solids* **1987,** *93,* 387.
19. Lippert, J. L.; Melpolder, S. B.; Kelts, L. M. *J. Non-Cryst. Solids* **1988,** *104,* 139.
20. Hoffmann, P.; Knözinger, E. *Surf. Sci.* **1987,** *188,* 181.
21. Yamauchi, H.; Kondo, S. *Colloid Polym. Sci.* **1988,** *266,* 855.
22. Burneau, A.; Barrès, O.; Gallas, J. P.; Lavalley, J. C. *Langmuir* **1990,** *6,* 1364.
23. Zhdanov, S. P.; Kosheleva, L. S.; Titova, T. I. *Langmuir* **1987,** *3,* 960.
24. Baumgarten, E.; Wagner, R.; Lentes-Wagner, C. *Fresenius Z. Anal. Chem.* **1989,** *335,* 375.
25. Burneau, A.; Barrès, O.; Vidal, A.; Balard, H.; Ligner, G.; Papirer, E. *Langmuir* **1990,** *6,* 1389.
26. Gallas, J. P.; Lavalley, J. C.; Burneau, A.; Barrès, O. *Langmuir* **1991,** *7,* 1235.
27. Legrand, A. P.; Hommel, H.; Tuel, A.; Vidal, A.; Balard, H.; Papirer, E.; Levitz, P.; Czernichowski, M.; Erre, R.; Van Damme, H.; Gallas, J. P.; Hemidy, J. F.; Lavalley, J. C.; Barrès, O.; Burneau, A.; Grillet, Y. *Adv. Colloid Interface Sci.* **1990,** *33* (2–4), 91–330.
28. Zaborski, M.; Vidal, A.; Ligner, G.; Balard, H.; Papirer, E.; Burneau, A. *Langmuir* **1989,** *5,* 447.
29. Fripiat, J. J. In *Soluble Silicate*; Falcone, J. S., Jr., Ed.; ACS Symposium Series 194; American Chemical Society: Washington, DC, 1982; p 165.
30. Young, G. J. *J. Colloid Sci.* **1958,** *13,* 67.
31. Hockey, J. A. *Chem. Ind. (London)* **1965,** p 57.
32. Yates, D. E.; Healy, T. W. *J. Colloid Interface Sci.* **1976,** *55,* 9.
33. Himmel, B.; Gerber, Th.; Bürger, H. *J. Non-Cryst. Solids* **1987,** *91,* 122.
34. Humbert, B. Thesis, Université de Nancy I, Nancy, 1991; Burneau, A.; Humbert, B. *Colloids and Surfaces,* in press.
35. Peri, J. B.; Hensley, A. L., Jr. *J. Phys. Chem.* **1968,** *72,* 2926.
36. Humbert, B.; Burneau, A.; Gallas, J. P.; Lavalley, J. C. *J. Non-Cryst. Solids* **1992,** *143,* 75.
37. Vasconcelos, W. L.; De Hoff, R. T.; Hench, L. L. *J. Non-Cryst. Solids* **1990,** *121,* 124.
38. Wyckoff, R. W. G. *Crystal Structures,* 2nd ed.; Interscience: New York, 1963; Vol. 1, pp 312–319.
39. Zhuravlev, L. T. *Langmuir* **1987,** *3,* 316.
40. Klier, K.; Shen, J. H.; Zettlemoyer, A. C. *J. Phys. Chem.* **1973,** *77,* 1458.
41. Van Roosmalen, A. J.; Mol, J. C. *J. Phys. Chem.* **1978,** *82,* 2748.
42. Van Roosmalen, A. J.; Mol, J. C. *J. Phys. Chem.* **1979,** *83,* 2485.
43. Furukawa, T.; Fox, K. E.; White, W. B. *J. Chem. Phys.* **1981,** *75,* 3226.
44. Stolen, R. H.; Walrafen, G. E. *J. Chem. Phys.* **1976,** *64,* 2623.
45. Burneau, A.; Barrès, O.; Gallas, J. P.; Lavalley, J. C. *Proceedings of the International Workshop on FTIR Spectroscopy*; Vansant, E. F.; Department of Chemistry, University of Antwerp, Belgium, 1990; p 108.

RECEIVED for review July 31, 1991. ACCEPTED revised manuscript December 3, 1991.

11

Surveying the Silica Gel Surface with Excited States

R. Krasnansky[1] and J. K. Thomas[2]

Department of Chemistry and Biochemistry, University of Notre Dame, Notre Dame, IN 46556

Time-resolved and steady-state fluorescence probing was used to study gas–solid and liquid–solid silica gel interfaces. The molecular surveying probes pyrene, 1-aminopyrene, pyrenecarboxylic acid, and 9,10-diphenylanthracene adsorbed at the silica gel surface give information about probe environment, mobility, and accessibility. Reactions of surface-bound arene singlet excited states with molecular oxygen were monitored over a range of temperatures; the reactions were assigned to a unique Langmuir–Hinshelwood mechanism. The kinetics reflect the details of oxygen adsorption and movement on the silica gel surface.

SURFACES ARE OF INTEREST BECAUSE OF their media-thickening tendency (*1*), chromatographic separation ability (*2*), and catalytic activity (*3*). Although surfaces have been long exploited, understanding the nature of surfaces has not always kept pace. Key questions about surface phenomena revolve around the understanding of the chemical environment present at, the mobility found on, and the molecular accessibility allowed at a surface.

Answers to the key questions about surface phenomena have been obtained by use of luminescence probing techniques. In general, a lumophore is isolated at an interface. On the basis of steady-state and time-resolved spectral properties of the lumophore in neat solution or in simple organized media (*4*), the energy, spectral shape, and time-resolved decay

[1]Current address: Rohm and Haas Company, Research Laboratories, 727 Norristown Road, Spring House, PA 19454
[2]Corresponding author

0065–2393/94/0234–0223$08.36/0

profile of a probe's emission are interpreted to address the key questions of local environment, mobility, and accessibility. Specific modifications of the lumophore probe impinge unique discriminating abilities on the probe. By virtue of their photophysical properties, pyrene and anthracene derivatives have gained a significant place among luminescence probes.

Because of its surface functionality, thermal stability, and at times porous intraparticle structure, silica gel presents an attractive surface for photophysical and photochemical study. This chapter deals with both surface functionality identification and with molecular mobility and reactivity occurring at the silica gel surface.

Pyrene has a nonallowed $0 \rightarrow 0$ transition (ground state to excited state) that is markedly medium-dependent. Media effects are readily monitored through pyrene's fluorescence vibrational structure (5). The compounds 1-aminopyrene (1-AP) and 1-pyrenecarboxylic acid (PCA) each possess two chromophores that interact in the excited state; the extent of the interaction depends on the media. The lone pair of the amine chromophore of 1-AP acts as an internal switch for photophysics. Previous work (6) showed that the photophysical behavior of 1-AP is dominated by protonation, or "blocking", of the lone pair (Figure 1). Protonation of the amino group leads to a complex, 1-APH$^+$, that exhibits photophysical properties similar to those of pyrene; the free 1-AP system exhibits different photophysics. In similar work (7), the photophysical properties of PCA have been correlated to its acid–base properties and media effects. The compounds 1-AP and PCA have been used to distinguish the relative population of geminal and nongeminal silanol functionality at the silica gel surface.

The nonporous silica gel Cab-O-Sil is a convenient system to study molecular geometry during the fluorescence quenching of ^{1}arenes* by oxygen at the gas–solid interface without the complication of partitioning

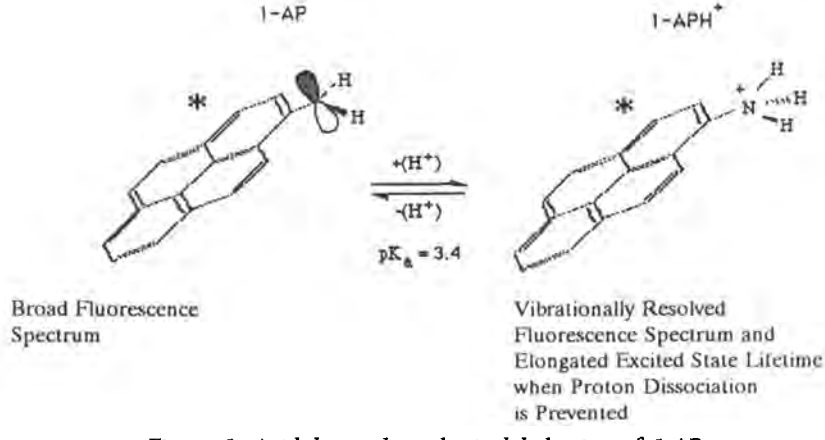

Figure 1. Acid–base photophysical behavior of 1-AP.

the probe between an external and an internal porous surface. When quenching molecules are present in both the gaseous and the adsorbed states, either a Langmuir–Rideal (*8*) reaction between a gas-phase molecule and a surface-bound molecule or a Langmuir–Hinshelwood (*9*) reaction between two surface-bound molecules may occur.

The fluorophores incorporated for the oxygen-quenching study were pyrene, monitoring the $^1B_{3u} \rightarrow {}^1A_{1g}$ transition (*10*), and 9,10-diphenylanthracene (DPA), monitoring the $^1B_{2u} \rightarrow {}^1A_{1g}$ transition (*10*, *11*). The adsorption of fluorophores onto the Cab-O-Sil surface is not homogeneous, but rather can be characterized by a distribution of adsorption sites; each adsorption site presents a microenvironment that is reflected by the unimolecular decay rate of a fluorophore residing at the site. The distribution of fluorophore unimolecular decays is modeled by a Gaussian distribution in natural logarithmic space about a mean unimolecular decay rate. The observable excited-state decay rate in the presence of quencher also has a Gaussian distribution. The oxygen quenching of surface-bound excited-state fluorophore is considered predominantly Langmuir–Hinshelwood.

Experimental Details

Instrumentation. Steady-state fluorescence spectra were obtained on an SLM–Aminco SPF-500 spectrofluorometer equipped with an LX300 UV illuminator, a 1200-grooves per millimeter grating, and a Hamamatsu R 928P photomultiplier tube in conjunction with a Zenith Z-368 computer. A neutral density filter, optical density 1.0, was placed in the excitation line to prevent photodecomposition of surface-bound fluorophore.

Time-resolved fluorescence decay profiles were obtained with a PRA Nitromite nitrogen flow laser, model LN-100, with a 0.12-ns full width at half-maximum, 70-μJ, 337.1-nm pulse. Emitted light was collected at 90° to the excitation line; a Kopp 4-96 band-pass filter removed collected scattered light. The monitoring wavelength, λ_{ob}, was selected with a Bausch and Lomb 33-86-02 monochromator equipped with a 1350-grooves per millimeter grating and detected by a Hamamatsu R-1644 microchannel plate with a response time of 0.2 ns. The signal was digitized via a Tektronix 7912HB programmable digitizer equipped with a 7B10 time base and either a 7A16A amplifier (response time 1.6 ns) or a 7A23 amplifier (response time 0.7 ns). Decay profile simulations were performed on a Zenith Z-368 computer by a nonlinear least-squares fitting method.

Sample Preparation. Samples were prepared by exposing the silica gel, previously dried at 150 °C for 24 h, to either cyclohexane or pentane solutions containing selected amounts of the fluorophore. The solvent was carefully removed under vacuum when required. Complete probe adsorption of liquid–solid samples was verified with absorption spectroscopy. Less than 0.07% of the silica surface was typically covered by the probe. Immediately before data collection, dry samples were evacuated under vacuum at 125–130 °C for 30 min. The total dehydration procedure was sufficient to remove the physisorbed water while leaving the surface silanol functionality intact (*12*). Selected amounts of oxygen were introduced into a

constant-position sample call by a series of stopcock manipulations and a vacuum line. Liquid–solid samples were deoxygenated ($[O_2]_{final} < 10^{-6}$ M) by bubbling the samples with solvent-saturated nitrogen for 30 min.

Various temperatures were achieved by incorporation of a quartz Dewar flask and a stream of chilled nitrogen gas. Nitrogen was cooled by passing the gas through a coiled copper tube submerged in liquid nitrogen. The sample temperature was monitored via a thermocouple attached to the sample cell wall and varied by regulating the nitrogen gas flow. Exterior Dewar fogging was prevented with a second, room-temperature stream of nitrogen.

Oxygen adsorption isotherms were obtained with a differential pressure analysis apparatus. The apparatus consisted of equal-volume spheres connected by a meter-high U-tube, filled halfway with distilled and degassed dimethylpolysiloxane, and a series of three-way stopcocks. Each sphere possessed a cell port equipped with a two-way stopcock. The total volumes were calibrated such that the volume of the left sphere equalled that of the right. A sample of known weight was placed in one of the cells, and the whole system was evacuated. With the two-way stopcocks closed, the system was equilibrated with a given amount of oxygen; the left and the right spheres were then isolated, and the two-way stopcocks were opened. The sample and the empty reference cells were equivalently submerged into various chilling baths. The amount of gas adsorbed was determined from the difference in the heights of the dimethylpolysiloxane columns and a calibration curve. The bulk pressure was measured with a Hastings vacuum gauge equipped with a DV-300 Raydist gauge tube.

HS-5 Cab-O-Sil having a Brunauer–Emmett–Teller surface area (S_{BET}) of 325 ± 25 m^2/g, an accessible pyrene surface area (S_{pyrene}) of 348 ± 40 m^2/g, and a particle diameter of 0.008 mm was donated by the Cabot Corporation. Mathenson Coleman and Bell silica gel (MCB) possesses an S_{BET} of 672 ± 70 m^2/g, an S_{pyrene} of 250 ± 50 m^2/g, and a mesh of 28–200. Each silica has a silanol concentration of 4.9 ± 0.9 silanols per square nanometer (*13*). Pyrene was purchased from Aldrich and passed three times down an activated silica gel–cyclohexane column. A sample of 1-aminopyrene (97%) was purchased from Aldrich, recrystallized from ethanol, and passed down an activated silica gel–benzene column. The 9,10-diphenylanthracene (99%), high-performance liquid chromatography grade cyclohexane, and gold label pentane were used as received from Aldrich. Oxygen was used as received from Mittler. Dimethylpolysiloxane was purchased from Sigma. A vacuum of 10^{-4} torr (10^{-2} Pa) was achieved with a Duo-seal model 1400 vacuum pump.

Results and Discussion

Photophysics of Pyrene on Various Silica Gel Surfaces. Pyrene gives information about its environment via changes in its fluorescence fine structure (*14*). Typically, five vibronic bands are identified; the ratio of the III band at 392 nm to the I band at 372 nm, the III/I ratio, increases in noninteracting (nonpolar) media with a concomitant increase in fluorescence lifetime (*15*). The versatility of the pyrene probe arises from the "forbiddenness" of the $S_0 \rightarrow S_1$ transition; any intensity for the transition comes from vibronic coupling with higher excited states (*10*). Interactive or polar solvents, via their interaction with the arene, increase the intensity of the $0 \rightarrow 0$ transition in both the absorption and the emission.

This increase in intensity is reflected in the increase in peak I with respect to the change in peak III. Pyrene adsorbed on a silica gel surface exhibits a typical III/I ratio of 0.58 (*15*). This value is between the values observed for pyrene in water and in methanol and reflects the interaction of the arene probe with the surface silanol functionality of the silica gel surface. Similar data are obtained on solid Al_2O_3.

Photophysics of 1-Aminopyrene on Various Silica Gel Surfaces. Figure 2 presents the fluorescence spectra of 1-AP adsorbed on MCB and FS-662 silica gel in cyclohexane. The fluorescence spectrum of MCB-bound 1-AP is quite typical of 1-APH^+, whereas the fluorescence spectrum of FS-662-bound 1-AP is quite typical of 1-AP. The surface-bound 1-APH^{+*} decays with an inherent unimolecular lifetime of 135 ± 2 ns, and the surface-bound 1-AP^* decays with an inherent unimolecular lifetime of 4.9 ± 0.1 ns. The different photophysical behavior of the 1-AP indicates that the adsorption sites for 1-AP are different on these silica gel samples at the given probe loadings.

Moderate heat treatment of the MCB silica gel at 450 °C for 24 h, a temperature below the sintering temperature, alters the surface such that the fluorescence spectra of 1-AP adsorbed on this surface have characteristics of both 1-AP and 1-APH^+; a heating temperature of 650 °C yielded an adsorbed 1-AP spectrum identical to that of 1-AP adsorbed on FS-662. A several-hour concentrated nitric acid treatment of the FS-662 silica, followed by washing with water until the wash maintained a neutral pH and drying, alters the surface such that the fluorescence spectrum of 1-AP adsorbed to this surface resembles that obtained from the MCB surface.

The thermal (*16*) and the chemical (*17*) treatments of the silica gels alter the degree of clustering of the silanol functionality on the silica surface. The available surface silanol functionality is shown in Figure 3. Hair et al. (*17, 18*) showed that the geminal silanol configuration gives rise to an adsorption site that, when occupied by aniline, yields a protonated adsorbed form of aniline; a similar correlation would account for the observed photophysical behavior of 1-AP on the silica gel surfaces. Milosavljevic and Thomas (*7*) used PCA to probe the microacidity of the silanol functionality. Scheme I shows the photophysics of PCA. In particular, the observed fluorescence decay rate constant was diagnostic for the determination of the apparent pH of the microenvironment. MCB-bound PCA demonstrated a neutral form, singly protonated carboxylic acid group fluorescence, whereas FS-662-bound PCA demonstrated a mixed anionic–neutral fluorescence. The observed fluorescence decay rate constants of 1.9×10^8 s^{-1} and 3.8×10^7 s^{-1} correspond to an apparent pH of 1.6 and 4.1 for the microenvironments of the geminal and nongeminal silanols, respectively.

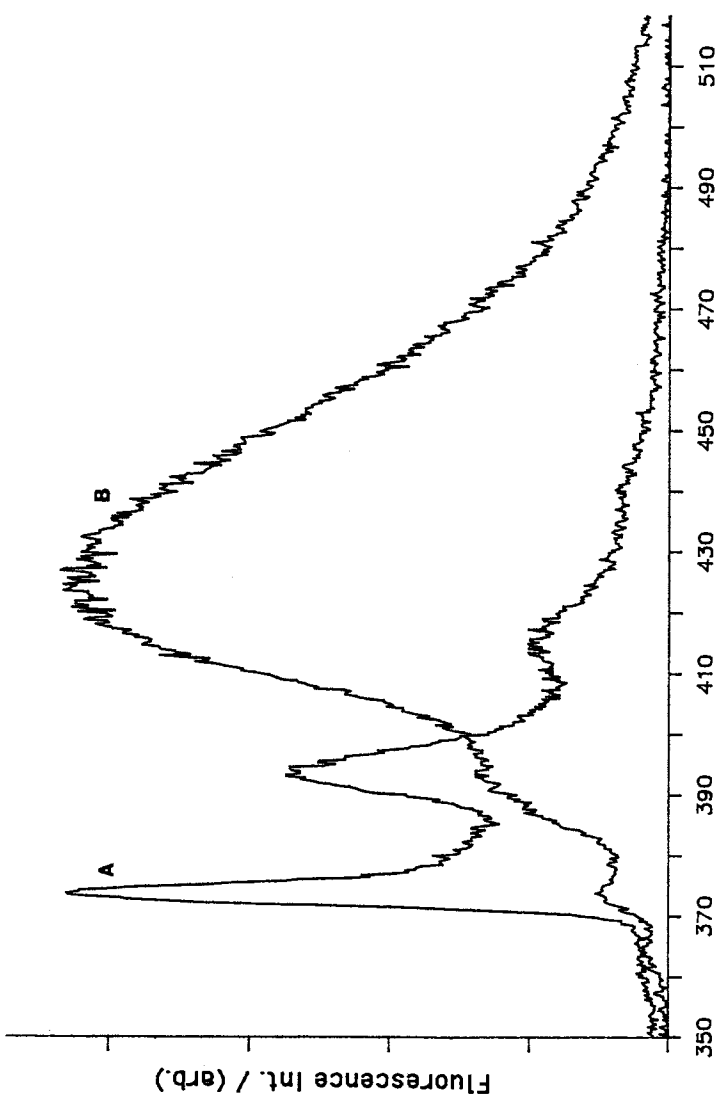

Figure 2. Fluorescence spectra: 1.9×10^{-7} mol/g 1-AP on (A) MCB and (B) FS-662 silica gel in deoxygenated cyclohexane at an excitation wavelength (λ_{ex}) of 337 nm.

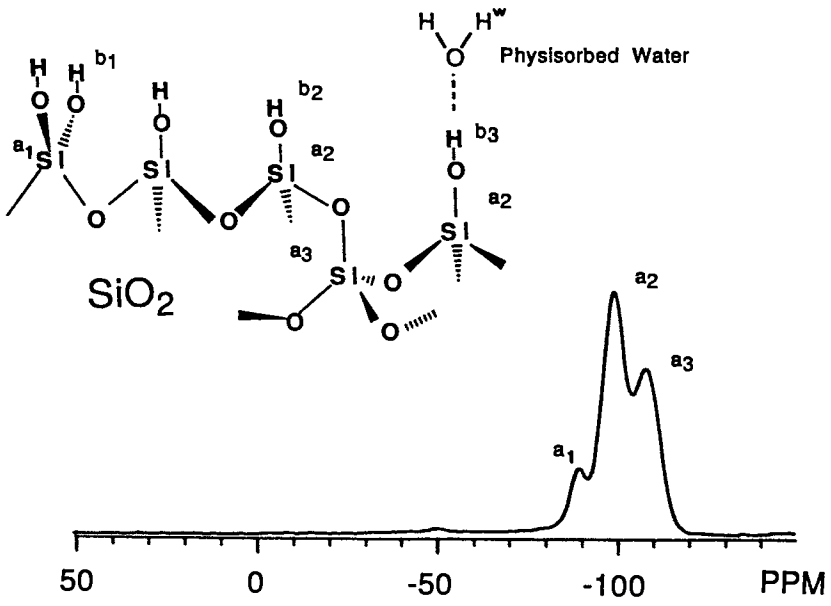

Figure 3. An 11.88-MHz ^{29}Si CP MAS NMR spectrum of MCB silica gel evacuated at 100 °C with a pictorial view of the silica gel surface.

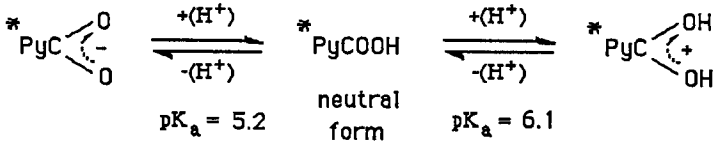

Scheme I. Acid–base photophysical behavior of PCA.

The ^{29}Si NMR (*19*) cross-polarization magic-angle spinning (CP MAS) and ^{1}H NMR magic-angle spinning with multiple-pulsed line narrowing (CRAMPS for combined rotation and multiple-pulse spectroscopy) techniques of Maciel et al. (*20, 21*) indicate that FS-662 silica gel has 9% of its silanol functionality in the geminal configuration. Figure 3 presents the ^{29}CP MAS NMR spectrum of the MCB silica gel. The percentage of MCB surface silanol functionality in the geminal configuration was determined to be 23%. Figure 4 presents the ^{1}H CRAMPS NMR spectra of the MCB silica gel sample dried under vacuum at both 100 and 500 °C as well as signal deconvolution. The deconvolution clearly shows the resolution of a fourth set of transitions that are present with the MCB silica at 396.6 Hz but not with FS-662. The 396.6-Hz ^{1}H transition is interpreted as originating from the geminal silanol configuration. The geminal configura-

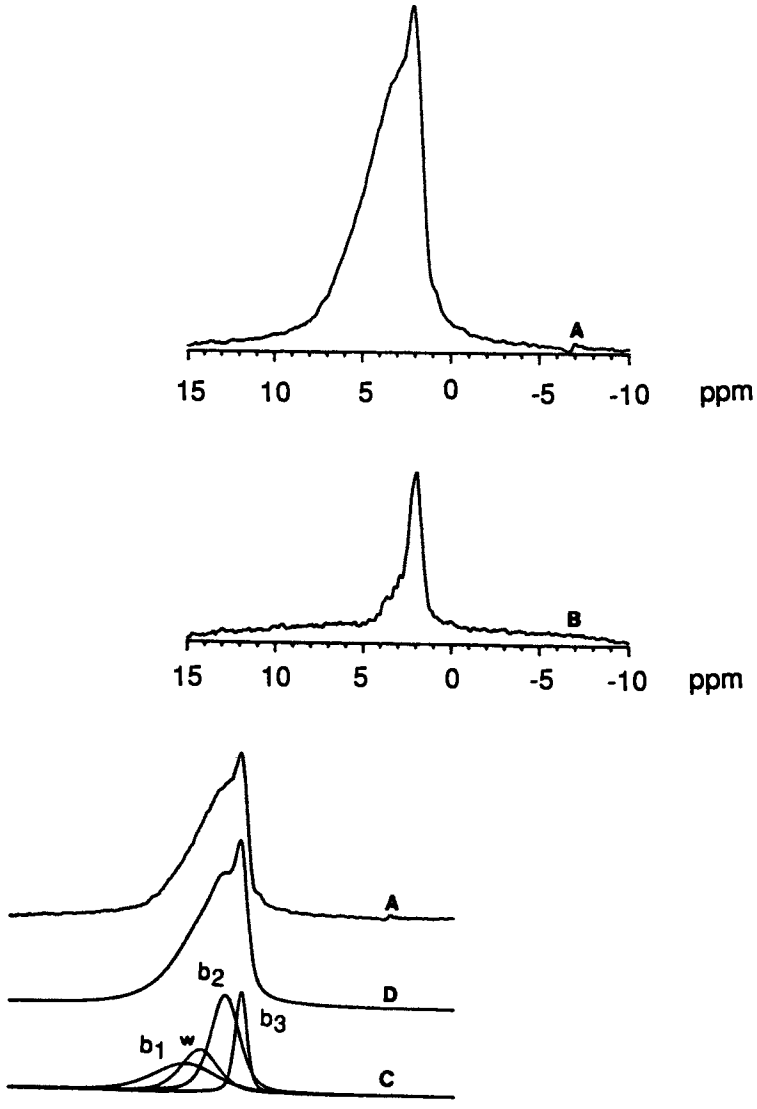

Figure 4. 187-MHz ^1H CRAMPS spectra of MCB silica gel (A) evacuated at 100 °C and (B) evacuated at 500 °C. Plot C is a deconvolution of spectrum A, and plot D is a computer simulation based on C.

tion is completely removed, and the hydrogen-bonded vicinal configuration is partially removed, by heating of the MCB silica at 500 °C. The redistribution of surface silanol functionality as observed by NMR spectroscopy supports the redistribution observed by photophysical probing technique. The ^1H CRAMPS NMR analysis of the MCB silica gel yields a

surface silanol functionality distribution of 30% geminal, 48% vicinal, and 22% isolated.

The higher acidity geminal silanol configuration is seen to mandate the photophysical behavior of 1-AP. Increasing the surface 1-AP concentration progressively increases the contribution of the neutral form to the fluorescence spectrum of MCB-bound 1-AP. The redistribution of spectral character equates to a titration of the geminal configuration. The percentage of silanols that exist in the geminal configuration is

$$\%\text{geminal} = 100\left(\frac{2[\text{1-AP}]_{\text{titration}}N(1 \times 10^{-18})}{S_{\text{probe}}[\text{silanol}_{\text{total}}]_{\text{surface}}}\right) \quad (1)$$

where S_{probe} is the probe-accessible surface area in square meters per gram, $[\text{1-AP}]_{\text{titration}}$ is the titration point in moles per gram, N is Avogadro's number, and the surface silanol concentration ($[\text{silanol}_{\text{total}}]_{\text{surface}}$) is taken as 4.9 silanols per square nanometer; the factor 2 accounts for two silanols constituting each geminal configuration. Deconvolution of the room-temperature fluorescence spectra at various probe loadings and use of equation 1 initially indicated that only 0.1% of the MCB silanols were in the geminal configuration, a conclusion in disagreement with the NMR spectroscopy study. As in solution, dropping the temperature increases the proportion of the fluorescence spectrum attributable to the 1-APH^{+*} species (Figure 5). The temperature redistribution of the fluorescence spectrum indicates that a deprotonation of the 1-APH^{+*} state competes with fluorescence of 1-APH^{+*}. The deprotonation accounts for the dramatic undercounting of geminal configurations. The deprotonation is apparently frozen out at 77 K; unfortunately, the high 1-AP loading required to reach the true titration point introduces self-absorption problems to the fluorescence study. The absorption process, however, occurs on a time scale at which deprotonation does not occur. Figure 6 presents the ratio of observed protonated form to neutral form of 1-AP on FS-662 as a function of probe loading and as monitored by deconvolution of the absorption spectra. Figure 6 and equation 1 indicate that 3% of the FS-662 silanol configurations are geminal, a result in agreement with the NMR spectroscopy study. The lower counting of the absorption technique reflects the blocking of a proportion of the silanol functionality by the pyrene.

Gaussian Distribution Model. As reported earlier (22), neither pyrene nor DPA fluorophore yields monoexponential unimolecular decays once adsorbed onto the silica gel surface. The low surface coverage and the absence of pyrene excimers indicate that the surface probe exists as an isolated species. Previously, deviations from the first-order decay kinetics

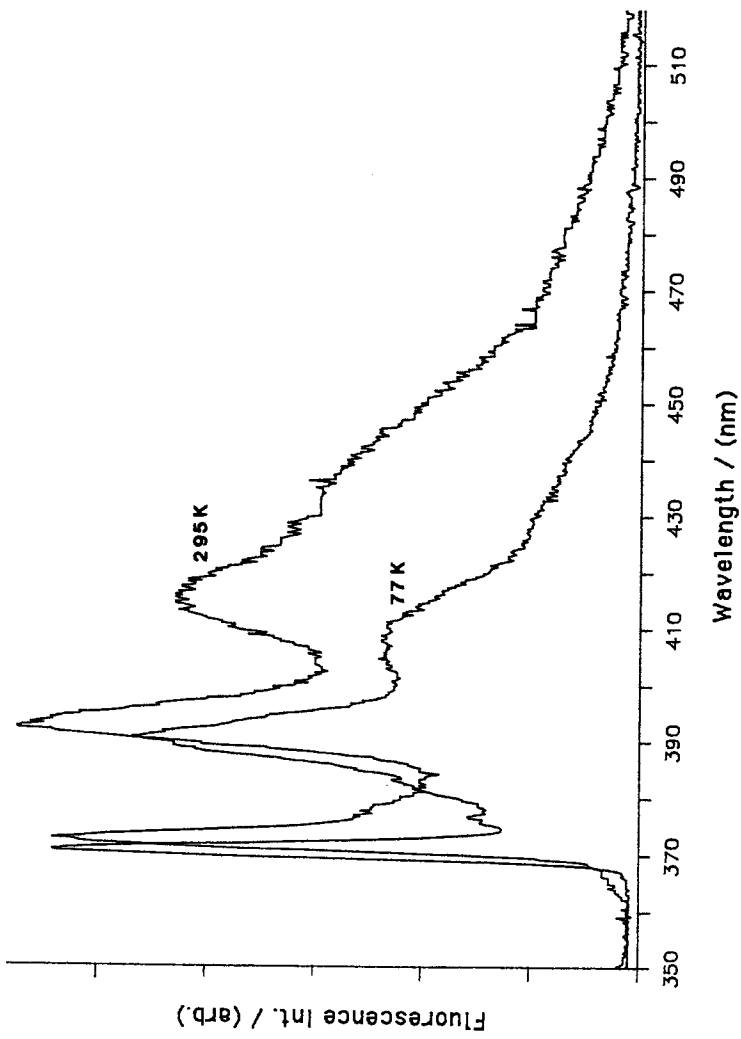

Figure 5. Fluorescence spectra: 9.82 × 10⁻⁷ mol/g 1-AP on dry MCB silica gel under vacuum; excitation wavelength was 337 nm at 295 and 77 K.

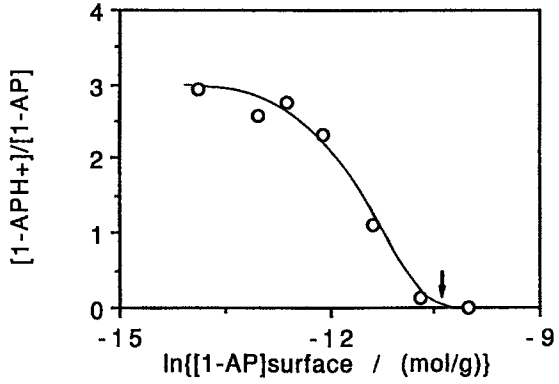

Figure 6. Plot [1-APH+]/[1-AP] versus ln [1-AP], for 1-AP adsorbed on FS-662 silica gel in deoxygenated cyclohexane monitored by deconvolution of absorption spectra.

were treated by invoking a multiexponential model (23). The biexponential luminescence decay function is

$$I(t) = I(0)\{A \exp(-k_1 t) + [1\text{-AP}] \exp(-k_2 t)\} \quad (2)$$

where $I(0)$ is the initial fluorescence intensity and $I(t)$ is the fluorescence intensity at time t. The physical interpretation of the given biexponential model mandates that the probe molecule is partitioned by a percent factor A between two uniquely identifiable environments characterized by the rate constants k_1 and k_2. The biexponential model is weakened by its intrinsic assumption of two possible environments. Each additional exponential term added to the model also brings an additional partitioning factor. Because, in the absence of two chemically unique adsorption sites, true representation of multiple adsorption sites on a surface would require the summation of each adsorption site, the number of variables in the decay assimilation quickly increases to the point where an interpretation of those values becomes questionable. Albery et al. (24) approached the problem of mathematically assimilating heterogeneous systems by expanding the work of Scott et al. (25) and laid the foundation for the development of the Gaussian distribution model. Heterogeneous systems can be characterized through a mean rate constant, $\bar{k}$, and a distribution parameter, γ. The dispersion in the first-order rate constants for $-\infty \leq x \leq \infty$ becomes

$$\ln k = \ln \bar{k} + \gamma x \quad (3)$$

The observed decay profile is composed of the summation of the contributions from each microscopic species. Integration over the distribution $\exp(-x^2)$, when the fluorescence intensity is proportional to the probe's excited state concentration, yields

$$\frac{I(t)}{I(0)} = \frac{\int_{-\infty}^{\infty} \exp(-x^2) \exp[-\bar{k}t \exp(\gamma x)]\, dx}{\int_{-\infty}^{\infty} \exp(-x^2)\, dx} \tag{4}$$

where

$$\int_{-\infty}^{\infty} \exp(-x^2)\, dx = \sqrt{\pi}$$

and x is the integration range. After transformation of the variable, $x = \ln(\lambda)$ for $x < 0$ and $x = -\ln(\lambda)$ for $x > 0$, the integration of the numerator of equation 4 can be carried out by using the extended Simpson's rule (26); division of this integration by the denominator yields equation 5:

$$\frac{I(t)}{I(0)} = \frac{1}{\sqrt{\pi}} \int_0^1 g(\lambda)\, d\lambda$$

$$g(\lambda) = \lambda^{-1} \exp\{-[\ln\lambda]^2\} \{\exp(-\bar{k}\, t\, \lambda^{\gamma}) + \exp(-\bar{k}\, t\, \lambda^{-\gamma})\}$$

$$\frac{I(t)}{I(0)} = \frac{0.2}{3\sqrt{\pi}} \{ 2[g(0.1) + g(0.3) + g(0.5) + g(0.7) + g(0.9)] + g(0.2) + g(0.4) + g(0.6) + g(0.8) + \exp(-\bar{k}\, t) \} \tag{5}$$

A representation of the Gaussian model is shown in Figure 7.

The Gaussian model was found to describe the photophysical behavior of both pyrene and 9,10-diphenylanthracene adsorbed on silica gel well. The physical interpretation of the Gaussian model in these systems would be that each probe experiences slightly different geometric perturbations due to surface irregularities on the scale of the probe's cross-sectional area or various surface-bound strengths. The Gaussian model permits the removal of the constraint of a very limited number of types of adsorption sites found in the biexponential model and leaves only two variable parameters, $\bar{k}_{obs}$ and γ, in the mathematical simulation of the decay profile.

Bimolecular quenching reactions of excited states are typically represented by the pseudo-first-order reaction kinetics, equation 6a. When a distribution of probe environments exists, the difference between the macroscopic fluorescence decay profile observed and microscopic fluores-

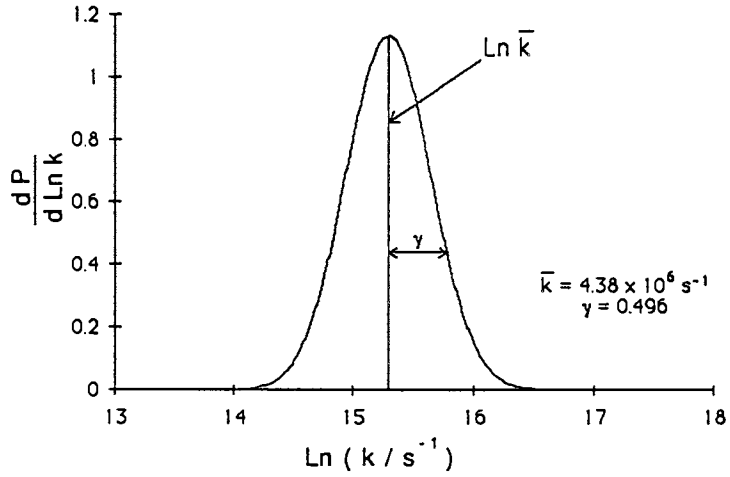

Figure 7. Representation of the Gaussian distribution model.

cence decay rates present must be recognized. The composite distribution of both unimolecular decay rates and the respective bimolecular reaction rates are combined in the distribution of observable decay rates. Hence, the parameters in equation 6a have to be redefined in the Gaussian distribution terminology to yield equation 6b.

$$k_{obs} = k_0 + k_q \text{ [quencher]} \tag{6a}$$

$$\bar{k}_{obs} = \bar{k}_0 + k'_q \text{ [quencher]} \tag{6b}$$

Whereas the observed decay profile no longer is characterized by a single decay rate, the steady-state fluorescence intensity becomes dependent on both γ_{obs} and $\bar{k}_{obs}$. The typical Stern–Volmer plot is no longer represented by equation 7a, but rather by equation 7b, where $\bar{k}_{obs}$ is defined by equation 6b, k'_q is the bimolecular quenching rate constant, $\bar{k}_0$ is the probe's mean excited-state unimolecular decay rate constant, $\bar{k}_{obs}$ is the mean observed decay rate constant, γ_0 is the distribution parameter of the Gaussian for the unimolecular decay, and γ_{obs} is the distribution parameter for the observed unimolecular decay rate.

$$\frac{I_0}{I} = 1 + \frac{k_q}{k_0} \text{ [quencher]} \tag{7a}$$

$$\frac{I_0}{I} = \exp\left(\frac{\gamma_0^2 - \gamma_{obs}^2}{4}\right) \frac{\bar{k}_{obs}}{\bar{k}_0} \tag{7b}$$

Reference 27 formally addresses the mathematical derivations associated with the Gaussian distribution model as applicable to luminescence probing.

Oxygen Quenching of Singlet Excited States of Pyrene and DPA (27). Because of the dramatic difference in unimolecular decay rates of pyrene and DPA, a large concentration range of oxygen could be examined and compared. Steady-state and time-resolved oxygen-quenching studies were performed at various temperatures and correlated as a function of bulk gaseous oxygen concentration. Oxygen pressures were converted to concentration units through the ideal gas equation to account for density changes at the various temperatures.

The temperature dependence on the steady-state quenching is typified by DPA (Figure 8). There was a dramatic increase in the degree of quenching at a given concentration of oxygen with a decrease in temperature when oxygen gas-phase concentrations were used as the independent variable.

The Gaussian distribution model was applied to the decay profiles at various concentrations of oxygen. Time-resolved fluorescence decay

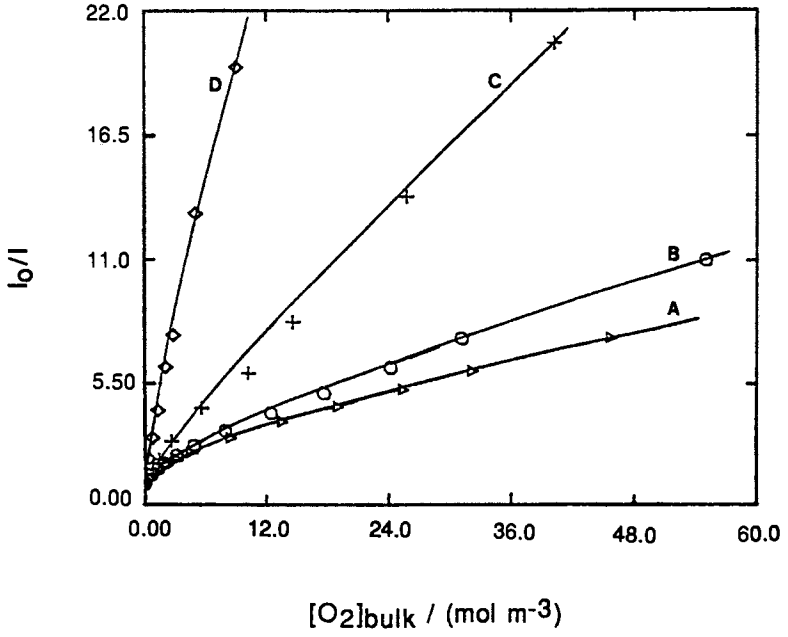

Figure 8. Steady-state oxygen quenching of 7.76 × 10⁻⁷ mol/g DPA on Cab-O-Sil (λ_{ex} = 365 nm and λ_{ob} = 390–520 nm) at (A) 23, (B) −27, (C) −50, and (D) −90 °C.

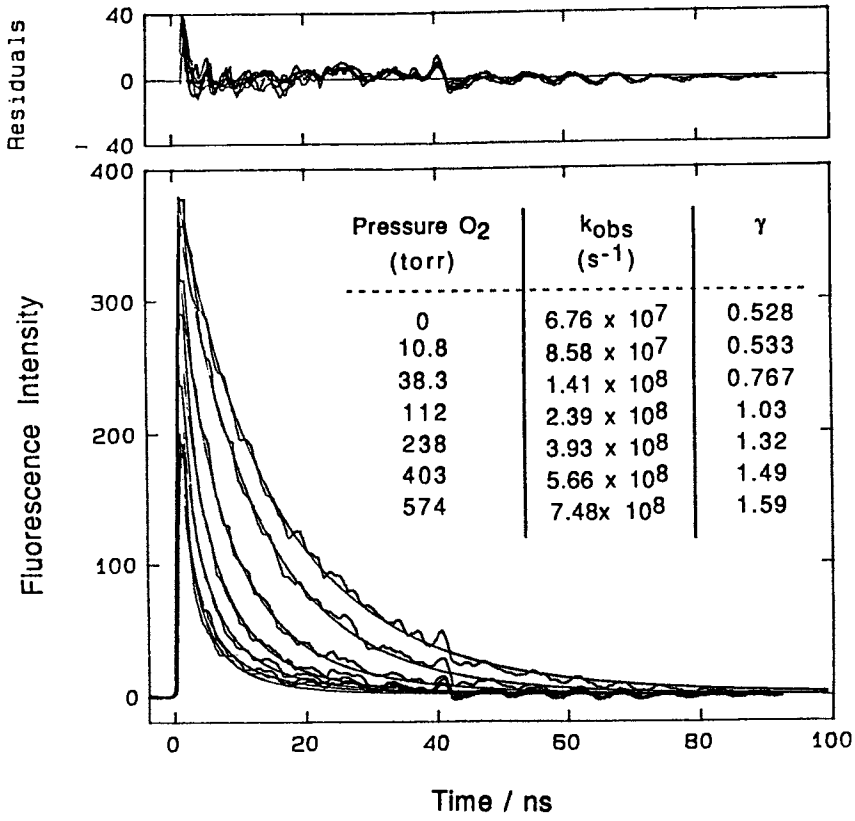

Figure 9. Transient fluorescence decay profile of 4.76 × 10^{-7} mol/g DPA on Cab-O-Sil, with Gaussian model simulated decay profiles at 18 °C and various pressures of oxygen (λ_{ex} = 337 nm and λ_{ob} = 430 nm).

profiles for the oxygen quenching of the DPA–Cab-O-Sil system are shown in Figure 9. Initial intensities of the fluorescence decay profiles are fixed at the value obtained in the absence of quencher to indicate that the quenching is dynamic in nature; short time intervals in the decay profiles are lost in the response time of the system. When the quenching is plotted in terms of bulk gaseous oxygen concentrations, as would be appropriate for a Langmuir–Rideal scheme, there is an increase in quenching efficiency with a decrease in temperature (Figure 10). Simulation of the fluorescence decay becomes difficult at high degrees of fluorophore quenching because an uncertainty in initial fluorescence intensity arises from an instantaneous component that enters the quenching scheme.

Recently, Turro and co-workers (*28*) derived the expressions for the bimolecular rate constant for a Langmuir–Rideal type quenching scheme both for a smooth surface, equation 8a, and for a porous solid in the

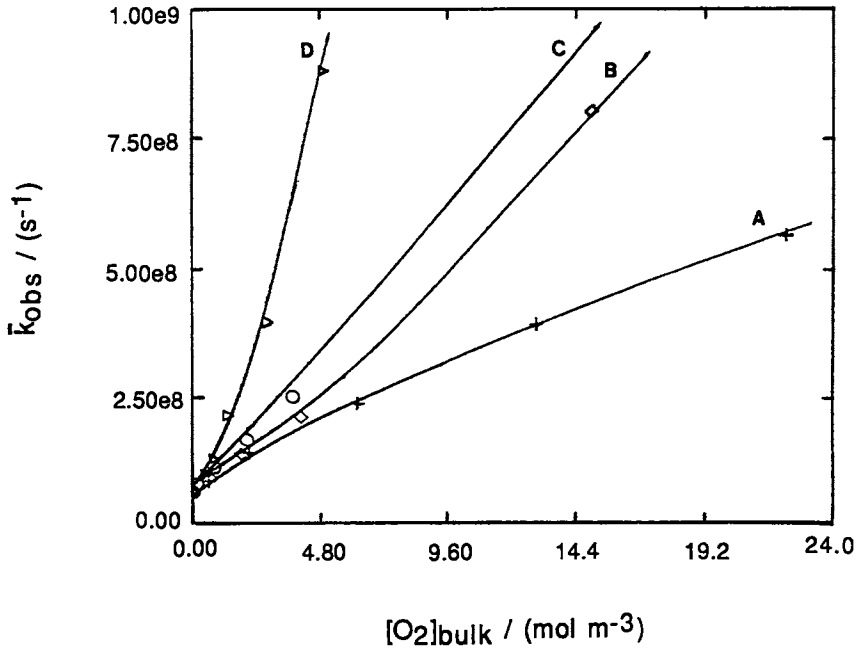

Figure 10. Time-resolved oxygen quenching in 4.76 × 10^{-7} mol/g DPA (λ_{ex} = 337 nm and λ_{ob} = 430 nm) showing the response of $\bar{k}_{obs}$ to bulk gaseous oxygen concentration at (A) 18, (B) −28, (C) −50, and (D) −83 °C.

Knudsen regime, where the pore diameter is much less than the gas-phase mean free path, equation 8b.

$$-\frac{d[\text{probe}^*]}{dt} = \frac{1}{4}\frac{\alpha < v > \sigma_{\text{probe}}}{kT} P_q [\text{probe}^*] + \frac{[\text{probe}^*]}{\tau_0} \tag{8a}$$

$$-\frac{d[\text{probe}^*]}{dt} = \frac{4}{6}\frac{\pi \alpha r_{ab} g R_p < v >}{kT} P_q [\text{probe}^*] + \frac{[\text{probe}^*]}{\tau_0} \tag{8b}$$

where

$$< v > = \left(\frac{8 k T}{\pi m_w}\right)^{1/2}$$

α is the efficiency of the bombardment reaction, σ_{probe} is the cross-sectional area of the probe, r_{ab} is the interaction radius for the reactants, g is a geometric factor ($g > 0$), R_p is the pore radius, τ_0 is the lifetime of the probe in the absence of quencher, P_q is the bulk gaseous quenching pressure, m_w is the molecular mass in kilograms per molecule of the gas, T

is the absolute temperature, and k is the Boltzmann constant. Converting pressures to concentration units through the ideal gas law and substituting for the mean velocity $<v>$ gives equations 9a and 9b (R is the ideal gas constant) from equations 8a and 8b, respectively.

$$k_q = R\,\sigma\,\alpha\,(2\,\pi\,m_w\,k)^{-1/2}\,\sqrt{T} \tag{9a}$$

$$k_q = \frac{4}{3}\,R\,R_p\,r_{ab}\,\alpha\left(\frac{2\,\pi}{m_w\,k}\right)^{1/2}\sqrt{T} \tag{9b}$$

Equations 9a and 9b show that a gas-phase bombardment quenching mechanism predicts that the quenching efficiency will increase with the square root of temperature; both probe systems show decreasing oxygen quenching efficiencies with increasing temperatures.

Oxygen Adsorption Isotherms. Oxygen adsorption isotherms on the Cab-O-Sil surface at various temperatures up to −47 °C were measured. The isotherms obtained followed Langmuir adsorption at the temperatures examined. Theoretical treatment of the oxygen adsorption isotherm data (27) yields a heat of adsorption of 3.54 kcal/mol (14.8 kJ/mol) and the assimilation times of 23.2, 44.1, 99.5, and 238 ps at −47, −64, −80, and −98 °C, respectively.

Langmuir–Hinshelwood Approach to Oxygen Quenching. Surface oxygen concentrations for the various gaseous bulk oxygen concentrations were determined with the adsorption isotherm parameters. From a steady-state point of view, the amount of oxygen adsorbed on the silica surface in the range where quenching occurs is quite low; at ambient temperatures, the surface quencher concentration even approaches the surface probe concentration. The amount of time a given oxygen resides on the surface is also quite short. Such short assimilation times would not be expected to yield the observed dynamic quenching if the oxygen initially present on the surface at the moment of probe excitation was completely responsible for the quenching of the probe's excited state. The probe's excited-state lifetime is immensely greater than the assimilation time of the oxygen. The number of times an adsorbed oxygen is replaced, at some other arbitrary surface location, by an oxygen from the gas phase is great during the lifetime of the probe. The random placement of oxygen on the surface would be crucial in describing the apparent surface migration distance incurred during the lifetime of the probe's excited state. A large surface oxygen exchange rate also upholds pseudo-first-order conditions.

Figure 11 shows that the observed decay rate constants of both DPA and pyrene vary linearly with surface oxygen concentration when surface oxygen concentration is used as the independent variable. The bimolecular

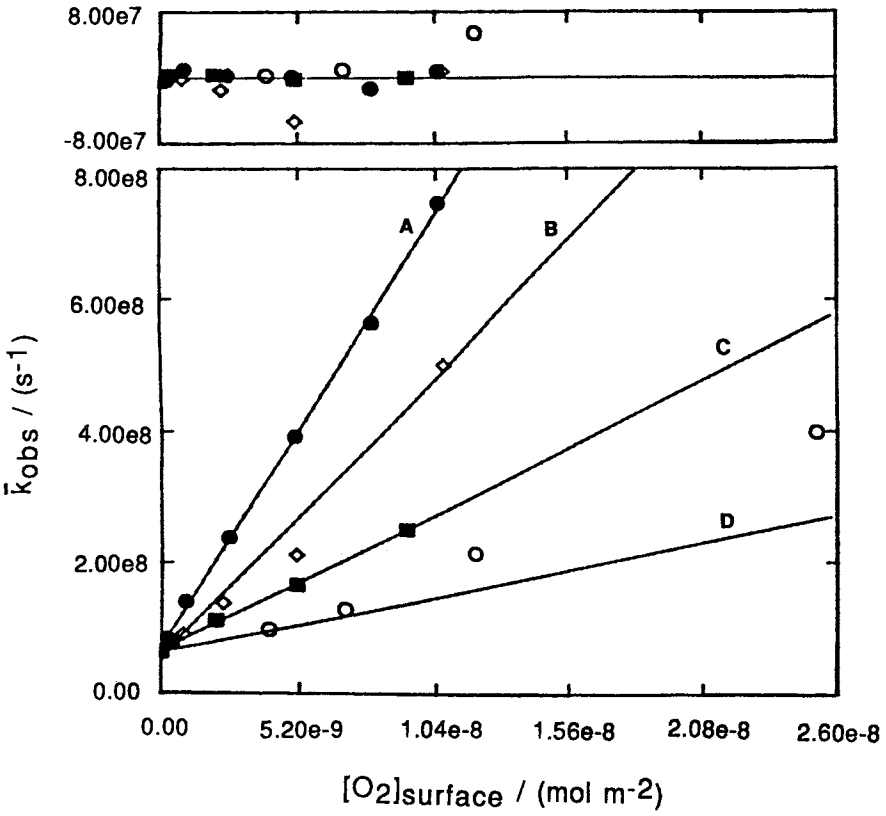

Figure 11. Time-resolved oxygen quenching ($\lambda_{ex} = 337$ nm) with a Gaussian fit of 4.76×10^{-7} mol/g DPA ($\lambda_{ob} = 430$ nm) at (A) 18, (B) −28, (C) −50, and (D) −83 °C.

quenching rate constants obtained from the slopes of these plots decrease with a decrease in temperature, as would be expected for a Langmuir–Hinshelwood mechanism. Under higher probe surface coverage conditions, it has been shown through the formation of static, as opposed to dynamic, excimers of pyrene on the silica gel surface that the fluorophore does not migrate on the time scale of the excited state (29); all motion, therefore, arises from the motion of the oxygen. An Arrhenius treatment of the observed quenching rate constants yields activation energies for the bimolecular Langmuir–Hinshelwood type quenching reaction of 3.31 and 2.31 kcal/mol (13.8 and 9.67 kJ/mol) for the pyrene–Cab-O-Sil/oxygen and the DPA–Cab-O-Sil/oxygen systems, respectively. A representation of the dynamics of the oxygen quenching is presented in Figure 12.

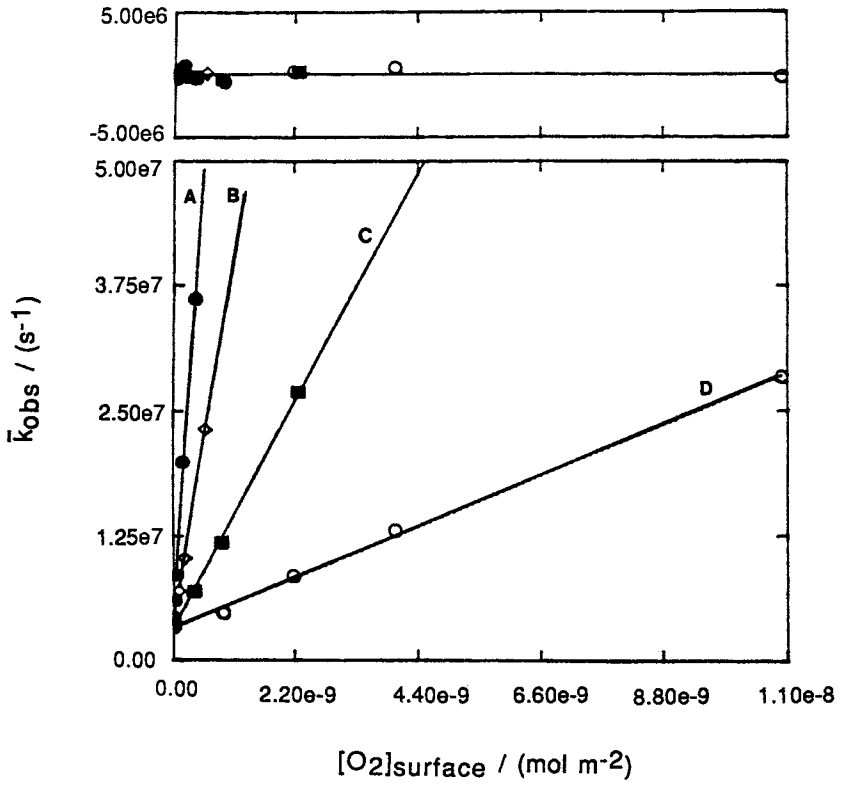

Figure 11.—Continued. Time-resolved oxygen quenching with Gaussian fit of 4.74×10^{-7} mol/g pyrene (λ_{ob} = 397 nm) at (A) 19, (B) −26, (C) −66, and (D) −92 °C on Cab-O-Sil.

The silica surface plays a role in the quenching scheme analogous to the solvent cage in solution. The interaction time of the probe and quencher is increased, and excess translational, vibrational, and rotational energy of the oxygen is dissipated by the adsorption process. The adsorption process, thus, increases the quenching probability.

Conclusions

Luminescence probing techniques have demonstrated their versatility in characterizing the environment found on, the mobility and accessibility allowed at, and the reactivity occurring at gas–solid and liquid–solid interfaces. Pyrene can be used to monitor the interactive nature of the silica surface, and 1-AP and PCA faithfully distinguish the silanol functionality present at the silica gel surface. MCB silica gel possesses a higher relative geminal silanol concentration compared to the FS-662 silica gel;

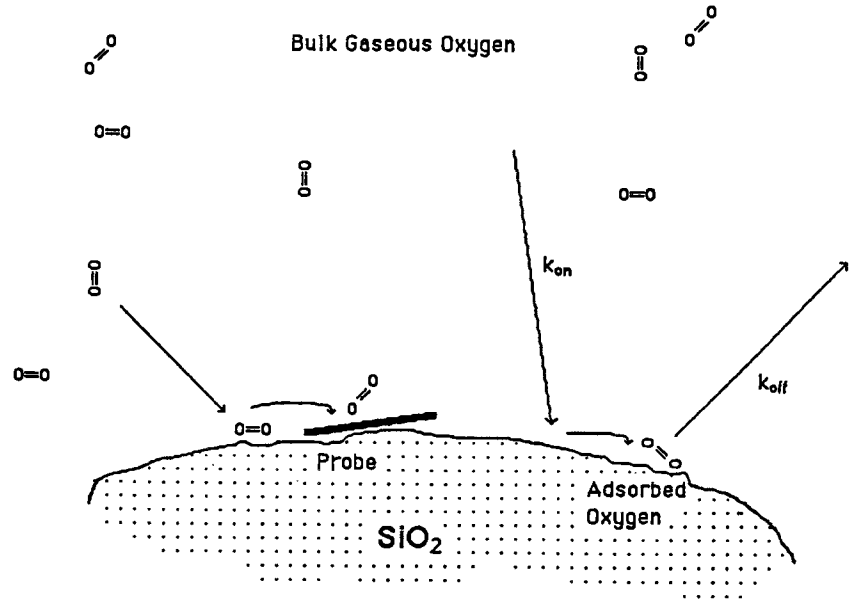

Figure 12. Oxygen quenching of Cab-O-Sil bound fluorophore.

this greater concentration gives rise to strong hydrogen bonding to the weak 1-AP base. Protonation of the amine's lone pair stops the mixing of the bichromophoric excited states and causes photophysical behavior typical of an isolated, or more correctly an inertly substituted, pyrene moiety.

The heterogeneous adsorption and the bimolecular quenching of the Cab-O-Sil bound pyrene and DPA by molecular oxygen were computer-simulated with a Gaussian distribution model. The bimolecular quenching rate constants followed the opposite trend with temperature when the gas-phase concentrations of oxygen were used as the independent variable as mandated by a Langmuir–Rideal mechanism. The bimolecular quenching rate constant followed the expected trend with temperature when surface concentrations of oxygen were used as the independent variable as mandated by a Langmuir–Hinshelwood mechanism. The quenching observed could not be accounted for by the oxygen present on the surface at the time of excitation; the exchange of surface-bound oxygens with oxygens from the bulk gas reservoir during the lifetime of the excited state had to be recognized. We assign the predominant quenching of the singlet excited states of pyrene and DPA located on the Cab-O-Sil surface by oxygen to a modified Langmuir–Hinshelwood scenario.

Acknowledgments

We are grateful to the NSF (Grant CHE–8911906) and the EPA for financial support of this work and to the Cabot Corporation for donation of Cab-O-Sil. We thank Bratoljub H. Milosavljevic from the Boris Kidrich Institute for Nuclear Science in Belgrade, Yugoslavia, and Kasuhide Koike from the National Research Institute for Pollution and Resources in Onogawa, Tsukuba, Japan, for their stimulating discussions. Finally, we thank the Colorado State University NMR facility for acquiring the NMR spectra.

References

1. Wightman, J. D.; Chessick, J. J. *J. Phys. Chem.* **1962,** *13,* 1217. Sirianni, A. F.; Meadus, F. W.; Puddington, I. E. *Can. J. Chem.* **1964,** *42(12),* 2916.
2. Kirkland, J. J. *Anal. Chem.* **1965,** *37,* 1458. Kirkland, J. J. *Chromatogr. Sci.* **1969,** *7,* 7. Kirkland, J. J. *Chromatogr. Sci.* **1972,** *10,* 593. Nikitin, Y. S. *Anal. Chem.* **1964,** *36(8),* 1526. Kirkland, J. J. *Chromatogr. Sci.* **1970,** *49,* 84.
3. Stiles, A. B. *Catalyst Supports and Supported Catalyst, Theoretical and Applied Concepts*; Butterworths: Boston, MA, 1987.
4. Organized media is defined as a chemical system that possesses a certain degree of self-assembly.
5. Thomas, J. K. *The Chemistry of Excitation and Interfaces*; ACS Monograph Series 181; American Chemical Society: Washington, DC, 1984.
6. Hite, P.; Krasnansky, R.; Thomas, J. K. *J. Phys. Chem.* **1986,** *90,* 5795.
7. Milosavljevic, B. H.; Thomas, J. K. *J. Phys. Chem.* **1988,** *92,* 2997.
8. Rideal, E. K. *Proc. Cambridge Philos. Soc.* **1939,** *35,* 130.
9. Hinshelwood, C. N. *Kinetics of Chemical Changes*; Clarendoni: Oxford, England, 1940; p 187.
10. Pariser, R. *J. Chem. Phys.* **1955,** *24(2),* 250.
11. Birks, J. B. *Photophysics of Aromatic Molecules*; Wiley-Interscience: New York, 1970; p 71.
12. Iler, R. K. *The Chemistry of Silica Gel: Solubility, Polymerization, Colloid and Surface Properties, and Biochemistry*; Wiley: New York, 1979; p 630. Sindorf, D. W.; Maciel, G. E. *J. Am. Chem. Soc.* **1983,** *105,* 1487.
13. Zhuravlev, L. T. *Langmuir* **1987,** *3,* 316.
14. Kalyanasundaram, K.; Thomas, J. K. *J. Am. Chem. Soc.* **1977,** *99,* 2039.
15. Thomas, J. K. *J. Phys. Chem.* **1987,** *94,* 553; Beck, G.; Thomas, J. K. *Chem. Phys. Chem.* **1985,** *94,* 553; Bauer, R. K.; de Mayo, P.; Okada, K.; Ware, W. R.; Wu, K. C. *J. Phys. Chem.* **1983,** *87,* 460. Bauer, R. K.; de Mayo, P.; Natarajan, L. V.; Ware, W. R. *Can. J. Chem.* **1984,** *62,* 1279.
16. Young, G. T. *J. Colloid Sci.* **1958,** *13,* 67.
17. Anderson, J. H.; Lambard, J.; Hair, M. L. *J. Colloid Interface Sci.* **1975,** *50(3),* 519. de Mayo, P. *Pure Appl. Chem.* **1982,** *54(9),* 1623. Iler, R. K. *The Chemistry of Silica*; Wiley: New York, 1979; pp 109–211.
18. Hair, M. L.; Hertle, W. J. *J. Phys. Chem.* **1969,** *73,* 4269.
19. Sindorf, D. W.; Maciel, G. E. *J. Am. Chem. Soc.* **1983,** *105,* 1487.
20. Bronnimann, C. E.; Zeigler, R. C.; Maciel, G. E. *J. Am. Chem. Soc.* **1988,** *110(7),* 2023.
21. Sindorf, D. W.; Maciel, G. E. *J. Phys. Chem.* **1982,** *86,* 5208.

22. Bauer, R. K.; de Mayo, P.; Okada, K.; Ware, W. R.; Wu, K. C. *J. Phys. Chem.* **1983,** *87,* 460.
23. Lochmuller, C. H.; Colborn, A. S.; Hunnicatt, M. L.; Harris, J. M. *J. Am. Chem. Soc.* **1984,** *106,* 4077.
24. Albery, W. J.; Bartlett, P. N.; Wilde, C. P.; Darwent, J. R. *J. Am. Chem. Soc.* **1985,** *107,* 1854.
25. Scott, K. F. *J. Chem. Soc. Faraday Trans. I* **1980,** *76,* 2065.
26. Riddle, D. F. *Calculus and Analytic Geometry,* 3rd ed.; Wadsworth Publishing: Belmont, CA, 1979; p 219.
27. Krasnansky, R.; Koike, K.; Thomas, J. K. *J. Phys. Chem.* **1990,** *94,* 4521.
28. Drake, J. M.; Levitz, P.; Turro, N. J.; Nitsche, K. S.; Cassidy, K. F. *J. Phys. Chem.* **1988,** *92,* 4680.
29. Hara, K.; de Mayo, P.; Ware, W. R.; Weedon, A. C.; Wong, G. S. K.; Wu, K. C. *Chem. Phys. Lett.* **1980,** *69(1),* 105. Krasnansky, R., Ph.D. Thesis, University of Notre Dame, 1990.

RECEIVED for review October 3, 1990. ACCEPTED revised manuscript January 31, 1992.

12

Surface Chemistry and Surface Energy of Silicas

Alain M. Vidal and Eugène Papirer

Centre de Recherches sur la Physico-Chimie des Surfaces Solides, Centre National de la Recherche Scientifique, Mulhouse, France

The establishment of relationships between the surface chemistry and the surface free energy of silicas is important for practical applications of these materials. Inverse gas chromatography, either at infinite dilution or finite concentration, appears to be an effective method for the detection of changes of surface properties induced by chemical or thermal treatments. Silicas of various origins (amorphous or crystalline) with surface chemistries modified by chemical (esterification) or heat treatment were compared. The consequences of these modifications on surface energetic heterogeneities were assessed.

SILICA EXISTS IN A BROAD VARIETY OF FORMS, in spite of its simple chemical formula. This diversity is particularly true for divided silicas, each form of which is characterized by a particular structure (crystalline or amorphous) and specific physicochemical surface properties. The variety results in a broad set of applications, such as chromatography, dehydration, polymer reinforcement, gelification of liquids, thermal isolation, liquid-crystal posting, fluidification of powders, and catalysts. The properties of these materials can of course be expected to be related to their surface chemistry and hence to their surface free energy and energetic homogeneity as well. This chapter examines the evolution of these different characteristics as a function not only of the nature of the silica (i.e., amorphous or crystalline), but also as a function of its mode of synthesis; their evolution upon modification of the surface chemistry of the solids by chemical or heat treatment is also followed.

0065–2393/94/0234–0245$08.00/0

Only two kinds of functional groups can be found on silica surfaces: siloxane bridges and hydroxyls (silanols). However, among the hydroxyls, different types can be identified, namely single free silanols, geminal hydroxyls, hydroxyl pairs associated through hydrogen bonding (either vicinal or brought together, for example, at points of contact between particles or in micropores), inner hydroxyl groups, and adsorbed water (*1–3*).

Various methods, either chemical (*4–8*) or physical (*9–15*), can be used for the determination of these surface groups, and their number and type can be easily modified by chemical (e.g., esterification upon reaction with alcohols) or heat treatment. However, for heat treatment, as shown by Fripiat (*16*), the modification of the surface chemical properties is much more complex than would be expected when only considering the curves relating weight loss to temperature. Thus it should be of interest to relate the evolution of surface silanol groups to the surface free energy of silica samples.

The surface free energy of a solid (γ_s) can be expressed as a sum of two components: γ_s^d (the dispersive component), describing London-type interactions, and γ_s^{sp} (the specific component), including all other interactions (H-bonding, polar, and so forth).

$$\gamma_s = \gamma_s^d + \gamma_s^{sp}$$

Two methods can be used for the assessment of the γ_s of divided solids: contact-angle measurements and adsorption processes. The drawbacks of the contact-angle measurements are associated with surface roughness of the samples. As for the adsorption process, determination of the components of the surface free energy of the solid is based on interpretation of adsorption isotherms, either complete (calculation from spreading pressures) or only from the first linear part of the isotherm. In this respect, inverse gas chromatography (IGC), which appears to be the technique of choice (*17*), was extensively used in this study.

Experimental Details

Materials. Eight silicas from different synthesis processes were studied:

1. Five amorphous silicas:
   - A, a fumed silica, Aerosil 200 (Degussa, 200 m^2/g)
   - P, a precipitated silica, Zeosil 175 MP (Rhône-Poulenc, 175 m^2/g)
   - G, a gel of silica, RP1 (Rhône-Poulenc, 230 m^2/g)
   - C, a colloidal silica, FDR (Rhône-Poulenc, 10 m^2/g)
   - F, a fibrillar silica (*18*), FATM 220/1 (180 m^2/g)

2. Three crystalline silicas:
   - L_1, synthetic (*19*) H_2SiO_5 (84 m^2/g)
   - L_2, synthetic H-Magadiite (48 m^2/g)
   - L_3, synthetic H-Kenyaite (18 m^2/g)

A and F were high-purity silicas. All samples but A were slightly porous.

Alcohol-Modified Silicas. The silicas were modified by reaction with alcohols, either methanol (C_1) or hexadecanol (C_{16}), according to a method previously described (*8*). Degree of esterification was determined by elemental analysis, microgravimetry (weight loss associated with the pyrolysis of modified silicas), or radiochemistry (use of ^{14}C-labeled alcohols). The corresponding modified silicas were identified as XC_1 and XC_{16}.

Inverse Gas Chromatography and Heat Treatment of Silicas. Silica particles of adequate size (0.25–0.5 mm in diameter) obtained by compression and sieving were used to fill chromatographic columns (stainless steel, 30 cm long, 3 mm in diameter) connected to a gas chromatograph fitted with a flame ionization detector. Helium was used as carrier gas at a flow rate of 20 cm^3/min [the flow rate conditions were selected so as to have the best efficiency for the chromatographic columns (obtained at the minimum of the Van Deemter curve)]. Measurements were made at a column temperature of 60 °C. Thermal treatment of silica was done under helium flow by heating the column to the desired temperature. After being heated for 30 min, the column was cooled to the analysis temperature. With alkane probes, symmetrical retention peaks were observed. For polar probes, skewed peaks were usually recorded; for such peaks an integrator was used to determine the peak first-order moment. Calculation of γ_s^d and specific interaction parameters from chromatographic data were described elsewhere (*20*) and are only briefly described here.

When minute amounts of solute are adsorbed, the adsorption process can be described by the initial part of the adsorption isotherm, which is practically linear. Under these conditions Henry's law applies. It is then possible to relate the thermodynamic parameters of adsorption, such as the variation in free energy upon adsorption of the solute at zero coverage ($\Delta G°$), to the retention volume of the probe (V_N):

$$\Delta G° = -RT \ln (C' V_N)$$

where R is the gas constant, T is the temperature, and C' is a constant depending on the reference state for the adsorbed molecule.

It is known from earlier studies that $\Delta G°$ varies linearly with the number of carbon atoms of a homologous alkane series. It is thus possible from the preceding equation to calculate the adsorption free energy increment associated with one CH_2 group:

$$\Delta G_{(CH_2)} = -RT \ln [V_{N(n)} / V_{N(n+1)}]$$

where $V_{N(n)}$ and $V_{N(n+1)}$ are the retention volumes of n-alkanes with n and $n + 1$ carbon atoms, respectively. The quantity $\Delta G_{(CH_2)}$ can provide an estimation of the dispersive interactions between one CH_2 group and an adsorbent and is related to the γ_s^d of the solid by

$$\Delta G_{(CH_2)} = 6.023 \times 10^{23} \times a_{(CH_2)} \times 2[\gamma_s{}^d \gamma_{(CH_2)}]^{1/2}$$

where $a_{(CH_2)}$ is the surface area of a CH_2 group (0.06 nm^2) and $\gamma_{(CH_2)}$ is the surface tension of a surface made of CH_2 groups only, for example, polyethylene (35.6 mJ/m^2 at 20 °C). For interactions of polar probes with polar surfaces, the free energy of adsorption can be expressed by

$$\Delta G = \Delta G^d + \Delta G^{sp}$$

where ΔG^d and ΔG^{sp} are the contributions to the free energy of adsorption of the dispersive and specific interactions, respectively. The generally accepted way of separating London dispersion effects from specific effects, in infinite dilution chromatography, is to compare the chosen solute probe with an *n*-alkane of approximately the same geometry and polarizability. As a consequence, the specific interaction parameter I_{sp} is obtained by subtracting ΔG^d, corresponding to nonspecific interactions, from ΔG, measured by inverse gas chromatography:

$$I_{sp} = \Delta G^{sp} = \Delta G - \Delta G^d$$

The accuracy of the measurements was equal to ±0.001 min for the retention time, ±0.1 °C for the column temperature, ±20 Pa for the atmospheric pressure, and ±100 Pa for the pressure drop. Therefore, net retention volumes were known with a precision of about 5%. Consequently, the absolute error for free energy of adsorption and for the specific interaction parameter are estimated to be ±0.1 and ±0.2 kJ/mol, respectively.

Results and Discussion

London Component of the Surface Free Energy of Heat-Treated Silicas. Figure 1 shows the evolution of γ_s^d for the different types of silicas versus heat-treatment temperature. The origin of the sample as well as the thermal treatments applied are important in determining γ_s^d.

Amorphous silicas A, P, and G exhibit similar behaviors, corresponding to an increase of γ_s^d, from about 60–70 mJ/m^2 at 60 °C to 100 mJ/m^2 at 500 °C, followed by a decrease at temperatures up to 700 °C. These complex variations must be associated with complex chemical changes occurring on the surface of silicas upon heat treatment. Colloidal (C) and fibrous (F) silicas have similar general trends characterized by a continuous increase of γ_s^d up to 600 °C (e.g., sample C; at 600 °C γ_s^d is 160 mJ/m^2).

The evolution of γ_s^d for crystalline silicas is completely different from that of amorphous silicas. Starting from a very high value at low temperatures, it levels off between 200 and 400 °C, then increases again for higher heat-treatment temperatures. The extremely high values obtained, particularly for the L_2 sample (γ_s^d is in the 120–470-mJ/m^2 range), raise a fundamental question as they do not have a physical

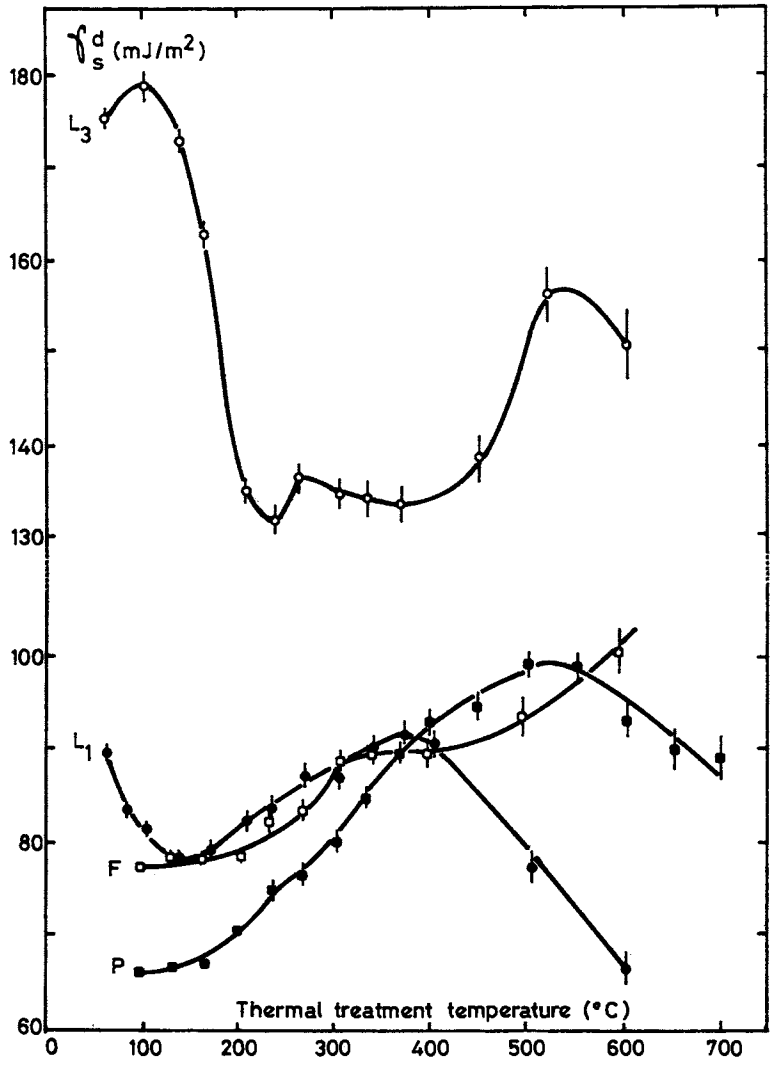

Figure 1. Evolution of the dispersive component of the surface free energy of silicas versus heat treatment temperature.

meaning. These results can be associated with the intercalation of the alkane probes between the sheetlike structure of crystalline silicas, a process that was demonstrated by use of branched alkanes.

The behavior of sample L_1 is a mix of that of crystalline and amorphous silicas, because it behaves as a crystalline silica at low temperature (60–200 °C) and as an amorphous silica above 200 °C (this behavior

parallels the evolution of its crystalline organization, which is unstable above 200 °C).

These curves point not only to the differences but also to the similarities exhibited by amorphous and crystalline samples. The main differences appear essentially at low treatment temperatures, at which the surface chemical properties of both types of silica are very much different. Interpretation of the evolution of γ_s^d versus temperature in amorphous silicas would suggest that the probes interact with siloxane bridges preferentially through dispersive interactions. This explanation was supported by Brinker et al. (*12, 13*), who identified by ^{29}Si NMR and Raman spectroscopies two types of silicon–oxygen species on the surface of silicas: tetra (unstrained) and trisiloxane (strained) rings. The trisiloxane rings, nonexistent at low temperature, form at intermediate temperatures and become prevalent in the 350–650 °C range. At higher temperatures trisiloxane cycles rearrange to yield less-strained cyclotetrasiloxane units.

The evolution of the physicochemical characteristics of the surface of amorphous silicas upon thermal treatment can be envisioned as follows. At room temperature the surface of the solids is covered by a multilayer of water, the external layers of which are eliminated at 30 °C under vacuum. At higher temperatures, only a monomolecular layer of water interacts with the surface (strongly with silanol groups, weakly with siloxane bridges). At about 100 °C, part of the water is evacuated, and thus the exposed surface will be available for interactions with alkane probes, a process associated with an increase of γ_s^d. At 250 °C all of the physically adsorbed water, but not molecules trapped in pores, has been eliminated. The phenomena observed between 250 and 500 °C can probably be attributed to the condensation of vicinal silanols (*8*), which yield trisiloxane cyclic compounds. At 500 °C, geminal silanols begin to disappear (*21*) and trisiloxane rings rearrange to yield tetrasiloxane cycles. Thus, above 500 °C the γ_s^d plot may be taken to represent the condensation of geminal and isolated silanols, a process that may be the reason, or the consequence, of a surface rearrangement that occurs at temperatures up to 800 °C (*22*).

Specific Component of the Surface Free Energy of Heat-Treated Silicas. Specific interaction capacities of heat-treated silicas, that is, their ability to interact with polar molecules, were examined with chloroform (Lewis acid probe) and toluene and benzene (amphoteric molecules). Figure 2 provides examples of the evolution of the specific interaction parameter I_{sp} of the different silicas with chloroform as a probe.

All amorphous silicas except C showed an I_{sp} that decreased with temperature of treatment, with a more or less pronounced step in the 200–400 °C temperature range. This evolution, which parallels the silanol content of the solids (*23*), suggests that I_{sp} reflects the interaction of the probe with silanol groups. The I_{sp} of the silicas treated at the highest

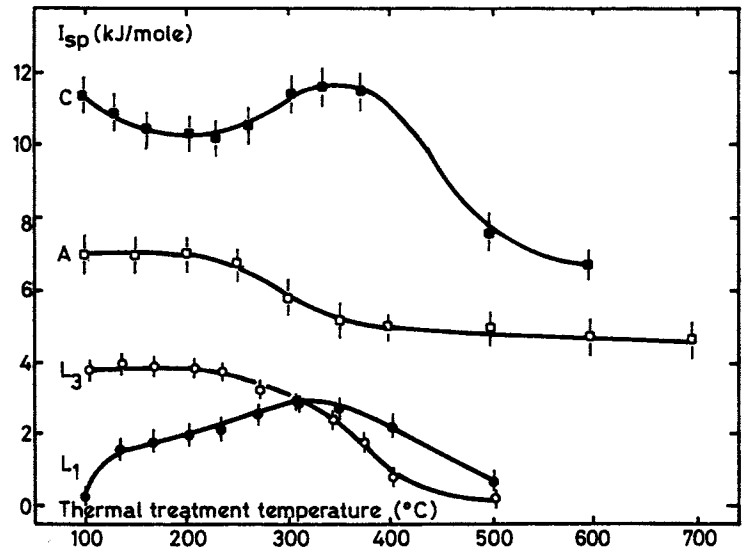

Figure 2. Evolution of the specific interaction parameter of silicas with chloroform versus heat treatment temperature.

temperature also appear to be quite different; thus, a nonequivalent surface chemical state of the various amorphous samples is implied.

In crystalline silicas the variation of I_{sp} versus temperature is much more complex. L_1 behaves as an amorphous sample, in agreement with the evolution of its crystalline structure with temperature, whereas L_2 and L_3 show maxima at 450 and 350 °C, respectively. Such a result means that interactions with chloroform are increasing while the total number of surface hydroxyls, which are theoretically responsible for these interactions, is decreasing. Thus, two antagonistic mechanisms have to be envisioned, one involving intercalation of the probe within the lamellar layers of the crystalline silicas (up to 350 °C; the interlamellar distance is decreased, and walls covered with silanol groups are thus closer—as a consequence their influence on inserted chloroform molecules will increase, yielding higher interaction parameters), the other (above 350 °C) associated with the condensation of hydroxyls, resulting in a loss of active sites and thus in a decrease of chloroform interactions [a process confirmed by ^{29}Si cross-polarization–magic-angle spinning (CP–MAS) NMR spectroscopy (*23*)].

Deactivation of silica surfaces by grafting of alkyl chains [esterification with short-chain (C_1) or long-chain (C_{16}) alcohols] was reported (*24*) to be associated with strong decreases in γ_s^d as well as I_{sp}, which for C_{16}-modified samples are very close to those exhibited by polyethylene (known to be a

surface of very low energy). Thus, the behavior of esterified silicas versus temperature was of interest.

Evolution of the Surface Free Energy of Esterified Silicas with Heat-Treatment Temperature. Figure 3 shows the evolution versus temperature of γ_s^d of initial and esterified G. The modifications are associated with a decrease of the dispersive component of the surface free energy, a process very much dependent on the number of carbon atoms of the grafted alkyl chain. Thus, the silica reacted with hexadecanol can be considered completely coated by a hydrocarbon layer, whereas the part of the surface that reacted with methanol, which is unhindered by the methyl grafts, remains available for further interactions. The curves also show the thermal stability of the grafted alkyl chains. Starting at about 250 °C, a steep increase of γ_s^d (particularly with C_{16}-modified silicas) is evident and is probably related to the pyrolysis of the grafted chains. This process seems to be completed by 500 °C, because the curves corresponding to the esterified samples merge with that of initial silica at this temperature. The increase in γ_s^d of the modified silicas can thus be considered to result from a combination of phenomena corresponding to the behavior of ungrafted silicas and to the degradation of the grafted alkyl chains.

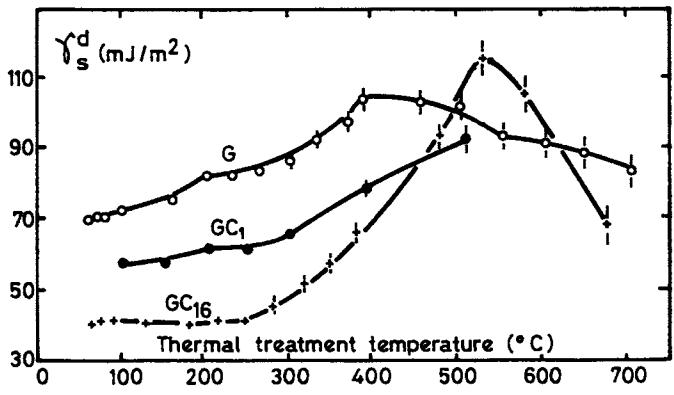

Figure 3. Evolution of the dispersive component of the surface free energy of esterified silicas versus heat treatment temperature. (Reproduced with permission from reference 26. Copyright 1990.)

Specific interaction parameters are strongly reduced upon surface modification (hexadecylated silicas have I_{sp} values close to zero). In methanol-reacted silicas, I_{sp} values decrease when heat-treatment temperature increases. This result suggests that after grafting with methanol, some free hydroxyls are still available for further interactions. This scenario is

also likely for C_{16}-grafted silicas, but for these silicas the residual silanol groups are completely shielded by the grafted chains and are thus inaccessible to the probes.

The results obtained with the different silicas point to the importance of the mode of preparation on their surface characteristics and thus on their surface heterogeneity. Understanding of the surface heterogeneity can be attained by calculation of the distribution function of the energy of adsorption of alkane molecules on the surface of the solids.

Distribution Function of Adsorption Energy. From chromatographic data it is possible to relate the amount of solute adsorbed on a solid to the equilibrium pressure and thus to plot its adsorption isotherm. For a heterogeneous surface, the experimentally measured adsorption isotherm can be described as a sum of local isotherms corresponding to different surface-active sites. The isotherm can then be represented by the following integral equation:

$$V(p) = \int_0^\infty \theta(p, \epsilon)\, \phi(\epsilon) d\epsilon$$

where $\theta(p,\epsilon)$ is the local adsorption isotherm on sites corresponding to an adsorption energy ϵ, $\theta(\epsilon)$ is the distribution function of adsorption energy, and p is pressure (*25*, *26*). Thus, by knowing the complete isotherm and using an approximation of local isotherm, it is possible to calculate $\theta(\epsilon)$. Because these are physical adsorption processes, only alkane probes were considered. Figure 4 shows the distributions of energy measured on silicas A, G, and L_3 with hexane as a solute. The distributions are bimodal and point to the existence of two different types of adsorption site on the surface. Moreover, the distributions appear to be dependent on the nature of the silica. The distribution calculated for silica L_3 is much narrower than those of silicas A and G. This result is in agreement with the surface topology of hydroxyls, which are known to be homogeneously distributed on the surface of L_3, whereas A exhibits a flat but chemically more heterogeneous surface, and G, which has a higher silanol content, is very heterogeneous (*23*). However, it is difficult to assign the peak corresponding to a given energy of interaction to a particular type of surface functional group. Nevertheless, the distribution energy curves yielded by initial silica G were compared to those yielded by the same silica grafted with methanol (GC_1) and hexadecanol (GC_{16}). Esterification would be expected to be associated with a complex modification of the silica surface. It appears (Figure 5) that grafting is indeed followed both by a shifting of the distribution curve toward smaller energies (the longer the chains, the larger the shift) and by a decrease of the height of the peak corresponding to the smaller energy. These shifts can be related to a decrease of the

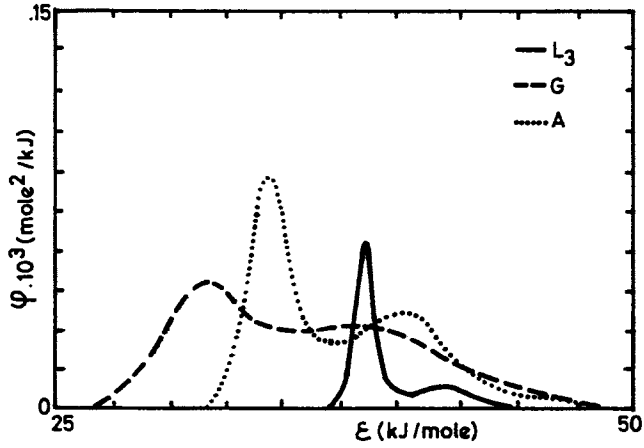

Figure 4. Distribution of the energy of adsorption of hexane for different silicas. (Reproduced with permission from reference 27. Copyright 1990.)

accessibility of the surface due to the steric hindrance of the grafted alkyl chains. Moreover, because the area under the curves is proportional to the number of adsorption sites, the decrease of peak height could be related to the decrease of the number of accessible silanols. As a consequence, the low energy peak could tentatively be linked with the energy of interaction between the alkane probe and surface hydroxyls.

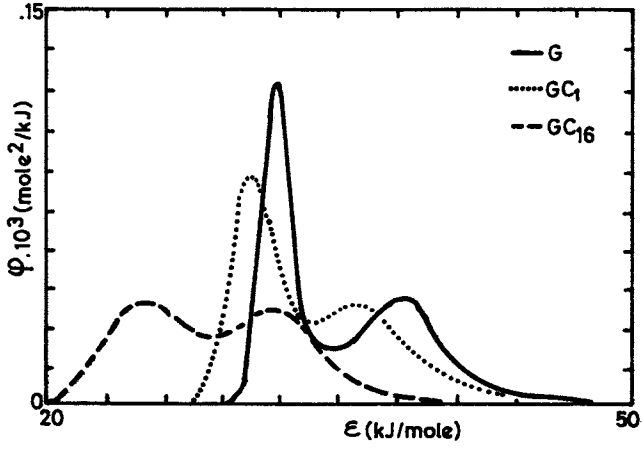

Figure 5. Distribution of the energy of adsorption of hexane for initial and esterified silicas. (Reproduced with permission from reference 27. Copyright 1990.)

Conclusions

The evolution of the surface free energy components of the different samples showed that the physicochemical surface characteristics of silicas and their surface heterogeneity are dependent on the mode of preparation. An approximation of surface heterogeneity was attained by calculation of the distribution function of the energy of adsorption of alkane probes on the solid surfaces.

References

1. Iler, R. K. *The Chemistry of Silica*; Wiley Interscience: New York, 1979.
2. Kondo, S. *Nippon Kagaku Kaishi* **1985**, *6*, 1106.
3. Wagner, M. P. *Rubber Chem. Technol.* **1976**, *49*, 703.
4. Hertl, W. *J. Phys. Chem.* **1968**, *72*, 1248.
5. Armistead, C. G.; Tyler, A. J.; Hambleton, F. H.; Mitchell, S. A.; Hockey, J. A. *J. Phys. Chem.* **1969**, *73*, 3947.
6. Evans, B; White, T. E. *J. Catal.* **1968**, *11*, 336.
7. Vidal, A.; Papirer, E.; Donnet, J. B. *J. Chim. Phys.* **1974**, *71*, 445.
8. Zaborski, M.; Vidal, A.; Ligner, G.; Balard, H.; Papirer, E.; Burneau, A. *Langmuir* **1989**, *5*, 447.
9. Morrow, B. A.; Cody, I. A. *J. Phys. Chem.* **1972**, *77*, 1465.
10. Hair, M. L. *J. Non-Cryst. Solids* **1975**, *19*, 199.
11. Sander, L.; Callis, J. B.; Field, L. R. *Anal. Chem.* **1983**, *55*, 1068.
12. Brinker, C. J.; Kirkpatrick, R. J.; Tallant, D. R.; Bunker, B. C.; Montez, B. *J. Non-Cryst. Solids* **1988**, *99*, 418.
13. Brinker, C. J.; Tallant, D. R.; Roth, E. P.; Ashley, C. S. *J. Non-Cryst. Solids* **1986**, *82*, 117.
14. Maciel, G. E.; Sindorf, D. W. *J. Am. Chem. Soc.* **1980**, *102*, 7606.
15. Miller, M. L.; Linton, R. W.; Maciel, G. E.; Hawkins, B. L. *J. Chromatogr.* **1985**, *319*, 9.
16. Fripiat, J. In *Soluble Silicates*; Falcone, J. S., Ed.; ACS Symposium Series 194, p 165.
17. Conder, J. R.; Young, C. L. *Physicochemical Measurements by Gas Chromatography*; Wiley Interscience: New York, 1979.
18. Aulich, H. A.; Eisenrith, K. H.; Urbach, H. P. *J. Mater. Sci.* **1984**, *19*, 1710.
19. Le Bihan, M. T.; Kalt, A.; Wey, R. *Bull. Soc. Fr. Minéral. Cristallogr.* **1971**, *94*, 15.
20. Papirer, E.; Balard, H.; Vidal, A. *Eur. Polym. J.* **1988**, *24*, 783.
21. Sindorf, D. W.; Maciel, G. E. *J. Am. Chem. Soc.* **1983**, *105*, 1487.
22. Feltl, L.; Lutovsky, P.; Sosnova, L.; Smolkova, E. *J. Chromatogr.* **1974**, *91*, 321.
23. Ligner, G.; Vidal, A.; Balard, H.; Papirer, E. *J. Colloid Interface Sci.* **1990**, *134*, 486.
24. Vidal, A.; Papirer, E.; Wang, M. J.; Donnet, J. B. *Chromatographia* **1986**, *23*, 227.
25. Rudzinski, W.; Jagiello, J.; Grillet, Y. *J. Colloid Interface Sci.* **1982**, *48*, 478.
26. Jagiello, J.; Ligner, G.; Papirer, E. *J. Colloid Interface Sci.* **1990**, *137*, 128.
27. Legrand, A. P. et al. *Adv. Colloid Interface Sci.* **1990**, *33*, 91.

RECEIVED for review October 3, 1990. ACCEPTED revised manuscript December 30, 1991.

13

Variable-Temperature Diffuse Reflectance Fourier Transform Infrared Spectroscopic Studies of Amine Desorption from a Siliceous Surface

Donald E. Leyden[1] and Kristina G. Proctor[2]

Condensed Matter Sciences Laboratory, Department of Chemistry, Colorado State University, Fort Collins, CO 80523

Variable-temperature diffuse reflectance infrared Fourier transform spectroscopy was used in conjunction with pyridine desorption studies to assess the acidity of a siliceous surface. An amorphous, porous silica substrate was investigated. The results contribute to an understanding of the acidic strength and the distribution of acidic sites on this material. A hydrogen-bonding interaction was observed between pyridine and the surface. Isothermal rate constants and an activation energy for the desorption process are reported and can be used as direct measures of surface site acidity.

SILICEOUS SUBSTRATES ARE USED EXTENSIVELY in industry and applied research. These materials can undergo a variety of chemical modifications that make them useful for applications such as catalysis and chromatography. An increased understanding of the nature of surface reactions and reaction products would facilitate current and future applications of these

[1]Current address: Philip Morris U.S.A., P.O. Box 26583, Richmond, VA 23261.
[2]Current address: Department of Chemistry, University of Southern Colorado, Pueblo, CO 81001.

0065–2393/94/0234–0257$08.00/0

substrates. Acquisition of such information requires innovative surface characterization methods.

One characteristic of interest is the surface propensity toward adsorption, hydrogen bonding, and acid–base interactions with chemical reagents. For example, surface silylation by alkoxysilanes may involve hydrolysis of the alkoxy groups by surface-adsorbed water. The overall rate of reaction (from dry, aprotic solvents such as toluene) may be limited by the rate of hydrolysis, which is likely dependent on the fraction of alkoxysilane associated with the substrate surface. A convenient measure of the distribution of a solute between the solvent and substrate is the chromatographic capacity factor (k') (*1*). Figure 1 shows a plot of the relative rate of hydrolysis for several alkoxysilanes (*n*-octyltriethoxysilane, 3-mercaptopropyltriethoxysilane, 3-cyanopropyltriethoxysilane, and 3-aminopropyltriethoxysilane) on the surface of controlled-pore glass versus the amount of silane adsorbed. The hydrolysis rate is followed by measuring the amount of ethanol produced in toluene solution. The amount of adsorbed silane is represented by the quantity $S[k'/(1 + k')]$, where S is the total amount of alkoxysilane in solution (*2*). The rate of hydrolysis of the silane alkoxy groups is linearly related to the fraction of the reagent adsorbed to the substrate for three of the compounds. However, in 3-aminopropyltriethoxysilane the rate of reaction is much faster than that predicted by the simple adsorption model. Knowledge of such differences is of considerable importance to a better understanding of the nature of surface substrate reactions.

Another area of interest is the acidity of siliceous substrates. Current methods of surface characterization provide a variety of information about the acidity of a surface. Visible indicators covering a range of pK_a values may be used to estimate the acidity as defined by the Hammett acidity function (*3, 4*). This method is vague in interpretation and can only provide a measure of relative acidic strength. Other methods involving the adsorption and desorption of gaseous bases can also assess relative acidic strengths. However, assignments to specific surface sites are subject to ambiguity of interpretation. These methods include differential thermal analysis (DTA) (*5*), thermal gravimetric analysis (TGA) (*6*), and titration calorimetry (*7*). The catalytic efficiency of a material can also be used to assess a general measure of surface acidity (*8, 9*).

Investigations of the acidity of specific surface sites may be accomplished by studies coordinated with spectroscopic methods, such as infrared (IR) spectroscopy, nuclear magnetic resonance (NMR) spectroscopy, or mass spectrometry (MS). Surface characterization with Fourier transform infrared (FTIR) spectroscopy can provide quantitative results with experimental methods that are easily performed. However, the transmission sampling techniques traditionally employed for infrared studies may introduce experimental artifacts on the analyzed surface (*10,*

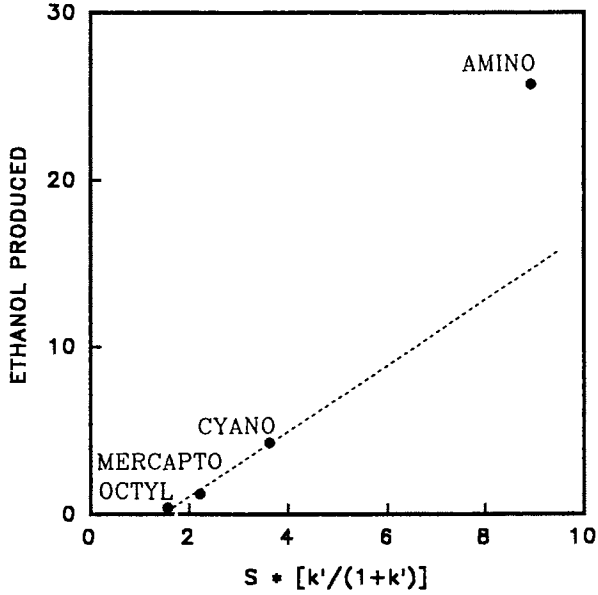

Figure 1. Relative amount of ethanol produced versus amount of silane adsorbed on the substrate, calculated from the chromatographic capacity factor k'.

11). To minimize this problem, self-supporting pellets are usually prepared, and the minimum pressure required to form a mechanically stable pellet is used. Although much information related to surface acidity has been obtained with transmission techniques, there remains some question regarding the extent of surface alteration due to sampling procedures.

Diffuse reflectance FTIR (DRIFT) spectroscopy provides an alternative to transmission infrared spectroscopy with respect to sampling procedures. DRIFT spectroscopy requires dispersion of the sample in a finely ground, nonabsorbing matrix such as KCl or KBr. The integrity of the sample surface is ensured because no pressure is used in the preparation. Variable-temperature DRIFT (VT-DRIFT) spectroscopy can be performed with commercially available, heatable–evacuable sample cells that can be interfaced for computer temperature control (*12*). Gaseous base adsorption and desorption processes can be followed directly; thus, specific surface sites can be identified and quantified and their acidic strength can be assessed. Previously, such results could be obtained only by combined methods such as IR–TGA (*13*) or IR–TPD–MS (TPD, temperature-programmed desorption) (*14*). Such combinations require variable-temperature experiments of independently prepared samples or elaborate instrumental design for measurements taken from the

same sample. VT-DRIFT spectroscopy provides a direct and independent means for the characterization of acidic surfaces in their native form.

This chapter describes the results of the acidity characterization of a selected silica surface with VT-DRIFT spectroscopy. Examples of the capabilities of the method are demonstrated by the qualitative determination of the adsorption and thermal desorption characteristics of pyridine on amorphous, porous silica gel. Procedures for the determination of isothermal desorption rate constants and activation energy of desorption are presented and discussed as a means of assessing acid site strength.

Experimental Details

Materials. Amorphous silica gel was used (J.T. Baker), 290-m^2/g surface area, 60–200 mesh, and 126-Å mean pore diameter. Pyridine (Baker, reagent grade) was used as received.

Instrumentation. Spectra were acquired with a Nicolet 60SX FTIR spectrometer, continuously purged with dry air and equipped with a liquid-nitrogen-cooled, wideband mercury–cadmium telluride detector. Coaddition of 100 interferometer scans at 8-cm^{-1} resolution was employed. The location of absorption maxima was confirmed by spectra taken at 1-cm^{-1} resolution. All spectra were converted into Kubelka–Munk units prior to use. Integration of peak areas was accomplished by using software available on the Nicolet 60SX. All peak areas were normalized to the 1870-cm^{-1} Si–O–Si combination band (*15*).

The diffuse reflectance accessory (model DRA-2CN, Harrick Scientific) was modified with a three-dimensional translational stage to optimally position the sample for maximum radiation throughput (*15*). The sample cell (model HVC-DRP, Harrick Scientific) was heated by a resistive heater contained within a post that housed a sample cup. The base of the sample cell also contained an external connector for evacuation and a second port, which was sealed with a septum and used for the introduction of pyridine by microsyringe. The sample cell cover contained a channel and connectors for water cooling and ZnSe windows (12 mm in diameter) for the IR radiation. The base and cover of the cell were sealed vacuum-right with an O-ring.

Temperature of the sample cell was monitored and controlled by an interface to an Apple II^+ computer. The temperature of the sample cell was sensed by an internal Fe–constantan thermocouple connected to a digital thermometer (Omega Engineering, model 199AJC-D). The digital value of the temperature was available as a binary decimal and was read by an input–output card (John Bell Engineering, model 79-295) in an expansion slot of the computer. The cell temperature was controlled to 1 °C by using software written in Applesoft and assembly languages and a signal to an exterior switch card that controlled the on–off status of a variable-voltage transformer.

Procedures. Prior to use, silica samples were calcined at 500 °C for 5 h in an open-ended tube furnace and stored in a desiccator after rehydroxylation. Samples were dispersed (15% w/w) in finely ground KCl by mixing in a Wig-L-Bug capsule without the grinding ball (Crescent Dental Manufacturing). Dispersions containing 4–6 mg of sample were spread over a bed of KCl in the sample cup and flattened by light compression with a smooth object. Samples were heated to 200 °C under

slight vacuum (100–150 mmHg, or 13–20 kPa) to remove physisorbed water then cooled to room temperature for the adsorption of pyridine. Liquid pyridine was introduced into the evacuated cell containing the sample at 25 °C by injection with a Hamilton microsyringe (0.5 μL). A volume of 3 μL resulted in saturation of the sample surface sites. Equilibrium occurred within 10 min under these conditions. The isothermal desorption of pyridine from silica gel was followed after adsorption of the base at room temperature. The sample cell was evacuated at room temperature to remove excess pyridine, and the temperature was then quickly ramped (30 s) and maintained at the desired temperature for the desorption. Spectra were recorded at intervals of 1, 5, 10, 20, and 30 min during the progression of 5-h desorption studies conducted at 50, 60, 70, 80, and 90 °C.

The possibility of interaction of pyridine with the dispersion matrix material was investigated by collecting spectra of pure KCl and of pyridine adsorbed on pure KCl before and after evacuation. All traces of pyridine were removed from the KCl spectrum following a few minutes of evacuation.

Results and Discussion

The surface of amorphous silica gel was qualitatively characterized by the adsorption of pyridine. Because pyridine is a weak base (pK_a 5.25), it selectively interacts with the more acidic surface sites. This interaction is relevant because metal oxide promoted catalysis is believed to occur by mechanisms involving acid-induced intermediate species (e.g., carbonium ions). Ring vibrations of pyridine give rise to infrared absorptions in the 1400–1700-cm^{-1} region. The absorption bands of pyridinium ion, covalently bonded pyridine, and hydrogen-bonded pyridine were assigned by Parry (*16*). These species are formed upon interaction with Brönsted acid, Lewis acid, and hydrogen-bonding sites, respectively. The absorption bands of these interactions are distinguishable and can serve as a tool for the qualitative identification of surface acidic sites.

The VT-DRIFT spectrum of silica gel in the silanol absorption region before the adsorption of pyridine is shown in Figure 2. The absorption band at 3740 cm^{-1} was assigned to silanols that do not hydrogen-bond to other silanols or to surface-adsorbed water (*17*). These sites are referred to as unassociated silanol sites. The absorption at 3740 cm^{-1} is slightly downshifted from that assigned to a freely vibrating silanol at 3750 cm^{-1} (*17*). The other absorption maxima observed at 3655 cm^{-1} and 3450 cm^{-1} arise from surface silanols that hydrogen-bond to each other and are hydrogen-bonded by surface-adsorbed water, respectively (*17*). These two groups of silanols are collectively referred to as associated silanols.

The VT-DRIFT spectrum of pyridine adsorbed on unmodified silica gel is shown in Figure 3, Absorption maxima are observed at 1595, 1485, and 1445 cm^{-1}. According to the assignments made by Parry (*16*), these bands indicate hydrogen-bond formation. The absorptions result from in-plane C–C stretching modes 8a, 19a, and 19b, respectively (*18*). The acidic strength of the surface sites is insufficient to generate pyridinium

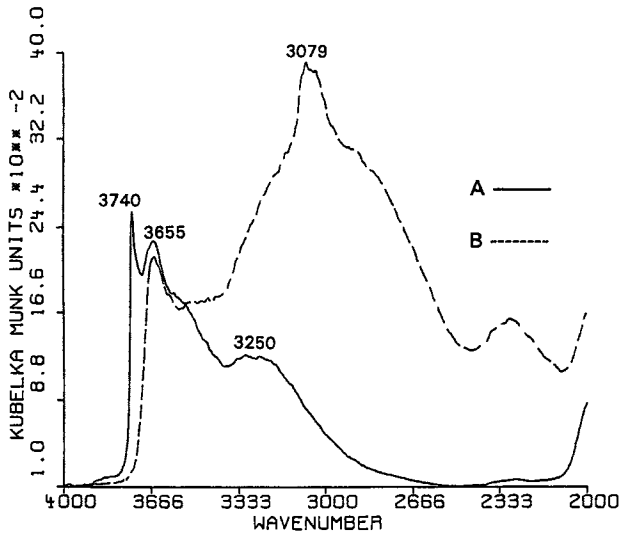

Figure 2. DRIFT spectrum of silica gel in the silanol absorption region at 25 °C (A) after removal of physisorbed water and (B) after adsorption of pyridine.

ion. This observation is consistent with previous studies of silica gel that used transmission infrared spectroscopic techniques (*19*).

The silanol absorption region changes as pyridine is desorbed from the silica gel surface. If pyridine is involved in reversible hydrogen-bonding with silanols, adsorbed pyridine should shift at least part of the unassociated silanol absorption to the associated silanol band. Conversely, desorption should shift the respective absorption band areas in the opposite manner. Figures 4 and 5 show results obtained upon desorbing pyridine from the silica gel surface. In Figure 4, the peak area of the unassociated silanol band increases in a linear relationship with pyridine desorption, as measured by the peak area of hydrogen-bonded pyridine. Conversely, the peak area for the associated silanol band decreases linearly with pyridine desorption in Figure 5. These data provide strong evidence that the unassociated silanols are the preferred sites of pyridine adsorption because they have greater acidic strength than the associated silanols.

The nature of the interaction between pyridine and surface silanols was investigated further by using VT-DRIFT. Hydrogen-bonded pyridine was desorbed from the silica gel surface isothermally, and the process was followed by using the integrated absorption of the band at 1445 cm^{-1}. According to the definition of the Kubelka–Munk function, this peak area is directly proportional to the surface concentration of hydrogen-bonded pyridine. The data were fit to integrated rate law equations representing zero-, first-, and second-order kinetics. As shown in Figure 6, an excellent

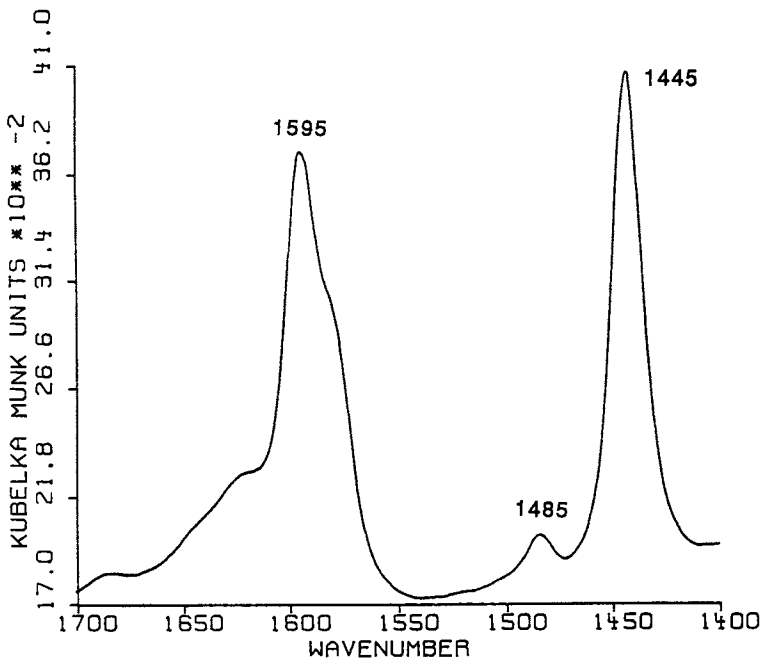

Figure 3. DRIFT spectrum of pyridine adsorbed on silica gel.

fit (linear correlation coefficient $r = 0.998$) was obtained when a reciprocal equation of the form $1/y = mx + b$ was used. The second-order rate law for this process can be expressed as

$$\frac{d[\text{HPYD}]}{dt} = -k_2[\text{HPYD}]^2 t$$

where [HPYD] is the concentration of H-bonded pyridine, k_2 is the second-order rate constant, and t is time. Integration of this rate law yields the integrated rate equation

$$\frac{1}{[\text{HPYD}]} = -k_2 t + c$$

in which a linear relationship between reciprocal concentration and time is predicted (Figure 6). The slope in Figure 6 represents the negative value of the second-order rate constant for the isothermal desorption process. This constant is a direct measure of the strength of the pyridine–silanol interaction and thus represents the degree of acidity of the surface acidic sites on amorphous silica gel.

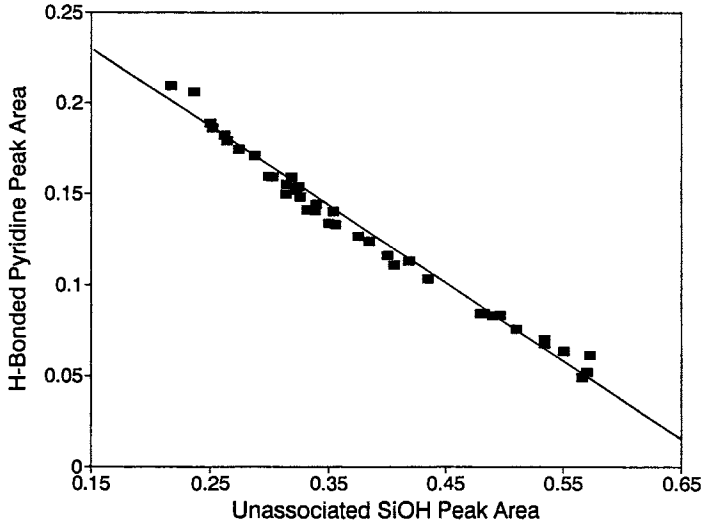

Figure 4. Appearance of unassociated silanol sites with desorption of hydrogen-bonded pyridine.

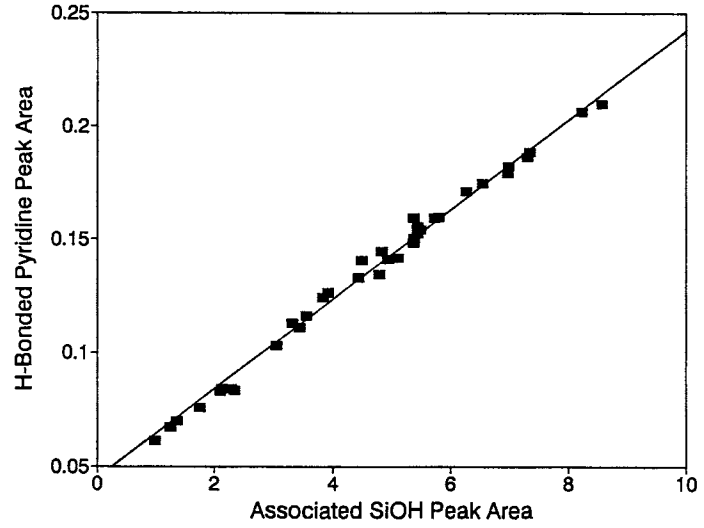

Figure 5. Disappearance of associated silanol sites with desorption of hydrogen-bonded pyridine.

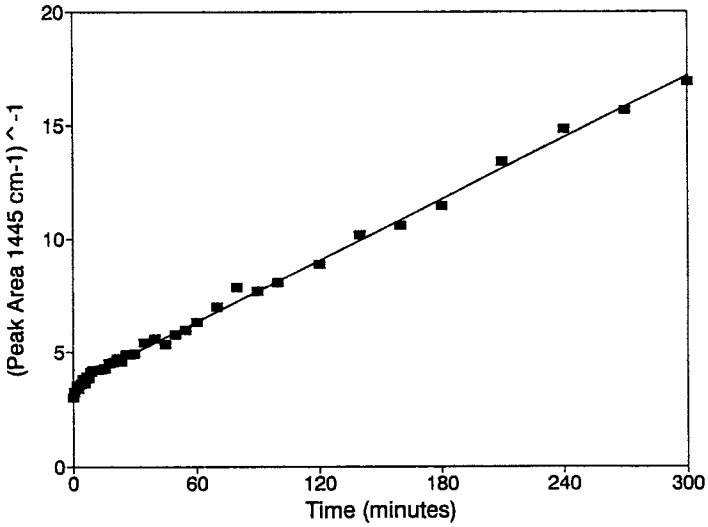

Figure 6. Reciprocal integrated absorption at 1445 cm^{-1} versus time for the desorption of pyridine from silica gel at 80 °C.

The observed second-order desorption of pyridine is believed to be evidence that the majority of surface silanols are paired on the surface in either a vicinal or geminal configuration. Further evidence for the pairing of the majority of silanols on the silica surface was presented elsewhere (*20*) and is in direct agreement with studies conducted by Peri and Hensley (*21*).

Isothermal desorption rate constants were determined from pyridine desorption studies conducted in the range of 50–90 °C. An Arrhenius plot of the natural logarithm of the second-order rate constants versus the reciprocal of the desorption temperature is shown in Figure 7. From these data, a value of 43.6 ± 4.2 kJ/mol is obtained for the activation energy of desorption. This value indicates a strong hydrogen bond between pyridine and surface silanols (22). The desorption activation energy may further be compared with the heat of adsorption of pyridine on silica, 45.2 ± 3.5 kJ/mol, obtained by Hertl and Hair (23). The close agreement between these values indicates that the activation energy for the adsorption of pyridine on silica is near zero.

Conclusions

Variable-temperature diffuse reflectance Fourier transform infrared spectroscopy provided qualitative and quantitative information concerning the acidity of surface sites on silica. Although the use of pyridine as a probe has been well known for many years, the ability of the technique to permit

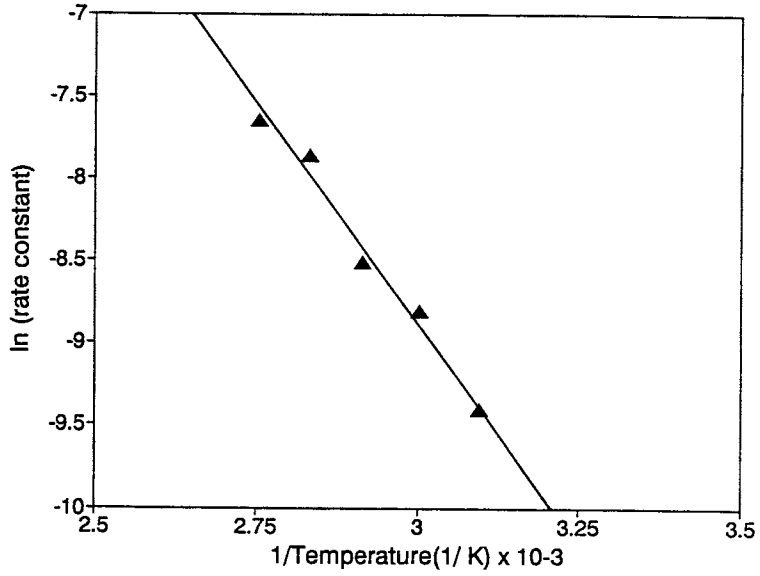

Figure 7. Arrhenius plot for the desorption of pyridine from silica gel.

easily accomplished investigations in a short period of time without disturbing the integrity of the sample is significant. Pyridine selectively adsorbs to the unassociated silanol sites that are more acidic than the sites hydrogen-bonded to surface water or other silanol sites. The activation energy for the desorption of pyridine is indicative of a strong hydrogen bond and is nearly equal to the heat of adsorption. Thus, the activation energy for the adsorption of pyridine is near zero.

Acknowledgments

This research was supported in part by Grants CHE–8513247 and CHE–8712457 from the National Science Foundation and funds from Dow Corning Corporation. The Nicolet 60SX FTIR spectrometer was purchased in part from a grant from the National Science Foundation (CHE–8317079).

References

1. Karger, B. L.; Snyder, L. R.; Horvath, C. *An Introduction to Separation Science*; Wiley: New York, 1973; pp 30–31.
2. Morrall, S. W. Ph.D. Thesis, Colorado State University, 1984, p 162.
3. Mishima, S.; Nakajima, T. *J. Chem. Soc. Faraday Trans. 1* **1986**, *82*, 1307.
4. Take, J.; Tsuruya, T.; Sato, T.; Yoneda, Y. *Bull. Chem. Soc. Jpn.* **1972**, *45*, 3409.

5. Stone, R.; Rase, H. *Anal. Chem.* **1957,** *29,* 1273.
6. Clark, A.; Holm, V. C. F.; Blackburn, D.M.; *J. Catal.* **1962,** *1,* 244.
7. Airoldi, C.; Santos, Jr., L.; *Thermochim. Acta* **1986,** *104,* 11.
8. Holm, V. C. F.; Clark, A. *J. Catal.* **1963,** *2,* 16.
9. Hattori, H.; Takahashi, O.; Takagi, M.; Tanabe, K. *J. Catal.* **1981,** *68,* 132.
10. Hambleton, F. H.; Hockey, J. A.; Taylor, J. A. G. *Nature (London)* **1965,** *208,* 138.
11. Blitz, J. P.; Murthy, R. S. S.; Leyden, D. E. *Appl. Spectroscopy* **1986,** *40,* 829.
12. Murthy, R. S. S.; Blitz, J. P.; Leyden, D. E. *Anal. Chem.* **1986,** *58,* 3167.
13. Ballivet, D.; Barthomeuf, D.; Pichat, P. *J. Chem. Soc. Faraday Trans. 1* **1972,** *68,* 1712.
14. Schwarz, J. A.; Russel, B. G.; Harnsberger, H. F. *J. Catal.* **1978,** *54,* 303.
15. Murthy, R. S. S.; Leyden, D. E. *Anal. Chem.* **1986,** *58,* 28.
16. Parry, E. P. *J. Catal.* **1963,** *2,* 371.
17. Hair, M. L. *Infrared Spectroscopy in Surface Chemistry*; Dekker: New York, 1967; pp 79–139.
18. Basila, M. R.; Kantner, T. R.; Rhee, K. H. *J. Phys. Chem.* **1964,** *68(11),* 3197–3207.
19. Scokart, P. O.; Declerck, F. D.; Sempels, R. E.; Rouxhet, P. G. *J. Chem. Soc. Faraday Trans. 1* **1976,** *75,* 359–371.
20. Proctor, K. G. Ph.D. Thesis, Colorado State University, 1989, pp 40–87.
21. Peri, L. B.; Hensley, Jr., A. L. *J. Phys. Chem.* **1968,** *72,* 2926.
22. Cotton, F. A.; Wilkinson, G. *Advanced Inorganic Chemistry*; Wiley-Interscience: New York, 1980; p 21.
23. Hertl, W.; Hair, M. L. *J. Phys. Chem.* **1968,** *72,* 4676.

RECEIVED for review November 13, 1990. ACCEPTED revised manuscript February 24, 1992.

14

Multinuclear NMR Spectroscopy Studies of Silica Surfaces

Gary E. Maciel, Charles E. Bronnimann, Robert C. Zeigler, I-Ssuer Chuang, David R. Kinney, and Ellen A. Keiter[1]

Department of Chemistry, Colorado State University, Fort Collins, CO 80523

$^{1}H \rightarrow {}^{29}Si$ cross polarization with magic-angle spinning is a valuable approach for observing local silicon environments on the silica surface. The ^{1}H combined rotation and multiple-pulse spectroscopy (CRAMPS) approach distinguishes clustered and isolated surface silanols. Correlations of the variations in ^{29}Si and ^{1}H peak intensities with silane loading level in silica gels derivatized with $(CH_3)_3SiCl$ suggest an incorrect model of the silica surface that is inconsistent with models derived from more detailed considerations. Other nuclides (e.g., ^{2}H, ^{13}C, and ^{15}N, along with ^{29}Si) provide valuable approaches for the characterization of local structure and motion in derivatized (silylated) silicas.

HIGH-RESOLUTION NMR SPECTROSCOPY TECHNIQUES FOR SOLIDS developed during the past 15 years (*1–4*) have been applied to the study of surfaces (*5*). NMR spectroscopy, with its typical focus on short-range (local) order (chemical structure), provides a powerful complement to diffraction techniques, which require long-range order (i.e., a high degree of crystallinity). Of course, NMR spectroscopy has notoriously poor intrinsic sensitivity properties, so it has typically been limited to systems that have relatively large numbers of the relevant nuclei ($\sim 10^{19}$) at the surface. Because most surface systems of technological interest (e.g., in catalysis and in separations) have high surface areas and are not highly regular at

[1]On leave from Eastern Illinois University.

0065–2393/94/0234–0269$08.00/0

the surface, NMR techniques are often well suited to their study. Silica surfaces often fall into this category.

The most generally useful line-narrowing technique in modern solid-state NMR spectroscopy is magic-angle spinning (MAS), in which the sample is mechanically rotated rapidly (thousands of revolutions per second) about an axis that makes an angle of 54.7° relative to the direction of the static magnetic field (*6–9*). Sufficiently rapid MAS brings about the coherent averaging of inhomogeneous line-broadening effects, such as the chemical-shift anisotropy (CSA) and inhomogeneous magnetic dipole–dipole interactions. This effect is a coherent, mechanical analog of the incoherent motional averaging accomplished by Brownian motion in liquids—the reason that high-resolution NMR spectroscopy enjoyed popularity for liquid samples for 25 years before it did for solids.

Underivatized Silica Surface

Figure 1 (bottom) shows the ^{29}Si (spin 1/2, 4.70% natural abundance) MAS NMR spectrum of the silica gel system (*10*). This spectrum shows a small peak at ~ −90 ppm due to $=Si(OH)_2$ groups at the surface, a large peak at ~ −100 ppm due to $\equiv Si-OH$ groups at the surface, and a large peak at ~ −109 ppm due to silicon atoms in the surface region with no directly attached hydroxyl groups. The lack of line broadening due to $^{29}Si-^{1}H$ dipolar interactions in this spectrum is due to the effects of both MAS and high-power ^{1}H decoupling. The fact that the large peak at ~ −109 ppm doesn't completely dominate the spectrum is due in part to the very high surface area of the silica gel sample (about 260 m^2/g), but primarily results from the fact that a highly effective surface-selective technique has been employed—cross polarization (CP) (*11–13*).

In the cross-polarization approach, spin polarization from a more abundant spin set that has a larger nuclear magnetic moment (in this case, ^{1}H) is transferred via a double-resonance method to a less-abundant spin set that has a smaller nuclear magnetic moment (in this case, ^{29}Si). The mechanism for the CP process in this double-resonance experiment involves a static component of the magnetic dipole–dipole interaction (in this case, a $^{1}H-^{29}Si$ dipolar interaction) and hence falls off rapidly with increasing distance. Therefore, because nearly all of the protons in this system are present at the surface as covalently attached OH groups or as physisorbed H_2O, there is a dramatic selectivity of the ^{29}Si spin polarization for the surface environment. On the basis of this approach, first used as a surface-selective strategy by Sindorf and Maciel (*13–19*), numerous studies of the effects of dehydration and rehydration or derivatization of the silica surface were carried out (*13–29*). Figure 1 (middle and top) shows examples of this approach.

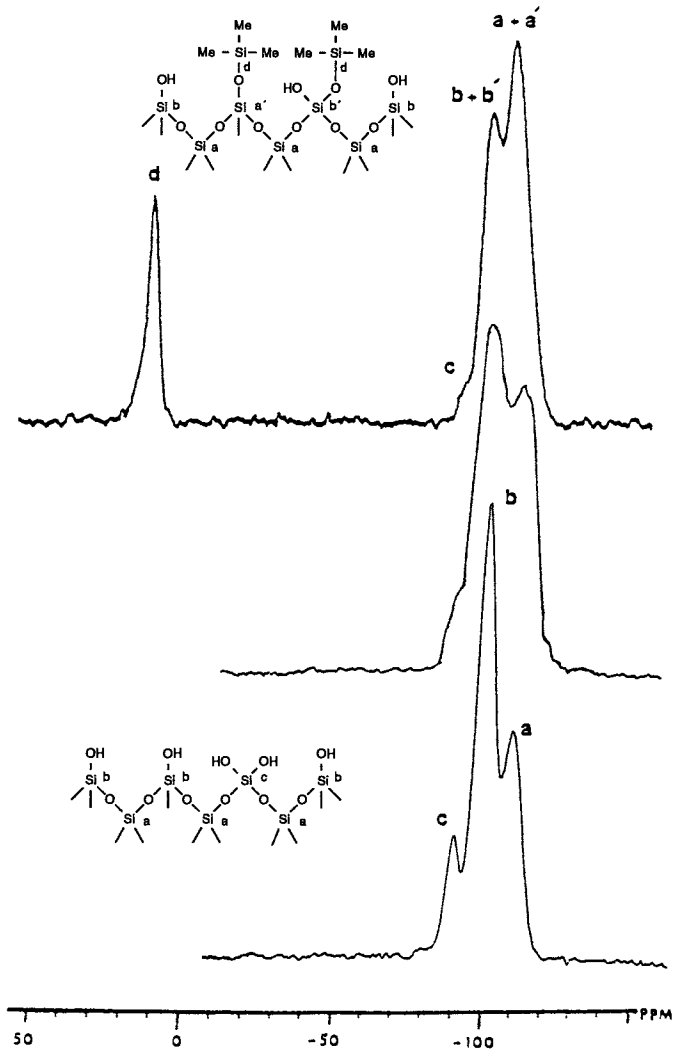

Figure 1. ^{29}Si CP–MAS spectra of hydrated Fisher S-157 silica gel (bottom), silica gel heated under vacuum at 200 °C (middle), and silica gel derivatized by $(CH_3)_3SiCl$ (top) (10).

The other magnetic nuclei present in significant numbers at the typical silica surface are ^{17}O (0.037% naturally abundant) and ^{1}H (99.99% naturally abundant). Oldfield and co-workers (*30, 31*) obtained $^{1}H \rightarrow {}^{17}O$ CP spectra of silica surfaces in experiments that normally require isotopic enrichment because the small nuclear magnetic moment (about 14% of that of ^{1}H) and quadrupolar broadening exacerbate both sensitivity and

resolution problems. ^{17}O NMR spectroscopy is likely to play a significant role in future NMR studies of the silica surface.

^{1}H NMR studies of silica surfaces have been numerous. The possibility of high local concentrations of protons (e.g., clustering of OH groups) can render the ^{1}H–^{1}H dipolar interactions homogeneous and thus limit the success of moderate-speed MAS in averaging the ^{1}H–^{1}H dipolar line broadening. Nevertheless, apparently useful ^{1}H MAS spectra on silica-type samples have been reported (*32, 33*), although some may be "distorted" in the manner indicated here (*34*). The possibility of line broadening or spectral distortions due to ^{1}H–^{1}H dipolar interactions can be largely eliminated by the use of multiple-pulse homonuclear dipolar line-narrowing techniques (*35*) in conjunction with MAS. This combination of techniques, combined rotation and multiple-pulse spectroscopy (CRAMPS) (*36*), is capable of providing line widths of 0.2–0.3 ppm in favorable cases, if there is not extensive line broadening due to (1) molecular motion, (2) unaveraged dipolar interactions with quadrupolar nuclei, or (3) large inhomogeneous effects from chemical inhomogeneities or magnetic susceptibility effects (*37, 38*).

Figure 2 shows ^{1}H CRAMPS spectra (*39*) of silica gels. Parts A, A′, and A″ of Figure 2 show that the spectrum obtained on the untreated sample can be computer-simulated as the sum of contributions from relatively sharp, symmetrical peaks centered at 1.7 and 3.5 ppm and an asymmetrical peak or band extending from about 8 to about 1 ppm. The spectrum of the silica gel after a 25 °C vacuum dehydration (Figure 2B) allows the peak centered at 3.5 ppm in Figure 2A to be easily identified as physisorbed water.

A CRAMPS-based ^{1}H technique that is extremely useful in the study of surfaces and greatly aids in identifying the origins of the other two peaks in the spectra shown in Figure 2 is a dipolar-dephasing experiment (*39*). In this experiment, a "dephasing period" is inserted between the initial pulse that first generates transverse ^{1}H magnetization and the CRAMPS detection period. During the dipolar-dephasing period, no multiple-pulse dipolar line narrowing occurs, so the ^{1}H magnetization evolves under the influence of whatever ^{1}H–^{1}H dipolar interactions may be present in the system. For those protons that are isolated from other protons (e.g., in isolated silanols), the magnetization is little affected by the dephasing period. However, the magnetization due to those protons that feel strong dipolar interactions with other protons (e.g., in clustered, H-bonded silanols or relatively stationary water clusters) should lose phase coherence and hence experience a substantial attenuation during a dephasing period of 50–100 μs. On this basis, the sharp peak at 1.7 ppm in the spectra of Figure 2 was identified as "isolated silanols", and the broad asymmetrical band was identified as "clustered silanols". It is interesting, and not

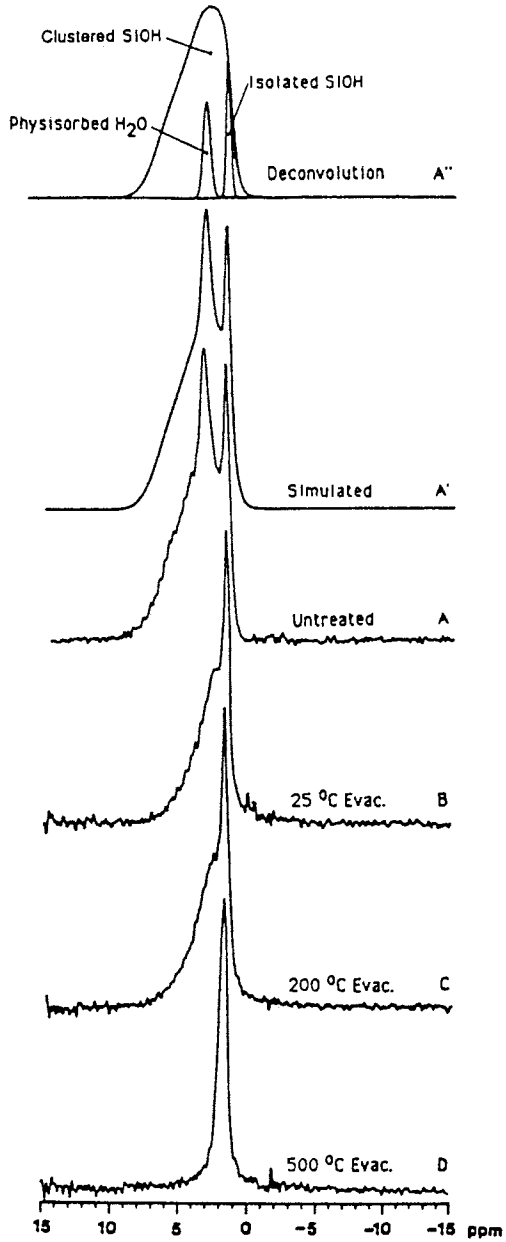

Figure 2. 187-MHz ^1H CRAMPS spectra of Fisher S-679 silica gel (A) untreated, (B) evacuated at 25 °C, (C) evacuated at 200 °C, and (D) evacuated at 500 °C. Plot A″ is the deconvolution of spectrum A; plot A′ is a computer simulation based on A″. (Reproduced from reference 39. Copyright 1988 American Chemical Society.)

surprising, that the isolated silanols are retained after sample evacuation at 500 °C (Figure 2D), whereas the "clustered" silanols are eliminated.

The silylation of a silica surface not only gives rise to a new, silane peak in the ^{29}Si spectrum (~15 ppm in Figure 1, top), but also causes an alteration of the intensities in the $=Si(OH)_2$, $\equiv SiOH$, and $=Si=$ peaks. These spectral changes permit the use of silylation for studying relative reactivities, as has been demonstrated by Sindorf and Maciel (*16, 18, 19*). The silylation process also changes the ^1H CRAMPS spectrum (*40*): new peak(s) due to the surface-attached silane moieties are introduced, and intensities in the silanol peaks are altered. Thus, the silylation process can be used to correlate ^1H and ^{29}Si NMR views of the silica surface. For this purpose, silylation by trimethylchlorosilane (TMCS) was used.

For TMCS-derivatized silicas with any but the lowest surface loading levels, the ^1H CRAMPS spectra are overwhelmed by the dominating $(CH_3)_3Si-O-$ peak; hence, $(CH_3)_3SiCl$ that was largely deuterated was employed to markedly attenuate this signal. Experiments of this nature were carried out as a function of the extent of silylation. Figure 3 shows the ^1H CRAMPS and ^{29}Si CP–MAS spectra obtained on a series of TMCS-derivatized silica gels with various $(CH_3)_3Si-O-$ loading levels. As the loading level increases, the relative intensities within the ^1H and ^{29}Si spectra are altered, the most conspicuous change being the increasing intensity of the sharp $(CH_3)_3Si-O-$ peaks at ~0.5 and ~15 ppm in the ^1H CRAMPS and ^{29}Si CP–MAS spectra, respectively. To compare changes in the various peak intensities as a function of $(CH_3)_3Si-O-$ loading level, deconvolutions of the ^1H and ^{29}Si spectra were carried out, and suitable corrections for spin dynamics were applied. On this basis, comparisons of the ^1H and ^{29}Si intensities of the individual contributing peaks can be made. These comparisons can be visualized from the plots given in Figure 4.

Comparisons of the trends in the upper and lower portions of Figure 4 reveal intensity patterns with the following *apparent* correlations: the sharp ^1H resonance of "isolated" surface OH groups *appears* to correlate with the ^{29}Si resonance of $=Si(OH)_2$ groups, and the broad ^1H peak of hydrogen-bonded (clustered) surface OH groups appears to correlate with the ^{29}Si resonance of $\equiv Si-OH$. This pattern suggests a surface structure in which there are large hydrogen-bonded clusters of $\equiv SiOH$ groups and isolated islands of $=Si(OH)_2$ groups on the surface.

However, this model is not entirely consistent with the CRAMPS-determined ^1H dipolar-dephasing behavior (*39*), the main basis for distinguishing between the clustered and isolated protons in ^1H CRAMPS spectra. This model is also inconsistent with related ^1H spin-diffusion behavior, as reflected in some preliminary $^1H-^{29}Si$ dipolar-dephasing experiments, ^{29}Si-detected $^1H-^1H$ spin-diffusion results, and ^{29}Si CP–MAS spectra detected in the absence of ^1H decoupling. Such experiments,

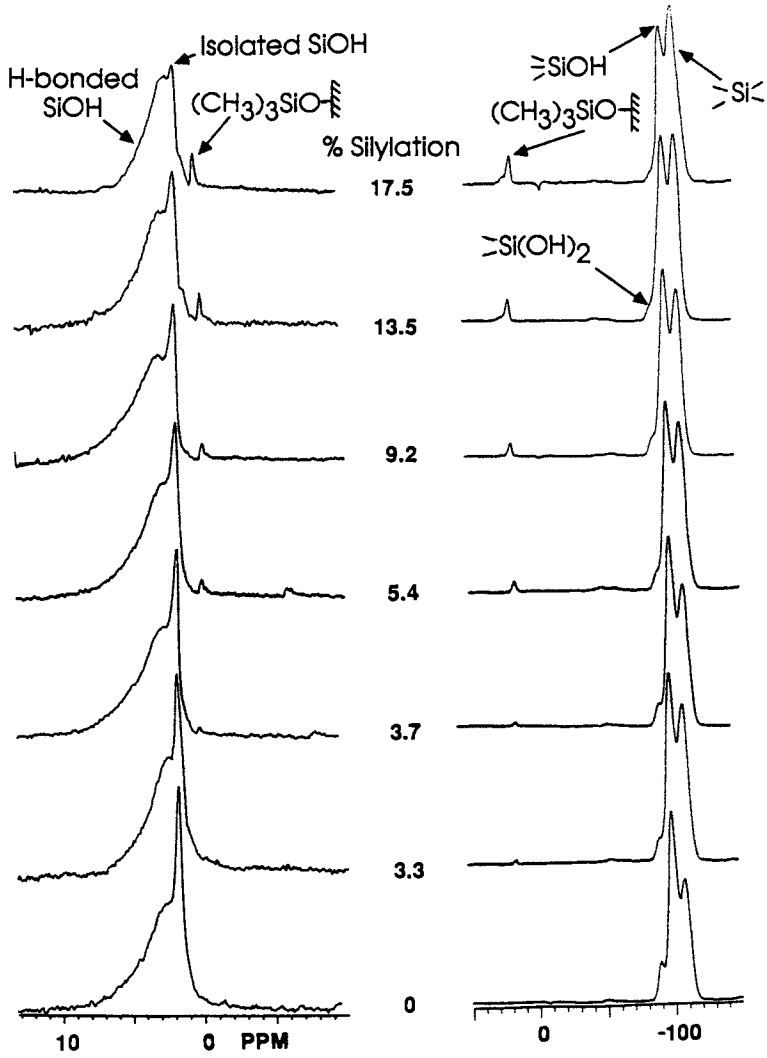

Figure 3. ^{1}H CRAMPS (left) and ^{29}Si CP–MAS spectra (right) of silica gel derivatized by $(CH_3)_3SiCl$ [perdeuterated, except for 1% $(C^1H_3)_3SiCl$]. Loading levels (percent silylation) are shown in the center.

which are reported in detail separately (*41*), indicate that the protons responsible for the broad ^{1}H CRAMPS peak identified with H-bonded silanols are the protons responsible for cross polarization of $=Si(OH)_2$ silicons and some $\equiv SiOH$ silicons. The protons identified as isolated silanols (non-H-bonded) in the ^{1}H CRAMPS spectrum are the protons responsible for cross polarization of the remaining $\equiv SiOH$ silicons in the ^{29}Si CP–MAS spectrum. These correlations, which are more compatible

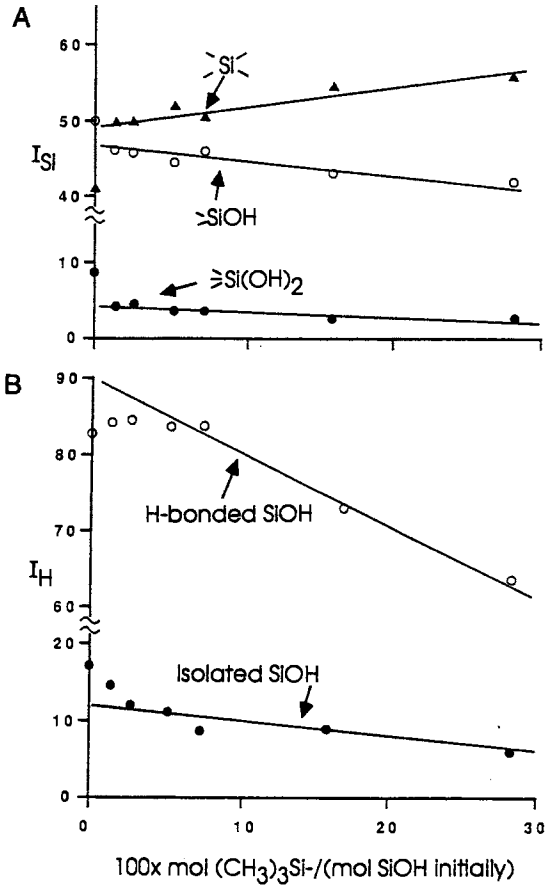

Figure 4. Signal intensities versus silane loading level (percent silylation) in derivatized silica gels shown in Figure 3: A, ^{29}Si CP-MAS intensities of =Si(OH)₂, ≡SiOH, and =Si=; and B, ^{1}H CRAMPS intensities of clustered (H-bonded) and isolated SiOH groups.

with the relevant infrared work (*42–44*), lead to a surface structure that we hypothesize to be composed of H-bonded =Si(OH)₂ and ≡SiOH groups along with other ≡SiOH groups that exist in somewhat more isolated, non-H-bonding sites on the surface. ^{1}H–^{1}H dipolar interactions and spin-diffusion interactions within the H-bonded silanols are much stronger—because of much smaller ^{1}H–^{1}H distances—than within the non-H-bonded ≡SiOH surface moieties. Future avenues that should be explored to clarify these points include ^{1}H multiple-quantum techniques (for estimating H-bonded cluster sizes) and ^{1}H–^{29}Si two-dimensional (2-D) chemical-shift correlation spectroscopy (for verifying or correcting tentative correlations).

Derivatized Silica Surfaces

In the preceding discussion, reference to derivatized silica surfaces focused entirely on the information that the silylation process can shed, via NMR spectroscopy, on the silica surface itself. With $(CH_3)_3SiCl$ as the derivatization agent, the gross nature of the $(CH_3)_3Si–O–$ attachment to the surface, or its behavior on the surface, is largely predictable via induction, without the need for NMR data. For some systems, especially when multifunctional silylation agents (X_nSiR_{4-n}, where $n > 1$) are employed, details of the attachment to the surface and the behavior of the attached moiety on the surface may be much less predictable. An example is provided by silica systems that have been derivatized by the (coupling) agent $(CH_3CH_2O)_3SiCH_2CH_2CH_2NH_2$ (APTS). Figure 5 shows ^{29}Si CP–MAS spectra of two series of APTS-modified silica samples (*24*). The variety of spectral patterns of the $\equiv Si\text{-}CH_2CH_2CH_2NH_2$ silicon resonance in the 45–70-ppm region of the ^{29}Si CP–MAS spectra reveals the range of APTS attachments to the surface and displays the power of ^{29}Si NMR techniques for elucidation of such details.

In contrast, ^{13}C CP–MAS spectra analogous to those in Figure 5 are generally less informative. However, the β-carbon (relative to the NH_2 group) is sensitive to the details of hydrogen bonding or protonation (Brønsted acid–base complex formation) of the NH_2 group at the surface (Figure 6). Of course, the ^{15}N (0.37% naturally abundant) chemical shift of the NH_2 group itself would be expected to be more sensitive to H bonding and protonation than ^{13}C chemical shifts. Figure 7 displays the natural abundance ^{15}N CP–MAS spectra of APTS-derivatized silica gels. The observed spectral differences presumably reflect the relative simplicity of the protonated form and the relatively complex distribution of hydrogen-bonded species present in the other two samples. These preliminary results indicate that the ^{15}N NMR spectroscopy approach is worth pursuing and may warrant the effort that will be required to synthesize the corresponding ^{15}N-labeled samples.

Another type of derivatized silica surface that has received considerable attention is C_{18}-derivatized silica gel; that is, silica gel that has been silylated with reagents such as $Cl(CH_3)_2Si(CH_2)_{17}CH_3$ (*45–51*). This system was studied via ^{13}C NMR (*47*) and ^{2}H NMR spectroscopy (*45*) as a function of surface loading of the C_{18} chains and of certain added liquids. The ability of cross polarization to select static components of a surface derivative relative to more mobile components—which would be emphasized by non-CP (single-pulse) techniques that rely on direct ^{13}C spin-lattice relaxation—can be seen in Figure 8, which provides a comparison between the single-pulse and cross-polarization ^{13}C MAS NMR spectroscopy results on four C_{18}–silica samples. Dramatic differences in line shapes and intensities, which can be interpreted at least qualitatively in terms of

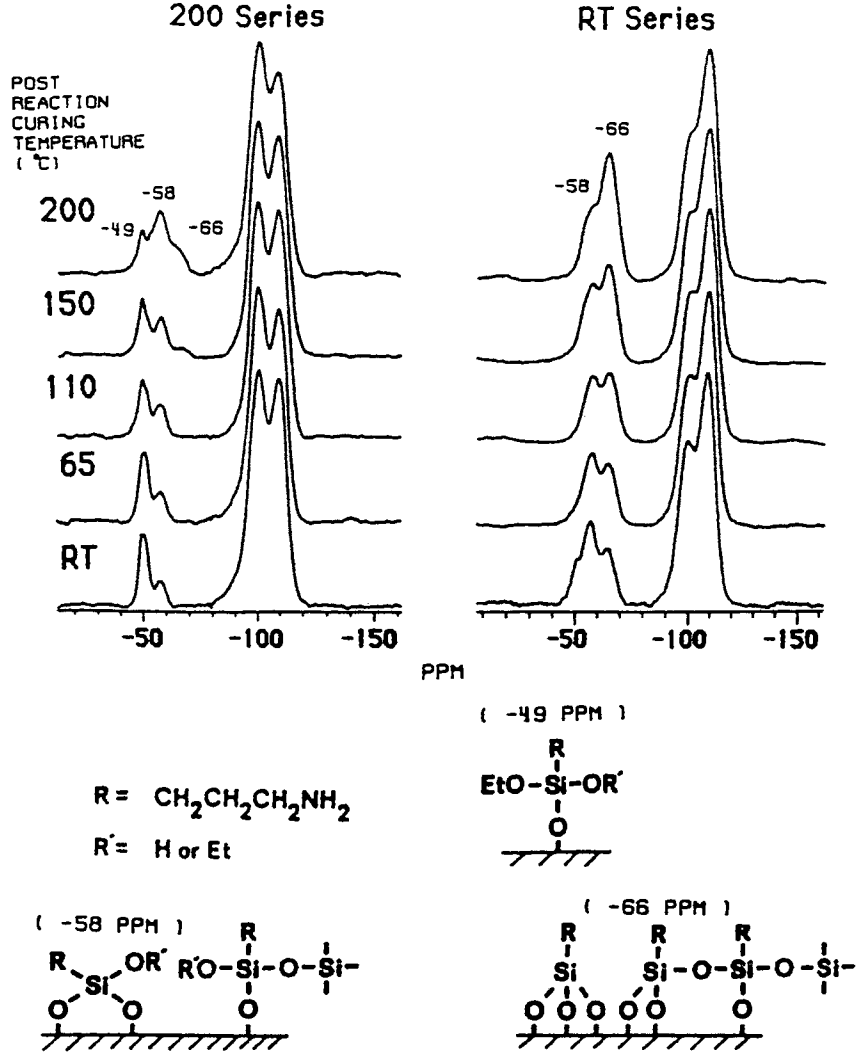

Figure 5. ^{29}Si CP-MAS spectra of APTS-modified silica gels. The spectra on the left and right correspond to silica gels dried under vacuum at 200 °C and room temperature, respectively, prior to reaction in dry toluene. The post-reaction treatment (curing) temperature is shown on the left (RT, room temperature). Structural assignments are given at the bottom. (Reproduced from reference 24. Copyright 1988 American Chemical Society.)

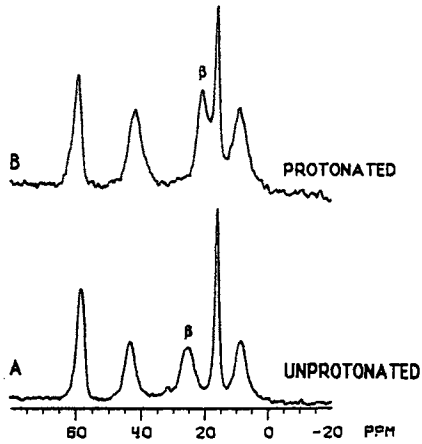

Figure 6. ^{13}C CP–MAS spectra of APTS-modified silica gels (A) and HCl-treated sample (B) (54).

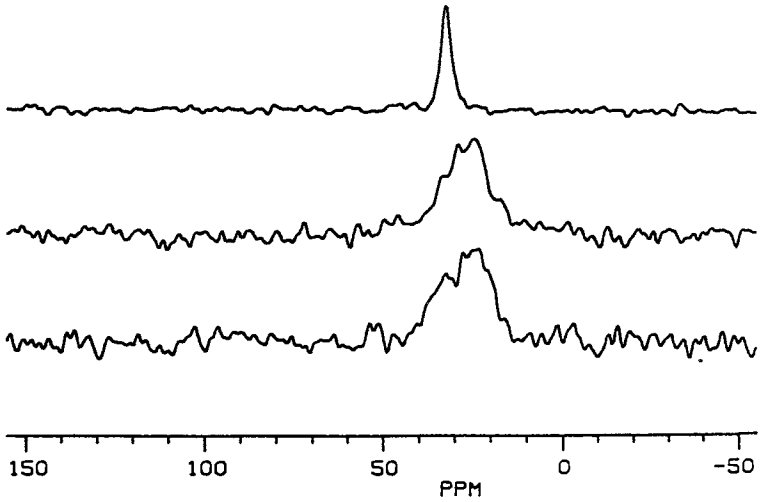

Figure 7. ^{15}N CP–MAS spectra (natural abundance) of APTS-modified silica gels (top) after treatment with H_2SO_4, (middle) untreated, and (bottom) after treatment with 0.1 M NaOH.

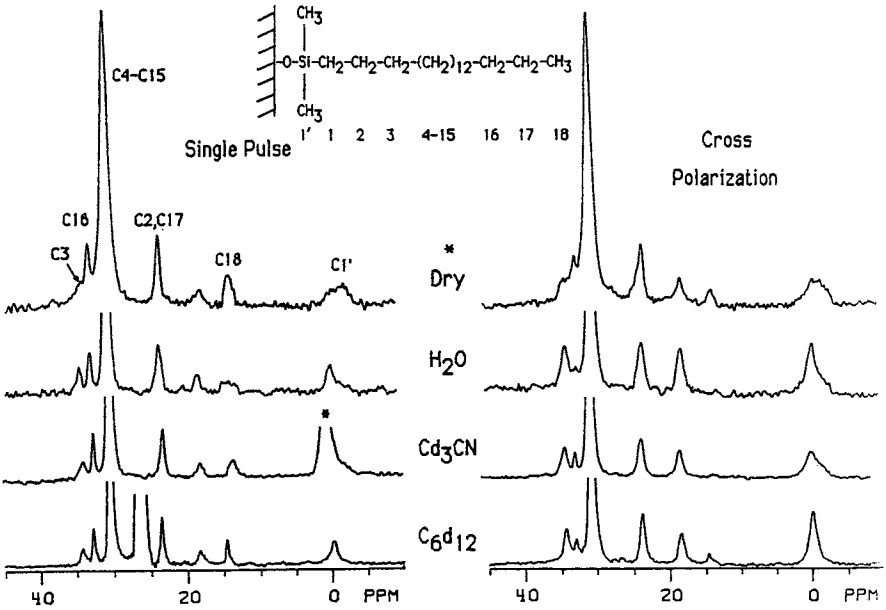

Figure 8. ^{13}C MAS spectra of C_{18}–silica samples, treated with the indicated liquids (55).

local motion within the C_{18} chain, can be noted readily in these comparisons. More detailed information on motion within the C_{18} chains is obtained by wide line ^2H NMR spectroscopy (a technique that does not have high resolution) on C_{18}–silica samples in which deuterium has been selectively substituted for protons. In this approach, the details of which are reported elsewhere (*45*), the line-narrowing effects of motion on the broad, quadrupole-based ^2H NMR line width of a mechanically static sample is modeled theoretically for specific trial motions to elucidate the detailed nature of the motion.

Experimental Details

^{29}Si and ^{13}C NMR measurements were made at 39.7 and 50.3 MHz, respectively, on a drastically modified Nicolet NT-200 spectrometer; a home-built CP–MAS probe with a sealed-tube MAS system based on the Gay design was used (*52*). ^{15}N NMR measurements were made on the same spectrometer at 20.3 MHz with a 2.5-cm^3 large-volume MAS system described previously (*53*). ^1H CRAMPS spectra were obtained at 187 MHz on a rebuilt NT-200 spectrometer described previously (*37, 38*); a probe with a MAS system based on the Gay design was used.

Acknowledgments

The authors gratefully acknowledge partial support of this research by the National Science Foundation (Grant CHE–9021003) and use of the Colorado State University Regional NMR Center (funded by NSF Grant CHE–8616437).

References

1. Mehring, M. *Principles of High Resolution NMR in Solids*, 2nd ed.: Springer-Verlag: New York, 1983.
2. Fyfe, C. A. *Solid State NMR for Chemists*; C.F.C. Press: Guelph, Canada, 1983.
3. Schaefer, J.; Stejskal, E. O. In *Topics in Carbon-13 NMR Spectroscopy*; Levy, G. C., Ed.; Wiley-Interscience: New York, 1979; Vol. 3, p 283.
4. Maciel, G. E. *Science* **1984**, *226*, 282.
5. Maciel, G. E. In *Heterogeneous Catalysis, Proceedings of the Second Symposium of the Industry–University Cooperative Chemistry Program of the Department of Chemistry, Texas A&M University*; Shapiro, B. L., Ed.; Texas A&M University Press: College Station, TX, 1984; pp 349–381.
6. Andrew, E. R. *Philos. Trans. R. Soc. (London)* **1981**, *A299*, 505.
7. Andrew, E. R. *Prog. NMR Spectrosc.* **1971**, *8*, 1.
8. Lowe, I. J. *Phys. Rev. Lett.* **1959**, *2*, 285.
9. Kessemeier, H.; Norberg, R. E. *Phys. Rev.* **1967**, *155*, 321.
10. Sindorf, D. W. Ph.D. Thesis, Colorado State University, 1982.
11. Pines, A.; Gibby, M. G.; Waugh, J. S. *J. Chem. Phys.* **1973**, *59*, 569.
12. Schaefer, J.; Stejskal, E. O. *J. Am. Chem. Soc.* **1976**, *98*, 1031.
13. Maciel, G. E.; Sindorf, D. W. *J. Am. Chem. Soc.* **1980**, *102*, 7606.
14. Maciel, G. E.; Sindorf, D. W.; Bartuska, V. J. *J. Chromatogr.* **1981**, *205*, 438.
15. Sindorf, D. W.; Maciel, G. E. *J. Am. Chem. Soc.* **1981**, *103*, 4263.
16. Sindorf, D. W.; Maciel, G. E. *J. Phys. Chem.* **1982**, *86*, 5208.
17. Sindorf, D. W.; Maciel, G. E. *J. Am. Chem. Soc.* **1983**, *105*, 1487.
18. Sindorf, D. W.; Maciel, G. E. *J. Am. Chem. Soc.* **1983**, *105*, 3767.
19. Sindorf, D. W.; Maciel, G. E. *J. Phys. Chem.* **1983**, *87*, 5516.
20. Linton, R. W.; Miller, M. L.; Maciel, G. E.; Hawkins, B. L. *Surface and Interface Anal.* **1985**, *7*, 196.
21. Miller, M. L.; Linton, R. W.; Maciel, G. E.; Hawkins, B. L. *J. Chromatogr.* **1985**, *319*, 9.
22. Rudzinski, W. E.; Montgomery, T. L.; Frye, J. E.; Hawkins, B. L.; Maciel, G. E. *J. Chromatogr.* **1985**, *323*, 281.
23. Caravajal, G. S.; Leyden, D. E.; Maciel, G. E. In *Chemically Modified Surfaces, Volume 1: Silanes, Surfaces and Interfaces*; Leyden, D. E., Ed.; Gordon and Breach Science Publishers: New York, 1986; pp 283–303.
24. Caravajal, G. S.; Leyden, D. E.; Quinting, G. R.; Maciel, G. E. *Anal. Chem.* **1988**, *60*, 1776.
25. Pfleiderer, B.; Albert, K.; Bayer, E.; Van de Ven, L.; de Haan, J.; Cramers, C. *J. Phys. Chem.* **1990**, *94*, 4189.
26. Akapo, S. O.; Simpson, C. F. *J. Chromatogr. Sci.* **1990**, *28*, 186,
27. Claessens, H. A.; de Haan, J. W.; Van de Ven, L. J. M.; deBruyn, P. C.; Cramers, C. A. *J. Chromatogr.* **1988**, *436*, 345.
28. Gangoda, M.; Gilpin, R. K.; Fung, B. M. *J. Magn. Reson.* **1987**, *74*, 134.

29. Bernstein, T.; Fink, P.; Mastikhin, V. M.; Shubin, A. A. *J. Chem. Soc. Faraday Trans. 1* **1986,** *82,* 1879.
30. Walter, T. H.; Turner, G. L.; Oldfield, E. *J. Magn. Reson.* **1988,** *76,* 106.
31. Timken, H. K. C.; Schramm, S. E.; Kirkpatrick, R. J.; Oldfield, E. *J. Phys. Chem.* **1987,** *91,* 1054.
32. Hunger, M.; Freude, D.; Pfeifer, H.; Bremer, H.; Jank, M.; Wendlandt, K.-P. *Chem. Phys. Lett.* **1983,** *100,* 29.
33. Köhler, J.; Chase, D. B.; Farlee, R. D.; Vega, A. J.; Kirkland, J. J. *J. Chromatogr.* **1986,** *352,* 275.
34. Dec, S. F.; Bronnimann, C. E.; Wind, R. A.; Maciel, G. E. *J. Magn. Reson.* **1989,** *82,* 454.
35. Waugh, J. S.; Huber, L. M.; Haeberlen, U. *Phys. Rev. Lett.* **1968,** *20,* 180.
36. Gerstein, B. C.; Pembleton, R. G.; Wilson, R. C.; Ryan, L. *J. Chem. Phys.* **1977,** *66,* 361.
37. Bronnimann, C. E.; Hawkins, B. L.; Zhang, M.; Maciel, G. E. *Anal. Chem.* **1988,** *60,* 1743.
38. Maciel, G. E.; Bronnimann, C. E.; Hawkins, B. L. *Advances in Magnetic Resonance: The Waugh Symposium*; Warren, W. S., Ed.; Academic Press: San Diego, CA, 1990; Vol. 14, pp 125–150.
39. Bronnimann, C. E.; Zeigler, R. C.; Maciel, G. E. *J. Am. Chem. Soc.* **1988,** *110,* 2023.
40. Bronnimann, C. E.; Zeigler, R. C.; Maciel, G. E. In *Chemically Modified Surfaces, Volume 2: Chemically Modified Surfaces in Science and Industry*; Leyden, D. E.; Collins, W. T., Eds.; Gordon and Breach Science Publishers: New York, 1988; pp 305–318.
41. Chuang, I.-S.; Kinney, D. R.; Bronnimann, C. E.; Zeigler, R. C.; Maciel, G. E. *J. Phys. Chem.* **1992,** *96,* 4027.
42. Peri, J. B. *J. Phys. Chem.* **1966,** *70,* 2937.
43. McDonald, R. A. *J. Phys. Chem.* **1958,** *62,* 1168.
44. Leyden, D. E.; Murthy, R. S. S.; Blitz, J. J.; Atwater, J. B.; Rachetti, A. In *Chemically Modified Surfaces, Volume 2: Chemically Modified Surfaces in Science and Industry*; Leyden, D. E.; Collins, W. T., Eds.: Gordon and Breach Science Publishers: New York, 1988; pp 633–642.
45. Zeigler, R. C.; Maciel, G. E. *J. Am. Chem. Soc.* **1991,** *113,* 6349.
46. Sindorf, D. W.; Maciel, G. E. *J. Am. Chem. Soc.* **1983,** *105,* 1848.
47. Zeigler, R. C.; Maciel, G. E. *J. Phys. Chem.* **1991,** *95,* 7345.
48. Jinno, K. *J. Chromatogr. Sci.* **1989,** *27,* 729.
49. Bayer, E.; Albert, K.; Reiners, J.; Nieder, M.; Müller, D. *J. Chromatogr.* **1983,** *264,* 197.
50. Albert, K.; Evers, B.; Bayer, E. *J. Magn, Reson.* **1985,** *62,* 428.
51. Bayer, E.; Paulus, A.; Peters, B.; Laupp, G.; Reiners, J.; Albert, K. *J. Chromatogr.* **1986,** *364,* 25.
52. Gay, I. D. *J. Magn. Reson.* **1984,** *58,* 413.
53. Zhang, M.; Maciel, G. E. *Anal. Chem.* **1990,** *62,* 633.
54. Caravajal, G. S. Ph.D. Thesis, Colorado State University, 1986.
55. Zeigler, R. C. Ph.D. Thesis, Colorado State University, 1989.

RECEIVED for review November 26, 1990. ACCEPTED revised manuscript December 19, 1991.

15

New Separation Methods for Characterizing the Size of Silica Sols

J. J. Kirkland*

DuPont, Central Research and Development Department, Experimental Station, P.O. Box 80228, Wilmington, DE 19880–0228

Both instrumental and chemical methods traditionally are used for characterizing the size of silica sols. Instrumental methods include electron microscopy, light scattering, turbidity–absorbance, centrifugation, and low-angle X-ray scattering. Chemical procedures involve gas adsorption, titrations, preferential precipitation, and rate of particle dissolution. Recent development of methods based on high-resolution separations has greatly widened the scope, accuracy, and precision of silica sol characterizations. These new methods include sedimentation field-flow fractionation (FFF), flow FFF, size-exclusion chromatography, hydrodynamic chromatography, and capillary-zone electrophoresis. Certain techniques (e.g., sedimentation FFF) permit the accurate determination of particle-size distributions, providing information that is not available by established characterization methods. The advantages and limitations of these new separation methods for characterizing the size of silica sols and other inorganic colloids are highlighted.

THE CHARACTERIZATION OF COLLOIDAL SILICA has been the subject of numerous studies involving both physical and chemical methods. Iler (*1*) summarized many of the available methods, with particular emphasis on chemical approaches. Other more recent reviews (*2–4*) featured instrumental methods that are useful for characterizing silica sols and other colloids. This chapter describes some of the relatively new separations

*Current address: Rockland Technologies, Inc., 538 First State Boulevard, Newport, DE 19804.

0065–2393/94/0234–0287$08.36/0

methods for characterizing silica sols. The merits and limitations of these methods are summarized so that the potential user can critically evaluate the capability of each approach for a projected application.

Sedimentation Field-Flow Fractionation

This method (SdFFF) is one of a family of field-flow fractionation (FFF) methods that were originally devised by Giddings at the University of Utah (*5*). Although the potential of SdFFF was predicted more than 20 years ago (*6*), only in the past few years has SdFFF become a useful laboratory tool. The emergence of commercial instrumentation has opened up the potential of this powerful tool for characterizing silica sols and a wide range of other colloidal particles, as well as soluble macromolecules (*7–14*).

SdFFF separations are carried out in very thin, open channels shaped like a belt or ribbon and suspended in a centrifuge. A schematic of a SdFFF apparatus is shown in Figure 1. Liquid mobile phase is precision-pumped through a sampling-valve loop containing the liquid mixture to be analyzed. The sample is swept from this sampling loop through a rotating seal into the channel within the centrifuge. Following separation in the channel, the individual sample components flow back through the rotating seal into a detector (typically a turbidimeter) that senses the particles. A computer controls the pump output, sample valve actuation, and rotor speed. It also acquires data from the detector and transforms this output to a true concentration profile. In addition, calculations and graphics are provided for displaying data on particle size and particle-size distribution.

The development of a typical SdFFF separation is illustrated in Figure 2. With the liquid mobile phase stopped and the channel rotating at an appropriate speed, the sample mixture is injected into the channel (Figure 2a). The channel is rotated in this mode for a "relaxation" or pre-equilibration period that allows the particles to be forced toward the accumulation wall at approximately their sedimentation equilibrium position. Sample particles that have a density greater than the mobile phase are forced toward the outer wall. Diffusion opposite to that imposed by the centrifugal force field causes the particles to establish a specific mean-layer thickness near the accumulation wall as a function of particle mass. (Typically, the average distance of the particle "cloud" from the accumulation wall is about 5–20 μm.) Liquid mobile phase then is flowed continuously through the channel with a characteristic bullet-shaped laminar flow profile (Figure 2b). Solvent and particles that are unaffected by the centrifugal external force field are intercepted by the average of all flow streams and elute first from the channel in one channel volume ("dead" volume). Small particles are engaged by faster flow stream more quickly than larger particles and are eluted first (Figure 2c). Larger particles near the wall are intercepted by slower flow streams and are

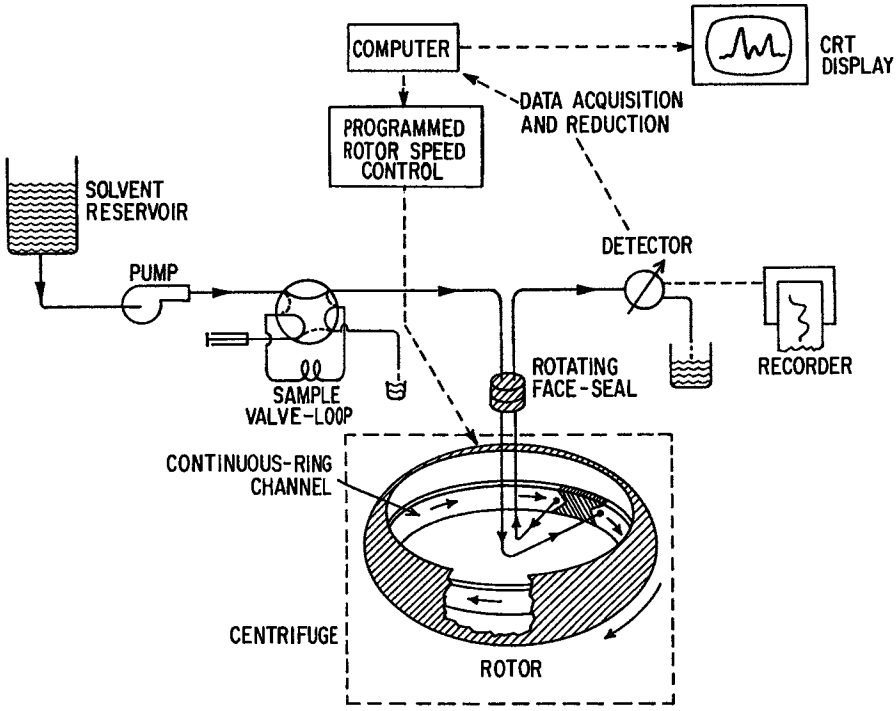

Figure 1. Schematic of SdFFF equipment. (Reproduced with permission from reference 36. Copyright 1982.)

eluted later (Figure 2d). Thus, particles elute from the channel in order of increasing effective mass.

The resulting fractogram provides information on the masses of the sample components by means of quantitative relationships describing SdFFF retention (5). Appropriate computer software permits the calculation of particle-size averages and particle-size distribution for the separated sample.

Force-field programming commonly is used in the SdFFF characterization of many colloidal particles to ensure that the entire particle-size distribution can be described in a convenient analysis time (*10, 15*). Constant force-field operation provides for the highest resolution of particles in the sample, with resulting highest precision. However, this mode of operation does not permit the rapid optimization of operating parameters for analyzing many samples. Also, characterization of samples with wide particle-size distributions is difficult with constant force-field operation. Force-field programming removes these limitations and provides a convenient and practical compromise for most applications.

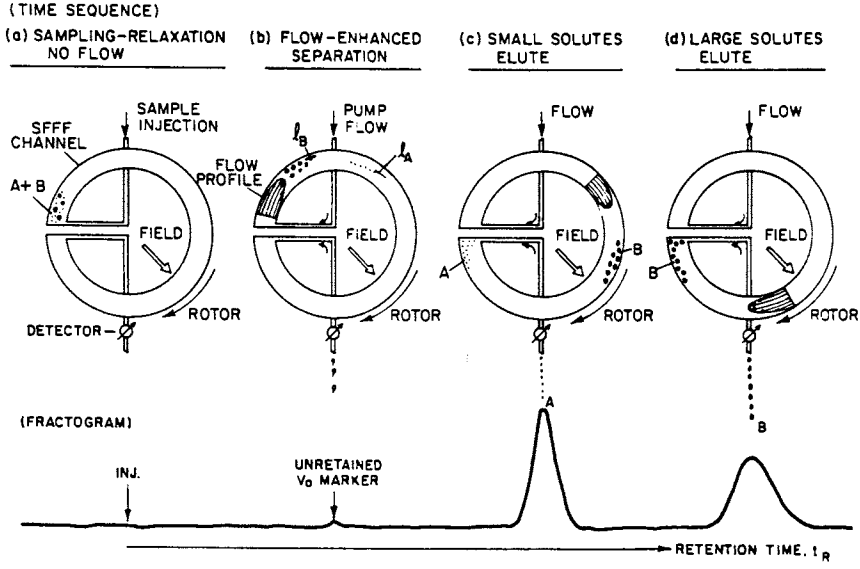

Figure 2. Development of a SdFFF separation. (Reproduced with permission from reference 36. Copyright 1982.)

A convenient and accurate method of force-field programming in SdFFF uses a time-delayed exponential decay (TDE–SFFF) procedure (*9*, *10*, *15*). In this method, mobile-phase flow is initiated after sample injection, and the initial force field is held constant for a time equal to τ, the time constant of the subsequent exponential decay. After this delay, the force field is decayed exponentially with a time constant τ. In the TDE–SFFF mode, a simple log-linear relationship is obtained with both particle mass (and size) as a function of retention time. This simple relationship permits a convenient calculation of the quantitative information desired for the sample.

An example of the use of the TDE–SFFF method for characterizing a silica sol sample is shown in Figure 3. The upper plot show the response of the turbidimetric detector as a function of separation time. The middle plot is the differential curve. Because the response of the turbidimetric detector is particle-size dependent, the detector output signal is transformed with known, quantitative light-scattering relationships to produce a plot of the relative concentration as a linear function of particle diameter. To the left of the bottom plot are various particle-size averages that were calculated for this sample. The weight- and number-diameter averages of 21.5 and 20.0 nm, respectively, indicate that this silica sol sample had a narrow size distribution (polydispersity of 1.075).

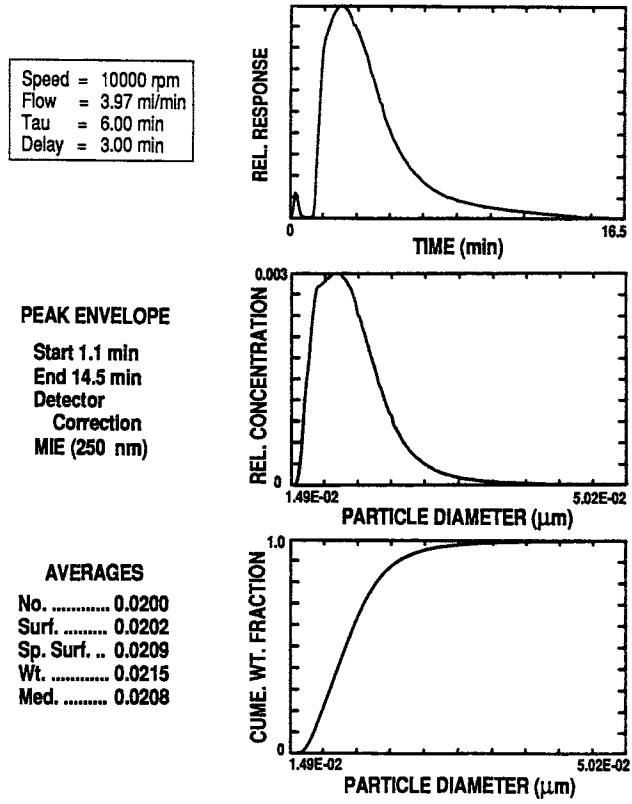

Figure 3. TDE–SFFF analysis of silica sol sample:mobile phase, 1 mM ammonium hydroxide; initial rotor speed, 10,000 rpm; mobile-phase flow rate, 3.97 mL/min; delay, 3.00 min; exponential decay time constant, 6.00 min; sample, 0.50 mL, 0.67%; and detection, UV, 220 nm.

Selecting the mobile-phase carrier is critical in characterizing silica sols by SdFFF. To prevent aggregation or particle flocculation, the pH should be in the range of 8–9, and the ionic strength should be low, generally <0.05. A convenient mobile phase is 1 mM ammonium hydroxide, which provides the proper pH (~8) and ionic strength. In addition, the positively charged ammonium ions adsorb to the negatively charged silica surface, so an environment that retards particle aggregation is created. Other satisfactory mobile phases include dilute organic buffers, for example, those containing ethanolamine or TRIS (tris(hydroxymethyl)aminomethane).

Advantages of SdFFF include accurate particle size distributions without the need for standards. Calculations require that the density of the colloid be known, although accurate and precise measurement of particle

density can also be performed by SdFFF if required (*16, 17*). SdFFF is capable of characterizing silica sols in the 10–1000-nm range. Particle distributions of almost 2 orders of magnitude can be measured in a single analysis by using programmed force-field methods.

The high resolution of SdFFF permits excellent discrimination between particle sizes. Narrow particle-size distributions with a 10–15% difference in size produce bands that can be resolved to baseline. This high level of resolution produces accurate size measurements. Computer-controlled SdFFF instruments are capable of data with excellent reproducibility—results with < 5% deviation (relative) are common. A typical analysis time for a silica sol is about 0.5 h. The SdFFF method can be applied to a wide range of colloidal particles, both inorganic and organic.

The SdFFF method is handicapped only by the somewhat high cost of equipment ($50,000–$100,000) and the need of the operator to acquire expertise that is not common to other more traditional instrumental methods. (Commercial equipment is available from Electronic Instruments and Technology, Inc., Sterling, VA, and FFFractionation, Inc., Salt Lake City, UT).

Flow Field-Flow Fractionation

This method (FlFFF) is another member of the field-flow fractionation family, with measurement capabilities somewhat like those of SdFFF (*18*). The basic field-flow fractionation separation process is retained in this method. Particles separate because they are intercepted by different flow stream velocities near the accumulation wall. However, in this FFF method, particles equilibrate at distances from the wall strictly as a function of their size (Stokes radius). The nearness to the wall is a balance of the cross flow in the channel pushing particles toward the wall and normal diffusion tending to move them away.

FlFFF separations are usually performed in thin channels constructed with flat beds. Figure 4 shows a schematic of a symmetrical channel (*19*). In this design, the force field is created by flowing a liquid across the channel perpendicular to the normal flow down the channel. This flowing is accomplished by using semipermeable membranes as both channel walls—solvent can flow through the membranes, but particles are retained within the channel for the separation. The remainder of the apparatus is quite similar to that previously described for SdFFF. Sample loading and detection is performed in the same manner.

A more recent and generally more advantageous design is an asymmetrical channel, shown schematically in Figure 5 (*20*). In this design, a single semipermeable membrane serves as the accumulation wall. A flat glass plate rather than a membrane is used at the top of the channel. The force field is again created by flow through the bottom membrane, but here the

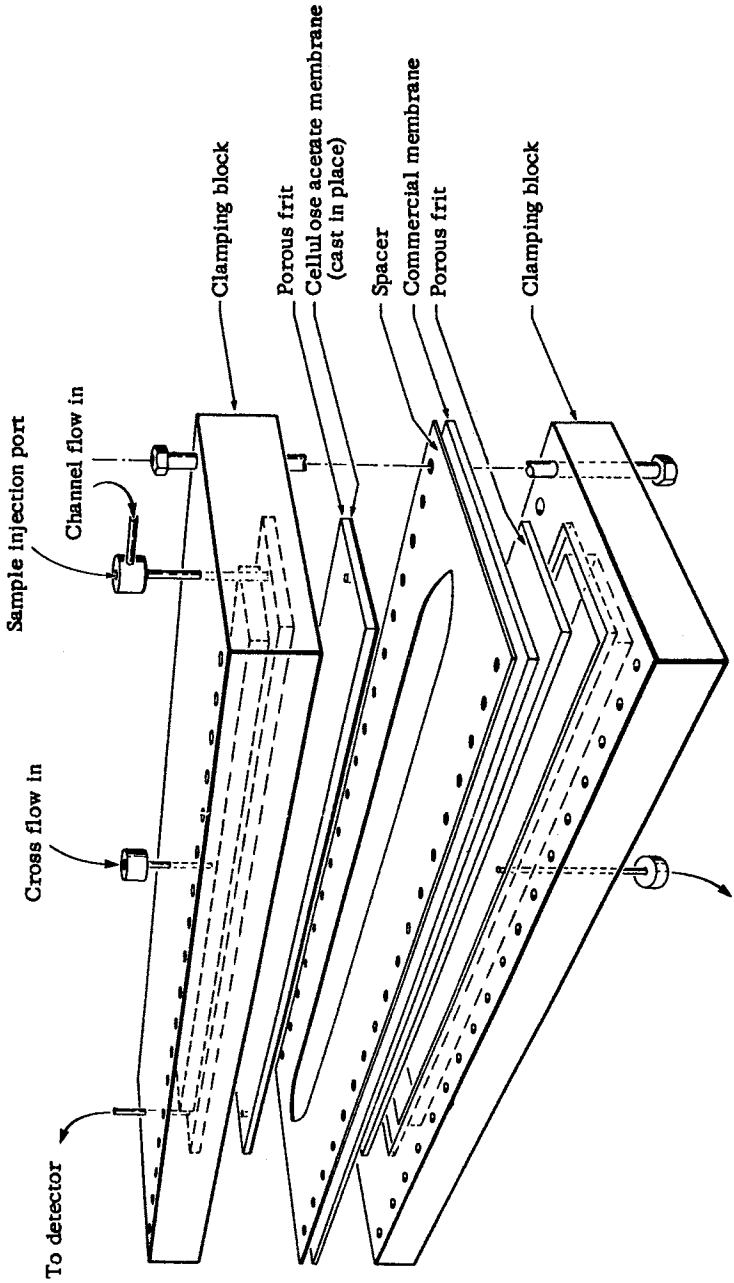

Figure 4. Symmetrical channel for FlFFF. (Reproduced with permission from reference 19. Copyright 1980.)

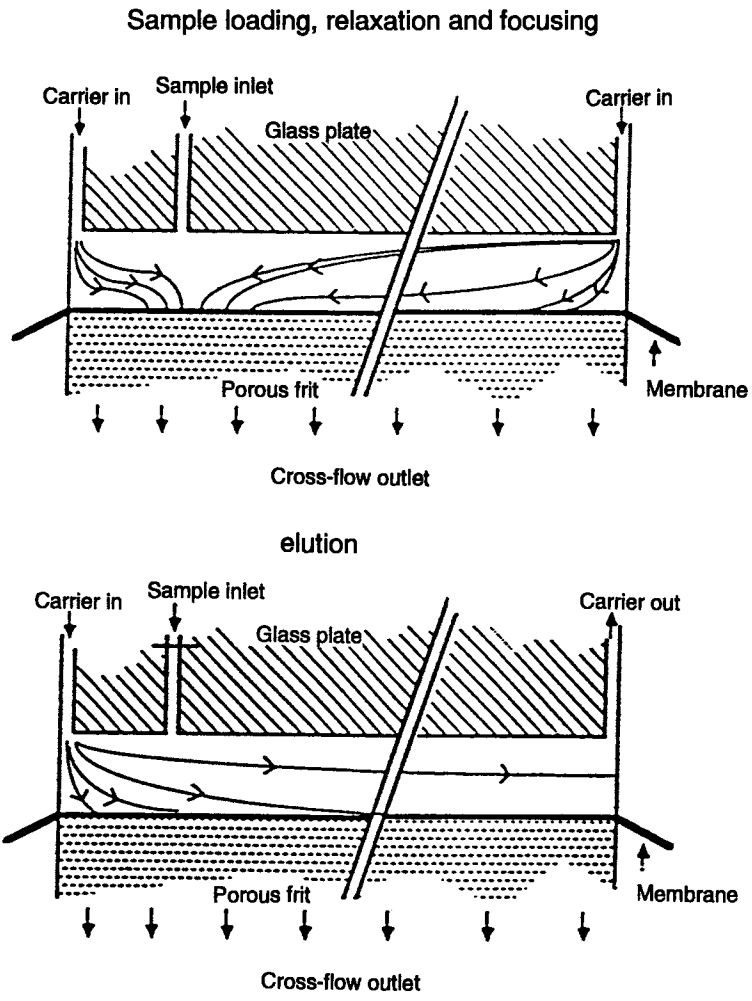

Figure 5. Asymmetrical channel for FlFFF. (Reproduced with permission from reference 20. Copyright 1989.)

flow velocity down the channel is asymmetrical. As a result of the mobile-phase carrier liquid being introduced at one end, the velocity of this liquid decreases as it proceeds down the channel. This change in mobile-phase carrier velocity somewhat complicates the retention theory for particles, but quantitative relationships for calculating particle size still are available (*21*).

A specific advantage of the asymmetrical channel design in FlFFF is that the injected sample can be prefocused into a very sharp band before

separation. The result of this band sharpening is higher separation resolution and improved accuracy of particle-size measurement. This band prefocusing step is schematically shown in the upper plate of Figure 5. With no flow, the sample is injected through a port slightly downstream from the incoming mobile phase. With suitable valves, carrier liquid is then pumped into both ends of the channel at flow rates appropriate to focus the normally diffuse sample in a narrow band slightly below the injection port. Flow is then reinitiated only on the inlet of the channel to carry out the separation in the normal fashion, as shown in the bottom plate of Figure 5.

Particle-size calculations are performed with quantitative relationships involving observed particle retention as a function of known experimental parameters (*21*). The fundamental calculated result of this retention is the diffusion coefficient distribution of the colloidal sample. Particle-size distribution can then be calculated; spheres are assumed with the relationship

$$d_p = \frac{2RTt_R}{(W^2N\pi\eta)\ \ln\{[z/L - (V_c + V_{out})/V_c]/[1 - (V_c + V_{out}/V_c]\}} \quad (1)$$

where d_p is the particle diameter, R is the gas constant, T is absolute temperature, t_R is the retention time of the particle, W is the channel thickness, N is Avogadro's number, η is the viscosity of the mobile phase, z is the focusing distance from the channel inlet, L is the channel length, V_c is the mobile-phase flow rate across the channel, and V_{out} is the flow rate out of the channel.

Figure 6 (*22*) shows the separation of a silica sol mixture by a symmetrical-channel FlFFF with a programmed (exponentially decayed) force-field technique. The advantage of this method is that a wide range of particle sizes can be accessed in a practical working time in a single experiment. Resolved bands for the individual narrow size-distribution silica sols in Figure 6 were obtained for this mixture under the operating conditions used. Also given are differential and cumulative particle-size distribution plots for the middle-sized component of this mixture, with a weight average of 0.21 μm and a polydispersity of 1.22 for this individual silica sol.

The advantages and limitations of FlFFF for characterizing colloids are quite similar to those described for SdFFF. Accurate particle size and particle-size distributions can be obtained without the need for standards. A range of particle sizes of about 10–1000 nm can be characterized in 0.5–1 h. An optimized FlFFF separation provides resolution and particle discrimination similar to that of SdFFF, with good long-term reproducibility. FlFFF has a somewhat wider range of applicability than SdFFF. Soluble organic macromolecules down to about 5000 daltons can be characterized by FlFFF, as well as particulates of many kinds.

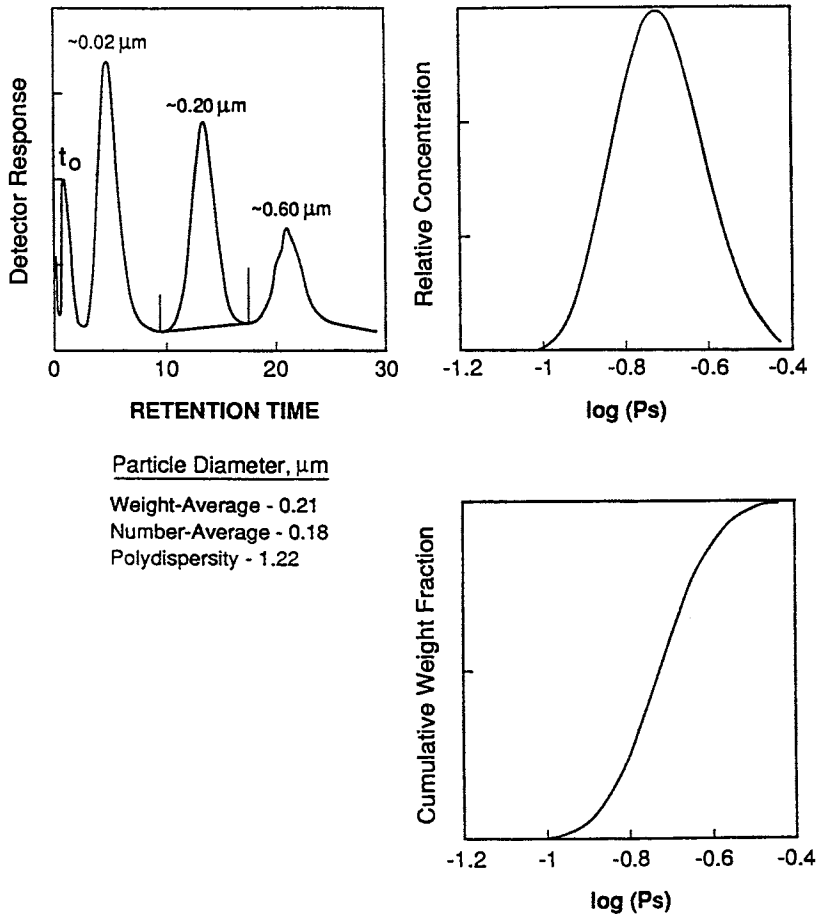

Figure 6. Separation of silica sol mixture by symmetrical-channel FFF with an exponentially decayed cross-flow force field. Retention time is given in minutes; Ps is the particle size. (Reproduced with permission from reference 22. Copyright 1992.)

Apparatus cost of FlFFF is somewhat less than that for SdFFF. Some special expertise is required for effective execution of the method. (Commercial equipment for FlFFF is now available from FFFractionation, Inc., Salt Lake City, UT.)

Size-Exclusion Chromatography

This characterization method (SEC) is effective and relatively simple for silica sols and other colloids. This technique is commonly used for

determining the molecular-weight distribution of a wide range of synthetic and natural macromolecules (23). However, its application for characterizing colloids has not been widely practices. SEC has been utilized to determine the particle-size distribution of various polymer lattices, but few applications of the method for characterizing silica sols have been reported (*24*, *25*).

The basic principle of SEC separations is illustrated in Figure 7. Separations are performed in a column packed with particles having pores mostly of a predetermined single size. A carrier mobile phase is passed through this bed so that liquid fills the pores inside and outside of the bed structure. As a mixture of colloidal particles passes through the packed bed, all colloids that are too large to enter the pores within the particles elute from the column first as a single band at the total exclusion volume. Intermediate-sized colloids (B in Figure 7) enter the pores and are retained according to the volume that can be accessed by the colloid—the smaller the colloid, the larger the volume that can be accessed within the pores and the more retained is the colloid (A in Figure 7). Solvent and very small colloids can access essentially all of the volume within the pores. These materials are most retained and elute last in the chromatogram as a single peak at the total permeation volume of the column. Thus, the fractionation range of the column is dictated by the size of the pores. All materials elute between the total exclusion and total permeation volumes, with fractionation occurring only in intermediate-volume selective-permeation range.

The apparatus used for SEC is relatively simple isocratic high-performance liquid chromatography (HPLC) equipment, as shown in Figure 8. The principal components are a precision high-pressure solvent delivery system, detector, and a column with particles having appropriate pore size. Detection is conveniently accomplished with a UV photometer or spectro-

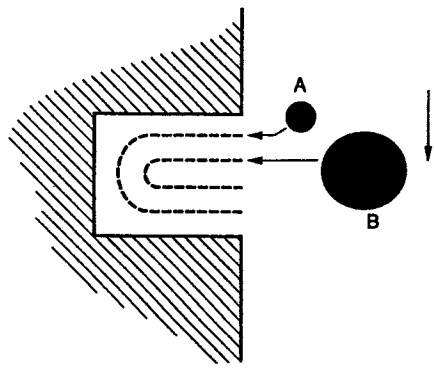

Figure 7. Size-exclusion fractionation within a single pore.

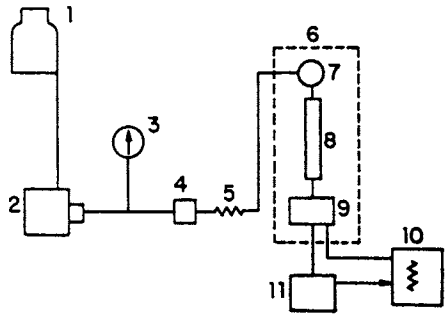

Figure 8. Schematic of typical apparatus for SEC: 1, mobile-phase reservoir; 2, solvent metering pump; 3, pressure gauge; 4 and 5, pulse damper; 6, thermostat; 7, sample injection valve; 8, SEC chromatographic columns; 9, detector; 10, recorder; and 11, computer.

photometer acting as a turbidimetric device. Alternatively, other units such as a light-scattering detector, densimeter, or refractive index detector can be used for many applications. Porous particles for the columns can be semi-rigid polystyrene–divinylbenzene (*24*) gels or rigid, porous silicas (*25*).

Quantitation of silica sol sizes is accomplished by means of a calibration plot. Theory predicts and experiments confirm a linear plot of the log of the particle diameter versus the retention (or elution) time of the colloid. This straight-line relationship is seen in the data in Figure 9 for a series of silica sols in the 8–25-nm range. Silica sols characterized by SdFFF were used as "standards" for this calibration plot. The column used for these separations contained porous spherical silica particles that had surfaces covalently coated with "diol" silane groups.

To determine the size of unknown silica sols with relatively narrow distributions, the retention time of the band for an unknown sample is compared to a peak-position calibration plot such as that shown in Figure 9. Just as for the determination of molecular weight for polymers, broad distributions of silica sols can be measured with appropriate software by using known calibration methods involving peak positions or by using known standards with broad distributions (*26*). However, commercial software for specifically characterizing silica sols and other colloids is apparently not yet available.

Selection of the mobile phase is critical in the characterization of silica sols by SEC. As with the other separation methods, pH should be slightly basic, and low ionic strength must be used to prevent particle aggregation. In addition, the mobile phase must interact with the surface of the packing-particle pores to neutralize undesirable charge effects. Negatively charged surfaces within the pore can result in ion-exclusion effects whereby

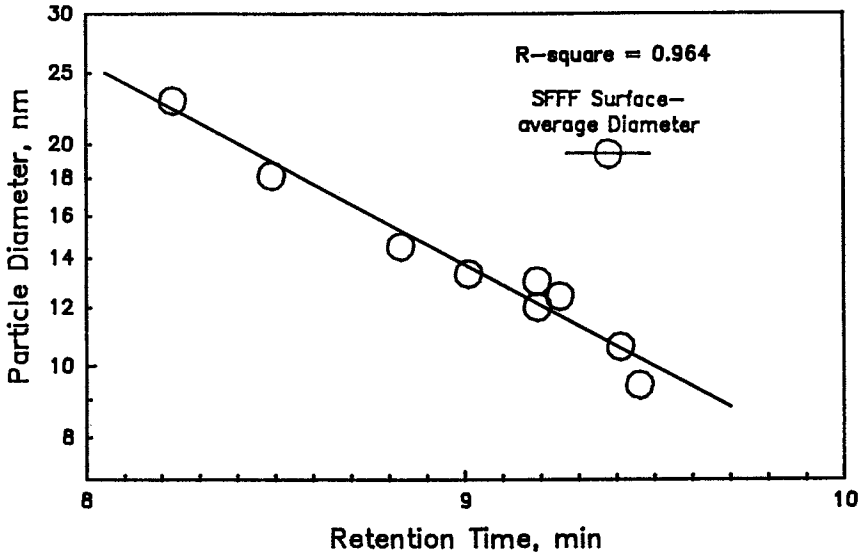

Figure 9. Size-exclusion calibration for silica sols: column, two 25 × 0.49 cm Synchropak-1000; mobile phase, 5 mM triethanolamine, pH 7.5; flow rate, 0.50 mL/min; sample, 0.020 mL, 0.6% in mobile phase; and UV detector, 240 nm.

negatively charged silica sols are unable to enter the pores for the desired size-exclusion process. Positively charged pore surfaces can result in irreversible retention of negatively charged colloids. For the data in Figure 9, 5 mM triethanolamine at pH 7.5 was found satisfactory. This mobile phase apparently levels out undesirable electrostatic effects so that the desired SEC mechanism can occur with this system.

Precision of the SEC measurement of silica sols can be improved by using an internal standard marker in the sample injected into the column for analysis. A totally permeating species such as potassium dichromate is convenient for this purpose. The marker serves to compensate for retention variations that can occur because of changes in flow rate, temperature, and other effects. With an internal retention marker, calibration and measurements are made with R_f values instead of retention times, as illustrated by the graph in Figure 10. R_f values are merely the ratios of the retention time of the marker to the retention time of the colloid peak, $t_{R,marker}/t_{R,colloid}$. For the data in Figure 10, a column of bare silica with 100-nm pores was used with a mobile phase of 0.01 M TRIS buffer, pH 7.0. A SEC chromatogram of a 32-nm silica sol (value from SdFFF) with the internal marker is shown in Figure 11. With this column and the R_f method, silica sols in the 10–50-nm range can be measured with reproducibilities of about ±2 nm (2σ).

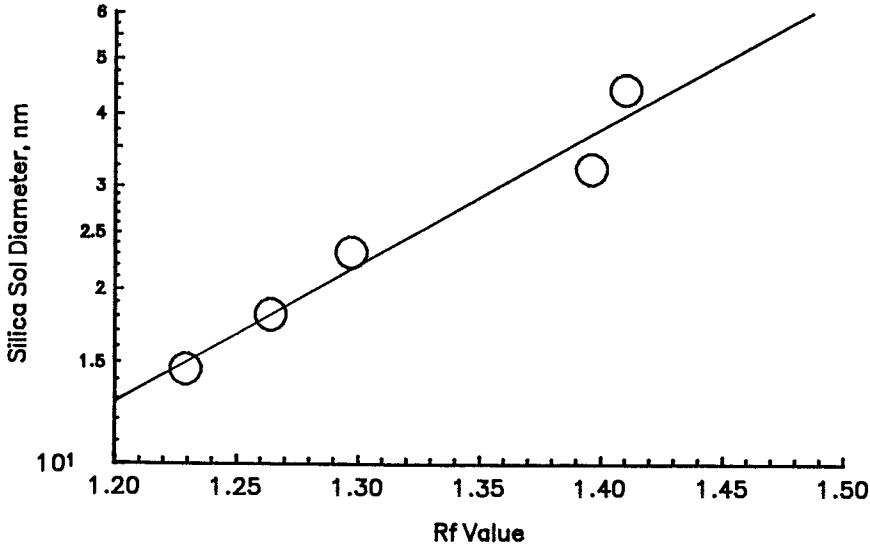

Figure 10. SEC calibration for silica sols, R_f method: column, two 25 × 0.62 cm Zorbax PSM-1000; mobile phase, 0.01 M TRIS, pH 7.0; flow rate, 1.0 mL/min; sample, 0.020 mL, 0.67% in mobile phase; and UV detector, 240 nm.

A strong positive feature of SEC is that instrumentation is readily available in the form of HPLC apparatus. No special experience is needed for those acquainted with this widely practiced method. Relatively unskilled operators can quickly learn to perform the analysis satisfactorily. Average particle sizes are quickly measured by the peak-position method. However, it is also feasible to determine particle-size distributions if appropriate computer software is available. Separation times are predetermined, because all species elute between the total exclusion and total permeation volumes (provided the desired SEC process is the only retention). No special method development is required, other than ensuring that the proper mobile phase–stationary phase combination is selected. Particle diameter is directly a function of retention or elution times.

A limitation of the SEC method is that standards are required. The method has lower resolution and particle discrimination than the FFF methods discussed earlier; poorer analysis precision results. A distinct limitation of the SEC method is that silica sol particles larger than about 60 nm cannot be analyzed by this approach. Silica sol particles of this size can enter larger-sized pores, but are partially or totally retained within the column. Presumably, particles of this size have such poor diffusion that attractive interaction with the pore walls (by van der Waals or other forces) cannot be overcome. Although silica particles smaller than about 2 nm can

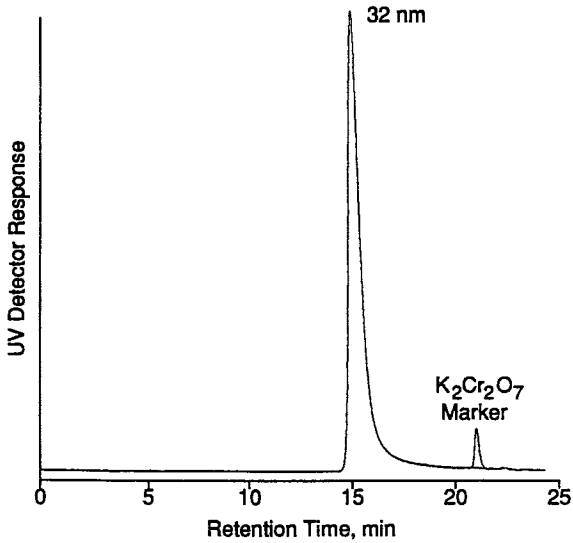

Figure 11. SEC calibration chromatogram of silica sol with marker; conditions as in Figure 10.

undergo the desired SEC process when columns of the correct pore size are used, such sols are difficult to detect by turbidimetry. Therefore, this level represents a practical lower limit of silica sol characterization by most separation methods. As noted earlier, for successful SEC the mobile phase must be carefully chosen, as for all of the characterization methods based on separations.

Hydrodynamic Chromatography

This separation method (HDC) was developed within the Dow Chemical Company in the early 1970s (*27*). This method has been utilized for determining the particle size of many polymer lattices (*27*, *28*), but it also can be used for characterizing a wide range of silica sols. Separation by the hydrodynamic effect is illustrated in Figure 12 (*29*). Colloids flowing between particles in a packed bed or within a capillary are subjected to different velocities as a result of the Poiseuille-like flow of the liquid mobile phase. Colloid particles are excluded from the wall interface, where the fluid velocity is lowest. Thus, larger colloid particles are intercepted by faster flow streams, have a higher mean velocity, and elute more quickly from the column compared to smaller colloids.

Equipment and technique for HDC of silica sols are essentially the same as for SEC. The difference is that the packed bed of the separating column is composed of nonporous, rather than porous, particles. Typically,

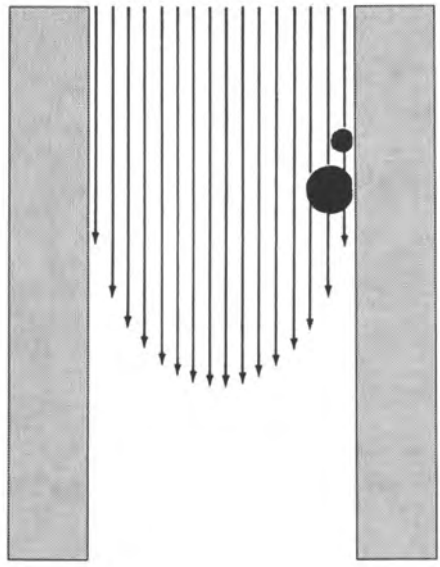

Figure 12. Hydrodynamic effect. (Reproduced from reference 29. Copyright 1982 American Chemical Society.)

these particles are polystyrene-based beads, but glass or dense silica beads also are effective. Alternatively, a long, narrow capillary can be used as the separating medium (*30*).

Relatively small fractionating volumes are associated with HDC systems. Therefore, the R_f market method (*27*) typically is used to compensate for possible variations in the operating parameters during the separation. Figure 13 shows a HDC calibration plot that was obtained by the marker method. The arbitrary log sol diameter versus R_f plot produced a linear relationship for this series of 40–600-nm SdFFF-characterized sols as standards. With this particular HDC system, silica sols can be routinely measured with precisions of about ±15% (relative) with the peak-position calibration method. This precision level is a direct result of the relatively poor resolution of HDC separations.

Silica sol samples with wide particle-size distributions also can show a bias toward particle sizes larger than actual, largely because turbidimetric detectors respond much more strongly to larger sol sizes. As a result, the apex of the sol peak appears to be at a smaller retention time than actually is the case. This phenomenon causes the calculated size value to be somewhat higher than actual for sols that do not have a narrow size distribution.

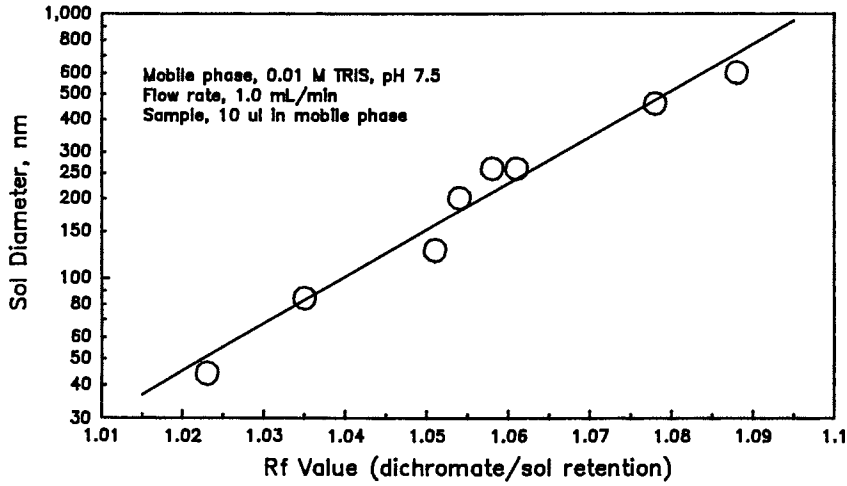

Figure 13. Hydrodynamic calibration for silica sols: column, two 25 × 0.94 cm columns of 20-μm glass beads; marker, 1 mM potassium dichromate; sample, 0.40% in mobile phase; and UV detector, 260 nm.

With the HDC method, no special instrumentation or experience is needed for the simple peak-position method, and elution of the sol is directly correlated to particle size. Good repeatability for the peak-position method is experienced if an internal marker is used. HDC can be used with silica sols in the range of about 6–600 nm. The upper limit of sol size has not been clearly defined. However, experiments have suggested that sols ≥600 nm do not completely elute from a packed bed of 20-μm glass beads.

The utility of HDC is somewhat limited by the relatively poor resolution and particle-size discrimination of the method, which restrict the precision of HDC in silica sol characterization. In principle, accurate particle-size distributions of silica sols also are possible with the HDC method. However, for such characterizations special software with corrections for the extensive band dispersion in HDC is required, along with a suitable band deconvolution method (*28*). Commercial HDC apparatus with this sophisticated software package apparently is no longer available. Standards are generally required, although quantitative retention relationships have been reported for capillary HDC systems in characterizing polymers (*37*). As with all of the other separation methods, careful selection of the mobile phase is required in HDC. Mobile phases generally are the same as those used for the FFF methods and SEC.

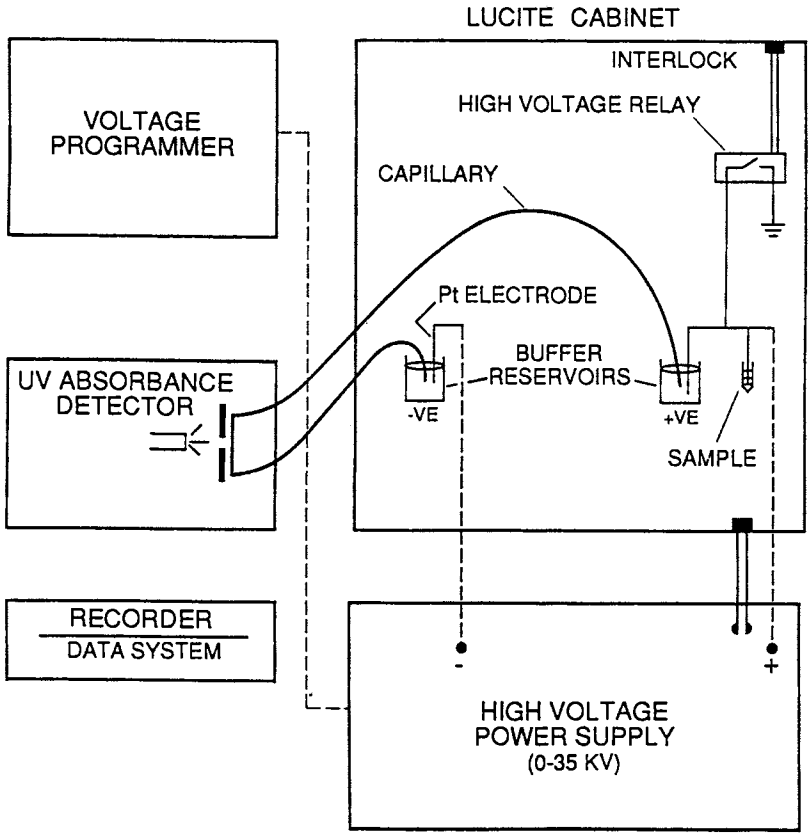

Figure 14. Schematic of CZE apparatus. (Reproduced from reference 34. Copyright 1988 American Chemical Society.)

Capillary-Zone Electrophoresis

This new separations method (CZE) is rapidly gaining distinction for separating a wide range of ionizable species because of its very high resolution (*32*). The usefulness of CZE for characterizing silica sols has been explored (*33*).

A schematic of a simple CZE apparatus is shown in Figure 14 (*34*). In CZE, small fused silica or glass capillaries 50–100 μm in diameter are used as the separating medium. Capillary forces at the interface between the buffer and the capillary wall stabilize a liquid buffer in which the separation occurs, eliminating the need for a semirigid gel that is used in conventional slab-gel electrophoresis. The very narrow capillaries permit the use of high voltages (30 kV) with resultant small electrical currents. Heating is rapidly dissipated from the narrow capillary, so rapid separa-

tions are possible. In addition, because the process occurs in a UV-transparent capillary, a portion of the capillary can be used as an optical flow cell. Thus, on-line detection of separated bands can be accomplished by turbidimetry and other optical methods.

Migration of a charged species such as a silica sol down a capillary in CZE is described by the expression

$$v = \mu V/L \tag{2}$$

where v is the migration velocity, μ is the electrophoretic mobility of the charged species, V is the total applied voltage across the capillary, and L is the capillary length (*32*). The popularity of the CZE method is based on its potential to develop very large plate numbers, with attendant high separation resolving power. The plate number N achievable in CZE can be described by

$$N = \mu V/2D \tag{3}$$

where D is the diffusion coefficient of the particle (*32*). The length of the capillary does not directly affect separation efficiency. Thus, very high voltages are used across relatively short capillaries to achieve excellent separations in a short time (<0.5 h).

Silica sol standards are required for calibrating CZE retention. Figure 15 shows the correlation of CZE retention time with the surface area of several silica sols determined by a titration method (*35*). In this case, the silica sol diameter is directly related to the surface area by the expression

$$d_p = 2720/S \tag{4}$$

where d_p is the sol diameter in nanometers for silica with a density of 2.2 g/cm^3 and S is the surface area in square meters per gram.

The excellent fractionating power of CZE for silica sols is shown by the electropherogram in Figure 16. Sols ranging from ~5 to 250 nm were separated in a single experiment in about 23 min. The range of sols and the degree of separation can be controlled by selecting the mobile-phase ions and ionic strength, separating voltage, and other operating parameters (*33*).

The CZE method is capable of very high resolution and discrimination between silica sols—the highest of all of the methods discussed here. Resolving power is easily varied as needed by changing the voltage used in the separation or the ionic strength of the liquid within the capillary. Elution of the silica sols is correlated to the size (diffusion coefficient) of the silica sol. CZE will effectively separate over a wide particle-size range,

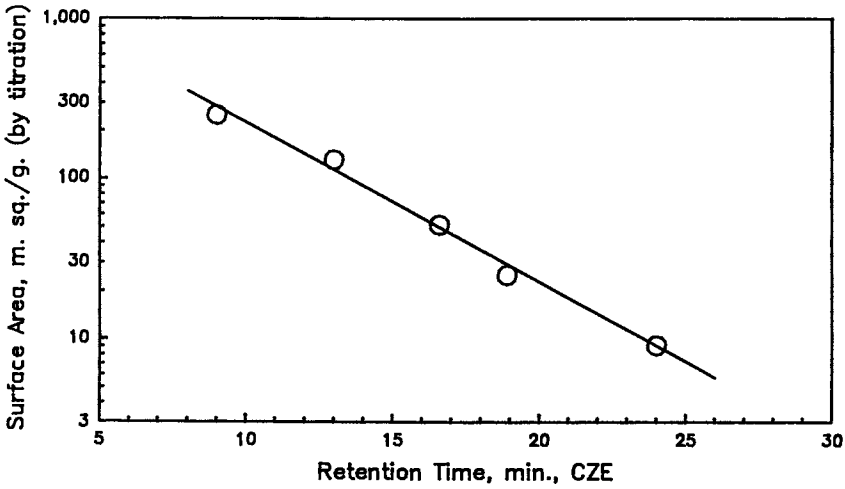

Figure 15. Correlation of silica sol surface area with CZE band retention: capillary, 60 cm × 50 μm; 30,000 V; mobile phase, 2.5 mM ammonium hydroxide and 4.7 mM ammonium chloride; and UV detection, 190 nm.

at least <6 to >600 nm. Limiting particle sizes for silica sols have not yet been determined.

Limitations of CZE for characterizing colloids include the need for standards to establish calibrations. Moderately expensive equipment is required, but appropriate commercial apparatus is now widely available. At present, CZE is not well-suited for routine analyses, and some special experience is needed to operate the equipment. Quantitative techniques are relatively crude at this stage of CZE development. Current quantitation is limited to peak-position measurements that provide estimates of the average particle size for narrow distributions. In theory, the determination

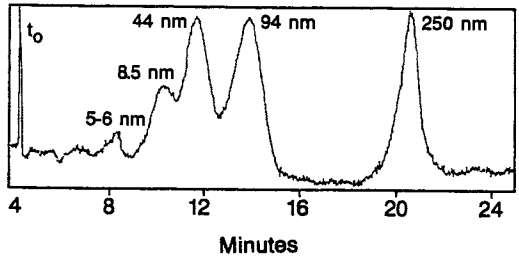

Figure 16. Separation of silica sols by CZE. Conditions as for Figure 15. (Courtesy of R. M. McCormick).

of particle-size distributions by CZE is feasible. However, appropriate software for this purpose has not yet been developed.

Conclusions

Table I summarizes the features of separations methods for measuring the size of silica sols. In theory, particle-size distribution measurements of silica sols could be devised for SEC, HDC, and CZE. However, these methods are currently restricted to estimating a particle-size average for relatively narrow distributions.

Table I. Separations Methods for Characterizing Silica Sols

Feature	*SdFFF*	*FlFFF*	*SEC*	*HDC*	*CZE*
Range (nm)	10–1000	10–1000	5–60	10–600	5–600
Quantitation strength	size, distribution	size, distribution	size	size	size
Equipment	commercial	commercial	commercial	commercial or research	commercial
Experience needed	moderate	high	low	low	high
Resolution and precision	high	high	moderate	poor to moderate	very high

References

1. Iler, R. K. *The Chemistry of Silica*; Wiley: New York, 1979; p 344.
2. *Modern Methods of Particle Size Analysis*; Barth, H. G., Ed.; Chemical Analysis Series, Vol. 73; Wiley: New York, 1984.
3. Allen, T. *Particle Size Measurement*, 3rd ed.; Chapman and Hall: London, 1981.
4. Kaye, B. H. *Direct Characterization of Fine Particles*; Wiley: New York, 1981.
5. Giddings, J. C.; Yang, F. J. F.; Myers, M. N. *Anal. Chem.* **1974**, *46*, 1917.
6. Giddings, J. C. *Separation Sci.* **1966**, *1*, 123.
7. Giddings, J. C.; Yang, F. J.; Myers, M. N. *Separation Sci.* **1975**, *10*, 133.
8. Yang, F. J.; Myers, M. N.; Giddings, J. C. *J. Colloid Interface Sci.* **1977**, *60*, 574.
9. Kirkland, J. J.; Yau, W. W.; Doerner, W. A.; Grant, J. W. *Anal. Chem.* **1980**, *52*, 1944.
10. Kirkland, J. J.; Rementer, S. W.; Yau, W. W. *Anal. Chem.* **1981**, *53*, 1730.
11. Kirkland, J. J.; Dilks, C. H., Jr.; Yau, W. W. *J. Chromatogr.* **1983**, *225*, 255.
12. Schallenger, L. E.; Yau, W. W.; Kirkland, J. J. *Science*, **1984**, *225*, 434.
13. Giddings, J. C.; Caldwell, K. D.; Jones, H. K. In *Particle Size Distribution: Assessment and Characterization*; Provder, T., Ed.; ACS Symposium Series 332; American Chemical Society: Washington, DC, 1987; pp 215–230.
14. Mercus, H. G.; Mori, Y.; Scarlett, B. *Colloid Polymer Sci.* **1989**, *267*, 1102.
15. Yang, F. J. F.; Myers, M. N.; Giddings, J. C. *Anal. Chem.* **1974**, *46*, 1924.
16. Giddings, J. C.; Karaiskskis, G.; Caldwell, K. D. *Separation Sci. Technol.* **1981**, *16*, 607.
17. Kirkland, J. J.; Yau, W. W. *Anal. Chem.* **1983**, *55*, 2165.

18. Giddings, J. C. *Anal. Chem.* **1981,** *53,* 1170A.
19. Giddings, J. C.; Myers, M. N.; Caldwell, K. D.; Fisher, S. R. In *Methods of Biochemical Analysis,* Vol. 26; Glick, D., Ed.; Wiley: New York, 1980; pp 79–136.
20. Wahlund, K. G.; Litzen, A. *J. Chromatogr.* **1989,** *461,* 73.
21. Wahlund, K. G.; Giddings, J. C. *Anal. Chem.* **1987,** *59,* 1332.
22. Kirkland, J. J.; Dilks, C. H. Jr.; Rementer, S. W.; Yau, W. W. *J. Chromatogr.* **1992,** *593,* 339.
23. Yau, W. W.; Kirkland, J. J.; Bly, D. D. *Modern Size-Exclusion Liquid Chromatography;* Wiley: New York, 1979; Chapters 12 and 13.
24. Singh, S.; Hamielec, A. E. *J. Liq. Chromatogr.* **1978,** *1,* 187.
25. Kirkland, J. J. *J. Chromatogr.* **1979,** *185,* 273.
26. Yau, W. W.; Kirkland, J. J.; Bly, D. D. *Modern Size-Exclusion Liquid Chromatography;* Wiley: New York, 1979; Chapter 9.
27. Small, H. *J. Colloid Interface Sci.* **1974,** *48,* 147.
28. McGowan, G. R.; Langhorst, M. A. *J. Colloid Interface Sci.* **1982,** *89,* 94.
29. Small, H. *Anal. Chem.* **1982,** *54,* 892A.
30. Silebi, C. A.; Dosramos, J. G. *J. Colloid Interface Sci.* **1989,** *130,* 14.
31. Tijssen, R.; Bos, J.; van Kreveld, M. E. *Anal. Chem.* **1986,** *58,* 3036.
32. Jorgenson, J. W.; Lukacs, K. D. *Anal. Chem.* **1981,** *53,* 1298.
33. McCormick, R. M. *J. Liq. Chromatogr.* **1991,** *14,* 939.
34. McCormick, R. M. *Anal. Chem.* **1988,** *60,* 2322.
35. Sears, G. W., Jr. *Anal. Chem.* **1956,** *28,* 1981.
36. Kirkland, J. J.; Yau, W. W. *Science* **1982,** *218,* 121.

RECEIVED for review October 30, 1990. ACCEPTED revised manuscript December 11, 1991.

16

Characterization of Colloidal and Particulate Silica by Field-Flow Fractionation

J. Calvin Giddings[1], S. Kim Ratanathanawongs[1], Bhajendra N. Barman[2,3], Myeong Hee Moon[1], Guangyue Liu[1], Brenda L. Tjelta[1], and Marcia E. Hansen[2]

[1]Field-Flow Fractionation Research Center, Department of Chemistry, University of Utah, Salt Lake City, UT 84112
[2]FFFractionation, Inc., P.O. Box 58718, Salt Lake City, UT 84158–0718

Particle-size and mass distribution curves, along with information on particle porosity, density, shape, and aggregation, can be obtained for submicrometer- and supramicrometer-size silica materials suspended in either aqueous or nonaqueous media by field-flow fractionation (FFF). Narrow fractions can readily be collected for confirmation or further characterization by microscopy and other means. Among the silicas examined were different types of colloidal microspheres, fumed silica, and various chromatographic supports. Size distribution curves for aqueous silica suspensions were obtained by both sedimentation FFF and flow FFF and for nonaqueous suspensions by thermal FFF. Populations of aggregates and oversized particles were isolated and identified in some samples. The capability of FFF to achieve the high-resolution fractionation of silica is confirmed by the collection of fractions and their examination by electron microscopy.

PARTICLE-SIZE DISTRIBUTION AND OTHER PARTICLE CHARACTERISTICS, including degree of aggregation, shape, and porosity, strongly influence the properties of numerous forms of colloidal and particulate silica (*1*). The rapid and accurate measurement of these distributions and characteristics

[3]Present address: Texaco, Inc., P.O. Box 1608, Port Arthur, TX 77641

0065–2393/94/0234–0309$10.16/0

by conventional techniques (such as microscopy, light scattering, and sedimentation) has proven to be difficult or in many cases impossible; thus, alternate technologies should be considered. The capability of field-flow fractionation (FFF), a newer technology, to provide high-resolution particle-size distribution curves and particle densities is now well documented (*2–9*) and suggests that FFF might play a constructive role in silica characterization. The ability of FFF to separate out aggregates, impurities, and other complex subpopulations differing in particle mass, size, or density and to provide narrow fractions of these subpopulations for examination by microscopy and other means is entirely unique; this capability is important and may prove essential in meeting tightening demands for precise particle characterization. The extension of FFF methodology to the measurement of particle shapes and porosities, as discussed here, is illustrative of the potential versatility of FFF in providing multiple properties of the components of complex colloidal materials. The application of FFF to diverse silica materials, explored in this chapter, is an opportune combination of a challenging materials characterization problem and a relatively new and highly versatile particle characterization technology.

FFF is a family of chromatographic-like techniques that fractionate colloidal materials according to differences in physicochemical properties (*2–6*). These properties include particle mass, size, and effective density; the specific combination of properties controlling the fractionation depends on the subtechnique of FFF. In an FFF run, the particles in the sample are separated according to the relevant property (e.g., particle mass) and are eluted from the FFF flow channel in a well-defined sequence (e.g., from low mass to high mass). The relative amounts of the sample eluting at different times are measured by a detector, and the resulting fractogram (detector signal versus time curve) is converted into a property distribution curve such as a mass or size distribution curve.

Figure 1 shows, for illustrative purposes, the fractograms for two different size ranges of polystyrene latex microspheres. (Polystyrene latex standards with narrow size distributions are ideal probes for testing the resolving power and accuracy of particle characterization methods. Those techniques unable to resolve close-lying latex standards are generally unable to provide detailed size distribution information on silica or other particulate matter.) In the first fractogram, Figure 1a, submicrometer-size latex particles are separated according to size (or mass)—the smallest particles emerge first and the largest last—by sedimentation FFF with power programming (*10*). (The spin rate (revolutions per minute) versus time curve for the power program is also shown; the initial spin rate is 2000, the flow rate is 1.6 mL/min, and the parameters t_1 (predecay time), t_{sf} (stop-flow time), t_a (power programming time constant), and p (power parameter in power programming) are 5 min, 2 min, −40 min, and 8,

respectively.) Figure 1b shows the separation of supramicrometer-size microspheres at even higher resolution and speed with sedimentation–steric FFF. (Here the spin rate is 1100 rpm and the flow rate is 6.00 mL/min.) For particles in this size range, the elution sequence proceeds from large to small particles as shown in Figure 1b.

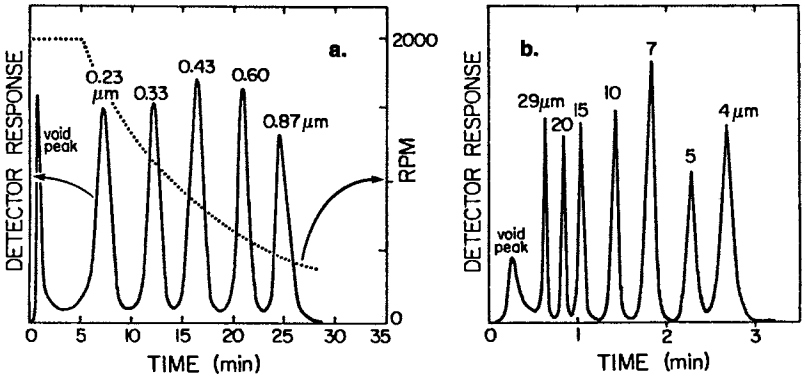

Figure 1. Illustration of the high resolving power of FFF for the separation of particles in different size ranges: a, submicrometer polystyrene latex microspheres fractionated by power-programmed normal mode sedimentation FFF; and b, supramicrometer-sized latex spheres fractionated by sedimentation–steric FFF.

Although field-flow fractionation was first developed in the 1960s (*11*), the first major study of colloidal silica by FFF was not reported until 1978 (*4*). At that time it was shown that the subtechnique of flow FFF could be used to fractionate colloidal silica down to a particle size of 0.01 μm (*see* Figure 2). The fractionation was verified by electron microscopy. Size distribution curves were obtained under different experimental conditions and shown to be consistent with one another. The effects of particle aggregation were examined.

Subsequent work on colloidal silica with sedimentation FFF was reported by Kirkland and co-workers (*7, 12*) and by Yonker et al. (*13*), who used various organic liquids as the FFF carrier.

In other work carried out on two different occasions, both sedimentation FFF (*14*) and flow FFF (*15*) were used to characterize the size distribution of chromatographic silicas having particles ranging up to approximately 20 μm in diameter. In more recent work (*16*), sedimentation FFF was used to obtain both the size and apparent density (thus giving the porosity and pore volume) of silica support particles used in chromatography.

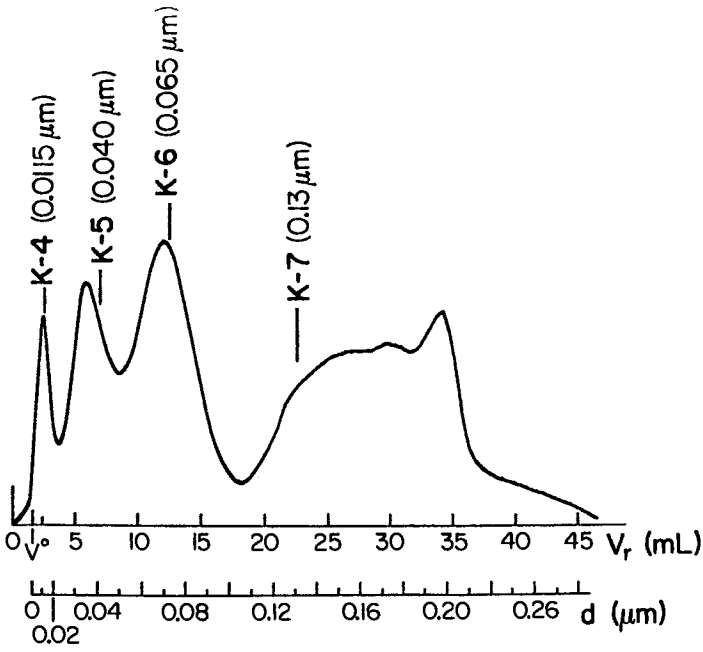

Figure 2. Early flow FFF fractograms of K-4, K-5, K-6, and K-7 colloidal silicas. The flow rates were $\dot{V} = 3.16$ *mL/h and* $\dot{V}_c = 11.1$ *mL/h; the void volume was 1.62 mL. (Reprinted with permission from reference 4. Copyright 1978 Academic Press.)*

In this chapter, both colloidal silica and coarser silica materials such as chromatographic supports are examined. The particle sizes range from 0.01 to 20 μm. An arsenal of FFF subtechniques was used, including sedimentation FFF, flow FFF, and thermal FFF. Although most of these studies involve aqueous suspensions, thermal FFF is shown to be capable of fractionating and characterizing nonaqueous suspensions of silica as well.

Theory

In FFF, particle size, mass, density, and so forth are determined by their relationship to particle retention time t_r, the time required for the passage of the particle through the FFF channel. The relationship between particle properties and t_r arises because a particle's position in the streamlines of a thin channel, and thus the particle's velocity, is determined by the force exerted on the particle by an external field directed at right angles to flow. The interactive force between the field and the particle can generally be expressed explicitly in terms of particle properties, thus a mathematical

relationship between these properties and the retention time is provided. The mechanism by which particles of different properties are differentially eluted, and thus the form of the mathematical relationship between particle properties and t_r, depends on the particle size range. The so-called normal mechanism (or normal mode) of FFF, producing the separation illustrated in Figure 1a, is applicable to particles ranging from about 1 nm in size up to a somewhat flexible upper limit generally set in the 1–2-μm size range. The steric mechanism (or steric mode), utilized in Figure 1b, has an adjustable lower limit of about 0.3 μm and extends upward, if necessary, beyond 100 μm.

In either the normal or steric mode of FFF, a small sample of suspended particles is injected into a stream of carrier liquid flowing through a thin ribbonlike channel. The particles are carried down the channel by the flow of carrier. However, the velocity of any given particle at any instant is determined by the position of the particle along the transverse (or thin) dimension of the channel as a consequence of the parabolic flow between the two flat walls confining the channel (*see* Figure 3). FFF, in either the normal or steric mode, operates by applying an external field or gradient across these channel walls and thus directed transversely across the channel. The field must interact with the particles and drive them toward one wall. By driving particles to different equilibrium positions or distributions, different particle types are carried along in different portions of the parabolic flow stream, which imparts a differential flow velocity to different particle subpopulations and results in their separation.

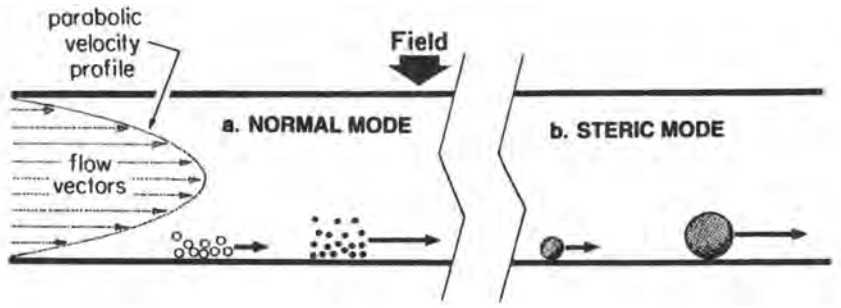

Figure 3. Diagram showing parabolic flow profile between FFF channel walls and the displacement by flow of particles according to (a) normal and (b) steric mechanisms.

Normal FFF. In normal mode FFF, used primarily for colloidal materials, the particles are driven toward one of the channel walls (the *accumulation wall*) by the external field. As the particle concentration

increases in the vicinity of the accumulation wall, diffusion begins to counteract the field-induced motion by driving particles away from the wall (Figure 3a). An equilibrium distribution is soon established in which the concentration c at any elevation x above the accumulation wall relative to the concentration c_0 at the wall is given by the exponential relationship (2–6)

$$\frac{c}{c_0} = e^{-x/\ell} \tag{1}$$

where the exponential ℓ equals the mean elevation of particles above the wall. The constant ℓ is related to the diffusion coefficient D, the field-induced velocity U, and the driving force F exerted by the field on a single particle according to the relationships

$$\ell = \frac{D}{U} = \frac{kT}{F} \tag{2}$$

where k is the Boltzmann constant and T is the absolute temperature. Because D, U, and F are related to the physicochemical properties of the particle, equations 1 and 2 establish a relationship between the distribution of particles along transverse axis x and these properties.

The velocity at which particles are swept through the channel, and thus their retention time t_r, also depends on the transverse distribution expressed by equations 1 and 2. More specifically, retention time t_r is given by

$$t_r = \frac{t^0}{6\lambda[\coth(1/2\lambda) - 2\lambda]} \tag{3}$$

which reduces to

$$t_r = \frac{t^0}{6\lambda} \tag{4}$$

when t_r is large compared to the void time t^0. Here λ is the dimensionless ratio of ℓ to channel thickness w; that is,

$$\lambda = \frac{\ell}{w} = \frac{kT}{Fw} \tag{5}$$

where the last equality (the relationship between λ and F) is based on equation 2.

The retention parameter λ is the critical link between the experimental retention time given by equation 3 (or equation 4) and the particle properties that determine the force F exerted on the particles by the field. The specific particle properties that are characterized by this relationship depend on the type of field applied. For a sedimentation field, F is related to the particle mass m by

$$F = m\left(\frac{\Delta\rho}{\rho_p}\right)G \tag{6}$$

where ρ_p is the particle density, $\Delta\rho$ is the difference between the particle and the carrier density, and G is the strength of the field measured as acceleration. For spherical particles of diameter d, F assumes the form

$$F = (\pi/6)d^3\,\Delta\rho\,G \tag{7}$$

This equation applies to nonspherical particles as well, provided d is interpreted as the effective spherical diameter of the particle, equal to the diameter of a sphere having the same volume as the particle.

By combining either equation 6 or 7 with equations 3 (or 4) and 5, the experimental retention time t_r can be related to particle mass m or diameter d. To fully utilize this relationship, the particle density ρ_p (and the resulting difference $\Delta\rho$ between ρ_p and the carrier density) must be known or obtained. This density is usually known to a good approximation. If it is not known, FFF methods have been developed for determining particle density values (*17*). However, uncertainties or complications introduced by the density dependence of sedimentation forces can be bypassed by using an alternate density-independent force in the FFF system, such as that utilized in flow FFF.

In flow FFF the particle is driven to the accumulation wall by the physical cross-flow of the carrier fluid. To implement this method, the walls of the channel must be permeable. A stream of carrier is then introduced through one wall and withdrawn from the opposite wall. The cross-flow fluid motion so generated is superimposed on the axial channel flow described earlier. This cross-flow displaces particles toward the accumulation wall as effectively as a sedimentation force. However, the driving force is density-independent; specifically,

$$F = 3\pi\eta d_s U \tag{8}$$

where U, defined earlier as the transverse displacement velocity induced by the field, is simply the cross-flow velocity of the fluid in flow FFF, and η is the viscosity. The particle property entering this equation is the Stokes diameter d_s, different (except for spheres) from the sedimentation FFF

diameter d. (Although diameter d is defined by the volume of a particle, d_s is defined by the friction coefficient and Stokes law, $f = 3\pi\eta d_s$.) By virtue of equations 8, 5, and 3, flow FFF can be used to calculate the diameter d_s for any particle eluting at time t_r independent of density.

A third and still different type of driving force that can be used in FFF is the effective force generated by a temperature gradient applied between the channel walls. The corresponding FFF subtechnique is known as thermal FFF. Although thermal FFF has been used primarily for the analysis of synthetic polymers, we have found that the method is applicable to particles suspended in organic liquids. The effective driving force for thermal FFF is given by

$$F = -D_T f \, dT/dx \tag{9}$$

where D_T is the thermal diffusion coefficient and dT/dx is the temperature gradient. Unfortunately, the dependence of D_T on particle properties is not fully understood, and thus empirical calibration has to be used to obtain size distribution and other data on particulate materials.

Steric FFF. In steric FFF, particles are driven almost to the point of contact with the accumulation wall (Figure 3b). The equilibrium position of these larger particles thus depends on their size. However, the particle position, and thus retention time, is complicated by hydrodynamic lift forces acting in opposition to the primary driving forces expressed by equations 7, 8, and 9. These lift forces, which increase with the flow rate, drive the particles a short distance away from the channel wall and thus into higher positions within the parabolic flow profile, where the flow velocity is greater than it would be for particles immediately adjacent to the wall (*18, 19*). The major role played by these lift forces and the greatly diminished role of Brownian motion (which is usually negligible for the large particles analyzed by steric FFF) distinguish the steric mechanism from the normal mechanism of FFF. Because the hydrodynamic lift forces are not well understood (*19*), and are thus difficult to incorporate into theory, there are no theory-based equations for retention time analogous to equations 3 and 4 for normal FFF. Instead, a semiempirical approach is used with constants established by experimental calibration. In particular, the retention time t_r is best expressed in the logarithmic form (*20*)

$$\log t_r = -S_d \log d + \log t_{r1} \tag{10}$$

where S_d is the diameter-based selectivity and t_{r1} is a constant representing the retention time of a particle of unit diameter. The value of S_d is somewhat less than unity when sedimentation is used as a driving force and somewhat greater than unity when cross-flow serves as the driving force

(*18*). Both S_d and t_{r1} are established by logarithmic plots of t_r versus d of well-characterized standards such as polystyrene latex beads. The value of t_{r1} depends on the field strength and, for sedimentation FFF, also on the particle density. It will be shown later that this dependence makes possible the determination of particle density and porosity values.

Experimental Details

A battery of six different FFF systems was used to provide a comparison of results obtained not only from different systems of the same type but from systems of entirely different types (i.e., with different primary force fields). The characteristics of the six systems are summarized in Table I. Included in the collection are two sedimentation FFF systems, three flow FFF systems, and one thermal FFF system. The characteristics and operation of these different categories of instruments are described in more detail in this section.

Sedimentation FFF. The two sedimentation FFF (or SdFFF) systems have similar specifications and design features that have evolved in two decades of work at the University of Utah. All have a horizontal rotation axis (radius 15.1 cm) that makes them suitable not only for the normal mode analysis of submicrometer-size particles, but also for the steric FFF of particles well above 1 μm in diameter (*see* Figure 1). System Sed I is a research instrument constructed at the University of Utah, and system Sed II is a commercial instrument (model S101) from FFFractionation. Although almost identical in design and performance, Sed I has been fitted with a special channel of reduced dimensions (*see* Table I). The reduced channel thickness (w = 127 μm) makes this instrument particularly effective for the rapid analysis (in the steric mode) of particles ranging from 0.5 to 40 μm in diameter (*see* Figure 1b). (Steric FFF in Sed II will fractionate particles up to ~80 μm.)

Conventional ancillary equipment was used with these sedimentation FFF systems. Sed I, for example, utilized a model 410 high-performance liquid chromatography (HPLC) pump from Kontron Electrolab (London) and a UV Spectroflow Monitor SF770 from Kratos Analytical Instruments (Westwood, NJ). Fractions of eluted silica were collected by means of a model FC-80K Microfractionator from Gilson Medical Electronics (Middleton, WI).

Flow FFF. The three flow FFF systems (Flow I, II, and III) are each constructed of two Lucite blocks with inset ceramic frits, a membrane, and a spacer. The frits provide a homogeneous distribution of cross-flow over the entire channel area. A membrane stretched over one frit surface serves as the accumulation wall and retains sample inside the channel. Systems Flow I and II were assembled with the YM-30 ultrafiltration membrane (Amicon, Danvers, MA) and Flow III with the Celgard 2400 polypropylene membrane (Hoechst-Celanese, Separations Products Division, Charlotte, NC). The frit of the second Lucite block defines the opposite (depletion) wall. The spacers, consisting of Teflon (Flow I) or Mylar (Flow II, Flow III), determine the channel thickness.

The flow FFF systems are characterized by the use of a second pump to drive carrier across the channel thickness; this setup provides the field that induces migration of sample toward the accumulation wall. The Flow I system was operated with an Isochrom LC pump (Spectra-Physics Inc., San Jose, CA) as the channel flow pump and a pulseless syringe pump (built in-house) as the cross-flow pump. Sample was injected via a Valco injector (Valco Instruments Co., Houston, TX) with a 20-

Table I. Field-Flow Fractionation Systems Used

System Designation	*System Type*	*System Source*	*Channel Dimensions (cm)*			*Void Volume (mL)*
			Thickness	*Breadth*	*Length*[a]	
Sed I	sedimentation FFF	FFFRC[b]	0.013	1.0	90.0	1.14
Sed II	sedimentation FFF	FFFractionation[c]	0.025	2.0	89.0	4.47
Flow I	flow FFF	FFFRC	0.018	2.1	38.5	1.35
Flow II	flow FFF	FFFRC	0.024	2.0	27.2	1.17
Flow III	flow FFF	FFFRC	0.013	2.0	27.2	0.63
Therm I	thermal FFF	FFFRC	0.022	2.0	46.5	2.02

[a]Tip-to-tip channel length.
[b]Field-Flow Fractionation Research Center, Department of Chemistry, University of Utah, Salt Lake City, UT 84112.
[c]FFFractionation Inc., P.O. Box 58718, Salt Lake City, UT 84158.

μL loop, and the eluted sample was detected at 254 nm with a UV–visible detector (UV-106, Linear Instruments, Reno, NV). The peripheral equipment employed in Flow II and III consisted of a Kontron model 410 channel flow pump, a syringe pump serving as the cross-flow pump, a Rheodyne (Cotati, CA) model 7010 pneumatic-actuated injection valve, and a model 757 Spectroflow UV–vis detector from Applied Biosystems (Ramsey, NJ) operated at 254 nm.

For some experiments, an evaporative light-scattering detector (ELSDII, Varex Corporation, Burtonsville, MD) was connected in series with the UV–vis detector of Flow I. The operating conditions were those recommended by the instrument manufacturer.

The main difference between the three flow FFF systems is the channel dimensions, given in Table I. Although systems Flow I and II were constructed with 254-μm spacers, the protrusion of the compressible membrane material into the channel space reduced the thickness w below this value. The w values reported in Table I are back-calculated from void volume measurements and subsequently confirmed by polystyrene standards. Flow I, with an initial w of 181 μm, was reassembled at one point, after which w was found to be 152 μm. This variation in w due to membrane compressibility was not observed when the thin polypropylene (25 μm) membrane was used in Flow III. In this case, the channel thickness equals the spacer thickness. Thus the measured and geometric void volumes are in good agreement.

Thermal FFF. The thermal FFF system (Therm I) is a unit of conventional design in which the channel volume is cut and removed from a Mylar spacer and the spacer is sandwiched between two chrome- and nickel-plated copper bars (*21*). The temperature gradient is instituted by heating one bar and cooling the other; temperature differences up to $\Delta T = 53$ K were utilized. Although the channel length and thickness (*see* Table I) are fairly typical for thermal FFF, the channel thickness is 3 times that commonly used in our laboratories. Although this added thickness causes some loss of resolution and speed, the capability for fractionating particles should be adequate for the work.

The carrier for the thermal FFF system was reagent-grade acetonitrile from EM Industries (Gibbstown, NJ). The flow of this carrier was driven by a model M-6000A pump from Waters Associates. A model CSI UV detector from Cole Scientific (Calabasas, CA) operating at 254 nm was used to detect the eluting particles. The signals were collected on an Omniscribe chart recorder (Houston Instrument, Austin, TX). A pressure regulator was used to maintain the channel pressure at 100 psi (700 kPa) above atmospheric pressure to provide solvent and signal stability when the operating temperature of the hot wall approaches the solvent boiling point.

Standards and Samples. The polystyrene standards used were obtained from Duke Scientific (Palo Alto, CA) and Seradyn (Indianapolis, IN).

The silica samples examined by different FFF subtechniques and systems are shown in Table II. These samples have particles that fall in three categories: nonporous colloidal microspheres, fumed silicas having a chainlike structure, and larger porous silica particles typical of chromatographic supports. The carriers and sample amounts injected for each type of silica analyzed by different FFF subtechniques are listed in Table III.

Preparation of the Cab-O-Sil fumed silica, a multistepped procedure, was as follows. The fumed silica powder (25–125 mg) was weighed into a 10-mL vial and then suspended in 5 mL of a 0.0016 M NaOH solution. After an initial 10-s vortex

Table II. Silica Samples Examined and FFF Systems Utilized

Sample Identity	*Source*	*Nominal Size (μm)*	*FFF System*
Colloidal silicas			
Ludox HS-30%	DuPont	0.012	Flow I, Flow II
TM		0.022	
SM		0.007	
Monospher 50	E. Merck	0.05	Therm I, Sed II
100		0.10	
150		0.15	
250		0.25	
500		0.50	
Nyacol 9950	PQ Corp.	0.1	Sed I, Sed II, Flow III, Therm I
Fumed silicas (chainlike network)			
Cab-O-Sil L-90	Cabot Corp.	0.22	Sed II, Flow III
M-5		0.17	
EH-5		0.14	
Chromatographic silicas (porous spheres)			
A. Hypersil-5 (136 Å)	Shandon	5	Sed I
B. Hypersil-5 (120 Å)	Shandon	5	Sed I, Flow II
C. Spherisorb	Phase Separations	5	Sed I, Flow II
D. Nucleosil	Machery-Nagel	5	Sed I, Flow II
E. Hypersil-3	Shandon	3	Sed I, Flow II

Table III. Summary of Carrier and Amount of Sample Injected

Sample	*System*	*Carrier*	*Amount Injected (μg per run)*
Ludox	Flow I	0.1% FL-70, 0.02% NaN_3; 0.001 M NH_4OH	60–120
	Flow II	0.01 M phosphate, pH 7.3	60–120
Monospher	Therm I	acetonitrile	40–70
	Sed II	0.1% FL-70, 0.02% NaN_3	40–70
Nyacol	Sed I	0.1% FL-70, 0.02% NaN_3	40
	Sed II	0.1% FL-70, 0.02% NaN_3	60
	Flow III	0.001 M NH_4OH	40
	Therm I	acetonitrile	70
Cab-O-Sil	Sed II	0.1% FL-70, 0.01% NaN_3; 0.02 M triethanolamine	560
	Flow III	0.001 M NH_4OH	500
Chromatographic silicas	Sed I	0.1% FL-70, 0.02% NaN_3	175–200
	Flow II	0.1% FL-70, 0.02% NaN_3	100

stage, the sample vial and a sonic probe were both immersed in a small water bath. Sonication was carried out for 5 min at 200 W. (The recommended procedure called for 2-min sonication at 480 W with a microtip inserted directly into the sample solution. This procedure was modified because we did not have a microtip.) Immediately before each injection the sample was vortexed for 10 s.

The aqueous carriers were made from doubly distilled deionized water. Most of these carriers contained a surfactant (FL-70, Fisher Scientific, Fairlawn, NJ) and a bacteriocide (sodium azide, NaN_3).

Scanning Electron Microscopy. Electron micrographs were obtained by using a Hitachi S-450 scanning electron microscope (Hitachi Scientific Instruments, Tokyo, Japan). Specimens were prepared by filtering an aliquot of each collected fraction (of interest) onto a 13-mm Nuclepore membrane filter. The filter was mounted on an aluminum stub and subsequently coated with a thin gold and palladium layer. The magnification and acceleration voltages varied from 25,000× and 30 kV for the fumed silica to 750× and 20 kV for the chromatographic silica.

Transmission Electron Microscopy. A Philips model 201 (Arvada, CO) transmission electron microscope was used as an alternative method for determining the particle sizes of Ludox silicas. Specimens were prepared on formvar-coated, 200-mesh copper specimen grids. Typical acceleration voltages and magnifications were 80 kV and 65,000×.

Data Analysis. The computer program used for data analysis was developed at the Field-Flow Fractionation Research Center. The underlying theory is similar to that discussed by Giddings et al. (*4*). For normal mode characterizations, the fractograms are converted to particle size distributions by using developed theory. However, for steric mode analyses, calibration curves are required (*15, 20*).

Results and Discussion

The application of FFF techniques to assorted silica samples including colloidal microspheres (Ludox, Monospher, and Nyacol), fumed silica, and chromatographic silica (*see* Table II) are discussed in this section. In several cases, different FFF systems are applied to the same samples, and the results are compared. The acquisition of size distribution data is emphasized, but the possibilities for measuring densities and porosities for spherical particles and structural factors for nonspherical silica are also discussed (and in one case demonstrated).

Ludox Colloidal Silica. Ludox colloidal silicas (DuPont) were among the first silica materials studied by FFF. In the first paper describing the applicability of FFF to colloidal silica (*4*), Ludox and related silicas were fractionated by flow FFF; the fractionation was verified by transmission electron microscopy (TEM). The theory behind the fractionation and the acquisition of size distribution data was developed, and evidence of aggregation was examined. An example of the fractionation of four colloidal silicas from that study is shown in Figure 2. The primary drawback of this earlier work was the lengthy runs, in some cases requiring over 10 h. Most of the experimental runs on Ludox described in this section were completed in less than 10 min.

To examine data reliability, two of the flow FFF systems (Flow I and Flow II) described in Table I were used. As shown in Table IV, five different sets of conditions corresponding to different flow FFF systems, carriers, flow rates, and detectors were used. The detectors employed were a UV detector (254 nm) and an evaporative light-scattering (ELS) detector. Studies were performed to identify a range of sample amounts that could be injected without overloading the channel. The quantities injected were 600, 120, and 60 μg. The effect of overloading (decreased retention time) was evident in the first case but not in the latter two cases. Less than 120 μg of Ludox silicas were injected throughout the remaining flow FFF studies.

Figure 4a shows the fractograms obtained for the three different Ludox silicas from Flow I and the experimental conditions corresponding to set 1 of Table IV. The cross-flow and channel flow-rates are listed as $\dot{V}_c$ and $\dot{V}$, respectively. The run times, following a stop-flow time of 40 s for relaxation, are only 5–10 min. Similar fractograms of these samples were generated by using the other sets of conditions defined in Table IV.

Standard data analysis software was used to convert the fractograms of Figure 4a into size distribution curves. The results are shown in Figure 4b. The mean diameters (corresponding to the first moments of the peaks) obtained from the different experimental sets are shown in the lower half of Table IV. These results are self-consistent and in satisfactory agreement

Table IV. Comparison of Mean Particle Diameters for Three Ludox Colloidal Silicas Measured under Different Experimental Conditions

Experimental Condition	*Set 1*	*Set 2*	*Set 3*	*Set 4*	*Set 5*
System	Flow II	Flow I	Flow I[a]	Flow I[a]	Flow II
Carrier	0.1% Fl-70 0.02% NaN_3	0.1% Fl-70 0.02% NaN_3	0.001 M NH_4OH	0.001M NH_4OH	0.01 M phosphate buffer
$\dot{V}$ (mL/min)	4.04	3.11	0.41	0.41	2.69
$\dot{V}_c$ (mL/min)	3.24	3.14	1.00	1.00	1.70
Detector	UV	UV	UV	ELS	UV
Sample diameter (nm)					
TM	30	31	31	30	34
HS-30%	18	19	18	18	18
SM	11	10	13	13	14

[a]Reassembled channel.

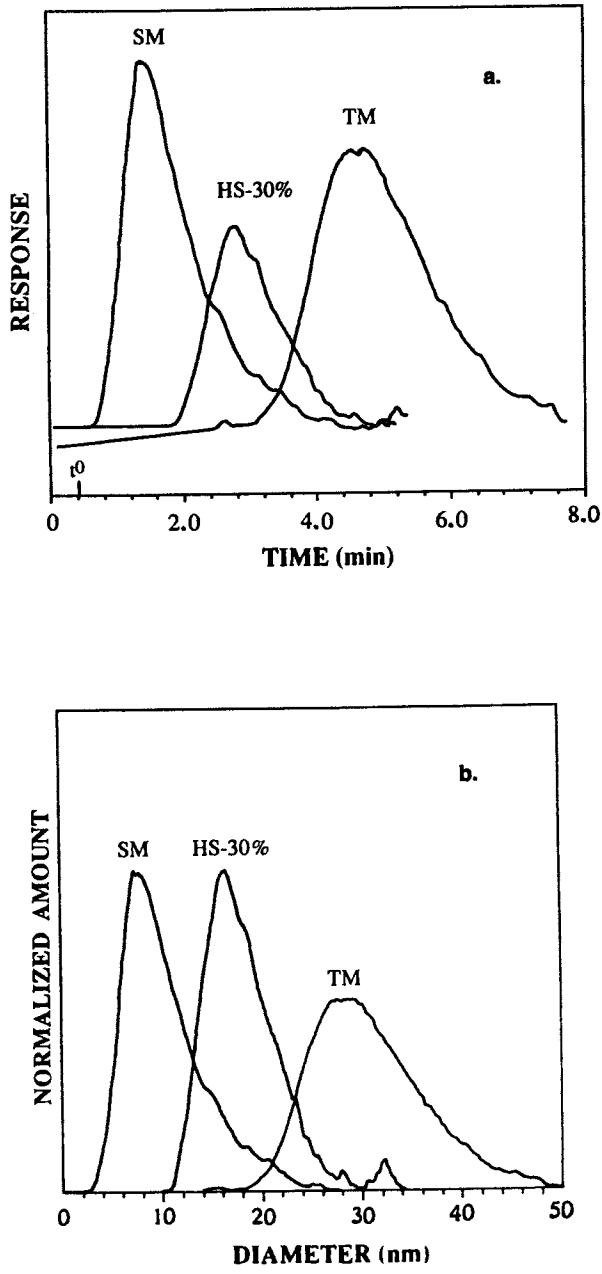

Figure 4. Flow FFF (system Flow I) characterization of three different Ludox colloidal silica suspensions: a, fractograms; and b, particle size distributions.

with the TEM measurements of 30, 18, and 12 nm for TM, HS-30%, and SM silicas, respectively.

Not only are the mean diameters consistent among the different experimental sets, but the entire size distribution curve appears generally to be quite reproducible. Figure 5 illustrates this point by showing the size distributions obtained both for TM and HS-30% in the experimental conditions of sets 1, 2, and 5. These size distributions were not normalized so that the different curves can be differentiated from one another. Although the discrepancies appear to be small, experimental set 5 provided broader distributions. However, theoretical calculations show that the system band broadening for set 5 conditions is excessive for the acquisition of accurate size distribution data. In particular, for TM the flow FFF system is calculated to generate only 69 theoretical plates, marginal for good fractionation. By contrast, set 1 and 2 conditions generate about 290 plates for TM, sufficient to produce accurate distributions. The observed increase in peak tailing for set 5 may also indicate a small degree of aggregation induced by the phosphate buffer.

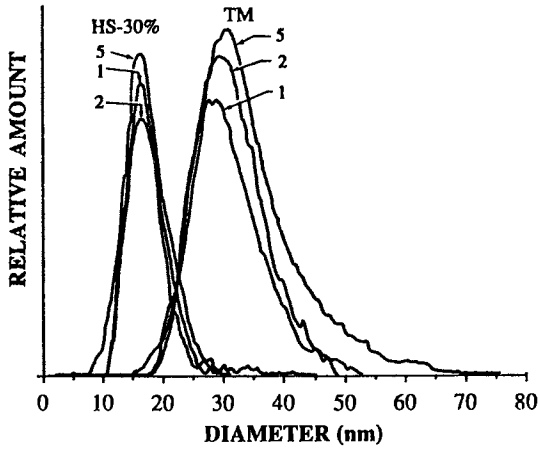

Figure 5. Comparison of the size distribution curves for two Ludox silicas obtained with two different flow FFF channels operated under three different sets of experimental conditions. The conditions are specified by matching the set numbers with those in Table IV.

The particle size distribution curves shown in Figures 4b and 5 were obtained without correcting the UV detector signal for light scattering (6, 22). With a light-scattering correction, the population size was shifted to significantly lower values. Unfortunately, in this particle size range the

light-scattering correction is remarkably sensitive to very low levels of light absorption, which cannot be assumed to be precisely zero.

To better evaluate the light-scattering correction, we compared the results obtained from the normal UV detector and the ELS detector; the latter, in theory, provides an absolute mass distribution curve. Figure 6 shows almost perfect agreement between the size distribution curves obtained from the UV and ELS detectors. Some, but certainly not all, of the (unexpected) agreement can be attributed to the use of nonoptimal flow rates, which provided less fractionation efficiency than the other experimental sets, as noted earlier. Clearly, the matter of applying light-scattering corrections to the signal from conventional UV detectors, particularly with colloidal silica, requires more study. When these corrections are made, the resulting diameters may or may not shift significantly relative to those reported here. These results show, nonetheless, that flow FFF is capable of producing meaningful and reproducible size distribution data for populations of colloidal silica spheres.

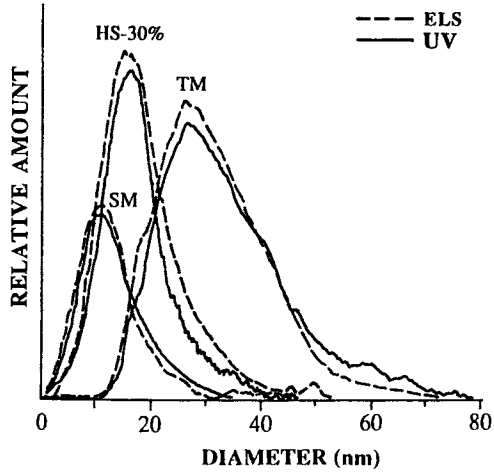

Figure 6. Comparison of size distribution curves of Ludox silicas obtained from Flow I with a conventional UV detector and an ELS detector.

Monospher Colloidal Silica. Superimposed thermal FFF fractograms (system Therm I) of various sizes of Monospher colloidal silicas (E. Merck) run in acetonitrile are shown in Figure 7. A ΔT of 53 K (cold wall temperature of 290 K) was used to obtain these data. The broadness and excessive tailing of the peaks suggests a high polydispersity for the particle populations. In addition, the proximity of elution of the Monospher 100 and 150 samples indicates that their mean sizes are not as different as

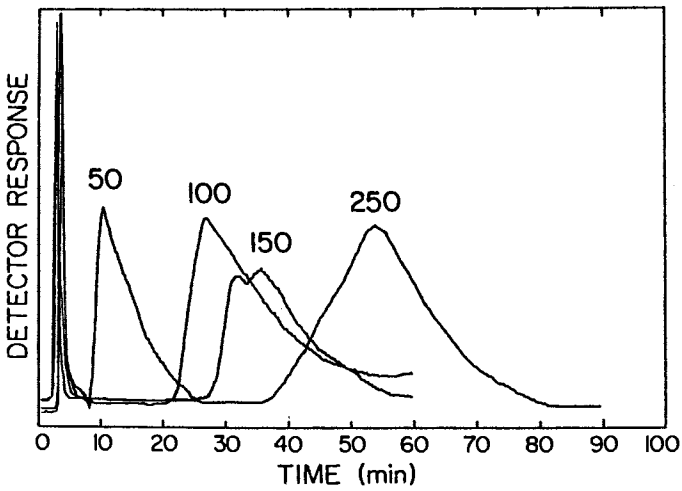

Figure 7. Fractograms of four different Monospher silicas suspended in acetonitrile by thermal FFF (system Therm I).

suggested by the nominal diameters (0.10 and 0.15 μm) reported in Table II. Although the thermal diffusion behavior of particles in liquids (reflected in the D_T term of equation 9) is not well understood, the systematic differential migration of different sizes of Monospher silicas illustrates the capability of thermal FFF for separating and characterizing particles in nonaqueous media (*21*).

The Monospher samples were further analyzed by sedimentation FFF. The fractogram shown in Figure 8 was obtained for a mixture of five different diameters of Monospher silica beads under the following power-programmed field conditions (*10*): $G_0 = 973.2$ gravities (2400 rpm), $t_1 =$ 10 min, $t_a = -80$ min, $t_{sf} = 6$ min, and $\dot{V} = 4.14$ mL/min. As in Figure 7, the Monospher 100 and 150 peaks are surprisingly close together. The broad and unusual slope of the peaks (including extra peaks) suggests that the population distributions for these samples are broad, possibly aggravated by aggregation.

The 250-nm sample was analyzed for possible aggregation. The fractogram shown in Figure 9 was obtained with a constant field of 15.2 gravities (300 rpm) and a flow rate of 4.0 mL/min. The micrographs in Figure 9 show the original sample and the fractions collected from a series of peaks as indicated on the fractogram. (In the absence of aggregation, a single peak would be expected.) The micrograph for the original sample shows uniform-sized beads, although many of them are in contact with one another. However, the clear presence of doublets and triplets in the second and third peaks, respectively, and of the assorted larger clusters in

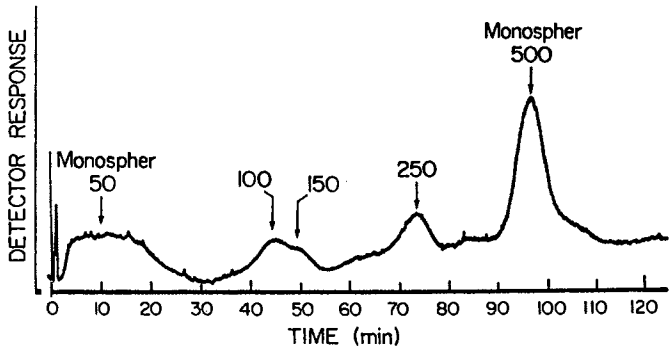

Figure 8. Separation of Monospher colloidal silicas with power-programmed sedimentation FFF (Sed II system).

the peak obtained by turning off the field, indicates that the 250-nm sample is highly aggregated. This result illustrates the capability of FFF to probe colloidal populations, both through fractionation and through the collection of fractions for further analysis.

Nyacol Colloidal Silica. Of the variety of Nyacol (Nyacol Products, Inc.) colloidal silicas, only Nyacol 9950 was investigated. According to the product bulletin, this "silica is present as amorphous spheres 100 millimicrons in size" (23). We undertook the further characterization of this material by using several FFF systems, including Sed I, Sed II, Flow III, and Therm I.

Power-programmed runs on Sed I and Sed II and constant-field runs on Therm I yielded broad and bimodal fractograms in all cases, a result that suggests that the colloidal material was distributed in two main population groups. The fractogram provided by the Sed I system [$G_0 = 973.2$ gravities (2400 rpm), $\dot{V} = 0.52$ mL/min, $p = 8$, $t_1 = 5$ min, $t_a = -40$ min, and $t_{sf} = 3$ min] is shown in Figure 10. This fractogram suggests that the size distribution is bimodal, with calculations showing that one mode is near 0.05 μm and another mode somewhat above 0.5 μm. To further elucidate this unexpected distribution, electron micrographs were taken of the original material and of three of the fractions collected at the positions indicated on Figure 10. These micrographs, shown at the top of Figure 10, verify the presence of both small and large particle populations. (The micrograph of the original sample was not properly focused to show the smaller particles.) Many of the particles in the larger population lie well above 0.5 μm in diameter, so significant steric effects may interfere with an accurate sizing of the second mode. Accordingly, a constant field run at 100 rpm and $\dot{V} = 0.2$ mL/min was instituted to reduce the excessive steric disturbances inherent in programmed runs made at high initial field

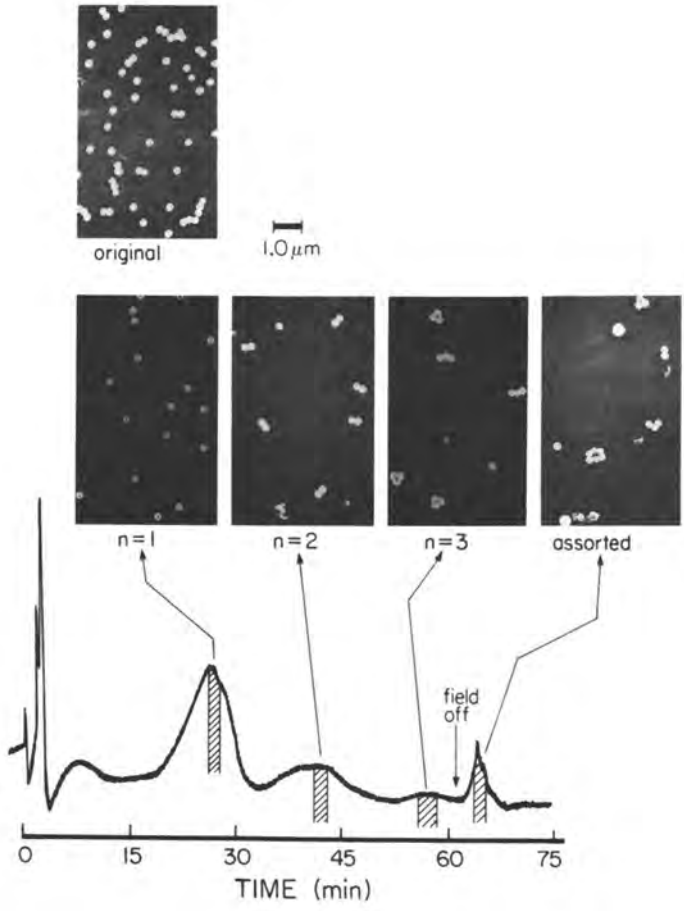

Figure 9. Sedimentation FFF (Sed II system) fractogram and electron micrographs of Monospher 250 aggregates.

strengths and high flow rates. This run yielded a mode at 0.63 μm, which is in reasonable agreement with the electron microscope results presented in Figure 10.

The Nyacol was also analyzed by the Sed II system, which was equipped with a thicker channel than Sed I (254 μm instead of 127 μm). Conditions similar to those described for the Sed I run were used, with the exception of $\dot{V} = 4.15$ mL/min. There is excellent agreement between Sed I and Sed II for the size distributions found in the vicinity of the first mode. However, the distributions of particles near the second mode are different, probably because of the variation in steric effects in the two runs.

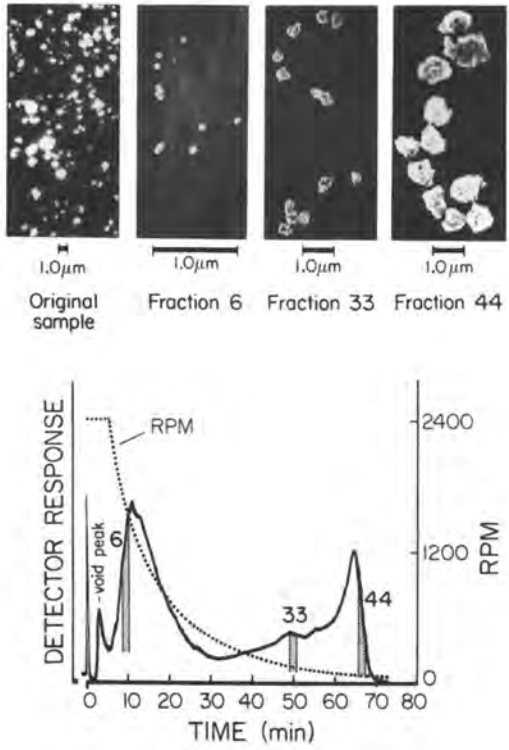

Figure 10. Fractograms and electron micrographs of fractions of Nyacol 9950 collected from a power-programmed sedimentation FFF (Sed I) run.

If the Nyacol particles are assumed to be solid spheres, correction for light scattering suggests that the population of larger particles constitutes only a small mass fraction of the sample. However, if the dominant population is made up of the smaller particles, then the principal mode clearly lies nearer a diameter of 0.05 μm than the 0.1 μm indicated by the manufacturer. A variety of runs on different instruments verified the former mode value; specifically, we obtained 0.058 μm for Sed I, 0.058 μm for Sed II, 0.043 μm for Therm I, and 0.041 μm for Flow III. (Experimental conditions for Therm I were $\Delta T = 53$ K and $\dot{V} = 0.60$ mL/min, and for Flow III were $\dot{V} = 0.51$ mL/min, and $\dot{V}_c = 0.41$ mL/min).

Cab-O-Sil Fumed Silica. Considerable work was done on the three fumed silica samples (Table II) by using both sedimentation FFF and flow FFF. Figures 11 and 12 demonstrate the effectiveness of both FFF systems in the fractionation of these chainlike particles. For both sedimentation and flow FFF, the L-90 sample was injected and fractions were

collected at various elution time intervals for further analysis by scanning electron microscopy. The micrographs included in Figures 11 and 12 show the expected elution order, from small to large particle size. The sedimentation FFF run shown in Figure 11 (Sed II system) utilized power field programming with the conditions $G_0 = 380.2$ gravities (1500 rpm), $\dot{V} = 2.05$ mL/min, $t_1 = 6$ min, $t_a = -48$ min, $t_{sf} = 5$ min, and $p = 8$. For the flow FFF analysis of Figure 12 (Flow III system), $\dot{V} = 0.50$ mL/min and $\dot{V}_c = 0.41$ mL/min.

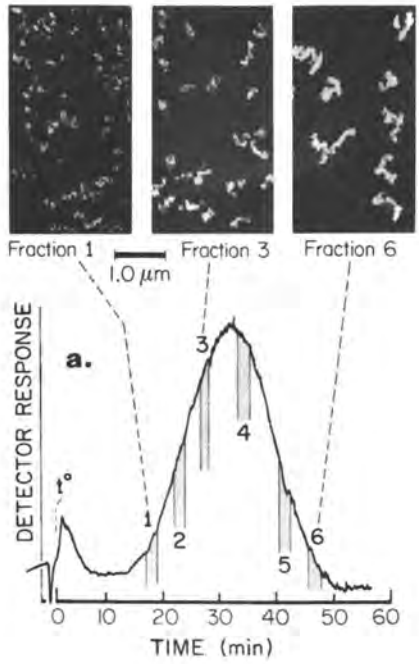

Figure 11. Fractograms and electron micrographs for collected fractions of Cab-O-Sil L-90 obtained by using sedimentation FFF (Sed II).

Figure 13 shows the particle size distributions acquired for the three fumed silicas by using the Flow III system. (No light-scattering correction was attempted for these irregularly shaped particles.) Superimposed on these plots is the size distribution of L-90 from the fractogram shown in Figure 11, obtained by using the Sed II system. (For the sedimentation FFF calculations, a density of 2.4 g/mL was used.) A broader size distribution of larger average diameter for flow FFF is observed than that for SdFFF. Such a difference is expected because, as noted in the "Theory" section, the two techniques measure different diameters (dis-

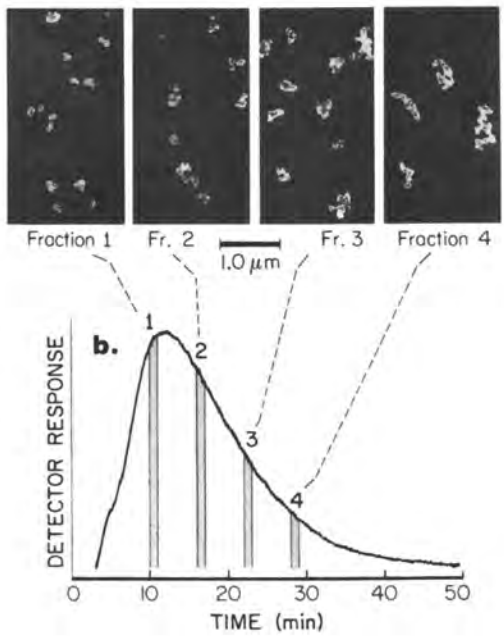

Figure 12. Fractograms and electron micrographs for collected fractions of Cab-O-Sil L-90 obtained with flow FFF (Flow III).

cussed later). Some of the difference, however, may arise from hydrodynamic effects or from particle interactions with the flow FFF membrane. (The latter explanations are suggested by an anomaly in the flow FFF of fumed silica, in which we have observed some dependency of the calculated particle size distribution on the channel flow rate.)

A summary and comparison of mean particle diameters obtained from the size distribution curves of SdFFF and flow FFF (d_{SED} and d_{FLOW}, respectively) with nominal values provided by Richard Geiger of Cabot Corporation based on image analysis d_{IA} is presented in Table V. (The images were generated with a JEOL TEM system and analyzed on a Kontron image analysis system. The Kontron system was used to determine the surface area of the projected image and to convert the area into an equivalent diameter. Weight-averaged mean diameters were then determined.) All the results are in approximate agreement with one another. Some size discrepancies are expected because different "sizes" are measured by different techniques. This important point should eventually lead to more detailed shape and structure analysis, as explained later.

As noted in the "Theory" section, retention in sedimentation FFF is determined by particle mass (*see* equation 6). Accordingly, the particle diameter emerging from sedimentation FFF calculations is the effective

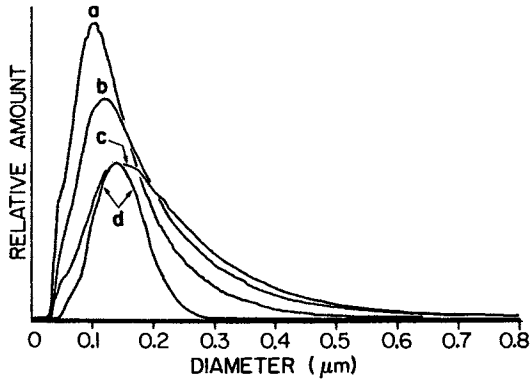

Figure 13. Particle size distributions of fumed silica samples obtained with flow FFF (a, EH-5; b, M-5; and c, L-90) and sedimentation FFF (d, L-90).

Table V. Comparison of Diameter Values Measured by Flow FFF, Sedimentation FFF, and Image Analysis

Sample	d_{SED}	d_{FLOW}	d_{IA}
L-90	0.15	0.20	0.22
M-5	0.14[a]	0.17	0.17
EH-5	0.12[a]	0.14	0.14

NOTE: All values are given in micrometers.
[a]Carrier was 0.02 M triethanolamine.

spherical diameter of the particle, which would be the diameter of a sphere occupied by the particle if it were fused into a spherical globule. Clearly, this diameter is smaller for these chainlike structures than that provided by most other methods, which to varying degrees measure the extension of the structure through space. Thus the average diameters reported in Table II based on the image area of the solid chains are larger than the modal diameter measured by sedimentation FFF. Flow FFF should yield a diameter (the Stokes diameter d_S; *see* equation 8) more nearly representative of the true hydrodynamic diameter of the particles and thus a diameter larger than that measured by sedimentation FFF. This is indeed the case, as shown by the results listed in Table V. The ratio of the diameters measured by these alternative methods to the SdFFF diameter should provide a measure of the bulkiness (or fractal dimension) of the chainlike structures. More work is obviously needed to exploit the comparison of methods.

Chromatographic Silica. Silica particles used for liquid chromatographic supports are generally porous spheres in the diameter range 2–20 μm. Important properties of these particles bearing on chromatographic performance include mean size, size distribution, presence of aggregates and fines, and particle porosity. All these characteristics should be accessible to measurement by FFF; most are described later.

Chromatographic silica was studied by FFF on several previous occasions. An early study using sedimentation–steric FFF yielded size and size distribution information (*14*) but undoubtedly incurred errors because it preceded recent calibration techniques developed to account for hydrodynamic lift forces (*20*). More recent work with flow FFF has provided size and size distribution information and has clearly signaled the presence of aggregates in one commercial sample (*15*). In a study (*16*) using sedimentation–steric FFF combined with microscopy, we developed a strategy for obtaining not only size distributions, but also porosity and porosity distributions. Some of the data derived from this study are summarized in Table VI.

Table VI. Application of Sedimentation–Steric FFF to Chromatographic Silica

Silica Support	*Apparent Density (g/cm³)*	*Porosity*	*Pore Volume (mL/g)*	*Mode Diameter (μm)*	*Diameter Range[a] (μm)*
A. Hypersil-5 (136 Å)	1.52	0.57	0.59	5.86	8.35–4.92
B. Hypersil-5 (120 Å)	1.49	0.59	0.66	6.13	7.59–5.18
C. Spherisorb	1.63	0.47	0.40	4.63	6.20–4.16
D. Nucleosil	1.45	0.62	0.75	4.71	5.92–4.04
E. Hypersil-3	1.49	0.59	0.66	3.43	4.95–2.88

[a]Range corresponds to 10–90% of cumulative mass distribution.
SOURCE: Reproduced from reference 16. Copyright 1991 American Chemical Society.

As suggested earlier, both sedimentation and flow FFF (in steric or hyperlayer modes) can be used to characterize particles in the size range of chromatographic silica. However, the two FFF approaches are more complementary than they are redundant. This is once again (as found also in the normal mode) a consequence of the different force laws that control particle behavior in the two systems. The driving force in flow FFF depends only on the Stokes diameter d_s as shown in equation 8. Thus for spherical silica particles, the diameter and diameter distribution, and nothing more, is characterized by flow FFF. However, the force acting on particles in a sedimentation FFF channel is a function of both particle diameter d and the density difference $\Delta\rho$ as shown by equation 7. Measurement by sedimentation FFF alone thus yields a mix of diameter and density information. However, if d can be established independently by other means (such as flow FFF or microscopy), then $\Delta\rho$ can be obtained

and the particle density (or density distribution) calculated. From the density values, porosities and pore volumes can be derived.

Figure 14 illustrates the fractionation of the chromatographic support Hypersil-5 (136-Å pore size) by sedimentation–steric FFF with system Sed I. The fractogram and the time intervals (6 s) in which fractions were collected from the eluting stream are shown. The electron micrographs of four of the resulting fractions confirm the high-resolution size fractionation; the largest particles are seen to emerge first and the smallest last, as expected of the steric mechanism. (A similar result is found with flow–hyperlayer FFF). Fractograms like that illustrated in Figure 14 combined with particle diameter measurements from one or more of the micrographs can be used to calculate particle densities as explained in reference 16.

Figure 15 shows the fractograms obtained from high-speed runs with sedimentation FFF (system Sed I) and flow FFF (Flow II) on five different chromatographic support materials. The fractograms look fairly similar, but, as noted earlier, they bear different information on size and density parameters. As already noted, the fractograms for sedimentation FFF (Figure 15a), when used in conjunction with microscopy, yield density and porosity information, as summarized in Table VI. With the density and thus $\Delta\rho$ known, the speed of the centrifuge can be adjusted such that the product $G\Delta\rho$ is the same for the porous silica particles as for various sizes of latex standards (such as those shown in Figure 1b) used for calibration. By this rotation speed adjustment (in which different rotation speeds are applied to different silica supports in Figure 15a to compensate for the various density differences), the particle diameter distribution can be obtained by using a calibration procedure based on equation 10. (The procedures are detailed in reference 20.) The results are shown for three chromatographic supports in Figure 16.

The same supports are analyzed somewhat more conveniently (with a similar calibration method) by flow FFF because density effects need not be considered (nor can density values be obtained). Flow FFF thus yields independent size distribution curves; these are also shown in Figure 16. The agreement in the two sets of distribution curves is excellent; this agreement suggests that these two totally independent methods are capable of providing reliable and accurate size distribution information for particles with $d > 1$ μm. (The small discrepancy around 2 μm may result from the fact that the Sed I system was accurately calibrated only down to 4 μm.)

Conclusions

Although FFF clearly has many advantages in the characterization of colloidal and particulate silica, a number of experimental difficulties must

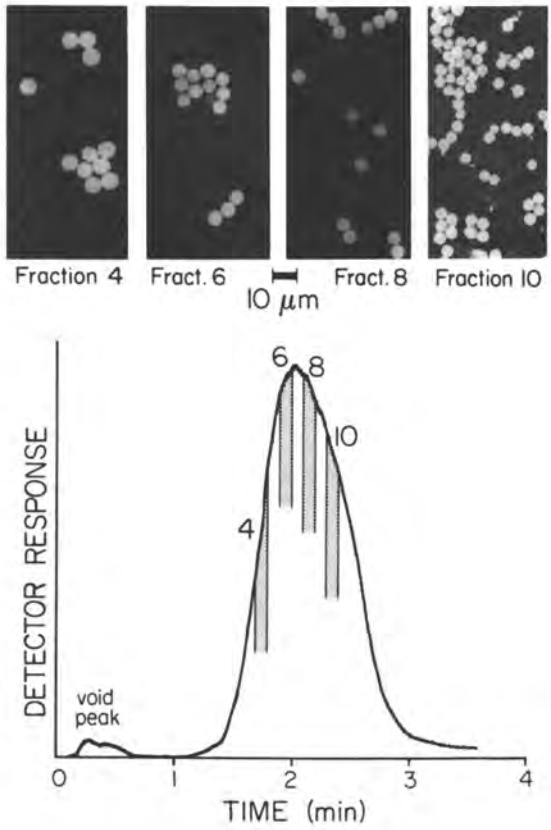

Figure 14. Fractogram from sedimentation FFF system Sed I of the chromatographic support Hypersil-5 (136-Å pore size) along with electron micrographs of particles collected in fractions 4, 6, 8, and 10.

still be resolved in certain areas. These results show, for example, that the quality of the experimental data, particularly for the Ludox and Cab-O-Sil silicas, would be greatly improved by finding detectors having higher sensitivity and by finding ways to remove the uncertainties of the light-scattering correction applied to conventional UV detectors. (Such uncertainties are common to many particle-sizing methods.) In addition, there are indications of occasional particle–wall interaction and adsorption problems found in the analysis of the colloidal materials, particularly with flow FFF.

Despite some present limitations, the data reported in this chapter demonstrate that FFF has some powerful and unique capabilities in silica characterization. The flexibility of FFF in analyzing particles at different size extremes is one asset. Perhaps the most outstanding advantage of FFF,

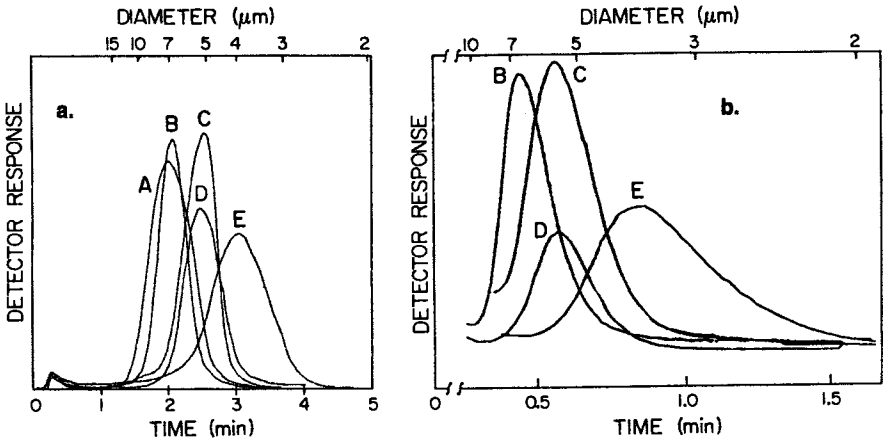

Figure 15. Fractograms of chromatographic silicas identified (by letter) in Table II obtained by using (a) sedimentation FFF system Sed I and (b) flow FFF system Flow II. The diameter scale at the top is obtained by using a calibration process based on equation 10 and the measured retention times of polystyrene latex standards. For sedimentation FFF, density compensation is carried out by adjusting the spin rate for each support material in accordance with its density (20). The corresponding spin rates utilized are A, 465; B, 479; C, 425; D, 500; and E, 475 rpm.

however, stems from its utilization of high-resolution fractionation and the associated capability of collecting narrow fractions for further examination by other techniques, such as microscopy. The fruits of this capability were demonstrated in the isolation and identification of colloidal aggregates, in the acquisition of particle densities and porosities for chromatographic silica, and so on. The possibility of obtaining detailed structural information on fumed silica is very likely to be realized by combining sedimentation FFF and flow FFF; fractions would be shunted from one system to another to exploit the complementary information they provide.

The capability of FFF to produce high-resolution (and thus detailed) size distribution curves in the submicrometer-size range is particularly important. Submicrometer-size distributions extending down to 5-nm diameter, as obtained from flow FFF, are generally very difficult to obtain by other techniques. For such small particles, electron microscopy is a primary tool, but electron microscopy can be used even more beneficially in combination with FFF, particularly if aggregation or other morphological features of the sample materials must be examined.

A more recent development in FFF, demonstrated by the results presented, is found in its capability of producing both rapid (often in 2–3 min) and accurate size distribution data for supramicrometer-size particles.

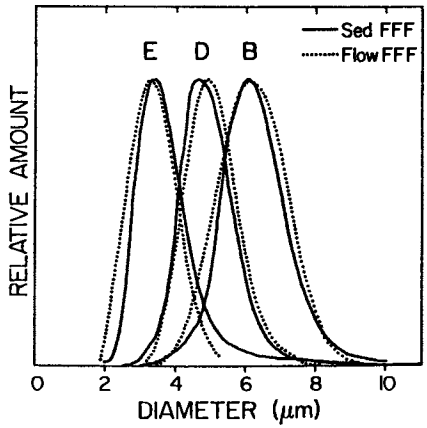

Figure 16. Comparison of size distribution curves of chromatographic silica obtained independently by sedimentation FFF and flow FFF. The three materials are B, Hypersil-5 (120-Å pore size); D, Nucleosil; and E, Hypersil-3.

The extension of this capability to the measurement (with the aid of microscopy) of particle densities and porosities in this size range, as described here, is also significant.

Acknowledgments

We thank Edward King of the Biology Department, University of Utah, for help and advice on electron microscopy; Richard Geiger of Cabot Corporation for providing the image analysis data for the Cab-O-Sil silicas; Andre Kumerrow of FFFractionation, Inc., for technical assistance; and the companies who contributed samples for this work. This work was supported by Grant CHE–9102321 from the National Science Foundation.

List of Symbols

c	particle concentration
c_0	particle concentration at accumulation wall
d	particle diameter
d_s	Stokes diameter
D	diffusion coefficient
D_T	thermal diffusion coefficient
F	driving force exerted by field on a particle
G	field strength measured as acceleration
G_0	initial field strength

k Boltzmann constant
ℓ mean particle elevation
m particle mass
p power parameter in power programming
S_d diameter-based selectivity
t_1 predecay time
t_a power programming time constant
t^0 void time
t_r particle retention time
t_{r1} retention time of particle of unit diameter
t_{sf} stop-flow time
T absolute temperature
U field-induced velocity
$\dot{V}$ channel flow rate
$\dot{V}_c$ cross-flow rate
x distance above accumulation wall
w channel thickness
ΔT temperature difference between hot and cold walls
$\Delta\rho$ difference between particle and carrier density
η viscosity
λ retention parameter
ρ_p particle density

References

1. Iler, R. K. *The Chemistry of Silica*; Wiley: New York, 1979.
2. Giddings, J. C.; Yang, F. J. F.; Myers, M. N. *Sep. Sci.* **1975**, *10*, 133–149.
3. Giddings, J. C.; Myers, M. N.; Yang, F. J. F.; Smith, L. K. In *Colloid and Interface Science*, Vol. IV; Kerker, M., Ed.; Academic Press: New York, 1976; pp 381–398.
4. Giddings, J. C.; Lin, G. C.; Myers, M. N. *J. Colloid Interface Sci.* **1978**, *65*, 67–78.
5. Giddings, J. C.; Karaiskakis, G.; Caldwell, K. D.; Myers, M. N. *J. Colloid Interface Sci.* **1983**, *92*, 66–80.
6. Yang, F.-S.; Caldwell, K. D.; Giddings, J. C. *J. Colloid Interface Sci.* **1983**, *92*, 81–91.
7. Kirkland, J. J.; Dilks, C. H., Jr.; Yau, W. W. *J. Chromatogr.* **1983**, *255*, 255–271.
8. Caldwell, K. D. *Anal. Chem.* **1988**, *60*, 959A–971A.
9. Giddings, J. C. *Chem. Eng. News* (October 10) **1988**, *66*, 34–45.
10. Williams, P. S.; Giddings, J. C. *Anal. Chem.* **1987**, *59*, 2038–2044.
11. Giddings, J. C. *Sep. Sci.* **1966**, *1*, 123–125.
12. Kirkland, J. J.; Yau, W. W.; Doerner, W. A.; Grant, J. W. *Anal. Chem.* **1980**, *52*, 1944–1954.
13. Yonker, C. R.; Jones, H. K.; Robertson, D. M. *Anal. Chem.* **1987**, *59*, 2573–2579.
14. Giddings, J. C.; Myers, M. N.; Caldwell, K. D.; Pav, J. W. *J. Chromatogr.* **1979**, *185*, 261–271.

15. Ratanathanawongs, S. K.; Giddings, J. C. *J. Chromatogr.* **1989,** *467,* 341–356.
16. Giddings, J. C.; Moon, M. H. *Anal. Chem.* **1991,** *63,* 2869–2877.
17. Giddings, J. C.; Karaiskakis, G.; Caldwell, K. D. *Sep. Sci. Technol.* **1981,** *16,* 607–618.
18. Giddings, J. C.; Chen, X.; Wahlund, K.-G.; Myers, M. N. *Anal. Chem.* **1987,** *59,* 1957–1962.
19. Williams, P. S.; Koch, T.; Giddings, J. C. *Chem. Eng. Commun.* **1992,** *111,* 121–147.
20. Giddings, J. C.; Moon, M. H.; Williams, P. S.; Myers, M. N. *Anal. Chem.,* **1991,** *63,* 1366–1372.
21. Liu, G.; Giddings, J. C. *Anal. Chem.* **1991,** *63,* 296–299.
22. Kirkland, J. J.; Rementer, S. W.; Yau, W. W. *Anal. Chem.* **1981,** *53,* 1730–1736.
23. Nyacol 9950 colloidal silica product bulletin, Nyacol Products, Inc., Ashland, MA 01720.

RECEIVED for review June 19, 1991. ACCEPTED revised manuscript December 26, 1991.

17

Interpretation of the Differences Between the Pore Size Distributions of Silica Measured by Mercury Intrusion and Nitrogen Adsorption

A. R. Minihan, D. R. Ward, and W. Whitby

Unilever Research Port Sunlight, Quarry Road East, Bebington, Wirral, Merseyside, L63 3JW, United Kingdom

Measuring the nitrogen sorption isotherms of a number of silicas both before and after analysis by mercury intrusion demonstrates that mercury intrusion can lead to compression of silica structures and that this compression can account for differences in pore size distributions measured by the nitrogen sorption and mercury intrusion techniques. These techniques are widely employed in the structural characterization of porous solids, often independently, despite the fact that very often the pore size distributions obtained by the two techniques fail to agree. Compression effects must be recognized because use of incorrect information can lead to misconceptions regarding the structure of a material.

MERCURY INTRUSION AND NITROGEN SORPTION are two common techniques used to analyze the structures of porous solids. However, they can give different pore size distributions or pore volumes for a given solid. Giles et al. (*1*) suggested that differences between pore size distributions as measured by mercury intrusion and by nitrogen sorption might be due to progressive rearrangement of the structure during mercury intrusion analysis followed by breakthrough into the voids between the globular particles when the particles reach a coordination number of 4. More recent work (*2*) on fume silicas and silica aerogels, which were examined by

0065–2393/94/0234–0341$08.00/0

mercury intrusion after enclosure in an impermeable membrane, demonstrated that the bulk of the intrusion that takes place with such materials is associated entirely with compaction of the powder particles.

The effect of mercury intrusion analysis on structure was examined for a series of silica xerogels with different pore size distributions. This analysis was achieved by applying nitrogen sorption analysis to the silicas both before and after mercury intrusion analysis. The study required the development of a method for the removal of mercury from a sample after the initial intrusion measurement that does not damage the structure. The results show the potential for an elastic deformation of the structure during compression as well as irreversible compression during mercury intrusion.

Experimental Details

Materials. The silica samples were selected on the basis of high purity, narrow pore size distributions, and availability with a large particle size, such that the inter- and intraparticle porosity regions are clearly distinguishable in the mercury intrusion curves. This feature allows the examination of the internal pore structure without the confusion of overlapping interparticle porosity. An experimental sample of silica [similar to silica produced by Crosfield Chemicals, Warrington, United Kingdom, as a support for Phillips ethylene polymerization (EP) catalyst] and a series of silicas manufactured by Crosfield for chromatographic applications (Sorbsil C60, Sorbsil C200, and Sorbsil C500) were examined. The surface areas of these materials, determined from the nitrogen adsorption isotherms by the Brunauer–Emmett–Teller (BET) equation (*3*), are shown in Table I. The effect of mercury intrusion on a sample of silica spheres (S980 G1.7, manufactured by Shell) was also examined. To eliminate any errors due to moisture sorption by the silicas, all samples were predried at 120 °C for at least 2 h and stored in a desiccator until used.

Table I. Surface Areas of Silica Samples

Sample	*BET Surface Area*
EP silica	301
Sorbsil C60	511
Sorbsil C200	299
Sorbsil C500	114

NOTE: Data are reported as square meters per gram.

Nitrogen Gas Adsorption Analysis. The apparatus used was a Micromeritics ASAP 2400, a fully automatic nitrogen gas sorption apparatus that can be programmed to measure gas adsorption and desorption isotherms and calculate surface areas and pore volumes by using a number of widely accepted procedures. All samples were outgassed initially at room temperature until a pressure of less than 100 mtorr (13 Pa) was achieved. Outgassing was completed by heating the samples to 120 °C and evacuating until a pressure of less than 5 mtorr (0.7 Pa) had been sustained for at least 2 h. The criteria for terminating the outgassing step was

the attainment of a stable pressure less than 5 mtorr and was not based on the outgassing time. Typical outgassing times were between 12 and 18 h, and the samples were held under vacuum until the start of the analysis. After outgassing, the samples were cooled under vacuum and the tubes were back-filled with helium before being transferred to the analysis ports.

The surface areas in Table I were obtained from the adsorption isotherms by using the BET method (3). The relative pressure range used for BET analysis was selected to give the best linear correlation with the BET function, and the surface areas were calculated by assuming a molecular cross section for the nitrogen molecule of 0.162 nm^2.

The pore size distributions were calculated by using the desorption isotherm, following the method of Barrett, Joyner, and Halenda (BJH) (*4*). In this procedure the Kelvin equation is used to calculate the radius r_p of the capillaries, which are assumed to be cylindrical:

$$\ln\left(\frac{p}{p_0}\right) = \frac{-nV_m\gamma}{r_pRT}\cos\Theta \tag{1}$$

Here V_m is the condensed molar volume (34.68 cm^3/mol for nitrogen); γ is the liquid–vapor surface tension (8.72×10^{-3} N/m for nitrogen); R is the gas constant; T is the temperature; p is the pressure of nitrogen above the sample; p_0 is the saturation vapor pressure of nitrogen at temperature T; and n is a unitless factor. The contact angle Θ is assumed to be zero, and the value of n is set to 2 for the desorption branch of the isotherm. The pore radius is then calculated from r_p by adding the thickness of the adsorbed layer present before capillary condensation takes place. This thickness (t) is calculated by using the Halsey (5) equation:

$$t = \sigma \sqrt[3]{\frac{5}{\ln\frac{p_0}{p}}} \tag{2}$$

A value of 0.354 nm is used for the average thickness σ of a single molecular layer of nitrogen. The algorithm used in the ASAP 2400 software is based on Faas's (*6*) implementation of the BJH method.

Mercury Intrusion Analysis. Mercury intrusion measurements were carried out with a porosimeter (Micromeritics 9220) capable of intruding mercury with intrusion pressures (p) up to 414 MPa (60,000 psi). Pore size distributions were calculated from the intrusion curve by using the Washburn (*7*) equation:

$$p = \frac{-2\gamma\cos\Theta}{r_p} \tag{3}$$

A value of 140 °C was used for the contact angle of mercury on the solid (Θ), and the surface tension of mercury (γ) was taken as 0.485 N/m. These values correspond to an effective working range for the instrument of 150 μm to 1.7 nm in pore radius. The samples were outgassed at room temperature to a pressure of 50 mtorr (7 Pa) immediately prior to analysis to facilitate filling the penetrometers with mercury. All data were fully corrected for mercury compression with calibrated penetrometers.

Experimental Procedure. Each sample was first characterized by both mercury intrusion and nitrogen sorption. Mercury intrusion measurements were replicated at least four times, and the solid residues from each analysis were collected and combined after the bulk of the mercury was decanted. These samples were washed free of mercury by using 50% nitric acid (25 mL per 0.5 g of solid) and then washed free of acid by filtering and reslurrying in demineralized water (six times with 50 mL per 0.5 g of solid). The washed samples were then rapidly cooled in liquid nitrogen and freeze-dried (Chemlab SB4). For comparison, samples of material that had not been analyzed with mercury intrusion were washed and dried in a similar manner to test for structural modification caused by the acid-washing technique.

After being dried, the samples were reexamined by nitrogen sorption and mercury intrusion, and a portion of the material was analyzed to determine the residual mercury levels. This analysis was achieved by acid digestion (10 mL of 50% aqua regia; sample sizes were approximately 0.2 g in all cases) in pressure-sealed poly(tetrafluoroethylene) (PTFE) tubes heated to 140 °C for 10 min in a microwave oven (CEM). The solutions were analyzed after suitable dilution in distilled water with a graphite furnace atomic absorption spectrometer (Perkin Elmer 5100-PC). The detection limit for this method is estimated to be 6 ppm of mercury on the dry solid.

Results and Discussion

The pore size distribution of the high-pore-volume silicas used for EP applications can be determined from the nitrogen adsorption isotherms by using the BJH method (*3*) described; a typical isotherm is shown in Figure 1. The isotherm has a "type A" hysteresis loop according to de Boer's classification (*8*), and this hysteresis indicates the pore structure has a uniform cylindrical form with no evidence of "ink bottle" pores. These structures, however, have a mercury intrusion curve similar to that shown in Figure 2. Three distinct regions of intrusion are usually observed; the first intrusion step at around 30 μm is associated with the voids between particles, and its exact position is dependent on the particle size distribution of the sample. This interparticle intrusion step is not of interest here, and the silicas selected for study were chosen because they have large particle sizes. Inter- and intraparticle pore size regions are thus easily resolved, and data interpretation in the remainder of this chapter concentrates solely on the internal porosity. The second and third intrusion steps are associated with the intraparticle porosity and should be directly comparable to the nitrogen desorption pore size distributions. Figure 3 shows such a comparison for the model EP-type silica.

These curves show that the pore size distributions measured by the two techniques are different, although the total pore volumes are similar. This observation suggests that although the two techniques are measuring the same pore structure, either the models used in the interpretation of the data are inappropriate and do not adequately describe the pore structure or the structure is modified during analysis. Earlier workers (*1*, *2*)

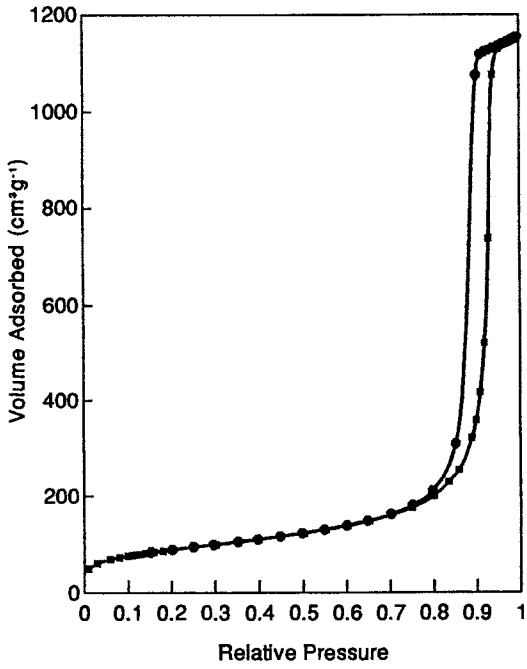

Figure 1. Nitrogen sorption isotherms of a typical high-pore-volume silica used in EP applications.

suggested that these differences are due to compression of the silica structure under the pressure applied in the mercury intrusion analysis. If this assessment is correct, such compression should be reflected in a change in the structure as determined by nitrogen sorption following the mercury intrusion experiment.

Effect of Mercury Removal Method on Silica Structure. To ensure that the washing technique used to remove the mercury from the samples after intrusion analysis does not alter the silica structures, some of the original samples of silica were treated in identical fashion and then reanalyzed by nitrogen sorption. Figures 4 and 5 show the nitrogen desorption pore size distribution curves of the Sorbsil C60 and Sorbsil C200 samples before and after such treatment. These results demonstrate that no significant structural modification results from the acid-washing treatment.

Analysis for residual mercury with the digestion method described indicated that only trace amounts of mercury remain on the samples after the initial washing (Table II). A detected level of 1000 ppm of residual mercury would result in an apparent loss in pore volume of 0.074 cm^3/g of

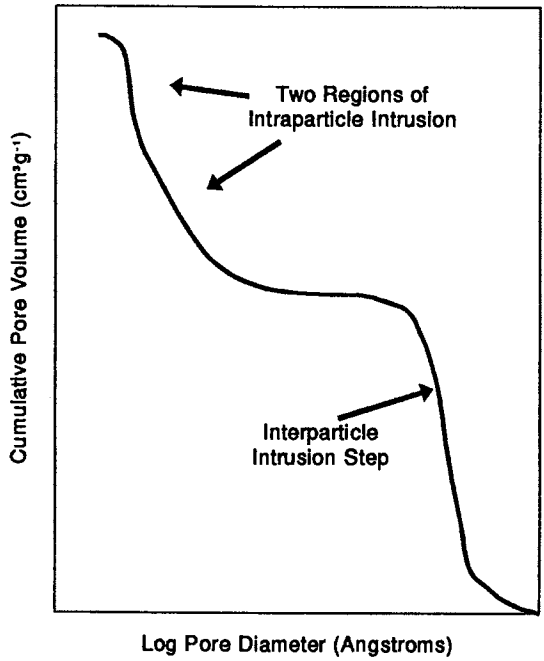

Figure 2. Mercury intrusion curve of a typical high-pore-volume silica used in EP applications.

silica. Thus the detected levels are always sufficiently low that any reduction in pore volume after intrusion cannot be explained in terms of residual mercury in the pore structure.

Effects of Mercury Intrusion. The facts that there is very little residual mercury in the solids after extraction and that the extraction method used does not cause any detectable structural modification have been established; now the earlier suggestion (*1*) that mercury intrusion causes compression of the pore structures can be examined.

Pore Structure of Sorbsil C500. Figure 6 depicts the internal cumulative pore volume as a function of pore diameter for Sorbsil C500. The total pore volumes as measured by the two techniques agree to within 0.05 cm^3/g; the pore volume measured by mercury porosimetry is slightly higher, possibly because this is an extremely wide-pored silica, with some pores too wide to be measured by nitrogen sorption.

As with the EP catalyst support, the nitrogen sorption technique (curve a) gives rise to a sharp, monotonic increase in pore volume over a narrow range of pore sizes, whereas the mercury intrusion technique

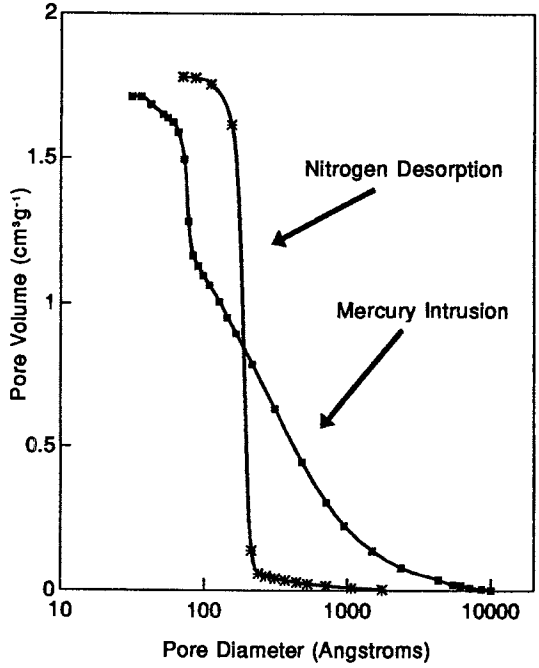

Figure 3. Comparison of the pore size distribution of a high-pore-volume silica measured by mercury intrusion and nitrogen desorption.

yields a broad, almost linear increase in pore volume at large (>50 nm) pore sizes followed by a sharp increase in pore volume at pore diameters in the range 30–50 nm.

Whereas this broad portion of the intrusion curve represents the majority of the pore volume for the EP catalyst support (Figure 3), it corresponds only to approximately 20% of the total pore volume for the C500 silica. This fact is consistent with the concept of a compression step followed by an intrusion step, because the crossover between compression and intrusion would be expected to occur at a lower pressure for the more highly aged, wider pore silica.

Curve c in Figure 6 represents the pore size distribution as measured by nitrogen desorption after mercury intrusion analysis and subsequent mercury removal. The mercury intrusion clearly results in a significant loss in pore volume, an observation consistent with an irreversible compression of the silica during the intrusion process. This loss in pore volume as measured by nitrogen desorption is 0.32 cm^3/g, a value corresponding fairly closely to the 0.4 cm^3/g that represents the broad–diffuse portion of the intrusion curve. The reanalysis by nitrogen sorption thus provides strong evidence that the silica is irreversibly co

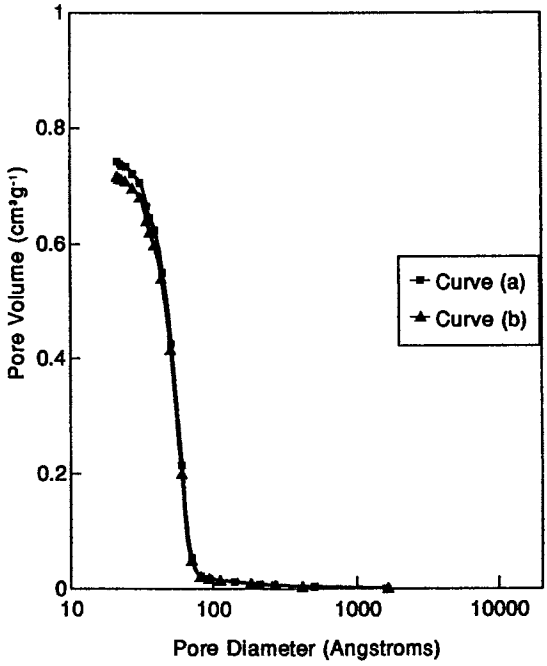

Figure 4. Effect of the mercury removal method on the pore structure of Sorbsil C60. Curve a is the material before treatment, and curve b is that after treatment.

mercury intrusion experiment. True intrusion into the pores only appears to occur when the work required to cause further compression is less than that required to force mercury into the pores. The intrusion pressure (and hence the apparent pore size) at which this situation occurs will be a function of the original pore size distribution and the strength of the silica structure.

Mercury Intrusion Experiments with Silica Spheres. These silica spheres (S980 G1.7 from Shell) were not examined in the same detail as were the other silica samples, but the photographs are included because they illustrate the effect of mercury intrusion on the integrity of the solid. These particular spheres have a typical pore volume of 1 cm^3/g and a pore diameter of 60 nm. The particles are also much larger than the Sorbsil materials (1.7 mm in diameter, compared to 40 to 60 μm for the Sorbsil materials).

Despite the fact that the pores in this material are quite large, the deformation caused by the compression effect is clearly demonstrated in Figure 7. The most noticeable feature in these pictures is the cracked and

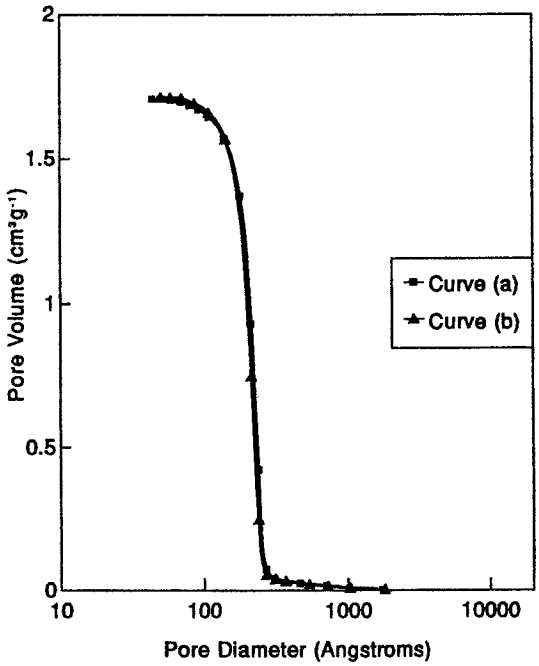

Figure 5. Effect of the mercury removal method on the pore structure of Sorbsil C200. Curve a is the material before treatment, and curve b is that after treatment.

Table II. Mercury Levels After Intrusion and Washing

Sample	*Mercury Level Detected*
EP silica	320
Sorbsil C60	90
Sorbsil C200	1300
Sorbsil C500	60

NOTE: Data are reported as parts per million.

broken nature of the particle surfaces and some slight indications of concave surfaces between the cracks. The integrity of the spheres is otherwise substantially maintained. These spheres have pores slightly larger than those of the Sorbsil C500, and a similar effect might be expected from the compression of the C500. Rather than create large cracks in the surface, however, the smaller particle size material probably simply fractures into even smaller pieces. If this breakdown occurs, internal porosity is lost in favor of interparticle porosity.

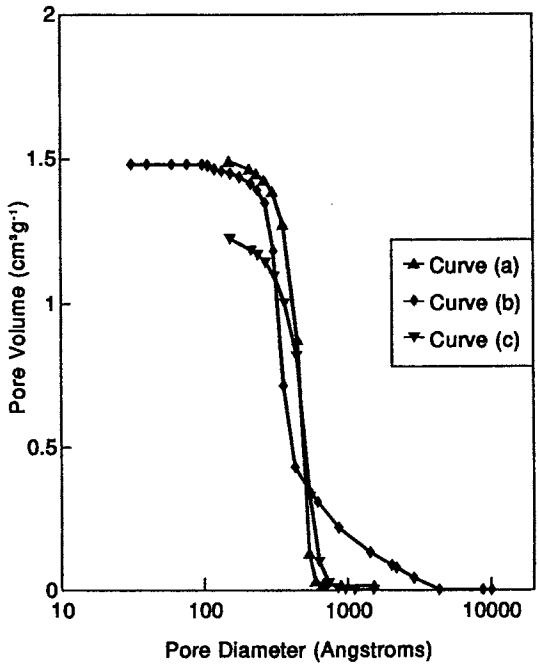

Figure 6. Effect of mercury intrusion on Sorbsil C500. The pore size distribution of the original material measured by nitrogen desorption is shown as curve a and that measured by mercury intrusion is shown as curve b. Curve c shows the nitrogen desorption pore size distribution after mercury intrusion and the removal of mercury.

Pore Structure of Sorbsil C200. The results obtained for the pore size distributions of Sorbsil C200 material are shown in Figure 8. Nitrogen adsorption (curve a) and mercury intrusion (curve b) again give different pore size distributions, the differences in the distributions being similar to those observed for the EP support (Figure 3). The internal pore volume as measured by mercury porosimetry is about 0.1 cm^3/g less than that obtained by nitrogen sorption. This difference may be due to the somewhat arbitrary choice of 1000 nm as the cutoff point between inter- and intraparticle porosity; some intrusion–compression may occur at larger pore sizes–lower pressures.

As was observed for the C500 silica, reanalysis of the pore structure by nitrogen sorption (Figure 8, curve c) following intrusion and removal of mercury indicates that the porosimetry experiment results in a permanent loss in pore volume and a shift to smaller pore sizes. In C200, however, this loss in pore volume no longer approximates that associated with the broad–diffuse area of the intrusion trace. Instead, the loss represents only

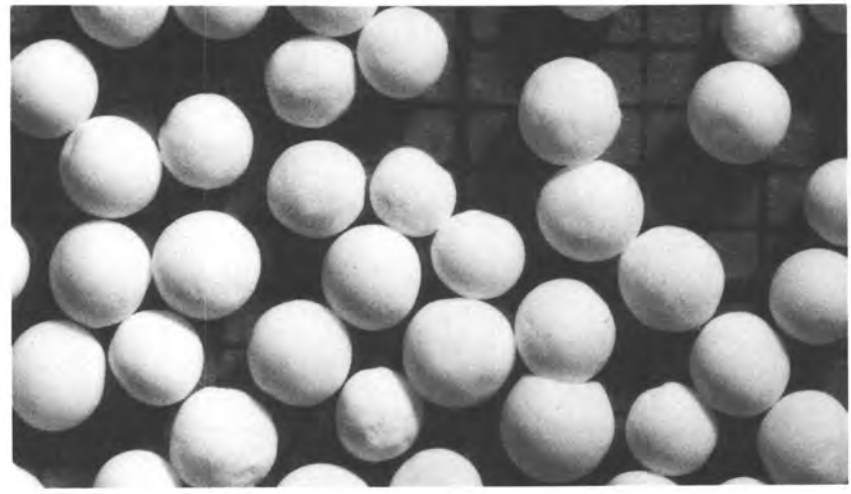

a

b

Figure 7. Effect of mercury intrusion on silica spheres (Shell). Top, starting material; and bottom, material after mercury intrusion (no attempt was made to remove the mercury).

about 40% of this region. Furthermore, a second intrusion experiment yields a trace (curve d) that confirms the loss in pore volume, but shows the same two regions, with an apparent compression phase followed by an intrusion step at virtually the same apparent pore size as in the initial intrusion experiment (curve b).

From this data the structure can be concluded to be compressed during the first mercury intrusion, but the compression region (i.e., the

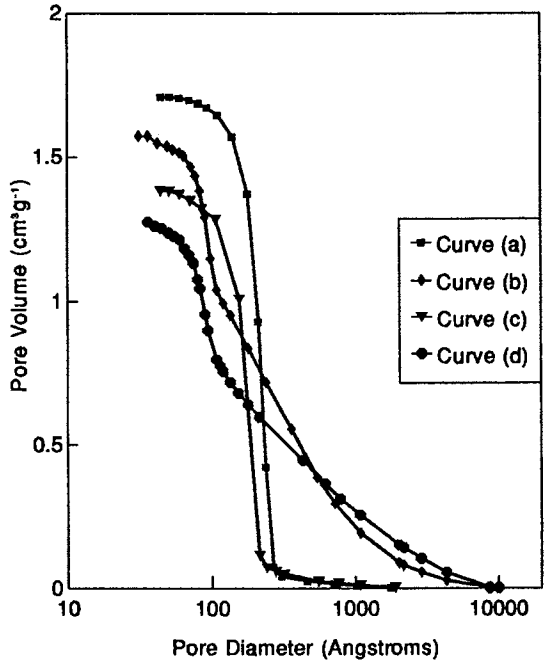

Figure 8. Effect of mercury intrusion on Sorbsil C200. The pore size distribution of the original material measured by nitrogen desorption is shown as curve a, and that measured by mercury intrusion is shown as curve b. The pore size distribution after removal of the mercury is shown as curve c (nitrogen desorption) and curve d (mercury intrusion).

initial gradual slope) must contain two contributions, one associated with an irreversible collapse and a second associated with elastic compression. In Sorbsil C500, the irreversible collapse appears to account for virtually all of this region, whereas the two phenomena are of approximately equal magnitude in C200 silica.

Pore Structure of Sorbsil C60. Examination of a silica with a relatively small pore size, such as Sorbsil C60, produces a different picture. The results (Figure 9) indicate differences in both pore size distributions and pore volumes as measured by nitrogen desorption (curve a) and mercury intrusion (curve b). Pore volumes measured by mercury intrusion are now significantly lower than those measured by nitrogen sorption, and the intrusion trace does not show a sharp step as the intrusion pressure increases, but rather only the initial gradual slope, which extends throughout the measured range of the intrusion plot (40–1000 Å pore diameter). This observation suggests that the structure is still being

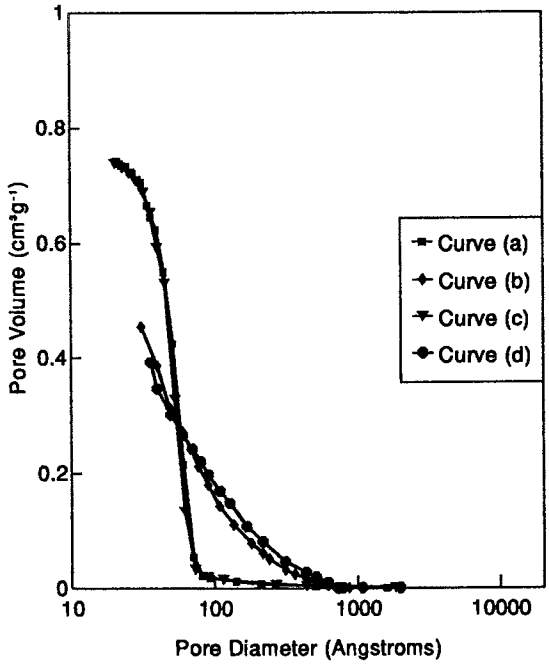

Figure 9. Effect of mercury intrusion on Sorbsil C60. The pore size distribution of the original material measured by nitrogen desorption is shown as curve a, and that measured by mercury intrusion is shown as curve b. The pore size distribution after removal of the mercury is shown as curve c (nitrogen desorption) and curve d (mercury intrusion).

compressed and that no intrusion has taken place when the upper pressure limit of the porosimeter has been reached.

Curves c and d in Figure 9 show nitrogen desorption and mercury intrusion traces, respectively, for pore size distributions after the initial intrusion experiment and subsequent mercury removal. In a surprising result, no permanent modification to the structure was caused by the initial intrusion experiment. In view of the results obtained with the silicas of larger pore size (Sorbsil C200 and C500), the results can be rationalized only in terms of a completely elastic compression of the structure during the intrusion experiment.

Conclusions

These results confirm the suggestions of earlier workers (*1*, *2*) that the mercury intrusion method can lead to structural deformation of solids during analysis. For silicas, there appears to be both an elastic deformation and an irreversible compression effect that contribute to the differences in

pore size distributions measured by nitrogen sorption and mercury intrusion. The irreversible compression appears to dominate in wide-pored silicas, which are presumably highly aged and therefore strong but brittle, whereas high-surface-area, low-pore-diameter silicas such as C60 undergo an almost completely elastic deformation.

With large-pore-size silicas (e.g., Sorbsil C500) the compressive effects of mercury intrusion are minimized because intrusion can take place into the pores at lower pressures. Pore volumes of such materials measured by mercury intrusion can be greater than those determined from nitrogen sorption because a significant fraction of pores lies outside the nitrogen sorption measurement range. Hence the pore size distributions measured by mercury intrusion can be more useful than the nitrogen sorption results.

Smaller pore size materials are subjected to greater compressive forces than wide-pore materials during mercury intrusion, because intrusion occurs at higher pressures and more marked structural changes occur before intrusion into the pores takes place. Some of this compression is an elastic deformation rather than an irreversible compaction. The pore sizes as measured by mercury intrusion for such materials are complex and depend not only on actual pore size distribution but on particle strength and deformability. As such, mercury intrusion is inappropriate for determining pore size distributions of these materials, although the technique can be used to determine total pore volumes as long as a sharp intrusion step is observed in the intrusion trace. Nitrogen sorption methods should therefore be used for the most realistic assessments of pore sizes for this type of material.

When the pore size of silicas is very small (as in C60), the compression of the structure caused by the mercury intrusion decreases the pore size to such an extent that it is outside the range for mercury intrusion analysis. The pore volumes measured represent only the compression region of the curve, and as a consequence the total pore volumes measured are lower than those measured for nitrogen. Nitrogen sorption methods are the only appropriate technique for this type of material.

The data presented show clearly the importance of using a combination of both mercury and nitrogen sorption methods if a complete understanding of porous solid structures is to be achieved. Even when mercury pore size distributions are capable of replication, they may not represent the true pore structure of the solid being examined.

Acknowledgments

We thank N. Whitehead for assistance in the development of the methodology for and determination of the residual mercury levels in the silica samples.

References

1. Giles, C. H.; Havard, D. C.; McMillan, W.; Smith, T; Wilson, R. In *Characterisation of Porous Solids*; Gregg, S. J.; Sing, K. S. W.; Stoeckli, H. F., Eds.; Society of Chemical Industry: London, 1979; pp 267–284.
2. Smith, D. M.; Johnston, G. P.; Hurd, A. J. *J. Colloid Interface Sci.* **1990,** *135,* 227–237.
3. Brunauer, S.; Emmett, P. H.; Teller, E. *J. Am. Chem. Soc.* **1938,** *60,* 309.
4. Barrett, E. P.; Joyner, L. G.; Halenda, P. P. *J. Am. Chem. Soc.* **1951,** *73,* 373–380.
5. Halsey, G. D. *J. Chem. Phys.* **1948,** *16,* 931.
6. Faas, G. S., Masters Thesis, Georgia Institute of Technology, Atlanta, GA, 1981.
7. Washburn, E. W. *Phys. Rev.* **1921,** *17,* 273.
8. de Boer, J. H. *The Structure and Properties of Porous Materials*; Butterworth: London, 1958; p 68.

RECEIVED for review December 18, 1990. ACCEPTED revised manuscript March 20, 1992.

18

Sol–Gel Processing of Silica

C. Jeffrey Brinker

Sandia National Laboratories, Albuquerque, NM 87185, and Center for Micro-Engineered Ceramics, University of New Mexico, Albuquerque, NM 87131

The sol–gel process for preparing silica and silicates from metal alkoxide precursors is reviewed and compared to the processing of aqueous silicates as described by Iler. Sol–gel processing combines control of composition and microstructure at the molecular level with the ability to shape material in bulk, powder, fiber, and thin-film form. In sol–gel processing of metal alkoxides, hydrolysis reactions replace an alkoxide group with a hydroxyl group. Subsequent condensation reactions involving the hydroxyl groups produce siloxane bonds. The structure of the evolving silicates is a consequence of the successive polymerization, gelation, aging, drying, and heating steps. Often the structures of polymers, gels, and dried gels (either xerogels or aerogels) may be characterized on the 1–20-nm length scale by a mass or surface fractal dimension. On longer length scales, dried gels are micro- or mesoporous, with surface areas often exceeding 800 m^2/g. During heating, these gels undergo continued polymerization, structural relaxation, and viscous sintering; dense amorphous silica essentially indistinguishable from its conventionally prepared counterpart ultimately results.

A SOL IS DEFINED AS A COLLOIDAL DISPERSION of particles in a liquid. A gel is a substance that contains a continuous solid skeleton enclosing a continuous liquid phase: the liquid prevents the solid from collapsing; the solid prevents (retards) the liquid from escaping. Thus the formal definition of sol–gel processing is the growth of colloidal particles and their linking together to form a gel. This definition has been expanded to include virtually all liquid-based processes for the preparation of ceramic materials. As illustrated in Figure 1, the formation of films, fibers, and

0065–2393/94/0234–0361$11.96/0

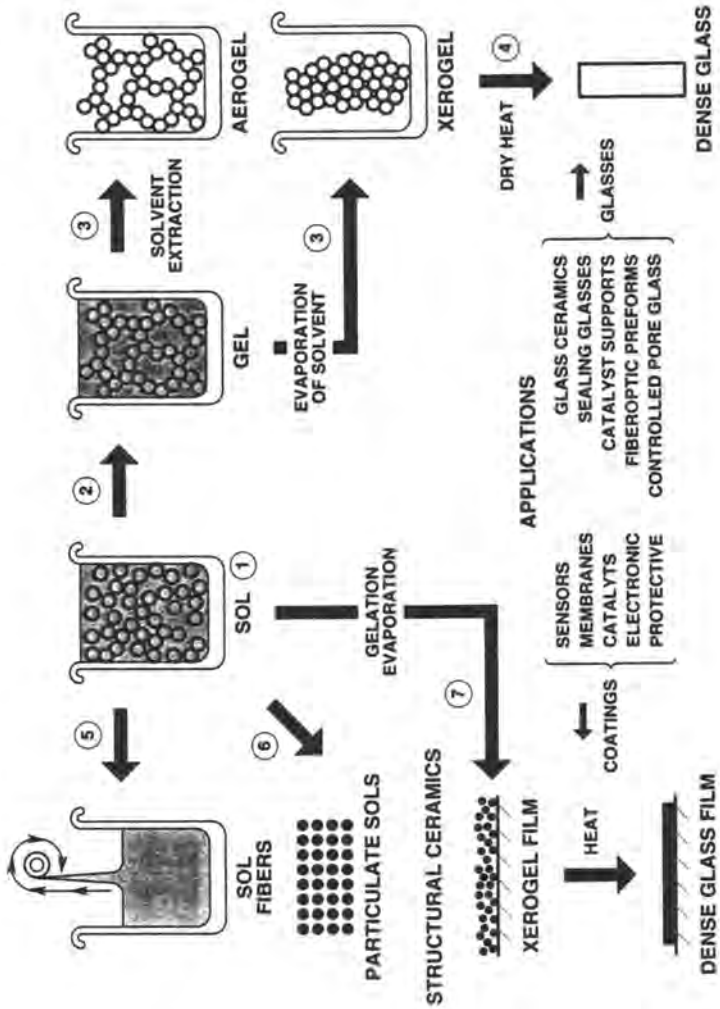

Figure 1. Illustration of the various stages of the sol–gel process. The numbers refer to the order in which these stages are presented in the text.

unaggregated particles are all considered sol–gel processes, even though gelation may not occur (particle formation), and often the sol is composed of polymers rather than particles (fiber formation).

The excitement of sol–gel technology derives from the ability to control composition and microstructure at the molecular level combined with the ability to shape the material at room temperature, for example, by casting bulk gels in precision molds, spinning fibers, or dip coating thin films (*1*). This chapter briefly reviews sol–gel technology for the preparation of silica and silicates (where silicate refers to any hydroxylated or alkoxylated forms of silica as well as multicomponent silicates, $M_xO{\bullet}SiO_2$). The discussion focuses on silicates prepared from metal alkoxide precursors. Where possible, comparisons are made with aqueous silicates as described by Iler in the classic monograph *The Chemistry of Silica* (*2*).

Additional information on sol–gel processing of ceramic materials in general includes review articles by Hench and West (*3*), Sakka (*4*), Masdiyasni (*5*), Roy (*6*), Zelinski and Uhlmann (*7*), and Zarzycki (*8*) as well as conference proceedings of the International Workshops on Gels (*9–14*), the International Conference on Ultrastructure Processing (*15–19*), and the Materials Research Society (MRS) Symposium on Better Ceramics Through Chemistry (*20–23*). Various applications of sol–gel processing are described in *Sol–Gel Technology for Thin Films, Fibers, Preforms, Electronics, and Specialty Shapes*, edited by Klein (*1*). The underlying physics and chemistry are described in *Sol–Gel Science* by Brinker and Scherer (*24*).

Hydrolysis and Condensation of Aqueous Silicates

The most weakly hydrolyzed form of silica detectable in aqueous solution is orthosilicic acid, $Si(OH)_4$ (*25*), although it is generally believed that protonation of silanols to form cationic species $\equiv Si(OH_2)^+$ can occur below about pH 2. Above pH 7, further hydrolysis involves the deprotonation of a silanol group to form an anionic species (*25*):

$$Si(OH)_4\ (aq) \rightarrow Si(OH)_3O^- + H^+ \qquad (1)$$

Because $Si(OH)_3O^-$ is a very weak acid, $Si(OH)_2O_2^{2-}$ is observed in appreciable quantities only above pH 12 (*25*).

By analogy to organic polymer systems, $Si(OH)_4$ may polymerize into siloxane chains that then branch and cross-link. However, Iler (*2*) states, "in fact, there is no relation or analogy between silicic acid polymerized in an aqueous system and condensation-type organic polymers." Iler recognizes three stages of polymerization: (1) polymerization of monomers to form particles; (2) growth of particles; and (3) linking of particles into branched chains, networks, and finally gels. Iler divides the polymerization process into three approximate pH domains: pH<2, 2–7, and >7. A pH of

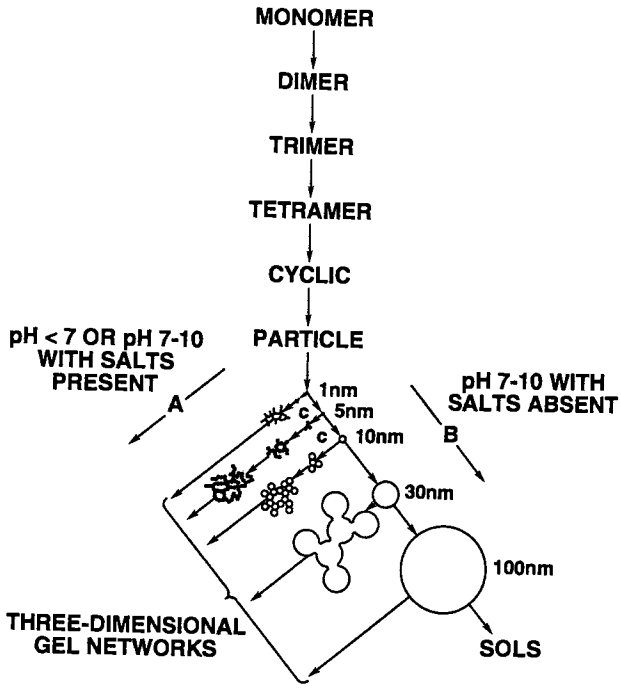

Figure 2. Polymerization pathway of aqueous silicates according to Iler (2). Stages of growth recognized by Iler: polymerization of monomer to form particles, growth of particles, and linking of particles together into branched chains, networks, and, finally, gels. (Reproduced with permission from reference 2. Copyright 1978.)

2 appears to be a boundary, because the point of zero charge (PZC), where the surface charge is zero, and the isoelectric point (IEP), where the electrical mobility of the silica particles is zero, both are in the range pH 1–3. A pH of 7 appears to be a boundary, because both the solubility and dissolution rates are maximized at or above pH 7, and because above pH 7 the silica particles are appreciably ionized (e.g., eq 1) so that particle growth occurs without aggregation or gelation. For all pH ranges, the addition of salt promotes aggregation and gel formation (2) (*see* Figure 2).

Because gel times decrease steadily between pH 2 and 6, it is generally assumed that polymerization above the IEP occurs by a bimolecular nucleophilic condensation mechanism (S_N2-Si) involving the attack of hydrolyzed, anionic species on neutral species (2):

$$\equiv SiO^- + \equiv Si{-}OH \rightarrow \equiv Si{-}O{-}Si\equiv + OH^- \qquad (2)$$

Because of inductive effects, the most acidic silanols. and hence the most likely to be deprotonated, are the most highly condensed species (*26*). Therefore condensation according to equation 2 occurs preferentially between more condensed species and less condensed, neutral, species. As suggested in Figure 2, this situation leads to a typical condensation pathway: monomer, dimer, trimer, and tetramer. Tetramers tend to cyclize because of the proximity of chain ends and the substantial depletion of the monomer population. Further growth occurs by addition of monomer and other low-molecular-weight species to cyclic species to create particles and by aggregation of particles to form chains and networks (*2*).

Growth above about pH 7 is distinguished from that below pH 7 by at least two factors: (1) Above pH 7, particle surfaces are appreciably charged, so particle aggregation is unlikely, whereas near the IEP there is no electrostatic particle repulsion, so the growth and aggregation processes occur together and may be indistinguishable. (2) Because of the greater solubility of silica and the greater size dependence of solubility above pH 7, growth of primary particles continues by Ostwald ripening, a process in which smaller, more soluble particles dissolve and reprecipitate on larger, less soluble particles. Growth ceases when the difference in solubility between the largest and smallest particles becomes negligible. Above pH 7, growth continues by Ostwald ripening at room temperature until the particles are 5–10 nm in diameter, whereas at lower pH growth stops after a size of only 2–4 nm is reached. Because of enhanced silica solubility at higher temperatures, growth continues to larger sizes, especially above pH 7 (*2*).

Because gel times decrease below the IEP, it is believed (*2*, *4*, *27*, *28*) that below about pH 2, condensation occurs by a bimolecular nucleophilic mechanism involving a protonated silanol:

$$\equiv SiOH_2^+ + HO-Si\equiv \rightarrow \equiv Si-O-Si\equiv + H^+ \qquad (3)$$

[Unlike in carbon chemistry, there is no evidence for a siliconium ion $\equiv Si^+$ (*29*).]

Hydrolysis and Condensation of Silicon Alkoxides

Tetramethoxysilane, $Si(OCH_3)_4$, abbreviated TMOS, and tetraethoxysilane, $Si(OCH_2CH_3)_4$, abbreviated TEOS, are the most commonly used metal alkoxide precursors in sol–gel processing of silicates (*24*). Silicate gels are most often synthesized by hydrolyzing the alkoxides dissolved in their parent alcohols with a mineral acid or base catalyst. At the functional group level, three bimolecular nucleophilic reactions are generally used to describe the sol–gel process (*24*):

$$\equiv Si{-}OR + H_2O \rightleftharpoons \equiv Si{-}OH + ROH \quad (4)$$

$$\equiv Si{-}OH + RO{-}Si\equiv \rightleftharpoons \equiv Si{-}O{-}Si\equiv + ROH \quad (5)$$

$$\equiv Si{-}OH + HO{-}Si\equiv \rightleftharpoons \equiv Si{-}O{-}Si\equiv + H_2O \quad (6)$$

The hydrolysis reaction (eq 4) replaces alkoxide groups with hydroxyl groups. Subsequent condensation reactions involving the silanol groups produce siloxane bonds plus the by-products alcohol (eq 5) or water (eq 6). The reverse of hydrolysis is esterification, in which hydroxyl groups are replaced with alkoxides. The reverse of condensation is siloxane bond alcoholysis (eq 5) or hydrolysis (eq 6).

The roles of acid or base catalysts are illustrated schematically in Figure 3 (*30*). The hydrolysis reaction appears to be specific acid or base catalyzed (*27, 29, 31*). Acid catalysts protonate the alkoxide group (eq 4), making a better leaving group (ROH) and avoiding the requirement for proton transfer in the transition state (*32*). Base catalysts dissociate water, producing a stronger nucleophile (OH^-) (*32*). The condensation reaction depends on the acidity of the silicate reactants. Above about pH 2, acidic silanols are deprotonated; strong nucleophiles, $\equiv SiO^-$, are created (*see* eq 2). Below about pH2, weakly acidic silanols or ethoxides are protonated, so good leaving groups (H_2O or ROH) are created and the requirement of charge transfer in the transition state (*see* eq 3) is avoided. The rate of siloxane bond hydrolysis increases above pH 4 and at very low pH (*2*). Similar behavior is expected for siloxane bond alcoholysis reactions. The esterification of silanols was reported (*33–35*) to proceed much faster under acid-catalyzed conditions.

Although making clear that there is no analogy between the polymerization of aqueous silicates and condensation-type organic polymers, Iler (*2*) suggested that such (molecular) siloxane networks "might be obtained under conditions where depolymerization is least likely to occur, so the condensation is irreversible and siloxane bonds cannot be hydrolyzed once they are formed." The solubility of silica is reduced by a factor of 28 when water is replaced by a 90 wt% methanol and 10 wt% water mixture (*2*); thus Iler's hypothesis might be realized under conditions in which silicon alkoxides are hydrolyzed with small amounts of water (generally, H_2O:Si ratios less than or equal to 4) especially below pH 7, at which the solubility and the dissolution rate are minimized (*see* Figure 3).

Evidence for molecular siloxane networks is abundant in numerous ^{29}Si NMR spectroscopy studies of alkoxides hydrolyzed under acidic conditions

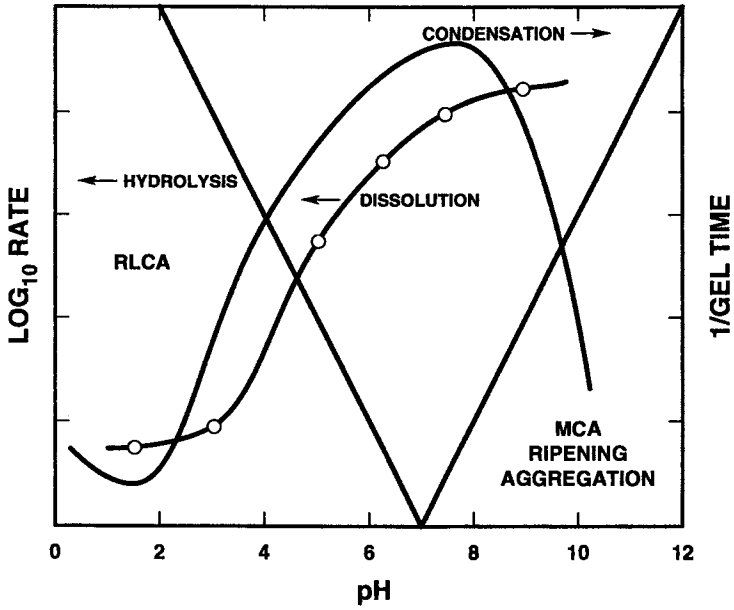

Figure 3. Illustration of the pH dependence of the hydrolysis, condensation, and dissolution rates of silica. Condensation rates are judged by the reciprocal of gel times. RLCA denotes reaction-limited cluster aggregation. (Reproduced with permission from reference 30. Copyright 1988.)

(*35–40*). Figure 4 (*41*) shows a sequence of ^{29}Si NMR spectra of TEOS hydrolyzed with 2 mol of water under acidic conditions in ethanol and for comparison a ^{29}Si NMR spectrum of a commercial aqueous silicate (Ludox). With time the TEOS sol becomes more highly condensed, as evident from the disappearance of monomer (Q^0) and the progressive formation of end groups and di-, tri-, and tetrasubstituted silicate species (Q^1–Q^4 species, respectively). However, even after 14 days, di- and trisubstituted species appear more prevalent than tetrasubstituted species. By comparison, ^{29}Si NMR spectra of aqueous silicates (Figure 4d) and base-catalyzed alkoxides (Figure 5) are dominated by monomer and tetrasubstituted species.

The prevalence of fully condensed Q^4 species in aqueous silicate sols (Figure 4d) is consistent with Iler's view (2) that particle growth occurs in a manner that maximizes the extent of internal condensation. Iler (2) stated that "at the earliest stage of polymerization, condensation leads to ring structures followed by addition of monomer and linking together of the cyclic polymers to (form) larger three-dimensional molecules. These condense internally to the most compact state with SiOH groups remaining on the outside." The paucity of Q^1–Q^3 species in the NMR spectra of

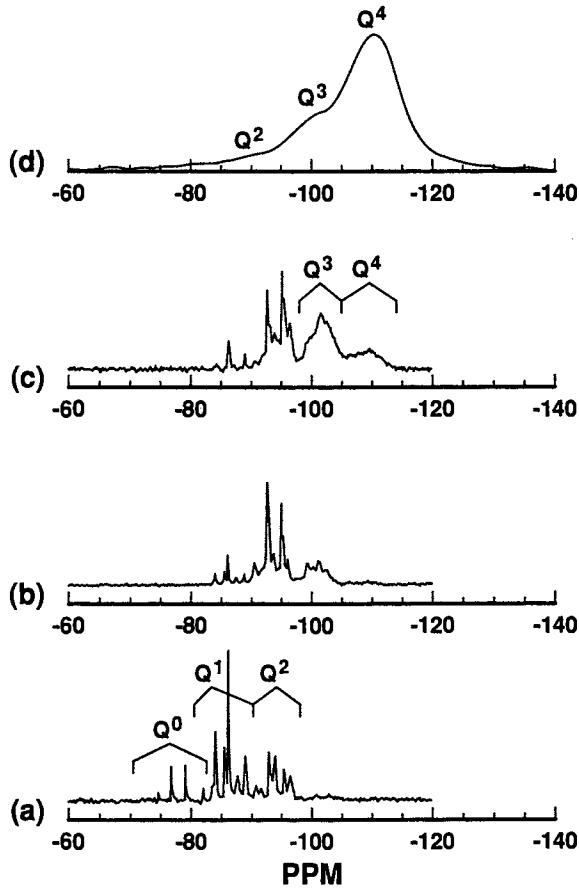

Figure 4. Comparison of ^{29}Si NMR spectra of an acid-catalyzed TEOS sol ($H_2O/Si = 2$) and a commercial aqueous silicate (Ludox HS40): (a) TEOS sol after 3 h; (b) TEOS sol after 3 days; (c) TEOS sol after 14 days of reaction; and (d) Ludox sol. Q notation refers to the number of bridging oxygens (–OSi) surrounding the central silicon atom (0–4). From Assink (41).

aqueous silicates and base-catalyzed alkoxides implies that under these conditions growth is dominated by the addition of monomer to highly condensed particles and that monomer addition is accompanied by extensive siloxane bond hydrolysis (ring opening) and reformation (so as to minimize Q^1–Q^3 species).

The distinction between particulate and polymeric silicate sols is also evident from small-angle scattering investigations (e.g., references 42–45) and from cryogenic transmission electron microscopy (cryo-TEM) investigations (*46*). Figure 6 compares small-angle scattering data obtained from a

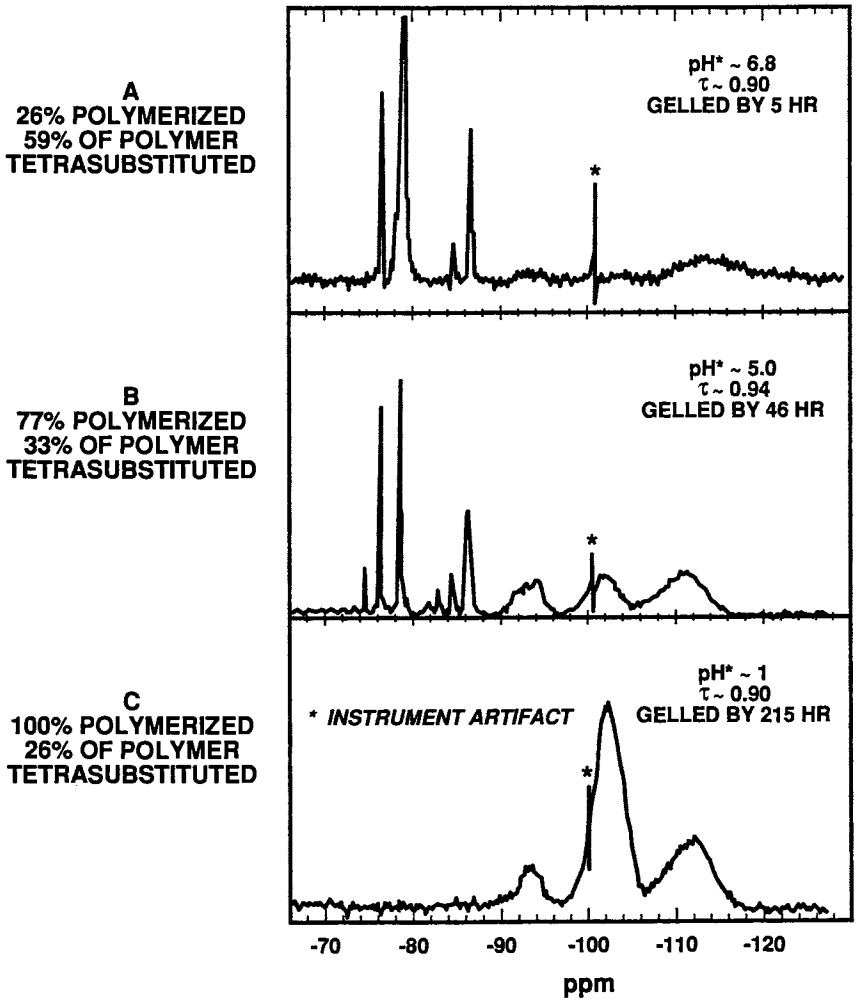

Figure 5. ^{29}Si NMR spectra of TEOS sols at $t/t_{gel} \geq 0.9$ for three different hydrolysis conditions. At pH ~1, all the monomer (~−70 to −80 ppm) is depleted; further growth must occur by CCA, whereas under neutral or basic conditions monomer persists and growth is biased to MCA. (Reproduced with permission from reference 40. Copyright 1986.)*

commercial aqueous silicate to that obtained from a variety of silicate sols prepared from alkoxides (*45*). The power–law relationships implied by the data can be interpreted on the basis of fractal geometry by the following expression (*43*):

$$P = -2D + D_s \tag{7}$$

where P is the Porod slope, D is the mass fractal dimension, and D_s is the surface fractal dimension (*47*). D relates an object's mass M to its radius r according to

$$M \sim r^D \tag{8}$$

Whereas for uniform (nonfractal) objects D would be the dimension of space 3, mass fractals are characterized by $D = D_s < 3$, so the density ρ of an object decreases with r as $\rho \sim 1/r^{(3-D)}$. D_s relates an object's area to its size. In three dimensions, D_s varies from 2 for a smooth (nonfractal) surface to 3 for a fractal surface that is so convoluted that it acquires the dimension of space. For nonfractal objects, $D = 3$ and $D_s = 2$, so $P = -4$, as shown by Porod and Kolloid (*48*).

Figure 6 shows that aqueous silicate sols are composed of uniform particles, whereas the various alkoxide-derived gels are either mass or surface fractals. These results have been rationalized by various reaction-limited kinetic growth models such as monomer–cluster aggregation (MCA) (*49*) and cluster–cluster aggregation (CCA) (*50*). In MCA, growth occurs by the addition of monomers to higher molecular weight species (clusters). In CCA, growth occurs by the addition of clusters to both monomers and other clusters. Reaction-limited conditions imply that the condensation rate is sufficiently low with respect to the transport (diffusion) rate that the monomer or cluster can sample many potential growth sites before reacting at the most favorable one (*49*). Reaction-limited conditions are obtained for most silicate synthesis schemes.

MCA requires a continual source of monomers, which, because of physical or chemical factors, condense preferentially with higher molecular weight species rather than themselves. Because growth occurs monomer-by-monomer under reaction-limited conditions, all potential growth sites are accessible; the result is compact, uniform (nonfractal) objects characterized by $P = -4$. ^{29}Si NMR spectra (e.g., Figure 5) show that a major requirement for MCA, namely, a source of monomer, is met for alkoxide-derived sols prepared at neutral or basic pH. As discussed earlier, the base-catalyzed condensation mechanism (eq 2) favors the reaction of low- and high-molecular-weight species, so the growth is biased toward MCA.

In CCA, monomers are depleted at an early stage of the growth process, so further growth must occur exclusively between clusters. Strong mutual screening of cluster interiors leads to ramified objects characterized by a mass fractal dimension $D \approx 2$ (Porod slope $P \approx -2$). As shown in Figure 6 for the two-step acid-catalyzed sample, Porod slopes of ~−2 are generally observed for silicate sols prepared from alkoxides under acid-

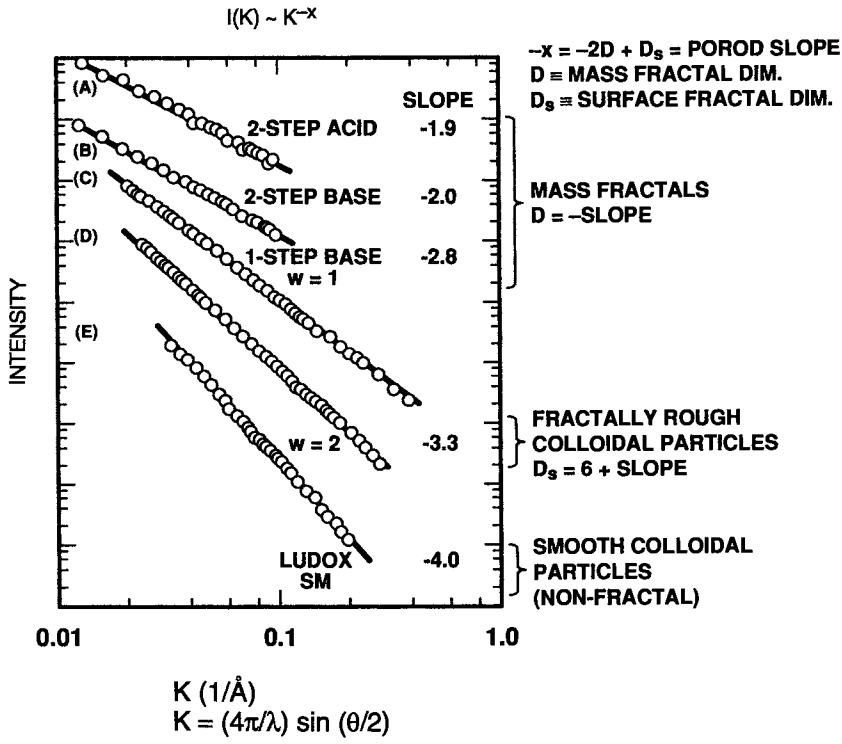

Figure 6. Log of scattered intensity versus log K *obtained by small-angle X-ray scattering (SAXS) for alkoxide-derived gels prepared under different hydrolysis conditions and a commercial aqueous silicate (Ludox SM). (Reproduced with permission from reference 44. Copyright 1985.)*

catalyzed conditions. Corresponding ^{29}Si NMR spectroscopy data for the two-step acid-catalyzed sample indicated that monomer was essentially depleted before the onset of measurable growth. Similarly, ^{29}Si NMR spectroscopy data presented in Figure 5 for an acid-catalyzed silica sol show that for normalized gel time $t/t_{gel} \sim 0.9$, the sol is 100% polymerized, so any further growth must occur by CCA. [In fact, ^{29}Si NMR spectroscopy showed that for these conditions monomer was depleted at a very early stage of the polymerization process, $t/t_{gel} = 0.01$ (*40*)].

MCA and CCA are just two of many plausible growth models, and the predictions of $P = -4$ and $P = -2$ for these two aggregation processes are not unique. However, the qualitative predictions of these models, namely, compact, uniform structures when growth proceeds in the presence of monomer and ramified, fractal objects in the absence of monomer, are generally observed.

Gelation and Aging

The gel point is defined as the time when an infinite, spanning polymer or aggregate first appears. For aqueous systems, Iler (*2*) observed the formation of three-dimensional gel networks below pH 7 or 7–10 with salts present (Figure 2) and attributed gelation to what is now known as ballistic cluster–cluster aggregation (*51*). As discussed later, gelation in both aqueous and alkoxide-derived sols is consistent with a percolative process involving cluster–cluster aggregates. The physical and chemical changes that occur after gelation but before complete drying are referred to as aging (*24*).

The first theory that attempted to derive the divergences in cluster mass and average radius accompanying gelation is that of Flory (*52*) and Stockmayer (*53*). In their model, bonds are formed at random between adjacent nodes on an infinite Cayley tree or Bethe lattice (*see* Figure 7). The Flory–Stockmayer (FS) model is qualitatively successful because it correctly describes the emergence of an infinite cluster at some critical extent of reaction and provides good predictions of the gel point. Although the polymerization of silicon alkoxides under acid-catalyzed conditions appears to produce molecular networks analogous to the organic polymers for which the FS model was developed, two inherent problems are encountered when adapting the FS approach to describe silicate polymers and gels. (1) Because of the nature of the Cayley tree, cyclic species are excluded, yet cyclic species are very prevalent in acid-catalyzed silicate sols (*36*) (*see* Figure 7). (2) Because cyclic configurations are avoided, the purely branched clusters formed on the Cayley tree are predicted to have a fractal dimension of 4 (*54*); a divergent density for large clusters results ($M \sim r^4$).

Because of problems with the FS approach, Stauffer (*55*) and de Gennes (*56*) advanced bond percolation as a description of polycondensation (*see* Figure 7). In the percolation model, bonds are formed at random between adjacent nodes on a regular or random d-dimensional lattice (*57*). In this approach, cyclic molecules are allowed and excluded volume effects are directly accounted for.

Aggregation of either particles (*see* Figure 2) or polymers is generally believed to account for the growth of clusters far from the gel point. As the clusters grow, their density decreases as $\sim 1/r$, so their volume fraction increases. Eventually, the clusters overlap and become nearly immobile. Further condensation involves a percolative process in which bonds form at random between large (~ 1 μm) aggregates, which are equivalent to nodes located on a random three-dimensional lattice. Martin and coworkers (*58*, *59*) have shown that the percolation model accounts for the static structure factor of alkoxide-derived silicate sols on the 25–400-nm length scale near the gel point. The evolution of properties in the vicinity

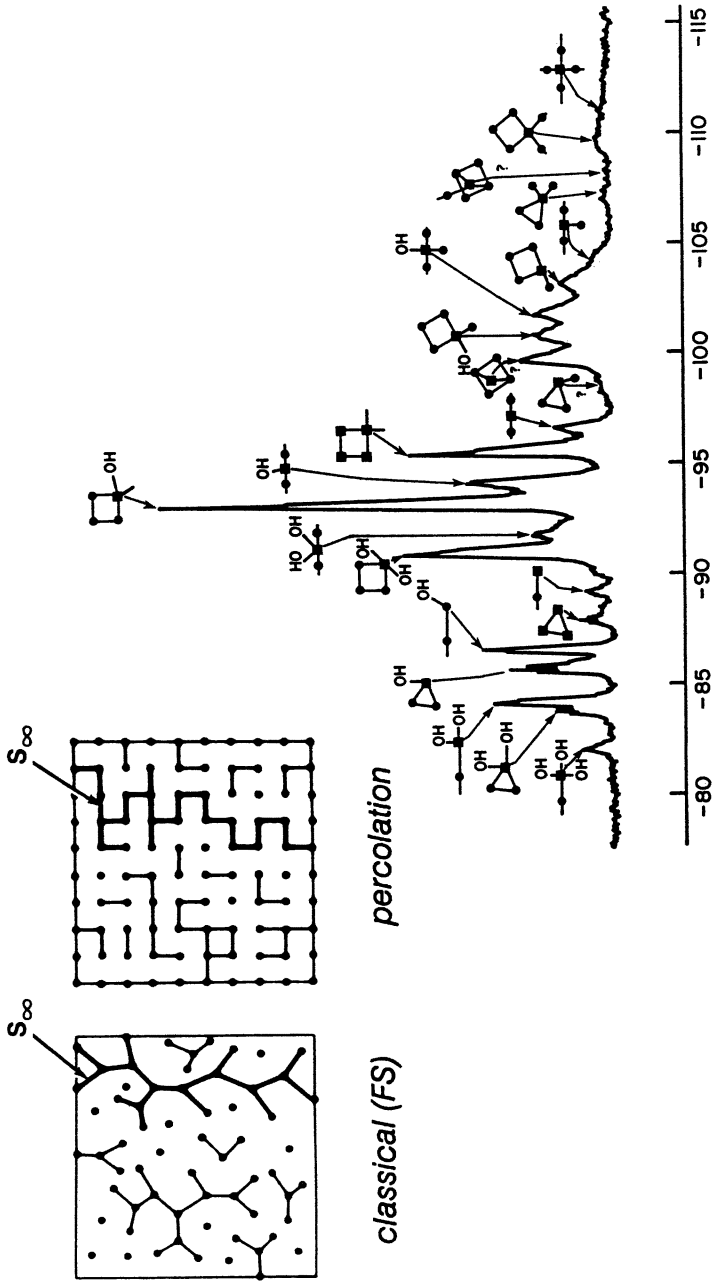

Figure 7. Illustrations of gelation according to the classical Flory–Stockmayer model and the percolation model. In the classical model, cyclic configurations are avoided, so the unphysical situation $M \sim R^4$ results. As illustrated by the ^{29}Si NMR spectrum of an acid-catalyzed TEOS sol (36), cyclic species are quite prominent sol components. (Reproduced with permission from reference 36. Copyright 1988.)

of the gel point is generally in agreement with critical behavior predicted by percolation theory and in contradiction to the classical theory (*24*).

As indicated in the percolation diagram in Figure 7, a relatively small fraction of the reactant species is part of the spanning network at the gel point. To incorporate more of the reactants in the gel network and thus impart strength and stiffness, gels are often aged prior to drying in either the mother liquor or other liquid. The aging process comprises (*60–62*) (1) continued polymerization; (2) syneresis; (3) coarsening; (4) phase separation; and in some cases (5) hydrolysis and esterification.

Polymerization continues both between monomers or polymers and the spanning network and within the network itself as reactive terminal groups diffuse into close proximity. This process appears to promote syneresis (sometimes called macrosyneresis) (*63*), the shrinkage of the gel network, resulting in expulsion of liquid from the pores. Scherer (*64*) states that the kinetics of syneresis depend on the driving force (polymerization), the mobility of the gel network, and the rate of fluid flow through the contracting network.

Iler's view of aging (*2*) is represented schematically in Figure 8a. The higher solubility of surfaces with positive curvatures causes dissolution there and reprecipitation on interparticle contacts that have negative curvatures and lower solubilities. This coarsening process, which is driven by a reduction in the solid–liquid interfacial energy, builds necks between particles that significantly strengthen the gel network. Figure 8b shows that aging an alkoxide-derived gel under basic conditions, where coarsening is enhanced, causes reorganization of a mass fractal ($D = 1.8$) into a surface fractal ($D_s = 3$) (*65*) accompanied by an *increase* in the solid–liquid interfacial area from about 900 to 1500 m^2/g (Figure 8c), as measured in situ by proton spin-relaxation techniques (*66*). Although coarsening occurs under these conditions, apparently the dissolution–reprecipitation process creates a microporous "skin" at the solid–liquid interface that accounts for the unexpected increase in surface area. As discussed later, this microporous layer collapses during drying because of capillary forces, and the dry gel (xerogel) surface area is less for the base-aged sample than the original sample aged in mother liquor, consistent with Iler's original view (Figure 8a).

One type of phase separation process is microsyneresis, illustrated in Figure 9 (*24, 67*). Microsyneresis, which is common in organic gels, results from a greater affinity of the polymer for itself than for the liquid. This situation can arise when a gel is aged in a liquid other than the mother liquor. For example, Davis and co-workers (*67*) showed that sequential aging of alkoxide-derived gels in alcohol and then water causes hydrolysis, polymerization, and phase separation. The reverse sequence (water and then alcohol) causes esterification, depolymerization, and solvation (*see* Figure 9). Macroscopic phase separation occurs when a base-catalyzed

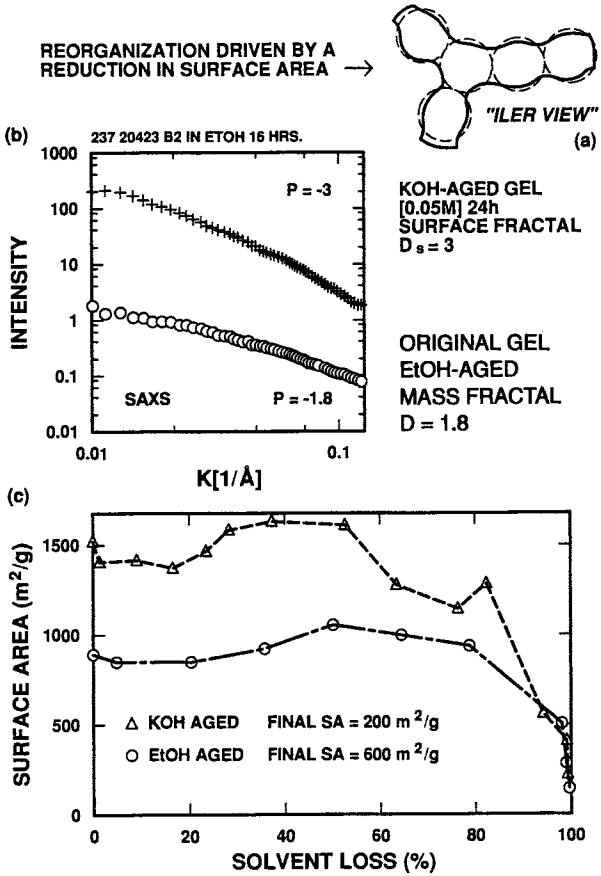

Figure 8. Part a, coarsened structure that results from aging a network of particles under conditions in which there is partial solubility of the condensed phase. Material is removed from surfaces with positive curvatures and deposited at interparticle contacts that have negative curvatures; "neck" formation results. (Reproduced with permission from reference 2. Copyright 1978.) Part b, Porod plots obtained by SAXS for an alkoxide-derived gel prepared at neutral pH in a 90% ethanol–10% water solvent (original gel EtOH-aged) and a similar gel aged for 24 h in 0.05 M KOH in ethanol (KOH-aged gel) (65). Part c, surface areas of EtOH- and KOH-aged gels as a function of percent solvent loss during drying; data obtained by proton spin relaxation methods. Final surface areas (SA) of fully dried gels were measured by using N_2 BET method. (Reproduced from reference 66. Copyright 1989 American Chemical Society.)

TEOS-derived gel is immersed in water. Unreacted TEOS present at the gel point phase separates into sufficiently large droplets that light scattering is observed (*61*). Artifacts of these droplets are observed by scanning electron microscopy (SEM) on fracture surfaces of the corresponding dried gels (*61*).

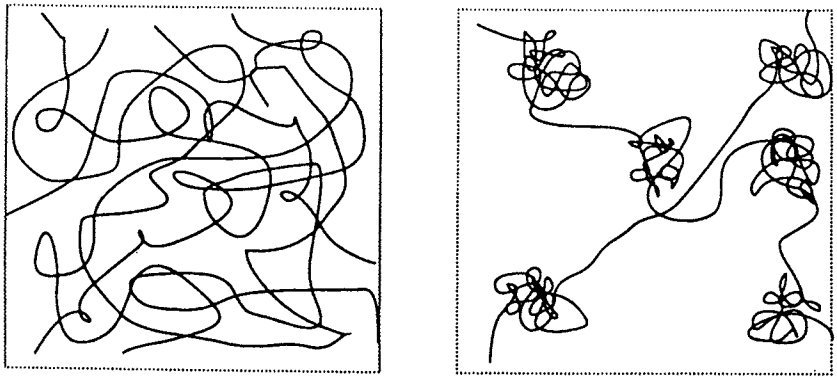

Figure 9. Representation of microsyneresis (24). *Immersion of a water-aged sample in ethanol is accompanied by partial esterification of the gel surface, network depolymerization, and solvation; smaller, more uniform pores result. The reverse process, immersion of an ethanol-aged sample in water, causes almost complete hydrolysis, network condensation, and apparent phase separation into water-rich and polymer-rich regions; larger pores with broader size distributions result. (Reproduced with permission from reference 67.)*

Drying

Drying is generally accomplished by evaporation to form a xerogel (from the prefix xero, meaning dry). Scherer (*68*) divides the evaporative drying process into several stages (*see* Figure 10). In the first stage, or constant rate period, the body shrinks to accommodate the liquid lost by evaporation, and the liquid–vapor interface remains at the exterior surface. The second stage begins when the body is too stiff to shrink, so the liquid recedes into the gel interior. Initially, a continuous liquid film remains that supports flow to the exterior, where evaporation continues to occur (first falling rate period). Eventually the liquid becomes isolated into droplets, so evaporation of liquid in the gel and diffusion of vapor to the exterior (second falling rate period) is required.

In gels, the first stage of drying, where the liquid–vapor interface (meniscus) remains at the exterior surface, continues while the body shrinks to as little as one-tenth of its original volume. The most important

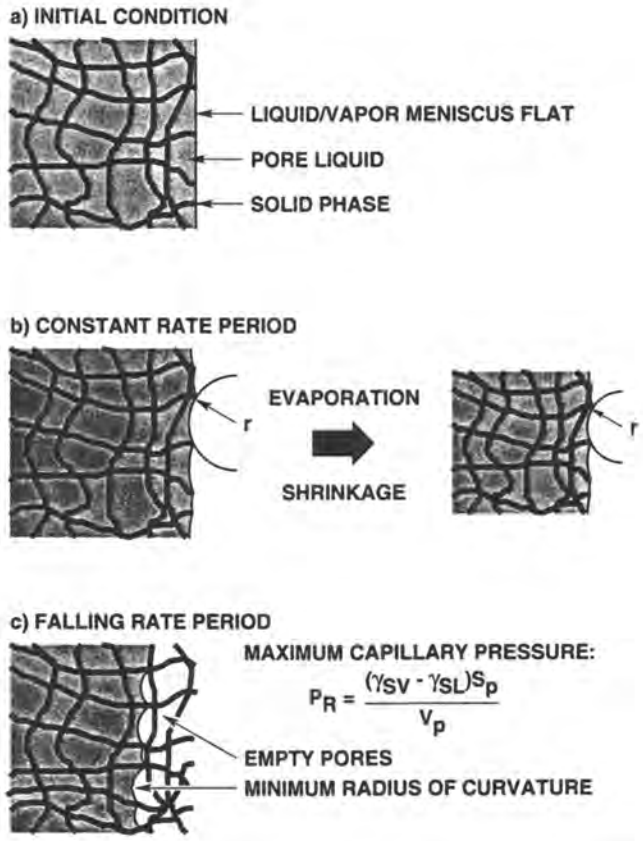

Figure 10. Illustration of drying process (24). *Capillary tension develops in liquid as it "stretches" to prevent exposure of the solid phase by evaporation, and the network is drawn back into liquid (a). The network is initially so compliant that little stress is needed to keep it submerged, so the tension in the liquid is low, and the radius of the meniscus* (r_c) *is large (b). As the network stiffens, the tension rises as* r_c *decreases. At the critical point, the radius of the meniscus becomes equal to the pore radius; the constant rate period ends and the liquid recedes into the gel (c). (Reproduced with permission from reference 24. Copyright 1990).*

pressure contributing to this shrinkage is the capillary pressure (P_c) that results from the radius of curvature (r_c) of the meniscus (68):

$$P_c = -2\gamma_{LV} \cos(\theta)/r_c \tag{9}$$

where γ_{LV} is the liquid–vapor interfacial energy (surface tension) and θ is the contact angle. Before evaporation begins, the meniscus is flat and $P_c = 0$. Capillary tension ($P_c > 0$) develops in the liquid as it "stretches" to

prevent exposure of the solid phase by evaporation. At the initial stage of drying the gel is quite compliant and the network shrinks in response to this tension, so r_c remains large. However, shrinkage is accompanied by continued polymerization reactions within the network. As the network stiffens, r_c decreases and P_c increases. The maximum capillary tension (P_R) is attained when r_c is equal to the hydraulic radius of the pore ($2V_P/S_P$, where V_P is the pore volume and S_P is the surface area) (*68*):

$$P_R = \gamma_{LV} \cos(\theta) S_P/V_P = (\gamma_{SV} - \gamma_{SL}) S_P/V_P \quad (10)$$

Any further drying causes the meniscus to recede into the gel interior.

Because the pore radius may approach molecular dimensions in some alkoxide-derived gels, P_R is an enormous tension, often exceeding several hundred megapascals. This tension is balanced by a compressive stress in the network that causes shrinkage. Despite the large magnitude of P_R, if P_R were uniform throughout the body, cracking would not be a major problem (*68*). Unfortunately, because of the low permeability of the network, it is difficult to draw liquid from the gel interior, so a pressure gradient develops. As the pressure gradient increases, so does the variation in free strain rate, with the surface tending to contract faster than the interior. The spatial variation in strain (or strain rate) causes the stress that leads to fracture (*68*).

Several strategies reduce the tendency of gels to crack during drying (*68*). Very slow drying reduces the gradient in strain by allowing the surface and interior to shrink at comparable rates. Aging strengthens the network and in some cases increases the pore radius, consequently reducing P_R. The use of surfactants or so-called drying control chemical additives (DCCA) (*69*) or, for example, the replacement of water with alcohol, reduces the pore fluid surface tension (or increases the contact angle), also reducing P_R. Supercritical drying (*70*) avoids liquid–vapor interfaces altogether and therefore capillary pressure.

Supercritical drying (also referred to as hypercritical drying) was first used by Prassas and Hench (*71*) to produce large silica monoliths without cracking. It involves the extraction of solvent above its critical point, where there is no distinction between liquid and vapor and, hence, no liquid–vapor interfacial energy ($\gamma_{LV} = 0$, so according to equation 10, $P_R = 0$). In some cases drying is accomplished with no measurable shrinkage of the network. The resulting dry gels are called aerogels, because air may constitute over 99% of the volume (*72*). Whereas Iler (*2*) referred to xerogels as "a contracted and distorted version of the gel originally formed in solution", aerogels should more closely represent the structure of the original gel. In support of this idea, Woignier et al. (*73*) found that the mechanical properties of aerogels are reasonably consistent with percola-

tion theory; for example, the Young's modulus (E) varies with density (ρ) as follows:

$$E \propto \rho^{3.7 \pm 0.3} \tag{11}$$

Structure and Consolidation of Dried Gels

For both particulate and polymeric gels, the removal of pore liquid during drying exposes an interconnected porous network within the gel that surrounds the solid or skeletal phase. The average dimensions of the pores and the thickness of the skeleton depend on the structure that existed at the gel point and the extent of rearrangement and collapse of this structure that occurred during aging and drying. Quite often the dimensions of the pores and skeletal phase constituting the dried gel are sufficiently small that, despite high volume percent porosities, xerogels and aerogels are transparent or translucent (*74*, *75*). In fact, primarily the small pore sizes and correspondingly the high surface areas of dried gels distinguish these materials from conventional porous ceramic green bodies or powder compacts. Table I (*24*) summarizes the porosities of several silicate xerogels and aerogels prepared from TEOS as determined from standard nitrogen adsorption–condensation measurements.

The structures of dried gels are determined on the molecular, mesoscopic, and macroscopic length scales by using a combination of solid-state magic-angle spinning (MAS) NMR, vibrational spectroscopy (IR and Raman), small-angle scattering spectroscopy, and nitrogen adsorption–condensation. Compared to wet gels, xerogels and aerogels are more highly condensed (*76*, *77*). However, because the surface coverage of terminal OH or OR groups on the amorphous silica surface generally exceeds ~4 per square nanometer (*2*), the high surface areas of alkoxide-derived gels require that a significant number of Q^2 and Q^3 silicon sites remain. On longer length scales, small-angle scattering investigations have shown that fractal structures existing at the gel point are more or less preserved in the desiccated gel (*78*). As discussed earlier, the absence of capillary pressure during supercritical drying causes fractal structures to be better preserved in aerogels than in xerogels (*73*).

When silica xerogels or aerogels are heated, they change size (ultimately shrink) and lose weight. Figure 11 compares the linear shrinkage and weight loss of two alkoxide-derived silica xerogels with that of a particulate xerogel prepared from a fumed silica (*79*). The particulate xerogel differs from the other two in that it is composed of comparatively large, fully polymerized particles, similar in many respects to xerogels derived from aqueous silica sols.

Table I. Summary of Porosity of Silicate Xerogels and Aerogels

Sample	*Pore Volume* (cm^3/g N_2 *STP*)	V_p[a]	*Surface Area* (m^2/g)	*Pore Diameter (Å)*		*Bulk Density*[b] (g/cm^3)
				Adsorption	*Desorption*	
Two-step acid-catalyzed xerogel	345	0.54	740	10–50	18	1.54
Two-step acid–base-catalyzed xerogel	588	0.67	910	10–100	46	0.99
Particulate (one-step base-catalyzed xerogel)	686	0.70	515	10–200	125	~0.6
Two-step acid–base-catalyzed aerogel	1368	0.82[c]	858	10–500[c]	186[c]	0.30

[a]Volume fraction porosity is based on the theoretical SiO_2 skeletal density of 2.2 g/cm^3.
[b]Measured at ~25% relative humidity.
[c]Because most of the adsorption occurs near P/P_0 near 1, pore volumes and pore size distributions may be inaccurate for aerogels.
SOURCE: Reproduced with permission from reference 24. Copyright 1990.

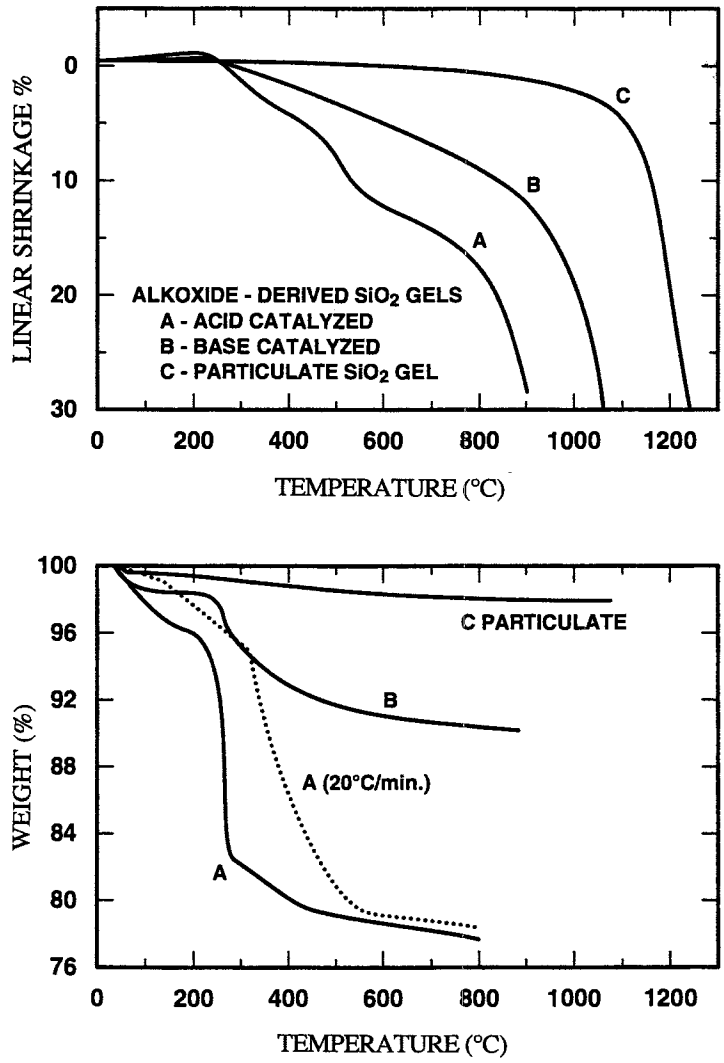

Figure 11. Linear shrinkage and weight loss versus temperature for three types of xerogels heated in air at 2 °C/min. Sample A, two-step acid-catalyzed xerogel; sample B, two-step acid–base-catalyzed xerogel; and sample C, particulate gel prepared from fumed silica. Weight loss of sample A was also measured at 20 °C/min. (Reproduced with permission from reference 79. Copyright 1984.)

The shrinkage curve can be divided into three approximate regions defined by the accompanying weight loss (*80*). Below about 150 °C, weight loss is attributed to desorption of physisorbed alcohol and water. There is little associated shrinkage; in fact, the most weakly condensed xerogels exhibit a measurable dilation because of their very high coefficients of linear thermal expansion [e.g., 470×10^{-7}/K for the acid-catalyzed sample in Figure 11 (*24*)]. By comparison, the particulate xerogel (sample C), which is composed of a fully condensed silica skeleton, shows essentially no change in length below 150 °C. At high temperatures (above 800–1000 °C, depending on the synthesis procedure), there is considerable shrinkage with little associated weight loss. In this region, shrinkage occurs primarily by viscous sintering (*81*). At intermediate temperatures, both shrinkage and weight loss are substantial for the alkoxide-derived xerogels. Shrinkage at intermediate temperatures is attributed (*80*) to continued condensation reactions and structural relaxation (*82*). Weight loss is attributed to the loss of water, the by-product of condensation, and pyrolysis of any residual organic compounds (*80*). The particulate gel shows little change in length or weight at intermediate temperatures, because it is composed of essentially fully polymerized silica.

Condensation reactions and structural relaxation, that is, the approach of the network structure toward its equilibrium configuration (*82*), cause the skeletal density (the density of the solid phase that is inaccessible to helium) to increase toward that of silica glass. Figure 12 shows that this skeletal densification accounts for all of the shrinkage observed at intermediate temperatures for a multicomponent borosilicate gel (*80*). The following data are skeletal densities of various xerogels after drying and the values approached (→) during heating:

- Commercial aqueous silica sols and gels (*2*), 2.20 → 2.30 g/cm^3
- Base TMOS (*58*), 2.08 → 2.20 g/cm^3
- Base NaBSi (*58*), 1.45 → 2.40 g/cm^3
- Acid TEOS (*59*), 1.70 → 2.20 g/cm^3
- NaAlBSi (*55*), 1.65 → 2.27 g/cm^3

These data (*2, 80, 83, 84*) indicate that skeletal densification at intermediate temperatures is observed in general for metal alkoxide derived silicate xerogels, whereas aqueous silicates have skeletal densities comparable to silica glass, and thus, like the fumed silica gel discussed earlier, exhibit little skeletal densification at intermediate temperatures.

Viscous sintering is a process of densification driven by interfacial energy (*81*). Material moves by viscous flow in such a way as to eliminate porosity and thereby reduce the solid–vapor interfacial area. The rate of viscous sintering is proportional to the surface area and inversely propor-

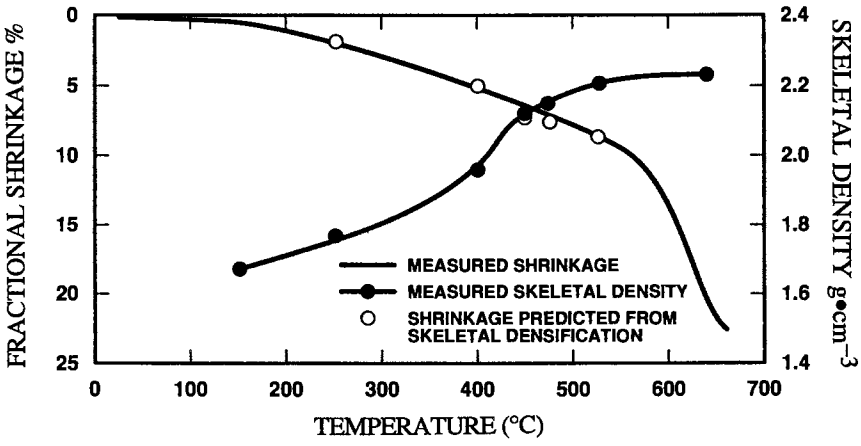

Figure 12. Linear shrinkage and skeletal density of a multicomponent borosilicate xerogel during heating in air at 2 °C/min. Skeletal densification accounts for all the shrinkage observed between 250 and 550 °C. (Reproduced with permission from reference 84. Copyright 1986.)

tional to viscosity and pore size. The differences in shrinkage observed in the high-temperature region in Figure 11 reflect differences in the rate of viscous sintering. The particulate gel has comparatively large pores, low surface area, and, because it is essentially fully polymerized silica, high viscosity. It begins to sinter substantially near 1100 °C, whereas the acid-catalyzed sample, characterized by small pores, high surface area, and low viscosity, begins to sinter below 800 °C.

The processes responsible for skeletal densification (polymerization and structural relaxation) also result in an increase in viscosity (*81*). Although skeletal densification occurs primarily at intermediate temperatures, it may continue at higher temperatures, where it has a dramatic effect on the kinetics of viscous sintering. Figure 13 (*79*) plots the change in viscosity versus bulk density for an alkoxide-derived silica gel (sample A in Figure 11) that was heated to the indicated temperatures at either 2 or 20 °C/min and held isothermally. These data, which were obtained by analysis of the shrinkage curves with a viscous sintering model developed by Scherer (*85*), illustrate several important trends commonly observed when sintering gels derived from alkoxides. (1) Unlike with well-annealed conventional glass, the viscosity is not a single-valued function of temperature. It increases isothermally by more than 3 orders of magnitude. (2) Because of the increasing viscosity, there is little associated densification. (3) Heating at a greater rate results in a lower viscosity and higher density at the beginning of the isothermal hold.

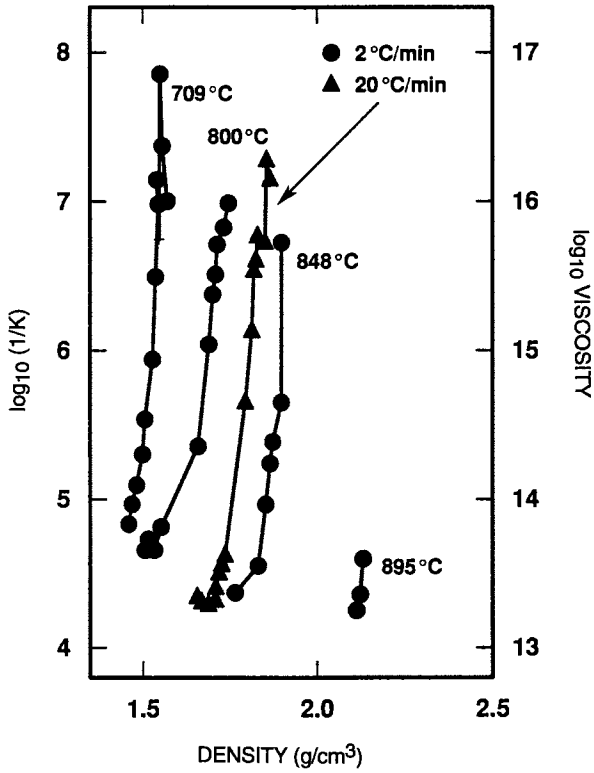

Figure 13. Sintering parameter (1/K) and viscosity according to Scherer model (85) of viscous sintering for two-step acid-catalyzed xerogel. Samples were heated to indicated temperatures at 2 or 20 °C/min and held isothermally. Corresponding bulk densities are plotted on the abscissa. (Reproduced with permission from reference 79. Copyright 1984.)

These trends reflect the competition between the rates of sintering, polymerization, and structural relaxation. Greater heating rates provide less time for viscous sintering, but also less time for polymerization and structural relaxation, processes that contribute to higher viscosity. Because the amount of viscous sintering is proportional to the integral of time divided by viscosity (*81*), the reduction in viscosity could more than compensate for the reduction in time, leading to the remarkable conclusion that faster heating promotes densification at lower temperatures (*24*). From a practical standpoint, the trends in Figure 13 demonstrate that the more efficient densification scheme involves heating at a constant rate rather than employing an isothermal hold.

The low temperatures and correspondingly high viscosities involved in viscous sintering of gels (normally near the glass transition temperature T_g,

defined by a viscosity of $10^{13.5}$ P) may permit the formation of metastable glasses (*24*). For example, because phase separation or crystallization normally require diffusion over distances of several nanometers (at least), it is possible that viscous sintering could be complete before any measureable phase separation or crystallization occurred. For example, homogeneous glasses have been prepared below 1000 °C in alkaline earth silicate systems that exhibit stable immiscibilities extending to over 2000 °C (*86–88*).

The possibility of preparing metastable glasses from gels by low-temperature sintering has provoked the question of whether or not sintered gels generally differ from the corresponding melt-prepared glasses. On the basis of a detailed comparison of the relaxation kinetics of sintered borosilicate gels and melted borosilicate glasses, it was concluded (*89*) that, once the gel was processed in the vicinity of T_g, it was indistinguishable from the melted glass. Previous conclusions to the contrary (e.g., references 90 and 91) have in general been related to subtle differences in composition, so such comparisons require that the compositions be identical (including the OH content).

Surface Structure and Chemistry

Because of their high surface areas, Iler (*2*) believed that the properties of porous gels are dominated largely by the surface chemistry of the solid phase. The surfaces of silica xerogels dried at 100 °C are terminated with hydroxyl groups (or in some cases, both hydroxyl and alkoxide groups). Zhuravlev (*92*) showed that the hydroxyl coverage of fully hydroxylated silica gels is 4.9 OH/nm^2, regardless of the surface area or manner of preparation. Although Iler (*2*) suggested that geminal silanols [$=Si(OH)_2$] do not exist on a dried surface, recent MAS ^{29}Si NMR spectroscopy results have shown that the hydroxylated silica surface is composed of Q^2–Q^4 silicon sites [for both aqueous (*93*) and alkoxide-derived (*77*) materials].

During the heat treatment procedures employed for consolidation, the surface is progressively dehydroxylated. Numerous Raman spectroscopy investigations (e.g., references 94–97 and Figure 14) have correlated surface dehydroxylation with intensification of a narrow Raman band at ~600 cm^{-1} labeled D2 (from its previous association with a defect). MAS ^{29}Si NMR spectroscopy experiments have in turn correlated the relative intensity of the D2 band with a reduction in the average Si–O–Si bond angle of Q^4 silicons (*77*). These results are consistent with the formation of cyclotrisiloxanes (three-membered rings) according to the following (*77*):

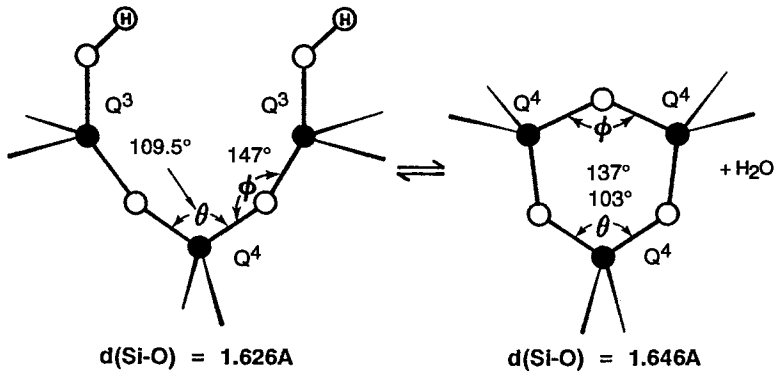

(12)

The concentration of the three-membered rings increases with surface area and the extent of dehydroxylation (*98*). Although the rings are strained, as evident from the reduced Si–O–Si and O–Si–O bond angles and increased Si–O bond length (compare the left and right sides of eq 12), such rings are apparently the preferred way to terminate the *dehydroxylated* silica surface (*99*), because they remain in high concentrations even in the vicinity of T_g (~1100 °C), where the silicate network is able to reconstruct (*100*). Because of their strain, the hydrolysis rate constant of cyclic trisiloxanes (reverse of eq 12) is about 75 times greater than the dissolution rate of conventional fused silica (*101*). As such, cyclic trisiloxanes are preferred sites for surface rehydration (*24*).

Normally, sintering commences before dehydroxylation is complete (*102*) so that a substantial hydroxyl content is retained in the fully densified gel. This situation is problematic when it is necessary to reheat the densified gel in the vicinity of its softening temperature, for example, in fiber drawing or sealing operations, because the evolution of water causes bloating. In addition, strong absorption in the IR spectrum due to O–H stretching vibrations significantly degrades the transmission of optical fibers. To avoid this situation, halogen treatments have been employed (*103, 104*): reaction of the hydroxylated silica surface with sources of chlorine or fluorine above their dissociation temperatures results in quantitative replacement of OH with F or Cl. Although Si–Cl vibrations do not absorb at wavelengths of interest for optical communications, evolution of chlorine may also result in bloating. The chlorine-bloating problem is mitigated by a second heat treatment in dry oxygen below the sintering temperature (1000–1100 °C). Because of the greater Si–F bond strength, significantly more fluorine can be incorporated in fully sintered gels without the bloating problems associated with chlorine.

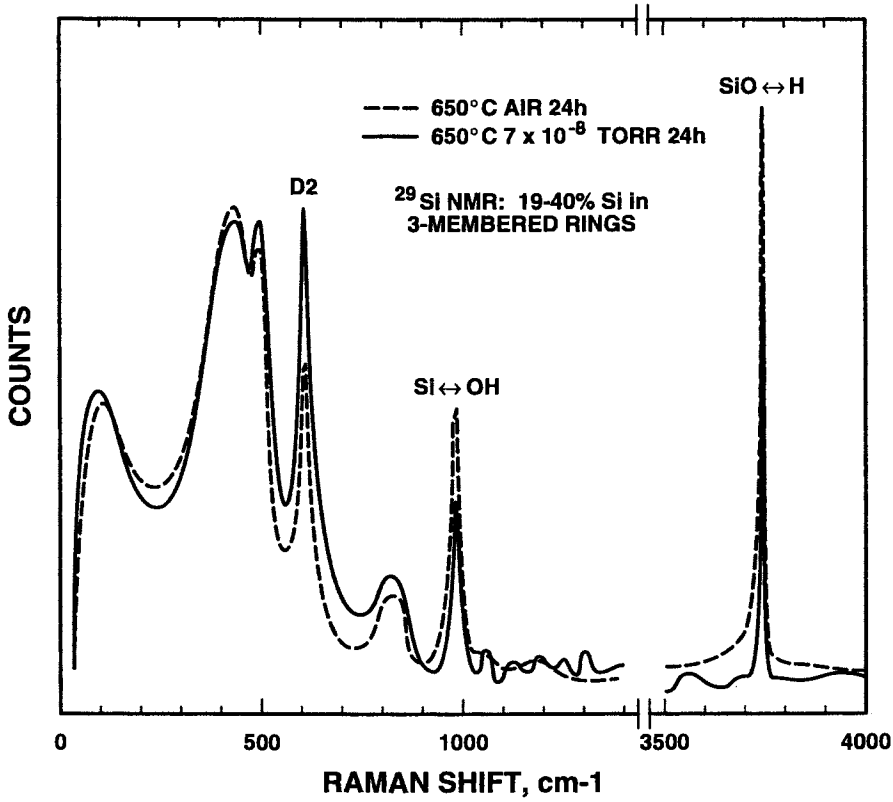

Figure 14. Raman spectra of silicate xerogel after a 24-h hold in air at 650 °C or after 24 h in air and 24 h in vacuum at 650 °C. Corresponding MAS ^{29}Si NMR spectra indicated that after the vacuum treatment up to 40% of the silicon atoms were contained in three-membered rings. (Reproduced with permission from reference 99. Copyright 1990.)

By definition, the intrinsically high surface area of gels requires that gases are accessible to a substantial portion of the solid phase. For example, in a gel with a Brunauer–Emmett–Teller (BET) surface area of 850 m^2/g, 65% of the silicon atoms are on a surface. The accessibility of the surface makes gas- or liquid-phase reactions a viable means of "bulk" compositional modification. This situation has been exploited by numerous researchers who have reacted silicate xerogels with ammonia to form oxynitride glasses without melting (*105–107*).

Fiber Formation

Some highly viscous, metal alkoxide derived sols can be drawn or spun into fibers useful for reinforcement or the production of refractory textiles.

Such sols are called "spinnable". Spinnable sols are generally prepared from ethanolic solutions of TEOS hydrolyzed with 1–2 mol of water under acidic conditions and aged in open containers (*108–110*). During aging the sols are concentrated by evaporation of alcohol. With time these sols show a progressive increase in the dependence of the reduced viscosity (η_{sp}/C) on the silica concentration (C) (*110*). Such behavior is illustrated in Figure 15, where the concentration dependence of the reduced viscosity of an silica sol prepared with $H_2O/Si = 1$ is compared to that of a particulate silica sol (Ludox) and sodium metasilicate, a chainlike silicate. After shorter periods of aging ($t/t_{gel} < 0.5$), the sol exhibits little concentration dependence of η_{sp}/C, consistent with a system of noninteracting spherical particles (e.g., Ludox):

$$\eta_{sp}/C = k/\rho \tag{13}$$

where k is a constant and ρ is the density of the particles. Further aging leads to extended, interacting polymers that exhibit a concentration dependence of the reduced viscosity described by the Huggins equation (*111*):

$$\eta_{sp}/C = \eta + k'(\eta)^2 C \tag{14}$$

where k' is a constant and η is the intrinsic viscosity.

Compared to particulate sols, spinnable sols also show a greater molecular-weight dependence of the intrinsic viscosity:

$$\eta = k'' M_n \alpha \tag{15}$$

where k'' is a constant that depends on the kind of polymer, solvent, and temperature, α depends on the polymer structure, and M_n is the number-average molecular weight. According to theory (*111*), $\alpha = 0$ for rigid spherical particles, $\alpha = 0.5$–1.0 for flexible chainlike or linear polymers, and $\alpha = 1$–2 for rigid rodlike polymers. Sakka (*108*) found $\alpha = 0.64$ or 0.75 for spinnable silica sols prepared from TEOS with H_2O:Si = 2 or 1, respectively.

The value of α can be re-expressed in terms of a mass fractal dimension according to the following relationship (*43*):

$$\eta \sim R_g^3/M_n \sim M_n^{(3/D)-1} \tag{16}$$

where R_g is the radius of gyration of the polymer. According to this expression, $\alpha = 0.64$–0.75 corresponds to $D = 1.83$–1.71, consistent with structures ranging from linear swollen polymers to swollen branched polymers. The ^{29}Si NMR spectrum of a spinnable silica sol (Figure 16) is

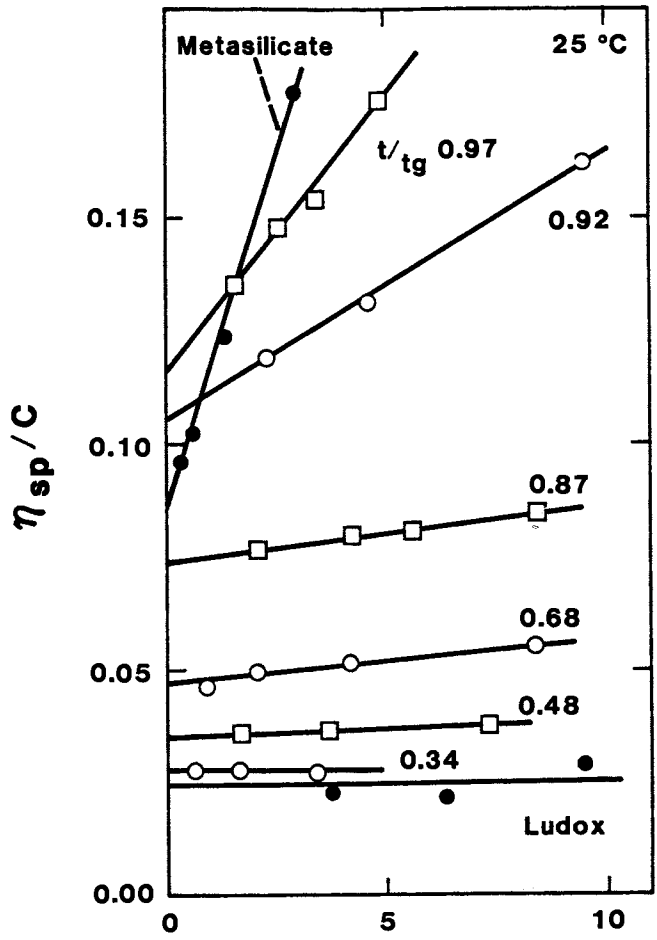

Figure 15. Concentration dependence of the reduced viscosity, η_{sp}/C, of an acid-catalyzed TEOS sol ($H_2O/Si = 1$) as a function of the normalized gel time t/t_{gel}. Data obtained for Ludox and sodium metasilicate are shown for comparison. (Reproduced with permission from reference 110. Copyright 1982.)

composed of Q^1–Q^4 species (*112*) indicative of randomly branched polymers, rather than strictly linear (Q^2) polymers or ladder (Q^3) polymers.

On the basis of these observations, the high viscosities required for spinnability are a result of swollen (extended) randomly branched polymers that exhibit a strong concentration and molecular weight dependence of the reduced and intrinsic viscosities, respectively. During aging, solvent evaporation increases both the concentration of the sol and the molecular weight; these increases in turn cause (eqs 14 and 15) the viscosity to

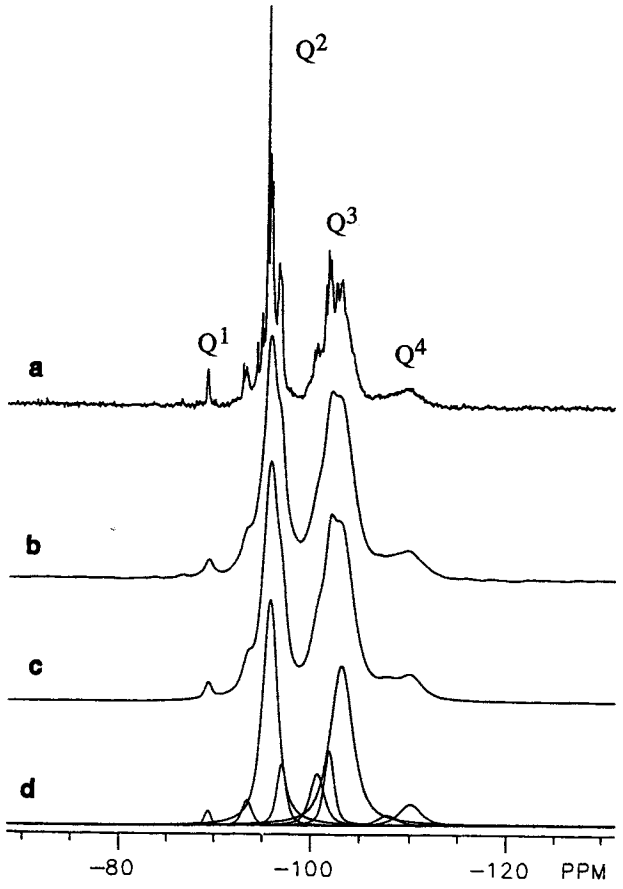

Figure 16. ^{29}Si NMR spectra of spinnable silica sol prepared from TEOS ($H_2O/Si = 1.5$). Spectrum a, experimental, 1.0-Hz exponential line broadening; spectrum b, experimental, 30-Hz exponential line broadening; spectrum c, computer simulation; and spectrum d, resonance components of computer simulation. (Reproduced with permission from reference 112. Copyright 1989.)

increase. However, premature gelation, which leads to elastic behavior and fiber fracture, is avoided because the combination of acid catalyst and low H_2O:Si results in highly esterified polymers that exhibit low condensation rates on the fiber-drawing time scale.

Particle Formation

As shown in Figure 2, polymerization of aqueous silicates at pH 7–10 in the absence of salt leads to the formation of unaggregated particles that

may exceed 100 nm in diameter (2). In this pH range, polymerization of monomer to oligomers and three-dimensional particles 1–2 nm in diameter occurs in only a few minutes. Once the concentration of monomer is substantially reduced, further growth occurs primarily by dissolution of smaller, more soluble particles and deposition of silica on larger, less soluble particles in a process called Ostwald ripening (2). Aggregation is avoided because the larger particles are charged and thus repel each other.

In Ostwald ripening, the rate of growth depends on the particle size distribution. At a given temperature, growth stops when the size of the smallest particles is so large that the difference in solubility of the largest and smallest particles becomes negligible. At room temperature, this occurs when the particles exceed 4–5 nm in diameter (2). Under hydrothermal conditions, where the solubility is enhanced, growth may continue to 150 nm (2). According to Iler (2), the distribution of particle sizes is generally not known, but a Gaussian distribution is assumed.

Larger particles with narrower size distributions can be prepared from alkoxides by using a method developed by Stober, Fink, and Bohn (SFB) (*113*). Dilute solutions of TEOS are hydrolyzed with large concentrations of water (H_2O:Si = 7.5 to >50) under quite basic conditions ([NH_3] = 1–7 M). The particles that form are spherical, and typically <5% of the particles differ by more than 8% from the mean size.

The growth of monodisperse particles is generally explained by the nucleation and growth model of La Mer and Dinegar (*114*). According to this model, the supersaturation of hydrous oxide is increased, for example, by hydrolysis and condensation, above the critical concentration (C_N), where nucleation is extremely rapid. Nucleation causes the supersaturation to be reduced below C_N, where further nucleation is unlikely. Growth continues on the existing nuclei until the concentration is reduced to the equilibrium solubility. The single burst of nuclei confers monodispersity to the sol; if nuclei continue to form throughout the growth stage, a broad distribution of particle sizes is expected.

Bogush and Zukoski (*115*) performed a careful study to elucidate the operative growth mechanism accounting for monodispersity in the SFB process. By analysis of the number density of particles, their size, and the molar volume of silica, they determined that C_N was exceeded during the complete course of the process, so nucleation continued during the growth period. To account for monodispersity under conditions that did not meet the criteria of the classic nucleation and growth model, Bogush and Zukoski (*115*) proposed a nucleation and aggregation model. Although negatively charged, the initial primary particles ($\leq$10 nm) are unstable because of their small size, so aggregation results. The larger, stable aggregates then sweep through the sol, picking up freshly formed primary particles and smaller aggregates. Monodispersity of the final particles is achieved through size-dependent aggregation rates.

Additional support for a nucleation and aggregation model is provided by cryo-TEM results of Bailey and Mecartney (*116*). By fast-freezing thin liquid films of sol, they were able to follow the evolution of particle growth in situ without artifacts introduced by drying. They concluded that particle growth occurs by addition of small, low-density particles to larger, colloidally stable "seeds". A similar hypothesis was made by Iler (*2*) on the basis of some very early TEM work by Radczewski and Richter (*117*) on sols prepared by hydrolysis of $SiCl_4$.

Film Formation

Prior to gelation, silicate sols can be deposited as thin films by such techniques as dipping or spinning. In dip coating, the substrate is normally withdrawn vertically from the coating bath at a speed U_0 (*118*) (*see* Figure 17). The moving substrate entrains the sol in a fluid mechanical boundary layer that splits in two above the bath surface, returning the outer layer to the bath. The entrained sol is thinned and concentrated by gravitational draining and vigorous evaporation of solvent (normally an alcohol–water mixture). A steady-state drying profile terminated by a well-defined drying line ($x = 0$ in Figure 17) develops when the upward flux due to entrainment of the sol on the moving substrate is just balanced by the fluxes attributable to evaporation and draining (*119*). The thickness (h) of the deposited film depends on U_0, the sol viscosity (η), and surface tension (γ_{LV}) according to the following relationship (*120*):

$$h \sim (\eta U_0)^{2/3}/\gamma_{LV}{}^{1/6}(\rho g)^{1/2} \tag{17}$$

where g is gravitational acceleration. Spin coating (*121*) differs in that the film thins primarily by centrifugation, which imposes a greater shear stress on the depositing sol and causes the evaporation rate to be greater because of forced convection caused by the spinning substrate.

The thin-film-forming process differs from the processes of gelation, aging, and drying described earlier for bulk gels (*see* Figure 1) in several fundamental ways (*118*):

1. Whereas drying normally follows gelation for bulk gel processing, in dip or spin coating, drying overlaps the processes of polymer growth, gelation, and aging. This overlap of the deposition and drying stages establishes a very brief time scale for coating (several seconds) compared to bulk gel formation and drying (typically days or weeks).
2. As in bulk systems, the structure of the dried film (xerogel) depends on the competition between capillary forces that tend to compact the structure and aging processes that

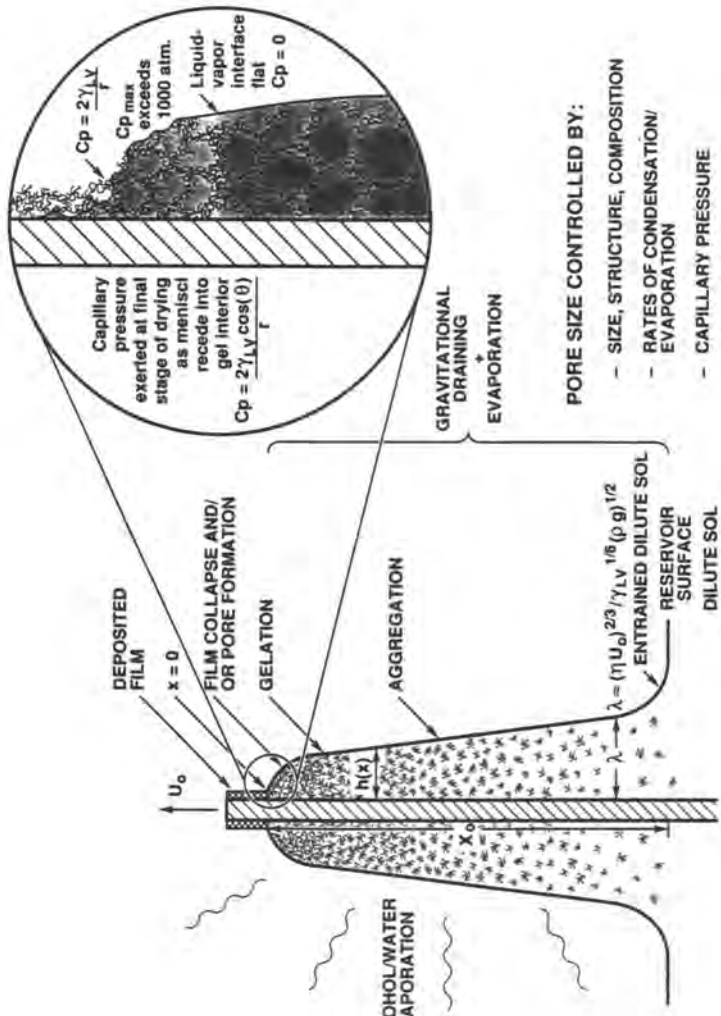

Figure 17. Illustration of sol–gel dip-coating showing sequential stages of deposition. Inset shows details of the final stage of drying.

stiffen the structure and thus increase its resistance to compaction. However, the brief duration of the coating process provides little time for aging, so films remain compliant and are compacted to a greater extent by capillary forces.

3. Gravitational or centrifugal draining combined with possible flows driven by surface tension gradients may impose very high shear rates on the depositing sol. After gelation, continued shrinkage of the constrained film due to drying, skeletal densification, or sintering creates tensile stresses within the film. By comparison, bulk gels are generally not subjected to high shear rates and are free to shrink isotropically.

Polymer growth during the deposition stage probably occurs by CCA, with trajectories ranging from Brownian (dilute conditions) to ballistic in the final 5% of the deposition process, where strong convective forces may exist because of rapid concentration of the inorganic phase (*119*). The gel point is ill defined but may be considered as the moment when the condensing network is sufficiently stiff to withstand flow due to gravity, yet still filled with solvent. From this point, further evaporation may collapse the film or create porosity within the film.

Compared to other thin-film-forming processes such as sputtering, evaporation, or chemical vapor deposition (CVD), sol–gel film formation has the advantage that both the composition and microstructure can be controlled on the molecular level. Thus, the films can be "tailored" for specific applications, for example, dense films for protective or optical applications and porous films for sensors or membranes.

The surface area, pore volume, and pore size of the deposited film depend on such factors as the size and structure (fractal dimension) of the entrained inorganic species, the relative rates of condensation and evaporation during deposition, and the magnitude of the capillary pressure (*122*). The fractal dimension influences porosity through steric control. Mandelbrot (*47*) showed that if two objects of radius R are placed independently in the same region of space, the number of intersections ($M_{1,2}$) is expressed as

$$M_{1,2} \propto R^{D1 + D2 - d} \tag{18}$$

where $D1$ and $D2$ are the respective fractal (or Euclidian) dimensions and d is the dimension of space, 3. According to this expression, if each object has a fractal dimension less than 1.5, the probability of intersection decreases indefinitely with R. These structures are "mutually transparent"

and, if deposited by dip or spin coating, should freely interpenetrate each other as they are concentrated on the substrate surface, so dense films result. If $D1$ and $D2$ are greater than 1.5, the probability of intersection increases algebraically with R. These structures are "mutually opaque". Strong screening of the cluster interiors prevents interpenetration, creating a porous structure much like an assemblage of "tumbleweeds".

Mandelbrot's relationship (eq 18) assumes that the objects are perfectly rigid and "stick" immediately and irreversibly at each point of intersection (chemically equivalent to an infinite condensation rate). In fact, fractal objects are more or less compliant, and the "sticking probability" is always $<<1$. These factors mitigate the criterion for mutual transparency; for example, if the condensation rate is reduced, screening is less effective, and objects with $D > 1.5$ can interpenetrate. Because the condensation rate of silica depends strongly on pH (*see* Figure 3), the "transparency or opacity" and ultimately the film porosity can be manipulated by the addition of acid or base catalyst (*24*).

For a particular withdrawal speed, U_o, the evaporation rate establishes the position of the drying line with respect to the reservoir surface (X_o in Figure 17) and thus the time scale. For reactive sols, a reduction in the evaporation rate provides more time for condensation reactions to occur, leading to stiffer networks that resist collapse by capillary forces. For colloidally stable sols (e.g., electrostatically stabilized SFB particles or highly esterified polymers), a reduction in the evaporation rate provides more time for ordering or interpenetration, leading to denser structures.

As in the case of drying bulk gels (illustrated in Figure 10), the maximum capillary pressure is exerted on the film network at the final stage of the deposition (drying) process, when liquid–vapor menisci recede into the film interior (*see* Figure 17). However, because of the short time scale of the coating process, film networks are more compliant than bulk gels, allowing more shrinkage to occur prior to the final stage. Thus, compared to bulk gels, the pore size is smaller and the maximum capillary pressure greater when the menisci finally recede into the film interior. It is conceivable that in some situations over 1000 atm (100,000 kPa) of pressure are exerted on the depositing film network. It is not surprising therefore that, under some conditions, film structures collapse to such an extent that no porosity is accessible to a nitrogen probe molecule (kinetic diameter ~0.4 nm) (*118, 123*).

A particularly illustrative example of the dependence of film microstructure on the size, structure, and condensation rate of the depositing silicate phase is that of a borosilicate sol deposited at pH ~3 after various periods of aging at 50 °C (*122*). The borosilicate species are characterized by a mass fractal dimension $D \simeq 2.4$. Aging at 50 °C causes them to grow in size as indicated by the plot of hydrodynamic radius versus aging time in Figure 18. Corresponding refractive indices of films deposited from the

aged sols are observed to decrease with increasing hydrodynamic radius. This behavior is consistent with a system of mutually opaque fractal clusters. Because the density of a mass fractal decreases with its size r as $\rho \sim 1/r^{(3-D)}$, the density (and refractive index) of an assemblage of noninterpenetrating (opaque) clusters would also decrease with r. For small r, the cluster density is greater and the effective screening (and opacity) is less, a situation that leads to much denser structures that have no accessible porosity (*123*). Denser structures are also obtained by reducing the pH of the coating bath from about pH 3 toward pH 1 immediately prior to deposition (*24*). The reduction in pH lowers the condensation rate. Thus branched structures are able to interpenetrate on the film deposition time scale, and compact films are produced.

Table II (*118*) shows that the surface area, pore volume, and pore size of the deposited films vary consistently with the aging times. Thus the film structures may be tailored for such applications as surface passivation, sensors, membranes, or catalysts by a simple aging process prior to film deposition. In addition, multiple deposition schemes involving different compositions or structures or both allow the formation of complex layered architectures potentially useful for optics, electronics, or sensors.

Summary

The structures of silicate polymers formed from alkoxides by the sol–gel process vary from weakly branched "molecular networks" to highly condensed particles that are similar to commercial aqueous silicates described by Iler (2). The sol–gel process combines this control of microstructure on molecular length scales with the ability to form specialized shapes such as fibers, films, monosized powders, and monoliths

Table II. Porosities of Films Prepared from Multicomponent Borosilicate Sols

Sample Aging Times[a]	*Refractive Index*	*%Porosity Ads. N_2*	*Median Pore Radius (nm)*	*Surface Area (m^2/g)*	*Applications*
Unaged	1.45	0	<0.2	1.2–1.9	dense, protective electronic and optical films
0–3 Days					microporous films for sensors and membranes
3 Days	1.31	16	1.5	146	
1 Week	1.25	24	1.6	220	mesoporous films for sensors, membranes, catalysts, optics
2 Weeks	1.21	33	1.9	263	
3 Weeks	1.18	52	3.0	245	

[a]Aging of dilute sol at 50 °C and pH 3 prior to film deposition.
SOURCE: Reproduced with permission from reference 118. Copyright 1990.

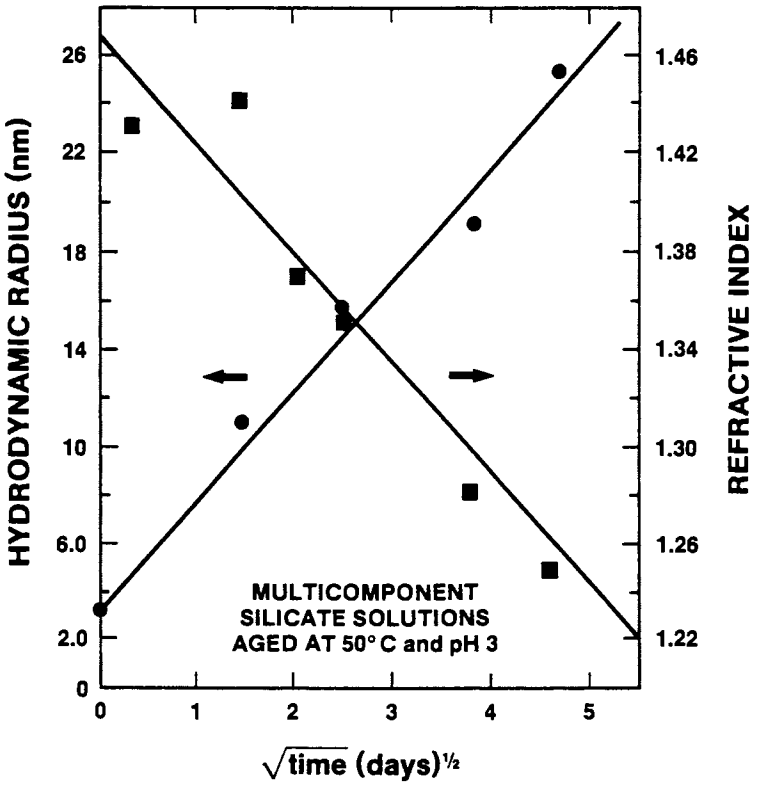

Figure 18. Reciprocal relationship between the hydrodynamic radius of multicomponent borosilicate species and the corresponding refractive index of films prepared from borosilicate sols as a function of root aging time at 50 °C and pH ~3. (Reproduced with permission from reference 1. Copyright 1988.)

at room temperature. Silica gels may be exploited for their porosity or consolidated to dense glasses indistinguishable from their melt-prepared counterparts. Sintering occurs in the vicinity of T_g and permits the formation of novel metastable materials. Iler's views on many of these aspects of the sol-gel process have been largely confirmed by recent experiments.

Acknowledgments

I have benefited from the continued support of the Department of Energy Basic Energy Sciences program "The Growth and Structure of Ceramic Precursors" and from associated collaborations with colleagues at Sandia National Laboratories (Roger Assink, Dale Schaefer, Keith Keefer, Joe Bailey, Carol Ashley, Alan Hurd, Scott Reed, and Dan Doughty) along with

George Scherer at Du Pont. This work was performed at Sandia National Laboratories and supported by the U.S. Department of Energy under Contract DE-AC04-76P00789.

References

1. *Sol-Gel Technology for Thin Films, Fibers, Preforms, Electronics, and Specialty Shapes*; Klein, L. C., Ed.; Noyes: Park Ridge, NJ, 1988.
2. Iler, R. K. *The Chemistry of Silica*; Wiley: New York, 1978.
3. Hench, L. L.; West, J. K. *Chem. Rev.* **1990,** *90,* 33–72.
4. Sakka, S. *J. Non-Cryst. Solids* **1985,** *73,* 651–660.
5. Masdiyasni, K. S. *Sagamore Army Mat. Res. Conf. Proc.* **1985,** *30,* 285–336. Baes, E. F.; Mesmer, R. E. *The Hydrolysis of Cations*; Wiley: New York, 1976.
6. Roy, R. *Science (Washington, DC)* **1987,** *238,* 1664–1669.
7. Zelinski, B. J. J.; Uhlmann, D. R. J. *Phys. Chem. Solids* **1984,** *45,* 1069–1090.
8. Zarzycki, J. In *Glass Science and Technology*; Ulhmann, D. R.; Kriedl, N. J., Eds.; Academic: Boston, MA, 1984; Vol. 2, pp 209–49.
9. *J. Non-Cryst. Solids* **1982,** *48,* 1–230.
10. *J. Non-Cryst. Solids* **1984,** *63,* 1–300.
11. *J. Non-Cryst. Solids* **1986,** *82,* 1–436
12. *J. Non-Cryst. Solids* **1988,** *100,* 1–554.
13. *J. Non-Cryst. Solids* **1990,** *121,* 1–492.
14. *J. Non-Cryst. Solids* **1992,** *147, 148,* 1–841.
15. *Ultrastructure Processing of Glasses, Ceramics, and Composites*; Hench, L. L.; Ulrich, D. R., Eds.; Wiley: New York, 1984.
16. *Science of Ceramic Chemical Processing*; Hench, L. L.; Ulrich, D. R., Eds.; Wiley: New York, 1986.
17. *Ultrastructure Processing of Advanced Ceramics*; Mackenzie, J. D.; Ulrich, D. R., Eds.; Wiley: New York, 1988.
18. *Ultrastructure Processing IV*; Uhlmann, D. R.; Ulrich, D. R., Eds.; Wiley: New York, 1992.
19. *Ultrastructure Processing V*; Hench, L. L.; West, J. K., Eds.; Wiley: New York, 1992.
20. *Better Ceramics Through Chemistry*; Brinker, C. J.; Clark, D. E.; Ulrich, D. R., Eds.; Elsevier: New York, 1984.
21. *Better Ceramics Through Chemistry II*; Brinker, C. J.; Clark, D. E.; Ulrich, D. R., Eds.; Materials Research Society: Pittsburgh, PA, 1986.
22. *Better Ceramics Through Chemistry III*; Brinker, C. J.; Clark, D. E.; Ulrich, D. R., Eds.; Materials Research Society: Pittsburgh, PA, 1988.
23. *Better Ceramics Through Chemistry IV*; Zelinski, B. J. J.; Brinker, C. J.; Clark, D. E.; Ulrich, D. R., Eds.; Materials Research Society: Pittsburgh, PA, 1990.
24. Brinker, C. J.; Scherer, G. W. *Sol-Gel Science*; Academic: San Diego, CA, 1990.
25. Baes, E. F.; Mesmer, R. E. *The Hydrolysis of Cations*; Wiley: New York, 1976.
26. Keefer, K. D. In *Better Ceramics Through Chemistry*; Brinker, C. J.; Clark, D. E.; Ulrich, D. R., Eds.; North-Holland: New York, 1984; pp 15–24.
27. McNeill, K. J.; DiCaprio, J. A.; Walsh, D. A.; Pratt, R. F. *J. Am. Chem. Soc.* **1980,** *102,* 1859.
28. Pohl, E. R.; Osterholtz, F. D. In *Molecular Characterization of Composite Interfaces*; Ishida, H; Kumar, G., Eds.; Plenum: New York, 1985; p 157.
29. Corriu, R. J. P.; Henner, M. *J. Organometallic Chem.* **1974,** *74,* 1–28.

30. Brinker, C. J. *J. Non-Cryst. Solids* **1988,** *100,* 30–51.
31. Aelion, R.; Loebel, A.; Eirich, F. *J. Am. Chem. Soc.* **1950,** *72,* 5705–5712.
32. Voronkov, M. G.; Mileshkevich, V. P.; Yuzhelevski, Y. A. *The Siloxane Bond*; Consultants Bureau: New York, 1978.
33. Brinker, C. J.; Keefer, K. D.; Schaefer, D. W.; Ashley, C. S. *J. Non-Cryst. Solids* **1982,** *48,* 47–64.
34. Brinker, C. J.; Keefer, K. D.; Schaefer, D. W.; Assink, R. A.; Kay, B. D.; Ashley, C. S. *J. Non-Cryst. Solids* **1984,** *63,* 45–59.
35. Pouxviel, J. C.; Boilot, J. P. *J. Non-Cryst. Solids* **1987,** *94,* 374–386.
36. Kelts, L. W.; Armstrong, N. J. In *Better Ceramics Through Chemistry III*; Brinker, C. J.; Clark, D. E.; Ulrich, D. R., Eds.; Materials Research Society: Pittsburgh, PA, 1988; p 519.
37. Lippert, J. L.; Melpolder, S. B.; Kelts, L. W. *J. Non-Cryst. Solids* **1988,** *104,* 139–147.
38. Artaki, I.; Bradley, M.; Zerda, T. W.; Jonas, J. *J. Phys. Chem.* **1985,** *89,* 4399–4404.
39. Klemperer, W. G.; Mainez, V. V.; Ramamurthi, S. D.; Rosenberg, F. S. In *Better Ceramics Through Chemistry III*; Brinker, C. J.; Clark, D. E.; Ulrich, D. R., Eds.; Materials Research Society: Pittsburgh, PA, 1988; pp 15–24.
40. Kelts, L. W.; Effinger, N. J.; Melpolder, S. M. *J. Non-Cryst. Solids* **1986,** *83,* 353–374.
41. R. A. Assink, personal communication.
42. Martin, J. E.; Hurd, A. J. *J. Appl. Cryst.* **1987,** *20,* 61–78.
43. Schaefer, D. W. *MRS Bull.* **1988,** *8,* 22–27.
44. Schaefer, D. W.; Martin, J. E.; Keefer, K. D. In *Physics of Finely Divided Matter*; Bocarra, N.; Daoud, M., Eds.; Springer–Verlag: Berlin, Germany, 1985; p 31.
45. Schaefer, D. W.; Keefer, K. D. In *Fractals in Physics*; Pietronero, L; Tosatti, E., Eds.; North-Holland, Amsterdam, Netherlands, 1986; pp 39–45.
46. Bailey, J. K.; Nagase, T.; Broberg, S. M.; Mecartney, M. L. *J. Non-Cryst. Solids* **1989,** *109,* 198.
47. Mandelbrot, B. B. *Fractals, Form, and Chance*; Freeman: San Francisco, CA, 1977.
48. Porod, G. *Kolloid Z.* **1951,** *124,* 83.
49. Keefer, K. D. In *Better Ceramics Through Chemistry III*; Brinker, C. J.; Clark, D. E.; Ulrich, D. R., Eds.; Materials Research Society: Pittsburgh, PA, 1986; pp 295–304.
50. Meakin, P. In *On Growth and Form*; Stanley, H. E.; Ostrowsky, N., Eds; Martinus-Nijhoff: Boston, MA, 1986; pp 111–135.
51. Sutherland, D. N. *J. Colloid Interface Sci.* **1967,** *25,* 373–380.
52. Flory, P. J. *J. Am. Chem. Soc.* **1941,** *63,* 3083; *J. Phys. Chem.* **1942,** *46,* 132.
53. Stockmeyer, W. H. *J. Chem. Phys.* **1943,** *11,* 45.
54. de Gennes, P. G. *Biopolymers* **1968,** *6,* 715–729.
55. Stauffer, D. *J. Chem. Soc. Faraday Trans. II* **1976,** *72,* 1354.
56. de Gennes, P. G. *Scaling Concepts In Polymer Physics*; Cornell Univ. Press: Ithaca, NY, 1979.
57. Zallen, R. *The Physics of Amorphous Solids*; Wiley: New York, 1983.
58. Martin, J. E.; Wilcoxon, J.; Adolf, D. *Phys. Rev. A* **1987,** *36*(4), 1803–1810.
59. Martin, J. E. In *Proceedings of Atomic and Molecular Processing of Electronic and Ceramic Materials: Preparation, Characterization, Properties*; Aksay, I. A.; McVay, G. L.; Stoebe, T. G.; Wager, J. F., Eds.; Materials Research Society: Pittsburgh, PA, 1987; pp 79–89.

60. Vega, A. J.; Scherer, G. W. *J. Non-Cryst. Solids* **1989,** *111*(2,3), 153–166.
61. Scherer, G. W. *J. Non-Cryst. Solids* **1989,** *109*, 183–190.
62. Yoldas, B. E. *J. Mater. Sci.* **1986,** *21*, 1087–1092.
63. Klimentova, Yu. P.; Kirichenko, L. F.; Vysotskii, Z. Z. *Ukr. Khim. Zh.* **1970,** *36*(1), 56–58 (Eng. trans.).
64. Scherer, G. W. In *Better Ceramics Through Chemistry III*; Brinker, C. J.; Clark, D. E.; Ulrich, D. R., Eds.; Materials Research Society: Pittsburgh, PA, 1988; pp 179–186.
65. Brinker, C. J.; Schaefer, D. W., unpublished work.
66. Glaves, C. L.; Brinker, C. J.; Smith, D. M.; Davis, P. J. *Chem. Mat.* **1989,** *1*, 34–40.
67. Davis, P. J.; Brinker, C. J.; Smith, D. M.; Assink, R. A.; Schaefer, D. W.; Tallant, D. R., submitted to *J. Non-Cryst. Solids.*
68. Scherer, G. W. *J. Am. Ceram. Soc.* **1990,** *73*, 3–14.
69. Hench, L. L. In *Science of Chemical Processing*; Hench, L. L.; Ulrich, D. R., Eds.; Wiley: New York, 1986; pp 52–64.
70. Kistler, S. S. *J. Phys. Chem.* **1932,** *36*, 52–64.
71. Prassas, M.; Hench, L. L. In *Ultrastructure Processing of Glasses, Ceramics, and Composites*; Hench, L. L., Ed.; Wiley: New York, 1984; pp 100–125.
72. Hrubesh, L. W.; Tillotson, T. M.; Poco, J. F. In *Better Ceramics Through Chemistry IV*; Zelinski, B. J. J.; Brinker, C. J.; Clark, D. E.; Ulrich, D. R., Eds.; Materials Research Society: Pittsburgh, PA, 1990; pp 215–319.
73. Woignier, T.; Phalippou, J.; Vacher, R. In *Better Ceramics Through Chemistry III*; Brinker, C. J.; Clark, D. E.; Ulrich, D. R., Eds.; Materials Research Society: Pittsburgh, PA, 1988; pp 697–702.
74. Wallace and Hench, L. L. In *Better Ceramics Through Chemistry*; Brinker, C. J.; Clark, D. E.; Ulrich, D. R., Eds.; Elsevier, North-Holland: New York, 1984; pp 47–52.
75. Russo, R. E.; Hunt, A. J. *J. Non-Cryst. Solids* **1986,** *86*, 219–230.
76. Klemperer, W. G.; Mainz, V. V.; Millar, D. M. In *Better Ceramics Through Chemistry II*; Brinker, C. J.; Clark, D. E.; Ulrich, D. R., Eds.; Materials Research Society: Pittsburgh, PA, 1986; pp 15–26.
77. Brinker, C. J.; Kirkpatrick, R. J.; Tallant, D. R.; Bunker, B. C.; Montez, B. *J. Non-Cryst. Solids* **1988,** *99*, 418–428.
78. Schaefer, D. W.; Keefer, K. D. In *Fractals in Physics*; Pietronero, L.; Tosatti, E., Eds.; North-Holland: Amsterdam, Netherlands, 1986; pp 39–45.
79. Brinker, C. J.; Drotning, W. D.; Scherer, G. W. In *Better Ceramics Through Chemistry*; Brinker, C. J.; Clark, D. E.; Ulrich, D. R., Eds.; Elsevier, North-Holland: New York, 1984; pp 25–32.
80. Brinker, C. J.; Scherer, G. W.; Roth, E. P. *J. Non-Cryst. Solids* **1985,** *72*, 345–368.
81. Scherer, G. W. In *Surface and Colloid Science*; Matijevic, E., Ed.; Plenum: New York, 1987; Vol. 14, pp 265–300.
82. Scherer, G. W. *Relation in Glasses and Composites*; Wiley: New York, 1986.
83. Tohge, N.; Moore, G. S.; Mackenzie, J. D. *J. Non-Cryst. Solids* **1984,** *63*, 95–104.
84. Brinker, C. J.; Roth, E. P.; Tallant, D. R.; Scherer, G. W. In *Science of Ceramic Chemical Processing*; Hench, L. L.; Ulrich, D. R., Eds.; Wiley: New York, 1986, 37–51.
85. Scherer, G. W. *J. Am. Ceram. Soc.* **1977,** *60*, 236–239.
86. Hayashi, T.; Saito, H. *J. Mater. Sci.* **1980,** *15*, 1971–1977.
87. Yamane, M.; Kojima, T. *J. Non-Cryst. Solids* **1981,** *44*, 181–190.

88. Bansal, N. P. *J. Am. Ceram. Soc.* **1988,** *71*(8), 666–672.
89. Scherer, G. W.; Brinker, C. J.; Roth, E. P. *J. Non-Cryst. Solids* **1986,** *82*, 191–197.
90. Weinberg, M. C.; Neilson, G. F. *J. Mater. Sci.* **1978,** *13*, 1206–1216.
91. Weinberg, M. C.; Neilson, G. F. *J. Am. Ceram. Soc.* **1983,** *66*(2), 132–134.
92. Zhuravlev, L. T. *Langmuir* **1987,** *3*, 316–318.
93. Fyfe, C. A.; Gobbi, G. C.; Kennedy, G. J. *J. Phys. Chem.* **1985,** *89*, 277–281.
94. Bertoluzza, A.; Fagnano, C.; Morelli, M. A.; Gottardi, V.; Guglielmi, M. *J. Non-Cryst. Solids* **1982,** *48*, 117–128.
95. Krol, D. M.; Van Lierop, J. G. *J. Non-Cryst. Solids* **1987,** *63*, 131–144.
96. Brinker, C. J.; Tallant, D. R.; Roth, E. P.; Ashley, C. S. In *Defects in Glasses*; Galeener, F. L.; Griscom, D. L.; Weber, M. J., Eds.; Materials Research Society: Pittsburgh, PA, 1986; pp 387–411.
97. Brinker, C. J.; Tallant, D. R.; Roth, E. P.; Ashley, C. S. *J. Non-Cryst. Solids.* **1986,** *82*, 117–126.
98. Wallace, S. Ph.D. Thesis, University of Florida, Gainesville, FL, 1991.
99. Brinker, C. J.; Brow, R. K.; Tallant, D. R.; Kirkpatrick, R. J. *J. Non-Cryst. Solids* **1990,** *120*, 26–33.
100. Bartram, H. E.; Michalske, T. A.; Rodgers, J. W., Jr. *J. Phys. Chem.* **1991,** *95*, 4453–63.
101. Bunker, B. C.; Haaland, D. M.; Michalske, T. A.; Smith, W. L. *Surf. Sci.* **1989,** *222*, 95–118.
102. Gallo, T. A.; Brinker, C. J.; Kelin, L. C.; Scherer, G. W. In *Better Ceramics Through Chemistry*; Brinker, C. J.; Clark, D. E.; Ulrich, D. R., Eds.; Elsevier: New York, 1984; pp 85–90.
103. Matsuyama, I.; Susa, K.; Satoh, S.; Suganuma, T. *Ceramic Bull.* **1984,** *63*, 1408–1411.
104. Rabinovich, E. M.; Wood, D. L.; Johnson, D. W., Jr.; Fleming, D. A.; Vincent, S. M.; MacChesney, J. B. *J. Non-Cryst. Solids* **1986,** *82*, 42–49.
105. Brinker, C. J.; Haaland, D. M. *J. Am. Ceram. Soc.* **1983,** *66*, 758–765.
106. Brow, R. K.; Pantano, C. G. *J. Am. Ceram. Soc.* **1987,** *70*, 9–14.
107. Kamiya, K.; Ohya, M.; Yoko, T. *J. Non-Cryst. Solids* **1986,** *83*, 209–222.
108. Sakka, S. In *Better Ceramics Through Chemistry*; Brinker, C. J.; Clark, D. E.; Ulrich, D. R., Eds.; Elsevier: New York, 1984; p 91.
109. Sakka, S.; Kamiya, K.; Makita, K.; Yamamoto, Y. *J. Non-Cryst. Solids* **1984,** *63*, 223–235.
110. Sakka, S.; Kamiya, K. *J. Non-Cryst. Solids* **1982,** *48*, 31–46.
111. Abe, Y.; Misono, T. *J. Poly. Sci. Chem.* **1983,** *21*, 41.
112. Brinker, C. J.; Assink, R. A. *J. Non-Cryst. Solids* **1989,** *111*, 48.
113. Stober, W.; Fink, A.; Bohn, E. *J. Colloid Interface Sci.* **1968,** *26*, 62–69.
114. La Mer, V. K.; Dinegar, R. H. *J. Am. Chem. Soc.* **1950,** *72*(11), 4847–4854.
115. Bogush, G. H.; Zukoski, C. F. In *Ultrastructure Processing of Advanced Ceramics*; Mackenzie, J. D.; Ulrich, D. R., Eds.; Wiley: New York, 1988; pp 477–486.
116. Bailey, J. K.; Mecartney, M. L. *Colloids and Surfaces*, submitted.
117. Radczewski, O. E.; Richter, H. *Kolloid Z.* **1941,** *96*, 1.
118. Brinker, C. J.; Hurd, A. J.; Frye, G. C.; Ward, K. J.; Ashley, C. S. *J. Non-Cryst. Solids* **1990,** *121*, 294–302.
119. Hurd, A. J.; Brinker, C. J. In *Better Ceramics Through Chemistry III*; Brinker, C. J.; Clark, D. E., Ulrich, D. R., Eds.; Materials Research Society: Pittsburgh, PA, 1988; pp 731–742.
120. Landau, L. D.; Levich, B. G. *Acta Physiochim, U.R.S.S.* **1942,** *17*, 42–54.

121. Bornside, D. E.; Macosko, C. W.; Scriven, L. E. *J. Imaging Technol.* **1987,** *13,* 122–129.
122. Brinker, C. J.; Hurd, A. J.; Ward, K. J. In *Ultrastructure Processing of Advanced Ceramics*; Mackenzie, J. D.; Ulrich, D. R., Eds.; Wiley: New York, 1988; p 223.
123. Frye, G. C.; Ricco, A. J.; Martin, S. J.; Brinker, C. J. In *Better Ceramics Through Chemistry III*; Brinker, C. J.; Clark, D. E.; Ulrich, D. R., Eds.; Materials Research Society: Pittsburgh, PA, 1988; pp 349–354.

RECEIVED for review October 19, 1990. ACCEPTED revised manuscript March 6, 1992.

19

The Chemistry of Hydrolysis and Condensation of Silica Sol–Gel Precursors

Bradley K. Coltrain and Larry W. Kelts

Corporate Research Laboratories, Eastman Kodak Company, Rochester, NY 14650–2110

A brief overview of sol–gel hydrolysis and condensation reactions and the evolving structures is presented. Results from existing literature are summarized, but emphasis is placed on recent and unpublished work. A sound knowledge of sol–gel chemical reactions is necessary for a thorough understanding of silicate polymer growth and control of material properties. This understanding is complicated by concurrent hydrolysis and condensation reactions. Many workers are contributing to this knowledge base. This chapter represents a summary of the state-of-the art in this area.

THE HYDROLYSIS AND CONDENSATION of silicon alkoxides is an area of intense interest. The sol–gel process uses high-purity monomers for low-temperature production of fibers, monoliths, coatings, and powders. Structures of the polymers produced in the sol ultimately dictate both gel and glass properties.

This chapter is a brief overview of silicon alkoxide hydrolysis and condensation and the resulting structures, emphasizing recent studies and unpublished work. Schmidt et al. (*1*) and more recently Brinker (*2*) have published excellent overviews of this chemistry; this chapter attempts to amplify and complement these reports.

A number of variables influence the structural evolution of silicate polymers: pH, solvent, water-to-silicon ratio (W), and monomer. Low-pH conditions with $W = 1–2$ are useful for fiber spinning; when $W = 4$ the sols

0065–2393/94/0234–0403$08.00/0

are useful as coatings, whereas high W values or high pH produces colloidal suspensions or powders. Monoliths are frequently produced by addition of drying control chemical additives (DCCAs), which enhance drying rates while reducing cracking due to drying stresses. The following discussion elucidates how the chemistry is controlled to dictate sol–gel properties.

The two fundamental chemical reactions of the sol–gel process are (1) hydrolysis:

$$\equiv\text{Si(OR)} + \text{H}_2\text{O} \underset{k_E}{\overset{k_H}{\rightleftharpoons}} \equiv\text{Si(OH)} + \text{ROH}$$

and (2) condensation:

$$\equiv\text{Si(OR)} + \text{(OH)Si}\equiv \underset{}{\overset{k_A}{\rightleftharpoons}} \equiv\text{Si–O–Si}\equiv + \text{ROH} \quad \text{(alcohol producing)}$$

$$\equiv\text{Si(OH)} + \text{(OH)Si}\equiv \underset{}{\overset{k_W}{\rightleftharpoons}} \equiv\text{Si–O–Si}\equiv + \text{H}_2\text{O} \quad \text{(water producing)}$$

k_H, k_E, k_A, and k_W are rate constants for hydrolysis, esterification, alcohol-producing condensation, and water-producing condensation, respectively. Usually, hydrolysis and condensation reactions are concurrent. The following discussion separates the two in an attempt to conceptually simplify the chemistry. In some cases, because the two reactions are interdependent, they are discussed together, especially when gel times are considered.

Hydrolysis

Aelion et al. (*3*, *4*) showed that hydrolysis of tetraethoxysilane (TEOS) is acid or base catalyzed with a minimum rate at pH 7. Studies of alkyltrialkoxysilane hydrolysis in buffered aqueous solutions indicate that hydrolysis is both specific acid and specific base catalyzed (*5*, *6*).

Trivalent siliconium ion (*1*, *7*) and pentavalent silicon species (*6*) were proposed as condensation intermediates. Gas-phase mass spectrometric reactions of TEOS indicate a surprising stability of both trivalent and five-coordinate $[(OEt)_4SiOH]^+$ species (*8*), but the trivalent species was incapable of initiating condensation, at least under these conditions. Although the gas-phase studies may not directly correlate with solution behavior, they do suggest that three- and five-coordinate species are at least possible.

Most results to date support the presence of a five-coordinate intermediate. Hydrolysis rates decrease with increasing bulkiness of the alkoxide (*5*, *9*). This feature and a large negative entropy of activation (−39 cal $deg^{-1}mol^{-1}$) (*5*) are consistent with associative mechanisms. Pohl and Osterholz (*6*) proposed initial protonation of an alkoxide under low-pH conditions followed by backside attack of a water molecule, producing a five-coordinate transition state with inversion at silicon. Flank-side attack without inversion was also proposed (*10*, *11*). At high pH, hydroxyl anions are proposed to attack the silicon atom to produce either a five-coordinate transition state or stable intermediate. The low-pH mechanism involves protonation of an alkoxide, so silicon atoms with electron-donating groups should hydrolyze more readily. Because –OH and –OSi groups are more electron withdrawing than –OR, the reactions become more difficult with increasing hydrolysis and condensation. The opposite is expected for high-pH conditions.

However, NMR studies, coupled with statistical modeling, contradict these arguments. Pouxviel and co-workers (*12*, *13*) studied acid-catalyzed reactions of TEOS with a variety of *W* values. Simulated kinetic curves for temporal evolution of various silicon species observed by ^{29}Si NMR spectroscopy were consistent with relative hydrolysis rate constants for sequential hydrolysis of the four –OEt substituents of 1:5.3:20:36. These trends were confirmed by more recent ^{1}H NMR spectroscopy (*14*), which yielded values for the four successive hydrolysis steps for TEOS of 0.0143, 0.064, 0.29, and 1.3 min^{-1}, respectively. Clearly these results indicate that inductive effects cannot be solely used to explain the relative hydrolysis rates. Steric bulk of the alkoxy substituent relative to hydroxy may have a dominant effect on hydrolysis rates.

Pouxviel et al. (*12*) demonstrated that higher *W* values ($W = 10$) enhance hydrolysis rates and thereby make hydrolysis under acid conditions nearly complete prior to condensation. At intermediate *W* ($W = 4$), hydrolysis and condensation proceed concurrently, and residual –OR groups remain; alcohol-producing condensation reactions become important. At low *W* values ($W = 1–2$), –OH sites are limited; thus reactions are retarded because both alcohol- and water-producing condensations require –OH groups.

Sols with low *W* values can be spun into fibers (*15*, *16*). Their spinnability was attributed to the presence of linear polymers (*15*). However, some work shows that linear polymers are not produced under these conditions. Using ^{29}Si NMR and small-angle X-ray scattering (SAXS) spectroscopy. Brinker and Assink (*17*) showed that TEOS–ethanol sols with $W = 1.5–1.7$ react via a random growth process leading to branched polymers. The polymers are more extended, producing a high-viscosity sol, which is stable against gelation for extended periods and is conducive

to spinnability. Sacks and Sheu (*16*) showed that spinnability is optimized when sols are highly shear thinning but not thixotropic.

Solvent effects are primarily due to polarity of the solvent and availability of labile protons (*18*). The solvent's ability to solvate or hydrogen-bond with available anions or cations greatly alters rates of reaction and particle size. The most thoroughly studied solvent effect is the use of DCCAs for production of monolithic gels. Orcel and Hench (*19*) and Jonas (*20*) studied the effect of formamide on a tetramethoxysilane (TMOS)–methanol system and concluded that increased viscosity and strong hydrogen bonding under both acidic and basic conditions reduced the hydrolysis rate.

This conclusion is supported by low-temperature ^{29}Si NMR work of Boonstra and co-workers (*21*) on a two-step TEOS–ethanol sol–gel system. The results indicate that formamide acts as a base to reduce H^+ concentration and the hydrolysis rate, but more importantly it also reduces the dimerization rate. In a two-step process, less than stoichiometric acidic water is added for hydrolysis, and condensation remains relatively slow. Dimerization is retarded, and so the number of free silanols available for condensation in the second step (addition of basic water) is enhanced. Thus, addition of formamide decreases the gel time by increasing the number of silanols for condensation. Gels with larger particle sizes and larger mean pore size are produced, and drying stresses are reduced.

Probably the most widely studied and important reaction variables are pH and catalyst. Pope and Mackenzie (*22*) studied the effects of catalysts on gel times of TEOS reactions. Such studies combine information on catalytic effects for both hydrolysis and condensation. The gel time of HCl-catalyzed TEOS reactions plotted as a function of pH is a sigmoidal shape (Figure 1). This plot is consistent with Iler's results for polymerization of $Si(OH)_4$ (*23*). Further, Pope and Mackenzie concluded that gel times depend on the catalytic mechanism of the catalyst as well as the pH, because sols catalyzed by HF and acetic acid have surprisingly short gel times (Table I).

Fluoride catalysis is well known (*22, 23*) and is proposed as due to the strong affinity of Si for F^-, small size of F^-, and ability of F^- to attack Si and expand its coordination sphere to 5 or 6. Increasing Si coordination may facilitate the loss of –OR groups, generate more electrophilic species, and thereby accelerate polymerization (*23, 24*).

Further, Jonas and co-workers (*24, 25*) have shown that TMOS polymerization is greatly enhanced by addition of NaF. A comparison of TMOS-derived gels generated at pH 6.4 with and without addition of NaF shows that F^- catalyzed gels are more branched in the early reaction stages and have more monomers, dimers, and trimers present at gelation. However, scattering results show fractal dimensions of about 2.2 for both systems, a result suggesting a similar reaction-limited cluster–cluster

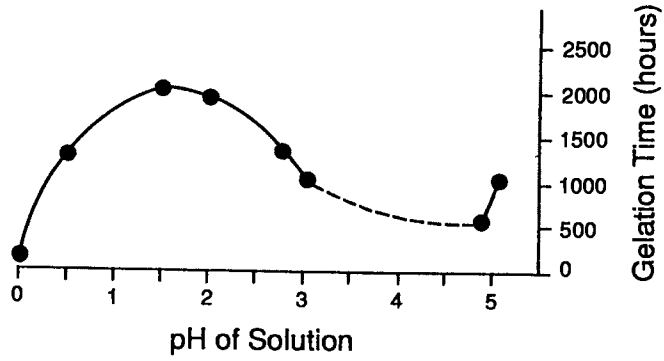

Figure 1. Gel time vs. pH for HCl-catalyzed TEOS sol (after ref. 22).

Table I. Gel Times and pH for TEOS Sols with Various Catalysts

Catalyst	*Initial Solution pH*	*Gel Time (h)*
HCl	0.05[a]	92
HNO_3	0.05[a]	100
H_2SO_4	0.05[a]	106
HF	1.90	12
HOAc	3.70	72
NH_4OH	9.95	107
No Catalyst	5.00	1000

[a]Between 0.01 and 0.05.
NOTE: TEOS:ethanol:water:acid = 1:4:4:0.05.
SOURCE: Modified from ref. 22.

growth model for both. The primary difference in structure was in the 100-Å range, with larger radii of gyration for F^- catalyzed systems.

Short gel times for acetic acid catalyzed sols is suggested (22) as due to displacement of –OR by an acetate ligand and subsequent attack by alcohol on the bound acetate, eliminating ethyl acetate and generating a silanol without hydrolysis:

$$Si(OR)_4 + CH_3COOH \xrightarrow{-ROH} (RO)_3SiO_2CCH_3 \xrightarrow{+ROH}$$

$$(RO)_3SiOH + CH_3COOR$$

Thus, two pathways were proposed for silanol production: hydrolysis as previously described and direct elimination of ethyl acetate.

Our work (26) shows that carboxylic acids have no unusual catalytic effect on gel times when gel time versus pH* (pH* was obtained with a

glass electrode in the reaction mixture) was plotted over the range of pH* = 0–7 for various catalysts (Figure 2). The reaction conditions of Mackenzie and co-workers (22, 27) were used (TEOS:ethanol:water:acid = 1:4:4:var; monomer and alcohol were mixed 30 min prior to water addition). The discrepancy in the catalytic effect of carboxylic acids results from Mackenzie and co-workers' comparison of acids at similar concentrations, which is difficult with the wide range of pK_a values. Acetic acid is weaker than HCl and thus provides a higher solution pH at the same concentration. This property is accentuated in alcohol because acetic acid acts as a weaker acid in alcohol (versus water) whereas HCl maintains a more constant acid strength (28). The sinusoidal curve obtained for gel time versus pH* plots for each of the acids is consistent with the results of Pope and Mackenzie (22) for HCl-catalyzed sols and with Iler for gelation of $Si(OH)_4$ (23). Some differences in gel times were observed near pH 2, similar to results reported by Iler for silicic acid gelation using various catalysts (23). However, the gel times for the sols catalyzed by carboxylic acid were not unusually short.

The silicon monomer chosen affects hydrolysis rates, gel times, and gel properties (2, 3, 27). Increasing steric bulk of the alkoxy ligands decreases hydrolysis rates by about a factor of 6 going from ethoxy to hexyloxy (3).

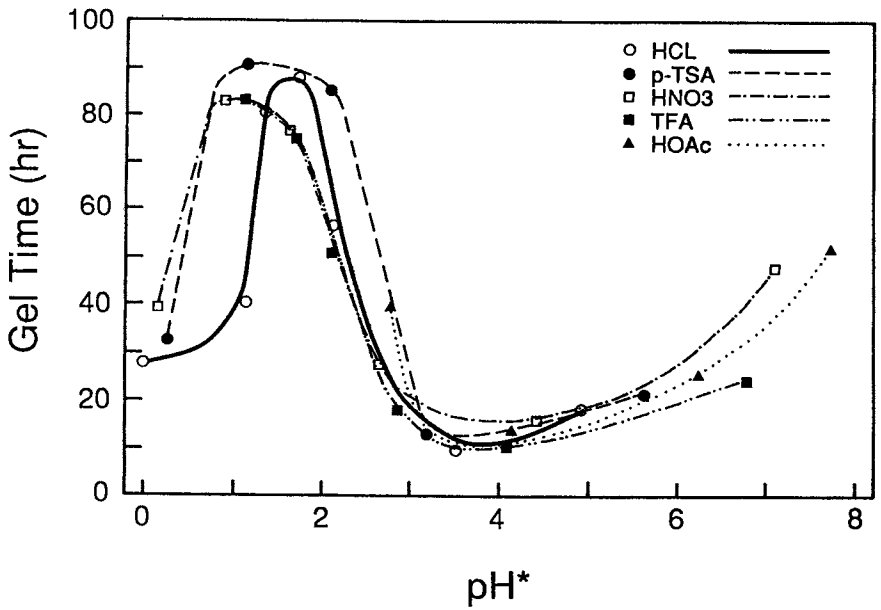

Figure 2. Gel time vs. pH for TEOS sols catalyzed by HCl, trifluoroacetic acid (TFA), p-toluenesulfonic acid (p-TSA), HOAc, and HNO_3.*

Differences in volume shrinkage, bulk density, and surface area are also reported for gels derived from different monomers (*27*).

Although TMOS sols gel faster relative to TEOS (160 versus 321 h), this property is not entirely due to hydrolysis rates, but also to the structural evolution of the sol (*29*). ^{29}Si NMR spectroscopic results show that TEOS-derived sols grow through intermediates containing more compact, cyclic structures than TMOS sols (Figure 3). Thus, TMOS polymers are more extended, chain-like structures that result in larger overlap of the polymers in solution and thus shorter gel times. These studies were done at low *W* values so residual –OR groups would be present. The increased steric bulk of the ethoxy groups may favor cyclization.

Substituting silicon tetraacetate, $Si(OAc)_4$, for TEOS in a typical sol–gel reaction (monomer:ethanol = 1:4, mixed 30 min prior to addition of 4 mol of 1.0 M HCl) results in a decrease in gel time from 242 to 1 h (*27*). This decrease is attributed to the generation of SiO_2 by direct attack of alcohol on the bound acetates. However, recent work (*30*) shows that

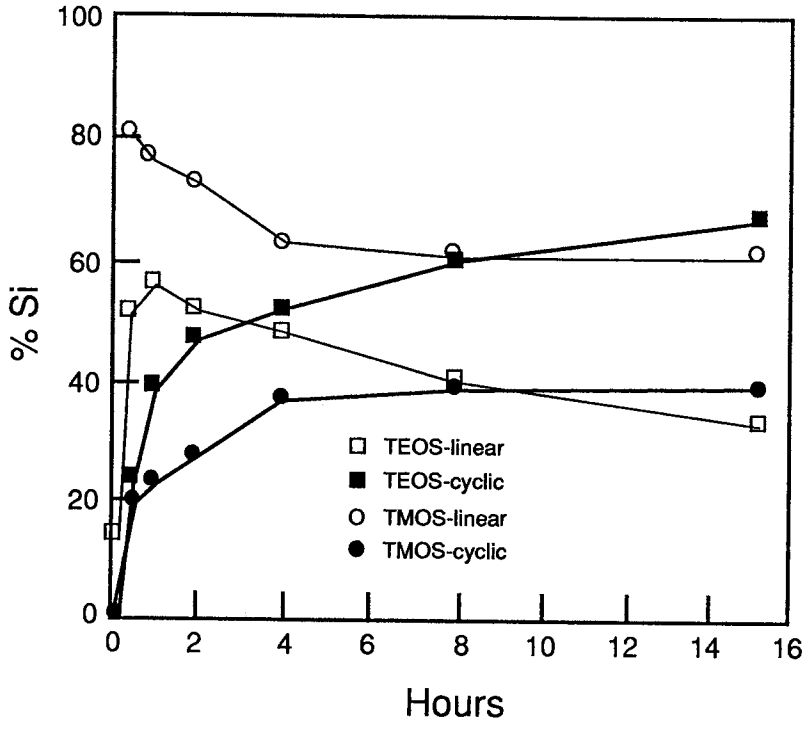

Figure 3. Linear vs. cyclic species calculated from ^{29}Si NMR spectra for TEOS–ethanol and TMOS–methanol sols (Si:water:acid = 1:2:0.02).

virtually no acetate ligands remain after reacting $Si(OAc)_4$–ethanol for 30 min (Figure 4). The acetates were replaced by ethanol via a rapid alcoholysis reaction. Also noteworthy is the lack of condensed silicon species in the ^{29}Si NMR spectrum and the absence of ethyl acetate in the ^1H NMR spectrum. Acetic acid was reported (*31*, *32*) to displace ethoxy groups on TEOS, but only upon refluxing. Acetate ligands are very stable on inorganic elements, such as Ti, that readily expand coordination to 5 or more (*33*). Bidentate ligation of acetate blocks reaction sites in such cases. $Si(OAc)_4$, however, has monodentate ligation (*34*), the ligands are much more labile, and alcoholysis is facile. Attack is possible on silicon as well as the carbonyl of the acetate ligand.

In this example, prior to water addition, alcoholysis causes the sol to consist primarily of TEOS in 4 equivalents of acetic acid. Thus the question becomes, why does TEOS gel much faster in acetic acid than in ethanol? Figure 5 shows ^{29}Si NMR spectra for the $Si(OAc)_4$–ethanol system just described and for TEOS in 4 mol of acetic acid, both spectra taken 45 min after addition of 4 mol of 1 M HCl. No evidence is seen in the NMR spectra for substitution of ethoxide ligands by acetate in the TEOS–acetic acid system. The two spectra are similar. (Additionally, the gel times for the two systems are nearly identical.) Condensation has proceeded rapidly to give a distribution of condensed species typical of acid-catalyzed sols. ^1H NMR spectra show rapid and nearly complete hydrolysis and the generation of ethyl acetate only after acidic water addition. Ethyl acetate arises from the acid-catalyzed reaction of free ethanol and acetic acid. The rapid gel time is not due to acetate ligation, but is apparently due to the very low pH of this system (acetic acid and HCl); below pH 2, condensation is catalyzed by H^+. Although water is a by-product in the generation of ethyl acetate, the rapid gel times could not be duplicated simply by increasing the water in TEOS–ethanol sols by the amount produced by the side reaction (determined by ^1H NMR spectroscopy). Additionally, solvent effects may play a role because the dielectric constant of the medium is reduced by acetic acid and ethyl acetate produced in the reactions.

Schmidt (*35*) demonstrated that alkyl substituents enhance ligand electron donation. Hydrolysis is enhanced under acidic conditions, but is retarded under basic conditions, by methyl substitution of ethoxysilane derivatives. This result is important for the generation of organic-inorganic hybrid materials. When TEOS is reacted with silicon monomers containing alkyl substituents (or organic polymers with trialkoxysilane groups), the relative reaction rates just described must be controlled to produce true hybrids and avoid "blocky" materials.

Recent work (*36*) shows the importance of this control. Methyltriethoxysilane (MeTEOS) and TEOS were mixed in equimolar amounts in ethanol followed by addition of 0.5 equiv of 0.15 M DCl. Such conditions

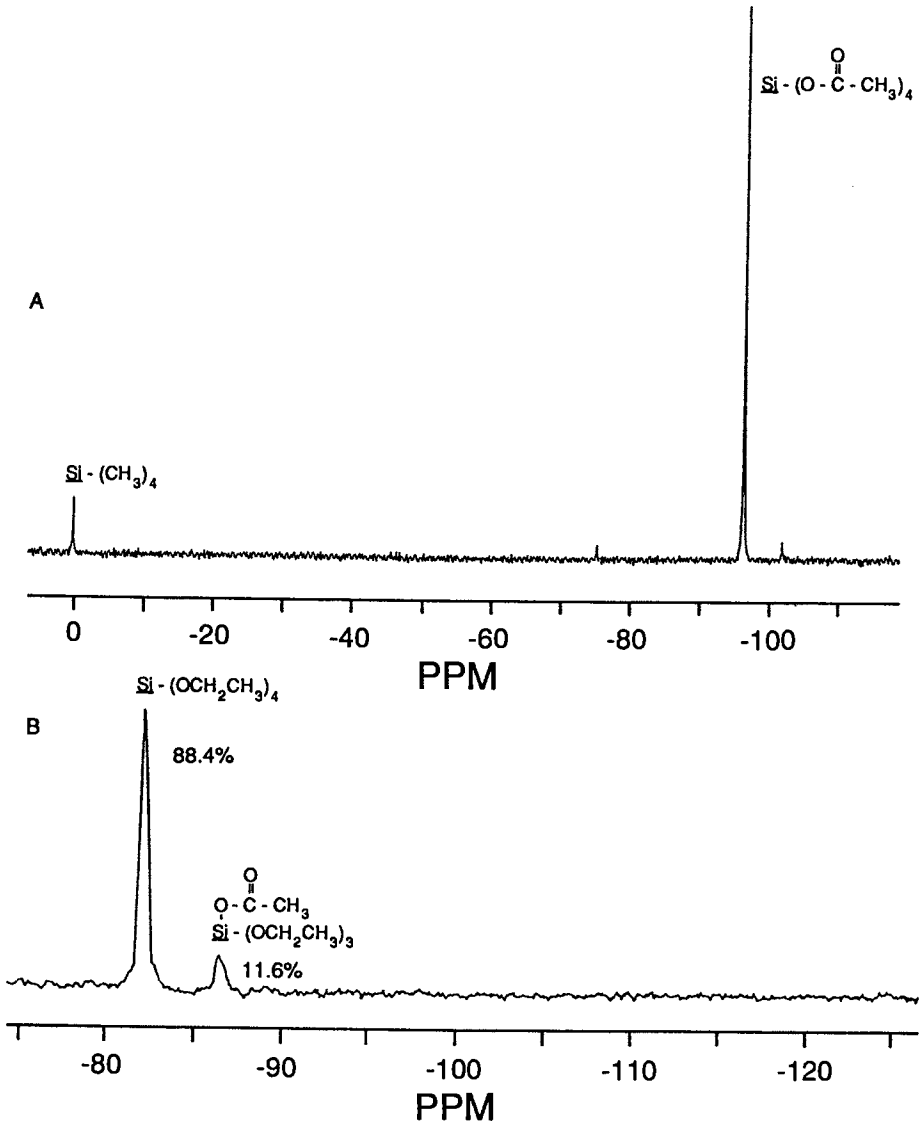

Figure 4. ^{29}Si NMR spectra of (A) $Si(OAc)_4$ in $CDCl_3$ and (B) $Si(OAc)_4$ in 4 mol of ethanol 30 min after mixing.

limit hydrolysis and condensation. Figure 6 shows the ^{29}Si NMR spectrum of this mixture 275 h after water addition. MeTEOS has reacted further as evidenced by the smaller T^0 vs. Q^0 peaks. After only 0.5 h 69% of the MeTEOS monomers have homodimerized, whereas only 31% have reacted with TEOS. Forty-four percent of the MeTEOS silicons have become

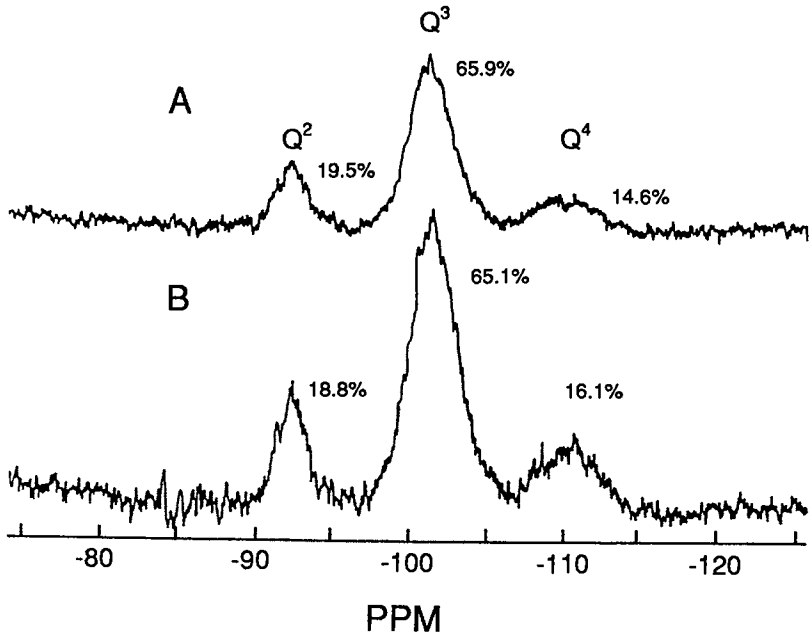

Figure 5. ^{29}Si NMR spectra of (A) TEOS–acetic acid sol and (B) $Si(OAc)_4$–ethanol sol, 45 min after addition of 4 equiv of 0.15 M HCl. Q refers to four possible condensation bonds; the exponent is the actual number of condensation bonds.

blocked with two other MeTEOS monomers. This outcome shows that mixing these two monomers together and adding sufficient water results in materials with MeTEOS- and TEOS-rich blocks. However, in our system (limited water) a point is reached where hydrolyzed MeTEOS reacts preferentially with hydrolyzed TEOS because late in the reaction the concentration of the TEOS is higher (most of the hydrolyzed MeTEOS has gone on to form oligomers). An understanding of the reaction variables affecting hydrolysis and condensation rates is needed to design and synthesize materials with new physical properties.

Reesterification, or the reverse of hydrolysis, is often important, particularly under acid conditions. Recent GC work on HCl-catalyzed TEOS sols at pH values ranging from 0.9 to 3.0 is shown in Table II.

Both hydrolysis and reesterification rates increase sharply as pH is lowered. These data show that the esterification reaction is important under these conditions as hydrolysis is only 3.5–6.0 times faster. This reaction results in acid-catalyzed gels frequently containing residual OR groups even though hydrolysis is nearly complete (2, *10*).

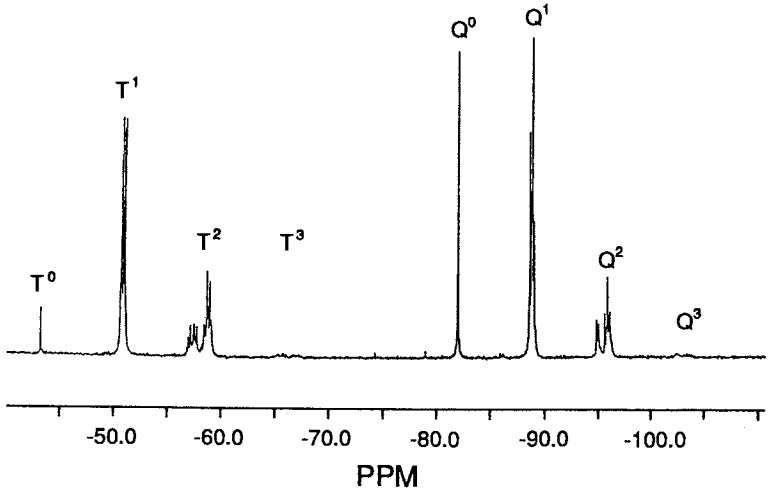

Figure 6. ^{29}Si NMR spectrum after 275 hr of 1:1 MeTEOS–TEOS in ethanol with 0.5 equiv of 0.15 M DCl–D_2O. **T** *and* **Q** *refer to the number of possible condensation bonds:* **T** *is three,* **Q** *is four; the exponent is the actual number of condensation bonds.*

Table II. Rate Constants from GC and Kinetic Model for HCl-Catalyzed Sols

pH	k_H	k_E	k_W	k_A
0.9	9.6	1.6	0.48	0.09
1.9	1.23	0.35	0.69	0.16
3.0	0.082	0.014	1.30	0.32

NOTE: TEOS:ethanol:water = 1:3.4:2. All values are in liters per mole hour.
SOURCE: Modified from ref. 37.

Condensation

Alcohol- or water-producing condensation generates a three-dimensional network. Pohl and Osterholtz (*6*) showed that condensation of alkylsilanetriols is specific acid and base catalyzed. Above the isoelectric point of silica (about pH 2.5) condensation proceeds by nucleophilic attack of deprotonated silanols on neutral silicates (*6*, *23*). Below the isoelectric point the reaction proceeds by protonation of silanols followed by electrophilic attack (*2*, *6*). These reactions favor less highly condensed sites, because these are the most electron rich, and lead to more extended, ramified structures. Above pH 2.5, reactions favor more highly condensed sites.

One important parameter influencing the structural evolution of silicate polymers is the "molecular separation" of the reactive species (*38*, *39*). Yoldas showed that TEOS concentration strongly influences the size of the silicate polymers. The effect is modified by the amount of water present; higher values of *W* result in higher degrees of polymerization. Concentrating the reacting solutions results in significant polymer growth if silanols are present, such as with high values of *W*.

The solubility of silica is also important. Figure 7 shows the relative dissolution rate for aqueous silicates as a function of pH (*23*). The rate is slow at low pH so there is little bond redistribution. SAXS studies coupled with computer simulations have shown that under these conditions reaction-limited cluster–cluster aggregation is favored and leads to branched structures with mass fractal dimensions (d_f) of about 2 (*2*, *40*, *41*). Recent wide-angle X-ray scattering (WAXS) and SAXS results show that acidic conditions generate primary particles of about 1-nm size, which in turn aggregate to form clusters with d_f of 1.75–2.14, consistent with reaction-limited or diffusion-limited cluster–cluster aggregation (*42*). These primary particles are proposed to consist of two silicate polyhedra made up of four six-membered rings (*43*).

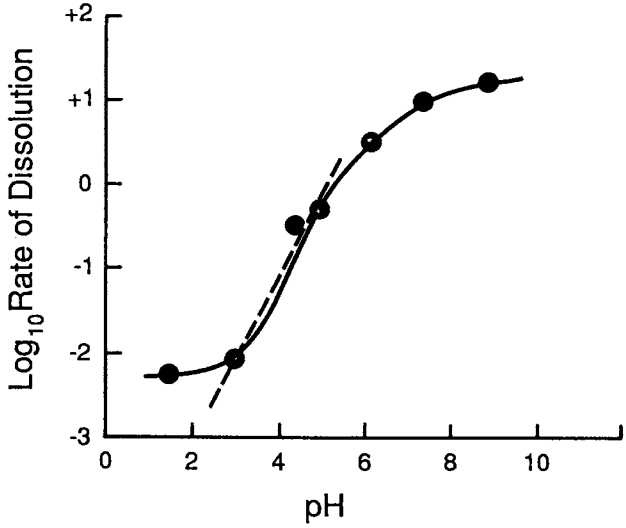

Figure 7. Silica dissolution rate as a function of pH (after ref. 23).

At pH >7, where the dissolution of silica is more favored, nucleation and growth is the predominant mechanism (*2*) Dissolution ensures a constant supply of monomers with high mobility. This feature, coupled with condensation being favored at more highly condensed sites, leads to

the generation of highly cross-linked, large particles stabilized by electrostatic repulsions. This dissolution reaction as well as slow hydrolysis accounts for monomers frequently being observed in base-catalyzed systems even past the gel point (*2*, *44*). ^{29}Si NMR spectroscopy shows that under basic conditions fully condensed or Q^4 species and monomers are the predominant species present. Under low pH conditions, no Q^0 or Q^1 and a distribution of Q^2, Q^3, and Q^4 species are present (if sufficient water is provided) (*44*).

Relative reaction rates of hydrolysis, condensation, reesterification, and dissolution must be understood and controlled to dictate structural evolution. However, accurate values for rate constants are difficult to obtain because of the enormous number of distinguishable reactions as next nearest neighbors are considered, and to the concurrency of these reactions. Assink and Kay (*45*) use a simplified statistical model assuming that the local silicon environment does not affect reaction rates, and the reactions for a particular silicon species are the product of a statistical factor and rate constant. These assumptions ignore steric and inductive effects. For example, this model predicts that the relative rate constants for the four sequential hydrolysis steps leading from TMOS to $Si(OH)_4$ would be 4:3:2:1. This model was applied to acid-catalyzed TMOS sols with W values ranging from 0.5 to 2.0. ^{29}Si NMR spectra on the temporal evolution of various silicon species show the model is in excellent agreement with experimental results. A lower limit for k_H was calculated as 0.2 L/mol-min. Values for k_W and k_A are 0.006 and 0.001 L/mol-min, respectively.

As mentioned earlier, Pouxviel and co-workers (*12*, *13*) studied acid-catalyzed reactions of TEOS with a variety of W values. The statistical model works better for TMOS than TEOS, possibly because of the increasing importance of steric factors with increasing bulk of the alkoxy substituent. Such effects are ignored in the statistical model. Although the relative hydrolysis rate coefficients for sequential hydrolysis of the four ethoxy groups was found by ^{29}Si NMR spectroscopy to be 1:5:12:5, reesterification reactions were ignored (*12*). Simulated kinetics curves including the effects of k_E yielded the relative hydrolysis rate constants of 1:5.3:20:36, as noted earlier (*13*). Reesterification rate constants increased steadily with increasing hydroxyl substitution. Condensation rate constants also increased with increasing hydroxyl substitution, but decreased with the degree of condensation. These relative trends are contrary to predictions based solely on inductive effects. These early applications of statistical models illustrate the complexity of sol–gel reactions and the fact that no variable can be readily ignored.

These trends were confirmed by more recent ^{1}H NMR work (*14*). Gel permeation chromatographic (GPC) data by the same authors showed that acid-catalyzed polymerization of TEOS with $W = 4$ produced monomodal

molecular weight distributions, whereas similar conditions with $W = 6$ produced bimodal distributions later in the reaction.

Kinetic measurements on the dimeric hexamethoxydisiloxane species generated values of $k_A = 0.0007$ L/mol-min and $k_W = 0.0011$ L/mol-min, versus 0.001 and 0.006 L/mol-min for the monomer (*46*). The alcohol-producing condensation reaction is about the same for monomers and dimers, but the water-producing condensation is significantly lower for dimers. This difference is probably due to both increased steric crowding in the dimer and the inductive effect of an –OSi ligand retarding the reaction, as described earlier. Steric and inductive effects are important variables on reaction kinetics.

Klemperer and co-workers (*47–50*) investigated a molecular building block approach to silica sol–gels by hydrolyzing and condensing $[Si_2O](OCH_3)_6$, $[Si_3O_2](OCH_3)_8$, and $[Si_8O_{12}](OCH_3)_8$. With low acid or base concentrations and higher W values, polymerization is rapid relative to depolymerization, and the primary structures of the starting materials are maintained. With lower W values and higher acid or base concentrations, polymerization and depolymerization reactions are competitive, and some redistribution occurs.

Recent studies on the sol–gel transition for TMOS show no drastic change in structure at the gel point (*51*). Percolation theory accurately accounts for gross structural features. Well past the gel point, motion remained at the molecular level and water freely diffused. Understanding and controlling structural evolution from the early reaction stages are important because these basic structures carry through to the gel state.

Conclusions

Structural control in sol–gel processes is complicated because many and diverse variables affect concurrent reactions differently. Inductive and steric factors contribute to the reaction rates. pH is probably the single most important variable in these reactions. It accounts for differences when DCCAs are used and for the rapid gel times in $Si(OAc)_4$ sols, as well as differences in the two predominant growth mechanisms: nucleation and growth and cluster–cluster aggregation.

When alkyl-substituted silicon alkoxides are used, other factors such as inductive effects on reaction kinetics become more important. The desire for new hybrid materials has made sol–gel science and technology one of the faster growing areas of chemistry. Although much has been learned, there remains a need for a better chemical understanding of the complex sequence of reactions.

References

1. Schmidt, H.; Scholze, H.; Kaiser, A. *J. Non-Cryst. Solids* **1984,** *63*, 1.
2. Brinker, C. J. *J. Non-Cryst. Solids* **1988,** *31*, 100.
3. Aelion, R.; Loebel, A.; Eirich, F. *J. Am. Chem. Soc.* **1950,** *72*, 124.
4. Aelion, R.; Loebel, A.; Eirich, F. *Recueil* **1950,** *69*, 61.
5. McNeil, K. J.; DiCaprio, J. A.; Walsh, D. A.; Pratt, R. R. *J. Am. Chem. Soc.* **1980,** *102*, 1859.
6. Pohl, E. R.; Osterholtz, F. D. In *Molecular Characterization of Composite Interfaces*; Ishida, H.; Kumar, G., Eds.; Plenum: New York, 1985; p 157.
7. Swain, C. G.; Estere, W. M., Jr.; Jones, R. H. *J. Am. Chem. Soc.* **1949,** *71*, 965.
8. Campostrini, R.; Carturan, G.; Pelli, B.; Traldi, P. *J. Non-Cryst. Solids* **1989,** *108*, 143.
9. Aelion, R.; Loebel, A.; Eirich, F. *J. Am. Chem. Soc.* **1950,** *72*, 5705.
10. Keefer, K. D. In *Better Ceramics through Chemistry*; Brinker, C. J.; Clark, D. E.; Ulrich, D. R., Eds.; Elsevier North Holland: New York, 1984; p 15.
11. Uhlmann, D. R.; Zelinski, B. J.; Wnek, G. E., ibid., p 59.
12. Pouxviel, J. C.; Boilot, J. P.; Beloeil, J. C.; Lallemand, J. *J. Non-Cryst. Solids* **1987,** *89*, 345.
13. Pouxviel, J. C.; Boilot, J. P. *J. Non-Cryst. Solids* **1987,** *94*, 374.
14. Hui, Y.; Zishang, D.; Zhonghua, J.; Xiaoping, X. *J. Non-Cryst. Solids* **1989,** *112*, 449.
15. Sakka, S.; Kamiya, K. *J. Non-Cryst. Solids* **1982,** *31*, 48.
16. Sacks, M. D.; Sheu, R. S. *J. Non-Cryst. Solids* **1987,** *383*, 92.
17. Brinker, C. J.; Assink, R. A. *J. Non-Cryst. Solids* **1989,** *111*, 48.
18. Artaki, I.; Zerda, T. W.; Jonas, J. *J. Non-Cryst. Solids* **1986,** *81*, 381.
19. Orcel, G.; Hench, L. L. *J. Non-Cryst. Solids* **1986,** *79*, 177.
20. Jonas, J. In *Science of Ceramic Chemical Processing*; Hench, L. L.; Ulrich, D. R., Eds.; Wiley–Interscience: New York, 1986; p 65.
21. Boonstra, A. H.; Bernards, T. N. M.; Smits, J. J. T. *J. Non-Cryst. Solids* **1989,** *109*, 141.
22. Pope, E. J. A.; Mackenzie, J. D. *J. Non-Cryst. Solids* **1986,** *87*, 185.
23. Iler, R. K. *The Chemistry of Silica*; Wiley: New York, 1979.
24. Winter, R.; Chan, J. B.; Frattini, R.; Jonas, J. *J. Non-Cryst. Solids* **1988,** *105*, 214.
25. Winter, R.; Hua, D. W.; Thiyagarajan, P.; Jonas, J. *J. Non-Cryst. Solids* **1989,** *108*, 137.
26. Coltrain, B. K.; Melpolder, S. M.; Salva, J. M. In *Ultrastructure Processing of Advanced Materials;* Uhlmann, D. R., Ulrich, D. R.; Eds.; Wiley: New York, 1992; p 69.
27. Chen, K. C.; Tsuchiya, T.; Mackenzie, J. D. *J. Non-Cryst. Solids* **1986,** *81*, 227.
28. Bates, R. G. *Determination of pH*; Wiley: New York, 1973.
29. Kelts, L. W.; Armstrong, N. J. *J. Mater. Res.* **1989,** *4*, 423.
30. Coltrain, B. K.; Kelts, L. W.; Armstrong, N. J.; Salva, J. M., unpublished results.
31. Sanchez, C.; Livage, J.; Henry, M.; Babonneau, R. *J. Non-Cryst. Solids* **1988,** *100*, 65.
32. Campero, A.; Arroyo, R.; Sanchez, C.; Livage, J. In *Ultrastructure Processing of Advanced Ceramics*; Mackenzie, J. D.; Ulrich, D. R., Eds.; Wiley: New York, 1988; p 327.
33. Doeuff, S.; Henry, M.; Sanchez, C.; Livage, J. *J. Non-Cryst. Solids* **1987,** *89*, 206.

34. Mehrotra, R. C.; Bohra, R. *Metal Carboxylates*; Academic: London, 1983.
35. Schmidt, H. *J. Non-Cryst. Solids* **1985,** *73,* 681.
36. Kelts, L. W.; Coltrain, B. K., unpublished results.
37. Ro, J. C.; Chung, I. J. *J. Non-Cryst. Solids* **1989,** *110,* 38.
38. Yoldas, B. E. *J. Non-Cryst. Solids* **1986,** *82,* 11.
39. Yoldas, B. E. *J. Polym. Sci. A: Polym. Chem.* **1986,** *24,* 3425.
40. Keefer, K. D. In *Better Ceramics through Chemistry II*; Brinker, C. J.; Clark, D. E.; Ulrich, D. R., Eds.; Materials Research Society: Pittsburgh, PA, 1986; p 585.
41. Brinker, C. J.; Keefer, K. D.; Schaefer, D. W.; Assink, R. A.; Kay, B. D.; Ashley, C. S. *J. Non-Cryst. Solids* **1984,** *63,* 45.
42. Himmel, B.; Gerber, Th.; Burger, H. *J. Non-Cryst. Solids* **1990,** *119,* 1.
43. Himmel, B.; Gerber, Th.; Burger, H. *J. Non-Cryst. Solids* **1987,** *91,* 122.
44. Kelts, L. W.; Effinger, N. J.; Melpolder, S. M. *J. Non-Cryst. Solids* **1986,** *83,* 353.
45. Assink, R. A.; Kay, B. D. *J. Non-Cryst. Solids* **1988,** *107,* 35.
46. Doughty, D. H.; Assink, R. A.; Kay, B. D. In *Silica-Based Polymer Science: A Comprehensive Resource*; Advances in Chemistry Series 224; Ziegler, J. M.; Fearon, F. W. G., Eds.; American Chemical Society: Washington, DC, 1990; p 241.
47. Klemperer, W. G.; Mainz, V. V.; Millar, D. M. *Mater. Res. Soc. Symp. Proc.* **1986,** *73,* 3.
48. Klemperer, W. G.; Mainz, V. V.; Millar, D. M. *Mater. Res. Soc. Symp. Proc.* **1986,** *73,* 15.
49. Klemperer, W. G.; Ramamurthi, S. D. *Mater. Res. Soc. Symp. Proc.* **1988,** *121,* 1.
50. Klemperer, W. G.; Ramamurthi, S. D. *Polym. Prepr.* **1987,** *28,* 432.
51. Winter, R.; Hua, S. W.; Song, X.; Mantulin, W.; Jonas, J. *J. Phys. Chem.* **1990,** *94,* 2706.

RECEIVED for review October 19, 1990. ACCEPTED for publication December 9, 1991.

20

Chemistry and Properties of Porous, Organically Modified Silica

Helmut Schmidt[1] and Harald Böttner[2]

[1]Institut für Neue Materialien, Universität des Saarlandes Gebäude 43, Im Stadtwald, D-6600 Saarbrücken, Germany
[2]Fraunhofer-Institut für Physikalische Messtechnik, Heidenhofstrasse 8, D-7800 Freiburg, Germany

Sol–gel techniques were used to prepare porous, organically modified silica materials. The introduction of organic groupings was carried out with alkoxysilanes as precursors; methyl and propyl amino groups were used. The results show that high-porosity materials can be synthesized; the microstructure strongly depends on reaction conditions such as composition, solvent, catalyst type, and concentration. Microstructure tailoring affects mechanical as well as adsorption properties, and custom-made materials such as abrasives and adsorbents with special properties were synthesized.

SILICA IS AN OXIDE with innumerable variations. On the basis of this structural variability, a variety of different types of materials have been prepared, such as compact fused silica, in the form of plates, fibers, or finely dispersed pellets, and porous materials. Because compact silica is mostly used for optical components or applications for which high chemical durability is required, porous and finely dispersed materials have completely different applications, for example, as fillers, adsorptive materials, or strengtheners in composites. Various aspects of the chemistry, physics, and applications of silica are described in detail in the book by Iler (*1*), with special consideration given to finely dispersed and porous materials.

The main preparation method for fused silica still involves melting technology, but a few other methods are used that involve sol–gel or

0065–2393/94/0234–0419$08.00/0

related routes (2). For fibers and coatings, sol–gel technology has become more and more important (3–5). For dispersed materials, pyrolytic and precipitation processes are the dominating technologies for large-scale production (6–7). To adapt these types of silica to a variety of special applications, various types of chemical surface modifications have been performed. A survey is given in reference 1. By surface modification (e.g., by organosilicon compounds) the hydrophobicity or hydrophilicity can be varied. For example, chromatographic materials (for reverse-phase chromatographic columns, for example) are prepared by reacting alkylsilanes that have well-defined alkyl chain-lengths (e.g., C_8) with the silica surface (Scheme I):

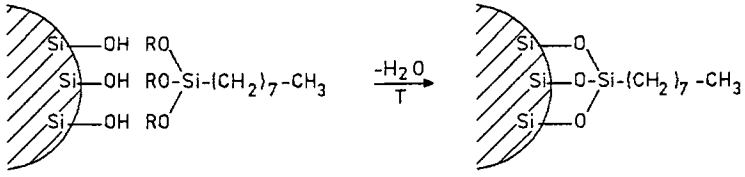

Scheme I.

This type of surface modification, if adequate functional groups are used, can be useful in incorporating silica particles into polymeric matrices (e.g., into rubber for tires) or in increasing the hydrolytic stability of high-surface-area silica (e.g., that used for membranes). Surface modification of silica is a very important principle and is widely commercialized.

General Considerations

Another principle of modification, the modification of the network by organic groups, is not as important now compared to the surface modification principle. The exchange of an –O– group of a $[SiO_4]^{4-}$ tetrahedron by a CH_3 group drastically changes the properties of the modified "glass" compared to fused silica. The density drops from about 2.2 (fused silica) to about 1.3 g/cm^3, and the thermal coefficient of expansion increases from 0.5×10^{-6} to 100×10^{-6} K^{-1}. Bulk materials modified by CH_3 are used as spin-on glasses for coating purposes in microelectronics. They can be oxidized to SiO_2 glassy films if desirable (*8*). The partial substitution of ≡Si–O– bonds by ≡Si–CH_3 groups leads to densification temperatures far below the densification of inorganic SiO_2 sol–gel films. The examples indicate an interesting effect of organic

modification of silica on properties as well as on structure. This chapter focuses on porous silica materials that have been bulk-modified by ≡Si–C– bonds and derived by sol–gel methods.

High porosity or high surface areas can be obtained by various preparation or special processing techniques, for example, by leaching of phase-separated sodium borosilicate glasses. Small dimensions of building units are required; small particles or small pores between units must be created (Figure 1). In materials with small pores between units, a high rigidity of material is required to avoid the collapse of the pores during the network synthesis.

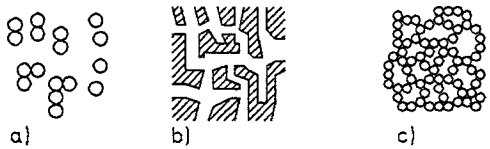

Figure 1. Model of high-surface-area materials: a, small particles; b, "reverse" system, small pores; and c, porosity generated by aggregation of small particles (a).

The required network rigidity results from the three-dimensional cross-linking of the $[SiO_4]^{4-}$ tetrahedrons. Bulk modification by introduction of organic units through ≡Si–C– bonds leads to a change of network connectivity and should also affect porosity or surface area. On the other hand, in this case the modification becomes an intrinsic property that should not be affected by surface corrosion (Scheme II), because after removal of the surface layer by hydrolytic processes, the following layer exhibits the corresponding structure and properties. The properties to be developed determine whether a surface or a bulk modification is more appropriate.

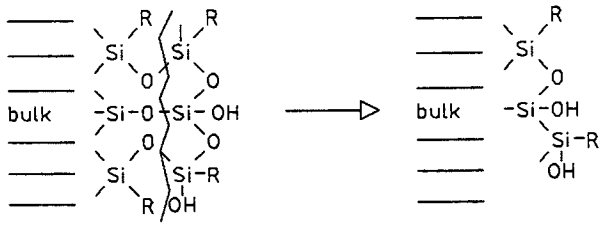

Scheme II. Model of corrosion of organic modification of silica ("bulk" denotes the $-CH_3$-modified structure).

Preparation of Porous Materials

Reactivity of Precursors in Sol–Gel Processes. If multicomponent systems are prepared by hydrolysis and condensation of alkoxide precursors in methanol, the reaction rates of hydrolysis and condensation (including aggregation) of the different components become very important for the distribution of the different components. The simple question of how CH_3 groups might be distributed within a porous two-component system with $Si(OR)_4$ and $CH_3Si(OR)_3$ or $(CH_3)_2Si(OR)_2$ as precursors leads to serious mechanistic problems. A comparison of the hydrolysis rates with acid catalysis indicates an increase with increasing number of organic ligands (*9–11*) and the opposite with bases. The effect on specific surface areas of the resulting materials is shown in Figure 2. Similar results with $(CH_3)_2SiO$-containing systems for membrane formation were obtained with ethanol.

The surface areas were measured by multipoint Brunauer–Emmett–Teller (BET) techniques. In NH_3-catalyzed materials, the fraction of micropores is extremely low (<1 vol %). In acid catalysis, the micropore content increased with decreasing surface area. The CH_3 content was determined by IR spectroscopic analysis of CH_3 groups only in NH_3-catalyzed composites could a loss of CH_3-containing units be observed.

The experimental process for synthesizing the porous materials was standardized as follows. The silanes were mixed in the ratios as indicated in MeOH (Me, methyl) as solvent, and then at room temperature 1 mol of water per ≡SiOR group was added. The water contained the indicated concentration of catalysts. The reaction mixture was stirred for 5 min and then stored in a closed flask. The two different catalysts show opposite tendencies with respect to increasing concentrations of CH_3 groups in the system. With NH_3, the surface areas decrease with increasing CH_3 group content in both systems (SiO_2–$CH_3SiO_{3/2}$ and SiO_2–$(CH_3)_2SiO$), but there is no significant difference between both systems.

In the acid-catalyzed systems, very high surface areas are observed in CH_3-containing composites. The effect of the HCl concentration is significant. In basic catalysis, the reaction conditions do not seem to influence structure and porosity to the same extent as in the acid case. In acid catalysis, the total surface area increases with decreasing gelling times and increases with increasing CH_3 concentrations. The gelling times are given in Table I.

The increase of surface area with increasing CH_3 concentration (decreasing network connectivity) can be explained by the interaction of CH_3-covered pore walls with water; this interaction leads to reduced interfacial tensions. Synthesis yields are a function of catalyst and composition (Figure 3). This fact can be explained by a reaction rate consideration. As shown in reference 9, the hydrolysis rate of the CH_3-

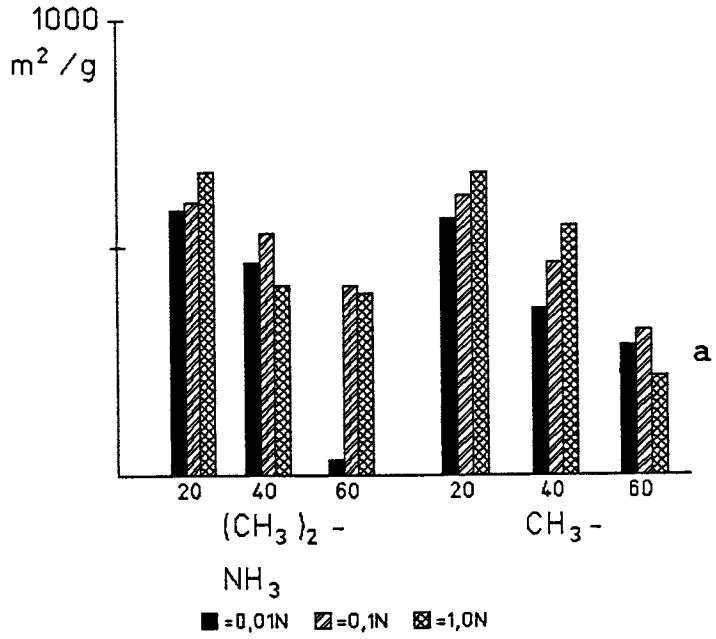

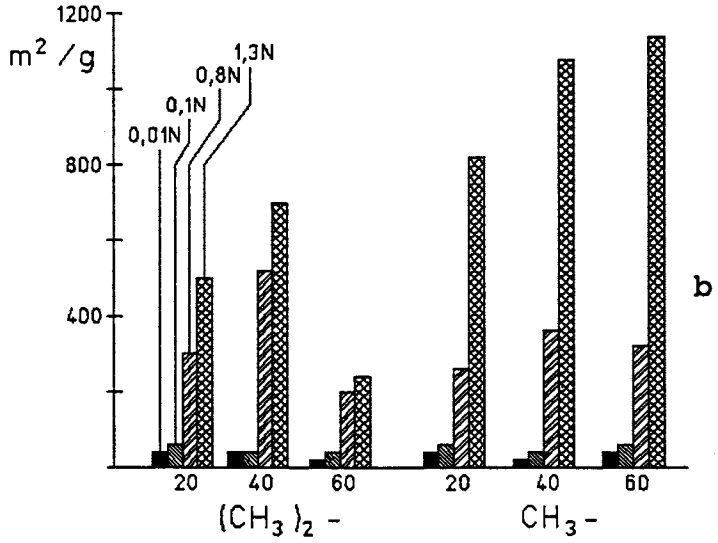

Figure 2. Effect of reaction conditions and composition on the specific surface area of -CH_3-modified silica [tetramethoxysilane (TMOS) as shown]. Part a: catalyst, NH_3; abscissa numbers, weight percent of $CH_3SiO_{3/2}$ or $(CH_3)_2SiO$. Part b: catalyst, HCl; abscissa numbers, same as in part a.

Table I. Gelling Times of Various Composites

Catalyst Type and Concentration	*80:20*	*60:40*	*40:60*
1 N NH_3 (2 N HCl)	~1 (~3 × 10^5)	~1 (~3 × 10^5)	~1 (~3 × 10^5)
0.1 N NH_3 (0.1 N HCl)	300 (~23 × 10^5)	~840 (~11 × 10^5)	~2700 (~13 × 10^5)
0.01 N NH_3 (0.01 N HCl)	1200 (~47 × 10^5)	~10^5 (~80 × 10^5)	~3 × 10^5 (~60 × 10^5)

NOTE: Times are reported in seconds. In the composite ratios, first number is the weight percent of SiO_2 in SiO_2–$CH_3SiO_{3/2}$.

substituted silanes in NH_3 catalysis drops rapidly. This decrease does not necessarily lead to longer gelation times because the gel formation could be caused by the tetraorthosilicate network only. As shown in reference 11, the condensation rate increases with higher pH values, leading to shorter gelling times in the composite sol compared to the acid-catalyzed case. Because of the low hydrolysis rates in the basic case, the gelling occurs mainly from the $Si(OR)_4$ hydrolysis and condensation, and the unhydrolyzed CH_3-containing precursors can evaporate if the gels are dried shortly after gelling. IR spectra in the base-catalyzed case show a corresponding decrease of the CH_3 signal in basic gels, too. If the composites are stored in a closed system for several weeks without drying after gelation to allow further reaction, higher yields can be obtained from basic catalysis, too. This process was carried out for surface area and H_2O adsorption measurements.

To support the hypothesis of weaker pore wall interaction in the CH_3-modified case, H_2O adsorption experiments were carried out on several

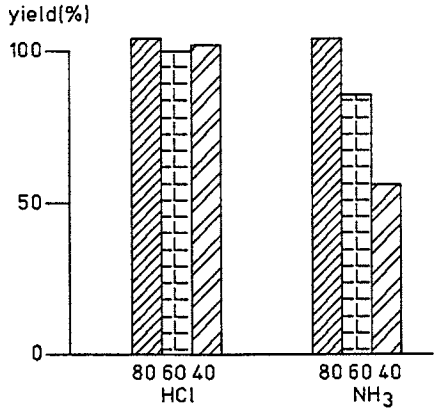

Figure 3. Percentage of product yield depending on catalyst and composition. The samples were dried after gelling to a constant weight at 110 °C; yields above 100% are due to residual water. Catalyst concentrations were 1.0 N NH_3 and 1 N HCl; abscissa numbers denote wt % SiO_2 in SiO_2–$CH_3SiO_{3/2}$ composites.

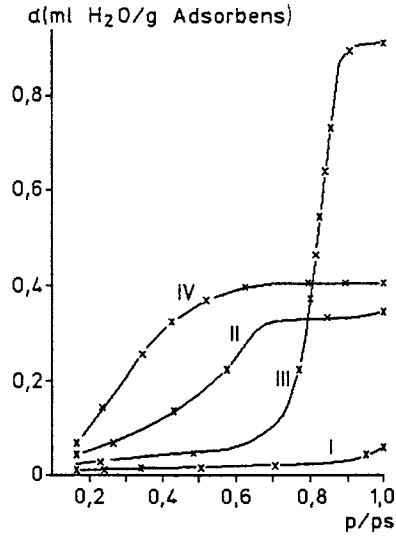

Figure 4. H_2O adsorption isotherms (partial pressure over saturation pressure) on four different silicas: I, CH_3-modified 300 m^2/g; II, $-CH_2-CH_2COOH-$, 800 m^2/g; III, $(CH_2)_3NH_2-$, 310 m^2/g; and IV, unmodified, 450 m^2/g.

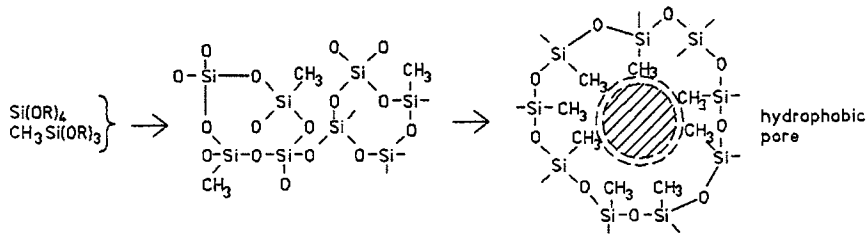

Scheme III. Self-arrangement of CH_3-modified systems.

porous silica gels with different compositions (Figure 4). The CH_3-modified system shows almost no H_2O adsorption, a result indicating extremely hydrophobic pores. Increasing hydrophilicity (II → IV) changes the adsorption behavior gradually. During the condensation step of the CH_3-containing gels, a self-adjustment of the system seems to take place, and the CH_3 groups "turn" to the inner pore walls (Scheme III).

In summary, high-surface-area systems can be prepared from $CH_3-Si\equiv/SiO_2$ and $(CH_3)_2SI=/SiO_2$ composites even if the network stiffness is expected to be decreased substantially, perhaps because of the decrease of interaction between hydrophobic (self-arranged) pore walls and H_2O and the reduction of interfacial forces.

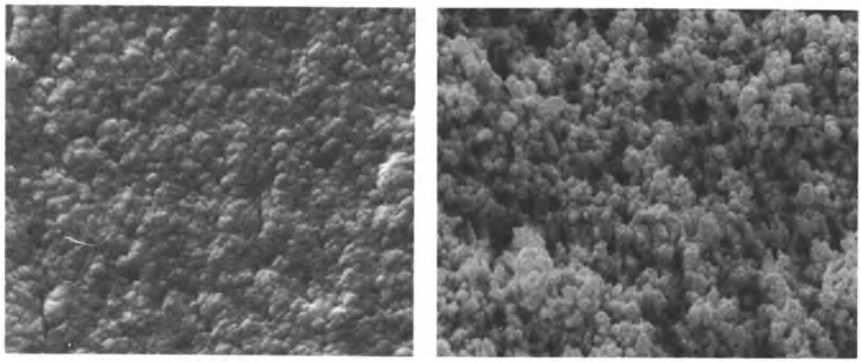

Figure 5. Images of gel surfaces: a, 0.1 N NH_3, 450 m^2; b, 6 N HCl, 270 m^2 g. The bar is 4 μm.

The influence of the catalyst does not only affect the physical properties; the morphology can be influenced, too. Figure 5 shows two gels with 60 wt % $(CH_3)_2SiO$ in a $(CH_3)_2SiO/SiO_2$ composite. Whereas the NH_3-catalyzed material is transparent, the HCl-catalyzed material is cloudy. Pore analysis shows a maximum at radius r of 4.2 and 500 nm. The larger radii can be of interest as "transport pores" for kinetics in liquid adsorption processes. This example shows how processing conditions can be used for the generation of special microstructure properties.

Preparation of Materials with Special Functions. The porosity not only defines the adsorption parameters of a material, but also its mechanical stability. On the basis of this idea and the hydrolysis and condensation kinetics and its effect on microstructure, an abrasive powder was developed (*12–13*) with an abrasion-controlling mechanism for human skin. The investigation of the synthesis parameter shows a direct connection between the composition and the mechanical properties of the granular material (Figure 6). As expected from the previous experiments, HCl had to be used to provide reproducible CH_3 concentrations and well-defined, reproducible material properties.

The increase of the abrasion number (not representing higher abrasion) at higher $(CH_3)_2SiO$ contents is misleading and due to the increasing elasticity of the grains, which is not covered by the test. For the hydrolysis and condensation step, HCl had to be used because NH_3 did not lead to satisfying products for reasons pointed out in the section "Reactivity of Precursors in Sol–Gel Processes". The abrasive material was incorporated into a soap matrix and is used for the medical treatment of acne papulo pustulosa very successfully. It has been on the market for several years as a commercial product (*14*).

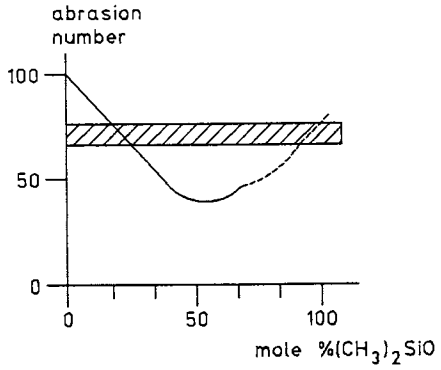

Figure 6. Abrasion numbers of a $(CH_3)_2SiO$–SiO_2 composite. The number represents the fraction of unaffected grains of an average diameter of 0.3 mm (in percentage) after a special abrasion test (15). The hatched area represents abrasive behavior recognized to be satisfying by test persons. The dashed line represents data that were not useful because of elasticity.

To customize the adsorption of functional molecules, the incorporation of organic groupings increasing the interaction between the adsorbent and the molecule to be adsorbed should be an adequate method. Several mechanisms can be taken into consideration, for example, an acid–base or a hydrophobic interaction mechanism. If larger molecules such as enzymes are considered, the pore size plays an important role, and the area of the accessible surface is an important parameter, too. To create basic sites, various types of silica with amino groups were synthesized by cohydrolyzing $(CH_3O)_3Si(CH_2)_3NH_2$, $Si(OC_2H_5)_4$, and optionally $(CH_3)_2Si(OC_2H_5)_2$ at room temperature with 50 vol % methanol as solvent.

Because amino groups act autocatalytically (*15–17*) in the presence of water, for acid catalysis an excess of HCl was used to overcompensate the formation of $-NH_3^+Cl^-$. In these cases, the gels were washed with methanol and water until no Cl^- could be detected in the filtrate. How far the incorporation of amino groups into silica could affect the adsorption of acid components was of interest. Lactic acid and a sulfonic acid (a commercially available dye named Telon Light Yellow) were chosen as test components (*18*). In Figure 7 the adsorption isotherm of lactic acid is shown. Unmodified SiO_2 does not have remarkable adsorption in aqueous solution under these circumstances. The result shows the effect of the amino modification quite clearly, because the lactic acid load of the adsorbent is remarkable, and it is difficult to adsorb small water-soluble molecules in an aqueous environment.

The kinetics of the adsorption are shown in Figure 8, which demonstrates an almost ideal breakthrough curve that indicates fast kinetics. The

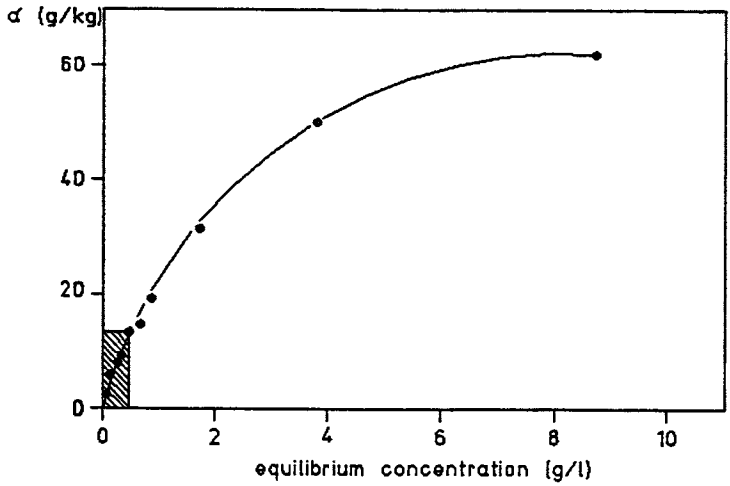

Figure 7. Adsorption isotherm of lactic acid on an amino-modified adsorbent. The composition was 5/95 (weight percent) in $NH_2(CH_2)_3SiO_{3/2}/SiO_2$. The mole surface was found to be 9.8×10^{-5} $-NH_2/g$; the method was that of reference 17. The BET surface area was 350 m^2/g; the hatched area indicates high loads even at low equilibrium concentrations.

breakthrough level represents almost the equilibrium value and does not depend on the flow rates used in the experiment. A glass tube 0.5 cm in diameter was used. Chemical analysis was carried out in steps of 5 mL to monitor the lactic acid concentration during the absorption experiment.

The sulfonic acid did not have remarkable adsorption under these circumstances. If, in addition to amino groups, a $(CH_3)_2Si=$ unit is incorporated, the adsorption rates increase remarkably. The best results were obtained with the composition SiO_2:$(CH_3)_2SiO$:amino = 40:60:2.5 with 9 N HCl as catalyst. The high concentration was found to lead to a maximum of load in a series of experiments with varying catalyst concentrations. The aromatic sulfonic acid could be loaded to 120 g per kilogram of adsorbent with an equilibrium concentration of 1.6 g/L and to 26 g/kg with 0.2 g/L (Figure 9). This fact can be attributed to a "double function" adsorption mechanism of a hydrophobic interaction of $-CH_3$ groups with the phenyl group of the sulfonic acid and the acid-based interaction. The kinetics of the flow experiments could be improved by microstructure tailoring (Figure 9) by variation of the catalyst concentration. Figure 9b shows the optimized microstructure with "transport pores" and a surface area about three times that of the adsorbent in Figure 9a.

Another interesting case is the adsorption of CO_2, which does not show dipole moment but is able to dissociate with water to an ionic compound

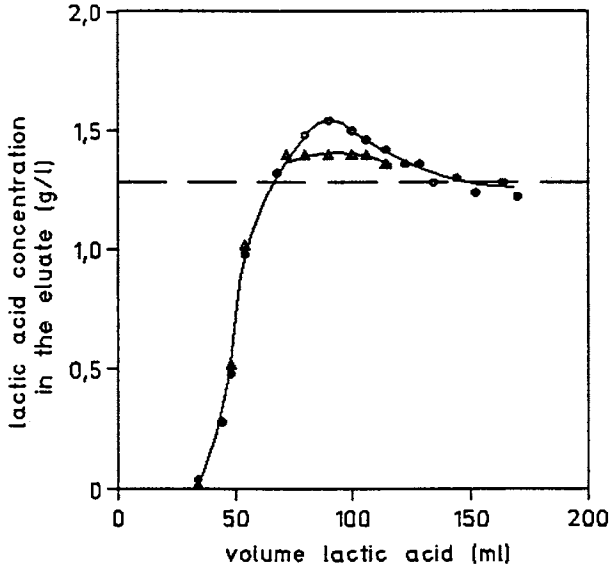

Figure 8. Breakthrough curves of a column-flow experiment. Flow rates were 2.0 (▲) and 0.83 (●) mL/min; 3 g of adsorbent was used. The dashed line indicates input lactic acid concentration.

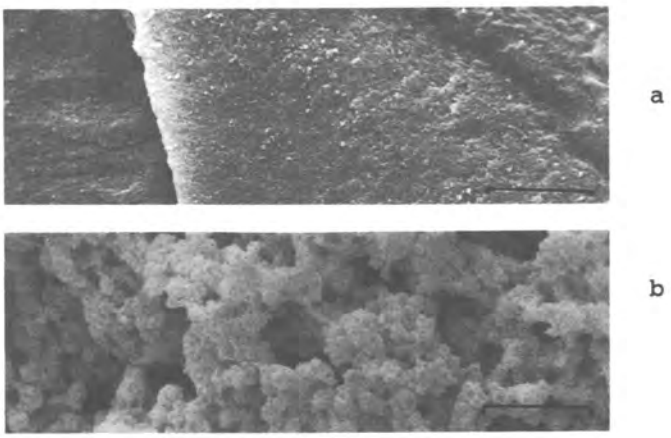

Figure 9. Amino- and CH_3-modified silica: a, 9 N HCl, 67 m^2/g; b, 12 N HCl, 188 m^2/g. The bars are 20 μm.

according to $CO_2 + H_2O \rightleftharpoons H_2CO_3 \rightleftharpoons H^+ + HCO_3^-$. The question arises whether amino groups in combination with water adsorbed to the pore walls are able to act in a dissociative way for the adsorption of CO_2 according to $H^+CO_3^- + H_2N- \rightarrow HCO_3^- + H_3N^+-$. Therefore, a series of adsorbents with varying $-NH_2$ concentrations were prepared, and the adsorption isotherms were determined. The influence of H_2O on the adsorption isotherms was determined by thermogravimetric analysis (TGA) with a N_2 gas flow loaded with water vapor. The adsorbents loaded with CO_2 were flushed with the H_2O-containing N_2, and the H_2O content of the gels was determined after the experiment. The evaluation of the mass balance and the amount of residual water led to the conclusion that the H_2O completely replaces the adsorbed CO_2. On the other hand, as a function of the NH_2 content, remarkable amounts of CO_2 were able to be adsorbed on adsorbents dried at 150 °C. These adsorbents show far lower OH peaks in the IR spectra than pure silica. This observation indicates that the ionic mechanism does not play any role, and a weak dipole interaction is postulated instead:

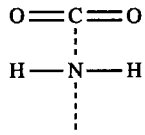

IR spectra, however, did not show a significant shift of the =C=O vibration. Figure 10 shows some of the most important results.

The NH_2 groups affect the amount of adsorbed CO_2 as well as the thermal behavior and illustrate the change of thermodynamics with composition. At higher pressures (not displayed in Figure 10), the amino-modified adsorbents show a saturation plateau around 5 bar CO_2 and a load of about 5–10 wt % CO_2, depending weakly on the surface area, whereas the CH_3-modified material (880 m^2/g) shows no significant plateau up to 15 bars (the end of the test) and a load of about 36 wt % at room temperature, which is an extremely high load. This observation leads to the question of whether these materials can be used for CO_2 storage or as propellants with CO_2. In reference 19, a heat pump is proposed; it uses two types of tailored adsorbents for CO_2 in a closed-system process.

The determination of the heat of adsorption shows higher values on adsorbents with amino contents above 10 mol % (e.g., SiO_2, 45 kJ/mol; 10 $-NH_2$, 43 kJ; 20 $-NH_2$, 58 kJ; 30 $-NH_2$, 65 kJ; experimental error, ±7%) and a decay as a function of the CO_2 surface coverage (e.g., in an adsorbent with 20 mol % $-NH_2$ from 58 kJ/mol ≡ 2 mL CO_2 per gram to 17 kJ/mol ≡ 10 mL CO_2 per gram). Thus, the amino-modified materials interact rather strongly in the first step with the CO_2, and the interaction decreases

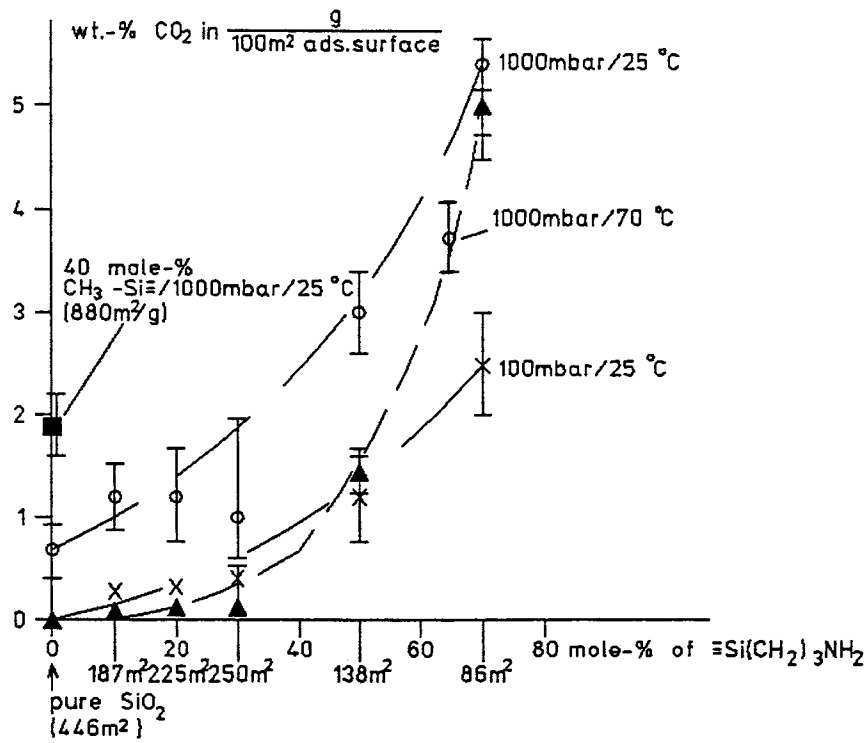

Figure 10. NH_2-containing silica with CO_2 at 100 and 1000 mbar and two different temperatures. The load is normalized on 100-m²/g surface area. Data of pure silica and a $-CH_3$-modified silica are given for comparison; the numbers with m² as units at the abscissa display the surface areas of the investigated adsorbents.

with increasing load; this observation suggests a population of various adsorption sites.

Conclusions

The organic bulk modification of silica can be used for tailoring specific surface properties. One advantage of this reaction route is the possibility to use a one-step process, but the reaction must be controlled very carefully. Multifunctional materials can be synthesized, too.

Acknowledgments

We thank the Bundesminister für Forschung und Technologie of the Federal Republic of Germany and Ruhrgas Company for financial support. We also thank J. Strutz for experimental work and helpful discussions.

References

1. Iler, R. K. *The Chemistry of Silica*; Wiley: New York, 1979; pp 462–714.
2. Hench, L. L.; West, J. K.; Zhu, B. F. In *SPIE Proceedings of Sol–Gel Optics*; SPIE: San Diego, CA, 1990; Vol. 1328, pp 230–240.
3. Sakka, S. In *Sol–Gel Technology for Thin Films, Fibers, Preforms, Electronics and Speciality Shapes*; Klein, L. C., Ed.; Noyes Publications: Park Ridge, NJ, 1988; p 140.
4. Achtsnit, H.-D.; Wegerhoff, W. Oral presentation at German Glass Forum Meeting, May 1990.
5. Scherer, G. W.; Brinker, C. J. *The Physics and Chemistry of Sol–Gel Processing*; Academic Press: New York, 1990; pp 204–209.
6. *Aerosil* (Technical Bulletin); Degussa: Hanau, Germany, 1970.
7. *Lab-O-Sil, CGEN-7*, Cabot Corporation: Boston, 1970.
8. Bagley, B. G.; Quinn, W. E.; Khan, S. A.; Barboux, P.; Tarascon, J.-M. *J. Non-Cryst. Solids* **1990,** *121*, 454.
9. Schmidt, H.; Scholze, H.; Kaiser, A. *J. Non-Cryst. Solids* **1984,** *63*, 1.
10. Kaiser, A.; Schmidt, H. *J. Membr. Sci.* **1985,** *22*, 257.
11. Schmidt, H.; Kaiser, A.; Rudolph, M.; Lentz, A. In *Science of Ceramic Chemical Processing*; Hench, L. L.; Ulrich, D. R., Eds.; Wiley: New York, 1986; p 87.
12. Coltrain, B. K.; Melpolder, S. M.; Salva, J. M. In *Proc. IVth Intl. Conf. on Ultrastructure of Ceramics, Glasses and Composites*; Uhlmann, D. R.; Ulrich, D. R., Eds.; Wiley: New York, 1989; pp 69–76.
13. Schmidt, H.; Kaiser, A.; Patzelt, H.; Scholze, H. *J. Phys.* **1982,** *43 (C9, suppl. 12)*, 275.
14. Kompa, H. E.; Franz, H.; Wiedey, K. D.; Schmidt, H.; Kaiser, A.; Patzelt, H. *Ärztliche Kosmetologie* **1983,** *13*, 193.
15. *Jaikin Neu*; Basotherm Company: Biberach-Riss, Germany, 1985.
16. Ravaine, D.; Seminel, A.; Charbouillot, Y.; Vincens, M. *J. Non-Cryst. Solids* **1986,** *82*, 210.
17. Schmidt, H.; Popall, M.; Rousseau, F.; Poinsignon, C.; Armand, M. In *Proc. 2nd Intl. Symp. on Polymer Electrolytes*; Stosati, B., Ed.; Elsevier: London; p 325.
18. Schmitt, H. W.; Walker, J. E. *FEBS Lett.* **1977,** *81*, 403.
19. Schmidt, H.; Strutz, J.; Gerritsen, H.-G.; Mühlmann, H. *German patent 35 18 738*, 1986.

RECEIVED for review October 19, 1990. ACCEPTED revised manuscript April 20, 1992.

21

Evaporation and Surface Tension Effects in Dip Coating

Alan J. Hurd

Ceramic Processing Science, Department, Sandia National Laboratories, Albuquerque, NM 87185-5800

Evaporation sets an important time scale for the formation of structure in sol–gel films during dip coating, and surface tension is the dominant driving force influencing that structure. The action and interplay of these two phenomena were evaluated by experiments with pure and binary solvents. From the optically measured thickness of the steady-state film profile, accelerated evaporation near the drying line that sets stringent constraints on the time available for network formation was found. In binary solvents, there is evidence for strong flows driven by surface tension gradients; this flow gives rise to capillary instabilities. Aided by these flows, differential evaporation leads to regions rich in the nonvolatile component near the drying line.

DIP COATING IS THE DEPOSITION OF A SOLID FILM on a substrate by immersion in a sol or solution, withdrawal, and drying. The simplicity of dip coating, a cousin of painting, belies the fact that films of very high quality can be applied. Indeed, optical-quality films of controlled index and thickness are readily obtainable with simple, inexpensive apparati. Complex shapes can be coated in one step; this simplicity is not always possible with evaporative or sputtering techniques. For bulky objects, dip coating is far easier to scale up than vacuum techniques. Finally, the admirable purity of solution chemistry, such as the popular sol–gel route, can be exploited.

According to a review by Schroeder (*1*), the technology of spin coating or dip coating inorganic sols to make stable films was pioneered in

0065–2393/94/0234–0433$08.00/0

Germany and became widely known after World War II. The physics involved in spin and dip coating has been reviewed (2) and remains under intense study (3, 4). The flexibility of sol–gel chemistry is demonstrated by the wide range of oxides and mixed oxides that have been used to form coatings (5, 6).

The term "controlled index" means that the refractive index can be made *smaller* than that of the bulk precursor by controlling the microstructure via the porosity. When silica is deposited, for example, the film index n can be varied over a wide range (7) from $n = 1.1$ to 1.5. This process control makes sol–gel coatings interesting for many optical, electronic, and sensor applications, but the evolution of the microstructure during film formation is not well understood, in spite of efforts to survey the variables (8, 9). This chapter reviews the important factors determining the microstructure of dip-coated films and explores at length two of them, evaporation and surface tension.

Although easy to accomplish, the process of dip coating is complex because it proceeds through overlapping stages: When the substrate is withdrawn slowly from a sol, a film of liquid, several micrometers thick at the bottom, becomes hydrodynamically entrained on the surface. If the solvent wets the substrate, the film thins through gravitational draining, capillary-driven flows, and evaporation. When the recession speed of the drying film (relative to the substrate) matches the withdrawal rate, steady-state conditions prevail, and the entrained film terminates in a well-defined drying line that is stationary with respect to the reservoir surface. As described later, the presence of this edge in the evaporating film leads to dramatic effects. Meanwhile, the precursors in the entrained liquid experience a rapidly concentrating environment; they tend to gel or jam through chemical or physical interactions. Most likely, a transient chemical or physical gel network occurs fleetingly in the thin liquid film under these conditions, and it is my view that the porosity of the deposited film is a remnant of this network.

Often the reservoir sol is unstable with respect to aggregation and gelation. However, the process of film formation forces reactions at a much accelerated rate: Although the bulk reservoir might require several hours or days to gel, the transit time from entrainment to drying line is of the order 10 s. Here is the first competition of time scales for film deposition. Clearly, network formation through the usual diffusion-limited and reaction-limited schemes can be frustrated by the accelerating effects of evaporation. In this context, the evaporation can be viewed as a strong force field coupling to the suspended particles—analogous to a centrifugal or electrophoretic field—and forcing them to crowd together. (The centrifugal acceleration causing an equivalent rate of crowding is as much as $10^6 g$.) When the crowding is rapid, particles do not have time to find low-energy configurations, so porous microstructures result. Thus, sol–gel

films can differ greatly in structure from bulk xerogels or aerogels (*10*) if desired.

Just before he died, Ralph K. Iler (personal communication, 1985) was working on a device for electrophoretically depositing particles with a controlled degree of order. In addition to the direct current field for deposition, he imposed an alternating current component. At low frequencies, the ac component tended to unsnarl packing defects, whereas at high frequencies it apparently created a dipolar interaction between particles.

Although the evaporation creates varying physicochemical states of the entrained sol with height from the reservoir, it is easy to show that in most situations the sol is essentially homogeneous across its thickness. [If it were not homogeneous, the particles might collect near the air interface of the entrained film as a sort of skin that would impede evaporation (*11, 12*).] In most situations the particles' transport by diffusion is fast enough to keep the concentration constant through the thickness: For a liquid film of thickness $\Delta r \approx 1$ μm and a diffusivity D_o of 10^{-6} cm^2/s (appropriate for a 10-Å moiety), it takes only a time $\Delta t \sim \Delta r^2/D_o = 10^{-2}$ s to relax thickness concentration gradients that might build up. For most positions on the film, this time scale can be considered short compared to other processes. Only very near the drying line itself would it be possible for concentration gradients normal to the substrate to "lock in". Some evidence suggests that such inhomogeneities exist (Fabes, B., personal communication and poster presentation at the Spring Meeting of the Materials Research Society, San Francisco, CA, 1990) through the thickness, but there does not appear to be a deep enough data base to conjecture about their origin.

Gravitational draining creates hydrodynamic shear throughout the entrained film. Unlike particle concentration, the shear rate is not the same throughout the thickness. In fact it must be zero at the air interface (because the gas cannot exert a shear force on the film, assuming, for the moment, no surface tension gradients exist) and nonzero at the substrate, which provides the force of lifting from the reservoir. Thus the shear rate must be maximal at the substrate: If z is the distance normal to the substrate and h is the thickness of the entrained liquid film, then the velocity (u) satisfying the Navier–Stokes equation $d^2u/dz^2 = 0$ is parabolic:

$$u = -u_0 \left(1 + \frac{h(x)\ z}{\lambda^2} - \frac{z^2}{\lambda^2}\right)$$

Here λ is a characteristic length of order 10 μm given by $\lambda^2 = \rho g/\eta u_0$, where ρ is liquid density, g is gravitational acceleration, η is shear viscosity, x is height and u_0 is substrate withdrawal velocity. The shear rate $\dot{\gamma}$ is due solely to gravitational back flow in the absence of surface-driven forces:

$$\dot{\gamma} = \frac{du}{dz} = -\frac{u_0}{\lambda^2} (h - z)$$

Thus, the shear is greatest near the reservoir, where the film is thickest, and next to the substrate wall z is 0.

It is interesting to consider whether shear-induced particle encounters are slow compared to diffusional transport. The relevant parameter is the Peclet number

$$P_e = \frac{6\pi a^3}{kT} \frac{du}{dz}$$

(for spheres of radius a, where k is the Boltzmann constant and T is the temperature), which is the ratio of these time scales. When P_e exceeds 1, it is well known that the structure of the dispersion is constantly forced by the shear to nonrandom states, typically ordered sheets or strings. For $P_e << 1$, diffusion randomizes the structure. Gravitationally driven shear is generally not strong enough to create "shear-induced ordering", even near the substrate at the base of the entrained film, where P_e is only 10^{-4}. However, shear driven by surface tension gradients can be quite large, so shear-induced order might be exploited to affect film microstructure (*13*) in coatings derived from colloidal suspensions (*14*).

Indeed, surface tension is arguably the dominant force in dip coating, at least at the point of entrainment and at the drying line where interfacial curvatures are significant. At the point of withdrawal from the reservoir, a meniscus forms to balance the pressure imposed by the curved surface against that of the gravitational "head". The relatively large volume of liquid pulled into the gravitational meniscus (radius of curvature about 1 mm) is indicative of the large surface tension of dip-coating liquids, and the effect (*15*) of surface tension is large enough to change the dependence of the entrained thickness $h(0)$ (proportional to deposited mass) on withdrawal speed u_0 from $u_0^{1/2}$ to $u_0^{2/3}$. The deposited *thickness* need not scale in this way with withdrawal speed because coating porosity can vary with other factors (*16, 17*). Between the meniscus and the drying line, the radius of curvature is too large (~10 km!) for surface tension to have any effect, but, at the drying line, capillary pressures are again significant.

Probably the most important surface tension effect is that of "capillary collapse" of the transient networks as they are invaded by the gas phase during the final phase of evaporation (*18*). This process is identical to the collapse of a sponge upon drying. The network can resist the invading menisci up to the point when their radii are small enough that the capillary stresses exceed the yield stress of the network (*19*). The network then compresses uniaxially until its modulus becomes high enough again to resist the capillary stress while the solvent is completely removed.

(Uniaxial compression is not the only possible mode of collapse. Large, stable pores could form, for example, by the lateral retraction of material.) By now the structure is denser and, possibly, completely different from that of the transient network. Nevertheless, the extent of capillary collapse can be controlled to some extent (*7*) by physical and chemical means to achieve a desired porosity.

Surprisingly large capillary pressures are theoretically possible in drying films. (In order of magnitude, there is little decrease in surface tension at a rapidly evaporating interface, or even a boiling one.) Because the final pore size can be smaller than 1 nm, the pressure in the liquid during the final stages of drying could exceed −100 atm (−10,000 kPa)! The negative sign indicates that the liquid is under tension. Although most liquids can support large tensions in small pores if no gas is present (*20, 21*) owing to suppression of nucleation, it is not clear how the liquid in open pores is similarly prevented or delayed from boiling away (*22a*). Nevertheless, strong evidence for suppressed vaporization is the hysteresis in adsorption isothermus of microporous solids (*20*): Liquid is reluctant to leave microsize cavities once it has filled them, because, presumably, the pores are smaller than a critical vapor nucleus. Moreover, recent experiments in deflection of sol–gel-coated beams (*22b*) indicates drying stresses of enormous negative pressure (2000 atm, or 21,000 kPa) generated by the capillary pressure.

The choice of solvent mixtures may be the route to controlling capillary forces. The main subject of the remainder of this chapter is the variety of effects that occur in mixed solvent systems during dip coating. These effects arise when differential volatility gives rise to concentration gradients, thence to surface tension gradients, which have surprisingly large effects on flow. A few of these effects are discussed. First a description is given of the evaporation constraints, because these determine, to first order, the local composition of the film.

Experiments on Evaporating Thin Films

Clean substrates of silicon were used to entrain liquid films of various compositions in a dip-coating geometry, as in Figure 1 with $\alpha = 0$. Interference images were obtained in reflection with monochromatic light. The liquid index of refraction and the angle of incidence were known, so the film thickness profiles were obtained from the position of the interference fringes.

The process of evaporation during dip coating was studied only recently (*2, 22a*), although the essential physics of evaporation has been well known for over a century. According to Fuchs (*23*), James Clerk Maxwell wrote an article on diffusion for the *Encyclopedia Britannica* in which he considered the stationary evaporation of a spherical droplet in an

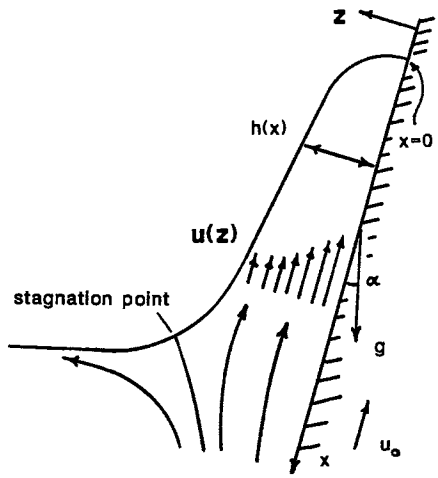

Figure 1. Geometry of dip coating. The angle of the substrate α can be adjusted to vary the effects of gravity g. *A stagnation point in the velocity field* u *occurs in the gravitational meniscus. The thickness* h(x) *is in the range 0 to 10 μm, and the height* x *is of order 1 cm. (Reproduced with permission from reference 22a. Copyright 1990.)*

which he considered the stationary evaporation of a spherical droplet in an infinite medium. (Maxwell was interested in wet bulb thermometry.) Not only did he realize that the rate of mass loss by the droplet is limited by vapor diffusion away from the surface, he correctly assumed that the vapor concentration at the surface of the drop is equal to its equilibrium saturation concentration (true when the vapor mean free path is small compared to the dimensions of the droplet). All that remains is to solve the steady-state diffusion equation for the vapor concentration c,

$$\nabla^2 c = 0 \tag{1}$$

on a sphere of radius a, with an additional boundary condition at infinity. The flux from the surface, which can be defined as a local evaporation rate (E), is governed through Fick's law by the vapor concentration gradients there:

$$E = \text{mass loss per unit area per unit time} = -D \frac{\delta c}{\delta r} \mid r = a \tag{2}$$

Although the diffusion constant D does not appear in the steady-state diffusion equation, it does appear in kinetic factors such as the time it takes for a droplet of a given initial mass to evaporate. The solution to equation 1

is a concentration c that decreases as r^{-1} from the droplet so that the total evaporation rate $4\pi a^2 E$ from equation 2 is proportional to the product aD. Thus, it is not the surface area that controls the rate of mass loss, but the radius.

Other geometries can readily be worked out. As a useful analogy, the concentration c in equation 1 can be viewed as the electrostatic potential around a conductor of potential c_0. The analog to the local evaporation rate is the electric field, evaluated at the surface of the conductor. By this analogy a fresh set of intuitive ideas can be brought to bear on evaporation problems. For example, it is not surprising that the vapor density around an infinite cylindrical source drops logarithmically with radial distance, and that the evaporation rate varies inversely with the radius of the cylinder. Similarly, the vapor concentration above an infinite sea drops linearly with distance, whereas the evaporation rate is constant everywhere on the surface.

Dip-coating geometries are not perfect one-, two-, or three-dimensional structures, however. Usually a sharp boundary is involved, such as the edge formed by the drying line. When coating on flat substrates, the film can be considered a thin, finite sheet. A dip-coating film can be approximated by a semi-infinite sheet, mathematically formed from a wedge in the limit that the wedge angle approaches zero. The edge carries a field singularity (*24*) of the form $r^{-1/2}$. In fact, for an arbitrarily shaped finite sheet, the field singularity remains $r^{-1/2}$ as long as the edge is locally straight on the scale of the sheet's thickness. This fact can be seen from the exact solution for the field above a thin disk, which can be readily shown to be encircled by a field singularity of the form $r^{-1/2}$, where r is the distance to the edge (*25*).

Such evaporation singularities can be very easily observed because the thickness profile of a thin liquid film locally reflects the rate of solvent removal. For very thin films, especially near the drying line, back flow due to gravitational draining can be neglected. The mass flux $h(x+dx)u_0$ carried into a fluid element dx, as shown in Figure 1, is balanced by the flux carried out by the substrate $h(x)u_0$ and the mass lost through evaporation $E(x)dx$; this observation leads to the continuity equation

$$\frac{dh}{dx} = \frac{E(x)}{u_0} \tag{3}$$

which can be integrated for $E \sim x^{-\eta}$ to give

$$h(x) \sim x^{1-\eta} \qquad (\eta < 1) \tag{4}$$

The thickness profile $h(x)$ of an evaporating ethanol film during dip coating (Figure 2) follows $h(x) \sim x^{1/2}$, giving $\eta = 1/2$ as expected for the edge of a sheet. Profiles of this type were derived from optical interferometry, including wedge fringes (Figure 3) and imaging ellipsometry (*26*). Optical profiles of evaporating sessile drops (Figure 4) also approach the substrate parabolically near the edge, as expected (*25*).

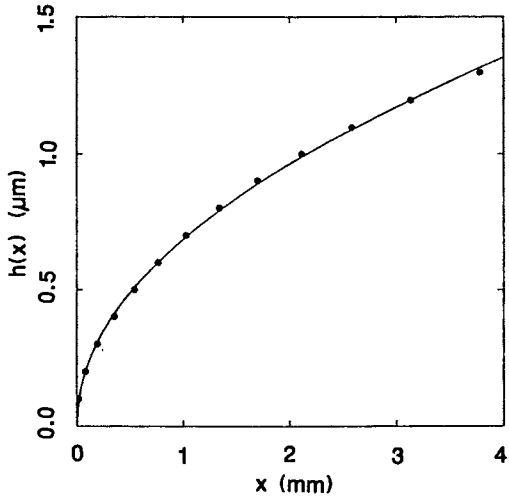

Figure 2. Thickness profile of dip-coated ethanol film. The profile is fit quite well by the form h ~ x^{η} *with* $\eta = 1/2$. *(Reproduced with permission from reference 22a. Copyright 1990.)*

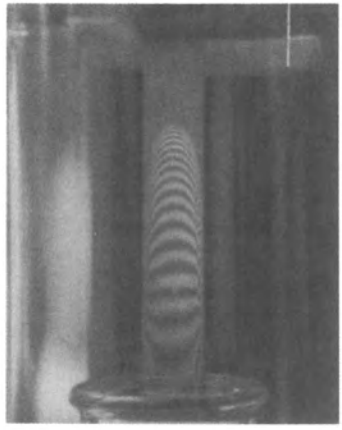

Figure 3. Optical interferogram of steady-state ethanol film. The drying line can be clearly seen.

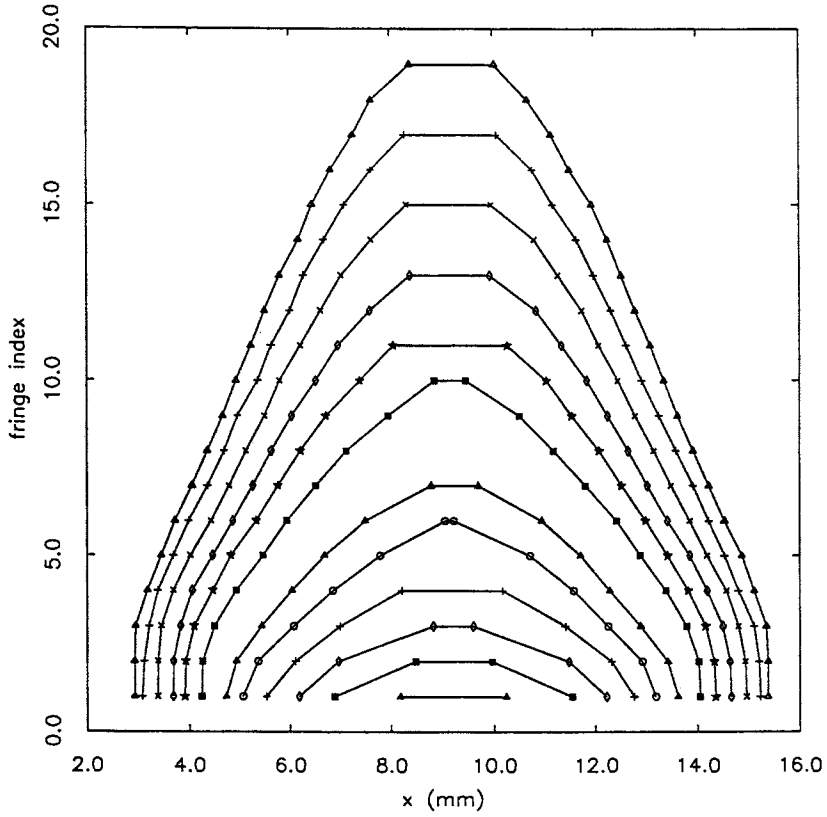

Figure 4. Thickness profiles of sessile methanol drop. A curve was drawn every 0.5 s. At the edge of the drop a parabolic section can be seen, as predicted by theory. (Each fringe index, or order, represents roughly 100 nm in thickness.)

An interesting case is $\eta = 1$, because it arises in fiber formation (27) and fiber coating. Ideally, according to equation 3, $h \sim \ln(x/x_0)$, where x_0 is the position of the drying line. In reality, the logarithmic profile is difficult to observe because small fibers do not entrain thick liquid layers owing to the large capillary pressures developed by the small curvature around the fiber itself. Nevertheless, it is possible to see the integrated singularity change with cylinders of decreasing radii (Figure 5). The needlelike singularity $\eta = 1$ should pertain as long as the radius of the cylinder is small compared to the height of the drying line.

Multicomponent Solvents and Surface Tension Gradients

A comparison of Figure 6, showing a film from a binary mixture of ethanol and water, with the pure ethanol film in Figure 3 shows a striking new

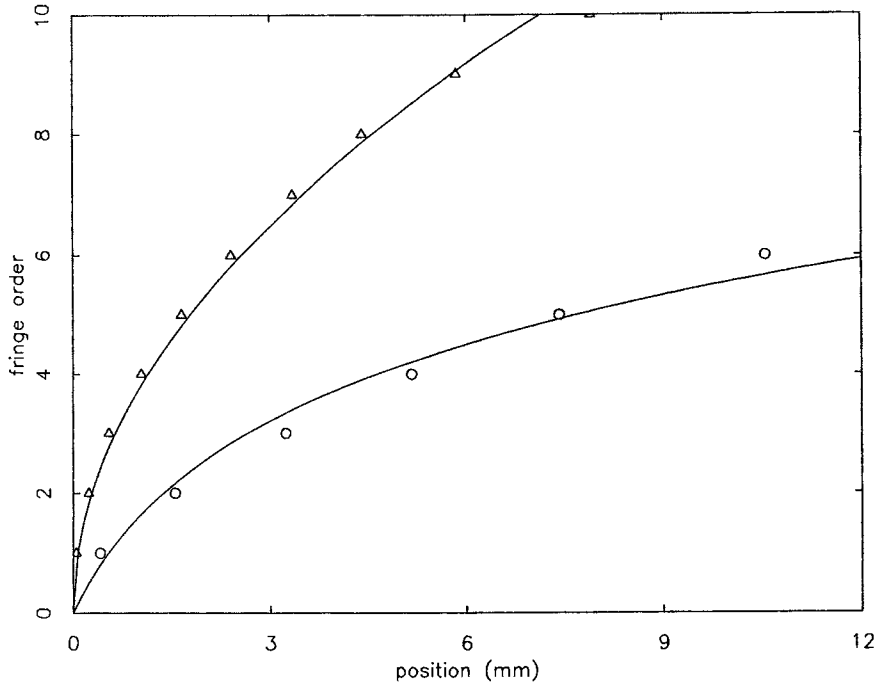

Figure 5. Thickness profiles of steady-state films on (triangles) a 1-cm strip and (circles) a 1.78-mm-diameter cylinder. The strip is well fit by a square-root function $h \sim x^{1/2}$, *whereas the cylinder, being near the needlelike geometric limit, is better fit by* $h \sim \ln(x\text{-}x_0)$.

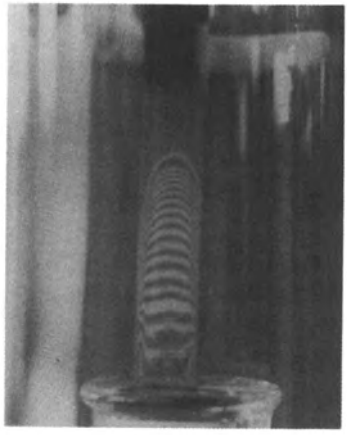

Figure 6. Optical interferogram of 82:18 (vol) ethanol–water film. A water-rich feature appears at the drying line.

feature at the drying line. The binary solvent has an additional "foot" extending from a false drying line, as shown in Figure 7. Doubling the amount of water in the reservoir (18% H_2O in Figure 6) doubles the extent of the foot. Clearly, then, the foot is a water-rich phase that outlasts the alcohol because of a lower volatility. The well-behaved wetting of the foot suggests that its composition is not pure water, which is very difficult to use to wet a substrate symmetrically without extensive hydrogen peroxide cleaning. This forgiving wetting nature, like that of pure alcohol, implies that the water-rich foot approaches a composition that contains at least some alcohol acting as a surfactant. Clearly the evaporating mixture is far from the boiling azeotrope, which for water and ethanol is 95% alcohol.

The binary mixture profile consists of two parabolas; thus, the evaporation of each component is unaffected by the vapor concentration of the other. That is, each component has an independent evaporation singularity. If the water-rich phase is denoted phase 1, and the ethanol phase 2, then the independent profiles are additive:

$$h_1 = a_1 x^{1/2} \qquad x > 0 \tag{5a}$$

$$h_2 = a_2 (x - x_2)^{1/2} \quad x > x_2 \,, \quad h = h_1 + h_2 \tag{5b}$$

$$h_2 = 0 \qquad x < x_2 \tag{5c}$$

where h is the total thickness and x_2 is the position of the false drying line (Figure 7). The volume fractions $\phi_1 = h_1/h$ and $\phi_2 = h_2/h$ are plotted schematically in Figure 8.

Differential volatility is not the only physics responsible for the "foot" feature of binary solvents. Flows due to surface tension gradients are clearly present. A simple linear mixing law (known to underestimate the gradients potentially present) for the total surface tension σ in terms of its constituents serves to estimate the magnitude of the flow,

$$\sigma = \phi_1 \sigma_1 + \phi_2 \sigma_2 \tag{6}$$

and, therefore, the surface tension gradients can be calculated,

$$\frac{d\sigma}{dx} = (\sigma_1 - \sigma_2) \frac{d\phi_1}{dx} - (\sigma_1 - \sigma_2)(x - x_2)^{-1/2} \quad (x > x_2) \tag{7a}$$

$$\frac{d\sigma}{dx} = 0 \quad (0 < x < x_2) \tag{7b}$$

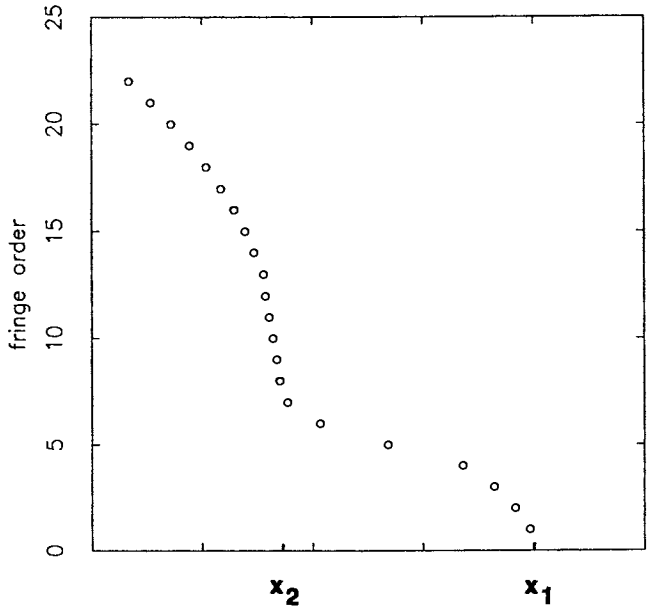

Figure 7. Thickness profile of 50:50 (vol) propanol–water film. The double-chin "phase separation" is due to differential volatilities and surface-driven flows. (Reproduced with permission from reference 13. Copyright 1991.)

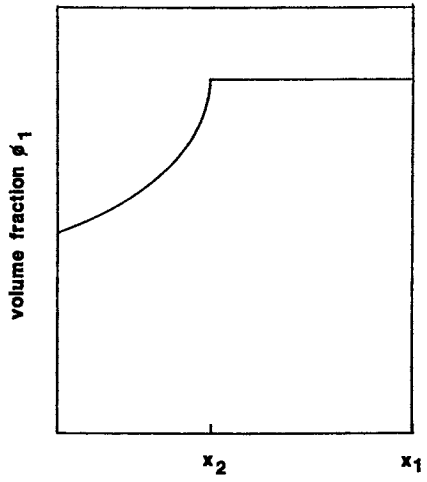

Figure 8. Schematic plot of volume fraction of water-rich phase ϕ_1 for propanol–water film, based on Figure 7.

assuming the no-flow profiles of equation 4 hold as adopted for equations 5a–5c. Not surprisingly, the abrupt disappearance of phase 2 at the false drying line x_2 leads to singular gradients.

But the simple no-flow picture of equation 4 can no longer hold in view of equations 7a and 7b. At the liquid–vapor boundary, the viscous shear force must balance the force imposed by surface tension gradients, $\eta du/dz = d\sigma/dx$ $(z = h)$. This boundary condition leads to a linear flow profile toward the drying line,

$$u = \frac{1}{\eta} \frac{d\sigma}{dx} z - u_0 \tag{8}$$

so the profiles h_1 and h_2 have to be recalculated. Profiles for static menisci of binary solvents have been calculated (*28*).

However, far from the singularity at the false drying line x_2, equation 8 should describe the physics accurately enough so that the strength of the surface-driven flows can be appreciated. Figure 9 shows the thickness profile of a binary mixture of toluene and methanol during film formation. The flows are strong enough to distort greatly the foot profile, creating, in fact, a thickened "toe" of toluene near the drying line. A crude estimation on the shear rate in the thin region is $\Delta\sigma/\Delta x \approx (10 \text{ dyne/cm})/(10^{-1} \text{ cm})$, hence $du/dz \sim 10^4 \text{ s}^{-1}$. For this sort of flow, P_e exceeds 1 for particles over 30 nm or so; thus shear-induced ordering would be expected.

Temperature gradients can often be considered small in dip coating; this assumption is not generally true in thin-film evaporation problems (*28*). However, because the substrate moves relatively rapidly past the

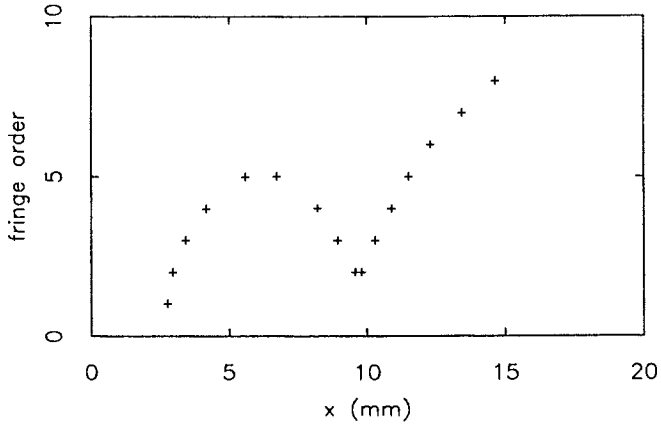

Figure 9. Thickness profile of 50:50 (vol) methanol–toluene film. A steady-state "bubble" of toluene forms because of strong surface-driven flows. (Reproduced with permission from reference 13. Copyright 1991.)

drying line, it constantly supplies energy for evaporation and renews the thermal field.

An interesting manifestation of surface flows in dip coating is a "rib instability" often observed near the reservoir in binary solvent systems and in some pure solvents (ethanol). Figure 10 shows a set of wavy interference fringes, indicative of a 20-nm thickness undulation that has a wave vector that runs perpendicular to the withdrawal direction. Typically, this undulation is a standing wave, but under some conditions (not well defined at this time) the ribs have been observed to fluctuate in position considerably. A study of the instability in water and methanol reveals that its wavelength is inversely dependent on the withdrawal velocity u_0 and that it is insensitive to solvent composition (Figure 11). An increase in u_0 fattens the entrained film (*18*); this result would be expected to increase the wavelength, not decrease it. Furthermore, although the instability has been observed rarely in pure solvents, it is more definite in binary mixtures; hence it is probably aided by surface-driven flows, but, as the data show, the wavelength is relatively insensitive to the mixture.

These observations suggest that the ribs are related to the "Plateau–Rayleigh instability" of cylindrical surfaces of liquids (29), such as a jet of water, the cylindrical surface for dip coating being the concavity in the gravitational meniscus. First treated in the 19th century by Plateau and Lord Rayleigh, this instability results from the fact that a cylindrical liquid surface can decrease its area by undulating longitudinally; from dynamic

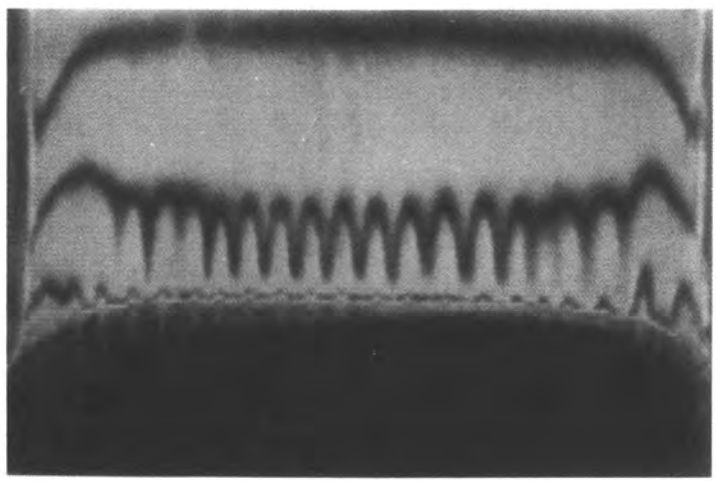

Figure 10. Imaging ellipsometry of rib instability near the reservoir meniscus (dark region).

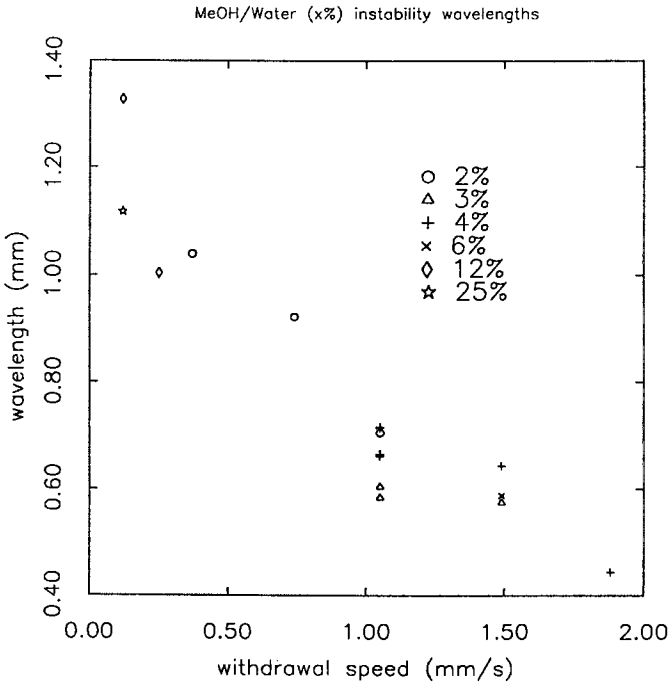

Figure 11. Wavelength of rib instability as function of withdrawal speed for several concentrations of methanol–water.

considerations, one particular wavelength emerges as the fastest-growing unstable mode (although not necessarily the wavelength that fully develops beyond the linear-response regime). Unstable conditions can exist for concave cylindrical surfaces, but the complex dynamics determining the wavelength represent an unsolved problem. Because higher withdrawal speeds decrease the wavelength and, eventually, smooth out the ribs altogether, it probably takes some time for the instability to organize. The balance point for this competition of time scales is generally within the processing window of typical dip-coating operations.

Summary: Time Scales

The limitation on structure formation in dip coating is best appreciated by considering the mean separation between two reactant molecules. By the conservation of nonvolatile mass, the concentration at x is inversely related to the entrained film thickness (22), and because the mean separation $\langle \Delta s \rangle$ is the inverse cube root of the concentration,

$$\Delta s \sim x^{1/6} \tag{9}$$

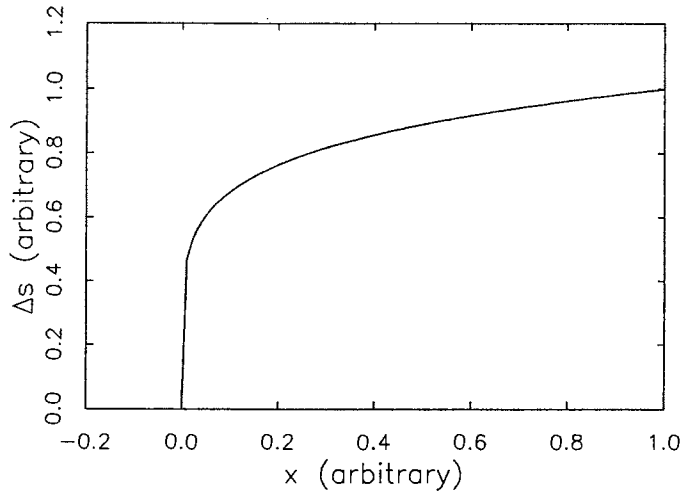

Figure 12. Interparticle distance near drying line. The square-root singularity in the evaporation rate gives rise to a rapid collapse of network structures following $x^{1/6}$.

From this precipitous function, shown in Figure 12, it is possible to understand the dominant factor for a molecule or particle entrained in the film. In the transit from reservoir to drying line, the first 98% of the trip is relatively bland: Δs decreases by only 50% during this phase. In only the last 2% of the transit time between entrainment and the encounter with the drying line, representing a few tens of milliseconds, the remaining interparticle distance is covered. Dense gel structures of the type developed in quiescent reaction-limited (low sticking probability) samples are unlikely to assemble under these conditions, because the precursors have less time to explore tight-fitting configurations. However, it would seem equally unlikely that delicate diffusion-limited (high sticking probability) structures would arise given the near-ballistic transport. Further, concentration fluctuations normal to the substrate might not have time to smooth out.

In any case, subsequent events usually overwhelm the situation. The capillary pressures during the final drying stage are so large that even the least tenuous structures will collapse partially. The reduction of surface tension at the drying line, perhaps by surfactants or by critical point methods, would appear to be a promising way to prevent complete collapse.

Acknowledgments

I thank Jeff Brinker for a long, satisfying collaboration on film formation, Randy Schunk for a critical reading of the manuscript, George Scherer for pointing out J. H. L. Voncken's work, and Don Stuart for tireless experimental work. This work was supported by Sandia National Laboratories under DOE Contract DE-AC04-76-DP00789.

References

1. Schroeder, H. In *Physics of Thin Films*; Haas, B.; Thun, R. E., Eds.; *Advances in Research and Development*; Academic Press: New York, 1969; Vol. 5, pp 87–141.
2. Scriven, L. E. In *Better Ceramics Through Chemistry III*; Brinker, C. J.; Clark, D. E.; Ulrich, D. R., Eds.; Materials Research Society: Pittsburgh, PA, 1988; Vol. 121, pp 717–729.
3. Schmidt, H.; Rinn, G.; Nass, R.; Sporn, D. In *Better Ceramics Through Chemistry III*; Brinker, C. J.; Clark, D. E.; Ulrich, D. R., Eds.; Materials Research Society: Pittsburgh, PA, 1988; Vol. 121, pp 743–754.
4. Brinker, C. J. *NATO ASI Ser. Ser. E* **1988,** *141,* 261–278.
5. Puyané, R.; González-Oliver, C. J. R. *Proc. SPIE Int. Soc. Opt. Eng.* **1983,** *401,* 307–311.
6. LaCourse, W. C.; Kim, S. *Ceram. Eng. Sci. Proc.* **1987,** *8,* 1128–1135.
7. Brinker, C. J. *Ceram. Eng. Sci. Proc.* **1988,** *9,* 1103–1109.
8. Bräutigam, U.; Bürger, H.; Vogel, W. *J. Non-Cryst. Solids* **1989,** *110,* 163–169.
9. Melpolder, S. M.; Coltrain, B. K. In *Better Ceramics Through Chemistry III*; Brinker, C. J.; Clark, D. E.; Ulrich, D. R., Eds.; Materials Research Society: Pittsburgh, PA, 1988; Vol. 121, pp 811–822.
10. Brinker, C. J.; Scherer, G. W. *Sol-Gel Science,* 1st ed.; Academic Press: Boston, MA, 1990; Chapter 13.
11. Brown, G. L. *J. Poly. Sci.* **1956,** *22,* 423–426.
12. de la Court, F. H. *Proc. Xth FATIPEC (Federations d'Associations de Techniciens des Industries de Peintures, Vernis, Emaux, et Encre d'Imprimerie de l'Europe) Congress* **1970**, pp 293–297.
13. Brinker, C. J.; Hurd, A. J.; Frye, G. C.; Schunk, R. P.; Ashley, C. S. *J. Ceram. Soc. Japan* **1991,** *99,* 862–877.
14. Floch, H. G.; Priotton, J. J. *Am. Ceram. Soc. Bull.* **1990,** *69,* 1141–1143.
15. Landau, L.; Levich, B. *Acta Physicochim. (URSS)* **1942,** *17,* 42–54.
16. Guglielmi, M. *Proc. SPIE Int. Soc. Opt. Eng.* **1989,** *1128,* 55–62.
17. Nisnevich, Ya. D. *Zh. Prikl. Khim.* **1986,** *59,* 1406–1409.
18. Poehlein, G. W.; Vanderhoff, J. W.; Witmeyer, R. J. *Polym. Prepr. Am. Chem. Soc. Div. Polym. Chem.* **1975,** *16,* 268–272.
19. Scherer, G. W. *J. Am. Ceram. Soc.* **1990,** *73,* 3–14.
20. Burgess, C. G. V.; Everett, D. H. *J. Colloid Interface Sci.* **1970,** *33,* 611–614.
21. Zheng, Q.; Durben, D. J.; Wolfe, G. H.; Angell, C. A. *Science (Washington, DC)* **1991,** *254,* 829–832.

22a. Hurd, A. J.; Brinker, C. J. In *Better Ceramics Through Chemistry IV*; Zelinski, B. J. J.; Brinker, C. J.; Clark, D. E.; Ulrich, D. R., Eds.; Materials Research Society: Pittsburgh, PA, 1990; Vol. 180, pp 575–581.

22b. Voncken, J. H. L.; Lijzenga, C.; Kumar, K. P.; Keizer, K.; Burggraff, A. J.; Bonekamp, B. C. *J. Mater Sci. (UK)* **1992,** *27,* 472–478.

23. Fuchs, N. A. *Evaporation and Droplet Growth in Gaseous Media*, 1st ed.; Pergamon Press: London, 1959.
24. Jackson, J. D. *Classical Electrodynamics*, 2nd ed.; Wiley: New York, 1975; Section 2.11.
25. Tranter, C. J. *Integral Transforms in Mathematical Physics*, 1st ed.; Chapman Hall: London, 1951; pp 50 and 99.
26. Hurd, A. J. In *Better Ceramics Through Chemistry III*; Brinker, C. J.; Clark, D. E.; Ulrich, D. R., Eds.; Materials Research Society: Pittsburgh, PA, 1988; Vol. 121, pp 731–742.
27. Sakka, S.; Kamiya, K.; Yoko, Y. In *Inorganic and Organometallic Polymers*; Zeldin, M.; Wynne, K. J.; Allcock, H. R., Eds.; American Chemical Society: Washington, DC, 1988; pp 345–353.
28. Parks, C. J.; Wayner, P. C. *AIChE J.* **1987,** *33*, 1–10.
29. Quéré, D.; di Meglio, J.-M.; Brochard-Wyart, F. *Science (Washington, DC)* **1990,** *249*, 1256–1260.

RECEIVED for review October 19, 1990. ACCEPTED revised manuscript March 24, 1992.

22

Formation of Uniform Precipitates from Alkoxides

C. F. Zukoski, J.-L. Look, and G. H. Bogush

Department of Chemical Engineering, University of Illinois, Urbana, IL 61801

The mechanism of precipitation of uniform particles through the hydrolysis and condensation of metal alkoxides is discussed. Final particle sizes were found to be sensitive to the reaction medium ionic strength and the surface potential of the growing particles. In addition, the rate of loss for soluble metal-containing species was found to be independent of the surface area of the growing particles. These observations imply that the major growth pathway is through agglomeration of small gel particles produced by reactions between soluble species that proceed independent of the presence of particles. Calculations that are presented support this growth mechanism.

THE LENGTH OF THE NUCLEATION PERIOD IN PRECIPITATION is commonly invoked as the primary control parameter for forming uniform particles in a reaction involving homogeneous nucleation and growth (*1–3*). In the model originally proposed by La Mer and Dinegar (*4*) for the mechanism of formation of sulfur sols, uniform size distributions result if all the particles are formed in a short burst of nucleation, and then particle growth occurs by a mechanism in which large particles increase in diameter more slowly than smaller particles (as occurs when growth is limited by diffusion to the particle surface). Despite the influence this model has had on studies of inorganic particle precipitation chemistry, the model has seen little corroboration and indeed has been brought into question for the sulfur sol for which it was developed (*5*). Although the La Mer mechanism would undoubtedly result in uniform particles, finding systems that meet the conditions required for the model to hold has been elusive.

0065–2393/94/0234–0451$08.00/0

Studies on the formation of polymer latex particles have provided an alternative mechanism whereby uniform particles can result from a homogeneous nucleation–precipitation reaction. In emulsion polymerization, an insoluble monomer is mixed with water and a water-soluble free radical initiator is added. Final particle size depends on reaction temperature, reagent concentration, and parameters controlling the colloidal stability of the growing particles (i.e., ionic strength and pH). The initial locus of the reaction is in the aqueous phase. Oligomers grow to a size at which they become insoluble and undergo a sol-to-gel transition. Because of their relatively low concentration, this transition involves only a few polymer molecules, and the gel phase grows by aggregation. The charge on the primary particles is small, but as the aggregation process proceeds, the charge per particle grows. As a consequence, aggregation rates of particles of equal size decrease, but the aggregation rate of particles of dramatically different size increases. The result is a bimodal particle (or gel-phase) size distribution, with one peak located at the primary particle size and the second peak representing particles that are stable to mutual coagulation and grow by scavenging smaller particles. Upon aggregation, the gel-phase particles coalesce, and thus the particles are able to retain a spherical shape. As the reaction proceeds, the growing particles reach a constant number density. These colloidally stable particles swell with monomer, and the locus of the reaction is transferred from the aqueous phase to the inside of the particle phase. Uniformity is achieved through control of the colloidal stability of the primary particles and aggregates of these particles (*6–8*).

A second organic analogy to the precipitation of inorganic particles occurs in dispersion polymerization. Here a solvent is chosen in which the monomer is soluble but the polymer is not. The reaction is initiated and proceeds through polymerization until the oligomers grow to a size at which they undergo a phase transition and precipitate to form polymer and solvent-rich phases. Uniform particles are achieved through the addition of steric stabilizers that control the aggregation of the growing gel phase (*9*).

The major distinction between the model of La Mer and that developed for uniform latex particles lies in the incorporation of colloidal stability of small particles. The La Mer model assumes that each nucleus is colloidally stable and survives at the end of the reaction at the center of a particle. The aggregation models argue that stabilizing primary small particles is difficult, but aggregation does not necessarily result in a broad particle-size distribution. When schemes for control of particle-size distribution are developed, the result of accepting the notion that colloidal stability can play an important role is that attention is focused away from the length of the nucleation period and towards the colloidal properties of the growing particles.

This chapter reviews our studies on the formation of uniform precipitates through the hydrolysis and condensation of titanium and silicon alkoxides. Our work has been aimed at elucidating whether uniformity is the result of the details of the chemistry or if particle-size distributions can be controlled by physicochemical means. In particular, the chapter focuses on experiments probing the length of the nucleation period in these systems and the effects of parameters that control particle interaction potentials. For the systems studied, the nucleation period appears to be a substantial fraction of the entire reaction period, and particle size is largely controlled by parameters related to particle interaction potentials. These results suggest that there are strong links between the physical chemistry underlying the formation of uniform latex particles and that controlling particle-size distributions of hydrous metal oxide precipitates (*10–14*).

Uniform Silica Particles

Stober et al. (*15*) developed a method of preparing remarkably uniform silica particles with sizes ranging from 50 nm to >1 μm in diameter. Their recipe involves hydrolyzing silicon alkoxides in aqueous alcoholic solutions containing ammonia. The resulting solids are amorphous and are 11–15% porous. We chose to use the hydrolysis and condensation of tetraethylorthosilicate, TEOS, in ethanol as a model precipitation reaction to study parameters leading to uniformity.

Our results (*10–12*) provide evidence that the La Mer mechanism is not at the heart of the uniformity of the resulting particles. Primarily, the rate of particle growth, the rate of loss of soluble silica (i.e., material that is able to pass through a 22-nm filter), and the rate of loss of TEOS (as determined from ^{29}Si NMR spectroscopy) are all well described by first-order processes with the same rate constant, k_1. These results are in keeping with those of Matsoukas and Gulari (*16*) and have been used to suggest that TEOS hydrolysis is the rate-limiting step in particle growth. The rate constant, k_1, was measured as a function of water and ammonia concentration. In addition, we found that the conductivity of the reaction medium first increases and then decreases. The rate of decrease in conductivity ($\sigma - \sigma_0$) is well fit by a first-order process with a rate constant with the same value as k_1. Here σ_0 is the initial conductivity of the reaction medium and σ is the suspension conductivity at reaction time t. The conductivity is found to be well modeled by (*11*, *12*)

$$\sigma - \sigma_0 = \{\exp(-k_1 t) - \exp(-k_2 t)\}$$

where k_2 has also been characterized over a wide range of water and ammonia concentrations. For all of the reactions studied, $k_2 \geq 10k_1$. The conductivity increase is taken as an indication of the hydrolysis of TEOS,

the production of silicic acid groups, and the subsequent deprotonation of these species by ammonia. Decreases in conductivity are associated with the loss of deprotonated silicic acid groups through condensation reactions. As a result of the strong link between the long time rate constant for the conductivity (i.e., k_1), and that measured for particle growth, as well as the rates of loss of soluble silica and TEOS, we feel conductivity is an accurate method of determining the relative amounts of hydrolyzed but uncondensed TEOS.

Soluble silica concentrations required for nucleation were determined by measuring the lag time for the increase of turbidity in a solution after the addition of TEOS. As the soluble silica concentration decreases toward the equilibrium value, C_{eq}, the lag time increases (but the final particle size is not greatly reduced). At an initial TEOS concentration of 5–10 times C_{eq}, the lag time becomes much longer than the time for the hydrolysis and condensation reactions to reach equilibrium. Thus, if the TEOS concentration exceeds 5–10 times C_{eq}, nucleation can proceed (i.e., 5–10 times C_{eq} represents the critical concentration that must be exceeded before appreciable nucleation is observed).

As the soluble silica concentration is considerably above this value for virtually the entire precipitation reaction (Figure 1), if nucleation does not occur throughout the reaction, the concentration of hydrolyzed TEOS must lie below the critical value. This situation may occur if the rate of hydrolysis is matched by the rate of deposition on particle surfaces. Two observations serve to discount this possibility. First, solution conductivities can be used to estimate the concentration of hydrolyzed TEOS. Using mobilities of KCl in water to characterize mobilities in the ions that give rise to the conductivity and assuming unit activity coefficients, we estimate that the concentration of hydrolyzed TEOS lies above the critical nucleation value for at least two-thirds of the time required for the soluble silica concentration to reach its final value (Figure 2). Second, if there is a balance between the rate of production of hydrolyzed TEOS and condensation of these species at particle surfaces, then absolute concentrations and rates of loss should depend on the surface area available for deposition. A series of reactions were performed in which particles were first precipitated and then diluted with their mother liquor such that their final particle density was decreased to a quarter of that in the as-precipitated suspension. TEOS was then added to these suspensions, and the rates k_1 and k_2 were determined. The absolute conductivity as well as the rate coefficients k_1 and k_2 were independent of particle density or even the presence of any seed particles (*12*). These results suggest that hydrolyzed TEOS concentration is above the critical nucleation level for much of the reaction and that there is a decoupling of reactions between soluble species and growth of particles. Consequently, hydrolysis and condensation reactions proceed independently of the presence of particles. Thus,

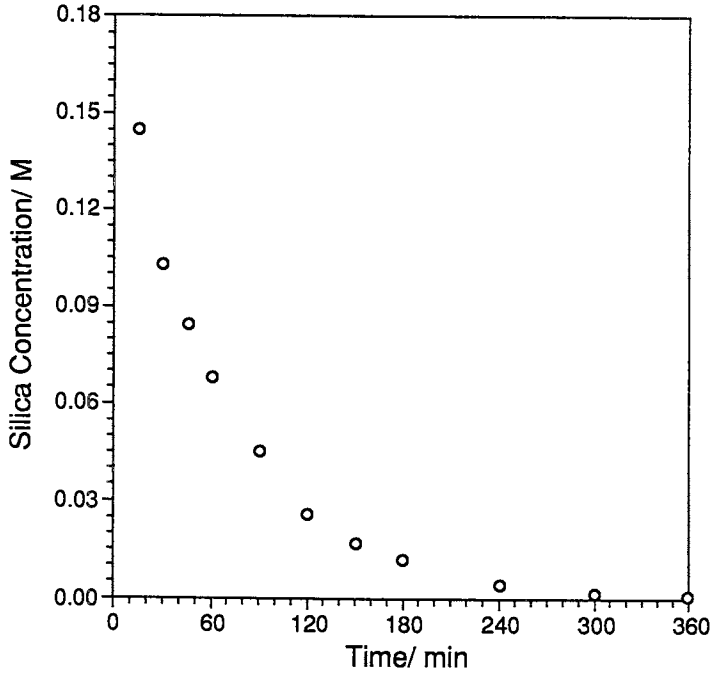

Figure 1. Soluble silica concentration as a function of time for a reaction at 25 °C for 0.17 M TEOS, 1 M NH_3, and 3.8 M H_2O ($C_{eq} = 2.4 \times 10^{-4} M$).

addition of soluble species to particle surfaces is not the major growth mechanism.

Studies by Klemperer and Ramamurthi (*17*) showed that under basic conditions silicon alkoxides react such that the molecular-weight distribution of soluble species remains peaked at the monomer level throughout the reaction. At early times, the reaction pathway is seen to follow the Flory–Stockmayer polymerization pathway developed for monomers with three to four reactive sites. The Flory–Stockmayer theory predicts the most probable molecular-weight distribution for monomers with various degrees of reactivity by assuming that all sites have equal reactivity and that there is no intramolecular cross-linking (*18*). Although these assumptions begin to break down early in the reaction, the results of Klemperer and Ramamurthi indicate that under basic conditions, there will be a few high-molecular-weight species produced through a cascade-like series of reactions. The fate of these high-molecular-weight species is key to the nucleation and growth of the silica particles.

The Flory–Huggins theory of polymer solubility suggests that if a polymer is growing in a poor solvent, when it reaches a critical molecular weight, a phase separation will occur in which a polymer-rich or gel phase

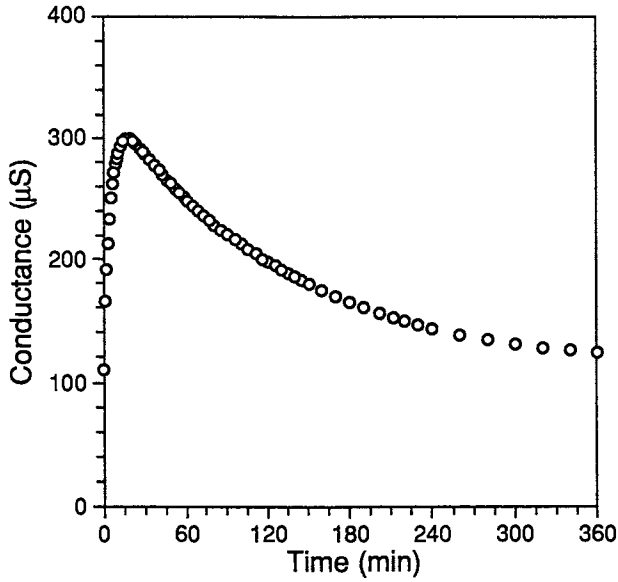

Figure 2. Conductivity of the reaction medium as a function of time after mixing (25 °C, 0.17 M TEOS, 1.0 M NH_3, and 3.8 M H_2O).

is formed, as is a polymer-poor, solvent-rich phase (*18*). If the high-molecular-weight species are sufficiently dilute, this phase separation may involve only a few polymers, and thus the phase-separated regions may be small. Continued growth of the gel phase will then occur through molecular addition and aggregation. Because the number of reactive sites in the gel particle is greatly reduced once the soluble polymer collapses, the rate of growth by molecular addition will be small. Instead, a more likely growth pathway of the gel phase may be by aggregation with continuing internal densification. The particle-size distribution of the gel phase will then be determined by kinetic parameters that control the size dependence of aggregation rates of gel particles.

This mechanism is hypothesized for the formation of uniform silica and titania particles, as it contains many of the elements observed in particle precipitation kinetics. Primarily, the continuous formation of high-molecular-weight species that undergo a phase transition at a critical size [as also suggested by the work of Bailey and Mecartney (*19, 20*)] to form nuclei helps to explain the decoupling of reactions between soluble species and the total surface area available for deposition. In this model, growing polymers remain soluble and thus would rather be surrounded by solvent than by other polymer species. Thus, these oligomers are not lost to particle surfaces until they reach a critical size, undergo a phase transition,

and become "sticky". Particle growth is then controlled by rates of aggregation between existing "gel" phase particles and freshly formed "gel" particles. Second, this mechanism suggests a pathway in which nucleation occurs for virtually the entire reaction period, in keeping with the experimental observations described earlier. Final particle-size distributions will be determined by parameters controlling the rates of aggregation of primary particles and the size at which aggregates become stable to mutual coagulation. Thus, without altering rates of reaction between soluble species, an increase in the ionic strength of the continuous phase would force particles to achieve a larger size before they become colloidally stable. As a consequence, final number densities of particles will be smaller and average diameters larger. To confirm these predictions, final particle sizes were measured as a function of ionic strength. Rate constants k_1 and k_2 were unchanged with [NaCl] up to 10^{-2} M. However, final particle diameters doubled (*12–14*).

Size-Dependent Aggregation Rates

Models of particle growth based on aggregation require a minimum-size particle—in this case, the primary particle size. Because of a current lack of understanding of the thermodynamic properties of high-molecular-weight inorganic species, methods of determining primary particle sizes in an a priori manner have not been developed for the polymer collapse model discussed earlier. However, for a system that more closely follows classical nucleation theory, methods of estimating nucleus sizes and solid–liquid surface tensions have been developed on the basis of critical nucleation concentrations (*21*). For TEOS and titanium alkoxides, critical nucleation concentrations occur in the range of 1–10 times $[C]_{eq}$, and classical nucleation theory suggests that nucleus surface tensions are on the order of 80–159 ergs/cm^2 and nuclei radii are 2–10 nm. As described later, these primary particle sizes are close to those required for an aggregation model to predict final particle diameters.

At the end of the precipitation reaction, the solid particles must be colloidally stable if a uniform particle-size distribution is to be observed. A question important to final uniformity is the particle size when this stability is achieved. The particles will always feel the long-range van der Waals attractive interactions. Interactions of an electrostatic or solvation origin can give rise to a repulsive barrier that can provide kinetic stabilization. At the end of the reaction, particles precipitated from TEOS and titanium alkoxides have final particle number densities, N_∞, of 10^{16}–10^{18} m^{-3}. These particles are suspended in a solvent with an ionic strength of approximately 10^{-4} M and have surface potentials of 10–35 mV. Our studies indicate that the particles also feel a short-range repulsive interaction that we have modeled as a solvation interaction with decay

length of 1 nm and contact interaction potential of $1–1.5 \times 10^{-3}$ J/m^2. With a Hamaker coefficient of $2.4kT$, classical Smoluchowski aggregation theory (22) can be used to determine the time required to halve the number density by aggregation,

$$t_{1/2} = 3\mu W_{ii}/4kTN_\infty \quad (1)$$

where μ is the continuous-phase viscosity, W_{ii} is the stability ratio for aggregation of two particles of size i, k is the Boltzmann constant, and T is temperature. If the La Mer model is used to describe particle growth, then N_∞ particles will be produced during the nucleation period and will have a radius on the order of 2–10 nm. Classical aggregation theory can be used to determine that for particles of this size, the stability ratio is about unity; thus, half the nuclei at a density of N_∞ will be lost by aggregation in 0.2–100 s, a time much shorter than the reaction period. Thus, it appears that while nuclei are very difficult to stabilize, particles grow by some mechanism such that at the end of the reaction they are colloidally stable.

As mentioned earlier, nuclei can grow through the addition of soluble molecules or by aggregation. A model was developed to determine if aggregation and continued nucleation alone can give rise to the particle-size distributions observed in the titania and silica precipitation reactions (*12*). A similar approach was taken by Harris et al. (*23*) for TEOS-derived silica and by Santacesaria et al. (*24*) for soluble-salt-derived titania. This model is based on the observed decoupling of reactions between soluble species (which are assumed to give rise to nuclei) and particle growth (which is assumed to occur by aggregation). Essentially, the model allows particles to nucleate and particles containing i and j primary particles to aggregate with a binary rate constant of $\beta(i,j)$. If $\beta(i,i)$ decreases as i increases but $\beta(1,i)$ increases with i, a uniform precipitate is predicted. In this model, primary particles of radius r_1 are formed at a rate $g_n(t)$, written

$$g_n(t) = g_s[\exp(-k_1 t) - \exp(-k_2 t)] \quad (2)$$

where $g_s = 3v(C_o - C_{eq})/[4\pi r_1^3(1/k_1 - 1/k_2)]$. Here v is the molar volume of the solid phase and C_o is the initial alkoxide concentration. The overall particle-size distribution evolves in time through a coupled set of equations linking the number density of particles containing k primary particles, $n(k,t)$:

$$dn(k,t)/dt = 1/2 \sum_{i=1}^{k-i} \beta(i, k-i)\, n(i,t)\, n(k-i,t) - n(k,t) \sum_{i=1}^{\infty} \beta(k,i)\, n(i,t) + \delta_{k,1}\, g_n(t) \quad (3)$$

Here $\delta_{k,1} = 1$ if k = 1 and is otherwise zero.

Smoluchowski aggregation rate kernels modified to account for hetero-aggregation in the presence of repulsive barriers become

$$\beta(i,j) = (1 + r_i/r_j)2\beta_s/[(4W_{ij}/W_{11})\, r_i/r_j] \quad (4)$$

with $W_{ij}/W_{11} = (r_{11}/r_{ij})(r_i/r_j)\exp[Jr_{11}(r_{ij}/r_{11} - 1)]$ for $r_i < r_j$. Here W_{11} is the stability ratio of primary particles and $r_{ij} = 2r_ir_j/(r_i+r_j)$. The variable $\beta_s = 8kT/3\mu W_{ii}$ is the characteristic aggregation rate constant from $8kT/3\mu W_{11}$. The parameter J is found from the slope of a $\log(W_{ii}/W_{11})$ versus $(r_{ii}/r_{11}) - 1$ curve. The stability ratio is found from particle interaction potentials, and J is found to increase with the maximum in the pair interaction energy.

Using measured surface potentials, estimates of Hamaker coefficients, and solvation parameters, the only unknown required for the aggregation model to make quantitative prediction of particle-size distributions is the size of the primary particle, r_1. Extensive calculations (*12*, *25*) indicate that equation 3 predicts a particle-size distribution that rapidly evolves into two peaks. The larger particles grow to a size at which they become stable to mutual coagulation, and after sufficient time a constant number density of colloidally stable particles is established. For a wide range of Jr_{11}, with k_1t_s and k_2t_s much smaller than unity, the final number density depends in a simple manner on parameters governing the solution to equation 3. Here $t_s = (g_s\beta_s)^{-1/2}$ is the characteristic time for nucleation and aggregation. For this range of conditions, the final number density of particles is well correlated by

$$N_\infty = 2.4 \times 10^{-2}(Jr_{11})^3 n_s \quad (5)$$

where $n_s = (g_s/\beta_s)^{1/2}$ is the characteristic number density scale. This model is similar to that developed by Feeney et al. (*8*) for emulsion polymerization of uniform latex particles. The breadth of the final particle size distribution is systematically narrower than that observed experimentally; this result emphasizes the conclusion that aggregation can result in uniformity.

As shown in Table I, reasonable estimates of particle interaction parameters provide a narrow range of values of J. The remaining unknown parameter, r_1, is used to force a fit between the final measured average size and that predicted from equation 5. Predicted values of r_1 fall in a physically meaningful range and are similar to those predicted by classical nucleation theory. Although the interaction potentials used in these calculations include estimated parameters, reasonable values have been used. These results indicate that particle growth by aggregation alone can reproduce experimentally observed final particle sizes. The model prediction of final average sizes rests on a prediction of final particle number density. Once N_∞ particles have been formed and are stable to mutual

Table I. Particle Interaction Parameters

Sample	$[Me(OR)_4]$ (M)	$[H_2O]$ (M)	$[NH_3]$ (M)	[HCl] ($M \times 10^4$)	$[Si]_{eq}$ ($M \times 10^4$)	$[Ti]_{eq}$ ($M \times 10^4$)	k_1[a] ($s^{-1} \times 10^4$)	k_2[b] ($s^{-1} \times 10^3$)	<D>[c] (nm)	δ_∞/<D>[d] (%)	ψ_o[e] (mV)	J' (nm^{-1})	W_{11}[g]	r_1[h] (nm)
A	0.17[i]	15	0.5	0	9 ± 1	NA[j]	4.2 ± 0.4	8.3 ± 0.9	269	8	−13	0.35	1.6	3.0
B	0.17[i]	15	1.0	0	4 ± 1	NA	9.5 ± 1.0	17 ± 2	343	6	−13	0.35	1.7	3.1
C	0.17[i]	15	2.0	0	7 ± 1	NA	17 ± 1	22 ± 2	453	2	−13	0.35	1.3	1.7
D	0.17[i]	15	3.0	0	6 ± 1	NA	23 ± 2	32 ± 3	459	1	−13	0.35	1.3	1.6
E	0.05[k]	0.25	0	0	NA	130	0.25	2	1100	13	11	0.30	1.4	1.7
F	0.05[k]	0.25	0	0.5	NA	150	0.25	2	820	13	18	0.37	1.5	1.7

[a] Rate constant for loss of soluble metal-containing species.
[b] Rate constant for initial increase in hydrolyzed alkoxide concentration. For reactions containing TEOT, k_2 is large and not easily measured. For these reactions, k_2 is an estimate.
[c] Measured final particle diameter.
[d] Measured standard deviation in diameter distribution divided by the average particle diameter.
[e] Surface potential determined from particle electrophoretic mobilities.
[f] Parameter controlling rate of aggregation of particles of like size.
[g] Stability ratio for primary particles of radius r_1.
[h] Primary particle size required for aggregation model to predict <D>.
[i] TEOS sample.
[j] NA, not applicable.
[k] TEOT sample.

aggregation, the particles can grow by any mechanism that relieves the supersaturation. For example, in the formation of polymer lattices, the stable particles swell with monomer and nucleation of primary particles stops. In the precipitation of silica and titania particles, the high supersaturations and the decoupling of rates of loss of hydrolyzed alkoxides suggest that primary particles may be continuously formed throughout the reaction. Final particle porosity and granular appearance supports our suggestion that aggregation acts as a major growth mechanism throughout entire reaction.

Uniform Titania Particles

The formation of uniform particles through the hydrolysis and condensation of titanium alkoxides has proven more elusive than for systems involving silica. Reports of uniform particle formation through the hydrolysis of tetraethylorthotitanate (TEOT) in aqueous ethanol by Barringer and Bowen (*26*, *27*) have been difficult to reproduce. Jean and Ring (*28*, *29*) developed a technique involving use of hydroxypropylcellulose in which uniform particles that are formed are fluffy and densify poorly. Considerable effort to prepare uniform particles following the techniques of Barringer and Bowen proved futile until we found that the growing particles are very sensitive to shear-induced aggregation. Subsequently, we have been able to reproduce the results of Barringer and Bowen if the degree of agitation to which the precipitating suspensions are exposed is kept at a low level.

The titania particles precipitate under reaction conditions very similar to those of the silica systems discussed earlier. A critical nucleation concentration of 1.5–3 times $[C]_{eq}$ is measured. This low supersaturation level is not reached until very late in the precipitation reaction (Figure 3). The rate of loss of soluble titania is also independent of the presence of solid surface area. Finally, on the basis of measures of particle surface potentials, nuclei of sizes less than about 20 nm are expected to be unstable and to rapidly aggregate. These results again indicate that during the precipitation of titania, nucleation may occur over much of the reaction period and final particle sizes may be determined by the aggregation of primary particles. These conclusions are supported by the transmission electron microscopy work of Diaz-Gomaz et al. (*30*).

The role of colloidal interactions is further supported by the observation that as the background concentration of HCl is raised to 10^{-3} M, the rate of loss of soluble titania is not altered, particle charge increases, and final particle size decreases (*13*, *14*). Again, these observations demonstrate the importance of colloidal stability during the precipitation of uniform particles.

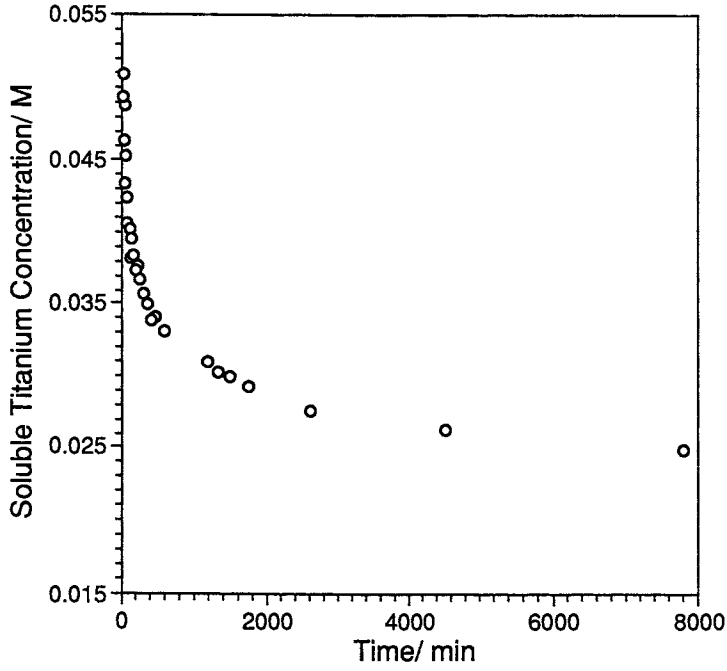

Figure 3. Soluble titanium concentration as a function of time for a reaction at 25 °C; 0.05 M TEOT and 0.25 M H_2O (C_{eq} = 0.025 M).

Shear-induced aggregation alters particle-size distributions after particles have reached a size at which they are stable to mutual aggregation by Brownian motion (i.e., aggregation is not observed in a quiescent fluid). In the absence of acid, the shear rate required to induce aggregation is 10 s^{-1}. Particles are observed to grow with a narrow size distribution until the average particle size is on the order of 600 nm. If the shear rate in the reactor is above 10 s^{-1}, large flocs are observed when particles exceed this size. At lower shear rates, the particles continue to grow, and at the end of the reaction, the particles have an average diameter of 1.3 μm with a standard deviation of approximately 15%.

Conclusions

Maintaining the stability of small colloidal particles has long been recognized to be difficult. Indeed, development of methods of stabilizing colloidal silica with a particle size under 10 nm was a major breakthrough. In the face of well-established models for colloidal interactions, researchers must demonstrate the stability of nuclei produced in precipitation reactions, rather than ask for evidence of their instability.

Silica particles precipitated from aqueous, basic alcoholic solutions to which silicon alkoxides have been added appear to grow as if the limiting reaction occurred at the particle surface (*12, 16*). However, the rate of loss of hydrolyzed TEOS is independent of particle surface area available for deposition. In addition, the concentration of soluble silica remains above the critical concentration required for nucleation until late in the precipitation reaction. These results and the observation that the final particles are uniform, with average size depending on ionic strength, lead us to conclude that the particles do not grow by the mechanism of addition of low-molecular-weight soluble species and that colloidal stability is important in the final particle-size distribution. Detailed calculations suggest that growth solely by aggregation of high-molecular-weight species [a mechanism that will result in changes in standard deviations in particle size distributions as observed in the seeded-growth studies (*12, 16*)] can result in particles of narrow size distribution. This model for particle growth provides a mechanism for the formation of a constant number of growing particles early in the reaction—a necessary step in the formation of uniform precipitates (*12, 23*). In addition, this model incorporates the physical chemistry of particle interaction potentials and aggregation and provides an obvious explanation of the final particle porosity. The density and ability of the primary particles to coalesce will be determined by the solution thermodynamics of growing silicon- and oxygen-containing molecules in mixed basic solvents, a field that has seen little exploration.

Precipitation of uniform titania particles follows a similar pathway in that the particles appear to be the result of reactions between soluble titania species that culminate in a sol-to-gel phase transition of high-molecular-weight species and the resulting aggregation of these primary particles. Under typical conditions in which the particles are precipitated from TEOT in ethanol, particles of narrow size distributions are initially observed to grow to a diameter near 600 nm. If the shear rate is kept below 10 s^{-1}, the particles continue to grow to >1 μm in size, with a relatively narrow final particle-size distribution. On the other hand, if the suspension is subjected to a larger shear rate, 600-nm particles aggregate and grow together, forming large open chains with well-formed interparticle necks. If particle surface charge is increased, final particle size is reduced, and a larger shear rate is required to induce aggregation. These results again provide graphic evidence that colloidal stability plays a major role in the formation of uniform precipitates.

The studies reviewed here show that precipitation of uniform particles requires two conditions to be met. First, at a point early in the reaction, a constant number of colloidally stable particles must be established. Second, these particles must remain stable to mutual coagulation throughout the subsequent reaction. If the primary particles formed are unstable with respect to larger particles, a short nucleation period is not a

prerequisite of a narrow final particle-size distribution. Indeed, continuous slow nucleation with the correct aggregation rate kernels can produce very uniform particles. If the nuclei are unstable and aggregation is very fast, a broad particle-size distribution may result. For colloidally stable nuclei, a short nucleation period will be important in establishing uniform precipitates. However, nuclei with 1–15-nm radii are difficult to stabilize under typical precipitation conditions.

Acknowledgments

This work was partially supported by a grant from the International Fine Particle Research Institute. We thank E. Lestan for help with the precipitation of titania. We also gratefully acknowledge stimulating conversations with W. Klemperer.

References

1. La Mer, V. K. *Ind. Eng. Chem.* **1952,** *44,* 1270.
2. Matijevic, E. *Acc. Chem. Res.* **1981,** *14,* 22.
3. Matijevic, E. *Ann. Rev. Mater. Sci.* **1985,** *15,* 483.
4. La Mer, V. K.; Dinegar, R. H. *J. Am. Chem. Soc.* **1950,** *72,* 4842.
5. Kerker, M.; Daby, E.; Cohen, G. L.; Krab, J. P.; Matijevic, E. *J. Am. Chem. Soc.* **1963,** *67,* 2105.
6. Fitch, R. M.; Kamath, V. K. *J. Colloid Interface Sci.* **1976,** *54,* 6.
7. Lichti, G.; Gilbert, R.; Napper, D. H. *J. Polymer. Sci.* **1983,** *21,* 269.
8. Feeney, P. T.; Napper, D. H.; Gilbert, R. G. *Macromolecules* **1984,** *17,* 2570.
9. Croucher, M. D.; Winnik, M. A. In *An Introduction to Polymer Colloids*; Kluwer Academic: Dordrecht, Netherlands, 1990.
10. Bogush, G. H.; Zukoski, C. F. In *Ultrastructure Processing of Advanced Ceramics*; Mackenzie, J. D.; Ulrich, D. R., Eds.; Wiley: New York, 1988; p 477.
11. Bogush, G. H.; Dickstein, G. L.; Lee, K. C.-P.; Zukoski, C. F. *Mater. Res. Soc. Symp. Proc.* **1988,** *121,* 57.
12. Bogush, G. H.; Zukoski, C. F. *J. Colloid Interface Sci.* **1990,** *142,* 1; **1990,** *142,* 19.
13. Zukoski, C. F.; Chow, M. K.; Bogush, G. H.; Look, J.-L. In *Better Ceramics Through Chemistry IV*; Zelinsky, B. J. J.; Brinker, C. J.; Clark, D. E.; Ulrich, D. R., Eds.; Materials Research Soc.: Pittsburgh, PA, 1990.
14. Look, J.-L.; Bogush, G. H.; Zukoski, C. F. *Faraday Disc., Chem. Soc.* **1990,** *90,* 345.
15. Stober, W.; Fink, A.; Bohn, E. *J. Colloid Interface Sci.* **1968,** *26,* 62.
16. Matsoukas, T.; Gulari, E. *J. Colloid Interface Sci.* **1988,** *124,* 252; **1989,** *132,* 13.
17. Klemperer, W. G.; Ramamurthi, S. D. In *Better Ceramics Through Chemistry III*; Brinker, C. J.; Clark, D. E.; Ulrich, D. E., Eds.; Materials Research Society: Pittsburgh, PA, 1988.
18. Flory, P. J. *Principles of Polymer Chemistry*; Cornell University Press: Ithaca, NY, 1953.

19. Bailey, J. K. In *Proceedings of the 47th Annual Meeting of the Electron Microscopy Society of America*; Bailey, G. W., Ed.; San Francisco Press: San Francisco, CA, 1989; p 434.
20. Bailey, J. K.; Mecartney, M. L. *Mat. Res. Soc. Symp. Proc.* **1990,** *180,* 153.
21. Nielsen, A. E. *Kinetics of Precipitation*; Pergamon: New York, 1964.
22. Russel, W. B.; Saville, D. A.; Schowalter, W. R. *Colloidal Dispersions*; Oxford University Press: Oxford, United Kingdom, 1989.
23. Harris, M. T.; Branson, R. R.; Byers, C. H. *J. Non-Cryst. Solids* **1990,** *120,* 397.
24. Santacesaria, E.; Tonello, M.; Storti, G., Pace, R. C.; Carra, S. *J. Colloid Interface Sci.* **1986,** *111,* 44.
25. Bogush, G. H., Ph.D. Dissertation, University of Illinois, 1990.
26. Barringer, E. A.; Bowen, H. K. *J. Am. Ceram. Soc.* **1982,** *65,* C199.
27. Barringer, E. A.; Bowen, H. K. *Langmuir* **1985,** *1,* 414; **1985,** *1,* 428.
28. Jean, J. H.; Ring, T. A. *Langmuir* **1986,** *2,* 251.
29. Jean, J. H.; Ring, T. A. *Colloids Surf.* **1989,** *29,* 273.
30. Diaz-Gomaz, M. I.; Gonzalez Carreno, T.; Serna, C. J.; Palaios, J. M. *J. Mater. Sci. Lett.* **1988,** *7,* 671.

RECEIVED for review December 18, 1990. ACCEPTED revised manuscript February 24, 1992.

23

Development of Silica Gels and Impact of Silica Research on Studies of Other Colloidal Systems

M. G. Sánchez

Department of Chemistry, The Johns Hopkins University, Baltimore, MD 21218

The development of silica gels is reviewed, from the pioneering work of Graham in the 19th century through the development by Patrick of an industrial manufacturing process in 1919. Emphasis is placed on the contributions of Iler and on the impact Iler's work had in the development of other inorganic colloidal systems.

THREE SCIENTISTS WERE PIVOTAL IN THE DEVELOPMENT OF SILICA GELS: Thomas Graham, Walter A. Patrick, and Ralph K. Iler. This chapter highlights their work and concludes with the impact they, particularly Iler, had on the development of other inorganic colloidal systems.

"The Century of Progress Exposition" held in 1933 in Chicago, IL, was one of the factors that induced the American Chemical Society to hold its fall meeting in that city. The meeting included a symposium on "The Century of Progress in Colloid Chemistry". On that occasion Ross A. Gortner, professor of agricultural biochemistry, University of Minnesota, presented a paper entitled "Colloids in Biochemistry: An Appreciation of Thomas Graham" (*1*), in which he traced many contributions of the 19th century scientist who originated the beautiful but complex field of colloids. Much of the material that follows was obtained from the Gortner reference.

0065–2393/94/0234–0469$08.00/0

Thomas Graham

It is difficult to establish with assurance the first publication that clearly deals with silica gels. "The Effects of Animal Charcoal on Solutions" (2), published in 1830 when Graham was only 25, is an early, well-documented reference. Graham modified animal charcoal by exhaustive extraction with dilute hydrochloric acid until only silica remained in the ash. He then studied the effect of this material on various solutions. He described the following observations:

- Ammoniacal copper solutions lose their blue color when put in contact with the extracted ash, and the copper cannot be removed from the material by subsequent extraction with strong ammonia.
- Silver is "adsorbed" from a solution of silver nitrate, and crystals of metallic silver appear on the surface of the material.
- Iodine is removed from a solution of iodine and potassium iodide. The material can be dried at a relatively high temperature without the appearance of iodine vapors. However, if the iodine–ash mixture is heated strongly in a closed flask, the iodine sublimes, but later upon cooling the "ash" readsorbs the iodine vapors.

As Gortner points out, "This paper is an outstanding contribution in the field of adsorption." Graham publications continued for many years—mainly in diffusion phenomena. His patient but steadfast pursuit combined with his thorough approach gradually provided the experimental foundation from which came his conception of the colloidal state of matter. In his 1861 paper "Liquid Diffusion Applied to Analysis" (3), Graham introduced in a systematic manner the concept of this new state of matter. The following excerpts from the introductory section show the insight and genius of the "father of colloid chemistry":

> The property of volatility, possessed in various degrees by so many substances, affords invaluable means of separation. . . . Similar in character to volatility is the diffusive power possessed by all liquid substances. . . . The range in the degree of diffusive mobility exhibited by different substances appears to be as wide as the scale of vapour tensions. Thus hydrate of potash may be said to possess double the velocity of diffusion of sulphate of potash and sulphate of potash again double the velocity of sugar, alcohol and sulphate of magnesia. But the substances named belong all, as regards diffusion, to the more "volatile" class. The comparatively "fixed" class, as regards diffusion, is represented by a different order of

> chemical substances marked out by the absence of the power to crystallize, which are slow in extreme. Among the latter are hydrated silicic acid, hydrated alumina and other metallic peroxides . . . when they exist in the soluble form.
>
> Low diffusivity is not the only property which the bodies last enumerated possess in common. They are distinguished by the gelatinous character of their hydrates. Although largely soluble in water, they are held in solution by a most feeble force. . . . As gelatine appears to be its type it is proposed to designate substances of the class as colloids and to speak of their peculiar form of aggregation as the colloidal condition of matter. Opposed to the colloidal is the crystalline condition. Substances affecting the latter form will be classed as crystalloids. . . . The distinction is no doubt one of intimate molecular constitution. . . . The solution of hydrated silicic acid, for instance, is easily obtained in a state of purity, but it cannot be preserved. It may remain fluid for days or weeks in a sealed tube, but is sure to gelatinize and become insoluble at last. Nor does the change of this colloid appear to stop at that point. . . . The colloidal is, in fact, a dynamical state of matter; the crystalloidal being the statical condition.

Some 26 pages later in that monumental paper, Graham addressed the "preparation of colloid substances by dialysis", and on the topic of "soluble silicic acid" he describes the preparation of dilute silica sols and their properties, including stability, gelation, and syneresis. In this paper, which ironically is primarily directed to the study of liquid diffusion, we witness the birth of colloidal chemistry.

Walter A. Patrick

About 50 years later, Walter A. Patrick, a professor of chemistry at the Johns Hopkins University who combined with his basic understanding of colloidal chemistry an inclination toward the practical, developed a laboratory method and ultimately an industrial process for the manufacture of silica gel. The process and product were patented in 1919 (*4*).

The Patrick silica gels were hard, transparent granules, stable to 700 °C, that possessed "ultramicroscopic" pores and exhibited high adsorptive capacities. The process (Figure 1) was commercialized by the Silica Gel Corporation, which eventually became part of the Davison Chemical Corporation, now a division of W. R. Grace & Co.

One of the key practical features of the Patrick process was the manufacturing flexibility it offered. By changing one or more of the washing and finishing parameters, such as pH, temperature, duration, aging, and so forth, the resulting gels could be profoundly modified. These variations were found primarily through empirical work. In the meantime,

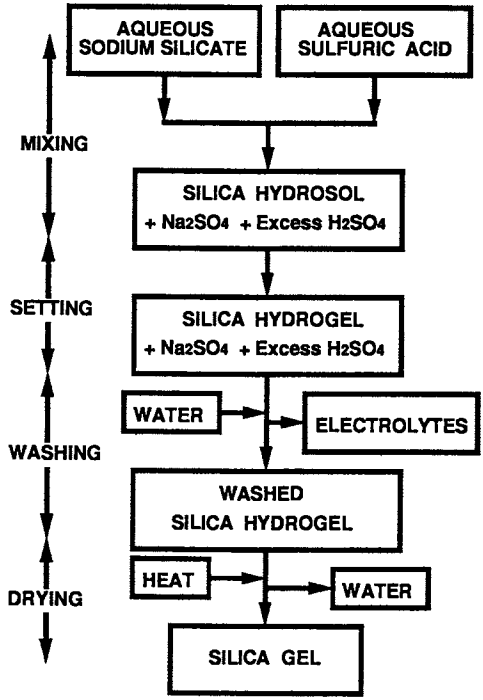

Figure 1. The Patrick silica gel process.

Patrick continued to unravel the fundamentals of silica gels, and until retirement circa 1960, he published extensively in the field. However, much work included in the theses of many of his doctoral students, although technically part of the open literature, seldom reached others and remains somewhat unknown. Contributions in such areas as light scattering during polymerization, gelation, and aging as well as dielectric loss of silica gels impregnated with alumina are examples.

Besides his important direct contributions and those of his many Ph.D. graduates, his early work made many grades of silica gel commercially available, and this availability had a profound impact on advances made by others in silica gels as well as in catalysis. Some specific examples are silica–alumina fluid cracking catalysts, which were developed from Patrick's silica hydrogels and provided the "high-octane aviation gasoline" during the second world war, and olefin polymerization catalysts, which use silica gel as supports. Many pigments, additives and other products were derived from the basic Patrick process.

In spite of these very significant achievements, the understanding of the phenomena that take place during silica gel preparation and of the resulting properties lagged far behind the empirical knowledge.

Ralph K. Iler

Iler's contributions, more than those of any other scientist of that period, narrowed the gap. His extensive experimental work and many papers and patents alone would give him a prominent place in the field. However, his major contribution is probably the order he brought to the empirical knowledge that existed prior to 1950. Through the publication of his first book, *Colloidal Chemistry of Silica and Silicates*, in 1955 (*5*), he transformed the field from "an empirical art with a modicum of science" to "a science with remnants of art". Researchers soon realized that this was a very valuable and rare book—not only for the specific information on silica, but also for the broad understanding it provided on inorganic colloidal systems in general.

Others contributed also to the transition from empiricism to science, but it was Iler's devotion to the field, systematic approach, inquisitive mind, and perception of overall harmony that made him the unquestionable leader of his time in inorganic colloidal chemistry. The understanding that followed the publication of his first book clearly transcended the silica system. The findings in silica were soon extended to other systems.

For example, the sol–gel process, which grew so fast in the late 1950s and the 1960s and continues to expand and generate new approaches and materials, began not by mere coincidence about 1 year after the publication of Iler's book. The term "sol–gel" was heard for the first time around 1956. It is believed to have been coined by researchers at the Oakridge National Laboratories (ORNL) (P.H. Emmett, personal communication, 1959).

The following section highlights some systems that were conceived and prepared in that period. Figure 2 shows some of the sols prepared (*6–8*) in the early days.

Some of the methods of preparation used during that period were catalytic hydrogen reduction of metal nitrate solutions at high temperatures; steam denitrification; high-temperature and high-pressure hydrolysis; electrodialysis at high temperature to remove solubilizing acids or bases; hydrolysis of alkoxides; peptization; urea or hexamethylene–tetramine hydrolysis; solvent extraction; and others. Two extensive reports with key references were presented at the 1968 panel held by the International Atomic Energy Agency in Vienna, Austria, in which the work on sol–gel methods performed by six firms in the United States (*9*) and by ORNL (*10*) was discussed. The intermediate objective of these programs was to produce gels from sols that had controlled micelle size, degree of hydration, and surface energy, and the ultimate goal was new ceramic materials.

Figure 3 shows a particularly interesting aqueous sol of uranium dioxide. It was prepared by electrodialysis from a uranyl chloride solution

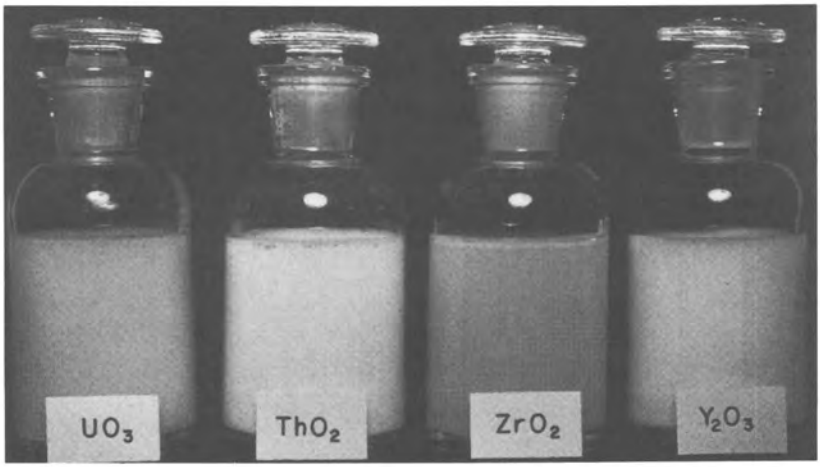

Figure 2. Early sols.

Figure 3. Aqueous sol of UO_2.

that contained excess HCl and flowed through the catholyte of an electrolytic cell, separated from the anolyte by an anion-selective membrane. The first step was the reduction of hexavalent to tetravalent uranium at the cathode. Further net removal of HCl by electrolysis resulted in nucleation, micelle growth, densification, and aggregation of UO_2. Temperature and programming of HCl removal, coupled with controlled aeration to prevent reduction to trivalent uranium, gave a sol of

the desired properties (*11*). It could readily be gelled with ammonia and converted into microspheroidal gel particles.

Figure 4 shows a transmission electron micrograph (TEM) of the UO_2 sol shown in Figure 3. The micelles were highly hydrated and exhibited a diameter of about 4–5 nm.

The sol properties were designed to achieve high surface reactivity in order to enhance sinterability of the gels obtainable by gelation. The fluid sol could be shaped prior to gelation, gelled in that shape, and sintered in hydrogen to prepare high-purity UO_2 products with a density in excess of 99% of the theoretical crystal density.

Figure 5 shows UO_2 microspheres about 100 μm in diameter prepared from a UO_2 sol. The uniformity in size, nearly perfect spherical shape, and high luster of the surface are evident. The microspheres were crystalline, with very small crystallite sizes that were not discernible by optical microscopy. They were dense and exhibited excellent mechanical properties (*12–14*).

Figure 6 is a TEM of a complex system consisting of micelles in which the core was a solid solution of UO_2 in ThO_2 and was coated with a silica layer. The surface properties of this system were essentially those of silica, but the principal components were actinide oxides (*15, 16*).

Techniques were also developed for the preparation of gels and ceramic solids of complex composition by mixing compatible sols prior to gelation or alternatively preparing sols in which various oxides were mixed within each micelle. The high degree of uniformity achievable in the resulting gels led to the formation of solid solutions at relatively low temperature. The very small diffusion distances required to achieve solid solutions offered previously unavailable means of preparing materials at low temperatures. The ceramic materials prepared by these methods combined high density with very small grain size; excellent mechanical properties resulted.

On the other end of the reactivity and sinterability scale, colloidal suspensions of very large micelle size were prepared. In these systems the objective was the preparation of high-pore-volume gels exhibiting bimodal pore size distribution for applications in catalysis. A gamma type alumina support is an example of this technique. The method used consists of preparing a hydrous gel of pseudoboehmite with ~30-Å crystallites aggregated to particles in the range of about 1–10 μm. The hydrous gel can be peptized with nitric acid to form a fluid colloidal suspension. This "sol" may be dropped into a column containing an upper layer of an immiscible organic solvent, such as an ammoniated hydrocarbon, in which the drops acquire a spheroidal shape as they fall. The ammonia brings about gelation of the outer layer of the droplets, which remain spheroidal as they cross into a lower aqueous phase of ammonium hydroxide at the base of the column, where neutralization is completed. The gelled droplets

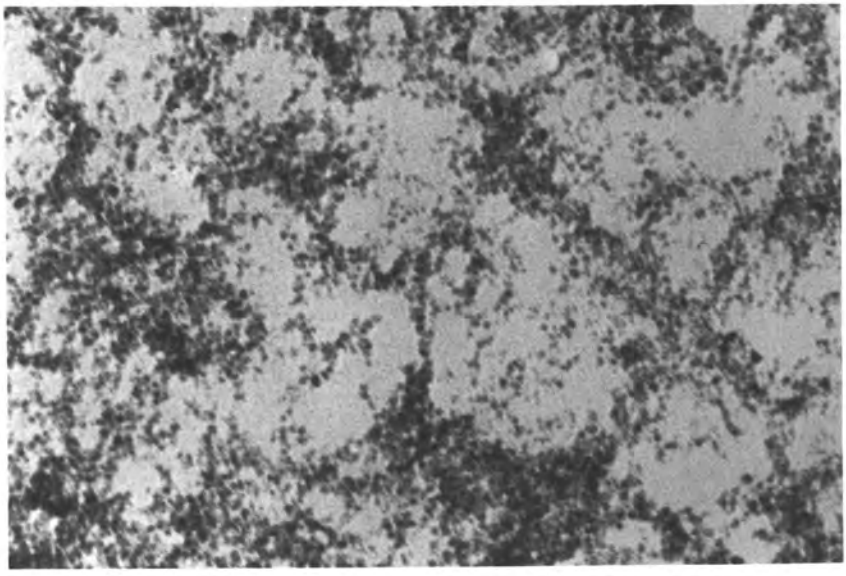

Figure 4. TEM of UO_2 sol shown in Figure 3.

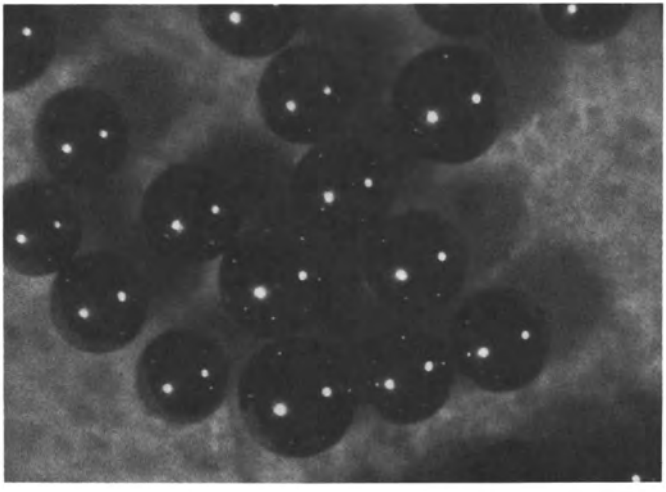

Figure 5. UO_2 microspheres.

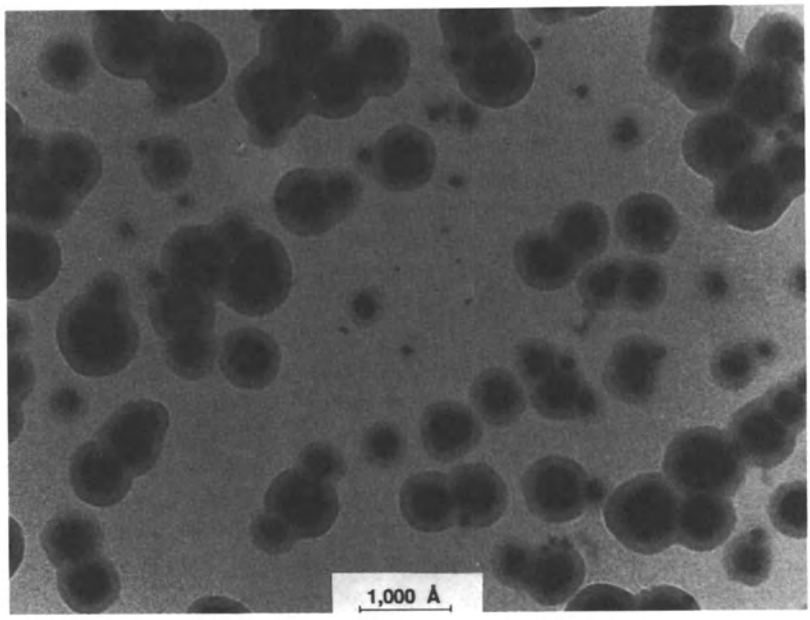

Figure 6. TEM of a complex system.

can be dried and calcined at high temperatures to achieve the particular transition alumina desired. This process can produce supports of different size and pore structure (*17*). The method was named "drop-gel" by N. R. Laine of Davison (Baltimore, MD).

Figure 7 shows spheroids of gamma type alumina about 3 mm in diameter used as supports in automobile exhaust catalysts.

Besides the broad spectrum of oxide gels and the ceramic materials prepared from them, work led to two other generic groups of new materials, the carbide and the nitride systems. In brief, by mixing oxide sols of very small micelle size with corresponding colloidal suspensions of carbon, intimately mixed sols and gels of oxides and carbon were prepared. High-temperature treatment in an inert atmosphere such as argon caused the oxides to be reduced and form dense metal carbide bodies (*18*). The products formed depended on the carbon-to-metal ratio in the mixed sol system and on the nature of the atmosphere used in the high-temperature firing step. The following equations, which use uranium dioxide sol as a typical heavy metal, illustrate the types of reactions that were carried out and the families of new materials that were developed.

1. preparation of metal monocarbides from metal dioxides and carbon sols fired in argon:

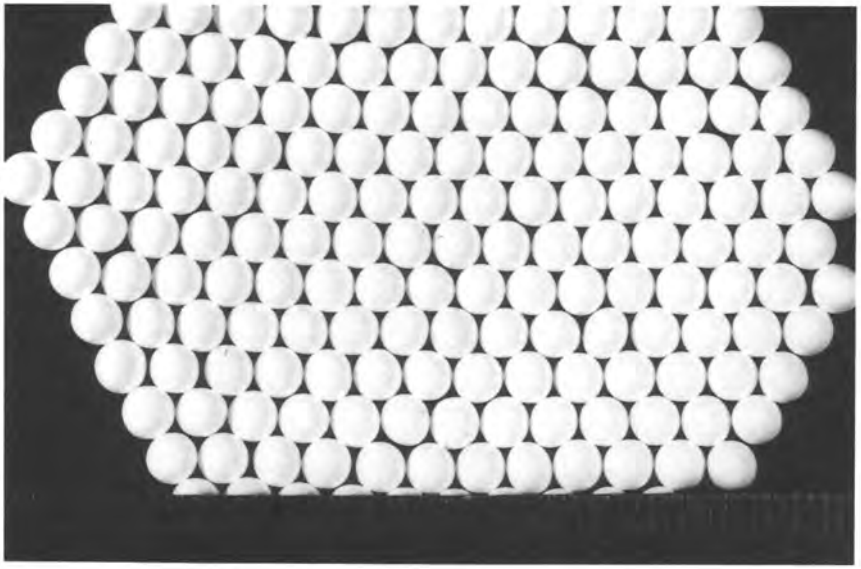

Figure 7. Alumina used in automobile exhaust systems.

$$UO_2 + 3\,C \rightarrow UC + 2\,CO\uparrow$$

2. preparation of metal dicarbides from metal dioxides and carbon sols fired in argon:

$$UO_2 + 4\,C \rightarrow UC_2 + 2\,CO\uparrow$$

3. preparation of metal mononitrides (*19*) from metal dioxides and carbon sols fired in nitrogen:

$$2\,UO_2 + 4\,C + N_2 \rightarrow 2\,UN + 4\,CO\uparrow$$

By controlling the carbon-to-metal ratio in the precursor mixed sols, a broad range of compositions can be prepared. Materials such as carbides, nitrides, solid solutions of carbonitrides, and multiple-phase systems with excess carbon were obtained. By using heavy metal oxide sols of very small micelle size and high surface reactivity, it was possible to produce some of the most refractory solids known at relatively low temperatures. Carbides, nitrides, and carbonitrides of U, Th, Zr, Hf, Y, the lanthanides, and so forth were prepared.

These colloidal approaches are being used today to synthesize advanced materials, such as high-critical-temperature ceramic superconductors (*20*).

References

1. Gortner, R. A. *J. Chem. Ed.* **1934**, *11*, 279–283.
2. Graham, T. *Quart. J. Sci.* **1830**, *1*, 120–125.
3. Graham, T. *Phil. Trans. R. Soc. London* **1861**, *151*, 204.
4. Patrick, W. A. U.S. Patent 1,297,724, 1919.
5. Iler, R. K. *Colloidal Chemistry of Silica and Silicates*; Cornell University Press: Ithaca, NY, 1955.
6. Sánchez, M. G. Canadian Patent 586,261, 1959.
7. Fitch, F. T.; Sánchez, M. G.; Vanik, M. C. U.S. Patent 3,091,592, 1963.
8. Fitch, F. T.; Smith, J. G. U.S. Patent 3,150,100, 1964.
9. Wymer, R. G. *Proceedings of a Panel on Sol–Gel Processes for Ceramic Nuclear Fuels: Status Report from the U.S.A.*; International Atomic Energy Agency: Vienna, Austria, 1968.
10. Wymer, R. G. *Proceedings of a Panel on Sol–Gel Processes for Ceramic Nuclear Fuels: Laboratory and Engineering Studies of Sol–Gel Processes at ORNL*; International Atomic Energy Agency: Vienna, Austria, 1968.
11. Hurley, F. R.; Tecotzky, M.; Vanik, M. C. U.S. Patent 3,691,087, 1972.
12. Cogliati, G.; De Leone, R.; Guidotti, G. R.; Lanz, R.; Lorenzini, L.; Mezi, E.; Scibona, G. *The Preparation of Dense Particles of Thorium and Uranium Oxide*; Third United Nations International Conference on Peaceful Uses of Atomic Energy; Vol. 11, A/CONF. 28/P/555; 1964.
13. Fitch, F. T.; Braun, A. B. U.S. Patent 3,331,785, 1967.
14. Flack, H. P.; Sánchez, M. G.; Lamberth, C. T. U.S. Patent 3,345,437, 1967.
15. Barrett, W. T.; Sánchez, M. G.; Vanik, M. C. U.S. Patent 3,097,175, 1963.
16. Fitch, F. T.; Sánchez, M. G.; Vanik, M. C. U.S. Patent 3,330,772, 1967.
17. Sánchez, M. G.; Ernest, M. V.; Laine, N. R. U.S. Patent 4,279,779, 1981.
18. Triggiani, L. V. U.S. Patent 3,518,328, 1970.
19. Gens, T. A.; Helton, D. M.; Clinton, S. D. *Laboratory Preparation of Uranium Nitride Microspheres by a Sol–Gel Technique*; ORNL-3879, Oak Ridge National Laboratory: Oak Ridge, TN, 1965.
20. Spencer, N. D.; Pan, W. H.; Rudesill, J. A. U.S. Patent 5,023,067, 1991.

RECEIVED for review October 19, 1990. ACCEPTED revised manuscript June 15, 1992.

24

Industrial Synthetic Silicas in Powder Form

Horst K. Ferch

Department of Applied Research and Technical Services, Silicas and Pigments, Degussa AG, Frankfurt on the Main, Germany

Pure synthetic silicon dioxide in powdered form is discussed. After a brief history, the significance of this product group is shown by the total production quantity in the Western hemisphere. A clear classification of synthetic silicas is given, and the principal differences between thermal and wet-process products are illustrated. After-treated silicas are also discussed. Various applications of synthetic silicas are described in detail. Questions about useful handling methods, registration, approval, and toxicology are addressed.

THE DEVELOPMENT OF SYNTHETIC SILICAS IN POWDER FORM took place in the 20th century. Nearly all of the manufacturing processes can be used on an industrial basis, although the extent to which they have been applied varies considerably. The ideas originated in North America and Germany (Table I) (*1*).

Mention was made in 1887 of electric arc silicas (2), and a detailed account by Potter has been available since 1907 (3). Industrial use of this process, which involves electricity costs, became possible only after further developments by the BFGoodrich Company (*4*).

Silica gels were first described in 1914 in the Göttingen thesis of Patrick (5), who then developed patents for methods of production in the United States (*6*) that were first implemented in 1920 (*7*). The first silica aerogels were made by Kistler in 1931 (*8*), and production was started in 1942 (9). Stöwener was an important early figure in silica gel production in Germany (*10*).

0065–2393/94/0234–0481$08.72/0

Table I. Overview of SAS

Process	*Raw Materials or Kind of After-treatment*	*Inventor*	*Commercial Name*
PYROGENIC OR THERMAL SILICAS			
Flame hydrolysis	$SiCl_4+H_2+O_2$	Kloepfer,1941	Aerosil, Cab-O-Sil
Electric arc	quartz + coke	Potter, 1907	Fransil EL, TK 900
SILICAS FROM WET-PROCESS			
Precipitation	water glass + acid	1940	Hi-sil, Ultrasil VN 3, Vulcasil, Zeolex
Spray drying	water glass + acid	approx. 1964	Ketjensil, Sipernat, Zeosil
Gels	acid + water glass	Patrick, 1914; Stöwener, 1924	Gasil, Sorbsil, Syloid
Overcritical conditions	acid + water glass	Kistler, 1931	Santocel
Hydrothermal process	sand + lime	1957	HK 125
AFTER-TREATED SILICAS			
Physical after-treatment	thermal		Syloid 73
Chemical after-treatment	coating		OK 412
Chemical after-treatment	reaction on the surface		Aerosil R 972, Sipernat D 17

NOTE: The term SAS here does not include any salts or synthetic sodium aluminosilicates (SSAS), which are not discussed in this chapter.

The first reinforcing silica for rubber, which was in the form of a calcium silicate and known as Silene, was introduced to the U.S. market as early as 1939 (*11*). The first reinforcing fillers for rubber articles available in West Germany after the Second World War were also calcium and aluminum silicates. The production of Hi-Sil, a silicate with a high silica content, started in 1946 (*12*). The first "pure" precipitated silica was brought onto the European market in 1953 and was called Ultrasil VN 3 (*13*).

Although the patent was not issued until 1942, aerosil was successfully produced for the first time by the original flame hydrolysis process in 1941

(*14*). The inventor, H. Kloepfer, told me that the idea behind this high-temperature hydrolysis had taken shape in 1934. The details of this process were published in 1959 and later (*15, 16*). In 1955, Flemmert (*17*) succeeded in exchanging the $SiCl_4$ used in the aerosil process with SiF_4. This Fluosil process was used in Sweden for about 15 years, and a recently built factory belonging to Grace commenced production in Belgium with this method in 1990.

Synthetic silicas in powder form are used in a wide range of applications. A breakthrough in certain fields was made possible only by the existence of these synthetic silicas, for example, the silicone rubber that was developed in the United States.

The existing market in 1990 in the Western hemisphere was estimated to be about 1 million metric tons per annum. Table II gives the approximate distribution of these products in powder form according to the different types. The capacity has doubled since 1974 (*1*). If the Eastern hemisphere is included, the value of 1 million metric tons per year increases by approximately 20%.

Table II. Estimated Distribution of Synthetic Silicas in Powder Form for 1990 in the Western Hemisphere

Silica Type	*Amount (1000 tons)*	*Percent of Total Amount*	*Percent of Total Value*
Precipitated	810	80	51
Fumed	100	10	33
Gels	90	9	15
Arc	<1	<1	<1
Total	1000	100	100

The large quantities of "fly ashes" that originate from the generation of energy in power stations and from the "silica fume" by-product of metallurgical processes should also be mentioned. Especially in toxicological literature, the terms "silica fume" and "fumed silica" are used synonymously; this usage is misleading, because the coarse particles of "silica fume", for instance, could cause irreversible changes in the lungs of mammals.

The production of "silica fume" for 1985 was 1.2 million metric tons per year (*18*). If an annual increase rate of 4% is calculated, this figure should have risen to 1.46 million metric tons per year by 1990. Fly ashes and silica fume were given off into the atmosphere on a virtually uncontrolled basis from about 175 production plants in 1985 (*19*). In addition, plasma processes have been used since 1968 to produce

synthetic silicas in powder form (*20, 21*), although these are of no technical relevance.

Nomenclature and Classification of Types

Until 1985 silicas were usually divided into two groups: natural and synthetic. Most of the naturally occurring SiO_2 modifications are crystalline, but this group also includes amorphous or mostly amorphous products, such as diatomaceous earth or kieselguhr. However, when the observations made at the end of the introduction are considered, this classification no longer proves sufficient, as fly ashes and silica fume are also synthetically produced, although not deliberately. These "airborne dusts" are not harmless (*22*).

For this reason, I submitted a proposal in 1985 (*23*) that a differentiation be made between "specifically produced" products and materials that necessarily accumulate. "Specifically produced" silicas are the desired main products, the quality of which is constantly monitored and controlled. This is not the case with the products that necessarily accumulate and are produced on an "uncontrolled" basis.

The products belonging to this uncontrolled group tend to be classified as amorphous (*22, 24, 25*). However, it was shown with the aid of X-ray diffractometer curves that dusts of this nature display the first signs of a short-range order, unlike the specifically produced products (*26*).

In the old classification system, the groupings were

- natural silicas (mostly crystalline)
- synthetic silicas (amorphous)

Under the new system, the classifications would be

- natural silicas
- specifically produced silicas
- uncontrolled dusts

Table III shows the categories used to classify synthetic silicas during the conference "Silica Fume in Concrete" held in 1987 at Montreal.

The term "synthetic amorphous silicas" (SAS) dates to 1985, when a number of people from the American Society for Testing Materials (ASTM) formed a working group called SAS. When discussing amorphous silicas, researchers differentiate between

- pyrogenic or thermal silicas and
- wet-process silicas.

Table III. Classification of Some SiO_2 Terms (Montreal 1987)

Term	*Origin*	*BET Surface Area (m^2/g)*
Fly ashes	power stations	~3
Silica fume	metallurgical processes	~15
Synthetic amorphous silicas	specifically produced	>50

Table IV. Principal Differences between Characteristic Properties of Pyrogenic and Wet-Process Silicas

Property	*Pyrogenic*	*Wet-Process*
SiOH density (per square nanometer)	2–3	~6
Drying loss (%)	2–3	~6
Ignition loss (%)	2	5
Aggregate particle size (μm)	—[a]	2–10
Impurities	slight	higher
Density (g/cm^3)	2.2	2.0
Pore volume	0	—[b]
Price	high	lower

[a]Not obtainable.
[b]Always present.

For many years there was considerable confusion regarding the nomenclature of SAS (*27*, *28*). The categories used here for the production processes of SAS were first published in 1968 (*29*) and were also maintained in reference 1. Further information about the historical details surrounding this chosen system of classification is given in reference 1. The basic categories used in classifying SAS are

1. pyrogenic or thermal silicas (also called fumed silicas)
2. wet-process silicas
3. after-treated silicas, which include
   - physical,
   - chemically fixed, and
   - coated treatment

Further details are given in Table IV.

Differences among the Types

A standard practice is to characterize SAS by physicochemical data (*1*). Some difficulties are encountered when the data given by different

manufacturers are compared: first, because test methods have not been generally adopted [dibutyl phthalate (DBP) adsorption, pore distribution, and methanol wettability], and second, because the correlations with the application-related properties, which are of interest to the user, are not widely known.

Nonetheless, it is possible to demonstrate several clear differences between pyrogenic and wet-process SAS (Table IV). The principal difference lies in the silanol group density given in the top line of this table, which in turn determines both the drying loss (generally expressed as moisture) and the ignition loss. Because pyrogenic silicas do not generally undergo a grinding process directly after production, it is not possible to state the agglomerate particle size of this group of products. Each method of analysis would provide a different result, depending on how the sample was handled prior to testing. The difference in the interstitial or pore volume is considerable: pyrogenic silicas are compact; that is, they have only an interparticle volume. Wet-process silicas always have a clearly definable share of internal pore volume.

The size of the specific surface area, which is often determined according to the Brunauer–Emmett–Teller (BET) method (*30*), is easily reproducible, but gives no indication as to the existence of an internal or external surface. The submicroscopic (and microscopic) pore volume is determined, for instance, according to the de Boer "*t*-curve method" (*31*, *32*)

Commercial pyrogenic silicas usually tend to be purer than wet-process silicas (Table V). Data of a very high-grade silica (silica in its purest form), which is only available in pilot-plant amounts at present, are included in Table V.

Table V. Comparison of SiO_2 Content and Total Impurities after 2 h at 1000 °C

SiO_2 Source	*SiO_2 (%)*	*Impurities (ppb)*
Wet-process method	98–99	<2,000,000,000
Pyrogenic method	>99.8	200,000
Aerosil in its purest form	>99.9999	<100

The differences between precipitated silicas and silica gels should be discussed. If the water-vapor adsorption behavior of two products with practically the same BET surface area is compared, distinct differences are apparent (Figure 1) (*33*).

The isotherms of silica gels can be recognized as being in the form of a standing "S", and those of precipitated silicas are shown as a lying "S".

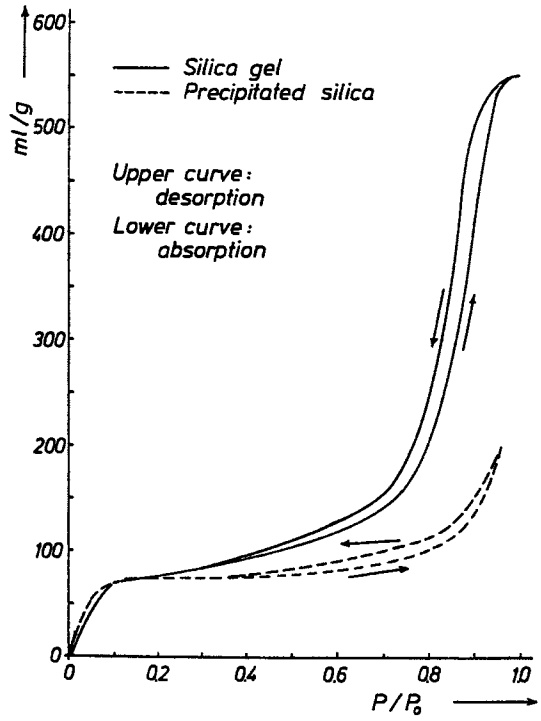

Figure 1. Water adsorption isotherms of a silica gel and a precipitated silica at room temperature. The existing pressure is p, *and the pressure in the saturated state is* P_0.

During the water-vapor adsorption, the silica gels approach the saturation point, whereas this point is not reached by the precipitated silicas.

The difference in the pore volumes is apparent if measured according to reference 31. Figure 2 gives pore distribution curves of the products shown in Figure 1. Figure 2 illustrates how precipitated silicas have relatively wide pores, and in particular a wide range of pore diameters, whereas silicas gels also have relatively narrow pores and display well-defined maximum peaks in the pore distribution curve (*33*). By means of physical after-treatment, it is possible to subsequently enlarge the pores of silica gels, so that these products assume adsorptive properties normally restricted to precipitated silicas (*34*). A further distinct difference becomes apparent (*35*) if the specific surface area according to Carman (*36*) is measured as a function of the porosity ϵ, which plays an important role in the Carman equation.

Synthetic amorphous silicas were characterized by Von Buzagh (*37*) as early as 1937. In 1953, Iler (*38*) wrote about the convenience of differentiating between precipitated silicas and silica gels. Stauff elabo-

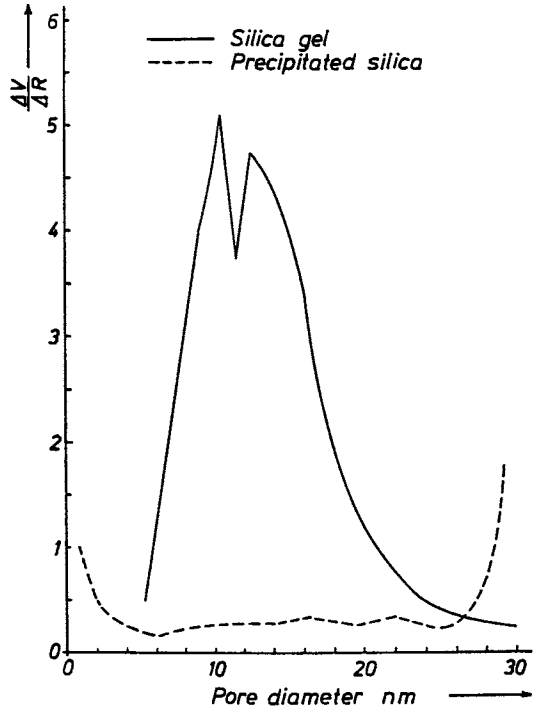

Figure 2. Comparison of the pore diameter distribution curves of a silica gel and a precipitated silica (33). V and R denote volume and radius, respectively.

rated on this subject in 1960 (*39*), and this work was endorsed by Iler in 1973 (*40*). The details are compiled in reference 1.

Electron microscopy is useful in studying silicas. Both transmission and scanning electron microscopy have greatly contributed to the understanding of the primary particle size and their distribution functions. These microscopies have also led to a considerable increase in knowledge regarding the points of adhesion that result in the formation of aggregates. However, electron microscopy cannot be used to differentiate between SAS in every case. This subject is dealt with in reference 41.

After-Treated Synthetic Amorphous Silicas

All forms of SAS may be after-treated. There are several kinds of possible after-treatment. Physical after-treatment—which does *not* include grinding in SAS—plays virtually no role here, although some such types were available on the market (e.g., Syloid 73).

The methods of after-treatment, together with the classifications used in the literature until 1973, were compiled in an article in 1976 that

includes nearly 100 references (*1*). The increase in patent literature on this theme has been particularly apparent. The materials that have been used for the chemical after-treatment of SAS and the date that their use was suggested are as follows (*1*):

- 1944, compounds containing chlorine
- 1951, silicone polymers and other polymers
- 1954, compounds containing oxygen
- 1968, compounds containing nitrogen

Kistler was the first person (1944) to suggest the use of chemical after-treatment (*42*), and the first industrially produced after-treated SAS was brought onto the market in 1962 (*43*). This product now bears the trade name Aerosil R 972.

The suggestions are of course given only in a rough and simplified form in the preceding list. For example, after-treatment with fluorinated compounds was also suggested (*44, 45*). A silica gel that has been after-treated with hydrofluoric acid develops hydrophobic characteristics to the same extent as Aerosil R 972, which is after-treated with dichlorodimethylsilane. Figure 3 (*46*) demonstrates the different behavior of Aerosil 130 (the untreated synthetic amorphous silica) and Aerosil R 972 for water adsorption.

Defining "hydrophobicity" is difficult. A comparison of the different test methods (*47*) shows that varying results are obtained. The level of the

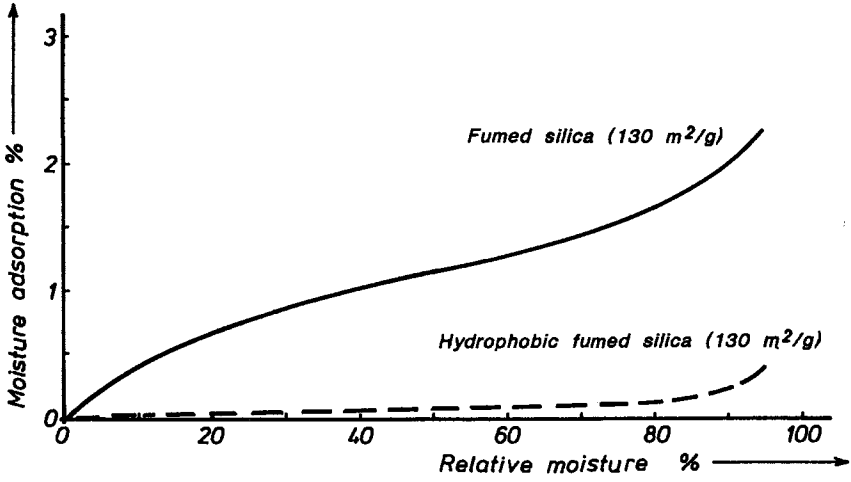

Figure 3. Water vapor adsorption isotherms at room temperature of the basic hydrophilic silica (top) and the hydrophobic grade produced with this material (bottom) (46).

carbon content, in particular, is not a measure for the degree of hydrophobicity. Until a few years ago, the terms "after-treatment" and "hydrophobicity" were synonymous when used in connection with SAS. However, because of the constant increase in the number of new after-treated products, new applications are being discovered for which hydrophobic properties are not required.

The use of chemically aftertreated SAS to improve special properties is discussed in a later section. Coating procedures, which do not involve firmly bonded groups or molecules on the surface of the synthetic amorphous silica as a result of a chemical reaction, are also important, particularly for SAS that are used as flattening agents in the coatings industry. Both silica gels (*48*) and precipitated silicas (*49*) may be coated with wax. This coating improves the suspension behavior and the redispersibility in liquid coatings and improves the scratch resistance or "nail hardness" of the dry coating film. During this coating process, the waxes are attached to the surface by means of adsorption (*33*).

Applications

As mentioned in the introduction, SAS are used in many fields. Only the most significant applications are discussed here. The extensive patent literature is not considered here. Figure 4 (*50*), published in 1982, gives an overview of the applications together with the types of SAS generally used in each case.

Improvement of Mechanical Properties. The most important application of SAS, and one of the oldest, is the control of the mechanical properties of rubber. SAS are important additives for both styrene–butadiene rubber (SBR) and natural rubber (NR), second in importance only to carbon black (*51, 52*). Figure 5 demonstrates the increase in tensile strength at room temperature for silicone rubber with various reinforcing fillers and kieselguhr. An improvement is also brought about in the mechanical strength of fluoroelastomers and other special kinds of rubber (*51*). Table VI summarizes the improvements that may be achieved in other fields.

Rheological Additives. SAS serve as excellent rheological additives in a large number of liquid, pastelike, or thermoplastic systems and in solids. Between 0.1 and 2% of the additive is used for applications of this kind, whereas between 3 and 33% is used for the carrier applications discussed in the following section. Table VII lists the applications in which SAS are used as rheological additives.

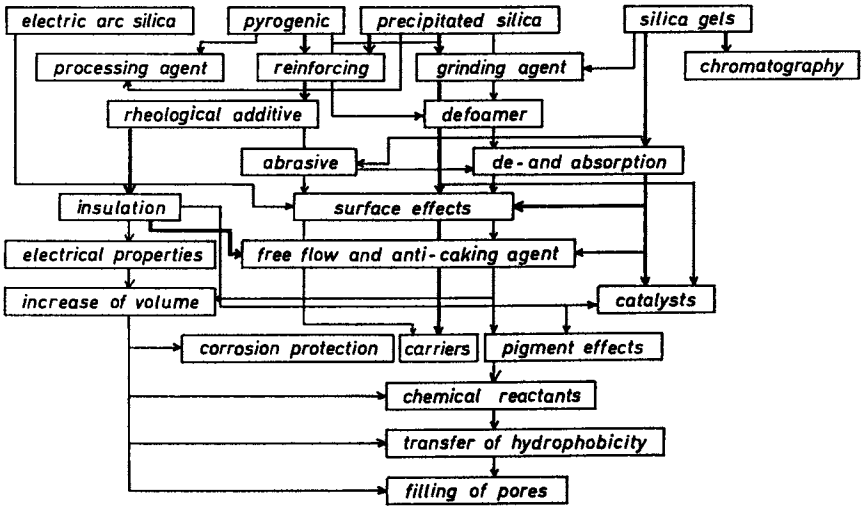

Figure 4. Overview showing the application of SAS. (Reproduced with permission from reference 50. Copyright 1982.)

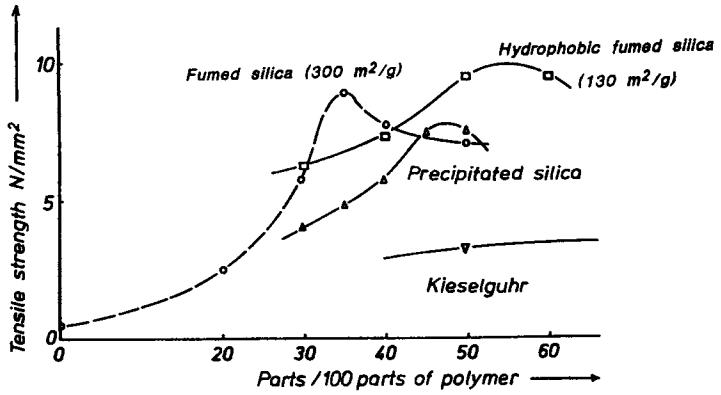

Figure 5. Increase in the tensile strength at room temperature of silicone rubber containing various fillers.

Carrier Applications. These applications are understood to mean fields of use in which the applied amounts of SAS exceed 2%. By far the most important application is choline chloride in a 60 or 75% aqueous solution that is transformed into a pressure-stable, free-flowing powder with the aid of spray-dried precipitated silicas. Another significant use is as plant protectants and pesticides; SAS are being used in a wide range of applications in this field. An overview of these applications is given in Table VIII (53).

Table VI. Improvement of Mechanical Properties by SAS

Application	*Improvement*
Thermoplastic materials	increase of hardness
	improvement of the form stability by increased temperatures
Adhesives	heat stability
Decorative paints	sanding of household paints
Toothpastes	tailor-made abrasiveness
Wettable powders (pesticides) and dusts	grinding additive

SOURCE: Reprinted with permission from reference 50. Copyright 1982.

SAS are also used in pharmaceutical applications, for example, in the conversion of plant extracts (such as extract valerianae) into free-flowing, pressure-stable powders that are then used to form tablets (*54*).

Surface Effects. The surface properties of coatings and printing inks can be changed, as can the properties of plastic films and the surface of paper. The coatings industry uses the largest quantity of SAS. An addition of SAS allows a controlled roughening of the coating surface that produces a flattened or matte effect (*55*) (Figure 6). This effect is of particular interest for furniture coatings, coil coatings, and clear finishes for artificial leather. The desired degree of flattening can be regulated according to the particle size and effective particle volume of the SAS chosen and by the amount of silica added. All types of synthetic amorphous silica are used in this particular field of application.

Two problems can occur during the processing and application of plastic films; these are known as "blocking" and "slip". Blocking describes the state that occurs when two films lying on top of each other are difficult to separate because of unwanted adhesion. It is particularly important to prevent this effect with video tapes and other such films.

Slip describes the gliding motion of thick plastic films used for packaging; heavy goods piled on top of one another are in danger of sliding if the surface of these packaging films is too slippery. SAS are also used during the manufacture of cellulose films to reduce surface slip (*33*). Another field of application is in the coating of high-grade papers that are used, for example, in the ink-jet or photocopying processes. An improvement in the adsorptive capacity of the paper results in a high uniformity of the surface (*57*).

As a rule, 3–7% of synthetic amorphous silica is required for applications in the coatings sector, whereas 0.2–2% is needed in the other

Table VII. Fields in Which SAS Are Used To Improve Rheological Behavior

Field	*Type*[a]	*Improvement*
Liquid systems		
Adhesives	pp, ps, sg	brushability, no cobwebbing
Coatings and inks	ps, (sg, pp)	thixotropy, formation of yield points, sharper points
Effect coatings	ps	reinforcing the effects
Gel coats and casting resins	ps, (sg)	thicker layers, no sagging, prevention of sedimentation
Toothpastes	pp, ps, (sg)	workability
Powders		
Coffee, milk and fruit powders	ps, pp, sg	free flow, prevention of caking
Fire extinguishers	ps, pp	free flow, prevention of caking
Garlic, tomato and other powders	ps, sg	free flow, prevention of caking
Inorganic salts, fertilizers	pp, ps	free flow, prevention of caking
Powder coatings, fluid bed systems, toner powders	ps, (pp)	free flow, prevention of caking
Spices, vitamins, amino acids	ps, (pp, sg)	free flow, prevention of caking
Tablets	ps, (pp, sg)	free flow, prevention of caking
Wettable powders	pp, (ps)	free flow, prevention of caking
Thermoplastic Systems		
Plasticized PVC	pp, (sg)	prevention of plate-out

[a]Abbreviations are ps, pyrogenic silica; pp, precipitated silica; and sg, silica gel. Abbreviations in parentheses refer to less-significant applications.

fields of application. The market shares for the coatings, plastics, and paper sectors in 1990 were in the ratio 10:5:1, respectively.

Pigment Effects. These effects are achieved in practice only with precipitated silicates. This effect is of special significance in emulsion or latex paints and in paper coatings. These applications play a more minor role in the United States than they do in Europe and Asia. Part of the titanium dioxide content in the paint and paper-coating applications is substituted with precipitated silicates without causing a deterioration in the brightness or opacity. The amount of silicate added must not exceed

Table VIII. Most Important Uses of Silica in the Formulation of Plant Protectants and Pesticides

Form Applied	*Active Ingredient Content*	*Particle Size*	*Typical Use*	*Typical SiO_2 Concentration (%)*
Dust	<2%	<45 μm	free-flow agent	<3
			grinding additive	<10
Dust concentrates	40–90%	<45 μm	free-flow agent,	<3
			carrier and grinding additive	<40
Wettable powders	30–80%	<45 μm	carrier,	15–35
			grinding additive,	<10
			free-flow agent	<3
Granules	<5%	<3 mm	anticaking agent	<3
Water-dispersible granules	5–80%	<3 mm	carrier,	15–35
			grinding additive,	<10
			free-flow agent	<3
Suspension concentrates and flowables	30–60%	<5 μm	suspension stabilizer,	approx. 0.5
			control of crystalline growth	approx. 0.1

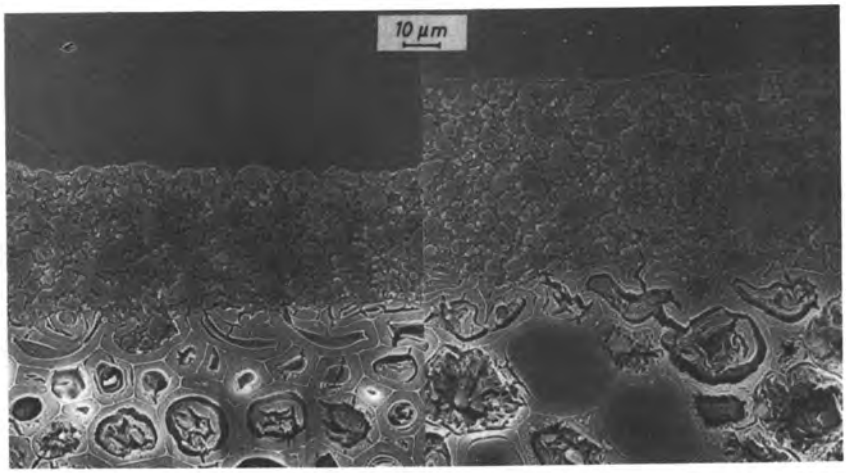

Figure 6. Scanning electron micrographs depicting microtome sections of wood glazes on absorbent wood: left, control paint; right, paint containing 1.5% fumed silica related to the total coating mass. The presence of this material prevents the coarser SiO_2 particles of the flattening agent from settling.

5% of the total paint because of the high oil adsorption of these silicates (*56, 57*). This application is gaining in importance as a result of the current shortage of TiO_2 on the market and the constantly rising price of TiO_2. Precipitated silicates and silicas are also being used more and more in the paper pulp itself. Because of differing demands, a clear regional splitting can be observed. The main area of use is Japan, followed by Europe. Only recently has the use increased in the United States and Canada. For price reasons, the amounts added in these applications are 1–2%. The main improvement is in the printability; the increased brightness is of less significance.

Electrical Effects. By means of adsorption, pyrogenic SAS reduce the number of charge carriers that contribute to the conductivity in poly(vinyl chloride) (PVC) high-voltage cables. As Figure 7 shows, this change brings about a reduction in the dielectric losses; that is, the cables can be used at higher temperatures (*33*). When used in high-temperature vulcanization (HTV) silicone rubber, these pyrogenic SAS affect the electrical properties as a whole far less than precipitated silicas do; thus, these silicas are not used in cable applications (*58*).

An increasing use is also being made of pyrogenic silicas in the prevention of electrostatic charges in powdered substances (*33*). These silicas play an important role, for instance, in the pharmaceutical industry,

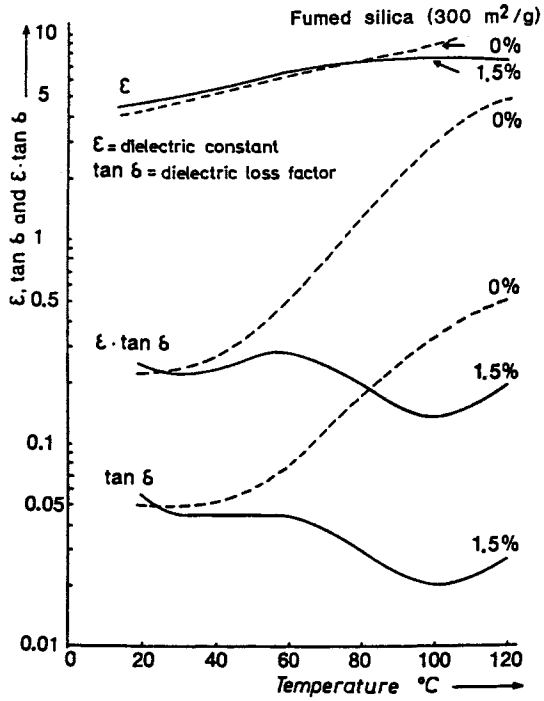

Figure 7. Dielectric properties of plasticized PVC with and without a fumed silica (300 m²/g) as a function of temperature.

where they are used to maintain an undisturbed process of making tablets, or in the grinding of sulfur for pesticides.

After-treated pyrogenic SAS have been used lately to an increasing extent to regulate the triboelectric properties of toner powders. The extent of the effects that can be attained is shown in Table IX.

Adsorption. The adsorption of water vapor from mixtures of gas is the main application in industrial practice. This field is the domain of silica gels (Figure 1). The economic advantages afforded by the use of silica gels are further increased by the ability to regenerate the wet silica gels. Silica gels are not only used in dynamic applications of this nature, but are also used for static applications, such as in the protection of chemicals or in the production of insulating glass for double glazing.

A less significant but nevertheless interesting application is the use of SAS to adsorb certain substances in beer to prevent the beer from becoming cloudy as a result of lengthy periods of storage or excessive cooling. Both silica gels and precipitated silicas are used for this application. Approximately 50–100 g/hL are required. This field of application is

Table IX. Charge-to-Mass Ratios of Aerosil 200 and Some After-Treated Silicas Based on This Material

Sample	*Ratio (μC/g)*	*Relative*[a]
VT 501	−560	311
VT 502	−530	294
VT 500	−400	222
R 974	−330	183
R 811	−230	128
Aerosil 200	−180	100
X	−150	83
Y	−50	28
VT 330	−9	9

[a]Percent of aerosil 200 value.

also undergoing changes. Europe has been the main area of use, but now the United States, Japan, and Australia are gaining in significance.

Similar use is made of pyrogenic SAS in the adsorption of blood components (γ-globulins) from human blood to increase the storage stability of the specially produced blood products. As in the application of SAS in breweries, the SAS do not remain in the beer or in the blood, but are removed almost without trace by filtration and centrifugation.

Catalysis. The production of catalyst supports for a wide range of applications will remain an important field for silica gels in the 1990s. Specially purified silica gels are shaped, dried, and coated. Because of their inferior deformability and stability, molded tablets of other SAS play a subordinate role in the manufacture of catalyst supports (e.g., for the polmerization of olefins). However, the use of pyrogenic SAS for this application is also growing, as the large number of patent applications proves (*59*). As with adsorption processes, the size of the pore volume remaining after the deformation is of utmost importance. The systems SiO_2–Ni, SiO_2–Pt, and SiO_2–Ag are of particular interest. Although hydrogenation and reduction are the primary reactions connected with SAS, work has also been carried out on oxidation and polymerization reactions (*60*). The so-called "spillover effect" on Pt-coated Aerosil is also worthy of note: ethylene is converted to dideuteroethane with the aid of D_2 (*60*).

Use of After-treated SAS for the Improvement of Properties. After-treated, mainly hydrophobic SAS can be used in a large number of applications to produce special effects that cannot be achieved at all (or not as effectively) with the hydrophilic source silicas. An example is the improvement of the corrosion protection of primers for the car industry

(*61*). Figure 8 shows a typical effect. A well-defined hydrophobic effect brought about by after-treated SAS is used to regulate the water balance of offset printing inks (*62*).

Figure 8. Zinc dust paints based on an epoxy ester after a 168-h salt spray test in accordance with DIN 50 021 and ASTM B 117-64: left, control paint; right, paint containing 2% Aerosil R 972 related to zinc dust mass.

Special effects have also been established during the improvement of the free-flow properties of products in powder form. Unfortunately, it is not yet possible to predict under which conditions a hydrophobic synthetic amorphous silica will produce better results than a hydrophilic (i.e., untreated) one. A similar situation exists in the area involving the thickening of technically important resins [e.g., special unsaturated polyester or epoxy resins (*63*)].

Other Uses. Not all of the possible applications of SAS have been discussed here. A number of other applications are listed in alphabetical order in Table X. In the future, precipitated silicas may be used to a considerable extent for low-temperature insulations (e.g., for refrigerators). A moisture-resistant film with added silica has outstanding heat resistance and does not need any fluorinated hydrocarbons. SAS will likely be used as raw materials for pure silica glass for applications with rigorous requirements. The purity and uniformity of such SAS will have a great influence on the final properties. New applications will undoubtedly follow.

Summary. Table XI is an estimation of the consumption figures for the different fields of application. These values were based on the 1 million metric tons per year for 1990 (Table II). At the same time, an attempt was made to weight these values in such a way as to express the importance of the respective SAS types.

Table X. Other Uses for SAS

Application	*Type*[a]
Battery separators	pp
Chewing gum	ps, pp
Chromatography	sg
Cigarette filters	sg, ps
Control of crystalline growth	pp, ps
Defoamer	pp, ps, sg
Fish feed	pp, (ps)
Foundry additives	pp, ps
High-temperature insulation	ps
Instant soups	pp, (ps)
Matting of bulbs and fluorescent lamps	pp, ps
Phlegmatization of organic peroxides and explosives	pp, ps
Silica greases	ps
Special detergents	pp, ps
Stain remover	pp, ps
Suspension aid	ps
Thickening in car batteries	ps

[a]Abbreviations are defined in Table VII.

Table XI. Estimated Consumption of SAS in the Western Hemisphere for 1990

Application	*Consumption (metric tons/year)*	*Percent of Total*	*Type*[a]
Reinforcement	730,000	73.0	pp (ps)
Rheology	8,000	0.8	ps
Carrier	75,000	7.5	pp
Surface effects	25,000	2.5	ps, pp, sg
Pigment effects	50,000	5.0	pp
Electrical effects	7,000	0.7	ps
Adsorption	25,000	2.5	sg
Catalysis	30,000	3.0	sg
Hydrophobic grades	5,000	0.5	
Various	45,000	4.5	
Total	1,000,000	100.0	

[a]Abbreviations are defined in Table VII.

Handling of SAS

The need to observe the respective values for the maximum concentration of a substance at the place of work has meant that questions involving the handling of SAS have assumed an important role. The current value is set at 4 mg/m^3 of total dust, both in the United States and West Germany.

Handling is also gaining significance for ecological reasons. In Europe, about 25% of SAS is still being delivered in paper sacks. Difficulties arise with the polyethylene-coated paper sacks, which cannot be recycled at present. As a result of a yearly increase of 8% (1988) in total waste produced in West Germany, SAS consumers are encountering increasing difficulties and costs to dispose of the empty paper sacks. For this reason, it is of major importance that the pneumatic conveyance of SAS functions well. Distances of up to 300 m and differences in height of up to 25 m pose no great technical problems. Moreover, the weighing and measuring of SAS needs to be carried out both continuously and discontinuously with sufficient accuracy.

Mechanical conveyance—for example, with angle-type bucket elevators—is only recommended for granulated products, such as those used in the rubber industry.

Questions Regarding Registration and Approval

In the past, non-after-treated SAS bore the Chemical Abstracts Service (CAS) registry number 7631–86–9, aluminum silicates bore the number 58425–86–8, and calcium silicates the number 1344–95–2. SAS that were after-treated with dichlorodimethylsilanes were given the number 60842–32–2 (formerly 68611–44–9), and SAS after-treated with polysiloxanes the number 67762–90–7. Thanks to efforts by SASSI (Synthetic Amorphous Silica and Silicates Industrial Association), new numbers have been assigned since June 7, 1989, which are designed to allow a better differentiation between the amorphous and crystalline substances. The following numbers are now valid for the different types of SAS:

- for fumed amorphous silicas, 11.2945–52–5
- for precipitated silicas, 11.2926–00–8
- for silica gels, 11.2926–00–8

As these numbers are not yet listed in the legal inventories of toxic chemicals in the United States, Europe, Australia, and Canada, it is also necessary to give the old CAS registry numbers. This situation causes certain problems—at least in countries outside the United States.

Synthetic silicas are permitted for use in many countries as anticaking agents in foodstuffs in powder form. National regulations must be observed here. In the United States, silicon dioxide is used in an amount not to

exceed 2% by weight of the food and is a direct "food additive" (*64*). In West Germany, a direct allowance is given only for salt, chewing gum, and some other foodstuffs. Silica is registered in the European Community under E551 as a food additive. The peroral harmlessness of SAS for human beings is established by the World Health Organization–Food and Agriculture Organization with its classification "unlimited daily intake".

"Silica" is also mentioned in the United States as an indirect food additive without any limitation in reference 64, parts 175–178, for adhesives, components of coatings, paper and paperboard, organic polymers, production aids, auxiliaries, and sanitizers. In this respect, the guidelines in Germany are very similar.

Each subdivision of SAS (fumed, gels, and precipitated) is listed separately in several national pharmacopoeias, for example, in the USPXX-I/NFXVI and in the pharmacopoeia of the European Community.

The testing of SAS according to the National Institute of Occupational Safety and Health (NIOSH) test number 7601, for example, can never serve as an exact procedure for the differentiation of crystalline or amorphous silica. The test may be useful (to a certain extent) for determining the content of respirable or total dust in airborne samples in order to ascertain the approximate degree of risk for the human lung.

Toxicology

SAS can affect the health of a human being by skin contact, inhalation, or peroral intake.

Skin Contact. Employees coming into contact with SAS sacks or dusts occasionally complain of itchiness or reddening of the skin. The individual sensitivity of a worker certainly plays a role here. I have not heard of any permanent complaints or damage during my 32 working years. The results obtained for aerosil, for example, are compiled in reference 26, which includes numerous bibliographic references. In view of the possible occurrence of scleroderma, in 1989 the Industrial Injuries Insurance Institute for the Ceramics and Glass Industries said that no such case has been registered for more than 20 years (*65*).

Inhalation. In 1962, reports issued by a production plant for precipitated silicas in the United States (*66*) stated that employees who had worked for more than 16.5 years at a dust concentration of 0.35–204 mg of SiO_2 per cubic meter showed no signs of silicosis or any other dust-related lung disease. This statement was confirmed for precipitated silicas in West Germany after regular medical examinations were carried out on 131 employees who had worked for a maximum of 38 years (*26*). Similar findings were confirmed for arc silicas in 1982 (*67*). After exposure to the

pyrogenic aerosil for 14 years (*68*) and for more than 30 years (*26*), no silicosis had occurred. Furthermore, no signs of toxic effects were observed (*26*). On the basis of experience gained to date, no harmful side effects are to be expected with silica gels either.

It is interesting to note that in West Germany the "increased occurrence of bronchial carcinomas in patients with silicosis cannot be based on statistical records" (*65*). In other words, even if silicosis develops as a result of quartz dust, the silicosis cannot be associated with a cancerous disease. According to Mayer (*69*), the findings from animal experiments that showed that quartz dust also caused an increase in carcinomas cannot be applied to human beings.

Peroral Intake. The effect of orally ingested SAS plays a subordinate role in industrial toxicology (*70*). This fact is also taken into account by the WHO, which says the daily intake of SiO_2 is unlimited. None of the silicas are resorbed following oral administration. The LD_{50} for rats is therefore very large, as Table XII demonstrates.

Table XII. Acute Toxicity of Some SAS on Rats

Commercial Name	*Oral LD_{50} for Rats (mg/kg)*	*Institution*
Hydrophilic Aerosil types	>10,000	CIVO, TNO, NL (1979)
Hydrophobic Aerosil R 972	>5,000	Leuschner (1977)
Ultrasil VN 3 Calsil, Extrusil, and Pasilex (all hydrophilic)	>10,000	CIVO, TNO, NL (1979)
Coated OK 412	>1,000	Leuschner (1979)

SOURCE: Reprinted with permission from reference 65. Copyright 1987.

References

1. Ferch, H., *Chem. Ing. Techn.* **1976**, *48*, 922.
2. Anonymous *Am. Chem. J.* 1887, 9, 14.
3. Potter, H.N. U.S. Patent 875,674, 1907; 875,675, 1907.
4. BF Goodrich Co., German Patent 1,034,601, 1955; U.S. Patent 2,863,738, 1958.
5. Patrick, W. A. Thesis, Göttingen University, Germany, 1914.
6. Silica Gel Corp. U.S. Patent 1,279,724, 1918.
7. Patrick, W. A.; McGaunack, J. *J. Am. Chem. Soc.* **1920**, *42*, 946.

8. Kistler, S. S. *Nature (London)* **1931,** *127,* 741; *J. Phys. Chem.* **1932,** *36,* 52.
9. White, J. F. *Chem. Ind.* **1942,** *51,* 66.
10. IG-Farbenindustrie, German Patent 428,041, 1924.
11. Pittsburgh Plate Glass Co. U.S. Patent 2,287,700, 1942.
12. Boss, A. E. *Chem. Ing. News* **1949,** *27,* 677.
13. *75 Jahre Chemische Fabrik Wesseling AG*; Arch. f. Wirtschaftskunde GmbH: Darmstadt, Germany, 1955.
14. Degussa AG, German Patent 762,723, 1942.
15. White, L. J.; Duffy, G. J. *Ind. Eng. Chem.* **1959,** *51,* 232.
16. Wagner, E.; Brünner, H. *Angew. Chem.* **1960,** *72,* 744.
17. NYNÄS Petroleum, German Patent 1,208,741, 1955.
18. Anonymous *Minaeraçao Metalurgia* **1985** July, *49,* 466.
19. Anonymous *Metal Bulletin Monthly* **1985** July, 53.
20. Monsanto German Patent 1,940,832, 1968.
21. Lonza AG German Patent 2,337,495, 1972.
22. Regidor, M. Thesis, Grenoble, France, 1981.
23. Ferch, H. *Staub, Reinh. Luft* **1985,** *45,* 237.
24. Vitums, V. C.; Edwards, M. J.; Niles, N. R.; Borman, J. O.; Lowry, R. D. *Arch. Environ. Health* **1977,** *32,* 62.
25. Brambilla, C.; Brambilla, E.; Regaud, D.; Perdrix, A.; Paramelle, B.; Fourcy, A. *Rev. Fr. Mal. Resp.* **1980,** *8,* 383.
26. Ferch, H.; Gerofke, H.; Itzel, H.; Klebe, H. *Arbeitsmed., Sozialmed., Präventivmed.* **1987,** *22,* 6, 23.
27. American Cyanamid, U.S. Patent 2,114,123, 1938.
28. Burak, N. *Chem. Process UK* **1967,** *8,* 10.
29. Ferch, H. *IX. Fatipec-Kongreßbuch* **1968,** 144.
30. Brunauer, S.; Emmett, P. H.; Teller, E. J. *J. Am. Chem. Soc.* **1938,** *60,* 309.
31. De Boer, H. J. *J. Catalysis* **1965,** *4,* 646.
32. De Boer, H. J.; Lippens, B. C.; Linsen, B. G.; Brockhoff, J. C. P.; Van Den Henvel, A.; Osinga, Th. J. *J. Coll. Interf. Sci.* **1966,** *21,* 405.
33. Ferch, H. In *Lehrbuch der Lacke und Beschichtungen*; Kittel, H., Ed.; W. A. Colomb Verlag: D-Oberschwandorf, **1974**; Vol. 2.
34. W. R. Grace German Patent 1,036,220, 1955.
35. Kindervater, F. *XII. Fatipec-Kongreßbuch* **1974,** 399.
36. Carman, P. C. *J. Soc. Chem. Ind. London,* **1938,** *57,* 825; **1950,** *69,* 134.
37. Von Buzagh, A. In *Colloidal Systems*; Technic. Press Ltd.: London, 1937; p 149
38. Iler, R. K. *Colloid Chemistry of Silica and Silicates*; Cornell University Press: Ithaca, NY, 1953.
39. Stauff, J. *Kolloidchemie*; Springer-Verlag: Berlin-Heidelberg, 1960.
40. Iler, R. K. In *Surface and Colloidal Science*; Matijevic, E., Ed.; Wiley: New York, 1973.
41. Ferch, H.; Seibold, K. *Farbe Lack* **1984,** *90,* 88.
42. Kistler, S. U.S. Patent 2,589,705, 1944.
43. Brünner, H.; Schutte, D. *Chem. Zeitg.* **1965,** *13,* 437.
44. Davison Chem. Co. U.S. Patent 2,625,492, 1950.
45. Wilska, S. *Suom. Kem.; Finland* **1959,** *32B,* 89.
46. Ferch, H. *Farbe Lack* **1979,** *85,* 651.
47. Ferch, H. *13th Eurocoat Congress; Nice, France,* **1987,** 128.
48. W. R Grace German Patent 1,006,100, 1957.
49. Degussa AG U.S. Patent 3,607,337, 1968.
50. Ferch, H. *Progr. Org. Coat; Switzerland,* **1982,** *10,* 91.

51. Parkinson, H. *Reinforcement of Rubbers*; Lakemann: London, 1957.
52. Bachmann, H. J.; Sellers, J. W.; Wagner, M. P.; Wolf, R. F. *Hi-Sil*; Columbia Southern Chemical Corp.: Barberton, Ohio, 1960.
53. Ferch, H.; Reisert, A.; Bode, R. *Kautschuk Gummi, Kunststoffe* **1986,** *39*, 1084.
54. Ferch, H.; Müller, K. H.; Oelmüller, R. In *Technical Bulletin Pigments No. 1*, 5th ed.; Degussa AG: Frankfurt, Germany, 1989.
55. Ferch, H. *Pharm. Ind. Germany* **1970,** *32*, 478.
56. Ferch, H.; Flach, V. *Wochenblatt f. Papierfabrikation* **1987,** *115*, 10.
57. Ritter, H. S. *Paint Varn. Prod.* **1963,** *53*, 31.
58. Ferch, H. *Verfkroniek; Netherlands,* **1965,** *38*, 9.
59. Bode, R.; Ferch, H.; Fratzscher, H. *Kautschuk Gummi, Kunststoffe* **1967,** *20*, 699.
60. Ferch, H.; Koth, D. *Chem. Ing. Techn.* **1980,** *52*, 628.
61. Lenz, D. H.; Conner, W. C. *J. Catalysis* **1987,** *104*, 288.
62. Ferch, H. *Farbe Lack* **1979,** *85*, 651.
63. Schumacher, W.; Gräf, H. *Farbe Lack* **1971,** *77*, 237.
64. *Code of Federal Regulations*, Title 21, Part 172, Section 480.
65. *Technical Bulletin Pigments No. 27*, 4th ed; Degussa AG: Frankfurt/M., Germany, 1987.
66. Mayer, P., personal communication.
67. Plunkett, E. R.; De Witt, B. J. *Arch. Environ. Health* **1962,** *5*, 469.
68. Ferch, H.; Habersang, S. *Seifen-Öle-Fette-Wachse* **1982,** *108*, 487.
69. *Technical Bulletin Pigments No. 64*, 3rd ed.; Degussa AG: Frankfurt/M., Germany, 1987.
70. Volk, H. *Arch. Environ. Health* **1960,** *1*, 125.

RECEIVED for review October 19, 1990. ACCEPTED revised manuscript January 3, 1992.

25

Adsorptive Properties of Porous Silicas

Martyn B. Kenny and Kenneth S. W. Sing[1]

Department of Chemistry, Brunel University, Uxbridge, Middlesex UB8 3PH, United Kingdom

Four main types of porous silica adsorbents have been identified: compacts of pyrogenic powders, precipitated silicas, silica gels, and zeolitic silicas. The importance of porosity relative to the adsorptive properties of each group is reviewed, with particular reference to the adsorption of nitrogen, argon, and water vapor. The differences in size and specificity of these adsorptive molecules may be exploited to explore the surface properties of each grade of silica. A notable feature of Silicalite I, which is the best known of the zeolitic silicas, is its remarkable hydrophobic character. Furthermore, the uniform tubular pore structure of this microporous silica is responsible for other highly distinctive properties.

AMORPHOUS AND CRYSTALLINE FORMS OF SILICA are now widely used as industrial adsorbents and catalyst supports. The preparation of a highly active and inexpensive silica adsorbent is not difficult, but the fine tuning of the adsorbent activity is somewhat more demanding. Hence, over the past 40 years the upgrading of the adsorptive properties of silicas has presented a challenge to many academic and industrial research workers.

The microstructure of various amorphous silicas was first discussed in a comprehensive manner by Iler in his early book *The Colloid Chemistry of Silica and Silicates* (*1*). Iler drew attention inter alia to the importance of the dense silica particle size and particle packing density in controlling the surface and colloidal properties of sols, gels, and precipitates. In particular, he showed how a change in coordination number of these globular

[1] Current address: Department of Chemistry, University of Exeter, Devon EX4 4QD, United Kingdom.

0065–2393/94/0234–0505$08.00/0

particles could affect the porosity and hence the adsorptive properties of the dried materials.

Since 1955, many others have extended these principles of particle packing, and now secondary and tertiary assemblages can be identified within the microstructures of certain silica gels and precipitates (2, 3). Iler had proposed (*1*) that the minimum size of the dense silica globule was about 1 nm. Later Barby (2), making use of transmission electron microscopy, came to the conclusion that in many amorphous silicas the primary particle size was indeed 1–1.5 nm.

In their pioneering studies of silica sols, Alexander and Iler (*4*) employed low-temperature nitrogen adsorption to determine the surface areas of the colloidal particles after removal of the aqueous medium. The Brunauer–Emmett–Teller (BET) areas were found to be only slightly larger than the values obtained from the particle size distributions as determined by light scattering and electron microscopy. These remarkable measurements indicated little change in the particle size or shape after the stabilized silica sols were carefully dried.

Before the distinctive adsorptive properties of porous silica can be described, the different ranges of pore size that are of special importance to the mechanisms of physisorption must be identified. Micropores are the pores of the smallest width ($d < 2$ nm); mesopores are of intermediate size ($d \sim 2$–50 nm); macropores are the widest pores ($d > 50$ nm) (5). Amorphous silica gels tend to be mesoporous or microporous, whereas the crystalline zeolitic silicas possess intracrystalline microporosity. The precipitated silicas are macroporous and also, to a small extent, microporous. These and other aspects of the microstructures will be discussed in the following sections.

Compacts of Pyrogenic Powders

From the standpoint of gas adsorption, the pyrogenic silicas can be regarded as essentially nonporous. Transmission electron microscopy has revealed that the high-temperature arc silicas, and to a lesser extent the flame-hydrolyzed "fume" silicas (e.g., Degussa Aerosils), consist of discrete spheroidal particles. According to Barby (2), these globules are in fact composed of primary particles of about 1 nm. The coordination number is so high that there is virtually no microporous structure; in their original, loosely packed state, these powders give physisorption isotherms (e.g., nitrogen at 77 K) of Type II in the Brunauer (*6*) and International Union of Pure and Applied Chemistry (IUPAC) (5) classification (Figure 1). This type of isotherm is associated with unrestricted monolayer–multilayer adsorption, the stage of monolayer completion being indicated by point B in Figure 1 (*7*).

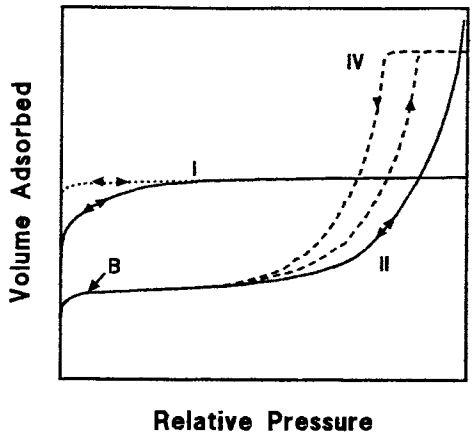

Figure 1. Types of physisorption isotherms given by porous and nonporous solids.

Well-defined pore structures are developed as a result of compaction of the fume silicas (*8*, *9*). If the compaction pressure is not too high [~10 tons in.$^{-2}$ (245 giganewtons m^{-2})] the nitrogen isotherm becomes similar to Type IV in Figure 1. The initial part of the isotherm is scarcely changed: The area of particle–particle contact is low, so there is little overall loss of surface area. However, at higher relative pressures capillary condensation occurs in the newly created mesopores and causes the isotherm to swing upwards away from the original (Type II) path until the pores are all filled and the isotherm reaches a plateau.

Very small particles of fume silica were compacted in the work of Avery and Ramsay (*8*), who found that high compaction pressures resulted in the conversion of the isotherm type from IV to I. A drastic loss of BET area accompanied this change (from 630 to 219 m^2/g), and Avery and Ramsay concluded that this change was associated with a marked increase in particle packing density. The shape and reversibility of this Type I isotherm was a clear indication that the effective pore width had been reduced to below 2 nm, that is, that the compact had become microporous.

Clearly, highly active mesoporous or microporous silicas cannot be produced by the compaction of nonporous powders, but Avery and Ramsay's (*8*) and other compaction studies (*10–12*) confirmed the importance of particle coordination in determining porosity and hence, adsorptive properties.

Precipitated Silicas

The surface properties of precipitated silicas have not been studied in as much detail as those of the fume silicas or gels. On the other hand, the

extensive patent literature is an identification of the industrial importance of these materials (*2*, *3*).

The gas adsorption measurements by Zettlemoyer and co-workers (*13*, *14*) appeared to indicate that some precipitated silicas (e.g., HiSil 233 from Pittsburgh Plate Glass Company) behaved as nonporous adsorbents. Thus, reversible Type II isotherms of nitrogen and argon were obtained by Bassett et al. (*14*), who concluded that unrestricted monolayer–multilayer adsorption had occurred. More recent work (*15*) showed that this interpretation is probably an oversimplification of the physisorption process.

In contrast to the behavior of the pyrogenic silicas, the level of nitrogen physisorption by several precipitated silicas was especially sensitive to change of outgassing temperature. Analysis of the adsorption data by the conventional BET method indicated an apparent increase in the surface area of ~26% over the range of outgassing temperature of 25–200 °C (*see* Figure 2). A more rigorous interpretation of the nitrogen isotherms, by application of the: α_s-method (*16*), revealed that this change was misleading and that the increase in BET area was associated with the development of microporosity (*15*). A_s is the external area obtained by affiliation of the α_s-method (*16*), and V_{mic} is the derived micropore volume.

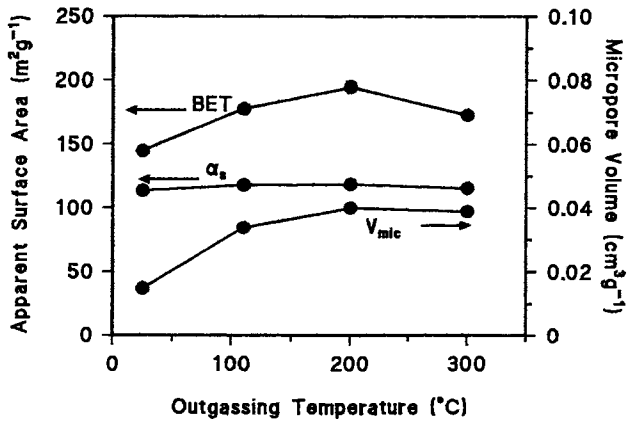

Figure 2. The effect of outgassing temperature on the BET area, α_s external area, and micropore volume (V_{mic}) for precipitated silica VN3.

The behavior of the precipitated silicas with respect to the adsorption of water vapor was even more anomalous (*17*, *18*). Kiselev (*11*) and others (*19*) had demonstrated that in the fully hydroxylated form, a wide range of nonporous pyrogenic silicas gave rise to a common reduced water isotherm (i.e., adsorption per unit area versus relative pressure). However, in the

precipitated silicas, the level of water adsorption was much higher than expected for monolayer adsorption. There seemed little doubt that water molecules were able to penetrate into very narrow pores that could not accommodate nitrogen or other molecules (*17*).

The abnormal behavior of the precipitated silicas appears to be due to the presence of trapped hydroxyl groups within the secondary particles. Thus, although the primary globules are densely packed within the secondary agglomerate, they apparently remain partially hydroxylated. The internal hydroxyls undergo hydrogen-bonding with water molecules, which are able to move in and out of the secondary particles. It is evident that the removal of these hydrogen-bonded water molecules also leads to the development of the small micropore volume.

Silica Gels

A large number of gas adsorption studies (*2*, *3*, *7*, *11*, *20*) have been reported on high-area silica gels, but unfortunately much of this work was carried out on ill-defined samples of unknown origin. Silica hydrogels are usually prepared by reacting silicate and acid in an aqueous medium. The properties of the final product (normally a xerogel) are controlled by the conditions under which the condensation–polymerization reaction occurs and by the after-treatment (washing and removal of the liquid phase). Syneresis takes place when the wet hydrogel is allowed to stand, and considerable further shrinkage of the solid accompanies the hydrogel–xerogel conversion.

The dependence of the xerogel porosity on the conditions of gelation has been investigated (*22*). In the early work of Sing and Madeley (*21*, *22*) a microporous product was obtained from the hydrogel prepared from sodium silicate and sulfuric acid at pH 3.5. Mesoporous structures developed when the reaction was carried out at higher pH (~6). On the other hand, changes in the silicic acid concentration over a wide range had very little effect, provided that the gelation was conducted in a buffered aqueous medium (*21*).

Acid washing appears to result in partial depolymerization of the hydrogel (*23*, *24*), which in turn leads to some enhancement in the adsorption activity. The effect is illustrated by the results in Figure 3. In this case, the original hydrogel was prepared at pH 5.4 and portions were then subjected to different forms of after-treatment (*25*). Soaking in HCl (at pH 2.0 for 24 h) resulted in significant upward movement of the nitrogen isotherm, that is, increase in both the BET area (from 284 to 380 m^2/g) and the pore volume (from 0.44 to 0.55 cm^3(liquid)/g). However, the shape of the hysteresis loop remained almost unchanged, a result suggesting that the mesopore size distribution was not altered to any significant extent.

The most striking result illustrated in Figure 3 was obtained when the hydrogel was washed with ethyl alcohol. The vacuum-dried alcogel so obtained gave a very much larger uptake of nitrogen over the complete range of relative pressure. A twofold increase was evident in both the BET area and pore volume. Thus, by replacing water as the continuous liquid phase, it was possible to reduce the capillary forces that normally bring about a drastic shrinkage of the open hydrogel during normal drying.

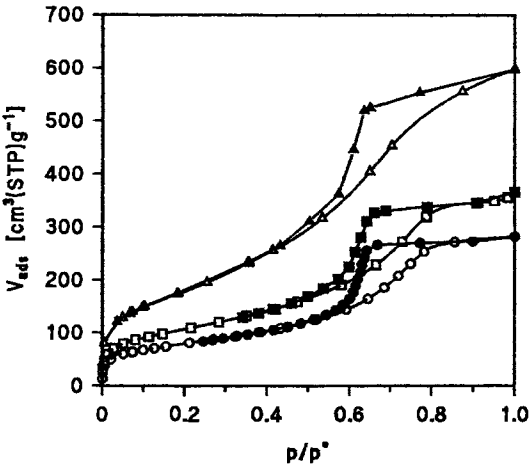

Figure 3. Nitrogen isotherms (77 K) for xerogel (○ and ●), acid-washed xerogel (HCl, pH 2.0, 24 h) (□ and ■), and alcogel (△ and ▲). Clear symbols denote adsorption; dark symbols denote desorption.

The alcogel featured in Figure 3 had a BET area of 641 m^2/g and a pore volume of 0.93 cm^3(liquid)/g. An even larger pore volume can be obtained if the fluid phase is removed under supercritical conditions to give an aerogel, that is, a product having a very low particle coordination number. Such materials are macroporous and have a high surface area (Table I), but they are usually mechanically weak and unstable when exposed to water vapor. The upper limiting surface area of a silica composed of discrete primary particles would be ~2000 m^2/g, but so far it has not been possible to obtain areas approaching this magnitude.

Conventional silica gels [termed S-type by Barby (2)] are produced by the roasting (or oven-drying) of low-density hydrogels, which undergo drastic shrinkage with considerable loss of pore volume and surface area. A different type of adsorption is produced from the same initial hydrogel if it is subjected to hydrothermal aging prior to the final drying. In this case packing and fusion of the primary particles takes place (26), so that after drying the pore space is largely confined to the interstitial space between

the secondary particles. The resulting G-xerogel has a somewhat lower surface area and larger and more uniform mesopore volume (Table I and Figure 4).

Table I. Typical Surface Areas and Pore Volumes of the Silica Gels

Type	*Porosity*	*BET-area* (m^2/g)	*Pore Volume* (cm^3/g)
Aerogel	macro	800	2.0
G-xerogel	meso	350	1.2
S-xerogel	meso	500	0.6
S-xerogel	micro	700	0.4

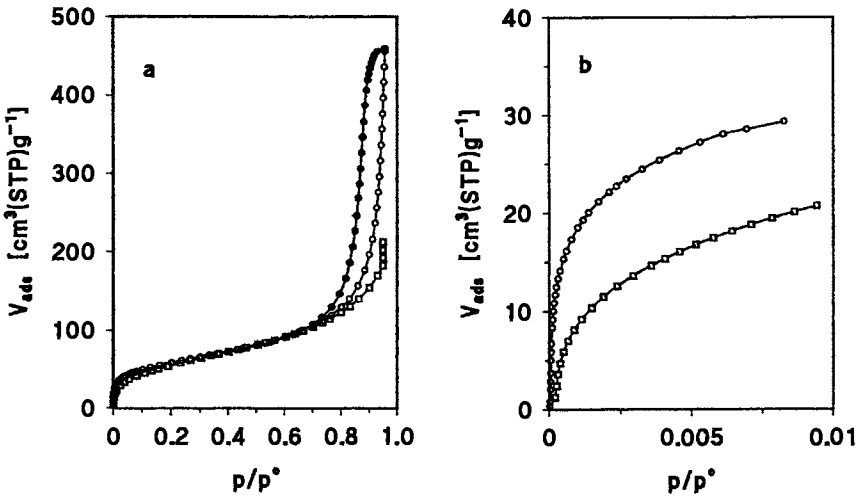

Figure 4. Part a: Nitrogen (○ and ●) and argon (□) isotherms at 77 K for a mesoporous silica. Part b: detailed low relative pressure data. Clear symbols denote adsorption; dark symbols denote desorption.

Low-temperature nitrogen adsorption is normally used for the determination of surface area and pore size distribution of porous materials. However, specific field-gradient quadrupole interactions play a significant role in the adsorption of nitrogen on hydroxylated silicas or other polar surfaces (*7*). Accordingly, some authors (*14*, *27*) have proposed that a nonpolar adsorptive such as argon should be used instead of nitrogen for the determination of surface area.

The difference in shape of the nitrogen and argon isotherms, both determined at 77 K, on a mesoporous silica is illustrated in Figure 4a. In the middle range of relative pressure, the isotherms follow almost identical

paths. The divergence at relative pressure $p/p^\circ > 0.7$ is associated with the onset of capillary condensation of nitrogen in the mesopores and confirms that argon cannot be employed at 77 K for the assessment of the mesopore size distribution (*7*). Of particular interest is the difference in shape of the isotherms at $p/p^\circ < 0.2$, that is, in the monolayer region. The use of high-resolution adsorption (HRADS) (*28*) allowed the initial part of the isotherm to be explored in considerable detail (*see* Figure 4b): It reveals that the nitrogen isotherm is extremely steep at fractional coverages <0.1 and at $p/p^\circ < 10^{-4}$. This steepness is probably due to localized adsorption on the highest energy sites of the surface. These results are consistent with calorimetric measurements of differential enthalpies of adsorption (*27*, *29*) and indicate that the surface was more heterogeneous with respect to the adsorption of nitrogen than argon. On the other hand, the lack of a well-defined point B suggests that argon is less reliable than nitrogen for the determination of surface area (*7*, *30*).

Zeolitic Silicas

A number of microporous polymorphs of crystalline silica can now be prepared. One procedure is to attempt the dealumination of a readily available zeolite; another approach involves direct synthesis, for example, of ZSM-5, in the form of Silicalite I (*31*). The considerable amount of recent interest shown in these Al-free zeolites (or porotectosilicates) has been stimulated by the uniformity of their channel structures and their hydrophobic nature.

These features are illustrated by the results of argon, nitrogen, and water measurements on Silicalite I [Figure 5a and Table II (*32*)]. The low-pressure steepness (high affinity) of the nitrogen and argon isotherms is indicative of the filling of very narrow micropores, but at higher relative pressure these isotherms are of very different shape. The hysteresis loop in the range $p/p^\circ \sim 0.1$–0.2 is a characteristic feature of the nitrogen isotherm and is probably associated with a phase transition from a liquidlike to a solidlike structure (*33*, *34*). The loop at higher relative pressure is the result of capillary condensation in the secondary pore structure outside the intracrystalline pores. Use of the HRADS technique reveals that further phase changes take place at very low relative pressures with both nitrogen and argon (Figure 5b) and also that the uptake of nitrogen occurs at lower relative pressures than argon, probably because of the stronger adsorbate–adsorbate interactions of the nitrogen quadrupoles and also the quadrupole interaction with any residual surface hydroxyl groups.

The uptake of water vapor by Silicalite I is remarkably low over the complete range of relative pressure. If we allow for the secondary pore filling, the amount of water adsorbed within the Silicalite I crystals seems

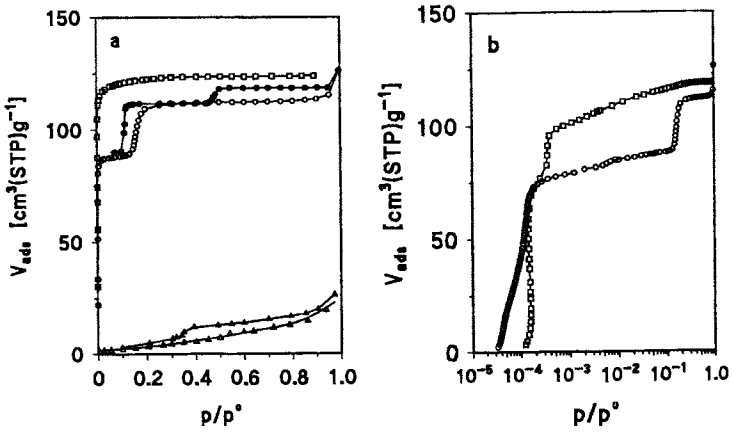

Figure 5. Part a: Nitrogen (77 K) (○ and ●), argon (77 K) (□) and water vapor (298 K) (△ and ▲) isotherms for Silicalite I. Part b: detailed low relative pressure data. Clear symbols denote adsorption; dark symbols denote desorption.

Table II. Pore Volumes at $p/p^\circ = 0.95$ of Molecular Sieve Silicas

Adsorbent	*Nitrogen*	*Argon*	*Water Vapor*
Silicalite I	0.18	0.16	0.02
Microporous silica 3[a]	0.10	0.08	0.09
Precipitated silica VN3	0.12[b]	—	0.11[b]

NOTE: All values are given in cubic centimeters per gram.
[a]From reference 32.
[b]Data were recorded at $p/p^\circ = 0.80$.

negligible (Table II). An explanation for these anomalous results must take into account the pore geometry in relation to the hydrogen-bonded structure of water. Thus, the intracrystalline pores of Silicalite I are tubular (intersecting straight and sinusoidal channels) of diameter ~0.55 nm, and most likely, an array of water molecules cannot be adsorbed without considerable distortion of the directional hydrogen bonds. In our view (35), it is of particular significance that the uptake of water within the slit-shaped pores of 0.5–0.6-nm width in molecular sieve carbons is much greater and consistent with the thickness of an undistorted thin "slab" of water. Therefore, Silicalite I is more hydrophobic than any form of microporous carbon available at present. Although further progress can be made in the refinement of the pore size distribution of amorphous mesoporous silicas, the development of well-defined microporous silicas

will depend on the preparation of new zeolitic structures and improvements in crystallinity of the existing zeolitic silicas.

Note added to proof: The recent disclosure by Mobil Scientists (*36*) of a new family of highly uniform mesoporous silicas is of great potential significance. One member, MCM-41, has been shown (P. J. Branton, P. G. Hall, K. S. W. Sing, unpublished work) to give a *reversible* Type IV nitrogen isotherm and to possess a very narrow range of pores.

References

1. Iler, R. K. *Colloid Chemistry of Silica and Silicates*; Cornell University Press: Ithaca, NY, 1955.
2. Barby, D. In *Characterisation of Powder Surfaces*; Parfitt, G. D.; Sing, K. S. W., Eds.; Academic Press: London, 1976; p 353.
3. Iler, R. K. *The Chemistry of Silica*; John Wiley & Sons: New York, 1979.
4. Alexander, G. B.; Iler, R. K. *J. Phys. Chem.* **1953,** *57*, 932.
5. Sing, K. S. W.; Everett, D. H.; Haul, R. A. W.; Moscou, L.; Pierotti, R. A.; Rouquérol, J.; Siemieniewska, T. *Pure Appl. Chem.* **1985,** *57*, 603.
6. Brunauer, S.; Deming, L. S.; Deming, W. S.; Teller, E. *J. Am. Chem. Soc.* **1940,** *62*, 1723.
7. Gregg, S. J.; Sing, K. S. W. *Adsorption, Surface Area and Porosity*; Academic Press: London, 1982.
8. Avery, R. J.; Ramsay, J. D. F. *J. Colloid Interface Sci.* **1973,** *42*, 597.
9. Gregg, S. J.; Langford, J. F. *J. Chem. Soc. Faraday Trans. 1* **1977,** *73*, 747.
10. Gregg, S. J. *Chem. Ind. (London)* **1968,** 611.
11. Kiselev, A. V. In *The Structure and Properties of Porous Materials*; Everett, D. H.; Stone, F. S., Eds.; Butterworths: London, 1958; p 68.
12. Gregg, S. J.; Sing, K. S. W. In *Surface and Colloid Science*; Matijevic, E., Ed.; Wiley: London, 1976; Vol. 9, p 231.
13. Zettlemoyer, A. C. *J. Colloid Interface Sci.* **1968,** *28*, 343.
14. Bassett, D. R.; Boucher, E. A.; Zettlemoyer, A. C. *J. Colloid Interface Sci.* **1968,** *27*, 649.
15. Carrott, P. J. M.; Sing, K. S. W. *Adsorption Sci. Technol.* **1984,** *1*, 31.
16. Sing, K. S. W. *Chem. Ind. (London)* **1967,** 829.
17. Carrott, P. J. M.; Sing, K. S. W. *Adsorption Sci. Technol.* **1986,** *21*, 9.
18. Carrott, P. J. M., Ph.D. Thesis, Brunel University, Uxbridge, Middlesex, England, 1980.
19. Baker, F. S.; Sing, K. S. W. *J. Colloid Interface Sci.* **1976,** *55*, 605.
20. Everett, D. H.; Parfitt, G. D.; Sing, K. S. W.; Wilson, R. *J. Appl. Chem. Biotechnol.* **1974,** *24*, 199.
21. Sing, K. S. W.; Madeley, J. D. *J. Appl. Chem.* **1953,** *3*, 549.
22. Sing, K. S. W.; Madeley, J. D. *J. Appl. Chem.* **1954,** *4*, 365.
23. Mitchell, S. A. *Chem. Ind. (London)* **1966,** 924.
24. Neimark, I. E.; Sheinfain, R. Yu.; Krugilkova, N. S.; Stas, O. P. *Kolloid Zhur.* **1964,** *26*, 595.
25. Wong, W.-K., Ph.D. Thesis, Brunel University, Uxbridge, Middlesex, England, 1982.
26. Kiselev, A. V. *Disc. Faraday Soc.* **1971,** *52*, 14.
27. Rouquerol, J.; Rouquerol, F.; Peres, C.; Grillet, Y.; Boudellal, M. In *Characterisation of Porous Solids*; Gregg, S. J.; Sing, K. S. W.; Stoeckli, H. F., Eds.; The Society of Chemistry and Industry: London, 1979; p 107.

28. Pieters, W. J. M.; Venero, A. F. In *Catalysis on the Energy Scene*; Kaliaguine, S.; Mahay, A., Eds.; Elsevier: Amsterdam, Netherlands, 1984; p 155.
29. Furlong, D. N.; Sing, K. S. W.; Parfitt, G. D. *Adsorption Sci. Technol.* **1986,** *3,* 25.
30. Carruthers, J. D.; Payne, D. A.; Sing, K. S. W.; Stryker, L. J. *J. Colloid Interface Sci.* **1971,** *36,* 205.
31. Flanigan, E. M.; Bennett, J. M.; Grose, R. W.; Cohen, J. P.; Patton, R. L.; Kirchner, R. M.; Smith, J. V. *Nature (London)* **1978,** *271,* 512.
32. Dollimore, D.; Heal, G. R. *Trans. Faraday Soc.* **1963,** *59,* 1.
33. Muller, U.; Unger, K. K. In *Characterisation of Porous Solids*; Unger, K. K., Ed.; Elsevier: Amsterdam, Netherlands, 1988; p 101.
34. Muller, U.; Reichert, H.; Robens, E.; Unger, K. K.; Grillet, Y.; Rouquerol, F.; Rouquerol, J.; Pan, D.; Mersmann, A. *Fresenius Z. Anal. Chem.* **1989,** *333,* 433.
35. Kenny, M. B.; Sing, K. S. W. *Chem. Ind. (London)* **1990,** 39.
36. Kresge, C. T.; Leonowicz, M. E.; Roth, W. J.; Vartuli, J. C.; Beck, J. S. *Nature (London)* **1992,** *359,* 710.

RECEIVED for review October 19, 1990. ACCEPTED revised manuscript December 26, 1991.

26

Silica Gels from Aqueous Silicate Solutions

Combined ^{29}Si NMR and Small-Angle X-ray Scattering Spectroscopic Study

Peter W. J. G. Wijnen[1], Theo P. M. Beelen, and Rutger A. van Santen*

Schuit Institute of Catalysis, Eindhoven University of Technology, P.O. Box 513, 5600 MB Eindhoven, The Netherlands

The use of modern spectroscopic techniques in the study of the formation of aqueous silica gels is described. The oligomerization process of monomeric silicic acid was studied by silicon-29 NMR spectroscopy; at high pH values cyclic trimeric silicate species were favored compared to the linear structure. Aggregation of primary silica particles of molecular size (<1 nm) was studied by analysis of small-angle X-ray scattering patterns. All systems studied (pH 4.0) indicate reaction-limited aggregation. Polyvalent cations influence the rate of aggregate formation in a negative way: aluminum at low concentrations (1 mol %) significantly inhibits aggregation. A new model for the aging process that proposes that monomeric silicic acid is transported (via solution) from the periphery of the aggregate into the core of the solution is given.

THE FORMATION OF AMORPHOUS SILICA GELS is an important process in modern industry because of their many applications. Most investigations in the field of silica gel preparation have contributed to the development of a physical chemical understanding of silica gel formation. As such, many

[1]Current address: Experimental Station, DuPont (Nederland) B. V., P.O. Box 145, 3300 AC, Dordrecht, Netherlands.
* Corresponding author

0065–2393/94/0234–0517$08.00/0

procedures to synthesize silica gels tailor-made to the demands of specific applications have resulted (*1*).

Although much phenomenological and empirical knowledge is available, the polymerization process is still lacking in molecular chemical descriptions (*1–3*). The preparation of silica has more or less become an art rather than a science based on fundamental knowledge of the preparation conditions. Insights into the underlying principles and molecular chemical aspects of silica gel formation are still limited. Understanding of the molecular chemical aspects of silica gel formation is required because small variations in preparation conditions and precursor solutions can result in different structural properties of the final product. Furthermore, the molecular aspects of silica gel formation also play a role in the synthesis of crystalline, microporous silicates and aluminosilicates (zeolites) (*4*), a process still poorly understood.

This chapter presents in situ spectroscopic investigations on the formation of silica gels from aqueous silicate solutions. The processes discussed deal with (1) the formation and growth of primary particles by polycondensation of small (monomeric) silicate anions, studied by silicon-29 NMR spectroscopy; (2) the aggregations of these primary particles into ramified silica aggregates and the role of cations in the aggregation process, studied by small-angle X-ray scattering (SAXS); and (3) the reconstruction of silica aggregates through chemical processes, studied with both silicon-29 NMR spectroscopy and SAXS. These three processes can be regarded as the key processes in formation of silica gels, and as such this chapter addresses the need for a more fundamental description of the process of silica gel formation.

Silicon-29 NMR Spectroscopy

Most commercial production processes of silica gel make use of aqueous silicate solutions. In contrast to alcoholic precursor solutions previously used to study the hydrolysis and oligomerization processes of the monomeric precursor (*2*), aqueous silicate solutions (water glass) contain a broad spectrum of structurally different silicate species, all present as essentially dissolved silica. To probe the local atomic environment of silicon nuclei and investigate the degree of polymerization of silicate species, silicon-29 NMR spectroscopy has been applied since the early 1970s (*5*). The large number of structurally different silicate species observed by ^{29}Si NMR spectroscopy contributes to the fact that the observed resonance lines of commercial water-glass solutions are rather broad: overlapping and small differences in resonance frequency of the different lines cause substantial line broadening. More alkaline solutions of aqueous silicate give rise to better resolved spectra (*6*). Furthermore, the concentration of small oligomeric and monomeric silicate anions is increased with respect to the

concentration of these anions in silicate solutions of lower alkalinity as a consequence of the higher alkalinity. Increasing pH values give rise to more depolymerized species.

Oligomerization of Aqueous Monomeric Silicic Acid. Because polymerization of the water-glass solution gives rise to a broad distribution of silicate anions and thus results in poorly resolved ^{29}Si NMR lines, the application of ^{29}Si NMR spectroscopy in this type of reaction provides minor information about the different oligomerization steps and the reaction mechanism of monomeric silicic acid. Therefore a different approach to the study of aqueous silicate solutions was applied. Because of the slow dissolution of amorphous silica gel in alkaline solutions, a gradual increase in the concentration of monomeric silicic acid can be expected. In Figure 1, typical NMR spectra of such a dissolution process are presented. In this example, amorphous, pyrogenic silica gel (Aerosil 200; Degussa) was dissolved in aqueous tetramethylammonium hydroxide (TMAOH; Janssen Chimica). TMAOH was chosen as the base because silicate species present in aqueous tetramethylammonium silicate solutions show a high degree of monodispersity: the number of different silicate species is rather small compared to alkali metal silicate solutions (*7*), and this choice facilitates identification of oligomers and oligomerization pathways. Initially (Figure 1a) a single resonance line is observed, which is attributed to monomeric silicate anions. Because of the gradual dissolution of the amorphous gel matrix, an increase in monomeric silica concentration is detected. Once a certain concentration of monomeric silicic acid has been reached, oligomerization of the monomers occurs and is reflected in the occurrence of a second resonance line. This line corresponds to dimeric silicate species. Further oligomerization takes place as a result of ongoing monomer dissolution.

From the development of resonance lines in the different spectra, a qualitative reaction mechanism can be extracted for the oligomerization process. In this mechanism, formation of cyclic structures is a predominant phenomenon. In the presence of TMA cations, no linear trimeric silicate anions are found in the silicate solutions, as can be deduced from Figures 1d through 1h. The use of alkali metal hydroxides as bases shows, aside from the cyclic trimeric silicate anion, the linear structure; the relative concentration of each depends on the alkalinity and the alkali metal used. The formation of cyclic trimeric silicate anions occurs before formation of the linear trimeric species (*6*). The formation of double-cyclic silicate anions can be observed in Figure 1e; two cyclic trimeric silicate anions combine to form the prismatic hexameric silicate anion (Q^3_6). This prismatic hexameric silicate anion forms, through addition of two monomers or one dimer, the well-known cubic octameric silicate anion. This cubic octameric silicate anion has been proposed to be predominantly

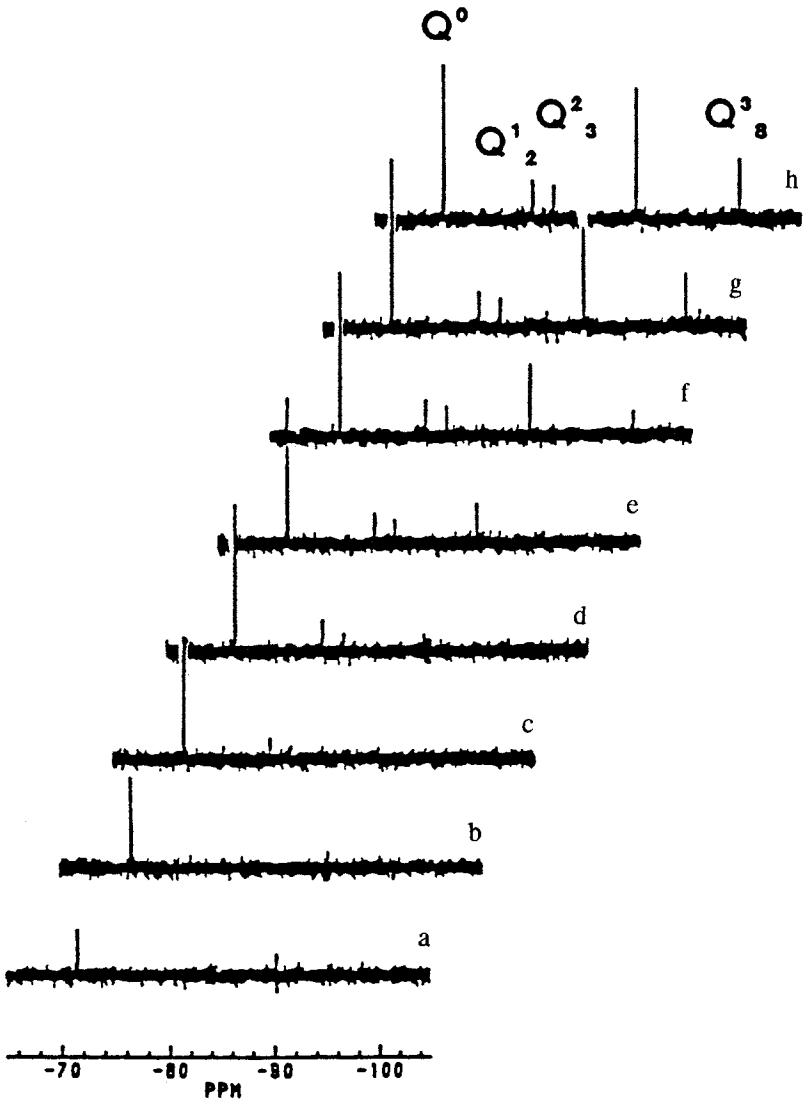

Figure 1. Dissolution of amorphous silica gel in aqueous tetramethylammonium hydroxide ($TMA_2O:SiO_2:36H_2O$) after (a) 83, (b) 250, (c) 833, (d) 1083, (e) 1250, (f) 1500, (g) 1666, and (h) 1833 min from initial mixing. The initially highly viscous suspension of tetramethylammonium silicate was introduced in zirconia magic-angle spinning NMR rotors and analyzed with a Bruker CXP-300 NMR (7.05) spectrometer. Five hundred free-induction decays were averaged that applied 45° pulses with a 10-s pulse delay. Magic-angle sample spinning was applied to average any chemical shift anisotropy arising from the highly viscous suspension.

stabilized by the tetramethylammonium cation. However, here it is shown that aside from stabilization of the Q^3_8 anion by TMA, other cyclic structures such as Q^3_6 and Q^2_3 are preferentially formed in aqueous silicate solutions containing tetramethylammonium cations. The observation that tetramethylammonium cations direct the oligomerization pathway may well be linked with the observation that during zeolite synthesis the zeolite structure needs to be built in a certain well-defined fashion. Cations in general will have an effect on the way oligomerization proceeds in aqueous silicate solutions.

Influence of Alkali Metal Hydroxides on Dissolution Rate. In a study (*6*) of the dissolution of amorphous silica gels in aqueous alkali metal hydroxides, the rate of dissolution was found to depend on the cation used in the dissolution reaction. A maximum in dissolution rate was found for potassium hydroxide solutions, whereas both intrinsically smaller and larger cations (lithium–sodium and rubidium–cesium) showed slower dissolution rates, as can be concluded from the concentration of dissolved silicate species (normalized peak areas) as a function of alkali metal cation (Figure 2). This result is contradictory to the expectation that a monotonic increase or decrease in dissolution rate is to be observed for the different cations used. One major effect that occurs at the high pH values of this study is that the majority of silanol groups (≡Si–OH) at the surface of the silica gel are ionized by hydroxyl anions present in the highly alkaline solution. This result implies that a large surface charge will be present on the silica. Because in aqueous solutions at high pH values contra-ions (cations) for the hydroxide (normally sodium) are present, the negative surface charges will be compensated by (alkali metal) cations.

Because the only variable changed in this dissolution study was the type of alkali metal hydroxide, differences in dissolution rate must be attributed to differences in adsorption behavior of the alkali metal cations. The affinity for alkali metal cations to adsorb on silica is reported (*8*) to increase in a continuous way from Cs^+ to Li^+, so the discontinuous behavior of dissolution rate cannot simply be related to the adsorption behavior of the alkali metal cations. We ascribe the differences in dissolution rate to a promoting effect of the cations in the transport of hydroxyl anions toward the surface of the silica gel. Because differences in hydration properties of the cations contribute to differences in water bonding to the alkali metal cations, differences in local transport phenomena and water structure can be expected, especially when the silica surface is largely covered by cations. Lithium and sodium cations are known as water structure formers and thus have a large tendency to construct a coherent network of water molecules in which water molecules closest to the central cation are very strongly bonded; slow exchange (compared to normal water diffusion) will

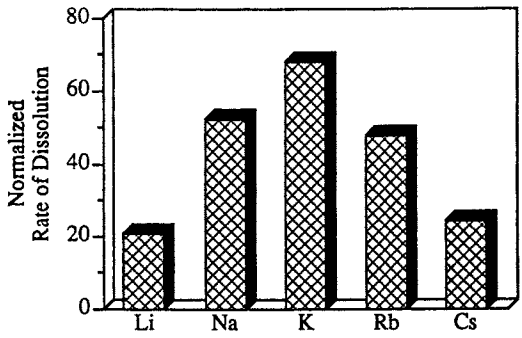

Figure 2. Normalized rate of dissolution of amorphous silica gel in alkali metal hydroxides as determined from the initial, integrated peak area of dissolved species (5 wt % silica suspensions; $M_2O:3SiO_2:180H_2O$). Other experimental details are given in the caption of Figure 1.

take place between water molecules in the nearest hydration shell and the bulk water molecules.

On the other hand, cesium, rubidium, and, to a lesser extent, potassium are known as water structure breakers; they cause the water molecules to be very disordered around the central cation. These larger cations have a small tendency to coordinate water molecules in a hydration shell, so lithium cations interact strongly with the (inner) hydration shell, whereas cesium cations barely have a hydration shell. As adsorption of (hydrated) cations will take place for aqueous silicate dispersions at high pH values, the state in which the adsorbed cations are present at the surface is crucial for promoting effects. Strong hydration forces (lithium) give rise to a slow exchange of water (hydroxyl) molecules, whereas no hydration (cesium) results in slow exchange as well. Potassium is the most favored alkali metal cation in transport reactions of hydroxyl anions towards the silica gel surface.

This phenomenon was confirmed by the introduction of symmetric tetraalkylammonium hydroxides in the dissolution of silica gel. In TMAOH the observed rate of dissolution was slow compared to the rate observed for cesium hydroxide dispersions, and cesium hydroxide has the lowest rate for the different alkali metal hydroxides. Results in Figure 3 clearly reveal an inhibition time between mixing of the silica gel with the aqueous TMAOH and the onset of dissolution. This observation is attributed to the strong interaction of the rather apolar TMA cation with the negatively charged silica gel surface. Because in this case no hydration shell is present, dissolution only occurs very slowly. The observed inhibition period of the dissolution reaction can be related to specific interactions of TMA cations with relatively large oligomeric species of the monomeric

silicic acid. From the time that prismatic hexameric silicate anions (double three-membered ring, Q^3_6) are present in the solution (*see* Figure 1e; $\delta = -89.2$ ppm), TMA cations migrate from the silica surface to the solution; this migration leaves an almost noncovered silica gel surface, and dissolution occurs as fast as in alkali metal hydroxide solutions. A speculative model for the increased affinity of TMA cations for the silicate solution is provided by the clathrate structure of TMA silicate solutions. In this model, oligomers of silicic acid (cubic octameric silicate) are surrounded by tetramethylammonium cations in such a way that the geometric nature of the silicate oligomer matches the structure of the hole induced by the arrangement of TMA cations (9).

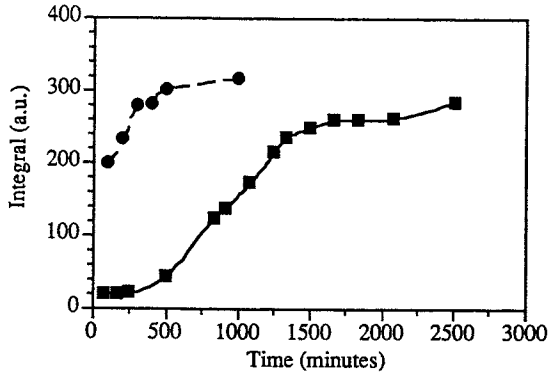

Figure 3. Total amounts of dissolved silicate anions (in terms of integrated peak area; a.u., arbitrary units) in solutions of cesium silicate (dashed line) and tetramethylammonium silicate as a function of reaction time (TMA_2O or $Cs_2O{:}3SiO_2{:}180H_2O$). The temperature was 25 °C; other experimental details are given in the caption of Figure 1.

Small-Angle X-ray Scattering

Silicon-29 NMR spectroscopy has thus been used to investigate the oligomerization of aqueous monosilicic acid. Prolonged polymerization of aqueous silicate solutions, however, yields a very broad distribution of polysilicic anions and colloidal structures (6, 7). This fact implies that with ^{29}Si NMR spectroscopy, only information with little detail on the ongoing polymerization process can be obtained, and so the polymerization process can be described only in a qualitative way in terms of relative changes in NMR line intensities and line widths. Therefore, a different spectroscopic technique was applied to study silica gel formation: small-angle X-ray scattering (SAXS) (*10*). As in X-ray diffraction, interference of scattered X-rays allows the identification of structural properties. From Bragg's

relation ($n\lambda = d \sin 2\theta$; λ is the wavelength, d is the interatomic separation, 2θ is the angle between the incident and diffracted light, and n is an integer), it can be seen that large structural features should be investigated at relatively small scattering (diffraction) angles (typically $2\theta < 5°$). Systems containing colloidal or subcolloidal particles can be studied at small scattering angles. Silica gels are constructed of a continuous network of particles of colloidal size (typically 3–50 nm in diameter). In the early 1980s, silica gels prepared from alcoholic precursor solutions (in contrast to the aqueous solutions discussed here) yielded scattering curves that were indicative of the formation of fractal structures (*11*).

Fractal Behavior in Silica Gel Chemistry. In fractal theory a structure can be described in terms of its fractal or broken dimensionality (*12*). This dimensionality, in contrast to the Euclidean dimensionality, which quantifies the space dimensionality embedding the structure, often has a noninteger value between 1 and 3. Fractal structures do not have a constant value for density; it gradually changes when traversing the system. For mass fractals, the way in which density varies is reflected in the fractal dimensionality D: density ρ varies with length scale r according to $\rho \propto r^{D-3}$. The fractal dimensionality can be used as a kind of fingerprint in the description of the process of aggregation of primary silica particles: different types of aggregation process result in different fractal dimensionalities (*13*).

Fractal behavior is reflected in a power-law relationship between scattered intensity I and scattering vector $\mathbf{Q}$ ($\mathbf{Q} = 2\pi/\lambda \sin 2\theta$). Therefore, in a log–log plot of scattered intensity versus scattering vector, fractality is observed as a linear region of the scattering curve; the slope of this linear part is, in general, smaller than 3 if the material is fractal with respect to the mass (variation of density within the structure) and between 3 and 4 if the material is fractal with respect to the surface area (*13–15*). In Figure 4, a computed small-angle scattering curve of a fractal system is presented (*16*). From deviations from power-law scattering at small and large scattering vectors, information is extracted concerning the size of the fractal aggregates and the size of the primary particles constructing the aggregate, respectively. These two parameters determined from in situ small-angle scattering curves are the structural properties that are determined by aggregation kinetics imposed by the precursor composition. A continuous increase in size of the silica aggregates was observed during the formation of silica gel (*17*). Moreover, after reaching the gelation point, the aggregate size still appears to increase as a function of time. At the gelation point, a continuous percolating network of silica particles exists in the solution, which has an infinite viscosity: twisting of the reaction vessel does not deform the meniscus.

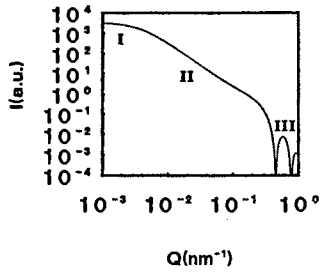

Figure 4. Simulated small-angle scattering curve from fractal geometry theorems (16). The small-angle scattering curve represents scattering from a fictitious fractal aggregate (R = 250 nm, D = 2.25, and the size of the primary building unit r_0 was 3 nm).

According to classical theories of gelation, a continuous aggregate of infinite size should be present at the gelation point. However, from the SAXS curves a determinable, finite size of the aggregates is extracted. This observation suggests that the growth process of silica aggregates has to be anisotropic. The finite size of fractal silica aggregates in silica gels might indicate the presence of elongated, intermingled structures with a finite (mean) aggregate radius. On the other hand, according to Martin and Hurd (*14*), SAXS on gelated, nondilute silica systems gives no information about the size of the aggregates, and so no conclusion should be drawn from the development of aggregate size at relatively long reaction times. From a certain reaction time near the gelation point, the solutions can no longer be considered dilute, so determination of aggregate sizes becomes disputable. However, this chapter focuses on qualitative differences in the evolution of aggregate size at reaction times that are short compared to the gelation time.

The size of primary particles can be extracted from the deviation of fractal behavior at large scattering vectors **Q**. In silica gels freshly formed from aqueous silicate solutions, no deviation from this fractal power law could be observed for **Q** values as high as 2 nm^{-1}. This result implies that the primary particles of freshly prepared silica gels are smaller than 2 mm, maybe even of molecular size. Oligomers present in the aqueous silicate solutions used as precursor solutions are not subject to further growth in acidic solutions, but merely aggregate into continuous networks of silicate particles. At low pH values (pH $\approx$ 4) aggregation of oligomers is a fast process in relation to growth of the primary particles.

Influence of Total Silica Concentration on Aggregation Kinetics. Dilution of the silicate solution would be expected to give rise to a crossover in the type of aggregation behavior of the primary silicate particles. For relatively concentrated systems ([SiO_2] $\approx$ 5 wt %), a

reproducible fractal dimensionality of $D = 2.20 \pm 0.05$ was measured (Figure 5). This value of the fractal dimensionality is in fairly good agreement with fractal dimensionalities obtained from computer simulations of reaction-limited cluster–cluster aggregation (*13*). In this limiting situation of reaction-limited aggregation, diffusion of particles or clusters of particles toward each other is faster than the kinetics of the chemical reaction between the particles. Dilution of the silicate solution in aggregating particles (total silica concentration) should therefore result in an increasing importance of the diffusion rate of the aggregating particles. So *reaction*-limited aggregation should change into *diffusion*-limited aggregation, as was observed by Aubert and Cannell (*18*) for colloidal silica solutions. This transition in type of kinetic aggregation process is accompanied by a difference in fractal dimensionality. Experimentally, however, no influence of the total silica concentration ($0.1 < [SiO_2] < 8$ wt %) on the fractal dimensionality was observed at the length scales (1–30 nm), temperature, and time scales investigated (Figure 5). This result implies that diffusion of particles in the aqueous silicate solution or suspension must be a fast process compared to the reaction kinetics between two aggregating particles, or internal organizations must be fast compared to aggregation. Concentrations lower than 0.1 wt % do not lead to aggregation processes.

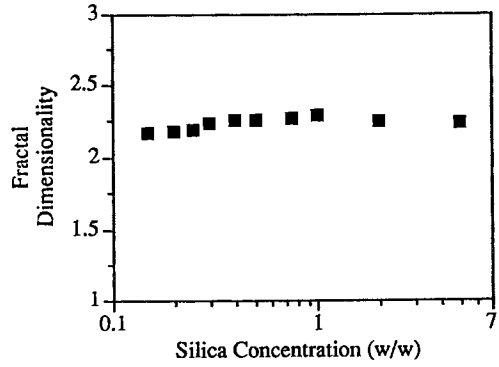

Figure 5. Fractal dimensionality of aqueous silica aggregates differing in total silica concentration obtained from SAXS spectra. The spectra were recorded after 5 days of reaction (pH 4.0 at 25 °C) in sealed polyethylene bottles. SAXS spectra were recorded at the Synchrotron Radiation Source of Daresbury Laboratories, United Kingdom, on beam line 8.2.

In contrast with these observations concerning the independence of fractal dimensionality from monomeric silicate concentration, the remarkable observation was made that the presence of oligomeric silicate anions

increases the rate of aggregate formation considerably (*17*). A decrease in the pH value of precursor solutions low in silica concentration (about 0.2 wt %), gives rise to oligomerization of the monomeric silicate anion. The oligomers formed appear to act as aggregation kernels for the silicate anions. The presence of these aggregation kernels induces rapid aggregation, as is reflected in the fractal dimensionality of the aggregates. Compared with usually observed fractal dimensionalities of aqueous silicate aggregates ($D = 2.2$), the fractal dimensionality of aggregates grown in solutions of low silica concentration and in the presence of oligomers is low ($D = 1.8$). This low fractal dimensionality points to a diffusion-limited cluster–cluster aggregation process. Reorganizations in the structural arrangement of the primary building units gradually cause an increase in fractal dimensionality to values observed for the reaction-limited cluster–cluster aggregation type (*19, 20*).

Influence of Polyvalent Cations on Aggregation Kinetics. This influence was investigated. No influence on the final fractal dimensionality of the gelating silicate solutions was observed for the cations investigated (Li^+, Na^+, K^+, Rb^+, Cs^+, TMA^+, Mg^{2+}, and Al^{3+}). The rate of aggregate growth, however, does strongly depend on the presence of polyvalent cations and hydrophobic monovalent cations (TMA) (*21*). Aggregation is retarded by addition of aluminum cations (Al:Si = 0.01) and to some lesser extent by addition of magnesium cations (Figure 6). This difference is understood in terms of the valency of the cations. Investigation of the influence of different concentrations of aluminum cations revealed that increasing aluminum concentrations cause the observed inhibition with respect to aggregate growth to diminish (Figure 7). Fast reaction between aluminum cations and silicate oligomers causes the silica particles to become charge stabilized. Aggregation is slow because of the charges of the primary particles. The structure of the aggregates is such that in a model of screened aggregation, initially low dimensionalities are observed. However, when the concentration of aluminum is increased, formation of homogeneous aluminosilicates causes charge stabilization to decrease. The aggregation kinetics resemble kinetics in solutions with no aluminum cations added.

Addition of tetramethylammonium cations results in an increase in aggregation rate, which can be attributed to the breaking of the local structure of water molecules surrounding the silicate particles. The activation energy of reaction between two primary particles is decreased.

Aging of Aqueous Silica Gels

So far, a discussion on the processes involved in the formation of silica gels has been presented. However before a silica gel, with its intrinsic

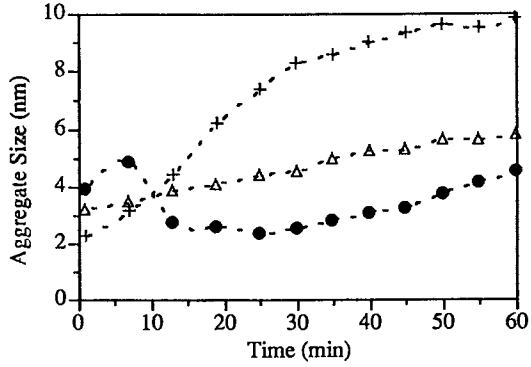

Figure 6. Size of aggregates as a function of reaction time for silicate solutions containing different cations: +, K only; Δ, Mg:Si = 0.01 mol/mol; ●, Al:Si = 0.01 mol/mol. The total concentration of silica was 5 wt %. Silica gels were prepared at pH 4.0 at room temperature (25 °C) by adding the silicate solution under vigorous stirring to a solution of hydrochloric acid (2 N) containing $MgCl_2$ or $Al_2(SO_4)_3$.

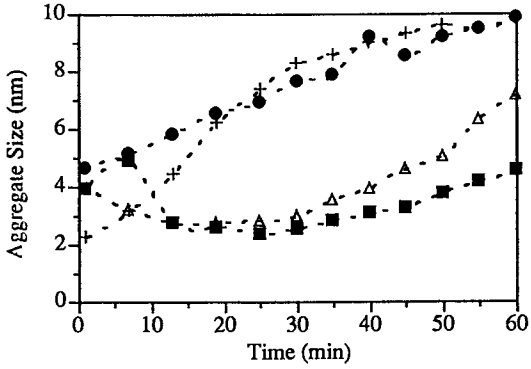

Figure 7. Size of aggregates as a function of reaction time for silicate solutions containing different concentrations of aluminum cations: +, K only, Al:Si = 0.0; ■, Al:Si = 0.01; Δ, Al:Si = 0.04; and ●, Al:Si = 0.10. The pH was 4.0, and the temperature was 25 °C. The total concentration of silica was 5 wt %. Silica gels were prepared at pH 4.0 at room temperature (25 °C) by adding the silicate solution under vigorous stirring to a solution of hydrochloric acid (2 N) containing different concentrations of $Al_2(SO_4)_3$.

properties of high specific surface area preserved, can be made, it must be aged in a way that prevents the framework of silica particles from collapsing upon drying. Until now, aging of aqueous silica gels was considered an Ostwald dissolution process of silicate units at surfaces with small radius of curvature (small particles) and subsequent deposition at surfaces with large or negative radius of curvature (large particles and

necks between particles, respectively) (*1*, p 228). In Figure 8, small-angle scattering curves of a freshly prepared and an aged aqueous silica gel are presented; different scattering characteristics are evident. In the scattering profile in Figure 8b, the scattering of primary particles can be distinguished (part III in Figure 2) from the case of freshly prepared silica gels, for which no scattering of primary particles can be observed (Figure 8a). Thus, the mean size of the scattering primary particles increases during aging from molecular level (<0.5 nm) to colloidal level (ca. 3–5 nm). The fractal dimensionality on the other hand has changed to a value smaller than the initial fractal dimensionality, so the gradient in density within the aggregates has become larger. Here dissolution is presumed to preferentially occur at peripheral positions in the aggregates, where the density in silica is low compared to the more dense core of the aggregates. Subsequent deposition of the monomeric species in the core of the aggregates causes the difference in density between the core (high) and the peripherals (low) to increase; a decrease in fractal dimensionality results.

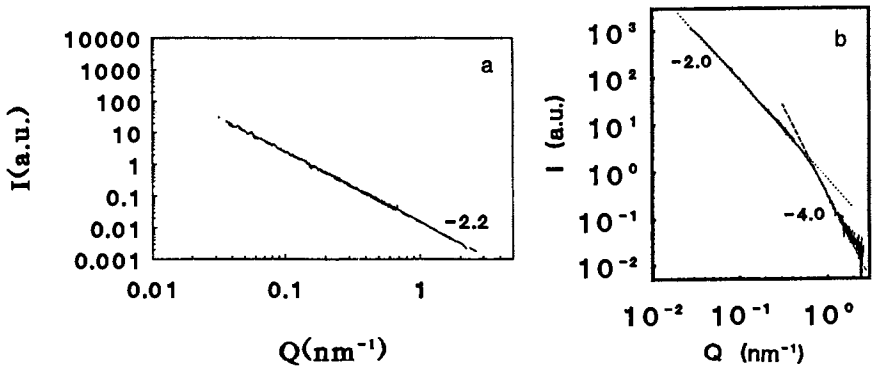

Figure 8. SAXS curves of a silica gel prepared at pH 3.9 from potassium water glass and hydrochloric acid: a, freshly prepared silica gel recorded after 2 h of reaction; b, same gel as in a, but after 1 year of aging at room temperature. The dotted line is a nonlinear least-squares fit of the fractal region in the curve and gives $D = 2.0$. *The dashed line is from the Porod law* ($I \propto Q^{-4}$). *In both a and b, two scattering curves measured at two different camera lengths (4.5 and 0.7 m) are combined to cover a broad scattering range (2 orders of magnitude in* Q *vector).*

The driving force for structure transformation can be related to the entropy of the structures (22). Very open structures are of highest entropy and thus will strive for a state that has less entropy. Because the structure of the silica aggregates is more or less rigid, the only way to decrease entropy is to gradually dissolve silica at places of highest entropy (i.e., the

low-density peripherals of the fractal structures) and to deposit the dissolved monomers at places with higher density (i.e., lower entropy). An increase in solubility of the silica aggregates will contribute to a faster process of structure reorganization. As such, aging of aqueous silica gels can be accelerated by higher pH values, high temperatures, and the presence of fluorine anions (*20*). The rate of dissolution of monomeric silicate anions is rate determining in the aging processes of aggregates formed by reaction-limited cluster–cluster aggregation. Interestingly, aging of aggregates formed by reaction-limited aggregation gives a decrease in fractal dimensionality with an increase in primary particle size. Aging of aggregates formed by diffusion-limited cluster–cluster aggregation results in an increase of fractal dimensionality at (nearly) constant primary particle size (*20*). The time scales on which both transformations take place are very different. Aging of aggregates grown by diffusion-limited aggregation is fast compared to aging of reaction-limited aggregates. Both transformations correspond to a decrease in system entropy and potential energy.

References

1. Iler, R. K. *The Chemistry of Silica*; Wiley: New York, 1979.
2. Brinker, C. J.; Scherer, G. W. *Sol Gel Science*; Academic: Boston, MA, 1990.
3. Hench, L. L.; West, J. K. *Chem. Rev.* **1990,** *90,* 33.
4. Barrer, R. M.; Coughlan, B. *Molecular Sieves*; Society of Chemical Industry: London, 1968.
5. Engelhardt, G.; Jancke, H.; Mäge, M.; Pehk, T.; Lippmaa, E. *J. Organometallic Chem.* **1971,** *28,* 293.
6. Wijnen, P. W. J. G.; Beelen, T. P. M.; De Haan, J. W.; Rummens, C. P. J.; Van de Ven, L. J. M.; Van Santen, R. A. *J. Non-Cryst. Solids* **1989,** *109,* 85.
7. Wijnen, P. W. J. G.; Beelen, T. P. M.; De Haan, J. W.; Van de Ven, L. J. M.; Van Santen, R. A. *Colloid Surf.* **1990,** *45,* 255.
8. Depasse, J.; Watillon, A. *J. Colloid Interface Sci.* **1970,** *33,* 430.
9. Keijsper, J. J.; Post, M. F. M. In *Zeolite Synthesis*; Occelli, M. L.; Robson, H. E., Eds.; Symposium Series 398; American Chemical Society: Washington, DC, 1989; pp 28–48.
10. Guinier, A.; Fournet, G. *Small Angle Scattering of X-rays*; Wiley: New York, 1955.
11. Brinker, C. J.; Keefer, K. D.; Schaefer, D. W.; Ashley, C. S.; Assink, R. A.; Kay, B. D. *J. Non-Cryst. Solids* **1982,** *48,* 47.
12. Mandelbrot, B. B. *The Fractal Geometry of Nature*; W. H. Freeman and Co.: San Francisco, CA, 1982.
13. Meakin, P. *Adv. Colloid Interface Sci.* **1988,** *28,* 249.
14. Martin, J. E.; Hurd, A. J. *J. Appl. Cryst.* **1987,** *20,* 61.
15. Schmidt, P. W. In *The Fractal Approach to Heterogeneous Chemistry*; Avnir, D., Ed.; Wiley: New York, 1989.
16. Teixeira, J. *J. Appl. Cryst.* **1988,** *21,* 781.
17. Wijnen, P. W. J. G. Ph.D. Thesis, Eindhoven University of Technology, Eindhoven, the Netherlands, 1990.
18. Aubert, C.; Cannell, D. S. *Phys. Rev. Lett.* **1986,** *56,* 738.

19. Wijnen, P. W. J. G.; Beelen, T. P. M.; Rummens, C. P. J.; Saeijs, J. C. P. L.; Van Santen, R. A. *J. Appl. Cryst.* **1991**, *24*, 759.
20. Wijnen, P. W. J. G.; Beelen, T. P. M.; Rummens, C. P. J.; Saeijs, J. C. P. L.; Van Santen, R. A.; *J. Colloid Interface Sci.* **1991**, *145*, 17.
21. Beelen, T. P. M.; Wijnen, P. W. J. G.; Rummens, C. P. J.; Van Santen, R. A. In *Better Ceramics through Chemistry IV;* Zelinski, B. J. J.; Brinker, C. J.; Clark, D. E.; Ulrich, D. R., Eds.; *Mat. Res. Soc. Symp. Proc;* Materials Research Society: San Francisco, CA, 1990; Vol. 180; pp 273–276.
22. Kaufman, J. H.; Melroy, O. R.; Dimino, G. M. *Phys. Rev. A* **1989**, *39*, 1420.

RECEIVED for review July 17, 1991. ACCEPTED revised manuscript December 27, 1991.

27

Surface Chemistry of Silica Coatings of Titania

D. Neil Furlong

CSIRO Division of Chemicals and Polymers, Private Bag 10, Clayton 3168, Australia

The dense silica (DS) process involves the exposure of titania particles to aqueous silica solutions of increasing silica concentration. The process is examined in this chapter by relating silica adsorption on titania surfaces to solution pH and concentration and to the various monomeric, multimeric, and polymeric species present in aqueous "solutions" of silica. Microelectrophoresis and gas adsorption studies reveal that adsorption of monomeric silica occurs via hydrated cation sites that constitute only approximately 40% of titania surfaces. These "anchoring" sites provide a base for complete surface coverage and buildup of silica multilayers (coatings), a buildup that occurs when the silica concentration is increased sufficiently at the chosen pH (around 10 in the DS process) to induce polymerization.

THE COATING OF SILICA FROM AQUEOUS SOLUTION ONTO TITANIA—an area of science and technology that has been underpinned by the Iler patent of 1959 (*1*) describing the composition and process for production of the so-called "dense silica coatings" (DS coatings)—is discussed in this chapter. The patent, though broad in its specifications with respect to the types of substrates that could be coated, was clearly targeted at the titania pigment business. Because of its technological impact, the patent spawned a period of research activity, reported in the open scientific literature mainly to the early 1980s, aimed at probing the nature of the DS deposition process and of the coatings themselves. Of course, many of these findings may already have been recorded in DuPont files. Nevertheless, the open research has proven very useful to the fundamental understanding of oxide–oxide

0065–2393/94/0234–0535$08.90/0

interactions, as well possibly to industry. In recent years relatively little new work on the details of deposition have appeared, although the properties and performance of various DS coatings remain very much of interest.

This chapter is a look back at a "parcel" of surface chemistry research that grew out of an extraordinarily useful piece of technology, and it focuses mainly on the specific chemical interactions of deposition. The characterization of the physicochemical properties and processing variables of DS coatings, particularly with regard to their use in pigments, is the focus of Chapter 28.

Why Coat Titania with Silica?

This question is easily answered if pigment performance is the main concern; the answer is improved dispersibility and paint film durability. Dispersibility relates mainly to the surface chemistry of the silica coating–paint film (2) interface and less to the specifics of titania–silica interactions and is not further considered here. The durability of paint films, on the other hand, relates more to the photoredox properties of titania and the consequent "damage" to organic resins in paint films. DS coatings were designed to provide a barrier to such photoredox reactions. Titania particles absorb ultraviolet light of wavelength below around 380 nm; these absorptions give rise to charge centers (valence band holes and conduction band electrons) with redox potentials appropriate for oxidation–reduction of organic media. The strong oxidizing potential of photogenerated surface holes at ca. 2.6 V (with respect to the normal hydrogen electrode) was particularly threatening to alkyd resins (3–5), for example, which formed the basis for paint films of the past.

The ability of surface photogenerated redox centers to participate in electron-transfer reactions with, for example, organic resins depends on titania particle size (relating to internal charge recombination rates that can also be influenced by metal ion dopants) and other parameters such as resin–surface affinity and availability of oxygen (6). However, paint film "chalking" (i.e., pigment–resin phase separation on exposure of the film to atmospheric ultraviolet rays) was a familiar sight when uncoated titania pigments were used. Uniform and coherent silica coatings of thickness around 2 nm or more presented a dielectric barrier to surface redox reactions and hence effectively retarded paint film chalking. Iler's DS coatings were such coatings. Although in the patent they were depicted rather stylistically (Figure 1), electron microscopy shows their real coherence and uniformity (Figure 2), and their retardation of resin oxidation has often been demonstrated (3–7).

Should a researcher not interested in pigment chemistry be interested in silica coatings on titania? It is interesting to digress at this point and

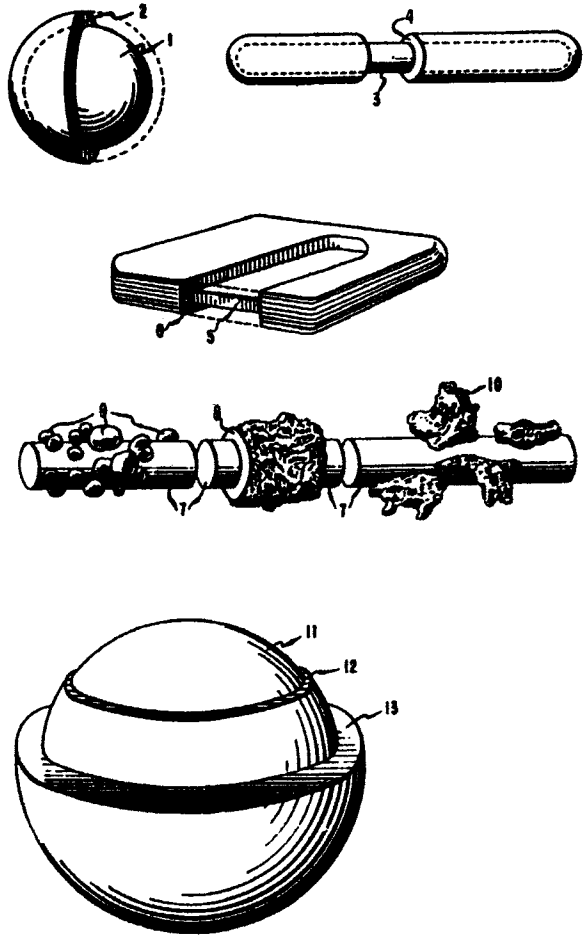

Figure 1. Schematic representations (1) of dense silica coatings formed by the Iler process.

consider briefly the question of coatings from the opposite viewpoint—useful photocatalysis. The photocatalytic power of titania particles has been investigated in a number of potentially useful organic oxidation reactions (*8–11*), the attraction of titania being its inherent chemical (i.e., dark) stability. In particular, titania has been central to the quest for efficient systems for the photolysis–photoreduction of water (*12*). Much that has been learned from the photocatalytic behavior of pigmentary titania has found its place in this very current sphere of research activity. For example, the efficient photooxidation of water requires the combina-

Figure 2. Transmission electron micrograph of dense-silica-coated titania particles: magnification, 200,000; 5.0 wt % silica loading. (Reproduced with permission from reference 23. Copyright 1979.)

tion of the photocatalytic power of titania with "hole-storing catalysts", such as ruthenium dioxide and vanadia. The main reason for this combination of catalysts is the need to harness the single electron-hole pair generated per absorbed photon with the desired multielectron reactions at the titania–medium interface. Hence, the laying down of an oxide catalyst onto colloidal particles of titania has become an important catalyst preparation procedure.

Of course silica coatings, being dielectric, will not be useful direct participants in water photolysis–photoreduction. This fact is demonstrated by the data of Tada et al. (*13*), reproduced in Figure 3, in which silica coatings ca. 1 nm in thickness [deposited by the so-called liquid-phase deposition or LPD process (*14*)] inhibit the photoreduction of aqueous silver ions. Researchers of aqueous photoredox chemistry have, however,

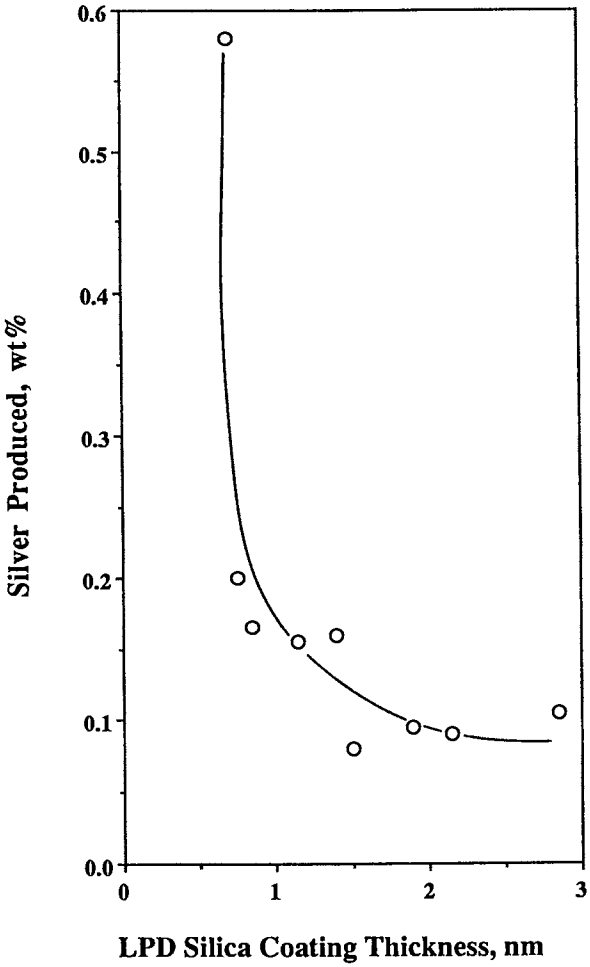

Figure 3. Dependence of the amount of Ag photodeposited on silica-coated titania particles on the thickness of silica coating. (Reproduced with permission from reference 13. Copyright 1989.)

used another aspect of silica surface chemistry to advantage—that is, the negative surface charge of silica when dispersed in aqueous solutions. Silica is negatively charged above ca. pH 2 (*15*), in contrast to titania, which has an isoelectric point around 5–6 (*16*). The surface charge of both silica and titania can be controlled by adjustment of the dispersion pH, and hence the adsorption of potentially photoreactive (ionic) solutes can be encouraged or retarded. When surface photochemical reactions involve a change of solute charge, the electric field at the silica– or titania–solution interface can enhance the separation of photochemical products; thus,

back-reactions are inhibited and the yields of useful products are improved. To date, such effects have been demonstrated only for either silica or titania alone (*17*). However, the potential for using partially silica-coated titania to give subtle control of useful interfacial photochemistry seems attractive. Therefore, the surface chemistry of silica-coated titania is useful in terms of the inhibition of surface photochemistry, as with pigments, and has potential for control of "preparative" surface photochemistry.

How To Coat Titania with Silica

The various "dry" processes such as vacuum evaporation or chemical vapor deposition (*18*) are not discussed here. These processes are central, for example, to semiconductor technology, but are not so readily used with titania powders. With titania (and other oxides) dispersed in aqueous solution, effective silica coating can be achieved (without really trying) merely by allowing an aqueous dispersion of titania to equilibrate in a Pyrex vessel (*19*). "Aqueous" silica that is leached from the Pyrex vessel will deposit onto particles. The leaching rate is greater at alkaline pH, and hence so is the coating rate. It is possible to completely mask titania surfaces in this manner, although even at high pH values the process is rather slow (on the scale of days) and somewhat irreproducible. Deposition by leaching is more often than not an undesirable process and not the basis of preparative coating technology. A number of other processes are used to prepare coatings and these include the Iler DS process (*1*) and the LPD process (*13*) of the Nippon Sheet Glass Company (Figure 4).

Iler approached DS silica coatings via a detailed and unparalleled understanding of the pH–concentration control of the aqueous chemistry of aqueous sodium silicate solutions (*20*). The preparation sequence shown in Figure 4a is one of a number in the Iler 1959 patent (*1*) and was used to prepare coated titania powders described later in this chapter. Variants on the original patent, some including coating additives other than silica (*21*), continue to appear in the patent literature. The "successful" binding of aqueous silica species to the surface of titania relates to the interactions between titania surfaces and the various silica–silicate species present in solution, and in particular to the progressive exposure of the titania surface to an increasing "aqueous silica" concentration. The concentration may be increased sufficiently during the coating procedure to cause precipitation of amorphous silica.

Proponents of LPD coatings have shown that this method produces effective coatings, but the number of characterization studies on both the process and the coatings have been far fewer than those on the Iler process. The silver reduction data (*13*) in Figure 3 suggest that these coatings are either not effectively uniform or are partially permeable to

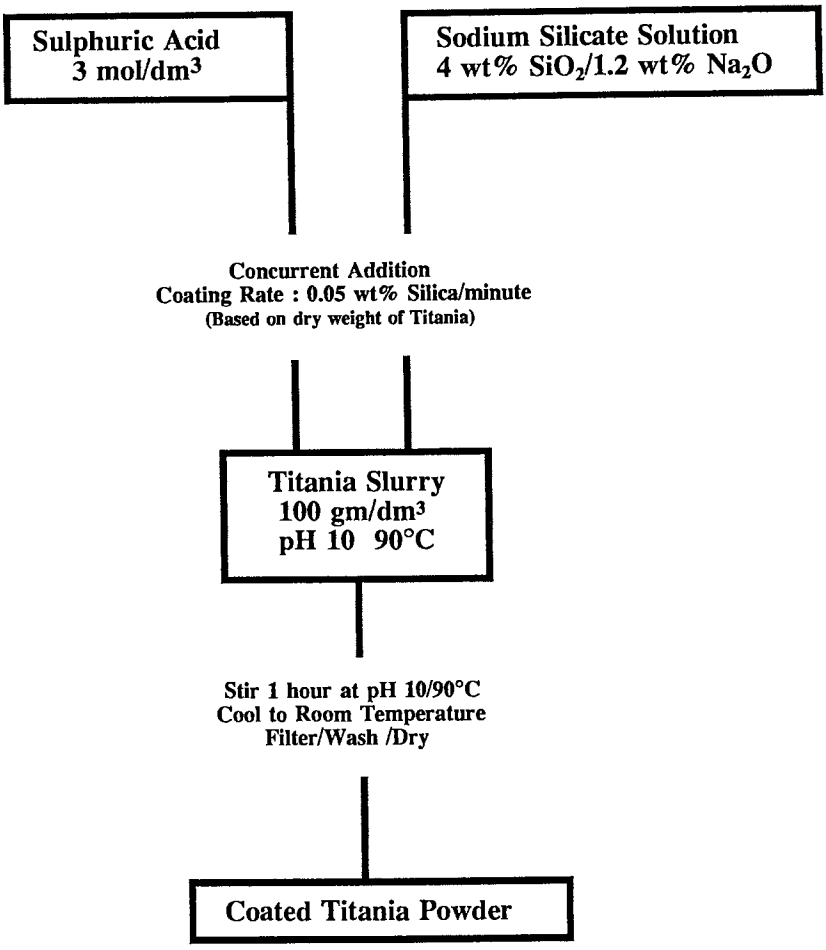

Figure 4. Sequences for preparation of (a) Iler DS coatings (1) on titania particles. Continued on next page.

aqueous ions. The use of fluoride solutions would intuitively render the LPD process less attractive from a processing point of view. A key difference between the LPD and DS processes is that the former exposes titania to supersaturated silica solutions at all stages of coating. The speciation chemistry of silica-supersaturated H_2SiF_6 solutions is much less well documented than is that of the aqueous silica solutions of the DS process.

Because of the wide industrial application of the Iler DS process, this chapter focuses on the silica–titania interactions in that process.

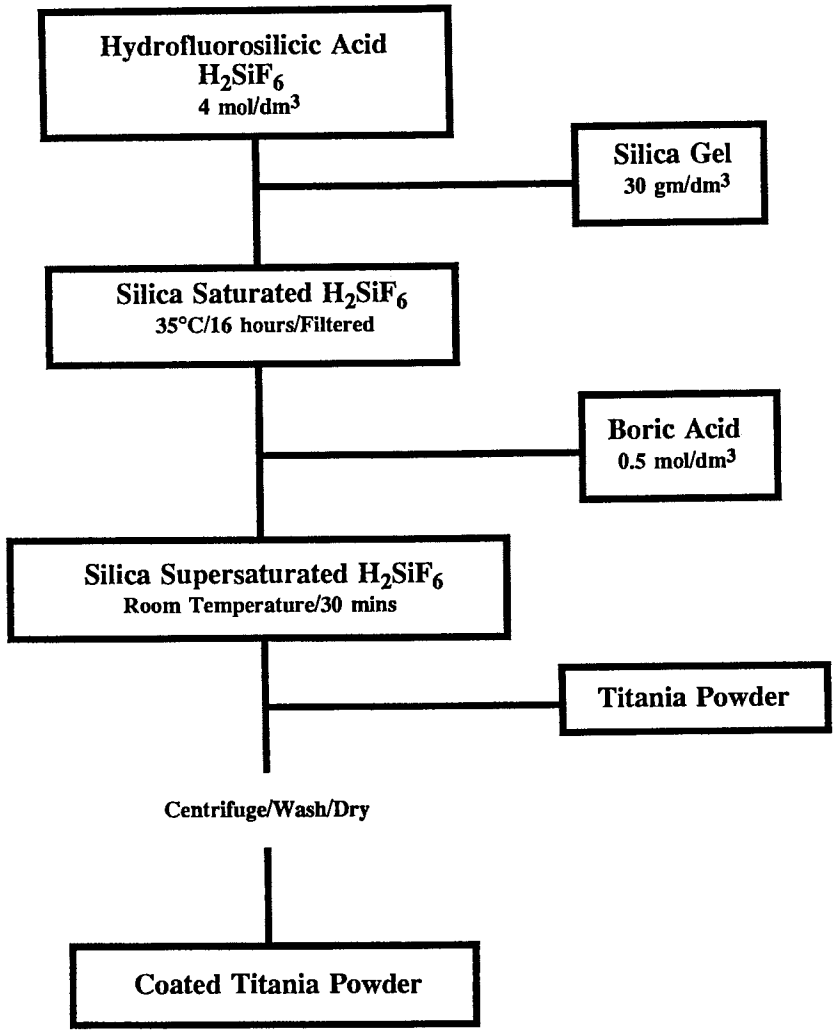

Figure 4.—Continued. Sequences for preparation of (b) LPD silica coatings (18) on titania particles.

Iler DS Deposition Process

Solution Chemistry of Aqueous Sodium Silicate. The Iler DS process is based on the exposure of the substrate particles to an increasing concentration of "aqueous" silica at 90–100 °C and a pH of ca. 9–10. The term "aqueous silica" hides much, in that it can include monomeric species (silicic acid and its conjugate bases), multimers, and fine particu-

lates (*20*). Although the direct experimental evidence describing the form of the multimers is somewhat inconclusive, it is generally felt that $Si_4O_6(OH)_6^{2-}$ is dominant. To gain an understanding of the types of silica species interacting with titania during DS deposition, a description of the pH–concentration domains of the various silica species is required. Figure 5 describes such a distribution at 25 °C and was compiled by Stumm et al. (*22*) from experimental equilibrium constants. "Indicators" (A, B, C, and D in Figure 5) have been added (*23*) to the Stumm diagram. These indicators arise from published light-scattering experiments and help to define the pH–concentration domain in which multimers are present as precursors to bulk precipitation of silica.

Figure 5 shows that the solubility of amorphous silica is independent of pH between 4 and 9; above pH 9 the solubility increases because of the formation of monosilicate, disilicate, and multimer ions. DS coatings are deposited at 90 °C—equilibrium constants are not available at this temperature. Silica solubility data are available (*24*), and hence it is

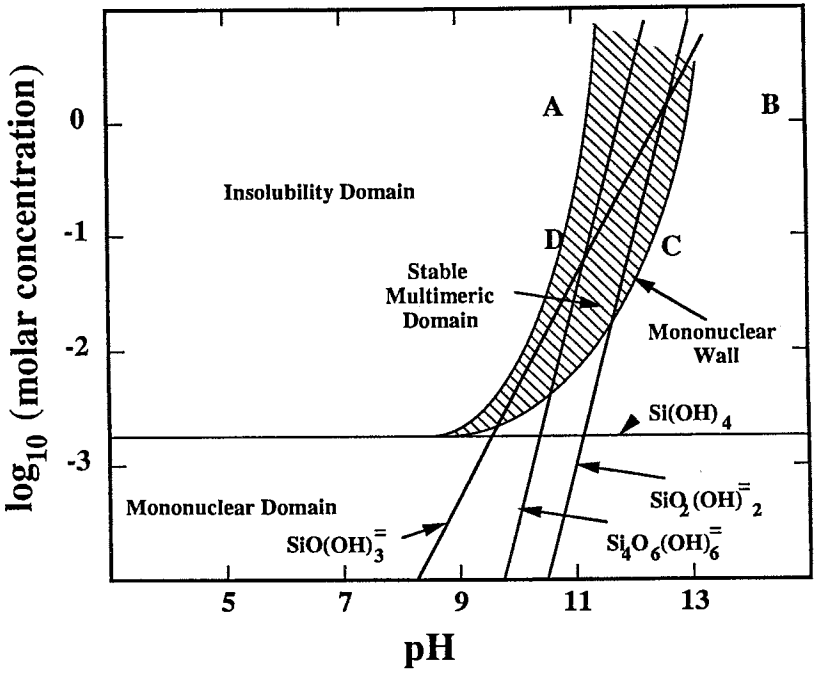

Figure 5. Calculated solubility diagram for amorphous silica at 25 °C. The monomolecular wall represents the lower limit for the stability of multinuclear silica species. Points A, B, C, and D are from experimental light-scattering data (20, 42) and provide confirmation of the region of existence of stable multimers. (Reproduced with permission from reference 23. Copyright 1979.)

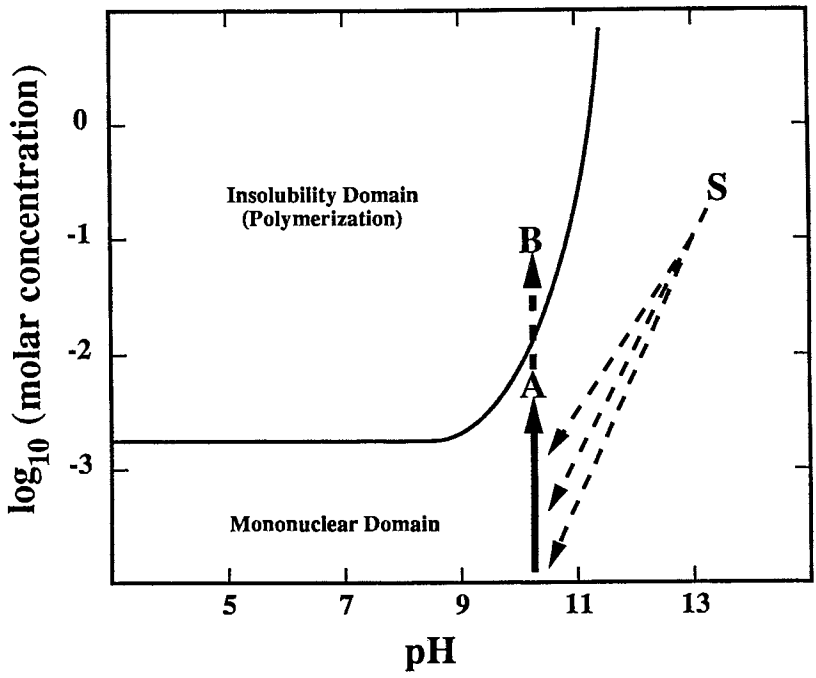

Figure 6. The course of a DS coating procedure (at 90 °C) related to the solubility domains for amorphous silica. S marks the concentration of sodium silicate solution (at pH ca. 13.5) added to the titania slurry. The vertical arrow represents the change in "aqueous silica" concentration during a coating procedure (at pH 10). Point A represents coating procedures that stop short of the precipitation edge, and point B represents those during which the edge is traversed. (Reproduced with permission from reference 23. Copyright 1979.)

possible to represent the insolubility–solubility domains of silica at this temperature (if not the details of individual speciation), as in Figure 6. The predominant reason behind Iler proposing that coatings be deposited at ca. 90 °C would be the increase by about a factor of 2.5 available in solubility compared to 25 °C, as well as possible "dehydration" and porosity aspects of resultant films (25). Included in Figure 6 are dashed lines that describe the "trajectory" of successive aliquots of aqueous silicate solution (pH ca. 13.5, point S) added to the titania slurry (at pH ca. 10). The steadily increasing silica concentration in the slurry is depicted by the solid vertical arrow in Figure 6.

In summary, in the DS process titania particles are exposed to an increasing concentration of monomeric silica species, and, depending on the coating level required (i.e., the total amount of silica added) this

concentration may be increased to the extent where precipitation of silica will occur. Multimeric species also may be present in part of the process.

Adsorption of Aqueous Silica onto Titania—pH and Concentration. A number of detailed experimental and modeling studies (*26–32*) have reported the adsorption of aqueous silicate onto oxides such as alumina and goethite and various other (often soil constituent) particulates such as fluorides. Studies of anion adsorption onto titania are not so common (*33*). This situation is somewhat strange given the technical importance of titania. The solubility of titania in water between pH 3 and 12 is only approximately 10^{-6} mol/dm^3 (*24*). Therefore, the formation of complexes between aqueous Ti(IV) species and aqueous silica will be insignificant in DS slurries. Such complex formation has often complicated the analysis of silicate adsorption on more soluble substrates (*29*) and makes it somewhat difficult to formulate generalized adsorption models (*32*).

In the adsorption study with titania (*33*), the levels of silica used were such that dispersions were always above the solubility limit for amorphous silica. Although the final concentration of "aqueous silica" in a typical DS preparation procedure might be between 10^{-2} and 10^{-1} mol/dm^3 and hence close to or above the solubility limit, the DS procedure certainly involves exposure of titania surfaces to soluble silica species prior to precipitation. Therefore, the value of the previous adsorption study (*33*) for understanding the details of DS deposition is limited. The final silica concentration reached depends on the levels of titania used and the degree of coating desired. Such "final" concentrations refer to added silica—in fact bulk precipitation may never occur even if the solubility edge of Figures 5 or 6 is traversed (*27*).

Figures 7, 8, and 9 describe changes in aqueous silica concentration, as the pH is lowered from ca. 13 to ca. 6, at various total silica concentrations (up to and including 10^{-2} mol/dm^3). Runs were performed in the absence and presence of titania. This series of experiments was performed at 25 °C (*34*), but nevertheless provides a framework for the understanding of DS deposition.

Concentration of 10^{-4} mol/dm^3 Aqueous Silica. This concentration is well below the "solubility edge" at all pH values—the blank result (Figure 7) confirms that no silica was precipitated when the pH was reduced from 13 to 7. In the presence of titania, adsorption occurred at all pH values, with a clear adsorption peak at pH 9.5. A similarly positioned adsorption maximum has been reported on goethite (*26, 27, 30*) and gibbsite (*26*) and interestingly also on some but not all fluoride minerals (*29*). By contrast, Howard and Parfitt (*33*) saw no such maximum on titania. However, as stated earlier, these workers were estimating adsorption in the presence of

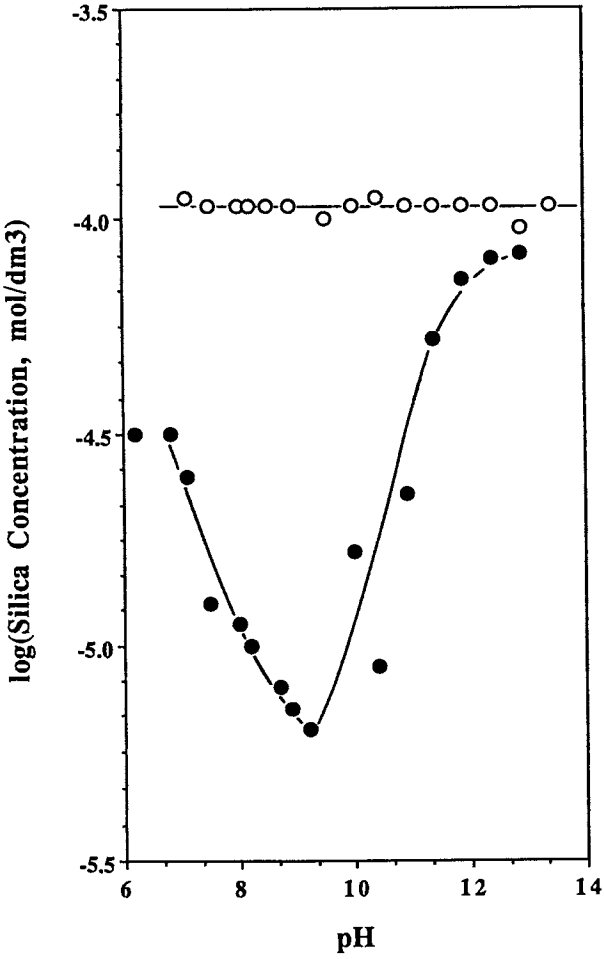

Figure 7. Aqueous silica concentration vs. pH for 10^{-4} mol/dm³ total silica with pH decreased from an initial value of 13.5: ○, sodium silicate solution (blank); ●, 20 m²/dm³ titania added (at pH 13.5).

precipitated silica, a somewhat different experimental system than that represented by Figure 7. Interestingly, Howard and Parfitt did observe desorption of silica when the pH was subsequently decreased from 10—results in accord with the data in Figure 7. At all the pH values in Figure 7 the titania particles will be negatively charged, hence adsorption is clearly not in response to electrostatic interactions, but rather in spite of them.

The adsorption maximum at pH 9–10 has been seen by others (26) as reflecting the first pK_a of silicic acid ($pK_a^1 = 9.45$ at 25 °C), although it has been argued by different workers that this maximum in turn was an

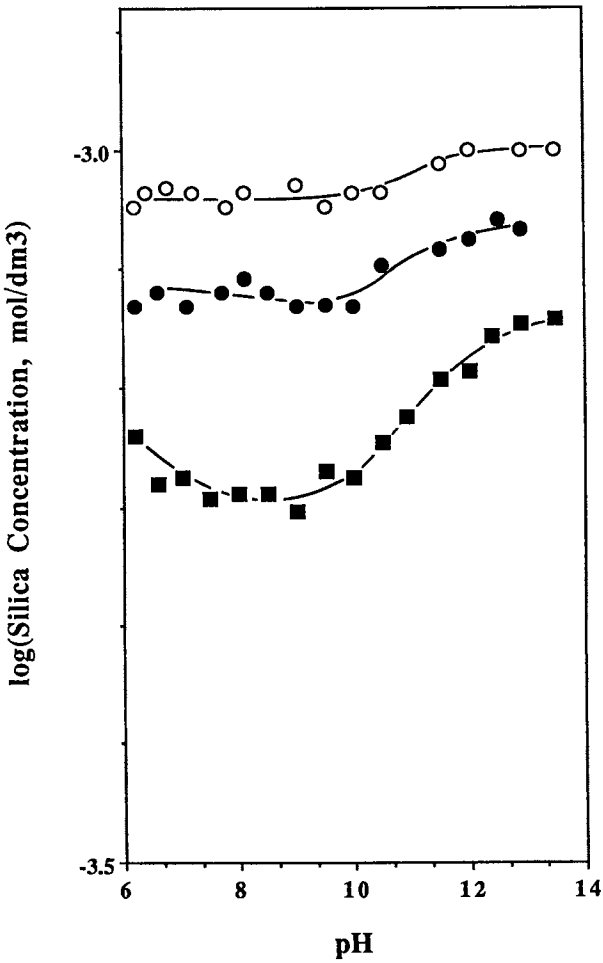

Figure 8. Aqueous silica concentration vs. pH for 10^{-3} mol/dm³ total silica with pH decreased from an initial value of 13.5: ○, sodium silicate solution (blank); ●, 20 m²/dm³ titania added; and ■, 60 m²/dm³ titania added (at pH 13.5).

indication that $SiO(OH)_3^-$ adsorbed alone (*29*) or that $Si(OH)_4$ and $SiO(OH)_3^-$ adsorbed concurrently (*26*). Early modeling studies (*26, 28*) related silica adsorption to exchange with substrate surface hydroxyl groups, although clearly this situation would not be the case for adsorption on fluoride minerals. Davis and Leckie (*30*) and others (*28*) alluded to the possibility of more than one type of surface adsorption site, although some workers (*28*) conceded that experimental verification may be difficult. Marinakis and Shergold (*29*) proposed the direct binding of aqueous $SiO(OH)_3^-$ to surface cation sites on calcium fluoride. Barrow and Bowden,

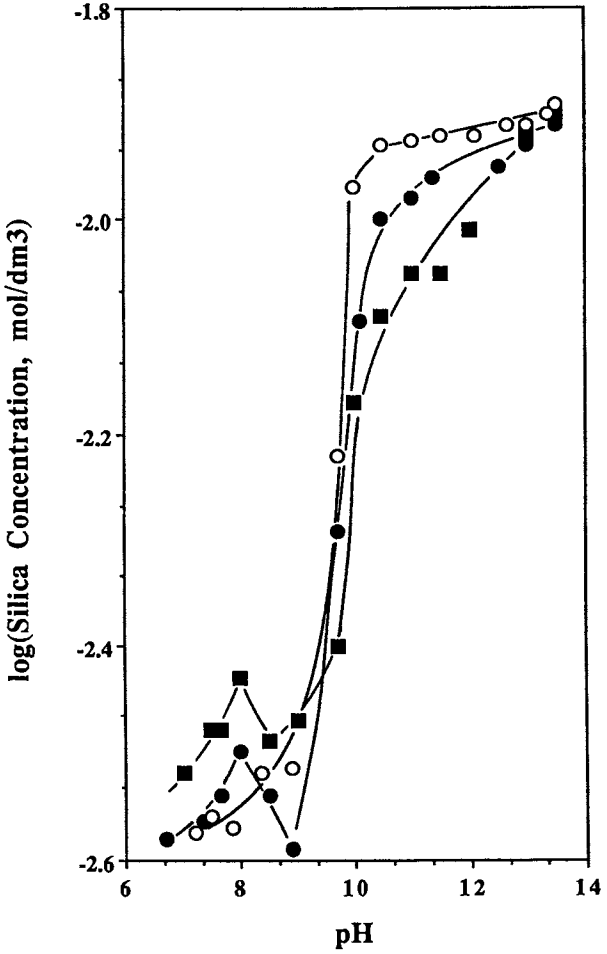

Figure 9. Aqueous silica concentration vs. pH for 1.25 × 10^{-2} mol/dm^3 total silica with pH decreased from an initial value of 13.5: ○, sodium silicate solution (blank); ●, 20 m^2/dm^3 titania added; and ■, 50 m^2/dm^3 titania added (at pH 13.5).

longtime contributors toward the understanding of anion adsorption, have extended (32) modeling work to specifically include both surface hydroxyls and surface cations (with coordinated water) on oxide surfaces. In so doing they concluded that the predominant adsorbing species is the divalent $SiO_2(OH)_2^-$ and rationalize this finding with the observed maximum in adsorption at around pH 9–12. They also state that the pK_a values for silicic acid (9.45 and 12.56) are close enough to make it difficult to clearly distinguish between the predominant adsorbing species at various pH values. In the experimental results represented in Figure 7 (total silica

concentration of 10^{-4} mol/dm^3), calculations show that $SiO(OH)_3^-$ is the greatly dominant species at pH 9.5. This fact leads to the conclusion, contrary to that of Barrow and Bowden (32), that $SiO(OH)_3^-$ is the predominant adsorbing species giving the observed adsorption maximum.

Concentration of 10^{-3} mol/dm^3 Aqueous Silica. This silica blank (Figure 8) showed a small decrease in concentration as the pH was decreased from ca. 12 to ca. 9–10; at lower pH values the concentration was constant. The aqueous silica diagram (Figure 5) shows an equilibrium solubility of ca. 2.5×10^{-3} mol/dm^3; hence the decrease evident in the blank seems unlikely to indicate precipitation. The likelihood is that silicon polyanions were removed from solution. In the presence of titania, some adsorption is apparent at all pH values. The adsorption peak is still evident at around pH 9, although much less so than in Figure 7. Hence it appears that monomer adsorption and multimer "precipitation" occurred concurrently in this slurry. The level of adsorption increased linearly with the increase of titania loading (Figure 8); this indicates that the adsorption density was independent of the equilibrium silica concentration in the range of 5.5 to 7.8×10^{-4} mol/dm^3 (see the adsorption isotherm in Figure 10). At a total silica concentration of 10^{-3} mol/dm^3 and pH 9–10, the dominant silica species is $SiO(OH)^{3-}$; $SiO_2(OH)^{2-}$ will be present as a very minor species. It seems then that the former is "controlling" when it comes to adsorption.

Concentration of 1.25×10^{-2} mol/dm^3 Aqueous Silica. At this concentration the precipitation edge for silica is at pH 10.0; this result is confirmed by the blank run in Figure 9, as was the limiting solubility of precipitated silica of ca. 2.5×10^{-3} mol/dm^3 at pH values less than 9. In the presence of titania, precipitation losses still dominate, although some extraction of silica occurs above the pH of precipitation, and the "maximum" in adsorption at pH ca. 9 is still evident.

Adsorption Isotherm at pH 9.5. The data in Figures 7–9 demonstrate how silica can adsorb onto titania as both monomers and polymers, the nature of the species depending also on the total concentration of "aqueous silica." Figure 10, showing the adsorption at pH 9.5, comes from many such uptake–pH experiments in which the equilibrium silica concentration did not exceed 10^{-3} mol/dm^3. Hence Figure 10 describes only monomer adsorption and indicates a limiting adsorption density of ca. 2.5×10^{18} molecules per square meter. This density corresponds to ca. 0.4 nm^2 per adsorbed silica species. The density of hydroxyl groups on titania surfaces corresponds to ca. 0.16 nm^2 per hydroxyl. Therefore, there is not a simple correlation between silica uptake and titania surface hydroxyls and adsorption does not proceed to complete surface coverage.

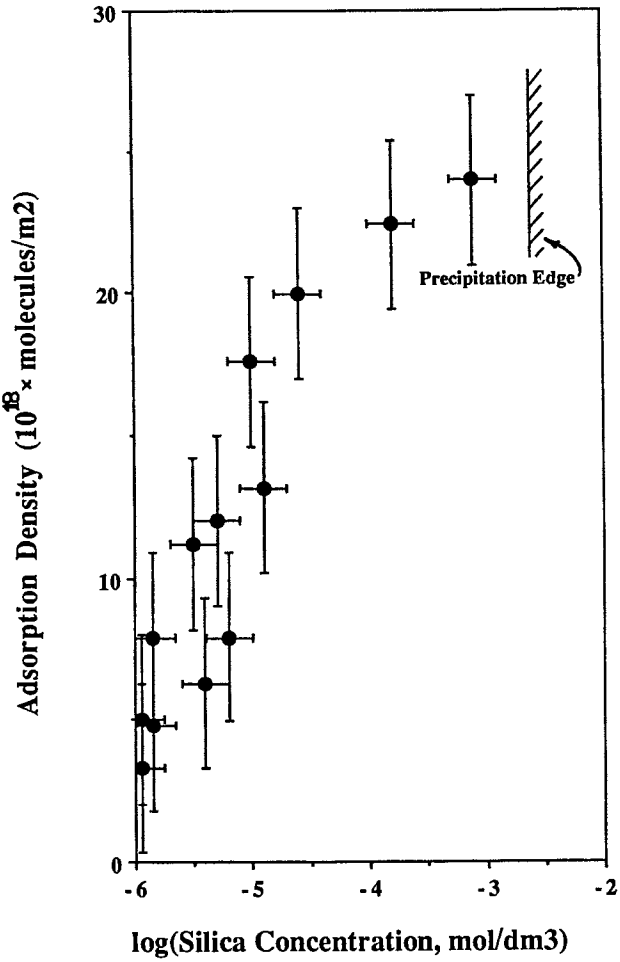

Figure 10. Adsorption isotherm for aqueous silica on titania at pH 9.5.

Howard and Parfitt (33) also observed that adsorption on titania did not proceed to complete surface coverage, stopping at a little less than half coverage. Similar incomplete coverage was also noted on geothite (27) and on some fluoride minerals (29). The adsorption density may be limited by the size of the adsorbing silicate species, although an area of ca. 0.4 nm^2 for the cross-sectional area of monomeric silica seems unreasonably large. There seems little other reason why all surface hydroxyls would not react equally with aqueous silica. As discussed, other surface sites may participate in adsorption (32). With the value of hindsight it can be said that silicate adsorption onto titania surfaces in fact occurs preferentially on

hydrated surface cation sites (known to be at a density of ca. 3×10^{18} per square meter); the following discussion presents experimental results that lead to this conclusion.

Interaction of Aqueous Silica with Titania. ***Microelectrophoresis.*** This method is useful for monitoring the surface charge characteristics of the "coated" titania either after or during deposition. There is a difference of ca. 3 pH units between the isoelectric point of titania (ca. pH 5) and that of silica (ca. pH 2), and the progressive shift in the isoelectric point as coating proceeds indicates the extent of silica coating. Figure 11 (23) shows such a progression for 0.6–5 wt % DS coatings on rutile particles ca. 0.1×0.4 μm in size (specific surface area 20 m^2/g). Such titania particles are not typical of commercial pigments (which are usually ca. 0.2 μm in diameter) but were useful for this "diagnostic" study in that they were very pure and without the normal pigmentary additives. Each coated titania was prepared according to the DS scheme (Figure 4a), and the level of silica incorporation was increased by increasing the amount of aqueous silicate solution added. Each coated titania powder was dried in air after preparation. The "final" silica concentration corresponded to point A on Figure 6 for the 0.62 wt % DS sample and increased to point B for the 4.99 wt % DS sample. Discrete coatings were only perceptible by electron microscopy for the 2.55 and 4.99 wt % DS samples (Figure 2). There was no evidence of "bulk" silica precipitation in any of the samples. Types of isoelectric point shift similar to those in Figure 11 are seen (23) when the electrophoretic mobility of the titania particles is determined, as a function of pH, in the presence of aqueous sodium silicate. Figure 12 is a compilation of isoelectric point data from both DS-coated titania and titania–aqueous silicate experiments.

Figures 11 and 12 show the following:

- The isoelectric point was apparently unaffected at low silica coverages—below ca. 0.5 wt %. This fact indicates that silica adsorbs preferentially onto surface sites in a manner that does not affect average surface charge–pH behavior. A similar suggestion was made by Kononov et al. (35) in describing silica adsorption onto fluorite.
- The addition of between 0.5 and 1.4 wt % silica resulted in a shift of isoelectric point proportional to the silica loading. This finding is consistent with the "rule of thumb" of electrokinetics that the isoelectric point of a mixed surface is the surface-area-weighted average of the isoelectric point values of the components (15). Hence it appears that this surface concentration regime corresponds to the completion of silica monolayer surface coverage of titania particles. This

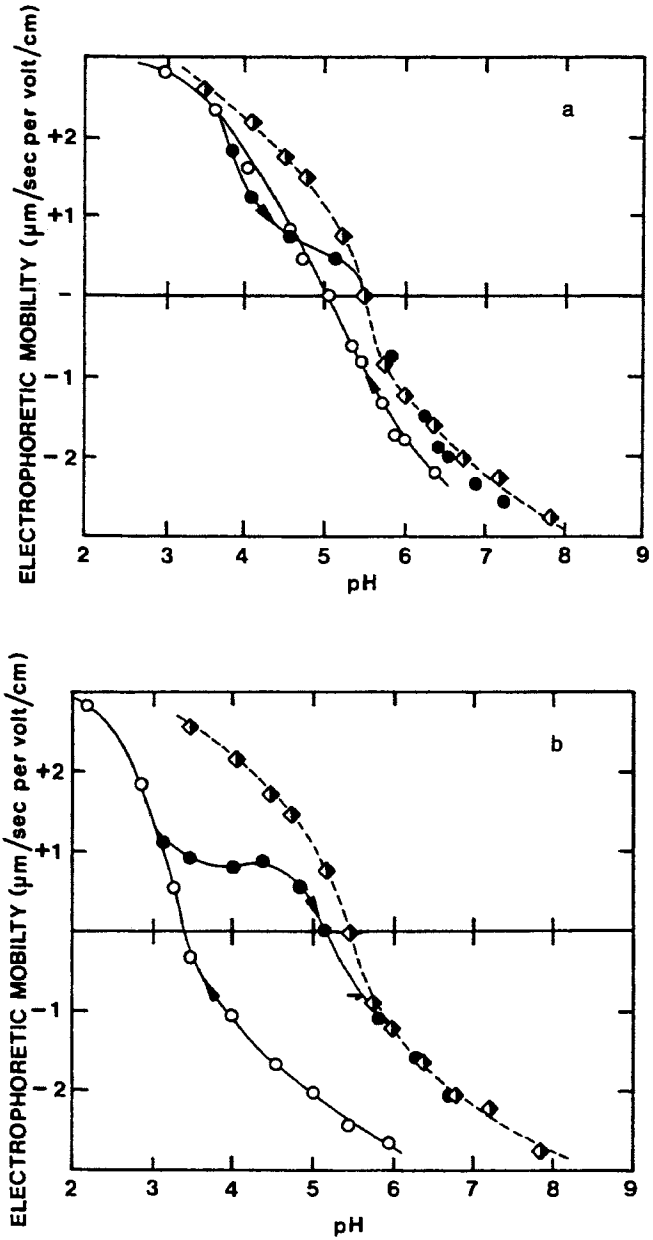

Figure 11. Electrophoretic mobility–pH curves for DS-coated titanias: ○, decreasing pH; ●, increasing pH; and ◈, uncoated titania. Silica loading was (a) 0.62 and (b) 1.35 wt %. (Reproduced with permission from reference 23. Copyright 1979.)

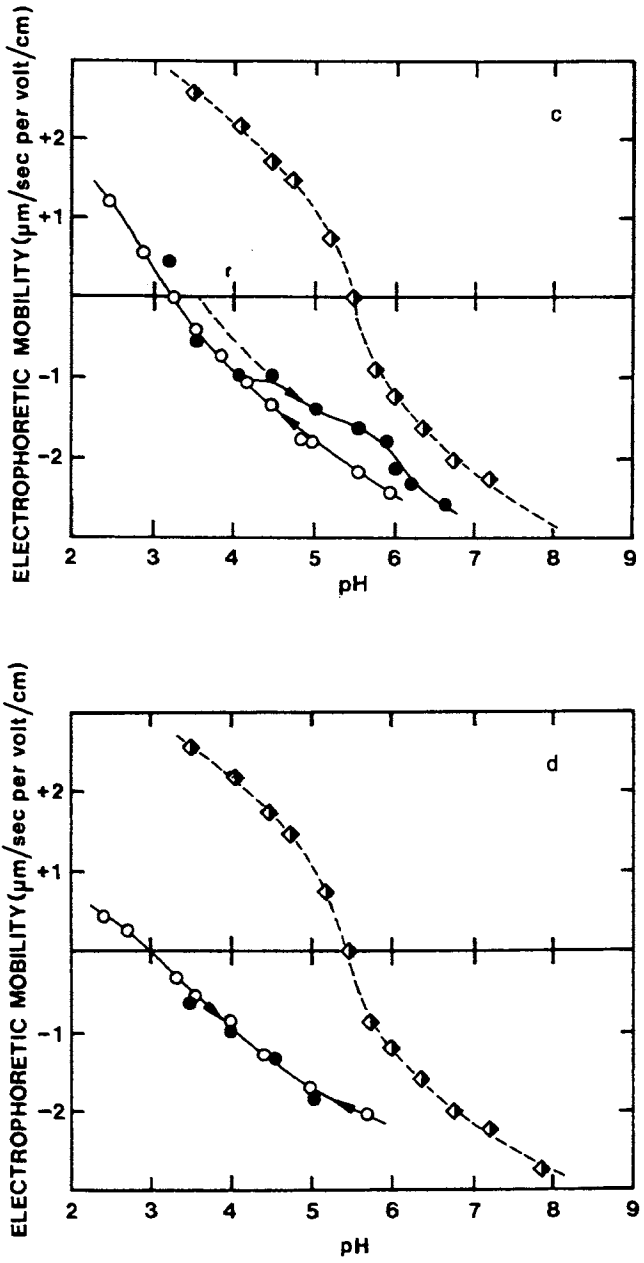

Figure 11.—Continued. Silica loading was (c) 2.55 and (d) 4.99 wt %.

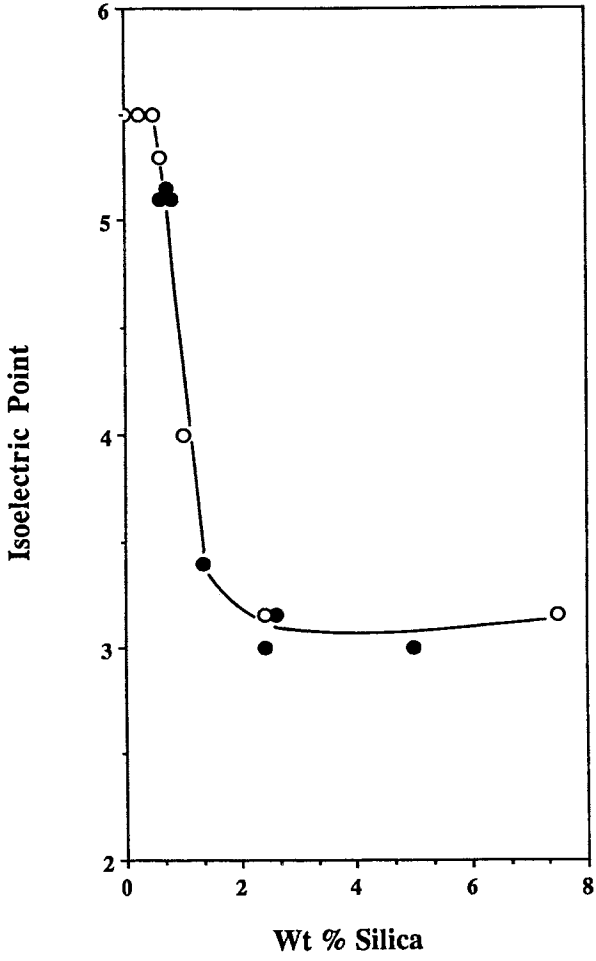

Figure 12. Isoelectric points of DS-coated titanias: ○, titania dispersed in aqueous silica; ●, dried, coated titania powders. The base titania was 20 m²/g.

relationship was confirmed by electron microscopy (*36*). Adsorbed silica in this concentration regime is relatively "fragile", in that it is apparently removed from titania particles during the "increasing pH" stage of the electrophoresis experiment (Figure 11).

- The particles exhibited a silica-like surface at greater than 1.5 wt % silica, and the silica coating was resistant to subsequent increases in pH.

If it is assumed that silica deposition results from 1:1 titania–silicate interactions, it can be shown (23) that the loading range of 0.5 to 1.4 wt % corresponds to ca. 40–100% monolayer coverage of titania particles; this result gives these interesting conclusions:

1. The first ca. 40% of surface coverage does not result in changes to surface-pH-dependent electrochemistry. As shown previously (37) with IR spectroscopy, ca. 40% of cations on the surfaces of rutile particles carry coordinated water molecules and the remainder are hydroxylated. The first type of surface site would not contribute to the pH dependence of surface charge—it seems from the electrokinetic data of silica-coated titanias that it is just these sites that preferentially adsorb aqueous silica. Such a finding is consistent with the observed maximum silica adsorption coverage (Figure 10). This specific silica–titania interaction is further discussed in the following "Gas Adsorption" section.
2. The electrokinetics of titania surfaces are completely converted to those of a silica surface with only one monolayer of silica. The indications are that silica binding proceeds beyond the level associated with the specific binding discussed earlier, although the adsorption isotherm (Figure 10) does not indicate such. Detailed assessment (23) of a wide range of coating experiments shows that complete surface coverage requires the concentration of aqueous silica to be increased to a level likely to induce polymerization, although the quantitative determination of the necessary concentration in a titania slurry at 90 °C and pH 10 (as in the DS coating procedure) is not possible. However, if the polymerization domain is avoided, adsorption of monomer inevitably leads only to partial surface coverage. It seems likely then that complete monolayer (and indeed subsequent multilayer) coverage occurs via the specific binding sites discussed earlier and not by interactions between aqueous silica species and surface hydroxyls on titania surfaces. If such anchoring sites are formed by exposure to monomeric silica, polymerization proceeds laterally across surfaces to effectively mask titania surface functionality at equivalent to monolayer coverage.

Gas Adsorption. Gas-phase infrared spectroscopy studies (37–39) of titania surfaces have revealed that surface cation sites on titania are dehydrated on outgassing between 150 and ca. 250 °C. Surface dehydrox-

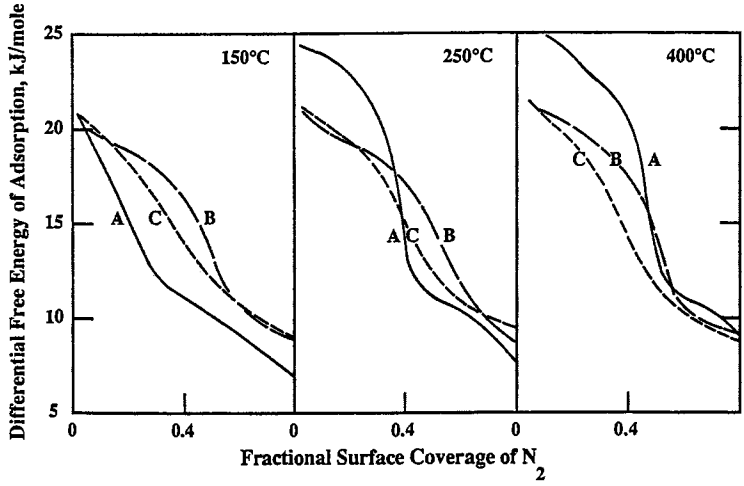

Figure 13. Differential energies of adsorption of nitrogen at 77 K plotted against nitrogen surface coverage. The outgassing temperature is indicated for each set of curves. Adsorbents were titania (curve A), titania with 0.6 wt % DS silica coating (curve B), and titania with 2.6 wt % DS silica coating (curve C). (Reproduced with permission from reference 41. Copyright 1980.)

ylation really only begins at above 250 °C and is essentially complete by 400 °C. Surface dehydration exposes very polar surface sites, and hence its evolution can be followed by measuring the energetics of interaction, for example, by using microcalorimetry with a polar probe gas (e.g., nitrogen). Representative microcalorimetry data (*40, 41*) for titania and DS-coated titanias are presented in Figure 13. The differential energy of nitrogen adsorption is plotted as a function of surface coverage by nitrogen (surface coverage deduced from the adsorption isotherm determined concurrently). For the present context the trends are clear. Curves A, for uncoated titania, demonstrate the emergence of "high-energy surface sites" when the outgassing temperature is increased from 150 to 250 °C and show that these sites occupy ca. 40% of titania surfaces (assuming, as is the norm, that nitrogen adsorption will proceed sequentially from "high" to "low" energy sites). Not surprisingly, for titania particles with a ca. 2-nm uniform DS coating (curves C), such active sites (not present on silica surfaces) are not uncovered on outgassing. The general form of the calorimetry curves for this sample over the outgassing range of 150–400 °C is very silicalike (*40, 41*). Interestingly, the titania particles with only around half-monolayer coverage of silica also show general silicalike behavior, and in particular there is no indication of active titania cation surface sites (curves B). Hence the gas adsorption microcalorimetry confirms the conclusions from microelectrophoresis; namely, silica deposition by the DS process proceeds via a

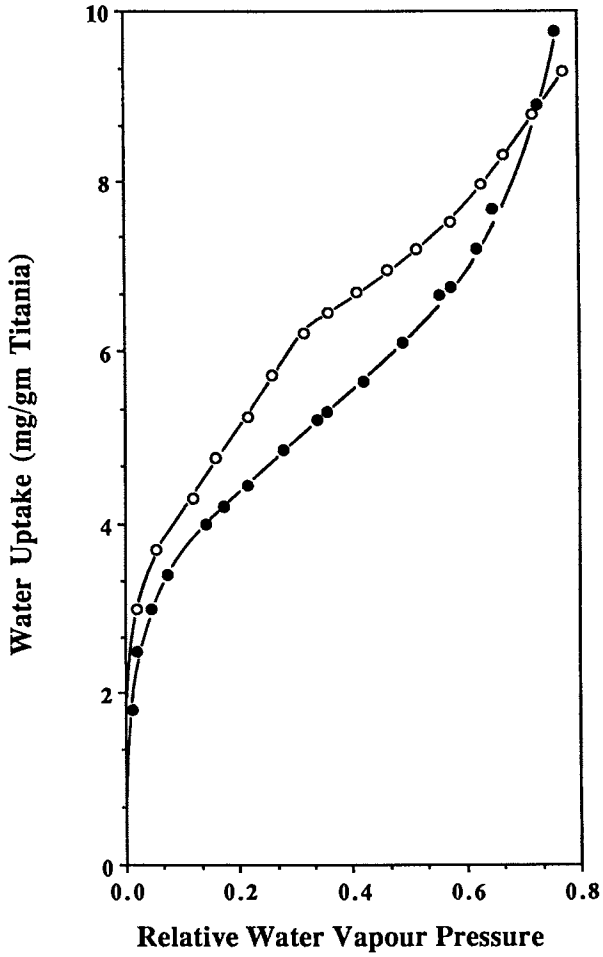

Figure 14. Adsorption isotherms of water vapor (at 25 °C) on titania (○) and 0.6 wt % DS-coated titania (●). The outgassing temperature was 150 °C. (Reproduced with permission from reference 42. Copyright 1986.)

specific solute–surface interaction as a precursor to "multilayer deposition". Undoubtedly, just such a sequence ensures coating adhesion and uniformity, two trademarks of the DS process.

The surface hydration–hydroxylation structure of titania, proved previously mainly by IR studies using dry titania powders, also seems to hold when these powders are dispersed in water. An interesting approach, therefore, is to probe directly the uptake of water from the gas phase by DS-coated rutile surfaces (*42*). Water adsorption isotherms are presented in Figure 14. The dual nature of titania surface sites, a property not seen

with other common oxides such as silica and alumina, leads to an unusual type of water adsorption isotherm for titania. The isotherm shows two distinct "knees" (Figure 14) connected by a region where adsorption increases linearly with the partial vapor pressure of water. The explanation for this adsorption behavior is rather complex (*42*) and beyond the scope of this chapter. This behavior is believed to be due to the presence of hydrated surface cation sites. What is noteworthy is that this rather specific behavior is not exhibited when ca. 40% of the titania surface is covered with DS silica.

Summary

Iler DS coatings have been a major success in the pigment world, and the Iler process may well be of value in the world of "useful" photocatalysis. Studies of silica adsorption on titania, via uptake and electrophoresis measurements and gas adsorption characterization procedures, have enabled an explanation of the nature of specific interactions between aqueous silica and titania. Binding is proposed to occur preferentially via hydrated cation sites on titania, and the occurrence of such binding is concluded to provide the basis for the subsequent surface polymerization necessary for the buildup of coherent multilayer silica.

Acknowledgments

As a young, raw researcher I was privileged to receive very positive encouragement from Ralph Iler. I have also benefited greatly by working with Tom Healy, Ken Sing, and Geoff Parfitt (deceased). Silicate adsorption data presented in this paper were the results of an honors program by Janice Grant of the University of Melbourne.

References

1. Iler, R. K. U.S. Patent 2,885,366, 1959.
2. Parfitt, G. D. *Croatica Chem. Acta*, **1980**, *53*, 333.
3. Simpson, L. A. *J. Oil Colour Chem. Assoc.* **1981**, *64*, 490.
4. Simpson, L. A. *Polymers Paint Colour J.* **1986**, *176*, 408.
5. Cutrone, L.; Moulton, D. V.; Simpson, L. A. *Pigment Resin Technol.* **1989**, *18*, 16.
6. Simpson, L. A. *Australian OCCA Proc. News* **1983** (May), 6.
7. Egerton, T. A.; King, C. J. *J. Oil Colour Chem. Assoc.* **1979**, *62*, 386.
8. Cundall, R. B.; Hulme, B.; Rudham, R.; Salim, M. S. *J. Oil Colour Chem. Assoc.* **1978**, *61*, 351.
9. Furlong, D. N.; Wells, D.; Sasse W. H. F. *Aust. J. Chem.* **1986**, *39*, 757.
10. Day, R. E.; Egerton, T. A. *Colloids Surf.* **1987**, *23*, 137.
11. Blatt, E.; Furlong, D. N.; Mau, A. W.-H.; Sasse, W. H. F.; Wells, D. *Aust. J. Chem.* **1989**, *42*, 1351.

12. *Photoinduced Electron Transfer*; Fox, M.A.; Chanon, M., Eds.; Elsevier: New York, 1988; Parts A through D.
13. Tada, H.; Saitoh, Y.; Miyata, K.; Kawahara, H. *J. Jpn. Soc. Colour Mater.* **1989,** *62*, 399.
14. Nagayama, H. Japanese Patent 58–161944, 1983.
15. Parks, G. A. *Chem. Rev.* **1965,** *65*, 177.
16. Furlong, D. N.; Parfitt, G. D. *J. Colloid Interface Sci.* **1979,** *69*, 409.
17. Furlong, D. N.; Johansen, O.; Launikonis, A.; Loder, J. W.; Mau, A. W.-H.; Sasse, W. H. F. *Aust. J. Chem.* **1985,** *38*, 363.
18. Nagayama, H.; Honda, H.; Kawahara, H. *J. Electrochem. Soc. Solid State Sci. Technol.* **1988,** *135*, 2013.
19. Furlong, D. N.; Freeman, P. A.; Lau, A. C. M. *J. Colloid Interface Sci.* **1981,** *80*, 20.
20. Iler, R. K. *The Chemistry of Silica*; Wiley: New York, 1979.
21. Jacobsen, H. W. Eur. Pat. Appl. EP 245,984, 1987.
22. Stumm, W.; Huper, H.; Champlin, R. L. *Environ. Sci. Technol.* **1967,** *1*, 221.
23. Furlong, D. N.; Sing, K. S. W.; Parfitt, G. D. *J. Colloid Interface Sci.* **1979,** *69*, 409.
24. Garrels, R. M.; Christ, C. L. *Solutions, Minerals and Equilibria*; Harper and Row: New York, 1965.
25. Iler, R. K., personal communication, 1984.
26. Hingston, F. J.; Pasner, A. M.; Quirk, J. P. *J. Soil Sci.* **1972,** *23*, 177.
27. Yokoyama, T.; Nakazato, T.; Tarutani, T. *Bull. Chem. Soc. Jpn.* **1980,** *53*, 850.
28. Sigg, L.; Stumm, W. *Colloids Surf.* **1980,** *2*, 101.
29. Marinakis, K. I.; Shergold, H. L. *Int. J. Mineral. Proc.* **1985,** *14*, 177.
30. Davis, J. A.; Leckie, J. O. *J. Colloid Interface Sci.* **1980,** *74*, 32.
31. Goldberg, S. *Soil Sci. Soc. Am. J.* **1985,** *49*, 851.
32. Barrow, N. J.; Bowden, J. W. *J. Colloid Interface Sci.* **1987,** *119*, 236.
33. Howard, P. B.; Parfitt, G. D. *Croatica Chem. Acta* **1977,** *50*, 15.
34. Grant, J. B. Sc. Thesis, University of Melbourne, 1980.
35. Kononov, O. V.; Barskii, L. A.; Ratmirova, L. P. *Russ. J. Phys. Chem.* **1973,** *47*, 1651.
36. Furlong, D. N., unpublished data.
37. Jones, P.; Hockey, J. A. *Trans. Faraday Soc.* **1971,** *67*, 2679.
38. Parkyns, N. D.; Sing, K. S. W. In *Colloid Science*; Everett, D. H., Ed.; The Chemical Society: London, 1975; Vol. 2, Chapter 1.
39. Parfitt, G. D. In *Progress in Surface and Membrane Science*; Danielli, J. F.; Rosenberg, M. D.; Cadenhead, D. A., Eds.; Academic: New York, 1976; Vol. 11, p 181.
40. Furlong, D. N.; Rouquerol, F.; Rouquerol, J.; Sing, K. S. W. *J. Chem. Soc. Faraday Trans. I* **1980,** *76*, 774.
41. Furlong, D. N.; Rouquerol, F.; Rouquerol, J.; Sing, K. S. W. *J. Colloid Interface Sci.* **1980,** *75*, 68.
42. Furlong, D. N.; Sing, K. S. W.; Parfitt, G. D. *Adsorption Sci. Technol.* **1986,** *3*, 25.

RECEIVED for review February 14, 1991. ACCEPTED revised manuscript January 30, 1992.

28

Dense Silica Coatings on Micro- and Nanoparticles by Deposition of Monosilicic Acid

Horacio E. Bergna, Lawrence E. Firment, and Dennis G. Swartzfager

DuPont Company, Wilmington, DE 19880–0228

The upper limit to the thickness of dense silica coatings on hydroxylated surfaces that can be obtained with conventional coating techniques was found to be extended significantly by coating with monosilicic acid. An example with submicrometer α-alumina particles as a substrate showed dense, uniform coatings up to at least 800 Å thick. The silica coatings and coating mechanism were characterized by chemical analysis, electrokinetic potential, nitrogen surface area (Brunauer–Emmett–Teller), particle size, X-ray photoelectron spectroscopy, diffuse reflectance Fourier transform infrared spectroscopy, secondary ion mass spectroscopy, and transmission electron microscopy.

SILICA COATINGS ARE APPLIED TO PARTICULATE MATERIALS to modify surface characteristics that interfere with the exploitation of desired bulk properties, as with titania pigments that may photocatalyze the degradation of their vehicle, surfaces of selective zeolite catalysts that may promote undesired reactions, and fillers for plastics that may not disperse in their matrix.

An upper limit to the thickness of dense silica coatings on hydroxylated surfaces can be obtained with some of the conventional coating techniques (*1*). We have found that this limit can be extended significantly by coating with monosilicic acid (MSA).

The deposition of silica from water was discussed by Iler (*2*). The mechanism of deposition of monomeric silica is different from that of the

0065–2393/94/0234–0561$08.00/0

deposition of colloidal particles. Monomeric silica is deposited from supersaturated solution in two known ways: as a deposit of $Si(OH)_4$ on a solid surface or as colloidal particles forming in the supersaturated solution.

Silanol groups SiOH condense with OH groups of MOH surfaces, where M is a metal that will form a silicate at the pH and temperature involved. The reaction is represented as follows:

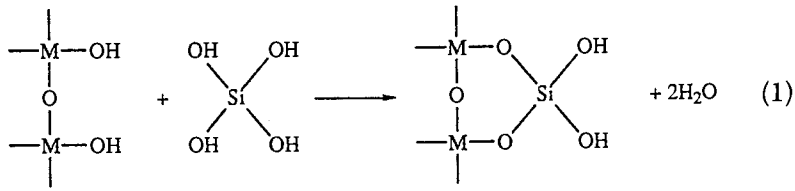

(1)

Further deposition of $Si(OH)_4$ is on silica, thus a layer of silica is built up.

The second known way of deposition of monomeric silica first involves polymerization in the solution. Iler described this deposition as follows: "If an insufficient area of a receptive solid surface is available to accept silica rapidly, and if the concentration of $Si(OH)_4$ is greater than 200–300 ppm (depending on pH), polymerization occurs with formation first of low polymers such as the cyclic tetramer; then these further condense to form small three-dimensional polymers which are colloidal particles" (*2*).

Monomeric silica is also deposited in a third way by living organisms as biogenic amorphous silica through still-unknown mechanisms. The underlying principles of nature's mechanism of deposition are being investigated as a first step to biomimetic processing of ceramics (*3*).

With the knowledge that monomeric silica is deposited from supersaturated solution as a deposit of $Si(OH)_4$ on a solid surface or as colloidal particles forming in the supersaturated solution, a general picture of the deposition of MSA on a hydroxylated surface may be visualized as occurring in three steps. In the first step, even before supersaturation it is assumed that at least some MSA may react with the hydroxylated surface (Figure 1). After supersaturation a number of mechanisms involving homonucleation and heteronucleation of MSA take place (Figure 2). Part of the MSA may react directly with the hydroxylated surface, and another part may nucleate to form hydrated silica polymers. The hydrated silica polymers may take several different paths depending on the conditions of the system. In one case, the hydrous silica polymer forms porous deposits on the hydroxylated surface. In another, the hydrous silica polymerizes further, either gelling or forming discrete particles of colloidal silica. Both the gel or the aquasol may attach to the hydroxylated surface, forming either "flaky" or porous deposits. Meanwhile, the MSA in solution may deposit in the interstices of the gel or in the interstices of the flaky or porous deposits formed on the surface by either the gel or the aquasol.

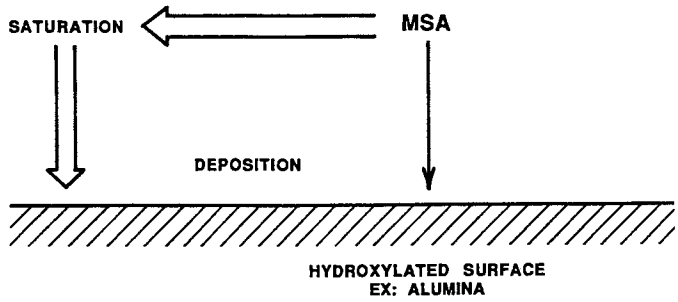

Figure 1. Silica deposition on hydroxylated surface; first step: before supersaturation.

What path the MSA follows is determined by factors such as composition of the substrate surface, addition rate of the MSA if it is being added to the system, slurry concentration if the system involves a dispersion of particles as substrates, ionic strength of the electrolyte solution in which the particles are dispersed, MSA concentration at any given time, and especially pH and temperature of the system.

If all these factors are properly controlled, MSA can be deposited on the hydroxylated surface, forming dense silica layers. Once a layer that completely covers the original hydroxylated surface is formed, any further deposition is on silica, thus an increasingly thicker dense silica layer is built up on the substrate surface (Figure 3).

In this chapter processes for coating α-alumina particles with MSA and for characterizing the coated particles to show the MSA is deposited as monomeric units to form a dense silica coating are described. The same procedures can be applied to coating titania and ρ-zeolite particles (*4*).

Experimental Details

Materials. MSA was prepared by the following procedure (*5*, *6*): a solution of sodium metasilicate was prepared by dissolving 30 g of pulverized, Fisher reagent grade $Na_2SiO_3 \cdot 9H_2O$ in 100 mL of 0.1 N NaOH. The silica content of this reagent, designated solution A, was 2.28%. A separate solution B was prepared, consisting of 0.025 N H_2SO_4, and was cooled to 0–5 °C. Meanwhile, a quantity of sulfonic acid cation-exchange resin (Dowex HCR-W2-H) was washed with distilled water until washings were colorless. A 1.5-g sample of the resulting washed resin was added to 100 mL of solution B in a beaker that was stirred and cooled in an ice bath at about 5 °C. At this point, 5 mL of solution A was added by intermittent jets of about 0.3 mL each, delivered by a 1-mL syringe and fine-tipped hypodermic needle. The pH of the resulting mixture was continuously maintained below 2.5 by delaying additions of solution A until the pH of the stirred, cooled mixture dropped below 2. After 5 mL of solution A had been added in this fashion, the pH of the mixture was about 2.15. The resulting clear solution of silicic acid was stored temporarily at 0–5 °C in an ice bath to prevent premature polymerization. The calculated concentra-

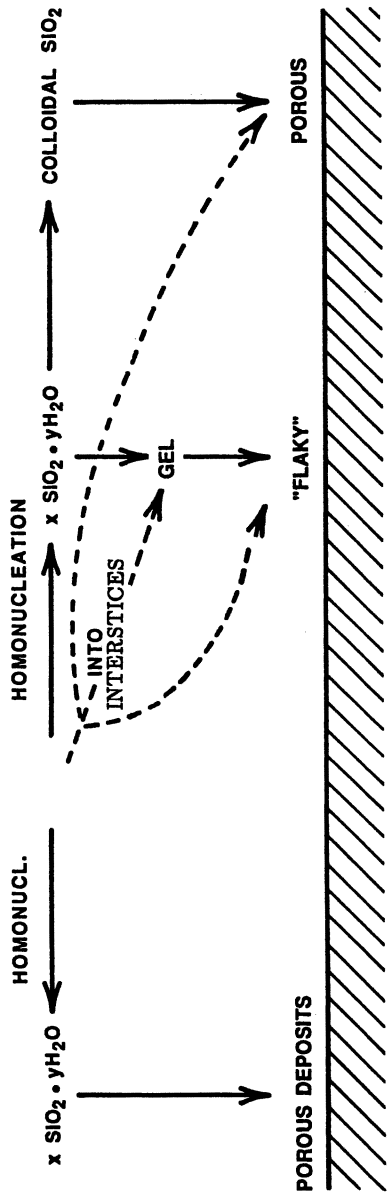

Figure 2. Silica deposition on hydroxylated surface; second step: after supersaturation.

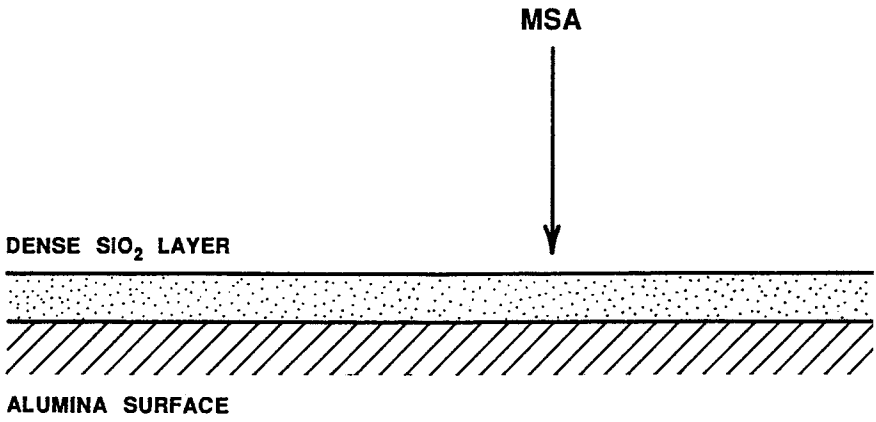

Figure 3. Silica deposition on hydroxylated surface; third step: after complete surface coverage.

tion of this solution of silicic acid was 3 mg of SiO_2 per milliliter. The same procedure was used to prepare silicic acid solution with a concentration of 2 mg of SiO_2 per milliliter.

The α-alumina was superground Alcoa A16 alumina classified by sedimentation in water and kept as a 10% aqueous slurry of pH 3.5–4.5. The Brunauer–Emmett–Teller (BET) specific surface area of the alumina product was 10–13.5 m^2/g.

Equipment. All coating experiments were performed in an automated reactor facility of a glass flask equipped with agitator, inlets for liquids, condenser, pH and temperature sensors, and controlling and recording instrumentation. The agitator consisted of a stir motor (Cole-Palmer model 4370-00) coupled to a glass stir rod with a Teflon blade positioned near the bottom of a glass flask. The flask was placed in a heating mantle, and the MSA was kept between 2 and 3 °C by a chiller with a circulating pump.

The aqueous alumina slurry was placed in the flask. The temperature of the slurry and MSA feed, the pH, the feeding rates of MSA and acid (concentrated HCl) or base (concentrated NH_4OH), and the stirring rates were controlled, measured, and recorded automatically (Kaye III Digitstrip recorder). The information obtained was monitored on the color screen of a Digital VT125 computer.

Procedure. Temperature of the alumina slurry was adjusted to 60 °C, and pH was maintained at 8.5 with automatic additions of dilute acid or base as needed. At this temperature and pH the MSA solution was added at a rate of ca. 2 g of SiO_2 per 1000 m^2 per hour to prevent formation of colloidal silica (*2*, *3*).

At the end of the MSA treatment, the slurry was allowed to cool to room temperature and centrifuged to separate the solid residue, made of coated alumina. The residue was washed by redispersing it in distilled water and centrifuging. The cake was dried in vacuum at 110 °C for 12 h.

Characterization Techniques. The dry samples of silica-coated alumina were analyzed by inductively coupled plasma–atomic emission spectroscopy

(ICP–AES). Specific surface area was determined by nitrogen adsorption (BET). Particle-size determination was made by low-angle forward scattering of light from a laser beam (Leeds and Northrup's Microtrac particle sizer) and by monitoring sedimentation with a finely collimated beam of low-energy X-rays and a detector (Micromeritics' Sedigraph 5100).

The samples were characterized by X-ray diffraction (XRD); transmission and high-resolution electron microscopy (TEM and HREM); microelectrophoresis; X-ray photoelectron spectroscopy (XPS), also known as electron spectroscopy for chemical analysis (ESCA); secondary ion mass spectrometry (SIMS); and diffuse reflectance Fourier transform (DRIFT) infrared absorption spectroscopy.

The transmission electron microscopy was done with a 100-kV accelerating potential (Hitachi 600). Powder samples were dispersed onto a carbon film on a Cu grid for TEM examination. The surface analysis techniques used, XPS and SIMS, were described earlier (7). X-ray photoelectron spectroscopy was done with a Du Pont 650 instrument and Mg K_α radiation (10 kV and 30 mA). The samples were held in a cup for XPS analysis. Secondary ion mass spectrometry and depth profiling was done with a modified 3M instrument that was equipped with an Extranuclear quadrupole mass spectrometer and used 2-kV Ne ions at a current density of 0.5 $\mu A/cm^2$. A low-energy electron flood gun was employed for charge compensation on these insulating samples. The secondary ions were detected at 90° from the primary ion direction. The powder was pressed into In foil for the SIMS work.

Electrokinetic potential of the alumina samples redispersed in 0.001 N KNO_3 was measured over a pH range between 2 and 9.5 with a Pen Chem System 300 instrument. The coated alumina powder was ultrasonically dispersed at 0.001 wt% into 300 mL of 0.001 N KNO_3 for ca. 15 min and immediately placed under N_2 atmosphere. A 50-mL portion was placed onto a titration stirrer under N_2 atmosphere that was fitted with a pH probe, a mechanical stirrer, and a port for addition of titrant. A portion of sample was pumped into the S3000 cell, which was fitted into a constant temperature bath set at 25 °C. This sample portion was used to rinse the cell of the previous sample. A second portion of sample was pumped into the cell. The pH was recorded and the zeta potential was measured. Two measurements were taken, one at the front stationary layer and the second at the back stationary layer. The histograms were then combined and averaged. The pH was adjusted with either 0.01 N KOH or 0.01 N HNO_3, and measurements were repeated for each desired pH value. Once all the desired pH versus zeta potential data were obtained, the data were transferred to an IBM PC and plotted. Estimates of isoelectric points (IEPs) were made from the plots obtained.

Infrared analysis of the coated and uncoated alumina particles was done by DRIFT with a 180° backscattering configuration and referenced to powdered (<30-μm particle size) KCl. A Nicolet 7199 interferometer operating at 4-cm^{-1} resolution was used to average 250 interferograms for an improved signal-to-noise ratio. The evacuated cell was capable of pressures of 10^{-6} torr (10^{-3} Pa) and temperatures to 400 °C.

Results

The original, uncoated α-alumina had a specific surface area of 10–13.5 m^2/g. Solid spherical particles of α-alumina 150 nm in diameter would have a surface area of 10 m^2/g. TEMs of the particles show that they are irregularly shaped and have a broad distribution of particle size between 0.1 and 0.8 μm (Figure 4).

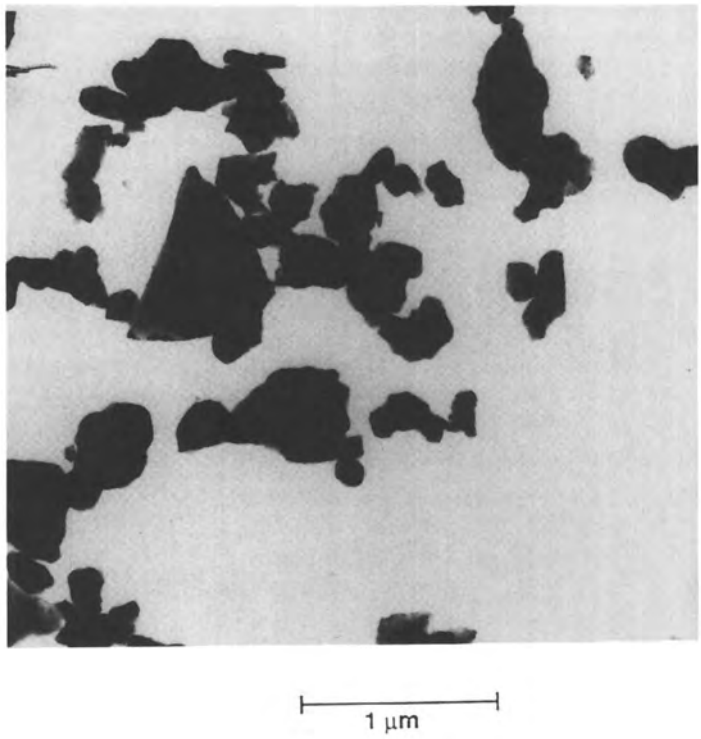

Figure 4. Transmission electron micrograph of superground, dispersed, and peptized Alcoa A16 α-alumina. (Reprinted with permission from reference 7. Copyright 1989.)

The silica content by chemical analysis, the specific surface area, and the particle-size analysis of the original alumina and the silica-coated products are included in Table I. For these alumina particles, theoretical monolayer coverage corresponds to 1 wt% silica. Within the error of the measurements, the specific surface area appears to remain fairly constant throughout the coating process. The constancy of surface area with silica level suggests that dense coatings are formed. Available particle-size measurements obtained by two different techniques suggest that the silica coating may cause some aggregation of the alumina particles at relatively low levels of silica and may become significant at higher coverages, starting at 6–9-wt% SiO_2.

Figure 5 shows plots of electrokinetic potential versus pH for the alumina samples at various levels of silica coverage and the changing character of the interface of the particles in aqueous solution with increasing coverage with silica, from pure alumina (IEP ca. 9.0) to pure silica (IEP ca. 2.0). Most of the change in electrokinetic potential has

Table I. MSA-Coated Submicrometer α-Alumina Particle-Size Analysis

Bulk Chemical Analysis (wt% SiO_2)	*BET Surface Area (m^2/g)*	D_{50} *(μm)*	
		Microtrac	*Sedigraph*
<0.05	10–13.4	0.5	0.3
0.12	10.8	0.5	0.3
0.32	12.3		0.13
0.55	12.5		0.12
1.19	14.4		
1.275	13.0		
2.03	14.0		0.26
2.55		0.55	0.08
2.69	9.8		0.42
3.72	13.4	0.44	0.42
4.89	13.5		
5.70	13.9	0.59–0.76	
6.60	13.7	0.62	0.54
8.14	11.7	0.89	0.71
8.41	13.5		0.60
23.38	9.9		1.35
27.0	10.5		

NOTE: No entry indicates that data were not determined. D_{50} is the 50th percentile of the size distribution.

occurred by 1-wt% silica loading; thus, most of the alumina surface has been covered by silica.

Figure 6 shows the infrared spectra of the surface of α-alumina particles before coating and after coating with 1-wt% of silica. The peak at 3743 cm^{-1} is characteristic of isolated surface Si–OH groups. The strong Si–OH absorption at the low 1% silica level shows that the silica is present largely at the particle surfaces as a coating.

Surface analysis results from XPS (ESCA) and SIMS as well as IEPS of samples with a coverage corresponding to 0.3–5.9-wt% SiO_2 are shown in Table II. At higher silica levels, the surface of the alumina particles is completely covered by a multilayer of silica and the thickness can be measured by TEM. Figure 7 shows, as an example, a micrograph of the coated edge of an alumina particle. These measurements are plotted in Figure 8 and included in Table III with BET results.

Figure 8 includes a plot of the calculated thickness of silica uniformly covering the surface of spherical alumina particles 150 nm in diameter (that is, spherical particles having approximately the specific surface area of the original α-alumina particles) as a function of silica weight percent. The formula for obtaining this plot is

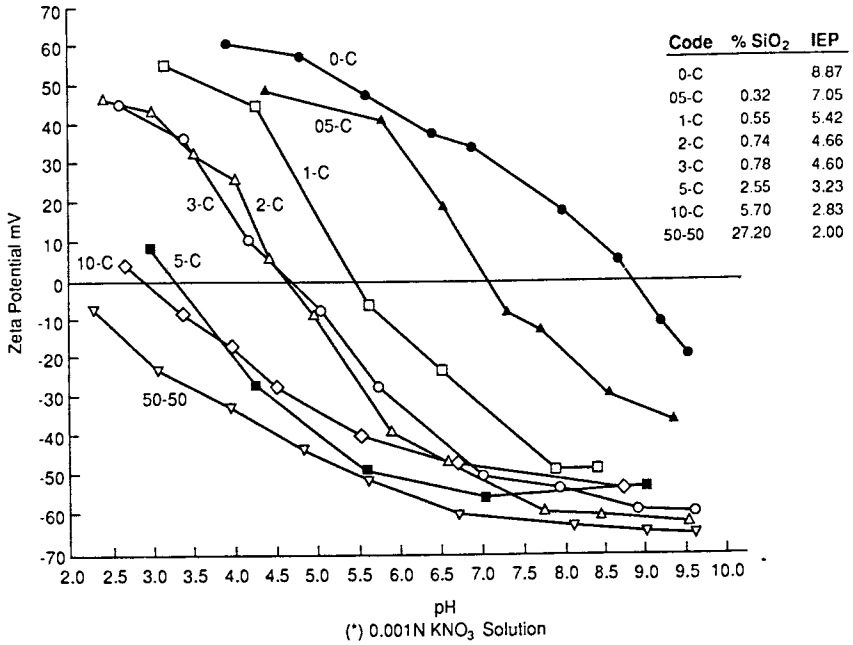

Figure 5. Electrokinetic (zeta) potential versus pH of alumina and silica-coated alumina particles dispersed in 0.001 N KNO_3 solution.

$$t = r\left\{\left[\frac{\rho_{Al}}{\left(\frac{1}{X_{Si}} - 1\right)\rho_{Si}} + 1\right]^{1/3} - 1\right\} \qquad (2)$$

where t is the coating thickness in nanometers; r is the particle radius, taken as 75 nm; ρ_{Al} is the density of α-alumina, 3.97 g/cm^3; ρ_{Si} is the density of the silica coating, taken as 2.2 g/cm^3; and X_{Si} is the weight fraction of silica in the coated particle.

A comparison of the results obtained by TEM, XPS, and SIMS was reported previously (6) and is included here for reference. In the 15–30-wt% range, there is good agreement between the coating thicknesses measured by TEM and the thickness calculated for uniform coating on spheres. Above 30 wt%, the thicknesses measured by TEM are much higher than the calculation. In this silica loading range, the measured surface area of the particles falls from about 12 (10–13.5) to 3 m^2/g. Apparently, in preparations at this high loading, the particles are agglom-

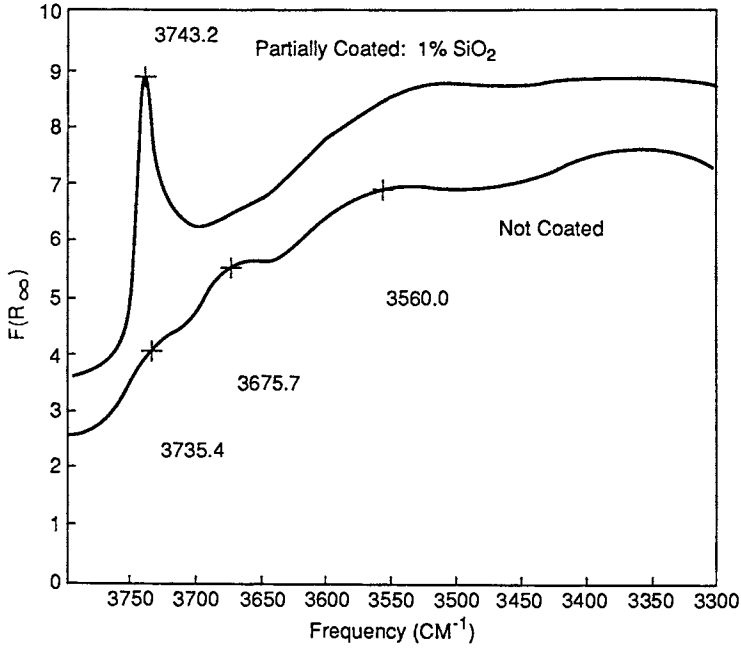

Figure 6. DRIFT spectra of the surface of α-alumina particles before and after coating with 1-wt% silica. $F(R_{\infty})$ *is the Kubelka–Munk function of reflectance.*

erated and the parameters of the calculation are no longer appropriate. Increases in average particle size were measured at lower silica levels, 6–9 wt%. Because there are fewer particles to coat, the coatings are thicker. We were unable to image without ambiguity coatings less than 35 Å thick.

Also plotted in Figure 8 is an estimate of thickness obtained from ratios of the Si and Al signals in the XPS spectra. This estimate results from the relationship between the measured Si:Al ratio and the thickness t of a uniform silica coating (*7*):

$$t = \lambda \ln (n_{Si}/n_{Al} + 1) \quad (3)$$

where n_{Si}/n_{Al} is the ratio of photoelectron signals from Si and Al multiplied by the appropriate sensitivity factors and λ is the electron mean free path.

There is quite good agreement between the TEM results, XPS results, and calculated thickness for the 10–20-wt% silica preparations. The low-silica region is plotted on an expanded scale in Figure 9; both the n_{Si}/n_{Al} ratios and the derived thickness are plotted. Over more than 2 orders of magnitude of n_{Si}/n_{Al}, there is good agreement between the XPS thickness and that calculated for uniform coating. Any deviations from a uniform

Table II. MSA Coating of Submicrometer α-Alumina Particles, First Stage: Hydrous Silica on Hydroxylated Alumina Surface

	XPS			SIMS		
W/O SiO_2	*Si:Al*	*Calculated Thickness (Å)*	*Coverage*	*Si:Al+Si*	*Approximate Average Thickness (Å)*	*IEP (pH)*
0.12	0.00	0.00	none			8.87
0.30	0.05	1.46	spotty	15	<5	
0.32	0.005	0.15	spotty			7.05
0.55	0.09	2.58	spotty	20	<5	5.42
0.74	0.09	2.58	spotty	30	5	4.66
0.785	0.10	2.86	spotty			4.60
1.19	0.09	2.58				
1.27	0.16	4.45		32	6	
2.03	0.31	8.10		57	6	
2.23	0.37	9.44	layer ca. 10 Å	60	7	3.0
2.55	0.44	10.94	layer ca. 11 Å	70	7–8	3.23
2.69	0.50	12.16		78	10	
4.89	0.95	20.00	layer 20 Å	85	25	
5.70						2.83

NOTE: No entry indicates that data were not determined.

Table III. MSA Coating of Submicrometer α-Alumina Particles, Second Stage: Hydrous Silica on First Silica Layer

Bulk Chemical Analysis (wt% SiO_2)	*HREM Thickness (Å)*	*BET Surface Area (m^2/g)*
Uncoated particles	—	10–13.4
5.70	35	13.9
12.90	60	
14.50	130	
22.50	150	
27.00	200	10.5
31.00	335	
	535	
54.00	830	3.0

NOTE: No entry indicates that data were not determined.

Figure 7. High-resolution electron micrograph of the coated edge of an alumina particle: total silica content, 14.5 wt% SiO_2; silica layer thickness, ca. 130 Å. (Reprinted with permission from reference 7. Copyright 1989.)

coating would decrease the n_{Si}/n_{Al} ratios and bring the XPS thicknesses below the calculated curve. The agreement is good even for coatings less than 1 nm thick, which approach atomic dimensions. These data show that the silica deposits as a molecular coating over a wide range of thicknesses.

Figure 10 shows SIMS depth profiles of surface composition versus time as the surface atoms are removed by 2-keV neon ion bombardment. There can be problems with quantitation of SIMS data associated with dependence of sputtering and ion yields on surface composition, but in this case of similar oxide coatings of substrates, these problems are minimized.

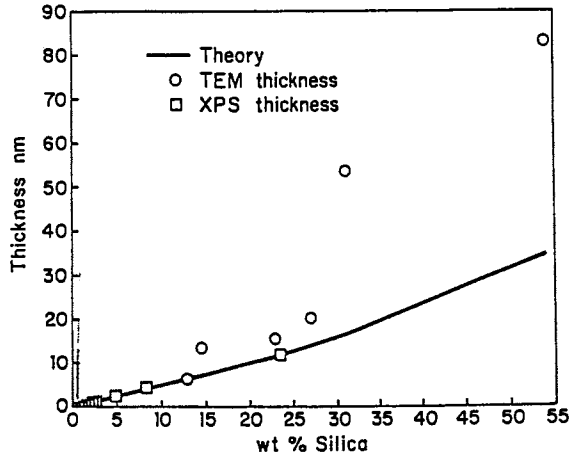

Figure 8. Silica layer thickness versus silica loading determined by TEM and XPS (ESCA) methods for silica-coated α-alumina particles. The theoretical curve was calculated for uniform silica coating of dense spherical α-alumina particles with equivalent 150-nm diameters. (Reprinted with permission from reference 7. Copyright 1989.)

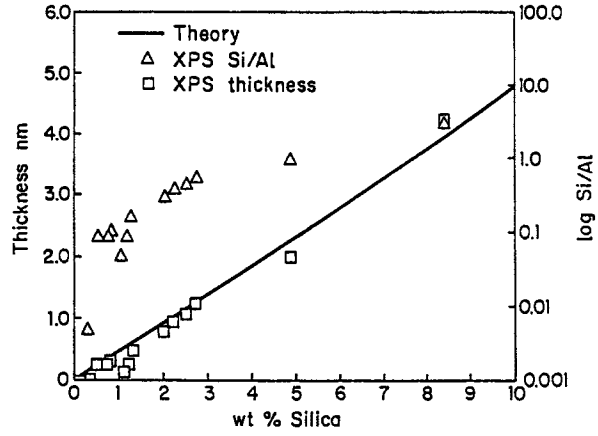

Figure 9. Low-silica region of an expanded scale plot of logarithm of Si:Al atomic ratio and derived XPS thickness versus silica loading. The theoretical curve was calculated for uniform silica coating of dense spherical α-alumina particles with equivalent 150-nm diameters. (Reprinted with permission from reference 7. Copyright 1989.)

The sputtering yields of SiO_2 and Al_2O_3 have been found to be similar (*8*). The abscissa is really in units of ion dose, but it was calibrated for depth by profiling through a 28-wt% coating thickness of 20 nm as measured by TEM. The calibration of ion dose to depth is then approximately 1×10^4 nm cm^2 C^{-1}. This calibration curve (compressed by a factor of 8) is shown,

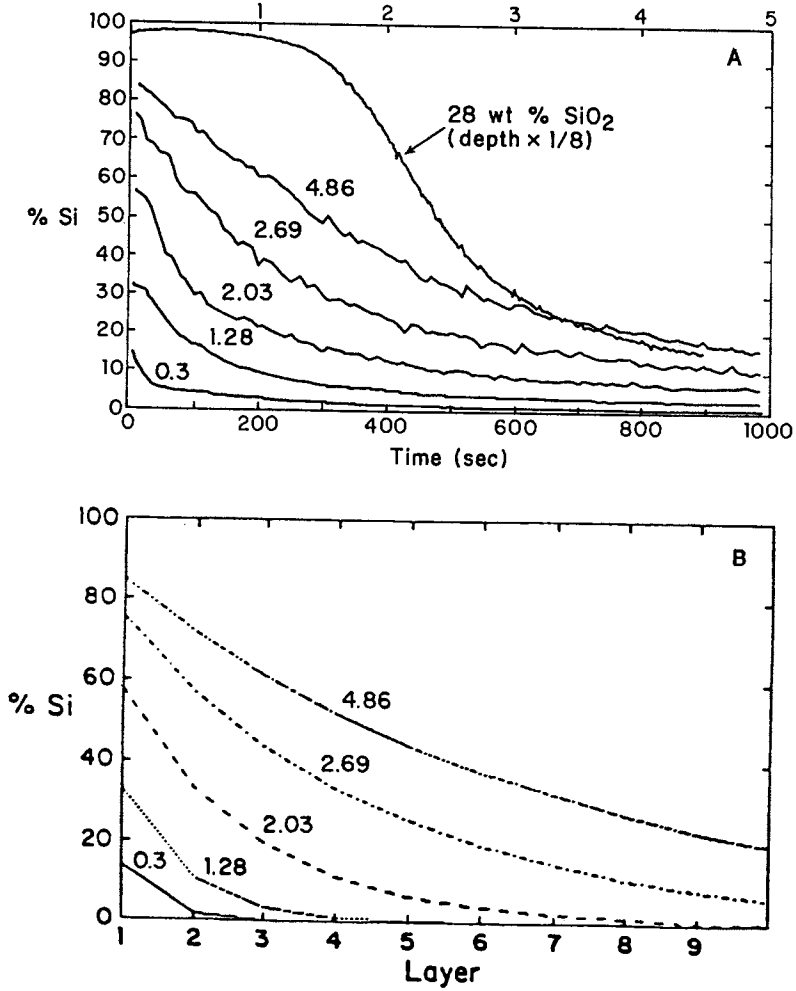

Figure 10. Depth profiles (A) of silica-coated alumina particles at different silica loadings obtained with SIMS. The calibration curve (28 wt% SiO_2) was compressed by a factor of 8. Model depth profiles (B) of silica-coated particles in the growth of the silica coating by random attachment of the silica units. The silica layer depth was converted to an approximate number of silica layers at 0.6 nm per layer. (Reprinted with permission from reference 7. Copyright 1989.)

along with some representative depth profiles of samples of lower silica content. The ordinate is in units of fractional coverage of the surface by silica ($n_{Si}/(n_{Si}+n_{Al})$). The coverage was calibrated at 100% silica with the signal from a thickly coated sample and at 0% with an uncoated sample; linear interpolation was used in between.

Discussion

In this work we tried to create conditions to deposit MSA on the hydroxylated surface of α-alumina in dense silica layers. The surface-sensitive electrokinetic measurements, DRIFT, SIMS, and XPS, show that the coating grows by deposition of molecular units on the surface of the alumina, whereas TEM, XPS, and surface area measurements show that thick, nonporous silica coatings can be grown. Characterization of particles coated with submonolayer or thicker MSA give insights into the nature of the coatings and the deposition mechanism.

At less than 5-wt% silica, there is some uncoated alumina surface. Just 1-wt% silica should be enough to coat the entire surface if it were deposited in a uniform monolayer (3.5 Å thick). The coatings become thicker even before complete coverage is obtained. Evidently, the silica is not deposited in complete layers on the alumina.

Although the silica is clearly not deposited complete layer by complete layer, the IEP, DRIFT, XPS, TEM, and SIMS data (Figure 5, 6, 9, and 10) show that the added silica is in the form of a coating on the alumina particles and is not present as an aggregated silica phase of silica particles. TEM data show this directly for coatings of large thickness. The other characterization methods show that the composition and chemistry of the particle surfaces are transformed from those of alumina to those of silica much more rapidly than the bulk composition is altered. For example, the SIMS data show that the particle surfaces are more than 80% silica when the bulk silica composition is 4.86 wt% (Figure 10). Also, if the silica was present as particles similar in size to the alumina particles and uniformly distributed through the alumina, the XPS-derived ratio n_{Si}/n_{Al} would approximate the bulk ratio of silica to alumina instead of the ratios 2 orders of magnitude higher that were measured.

IEP and SIMS characterizations can be used to compare the particle surface compositions dry and in aqueous solution. In Figure 11, the initial Si surface coverages and the IEP data are plotted together versus the amount of silica added. Schwarz et al. (9) showed a linear relationship between zero point of charge and silica content in a set of aluminosilicates. A more complex relationship is suggested by the curves in Figure 11 for these coated alumina particles, but the data suggest similar surface compositions in both dry and aqueous environments.

Plotted in Figures 8 and 9 is equation 2, the thickness calculated for uniform layers of silica on spherical alumina particles. The XPS- and TEM-derived coating thicknesses are in fair agreement with the assumption of complete coatings of constant thickness. The TEMs are consistent with the notion that the thick coatings are uniform. A comparison of model

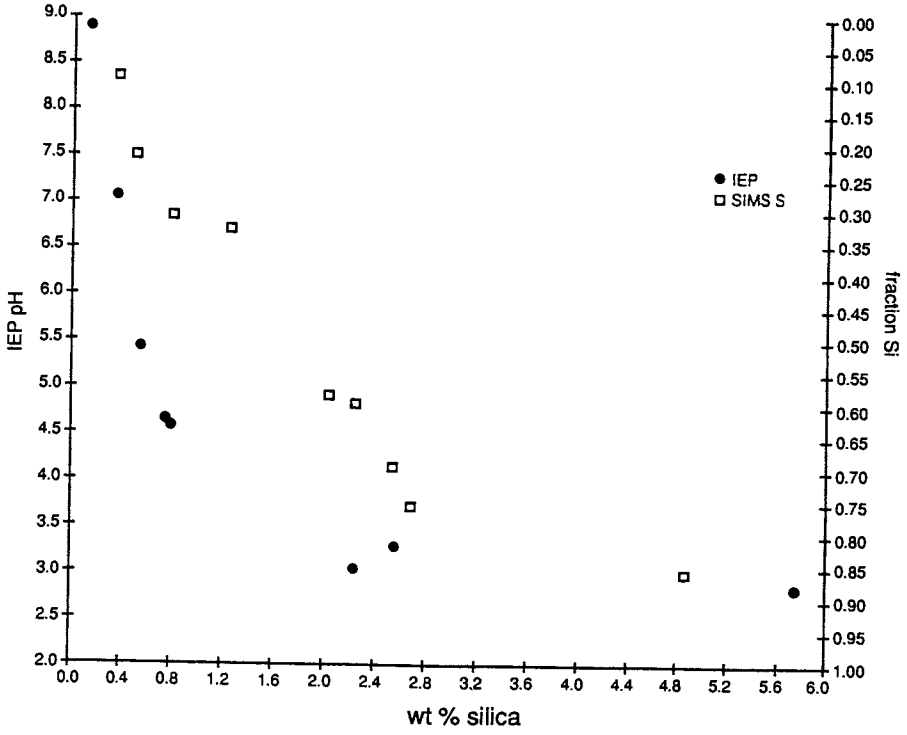

Figure 11. Relationship between isoelectric point, SIMS Si surface coverage, and total weight percent silica on the alumina surface. (Reprinted from reference 7. Copyright 1989.)

calculations and experiment shows that XPS is not sensitive to the details of the distribution of coating thicknesses (*7*).

The SIMS depth profile of the 28-wt% coating shows a plateau at nearly 100% Si for 10 nm before Al is detected (Figure 10). All of the alumina surface is covered at high loadings.

One mechanism of coating growth by random attachment of silica units to the particle surface with equal preference for bare alumina or previously deposited silica can be modeled. In this case, the rate of loss of alumina during growth is proportional to the fraction of alumina exposed. This mechanism predicts that the amount of bare alumina, n_{Al}, measured with SIMS should decay exponentially with added silica. A plot of $-\ln [n_{Al}]$ versus silica weight percent should yield a straight line. Such a plot is shown in Figure 12. The fraction of alumina exposed is merely 1 minus the silica fraction measured at the start of the depth profiles, as in Figure 10. The measurement is in good agreement with this model.

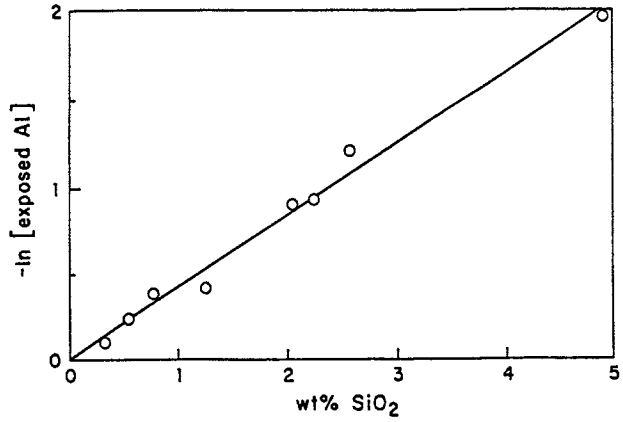

Figure 12. Plot of $-\ln [n_{Al}]$ as measured by SIMS versus weight percent silica. The linear plot indicates a random growth mechanism. (Reprinted from reference 7. Copyright 1989.)

Growth of the silica coating by random attachment of the silica units also predicts that the depth profiles will have a certain form. The amount of silica two layers thick will simply be the square of the fraction that is one layer thick. In general, the fraction of surface coated with N layers of silica would be

$$f(N) = f(1)^N \tag{4}$$

where $f(N)$ is the fraction of the surface covered N layers thick. Figure 10B compares model depth profiles calculated for the fractional coverages measured at the start of the depth profiles to the complete depth profiles. The only adjustable parameter was the conversion of silica layer number to depth, about 0.6 nm per layer. The size of a SiO_4 tetrahedron can be estimated to be 0.35 nm. The agreement between the calculated and observed profiles is quite good and gives good support to the random growth mechanism.

Random fixing of the silica units on the particle surface means either that the approaching units stick where they first contact the surface or that the adsorbed silica units are mobile but have no preference for where they become permanently fixed.

After complete coverage of the alumina surface is achieved at high silica loadings, the distribution of thicknesses will be Gaussian with a standard deviation of the square root of the average thickness. With the random growth mechanism established, the coating thicknesses and thickness distributions of silica coatings prepared in this way can be easily predicted.

Acknowledgements

W. B. Hambleton, Jr., designed and automated synthesis facility and prepared the coated alumina samples; E. E. Carroll, Jr., made the surface area measurements; M. L. and M. J. Van Kavelaar performed the TEM measurements; B. F. Burgess and the Galbraith Laboratories of Knoxville, TN, made the ICP–AES determinations; R. E. Johnson, Jr., and J. V. Hughes, Jr., made the electrokinetic potential measurements; D. B. Chase developed the DRIFT spectra; and P. E. Bierstedt performed the XPS tests. We are grateful to D. P. Button for encouragement and support to do his work. We dedicate this chapter to the late Ralph K. Iler, who was an invaluable source of inspiration at the early stages of our work with MSA and zeolites.

References

1. Button, D. P., private communication, 1986.
2. Iler, R. K. *The Chemistry of Silica*; Wiley: New York, 1979; p 87.
3. Ulrich, D. R. *Chem. Eng. News* **1990**, *68*, 40.
4. Bergna, H. E.; Corbin, D. R.; Sonnidesen, J. C. U.S. Patent 4,683,334.
5. Alexander, G. B. *J. Am. Chem. Soc.* **1953**, *75*, 2887.
6. Bergna, H. E.; Corbin, D. R.; Sonnidesen, J. C. U.S. Patent 4,752,596.
7. Firment, L. E.; Bergna, H. E.; Swartzfager, D. G.; Bierstedt, P. E.; Van Kavelaar, M. L. *Surf. Interface Anal.* **1989**, *14*, 46.
8. Betz, G.; Wehner, G. K. *Top. Appl. Phys.* **1983**, *52*, 11.
9. Schwarz, J. A.; Driscoll, C. T.; Bhanot, A. K. *J. Colloid Interface Sci.* **1984**, *97*, 55.

RECEIVED for review January 30, 1992. ACCEPTED revised manuscript May 7, 1992.

29

Applications of Colloidal Silica: Past, Present, and Future

Charles C. Payne

Nalco Chemical Company, One Nalco Center, Naperville, IL 60563–1198

Early uses of colloidal silica for catalysis, ceramics, paper and textile applications, strength enhancement in rubber, tobacco treatment, and medicine are discussed. A historical view of the development of applications is highlighted, and future uses are discussed.

WHEN THOMAS GRAHAM PREPARED SILICA COLLOIDS IN THE 1860s (*1*, *2*), he couldn't have envisioned its many applications today. The list of applications in Iler's 1979 edition of *The Chemistry of Silica* (*3*) is long and varied. Sometimes silica is used to promote adhesion and sometimes to prevent adhesion. These opposing properties from the same material indicate that applications involving silica sols can be quite complex. Bungenburg de Jong (*4*), in reviewing the origins of colloid science, pointed out that Graham introduced the term "colloids" for substances that "in solution" showed only a very slow diffusion velocity compared with other substances such as sugar and salts. Most of the early literature (*5*) made no distinction between silicates, polysilicates, and what ultimately has come to be known as colloidal silica. Colloidal silica has discrete particles that are generally somewhat spherical and amorphous.

Preparation Procedures

Early. Thomas Graham was not the first person to attempt to prepare a colloidal silica. As early as 1747, Pott made a "semisolution of silica", and as early as 1820, a reference is made to the preparation of a sol of "hydrated silica" (*6*). In 1853, a French researcher named Fremy (*7*)

0065–2393/94/0234–0581$08.00/0

prepared a dilute colloidal silica from silicon sulfide. By 1864, silica colloids were being prepared by the dialysis of gels and by the hydrolysis of silicate esters (*8*). All products were very dilute.

Colloidal silica technology proceeded slowly. The early products were not suitable for most applications because (1) only low silica concentrations were available, (2) the materials were not stable with time, or (3) the products did not have reproducible properties. By 1915, only one patent for preparation of a commercial colloidal silica had been issued (*9*). Using electrodialysis (Figure 1) to make a product, Schwerin marketed a 2.4% silica sol as a stable material. Schwerin suggested the use of this product for medicinal purposes but did not specify how or where it should be used.

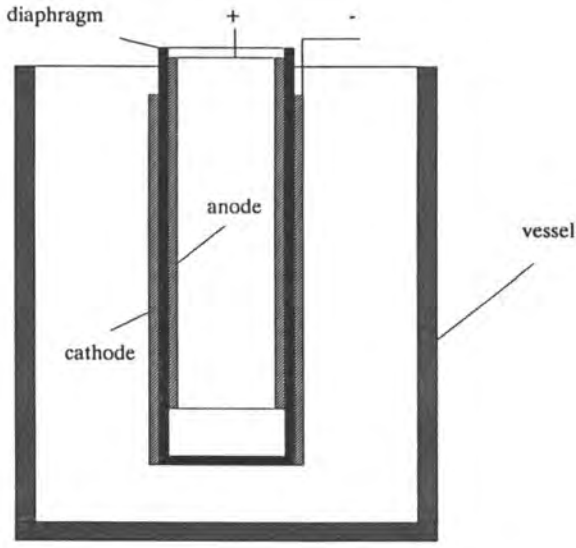

Figure 1. Electrodialysis cell of Schwerin (10).

1941 to 1963. The year 1941 was the turning point toward commercial silica sol production methods. Bird (*10*), at Nalco, found that low-molecular-weight silicic acids could be prepared by ion exchange. If a small amount of sodium hydroxide was added to these materials, particles were formed. These materials could then be concentrated with conventional evaporator techniques to about 27.5% silica. Nalco licensed the ion-exchange procedure to DuPont, which continued to work on preparation throughout the 1940s. Monsanto (*11–14*), during the years 1941 to 1951, continued to develop products by peptizing silica gels and thus prepared materials with a broad particle-size distribution, and by 1963 products containing 50% silica were prepared by gel peptization techniques.

The year 1951 is significant for the preparation of colloidal silicas other than by the conventional gel peptization technique. Using Bird's idea of preparing low-molecular-weight silicic acids by ion exchange, Bechtold and Snyder (*15*), two DuPont scientists under Iler's direction, developed the ingenious method of growing the particles to any given size while concentrating the products to up to 35% silica. This research, coupled with the work by Joseph Rule (*16*), another DuPont scientist, and his co-workers, determined the parameters needed to keep the products stable at high silica concentrations; thus, the Bechtold and Snyder process became a practical method that turned colloidal silica into a stable product with predictable properties. By 1959, commercial products were available with up to 50% silica concentrations. Rule's work was important in making stable products, but it was also important for using these materials in different applications.

Applications

To 1933. Griessbach (*17*) in 1933 summarized the various methods for preparing and using colloidal silicas up to that time. The methods of preparation of sols included dialysis, electrodialysis, gel peptization, and hydrolysis of the silicate esters or silicon tetrachloride. Silica sols were used in numerous applications at that time. Silica sols were a primary binder in the synthesis of catalysts used in the production of sulfuric acid or the dehydration of alcohols. In ceramics, they were used in glazes and other coatings. Cements and such materials as plaster of Paris could be coated with colloidal silica to improve their resistance to water and acidic substances. Colloidal silica was incorporated into paper and sprayed onto textiles or wood to either strengthen or protect the substrate. It was added to metal solutions such as silver or gold to improve stability so that these materials could be used in medicines. Silica in combination with surface-active agents also showed tendencies to emulsify, especially when the sol became destabilized and the viscosity of the system increased. Rubber latex emulsions were coagulated with colloidal silica to strengthen the final rubber product. A novel use for its time was the addition of colloidal silica to tobacco to help with the fermentation process and to aid in the adsorption of nicotine. Apparently, the fact that silica adsorbed and retained water helped to keep the tobacco fresh. The use of silica sols in medicine appears to be an area of great speculation in 1933. Colloidal silica was claimed to be useful for treating subcutaneous wounds, tuberculosis, and many circulation problems such as hardening of the arteries. Griessbach (*17*) also suggested the immobilization of such enzymes as those involved in the conversion of amylopectin into simple starches.

Many of these applications are practiced today. Other applications exist only for specialized situations. For example, silica sols are a desirable source of silica for catalyst substrates. For catalyst preparations, however, colloidal silica is generally used only for specialized applications.

Griessbach (*17*) showed that five companies produced silica sols in 1933. Most products were very dilute, and only one could be considered concentrated. The most concentrated sol available at that time was a product called Kieselsol I.G. (made by I.G. Farbenindustries), which contained 10% silica and was stabilized with ammonium hydroxide. The characteristics of most of the sols were undetermined. Moreover, the difficulty of making a reproducible product that would perform in a predictable manner for specific uses was technically impossible at that time. This difficulty, most likely, was the major reason that colloidal silica applications did not increase rapidly. Iler (*18*) pointed out that colloidal silica was not accepted for wide commercial use until methods were discovered for producing sols with high concentrations that would not gel or settle with time. The first steps to achieving that goal occurred in 1941 (discussed in the preceding section on preparation procedures).

1933 to 1955. Iler's 1955 edition of *Colloidal Chemistry of Silica and Silicates* (*5*) devotes seven pages to the uses of silica sols at that time. The areas of use included floor waxes, textiles, organic polymers, water treatment, and miscellaneous areas such as in cements and as a binder for luminescent materials used in television picture tubes.

Two areas of major interest in 1955 were paper antiskid and investment castings. Wilson (*19*) used colloidal silica to increase the friction between paper surfaces. In this application (Figure 2), the silica sol is typically diluted to 1–7% as silica solids and then applied to multiwall bags, corrugated boxes, and linerboards. Various methods of applying the silica sol were used. Typical applicators were sprays, segmented applicator rollers, knife blades, full roll coaters, sponges, and brushes.

Testing to ensure that the colloidal silica has been applied correctly consisted of determining either static or dynamic coefficients of friction with a slide angle tester (Figure 3). The coefficient of friction is defined as the numerical value for the tangent of the angle needed to start sliding (static) or the value needed to maintain sliding (kinetic).

Collins (*20*) used colloidal silica as a binder for investment casting applications. Investment casting techniques are useful for the production of aircraft parts, various industrial castings, dental and jewelry parts, and sporting equipment such as golf club irons and propellers for outboard motors. In a typical procedure, colloidal silica is mixed with a refractory grain such as quartz or alumina, with or without a gelling agent, formed into a ceramic mold, dried, and fired. Other investment castings with expendable patterns included ceramic shell molds; precoats for solid

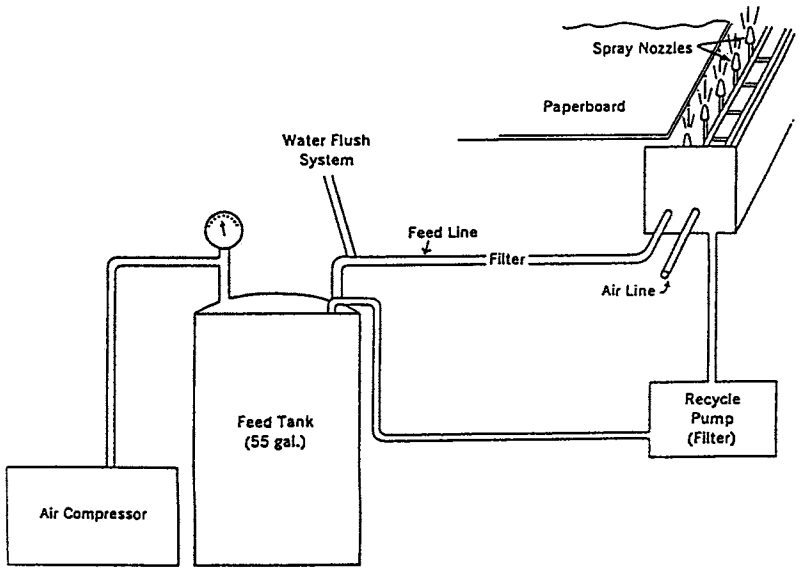

Figure 2. Spray unit for paper antiskid application.

molds; backups for solid molds, "tamp and pack" methods, and solid molds with no precoats.

Colloidal silica was used in general foundry applications such as gunning mixes, ceramic mold facings for core boxes and the like, mold washes, and semi-permanent molds with renewable facings. It was also used in the production of wallboard (Figure 4).

1955 to 1962. In 1962, Monsanto (*21*) reviewed the patent literature and listed the promising applications for colloidal silica at that time. They grouped the areas of application into the categories cellulosics, ceramics, electricity, floor waxes, flotation, insulating coatings, refractory molds, paints, photography, printing, paper, rubber, textiles, and miscellaneous; "miscellaneous" tends to involve some type of coating or inorganic–organic composition.

An area of interest at that time was the incorporation of colloidal silica into emulsion systems. Typical emulsions included floor waxes or rubber latices. Conventional wax compositions ordinarily included certain extenders or modifiers in the wax dispersions. These may comprise wax-soluble or water-dispersible resins (natural or synthetic). These formulations can produce coatings with a pleasing appearance; however, many lack slip resistance. The incorporation of colloidal silica into the formulation produces coatings that prevent slipping.

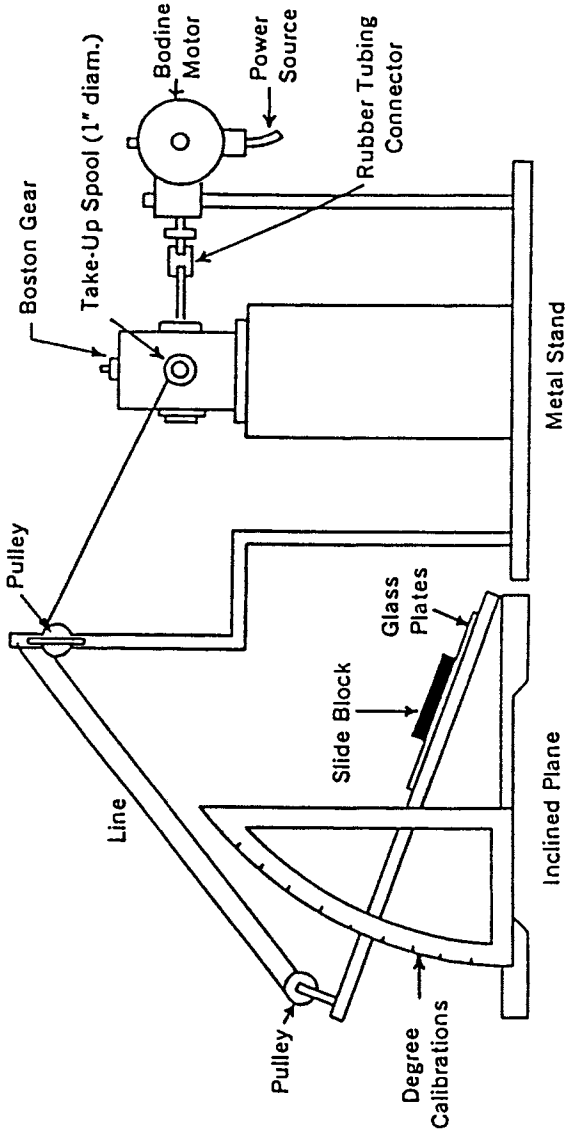

Figure 3. Testing equipment for skid resistance.

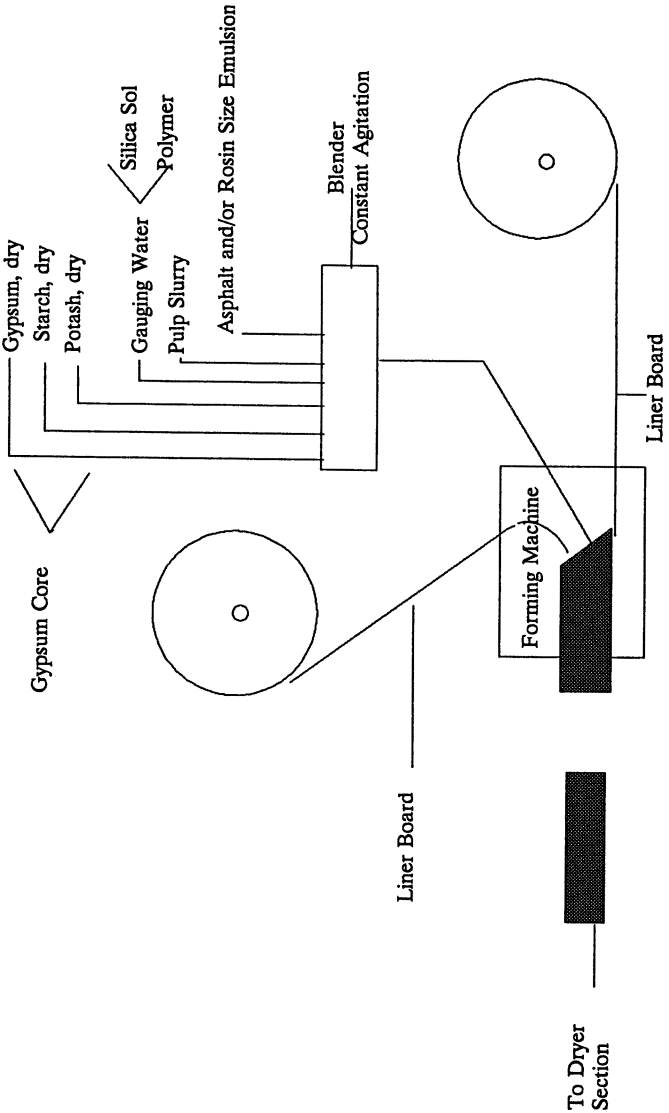

Figure 4. Typical flow diagram of wallboard production.

Iler (*22*, *23*) described typical formulations with Carnuba wax, which is dispersed in water containing colloidal silica, a fatty acid like oleic acid, triethanolamine, and potassium hydroxide. This composition can then be applied, for example, as a thin coating to linoleum floor. The product forms a lustrous coating without rubbing while providing a slip resistance.

Mixtures of rubber latices or elastomer foams were modified with colloidal silica to give improved properties. Typical processes involved drying, gelling, or coagulating the colloidal silica within the elastomer system. Silica sols were used with phenolic, formaldehyde-based, melamine, polyester, acrylic, vinyl or styrene polymer–copolymer, polyamide, and styrene–butadiene rubber systems to provide strength to films and coatings.

A typical rubber formulation, for example, that demonstrates the surface area properties of silica sol can be seen in the Talalay process for making foam rubber (*24*); the elastomer foam is in a latex form, to which is added an accelerator, an antioxidant, a vulcanizing agent, and carbon black. The mixture is then foamed, either mechanically or chemically, gelled, vulcanized to make the rubber, washed, and dried. The dried material is then postdipped in colloidal silica to reinforce the walls and prevent the crumbling effect seen on poorly made foam rubber pillows and so forth. Originally, a 20-nm silica sol was used. If a colloidal silica with a smaller particle size is used, the corresponding higher surface area allows less silica to be used in the system; thus the cost of the whole process is reduced.

1962 to 1979. When Iler's book, *The Chemistry of Silica*, came out in 1979 (*3*), the section on the applications for colloidal silica had increased to 21 pages, compared to seven pages in the 1955 book (*5*). The increase in the number of applications was largely due to the efforts of Iler. As technical manager of DuPont's colloidal silica area, Iler enlisted the help of some excellent researchers whose job it was to develop new application areas. As a result, numerous application patents were issued during this time period. The areas of application were many and varied during the period of 1962 to 1979. They can broadly be subdivided into binding and nonbinding systems. For example, silica sols are used as a binder for thermal insulation (Figure 5) or for catalyst manufacture and as a polishing agent for silicon wafers in a nonbinding application.

Stiles, McClellan, and Sowards (*25–28*) showed that colloidal silica is a good source of raw material for making the base catalyst. Silica sols have the advantage of a uniform distribution and known particle size. Thus, the catalyst manufacturer can predict the pore size and volume of the final product. Colloidal silicas also offer the advantage of low levels of sodium (compared to sodium silicate), a known catalyst poison, and therefore require less washing and processing to remove the unwanted cation. In

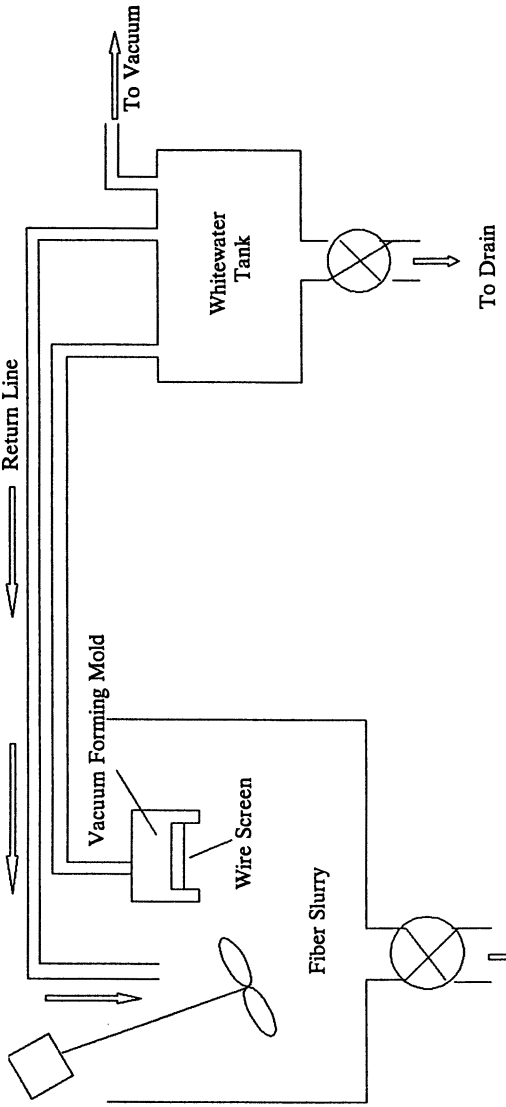

Figure 5. Vacuum forming process for preparing thermal insulation.

addition, colloidal silicas, because they are liquid, can be mixed with metal salts such as bismuth and molybdenum and spray-dried. Uniform dispersion of the silica with the expensive "active" metals gives a highly desirable catalyst with no "hot" spots. Consequently, high yields of expected products result. Such catalysts can be used in the conversion of propylene and ammonia to acrylonitrile (*29*, *30*).

One application area between 1962 and 1979 that has an impact on today's problems is the manufacture of wallboard. Wallboard was prepared by sandwiching a gypsum mixture between heavy papers. A typical core consists of gypsum, starch, potash, a pulp slurry, an asphalt or rosin-size emulsion, and gauging water (i.e., a colloidal silica plus polymer binder system). The mixture is blended together and placed between liners made on linerboard machines.

One way this application can be used to solve today's problems was presented early in 1990 by Air Products and Chemicals Inc. A power plant in Indiana was going to use a high-sulfur coal to generate its electricity. The acidic gas emissions, which consist of sulfur dioxide, was scrubbed with a limestone plus water mixture. The resulting calcium sulfite is oxidized to form calcium sulfate, which is then washed, centrifuged, rinsed, and dried. The final product is gypsum that contains less than 10% water. Because the average modern house is estimated to use 8000 square feet of wallboard, the process solves the gas emission problem while producing a low-cost construction material.

Colloidal silicas can also be used as a fine polishing abrasive for silicon wafers. Typical operations (*31*, *32*) involve feeding a dilute silica "slurry" (i.e., silica sol) that has been adjusted with a caustic agent onto a revolving polishing wheel containing a polishing pad. The silicon wafer is fixed to a polishing head and placed in contact with the polishing pad. As the system rotates, the high pH and the abrasive property of the colloidal silica removes silicon from the surface of the wafer. The resulting wafer has a mirrorlike surface onto which an electrical circuit can be placed.

Other applications of this time period can be found in Iler's discussion and references (*3*).

1979 to Present. The literature from 1979 to the present shows that the major application areas for colloidal silica involve coatings and "inorganic–organic compositions." Most of these compositions use the silica sol in a binder application. Japanese research far exceeds that of all other countries.

Coatings is a diversified application area involving a substrate and some type of surface covering. The type of substrate material to be coated can be plastics such as polycarbonate or polypropylene, metals, silicone rubber, ceramic- or refractory-like materials, fabrics like nylon and rayon, photographic films, paper materials, walls (painted or not), eyeglass lenses,

inorganic fibers such as fiberglass, stone for buildings, investment casting molds, leather or leather substitutes, and concrete surfaces. Typical coating materials tend to be polymeric in nature, although some application areas use the colloidal silica without organic polymers. For example, Nippon Steel Corporation (33) disclosed the use of a colloidal silica in combination with phosphates and chromic oxide or chromate to make a nondirectional magnetic film for steel sheets. Toshiba Silicone Company, Ltd. (*34*), on the other hand, uses a silane–colloidal silica mixture to coat glass lenses.

Inorganic–organic composition uses are similar to coatings uses except that no substrate is involved. A variety of mixtures can be used in which the colloidal silica is added to impart strength. An example of this type of system was disclosed by Asahi Glass Company, Ltd. (*35*); colloidal silica was added to isophorone diisocyanate and a pentaerythritol triacetate–tetraacetate mixture to produce a material for a polycarbonate plate.

Colloidal silica continues to be used in the conventional application areas such as catalysis, paper antiskid, refractory insulation, and photography. Its use, however, is dwarfed by that of coatings and inorganic–organic compositions.

The Future. Two types of silica sol products are needed in the 1990s: specialty products and organosols. Specialty products are used in high-technology areas. Price is generally unimportant if they work. Typical examples of specialty products are monodisperse sols [i.e., one particle size, low sodium, and low metal (aluminum, iron, etc.) concentrations, and no aggregation].

Monodisperse silica sols are important in the previously mentioned Talalay process for making foam rubber pillows. If a 4-nm silica sol is normally used, then a substitution of a 3.5-nm particle at the same silica dosage would theoretically increase the strength of the rubber by 14.3%. If, however, the particle size is changed from 4.5 to 5.0 nm, the strength of the rubber would decrease by 11 to 20% at the same silica dosage. Under these conditions, the crumbling effect of the foam rubber would return.

The second application area of interest is organosols. Organosols involve the use of nonaqueous systems, for example, in making magnetic colloids and recording media, high-technology ceramic composites, and catalyst supports (*36*). The high solid loadings, the lack of aggregation, and the improved uniformity of the colloid and the final product can only be obtained from colloidal systems. Silica organosols are dispersions of silica colloids in an organic solvent. Silica organosols can be used as a low-temperature binder (*37*), as an adhesion promoter (Schmidt, K. E., personal communication), or as a silica source for magnesia refractories. For example, magnesia refractories use silica as a binder to make high-temperature materials through the formation of a magnesium silicate

called Fosterite. If a silica sol in water is used, the magnesia grain reacts to form magnesium hydroxide. The reaction with silica then proceeds by a different phase diagram. The firing temperature must be raised to almost 2000 °F (1100 °C) before the cold crush strength increases with increasing firing temperature. When an organosol is used, the cold crush strength increases with increasing firing temperature immediately, as expected.

Currently, there are now greater demands on those industries in which colloidal silica has been used in the past to develop higher quality products. Thus, a cement to which colloidal silica was added to improve its strength properties years ago must now be UV-resistant and also have better than 90% reflectivity (*38*). One application of current interest is in the area of papermaking (*39–43*). Colloidal silica is mixed with starch and slurried paper fibers. It is then formed into paper on the wire of a paper machine. The addition of the silica sol to the system gives improved dewatering of the flocced slurry as well as a high retention of the paper fines and fillers. The result is lower heating costs for drying the paper and better mat formation. Considerable savings can be realized for the papermaker using this system. Greater retention properties mean that more recycled, and therefore cheaper, paper can be added to the paper furnish (formula) without sacrificing strength, because recycled paper contains more fines, and paper strength depends on fiber–fiber interactions.

Conclusions

Where will future applications come from? One source is universities, and a second is extension of existing applications. Some applications of colloidal silica originating in universities include the following:

- grinding aid for pharmaceutical formulations (Modena University, Modena, Italy, 1988) (*44*)
- stabilizing agent for organic compounds subject to temperature–humidity degradation conditions (Hamburg University, Hamburg, Germany, 1989) (*45*)
- mixtures (silica sol + montmorillonite clay) to give pillared clays with super galleries (Michigan State University, East Lansing, MI, 1988) (*46*)
- catalytic agent for hydrolysis of silane-coupling agents (Nihon University, Tokyo, Japan, 1988 (*47*)

Silica applications are, indeed, a global endeavor.

Extending ideas of other applications involves the technique known as an "association of ideas." For example, in U.S. Patent 4,637,867 (*48*),

colloidal silica is used as a dispersing agent (and probably a crystal modifier) for preparing fine crystal particles of maleic anhydride. This same idea can be used for making crumb rubbers in elastomer systems (*49*) into fine-grain emulsions in photographic systems (*50*).

One might argue that silica sols can easily be used as a dispersing agent, but that this kind of argument does not apply to other systems. The use of colloidal silica as a frictionizing agent, however, shows that the technique works for other systems. Historically, silica sols have been used in paper antiskid applications, floor waxes, hot pressing railroad engine drive wheels, and polishing applications. One Japanese researcher used the frictionizing properties of silica for improving nonwoven fiber blackboard erasers. Extending this same idea, why not use silica sols for cleaning cloths and floor mops or for rubber or nonrubber pencil erasers?

Historically, colloidal silica has been tried in many applications. In many cases, the reason that it is not used is not that it didn't work, but the cost of the products is more than the customer wants to pay for improvements. Colloidal silica has been used in the making of opals, in the balancing of large-diameter industrial saws, as an anticaking agent for explosives, and as a frictionizing agent for baseball bats to improve the hitting performance of minor league players. Colloidal silica will continue to be a versatile product with an applicability limited only by the imagination of the researcher.

References

1. Graham, T. *J. Chem. Soc.* **1862**, *15*, 216.
2. Graham, T. *J. Chem. Soc.* **1864**, *17*, 318.
3. Iler, R. *The Chemistry of Silica*; Wiley-Interscience: New York, 1979; pp 415–438.
4. Bungenburg de Jong, H. G. In *Colloid Science*; H. R. Kruyt, Ed.; Elsevier: New York, 1949; Vol. II, pp 1–5.
5. Iler, R. *The Colloidal Chemistry of Silica and Silicates*; Cornell University Press: New York, 1955; p 87.
6. Hauser, E. A. *Silicic Science*; Van Nostrand: Princeton, NJ, 1955; p 54.
7. Fremy, E. *Ann. Chem. Phys.* **1853** (3), *Bd. 38*, S 312–344.
8. Graham, T. *Ann. Chem.* **1862**, *Bd 123*, S860–861.
9. Schwerin, B. U.S. Patent 1,132,394, 1915.
10. Bird, P. U.S. Patent 2,244,325, 1941.
11. White, J. F. U.S. Patent 2,285,477, 1942.
12. White, J. F. U.S. Patent 2,375,738, 1945.
13. Trail, H. S. U.S. Patent 2,572,578, 1951.
14. Trail, H. S. U.S. Patent 2,573,743, 1951.
15. Bechtold, M F.; Snyder, O. E. U.S. Patent 2,574,902, 1951.
16. Rule, J. M. U.S. Patent 2,577,485, 1951.
17. Griessbach, R. *Chem. Ztg.* **1933**, 57, Nr 26, S 253–260, 274–276.
18. Iler, R. *The Colloidal Chemistry of Silica and Silicates*; Cornell University Press: New York, 1955; p 89.
19. Wilson, I. V. U.S. Patent 2,643,048, 1953.

20. Collins, P. F. U.S. Patent 2,380,945, 1945.
21. Monsanto Technical Bulletin I-237, *Monsanto Silicas for Industry*, 1962.
22. Iler, R. U.S. Patent 2,597,871, 1947.
23. Iler, R. U.S. Patent 2,726,961, 1955.
24. Talalay, A. et al. U.S. Patent 2,926,390, 1960.
25. McClellan, W. R. U.S. Patent 3,415,886, 1968.
26. Stiles, A. B.; McClellan, W. R. U.S. Patent 3,497,461, 1970.
27. Sowards, D. M.; Stiles, A. B. U.S. Patent 3,518,206, 1970.
28. McClellan W. R.; Stiles, A. B. U.S. Patent 3,678,139, 1972.
29. Callahan, J. L. U.S. Patent 2,974,110, 1961.
30. Callahan, J. L.; Szabo, J. J.; Gertisser, B. U.S. Patent 3,322,847, 1967.
31. Walsh, R. J.; Herzog, A. H. U.S. Patent 3,170,273, 1965.
32. Sears, G. W. U.S. Patent 3,922,393, 1975.
33. Nippon Steel Corp., Japanese Patent 57/192,222, 1982.
34. Toshiba Silicon Company, Ltd. Japanese Patent 60/166,355, 1985.
35. Asahi Glass Company, Ltd. Japanese Patent 60/137,939, 1985.
36. Smith, T. W. U.S. Patent, 4,252,671, 1979.
37. Bikadi, Z.; Guder, H. European Patent EP 390276, 1989.
38. Page, C. H.; Thanavala, D. N.; Thombare, C. H.; Kamat, R. D.; Bapat, V. S. Indian Patent 163,979, 1988.
39. Batelson, P. G. Canadian Patent 1,154,564, 1983.
40. Andersson, K.; Andersson, K; Sandstrom, A; Stroem, K.; Basla, P. *Nord. Pulp Pap. Res. J.* **1986**, *1* (2), 26–30.
41. Johnson, K. A. U.S. Patent 4,643,801, 1987.
42. Sofia, S. C.; Johnson, K. A.; Crill, M. S.; Roop, M. J.; Gotberg, S. R.; Nigrella, A. S.; Hutchinson, L. S. U.S. Patent 4,795,531, 1989.
43. Rushmere, J. D. U.S. Patent 4,798,653, 1989.
44. Forni, F.; Coppi, G.; Iannuccelli, V.; Vandelli, M. A.; Cameroni, R. *Acta Pharm Suec* **1988**, *25* (3), 173–180.
45. Krahn, F. U.; Mielck, J. B. *Int. J. Pharm.* **1989**, *53* (1), 25–34.
46. Moini, A.; Pinnavaia, T. J. *Solid State Ionics* **1988**, *26* (2), 119–123.
47. Nishiyama, N.; Asakura, T.; Houe, K. *J. Colloid Interface Sci.* **1988**, *124* (1), 14–21.
48. Herbst, R. U.S. Patent 4,637,867, 1987.
49. Payne, C. C., unpublished data.
50. Saleck, W.; Himmelmann; Huckstadt, H.; Meyer, R. Belgian Patent 766095, 1971.

RECEIVED for review February 19, 1991. ACCEPTED revised manuscript March 24, 1992.

30

The Uses of Soluble Silica

James S. Falcone, Jr.

West Chester University, Department of Chemistry, West Chester, PA 19383

The uses of soluble silica are reviewed in a concise manner. Ideas originally summarized by Ralph K. Iler are expanded and discussed with up-to-date references. Key technological factors associated with the application of soluble silica in the broad categories are described. The categories are: Adhesives, binders, and deflocculants; Cleaners and detergents; and Raw materials. These technological factors are related to current understanding of the chemical properties of these complex inorganic polymer solutions.

RALPH K. ILER (*1*), in *The Chemistry of Silica*, classified the uses of the soluble silicates into three categories:

- **Adhesives, binders, and deflocculants'** function is dependent primarily on the presence of polysilicate ions. The soluble silicate used has a ratio range of 2.5 to 4.0, where the ratio is defined as one-half of the ratio of moles of Si to moles of cation (e.g., Na^+ or tetramethylammonium ion, TMA^+).
- **Cleaners and detergents'** function is primarily due to controlled alkalinity using silicates with ratios generally lower than 2.5.
- **Raw materials** for the production of precipitated forms of silica, sols and gels from solutions with ratios equal to 3.3 or greater.

An analysis of the trends in U.S. production statistics for sodium silicates from the early 20th century to date is shown in Figure 1. It suggests a macro growth pattern in volume of roughly 10 million kg/year

0065–2393/94/0234–0595$08.00/0

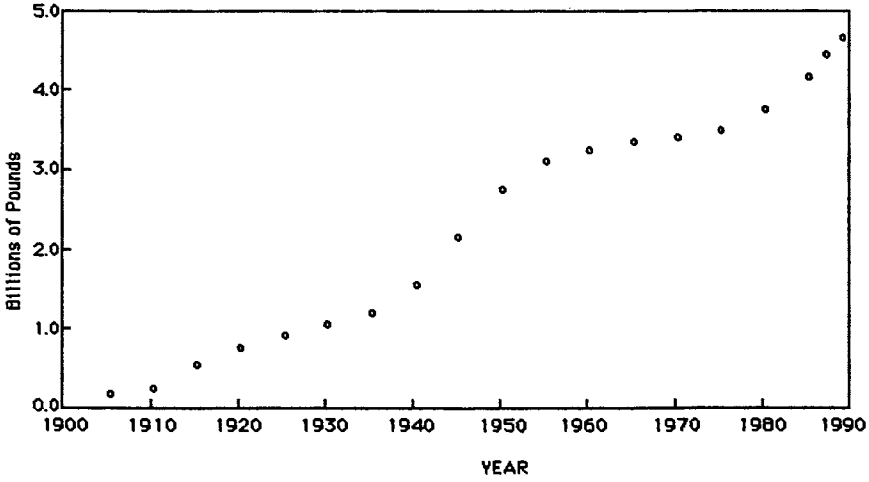

Figure 1. Sodium silicate production since 1900 as 40° Bé 3.3 ratio solution (data smoothed to show trends). CGR since 1925 is 2.6%.

when the silicate production is calculated as 40° Bé 3.2 ratio equivalent (Bé refers to the Baumé density scale). Growth plateaus as seen in the 1930s and the 1960s reflect, in a way, the three categories in the order described. In the first third of the century, silicate uses were predominantly in the first class. In mid-century there was a rise in the use of silicates in synthetic detergents. The overall volume of silicates grew after World War II in spite of great volume losses in applications of adhesives to both natural and synthetic organic polymers. New growth in production the final third of the century is due to increased use of soluble silicates as intermediates in making many classes of silica-based performance materials.

The diversity of uses for the alkali silicates is a result of both their structural complexity (2, 3) and their complex reactivity. One might view them (*4*) as silica dissolved and/or dispersed in an hydroxide ion-rich aqueous system. In the chemical processing industry (CPI), they are valued as a reactive source of $(SiO_2)_n$ structural units. Soluble silica as an intermediate can be reacted with acids and bases to form a wide range of final products ranging from seemingly simple condensed forms of relatively pure noncrystalline silica, precipitates, gels, and sols, to highly complex crystalline metallosilicates like those found in the broad class of aluminosilicates, zeolites. The key properties of an intermediate are likely to be silica concentration, ratio, supporting cation, type and level of impurities, and consistency in these factors. These factors will be particularly important in the manufacture of catalysts, highly selective sorbents, and

other high-performance materials where trace metals could effect final product performance.

When alkali silicates are used as components, rather than reactants, in systems where partial contributions to overall performance are the dominant role, the utility factors are generally not as easy to identify. This is because these systems usually depend on the surface and solution chemical properties of the wide range of highly hydrophilic polymeric silicate ions deliverable from soluble silicate products or their proprietary modifications. In most cases, however, one or two of the many possible influences of these complex anions clearly express themselves in final product performance at a level sufficient to justify their use.

These major values may be seen as resulting from the following broad functions: hydrogen ion buffering, metal ion complexation, and specific adsorption. The sodium silicates are salts of a weak acid, silicic acid ($pK_a \sim 9.8$), and a strong base, sodium hydroxide. Their chemistry is complicated by the fact that silicic acid is by no means a well-defined substance. In fact, it appears that silicic acid might be best viewed as a complex hydrous polymer which varies in Si, O, and H composition and connectivity between Si–O–Si or number of shared SiO_4 tetrahedra corners. These variations influence silanol acidity and number of bonded and non-bonded oxygen atoms. The possible structures are difficult to study directly and model quantitatively; however, they are indirectly observable from the patterns of behavior in systems containing them. Evidence from studies of the interactions of soluble silica, metal ions, and oxide surfaces strongly suggests the presence of a wide range of metastable soluble silica species influencing the balance of other interaction in the system. For example:

- Silica adsorbs on gamma–Al_2O_3 in a broad pH range (*5*, *6*), which might be explained by assuming that the silica species in solution have a similarly broad range of pK_a values (between 6 and 10). The silica adsorption does not exhibit the sharp maximum value normally seen for weak acids at the pH value equal to the acid's pK_a value. Silica adsorption was reduced by the presence of divalent metal ions, possibly as a result of reduced silicate species activity.
- The addition of solutions of soluble silica to oxide mineral suspensions increases the magnitude of the negative surface charge on the mineral particles with higher ratio silicates (increased oligomers and higher polymers) being more active. Soluble silica species also attenuate the influence of multivalent cations on the surface charge (*7*, *8*).
- Highly polymerized silicate anions appear to interact with metal ions in solution in a manner analogous to silica gel, and

the interaction decreases as the degree of silicate polymerization decreases (*9*). This behavior is consistent with Iler's generalization (*10*) that silica suspended in solutions of polyvalent metal ions begins to adsorb these ions when the pH value is raised to within 1 to 2 pH units of the hydroxide activity at which the corresponding metal hydroxide would precipitate. It is likely that much of the behavior of silica hydrogel and the larger soluble silicate polymers towards metal ions can be attributed to metal ion adsorption in the interfacial region of the larger silica oligomers/polymers. This results in localized concentration near the siliceous surface in excess of the metal ion hydroxide solubility product (*11*).

- It also is well known that the addition of acids and bases shifts the polymer equilibrium in solutions of silicates as a result of the following generalized scheme:

With these generalizations in mind, one can interpret the performance enhancements that are seen when soluble silicates are added to many industrial processes.

Controlled Buffer. By the appropriate choice of ratio of silica to NaOH, one can effectively buffer hydrogen ion activity in the important industrial range of 9 to 11. When systems performance is dependent on anionic surfactants and sequestrants, this property is valued greatly.

Corrosion Inhibition. The presence of soluble silica in water exposed to various metals leads to the formation of a surface less susceptible to corrosion. A likely explanation is the formation of 'metallosilicate complexes' at the metal water interface after an initial disruption of the metal oxide layer and formation of an active site. This modified surface is expected to be more resistant to subsequent corrosive action via lowered surface activity and/or reduced diffusion.

Red Water Control. Dissolved metal ions like iron and manganese play havoc with the aesthetics of ceramics systems that come into contact with waters containing them (e.g., bathtubs, wash basins, and stucco sprayed by lawn sprinklers). The addition of high-ratio silicates will effectively eliminate this problem through the formation of 'metallosilicate complexes,' which remain suspended in the water (*12*).

Bleach Stabilization. When added to hydrogen peroxide based bleaching systems, soluble silicates are known to significantly enhance bleach performance. Many hypotheses have been put forth to explain this process, including buffering, peroxysilicate complex formation, and modification of peroxide equilibrium. However, the most recent and plausible explanation is that the silicate inactivates iron and manganese species which catalyze peroxide decomposition (*13*).

Controlled Gelation. Solutions of soluble silica can be added to permeable matrices and jelled in place either by post-addition of acid, the action of acids in place, or the controlled reaction of a gelation agent added directly with the silicate. For example, CO_2 is used in foundry applications where silicate jelled by CO_2 gas binds sand to make metal molds. Hydrolyzable esters, like diacetin or triacetin, can be mixed with silicate solutions, yielding time-controlled setting systems. Recently, mixtures of portland cement and silicates have been used to gel liquid waste systems. Various proprietary systems involving soluble silica are used to accomplish objectives which involve stabilizing soils and blocking fluid flows. The strengths and set times of these systems are generally a function of the concentration of the silica and the pH value of the solution.

Coagulation–Dispersion. Soluble silica, particularly in the form called activated silica, is used in water treatment as a coagulant aide, where it improves the settling properties of alum-induced flocs, apparently via densification. In addition, silicate added by itself to a mineral suspension can cause beneficial conditioning, coagulation, or dispersion, depending on the treatment levels and system. Judicious use of silicate can lead to an enhancement of mineral flotation processes which employ hydrophobic collectors, generally by dispersion improvement and suppression of the flotation of unwanted oxides. This is done by maintaining negative surface charges and/or hydrophilic surfaces on unwanted components. However, silicates if overused can lead to total suppression of a mineral slurry due to the adsorption of silicate on all minerals, which causes all surfaces to become hydrophilic, and thus non-floating.

Anti-redeposition–Sacrificial Agent. The universal suppression described, while it is a negative in mineral flotation, becomes a positive value in such applications as de-inking and detergency, where the maintainance of particulate surfaces in a negative charge state aids in the intended separation action (e.g., soil from cloth and ink from pulp fiber). In a related manner, the presence of anionic polysilicates will often improve a system whose performance is dependent on the effectiveness of anionic surfactant or polyelectrolytes. This improvement is due to a sacrificial effect whereby the silicate preferentially "sorbs" on active sites in the system and helps to maintain high activity for the costly active ingredients which in the absence of silicate would be adsorbed.

Deflocculation. Soluble silicates suppress the formation of ordered structures within clay slurries, thus increasing the solids which can be incorporated into a clay water system. This interesting surface phenomenon finds practical expression in the manufacture of bricks and cement.

These examples attest to the diversity of values to be extracted from these important industrial materials. This brief review only highlights the applied chemistry in this system. The interested reader is directed to the general references that follow for further insight.

References

1. Iler, R. K. *The Chemistry of Silica*; Wiley: New York, 1979; p 667.
2. Dent Glasser, L. S.; Lachowski, E. E. *J. Chem. Soc. Dalton Trans.* **1980**, *393*, 390.
3. Falcone, Jr., J. S. In *Cements Research Progress—1988*; Brown, P. W., Ed.; American Ceramic Society: Westerville, OH, 1989; 277.
4. McLaughlin, J. R. "The Properties, Applications and Markets for Alkaline Solutions of Soluble Silicate", paper presented to CMRA in New York, May, 1976.
5. Hingston, F. J.; Atkinson, R. J.; Posner, A. M.; Quirk, J. P. *Nature (London)* **1967**, *215*, 1459.
6. Huang, C. P. *Earth Planet. Sci. Lett.* **1975**, *27*, 265.
7. Hazel, F. J. *J. Phys. Chem.* **1945**, *49*, 520.
8. Tsai, F.; Falcone, J. S. paper presented at ACS/CSJ Chem. Congress, Honolulu, HI, Apr. 6, 1979.
9. Falcone, Jr., J. S. In *Soluble Silicates*, ACS Symposium Series 194; Falcone, Jr., J. S., Ed.; American Chemical Society: Washington, DC, 1982; p 133.
10. Iler, R. K. *The Chemistry of Silica*; Wiley: New York; p 667.
11. Ananthapadman, K. P.; Sumasundaran, P. *Colloid and Surf.* **1985**, *13*, 151.
12. Browman, M. G.; Robinson, R. B.; Reed, G. D. *Environ. Sci. Technol.* **1989**, *23*, 566.
13. Colodette, J. L.; Rothenberg, S.; Dence, C. W. *J. Pulp and Paper Sci.* **1989**, *15*, J3.

Additional Reading

Falcone, Jr., J. S.; Boyce, S. D. In *Encyclopedia of Polymer Science and Engineering*, 2nd ed.; Kroschwitz, J. I., Ed.; Wiley: New York, 1989; Vol. 15, pp 178–204.

Liebau, F. *Structural Chemistry of Silicates*; Springer-Verlag: Berlin, Germany, 1985.

Dent Glasser, L. S. *Chemistry in Britain* **1982**, Jan, 33.

Ingri, N. In *Biochemistry of Silica and Related Compounds*; Bendtz, G.; Lindquist, I., Eds.; Plenum: New York, 1978; p 3.

Barby, D.; et al. In *The Modern Inorganic Chemical Industry*; Thomson, R., Ed.; Chemical Society: London, 1977; p 320.

Wills, J. H. In *Encyclopedia of Chemical Technology*, 2nd ed.; Wiley: New York, 1969; Vol 18, pp 134–166.

Vail, J. G., *Soluble Silicates*; ACS Monograph 116; Van Nostrand Reinhold Co., Inc.: New York, 1952; Vol. 1 and Vol. 2.

RECEIVED for review March 4, 1991. ACCEPTED revised manuscript December 19, 1991.

31

Silicon–Aluminum Interactions and Biology

J. D. Birchall

Department of Chemistry, Keele University, Keele, Staffordshire, ST5 5BG, United Kingdom

Silicon is listed as an essential element. Its removal from the diet of experimental animals has been shown to result in reduced growth rate (reversed on silicon supplementation) and changes to bone formation and the synthesis of collagenous connective tissue. However, in spite of much effort, no organic binding (e.g., to proteins) of silicon has been convincingly demonstrated under physiological conditions in which silicon exists as silicic acid, $Si(OH)_4$, and no biochemical rationale has been proposed to account for the effects of silicon deficiency. However, recent research indicates that a major role for silicon (as silicic acid) is to reduce the bioavailability of aluminum, which is toxic when it gains entry into biological systems, but which is normally largely excluded. The formation of subcolloidal hydroxyaluminosilicate species is shown to prevent the absorption of aluminum in fish via gill epithelia. The generality of this effect is discussed. The symptoms of silicon deficiency in experimental animals seem likely to result from aluminum toxicity, so that the environmental balance for the two elements may be critical. This chapter reviews the present position.

In Ralph K. Iler's magnum opus, *The Chemistry of Silica* (*1*), the final chapter is a review of silica in biological systems. Iler was fascinated by this least understood and most challenging aspect of silica chemistry, perhaps because of his instinctive feel for its fundamental importance. The headings within that last chapter reveal its sweep—from the "Origin of Life" to the "Essential Role of Silica in Mammals". He reviewed the concept of silicates as substrates for the formation of complex molecules

0065–2393/94/0234–0601$08.00/0

from simple compounds at the earliest stages in the formation of living organisms, including algae, fungi, insects, plants, mammals, and humans. He discussed the formation of biogenic silica in plants (phytoliths) and in the frustules or exoskeletons of diatoms and the fibrogenic effect of silica and silicates in the lung, the most important manifestation of toxicity. Silica being ubiquitous throughout biological systems, Iler was intrigued by the possibility that it plays a vital role. Silica is used as structural material in diatoms and some sponges, and its deposition in plants can be advantageous in strengthening, stiffening, and hardening leaf surfaces, stalks, or the barbs of nettles. As important as such a "mechanical" role is, it is not a biochemically fundamental one.

The element silicon is the second most abundant element in the earth's crust after oxygen. It is described in modern texts of bioinorganic chemistry as an essential trace element largely as a result of the classical experiments of Carlisle (*2*) and Schwarz and Milne (*3*). These workers, in independent experiments, maintained rats and chicks on a synthetic diet deficient in silicon. Using a similar technique, Schwarz had previously shown the essentiality of selenium and other elements. Silicon deficiency in the experimental animals produced a significant reduction in growth rate, reversed on silicon (as silicate) supplementation, with profound changes to the formation of bone and collagenous connective tissue such as cartilage. Since these experiments were reported (1972), there has been a search for the mechanism of action of silicon. The first hypothesis in explanation was based on the claim that silicon was bound in the biopolymers of connective tissue—collagen and polysaccharides—and acted as a labile cross-link, so influencing tertiary structure and integrity (*4*). However, the reported silicon content of isolated biopolymers declined as isolation and analytical techniques improved, so that this role became increasingly unlikely and the hypothesis untenable (*5*). Essential trace elements such as Fe, Cu, Se, and Zn have defined binding sites, usually within a protein structure, and the metal–protein complex is the functional entity, for example, an enzyme. However, in spite of much searching, no specific binding site for silicon has been found. No evidence exists for the formation of Si–C bonds in biological systems, and such chemistry as exists is that of silicic acid, $Si(OH)_4$. Organic complexes of silicic acid are few and are unstable at physiological pH (e.g., complexes with 1,2-dihydroxyphenols such as catechol). Much speculation (*5*) has occurred as to the possible binding of silicic acid to appropriately spaced hydroxyl groups on minority sugars in polysaccharides, but no convincing experimental evidence for such binding has been presented. (Reference 6 is a review of this topic.) By what mechanism, then, does silicon (as silicic acid) deficiency produce the reported pathological changes?

The Search for Mechanism

A key issue in the mechanism underlying the essentiality of an element is its location at tissue, cellular, and molecular levels, and as noted no *molecular* binding of silicon has been observed. Plasma contains silicic acid in the concentration range 5–10 μm/L, so that all tissue is exposed to it. Noting that osteogenesis was impaired in silicon-deficient experimental animals, Carlisle conducted a microprobe scan across a bone section and found silicon to be concentrated (0.5%) locally at the mineralization front (*7*). A major effect of silicon deficiency was on the synthesis of the preosseous, collagenous matrix that is mineralized to form bone proper. Carlisle noted that the activity of prolylhydroxylase (a key enzyme in collagen synthesis) in tissue cultures of cartilage from silicon-deficient chicks was low but was increased when silicon (silicate) was added to the culture (*8*). The conclusion drawn was that silicon was a cofactor in the proper functioning of this enzyme. The known cofactors for prolylhydroxylase are iron, oxygen, ascorbate, and 2-oxyglutarate, and it is extremely difficult to see how silicic acid can engage in any chemistry with any of these cofactors, or with the enzymic protein. However, the observed increase in activity prompted by silicic acid addition requires explanation.

The first clue to a possible explanation came from an entirely different direction. Hexokinase, with adenosine triphosphate (ATP)-Mg^{2+}, is involved in the first step in the metabolism of glucose, the formation of glucose-6-phosphate. The activity of hexokinase is low and can be raised by the addition of citrate (*9*). The low activity is due to contamination with aluminum, which binds to ATP 10^7 times more strongly than the required Mg^{2+} and blocks phosphate transfer. The role of citrate, a strong complexing agent for aluminum, is to remove aluminum from ATP and so allow Mg^{2+} to bind. Aluminum is almost as ubiquitous as silicon, and the two elements, in Iler's words, "have a unique affinity" (*1*). There appears to be no *organic* chemistry of silicon in biological systems, so the question becomes, Could the effects of its deficiency be related to inorganic chemistry, with aluminum (now known to be toxic) being the interacting metal?

A Test of the Concept: Prolylhydroxylase Activity

Prolylhydroxylase, the collagen synthesis enzyme that has low activity in silicon-deficient tissue, requires iron that cycles between Fe^{3+} and Fe^{2+}. The apoenzyme will bind aluminum (less strongly than iron), and the enzyme is then, of course, inactive. An experiment was conducted (*6*) in which the apoenzyme was presented with iron first and then aluminum, all other essential cofactors being present. Activity, as measured by hydroxyproline production, was reduced by 20% of the control level. When the

apoenzyme was presented with aluminum first and then iron, activity was reduced by 55% of the control levels. Silicic acid alone had no effect on the activity, which remained at the control level (Table I). However, when the "Al first" experiment was repeated in the presence of a sixfold excess of silicic acid (600 μM) over aluminum, the inhibiting effect of aluminum was completely suppressed. Clearly, in the presence of silicic acid, aluminum is removed from competition with iron for binding in prolylhydroxylase.

Table I. Effect of Silicic Acid on Inhibition of Prolylhydroxylase by Aluminum

Addition (100 μM)	*% Inhibition of Control*[a]
$Si(OH)_4$	0
Fe then Al	20
Al then Fe	55
Al + 600 μM ($Si(OH)_4$)	0

[a]Assays were done by measuring the release of ^3H as ^3H_2O from ^3H-prolylprotocollagen, which accompanies the hydroxylation of proline at position 4.

This experiment strongly supported the developing hypothesis that conditions in which silicon levels are (artificially) low allow the manifestation of aluminum toxicity. However, as will be shown later, aluminum challenges Ca^{2+} and Mg^{2+} rather than iron in vivo.

Aluminum in Biological Systems

Aluminum has long been regarded as innocuous. It is not used in biological systems and, strangely, for so ubiquitous an element, is largely excluded; iron, with a very similar charge-to-radius ratio, is essential and actively sought. The perception of aluminum as innocuous has changed over the past 2 decades. Aluminum is indisputably the agent responsible for the disorders observed in patients undergoing hemodialysis for renal insufficiency when aluminum-containing dialysate is used. Plasma aluminum can then rise from <1 μM to >5 μM with three potential consequences (*10*):

1. a microcytic anemia not responding to iron therapy, but responding to reduced plasma aluminum levels
2. a progressive deterioration in cognitive function with eventual dementia (dialysis encephalopathy).
3. a disorder of bone (dialysis osteomalacia) with inactive osteoblasts, bone pain, and spontaneous fracture. In this,

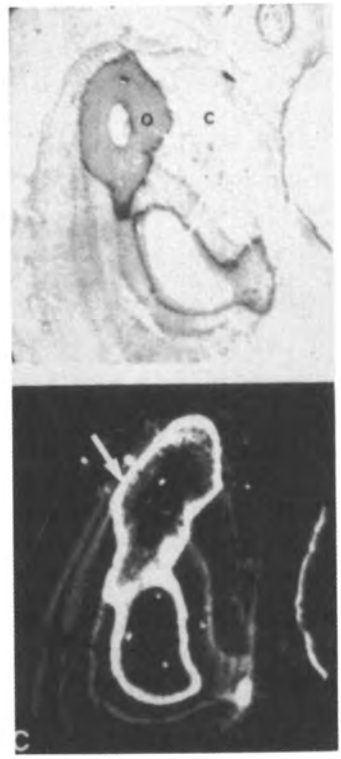

Figure 1. Aluminum (arrowed) at the growth front in bone from patient with dialysis osteomalacia. (Reproduced with permission from reference 35. Copyright 1990.)

aluminum is found at the growth front (Figure 1). (Silicon has been found in the same location).

Now that aluminum is recognized as the cause of these disorders, levels are carefully monitored, and aluminum is removed from dialysis fluid by reverse osmosis.

Aluminum is the major toxic entity for aquatic life in waters affected by "acid rain" and is the major cause of poor crop yields in acidic soils in which root growth is stunted (*11*, *12*).

The mechanisms underlying these effects are not well-understood, but there is a consensus that, once within the biological milieu, aluminum displaces Mg^{2+} from key sites where this metal is an essential cofactor and is involved in the disturbance of Ca^{2+} manipulation (*see* later).

In dialysis with aluminum-containing water, the metal bypasses the normal exclusion mechanisms, and in acidic waters high in aluminum

(5–10 μM), bioavailable aluminum is adsorbed at fish gill epithelia and then absorbed systemically. The dietary intake of aluminum in humans is of the order of 10–20 mg/day (*13*), but only a small fraction is absorbed in the gut. The exclusion mechanism is unknown. Absorption is increased by citrate and other aluminum-complexing agents.

The facts that aluminum ingress in dialysis gives rise to an encephalopathy, that aluminum levels are raised in the brains of patients with Alzheimer's disease (*14*), and that aluminum, colocalized with silicon, is found at the core of the senile plaques characteristic of Alzheimer's disease (*15*) have prompted concern that dietary aluminum can, in susceptible individuals, provoke or be a cofactor in Alzheimer's disease. In one recent epidemiological study (*16*), a relationship was found between the aluminum content of drinking water and the incidence of Alzheimer's disease. Two criticisms were made of this study: (1) a lack of dose–response correlation with near-maximum increase in Alzheimer's disease incidence at the lowest levels of aluminum concentration, and (2) even at the highest level of aluminum (>111 ppb) included in this study, the daily aluminum intake from water would be <0.5 mg, whereas the intake from food would be 10–20 mg. [In 1982, about 4×10^6 pounds of aluminum compounds were used as food additives in the U.S. (*17*).] This apparent paradox is resolved if the hypothesis that silicon limits aluminum bioavailability is adopted. Aluminum and silicon concentrations in potable water are inversely related. High aluminum and low silicon levels are found in soft waters from high, well-weathered, acidic catchment areas requiring aluminum coagulation treatment for clarification. Conversely, hard, mineralized waters from still-weathering geology are high in silicon, often 10-fold or more than the level in soft water. It has been proposed (*18*) that this epidemiological study in fact revealed a relationship between the silicon content of water and its role in suppressing the absorption of the aluminum contained in food.

A Test of the Al–Si Balance Hypothesis

Fish in acidic waters containing aluminum have high mortality due to gill damage and loss of osmo- and ionoregulatory function. In one experiment (*19*), Atlantic salmon fry were exposed to acidic water (pH 5) containing a toxic level of aluminum (ca. 7 μM) with low (0.60 μM) and high (93 μM) levels of silicon as silicic acid. The "pure", control water (at pH 5) contained low levels of both elements, 0.85 μM aluminum and 0.66 μM silicon. Survival curves are shown in Figure 2. In the 7 μM Al, low-silicon conditions, 50% of fish were dead within 26 h, and all fish were dead within 48 h. Gill damage was obvious, and the fish contained 2 μM Al per gram of dry mass. With the high silicon level, no fish died in the duration of the experiment, gill structure remained normal, and the fish contained

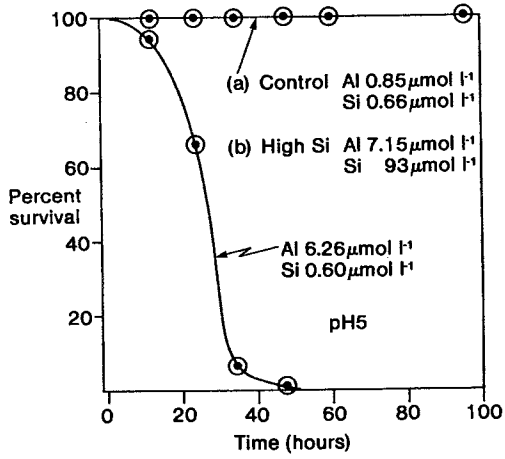

Figure 2. Survival curves for Atlantic salmon fry exposed to control (low Al) water and water containing ca. 7 μM Al with high and low silicic acid levels. The top curve shows both control and high-Si results. (Reproduced with permission from reference 35. Copyright 1990.)

only 0.40 μM Al per gram of dry mass, 10% less than that absorbed from the control water.

Clearly, in the presence of the high level of silicon, aluminum was prevented from binding at gill epithelial surfaces and systemic absorption. This exclusion occurred at the interface between creature and the external environment, and a fundamental question is, Is this a general effect, not only at the fish gill, but also at plant root membranes and in the gastrointestinal tract of mammals and humans?

The Exclusion Mechanism

Iler has remarked (p 193, ref. 1), that "there is a peculiar affinity between the oxides of aluminum and silicon". This affinity results from the isostructural nature of $(SiO_4)^{4-}$ and $(AlO_4)^{5-}$, which is responsible for the vast range of natural aluminosilicates and synthetic zeolites. Synthetic zeolites are synthesized by the reaction of aluminate and silicate anions at high temperature and pH. However, interactions occur between silicic acid and hydroxyaluminum ions in dilute ($<10^{-4}$ M) solution at near-neutral pH, and these interactions are of biological and environmental significance in reducing aluminum bioavailability. Hydroxyaluminum cations were shown (*20*) to react with silicic acid in solutions of pH 4 upwards to form clear solutions containing nondialyzable hydroxyaluminosilicate species with a limiting Si:Al ratio of about 0.5. A concentration of at least 100 μM $Si(OH)_4$ is required. When such solutions are heated, the poorly

crystalline mineral imogolite is precipitated. This unidimensional, tubular structure has the ideal composition $(HO)_3Al_2O_3$ SiOH and can be considered as a single gibbsite sheet with the inner surface hydroxyls replaced by silicic acid. The stable, clear, unheated solutions appear to contain fragments of this structure. The species have been detected by the infrared examination of solids recovered by freeze-drying solutions (*20*) and by ion-exchange experiments (*21*, *22*). Although the apparent solubility of aluminum is raised at the pH of normally minimum solubility in the presence of silicic acid (Figure 3), the hydroxyaluminosilicate species present limit the bioavailability of aluminum. The interaction of aluminum with various binding groups is reduced when silicic acid is present, as is illustrated by ion-exchange experiments using an iminodiacetate functional resin (Figure 4) (*22*). The fall in aluminum retention (Figure 4a) from about pH 7 is seen to correspond to the formation of hydroxyaluminosilicate species (Figure 4b). Similar results (*21*) were obtained with sulfonate and phosphonate functional resins with the pH of onset of reduced aluminum binding being >5 and >6.6, respectively. Such experiments reflect the stability of the hydroxyaluminosilicate species with respect to ligand–Al binding.

Fish gill epithelia and associated mucus contain such binding groups and, as in ion-exchange resins, aluminum binding is similarly reduced in the presence of silicic acid. This reduction is possibly aided by a pH more

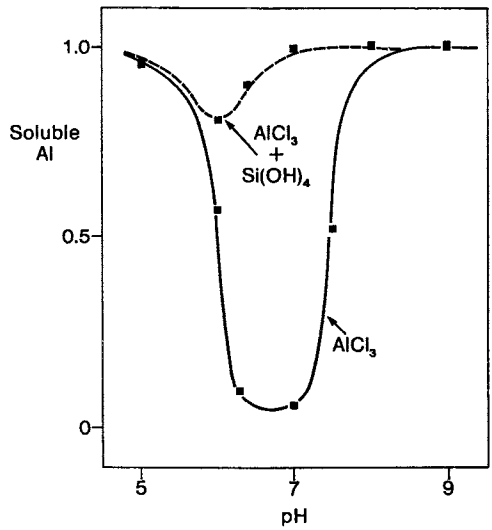

Figure 3. Fraction of aluminum remaining in 20-h-old solution after filtration through a 0.2-μM membrane as a function of pH. Solutions contained 0.1 mM $AlCl_3$ with and without 0.5 mM $Si(OH)_4$. (Reproduced with permission from reference 35. Copyright 1990.)

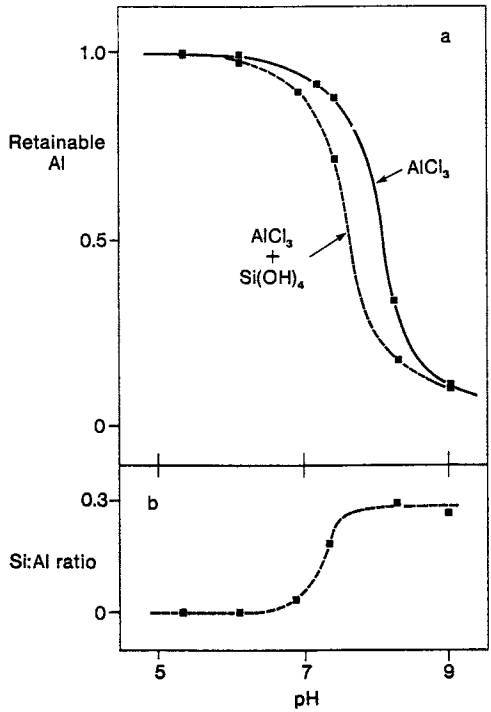

Figure 4. Part a: Fraction of aluminum retained on iminodiacetate functional resin as a function of pH. Solutions contained 0.1 mM $AlCl_3$ with and without 0.5 mM $Si(OH)_2$. Part b: The Si:Al ratio of the retained species. (Reproduced with permission from reference 35. Copyright 1990.)

alkaline than that of the bulk water within a boundary layer proximate to the gill surface and resulting from NH_3 and CO_2 excretion.

At pH 6.2, the formation of the solid hydroxide phase gibbsite limits the level of dissolved aluminum to about 10^{-7} M. The formation of imogolite reduces this level to 10^{-11} M, so that the formation of hydroxyaluminosilicate phases reduces the concentration of biologically available aluminum to levels well below those producing toxic effects.

The formation of hydroxyaluminosilicate species at near-neutral pH is unique. No interactions occur between silicic acid and Ca^{2+} or Mg^{2+} at less than pH 10, so that the transport and binding of these cations is unhindered. The interactions of Fe^{3+} with silicic acid at near-neutral pH are very different from those of aluminum. Acidic solutions containing Fe^{3+} (10^{-4} M) with a threefold molar excess of silicic acid remain clear on neutralization: no visible precipitate forms. Instead, Fe–O polymers are formed as spherical hydrated ferric oxide particles 10–15 nm in diameter,

stabilized against growth, aggregation, and precipitation by an adsorbed layer of silicic acid (*23*).

Such sols present iron in a readily available form to chlorotic plants, probably because the minute particles are easily reduced to Fe^{2+} and solubilized by root exudates (*24*). Thus, silicic acid distinguishes between aluminum and iron as regards biological availability. This ability to distinguish may have been important in primitive biological systems.

The Significance of the Environmental Si:Al Balance

Biological systems are not tolerant of internalized aluminum, which normally is excluded or, as in some plants, rendered immobile, possibly by binding to phytate. In mammals and humans, once internalized, aluminum is bound and carried in the iron-transport protein transferrin (*25*), which can bind two M^{3+} ions per molecule. Although aluminum is bound much less strongly than iron, (log K ca. 12 for Al^{3+} and log K ca. 20 for Fe^{3+}, where K is the stability constant) there is normally an abundance of transferrin with empty sites. Aluminum appears to be concentrated in cells and tissue with high transferrin receptor density, a conclusion supported by experiments using ^{67}Ga-loaded transferrin, in which the marker is found in areas of the rat brain with high receptor density (cerebral cortex, hippocampus, septum, and amygdala) (*26*). These areas are selectively vulnerable in Alzheimer's disease. Aluminum-loaded transferrin is internalized by cultured neuroblastoma cells (*27*) and, presumably, by cerebrovascular endothelial cells because aluminum crosses the blood–brain barrier. Aluminum has also been detected within osteocytes at the junction of osteoid and mineralized bone in patients with dialysis osteomalacia (*28*) and is almost certainly responsible for the low level of cellular activity. A key point is that ferritin is inefficient at loading with aluminum, so that there is no safe "sink" for the element. Events at the intracellular level ultimately responsible for toxicity remain unclear, but aluminum impairs glucose utilization and cholinergic activity in the rat brain (*29*). GTP–GDP (guanosine 5′-triphosphate–guanosine diphosphate) nucleotide exchange is inhibited by aluminum (*30*) and, in vitro, aluminum stimulates phosphatidylinositol (PtdIns) hydrolysis and inhibits PtdIns(4,5)P_2 (where (4,5)P_2 is inositol 4,5-bisphosphate) hydrolysis (*31*). In vitro, aluminum inhibits tetrahydrobiopterin synthesis (*32*). Significantly, aluminum has been reported to increase the permeability of the blood–brain barrier (*33*), and indeed, endothelial "leakiness" is a constant theme, as is alteration in the manipulation of Ca^{2+}. Recent experiments (*34*) suggest that this latter alteration may result from interference in the phosphatidylinositol-derived Ca^{2+} intracellular second messenger system. In rat pancreatic acinar cells, the microinjection of aluminum eliminated the acetylcholine-evoked mobilization of Ca^{2+} from cytoplasmic stores. Early experiments indicated

that this inhibitory effect of aluminum is absent in the presence of silicic acid. This Ca^{2+}-mobilizing system is ubiquitous in biological systems, and its alteration may account for many of the toxic effects of aluminum in plants, animals, and humans.

In view of these various effects of internalized aluminum, the exclusion of the element from biological systems is fundamentally important (*35*). The low solubility of aluminum at neutral pH is one mechanism, but acidity increases availability. Citrate (*36*) and other chelators [e.g. maltol (*37*)] appear to increase absorption in the gastrointestinal tract. An important question is, How general throughout biological systems is the observed effect of silicic acid in excluding aluminum from fish? Is this mechanism operating at plant root membranes and within the gastrointestinal tract?

Silicic Acid: Geochemistry and Health

The essential trace elements (and the toxic elements) are ultimately obtained from the earth's crust via crops and water, although human activity can modify occurrence and availability. The multidisciplinary subject of environmental geochemistry and health studies the relationship between disease epidemiology and geochemistry. Most success has come in understanding the relationship between trace-element deficiency in farm animals and local geochemistry, for example, the effects of Cu deficiency in cattle. The recognition of the goiter of iodine deficiency and the effects of fluorine on the incidence of dental caries are examples of success, as is the recognition of selenium deficiency as the cause of endemic cardiac myopathy in the Keshan district of China (*38*).

A negative association between silica concentration and the incidence of ischemic heart disease (IHD) has been reported (*39*, *40*) and is associated with the lower incidence of IHD in hard-water areas (*41*, *42*). Silicon is associated negatively with IHD mortality (correlation coefficient $r = 0.66$) and positively ($r = +0.68$) with water hardness (*42*). However, no explanation for this observation has been possible. A marked geographical variation occurs in the incidence of ischemic heart disease in the British Isles. A high incidence occurs in the north and west, and a low incidence in the south and east, the relative odds of a major IHD event in males changing from 1.0 in the south of England to 3.03 in Scotland (*43*). This difference reflects, inter alia, a difference in geology between the regions with hard water in the south and east and soft, peaty water from upland areas in the north and west. Silica concentration can differ by an order of magnitude (<10 to >200 μM). The water from upland catchment areas is frequently treated with aluminum for clarification, and with very low silicic acid levels, residual aluminum is likely to be biologically available.

However, with the major part of the intake of aluminum being food (and antacid medication), the important question is the effect of *silicic acid* in water on the absorption of the aluminum in food (*18*). The extent of exclusion would not then be a linear function of silicic acid concentration, because a minimum level of about 100 μM Si is required for the formation of stable hydroxyaluminosilicates, in which the Si:Al ratio is about 0.5 and which have minimum solubility (Figure 5).

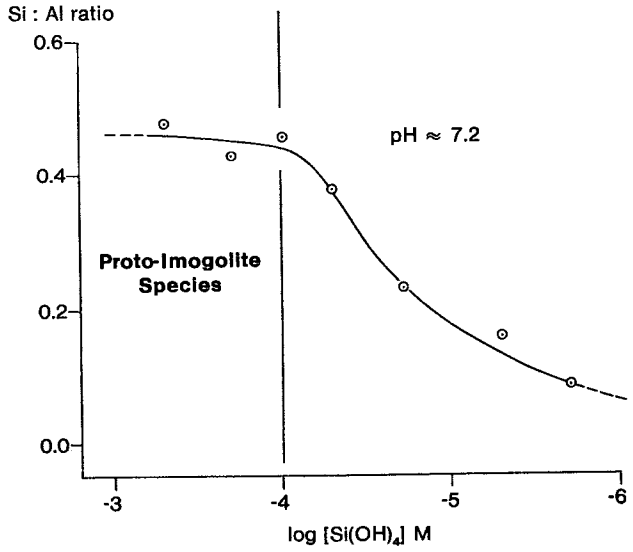

Figure 5. The Si:Al ratio of hydroxyaluminosilicate species formed in solutions containing 10 μM Al^{3+} at pH 7.2. All solutions were aged 20 h and held at 20 °C. (Private communication, J. S. Chappell).

Silicic acid is readily absorbed, and plasma levels rise rapidly following intake. In normal subjects excretion is rapid, average plasma levels are 5–10 μM, and all cells and tissues contain silicon, which may be concentrated in some cells or cellular compartments, for example, in the osteoblast. Little is known of the interactions between this silicic acid and internalized aluminum. With aluminum bound strongly to transferrin and the low plasma silicic acid levels, interaction is unlikely except at sites of local concentration. Codeposited aluminum and silicon (as amorphous aluminosilicate) has, so far as is known, been reported only at the core of senile plaques. Separate groups of workers report silicon in artery walls (*44*) and aluminum (*45*) in artery walls, but no studies have been made of the association and balance of the two elements in tissue. Such studies will be required if progress is to be made. Some workers have reported an

inverse relationship between the level of silicon in arterial tissue and the degree of sclerotic damage and calcification (*46*). The link between all these various observations may be the ability of internalized aluminum to increase the permeability of endo- and epithelial membranes and to alter intracellular Ca^{2+} manipulation and the ability of silicic acid to exclude aluminum from entry in biological systems and, possibly, its ability to modify the effects of internalized aluminum.

Conclusions

The most recent research indicates that in its biological effects, silicon (always as silicic acid) is inextricably linked with aluminum. Good evidence suggests that silicic acid reduces the absorption of manganese in plants and thereby moderates the toxicity associated with excess manganese (*47*, *48*). However, the predominant association is with aluminum because of the prevalence of the two elements and the unique affinity of one for the other. The need in primeval biological systems to "select out" aluminum thus probably involved high silicic acid levels at near-neutral pH, and it will be important to understand the anthropogenic disturbance of the interactions of these two elements that, with oxygen, constitute 80% of the earth's crust. This area is one of the most exciting in bioinorganic chemistry.

References

1. Iler, R. K. *The Chemistry of Silica*; Wiley: New York, 1979.
2. Carlisle, E. M. *Science* **1972**, *178*, 619–621.
3. Schwarz, K.; Milne, D. B. *Nature* **1972**, *239*, 333–334.
4. Schwarz, K. *Proc. Nat. Acad. Sci. USA* **1973**, *70*, No 5, 1608–1612.
5. Schwarz, K. In *Biochemistry of Silicon and Related Problems*; Bendz, G.; Lindqvist, I., Eds.; Plenum: New York, 1978; pp 207–230.
6. Birchall, J. D.; Espie, A. W. In *Silicon Biochemistry*; Ciba Foundation Symposium 121; Wiley: Chichester, England 1986; p 140–159.
7. Carlisle, E. M. *Science* **1970**, *167*, 179–280.
8. Carlisle, E. M.; Alpenfels, W. F. *Fed Proc.* **1984**, *43*, 680.
9. Viola, R. E.; Morrison, J. F.; Cleland, W. W. *Biochemistry* **1980**, *19*, 3131–3157.
10. Kerr, D. N. S.; Ward, M. K. In *Metal Ions in Biological Systems, Vol. 24; Aluminum and its Role in Biology*; Sigel, H.; Sigel, A., Eds.; Dekker: New York, 1988; pp 217–258.
11. Driscoll, C. T. *Environ. Health Perspec.* **1985**, *66*, 93–104.
12. Taylor, G. In reference 10, pp 123–163.
13. Jones, K. C.; Bennett, B. G. "Exposure Committment Assessment of Environmental Pollutants," Report No 33, Vol 4. Monitoring and Assessment Research Centre, King's College, University of London, London, 1985.
14. Crapper, D. R.; Krishnan, S. S.; Dalton, A. J. *Science* **1973**, *180*, 511–513.

15. Candy, J. M.; Oakley, A. E.; Klinowski, J.; Perry, R. H.; Fairburn, A.; Carpenter, T.; Atack, J. R.; Blessed, G.; Edwardson, J. E. *Lancet* **1986**, *i*, 354–357.
16. Martyn, C.; Barker, L. J. P.; Osmond, C.; Hams, E. C.; Edwardson, J. A.; Lacy, R. F. *Lancet* **1989**, *i*, 59–62.
17. Committee on Food Additive Survey Data, "Poundage of Uptake of Food Chemicals, 1982"; National Academy Press: Washington, DC, 1984.
18. Birchall, J. D.; Chappell, J. S. *Lancet* **1989**, *i*, 114.
19. Birchall, J. D.; Exley, C.; Chappell, J. S.; Phillips, M. J. *Nature* **1989**, *338*, No. 6211, 146–148.
20. Farmer, V. C.; Frazer, A. R.; Tait, M. *Geochim. Cosmochim. Acta* **1979**, *4*, 1417–1420.
21. Birchall, J. D.; Chappell, J. S. *Clin. Chem.* **1988**, *34/2*, 265–267.
22. Chappell, J. S.; Birchall, J. D. *Inorg. Chim. Acta* **1988**, *153*, 1–4.
23. Birchall, J. D.; Espie, A. W. In reference 6.
24. Demolon, A.; Bastiss, E. *Compt. Rend.* **1944**, *219*, 293–296.
25. Trapp, G. A. *Life Sci.* **1983**, *33*, 311–316.
26. Candy, J. M.; Edwardson, J. A.; Faircloth, R.; Keith, A. B.; Morris, C. N.; Pullen, R. G. L. *J. Physiol.* **1987**, *391*, 34.
27. Morris, C. M.; Candy, J. M.; Court, C. A.; Edwardson, J. A.; Perry, R. M.; Moshtaghie, A. A.; Skillen, A.; Fairbairn, A. *Biochem. Soc. Trans.* **1987**, *15*, 498.
28. Schmidt, P. F.; Zumkley, H.; Barckhaus, R.; Winterberg, B. In *Microbeam Analysis*; Russell, R. E., Ed.; San Francisco Press: San Francisco, CA, 1989; p 50–54.
29. Johnson, G. V. W.; Jope, R. S. *Toxicology* **1986**, *40*, 93–102.
30. Miller, J. L.; Hubbard, C. M.; Litman, B. J.; MacDonald, T. L. *J. Biolog. Chem.* **1989**, *264*, No 1, 243–250.
31. McDonald, L. J.; Mamrack, M. D. *Biochem. Biophys. Res. Comm.* **1988**, *155*, No. 1, 203–208.
32. Cowburn, J. D.; Blair, J. A. *Lancet* **1989**, *i*, 99.
33. Banks, W. A.; Kastin, A. J. *Lancet* **1983**, *ii*, 1227–1229.
34. Wakui, M.; Itaya, K.; Birchall, J. D.; Petersen, O. H. *Febs. Lett.* **1990**, *267*, No 2, 301–304.
35. Birchall, J. D. *Chem. Brit.* **1990**, *February*, 141–144.
36. Kruck, T. P. A.; McLachlan, D. R. In reference 10, pp 285–314.
37. Nelson, W. O.; Lutz, T. G.; Orvig, C. In *Environmental Chemistry and Toxicology of Aluminum*; Lewis, T. E., Ed.; Lewis Publishers: Chelsea, Michigan, 1989; pp 271–287.
38. Xu, Guang-Iu; Jiang, Yi-fang In *Proceedings of the First International Symposium on Geochemistry and Health*; Thornton, I., Ed.; Science Reviews Ltd, 40, The Fairway, Northwood, Middlesex, HA6 3DY, United Kingdom, 1985; pp 192–204.
39. Schroeder, H. A. *J. Am. Med. Assn.* **1966**, *195*, 81–85.
40. Schwarz, K.; Punsar, S.; Ricci, B. A.; Karvonen, M. J. *Lancet* **1977**, *i*, 538–539.
41. Masironi, R. *Phil. Trans R. Soc. Lond. B288*, **1979**, 193–203.
42. Pocock, S. J.; Shaper, A. G.; Powell, P.; Packham, R. F. In reference 38, pp 141–157.
43. Elford, J.; Thomson, A. G.; Phillips, A. N.; Shaper, A. G. *Lancet* **1989**, *i*, 343–346.
44. Carlisle, E. M. In reference 9, pp 123–139.
45. Zinsser, H. H.; Butt, E. M.; Leonard, J. *J. Am. Geriatr. Soc.* **1957**, *5*, 20–26.

46. Loeper, J.; Loeper, J. G.; Lemaire, A. *Press Med.* **1966**, *74*, 865–867.
47. Lewin, J.; Reimann, B. E. F. *Annu. Rev. Plant Physiol.* **1969**, *20*, 289–304.
48. Foy, C. D.; Chancey, R. L. *Annu. Rev. Plant Physiol.* **1978**, *29*, 511–566.

RECEIVED for review February 19, 1991. ACCEPTED for publication March 26, 1992.

32

Preparation and Uses of Silica Gels and Precipitated Silicas

Robert E. Patterson

The PQ Corporation, Research and Development Center, 280 Cedar Grove Road, Conshohocken, PA 19428

An overview of the nomenclature, manufacture, and uses of synthetic silica gels and precipitated silicas that are of significant commercial importance is presented. Typical manufacturing processes are reviewed, and differences in the structure of silica gels and precipitated silicas that come about as a result of their methods of production are discussed. Applications covered include uses as a reinforcing agent, carrier, anticaking and free-flow agent, thickener, adsorbent, defoamer, substrate, abrasive–polishing agent, antiblock agent, and flatting agent.

ILER DEVOTED ONE OF THE SEVEN CHAPTERS of *The Chemistry of Silica* (*1*) entirely to the manufacture, characterization, and uses of "silica gels and powders". In the 160 pages of Chapter 5, Iler covered so many products, processes, and applications that it is difficult for anyone not already in the field to distinguish between what is of commercial importance and what is of theoretical interest.

The aim of this chapter is more limited; the emphasis is to provide an overview of the uses of synthetic silica gels and precipitated silicas that are of significant commercial importance. Excluded from this discussion are naturally occurring silicas, including products such as diatomaceous earth and so-called "amorphous silica" minerals (which are actually microcrystalline). Also excluded are fumed and arc silicas, forms of synthetic silica made at high temperature (in contrast to silica gels and precipitated silicas, which are generally made in aqueous solution and consequently have surface chemical properties quite different from high-temperature silicas)

0065–2393/94/0234–0617$08.00/0

and products that are not properly classified as silicas (such as insoluble metal silicates). Chapter 24, by Ferch, covers fumed silicas as well as silica gels and precipitated silicas from a somewhat different perspective.

Nomenclature and Manufacture

In *The Chemistry of Silica* (*1*), Iler used the term *silica powders* as a broad category encompassing silica gels, precipitated silicas, and fumed or pyrogenic silicas. In this chapter, only gels and precipitates are covered, because silica gels and precipitated silicas both being produced by wet processes, possess physical and chemical properties that are similar enough to provide for substantial overlap in applications. In contrast, fumed silicas, which are produced by thermal processes, possess unique properties that confer performance characteristics that cannot generally be matched by wet-process silicas in specific applications.

Silica Gels. Silica gels and precipitated silicas can usually be distinguished on the basis of pore structure. Silica gels give a Type IV nitrogen adsorption isotherm, whereas precipitated silicas give a Type II isotherm (*2*). The general shapes of these isotherms are shown in Figure 1. Mercury intrusion–extrusion isotherms exhibit a hysteresis effect in gels because the stronger pore structure remains relatively intact, whereas in precipitates only the intrusion curve can be measured because the high pressure during intrusion breaks down the pore structure. However, in practice these terms refer to the method by which the powder was manufactured. All silica gels and precipitated silicas of major commercial importance are derived from sodium silicate, with the reaction conditions adjusted to yield one type of silica or the other.

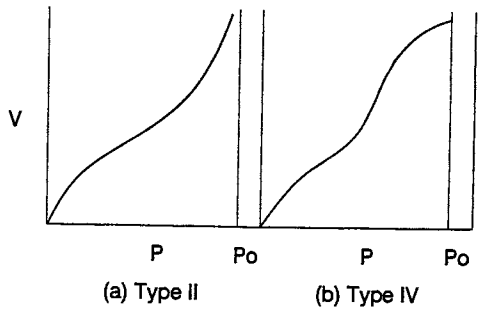

*Figure 1. Typical Brunauer adsorption isotherms for (left) precipitated silica (Type II) and (right) silica gel (Type IV) (*V*, volume adsorbed;* P*, pressure; and* P_o*, saturation pressure).*

Figure 2 shows a typical manufacturing process for silica gels. Silica gels are formed by the acidification of sodium silicate solution under conditions that form a three-dimensional network of silica polymers that entirely enclose the liquid phase. The liquid that forms just after the mixing of the acid and silicate is referred to as a *hydrosol*; in time the hydrosol sets into a rigid gel. If setting is rapid, *gel beads* are possible. With slower setting, a large gel mass is formed that must be crushed before further processing.

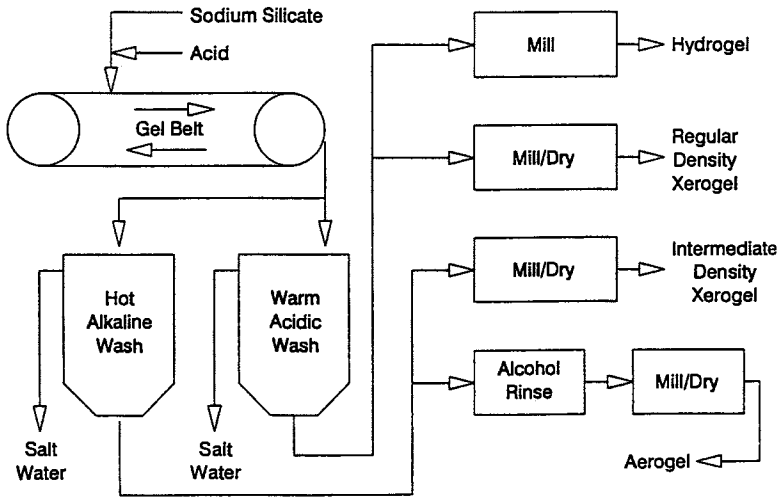

Figure 2. Typical manufacturing process for silica gels.

Silica hydrosols can be formed under a wide range of pH. In highly acidic solution, the silicic acid polymerizes to form nuclei that grow to 1–3 nm, which then aggregate into chains. As the pH of formation increases, these nuclei grow to a larger size, with less aggregation because of repulsion of the more negatively charged particles. Thus, the surface area of silica gels becomes lower as the pH of formation is increased.

After gelation is complete, the next step is to wash the raw gel to remove soluble salts. The conditions of washing affect other gel properties as well. If the washed gel is dried only enough to remove excess surface water, the product is called a *hydrogel* (Iler used the much less common term "aquagel"). Remarkably, hydrogels may contain up to 70% water (by weight), yet still remain relatively free-flowing. If the washed gel is substantially dried, the product is called a *xerogel*. Milling may accompany drying to achieve a desired particle-size distribution.

Silica gels are further distinguished by the degree to which their pore structure is reinforced during processing. Gels washed under acidic conditions retain their high surface area, often over 700 m^2/g. Such products are referred to as *regular-density* gels. When a regular-density gel is dried, surface tension forces cause the pore structure to collapse to a high degree. This collapse can be reduced by washing the gel under hot alkaline conditions, a process known as *hydrothermal treatment.* Because the solubility of silica in water increases rapidly above pH 8, reinforcement can occur through the deposition of dissolved silica at the juncture of primary particles owing to the reduction of solubility in areas having a negative radius of curvature. The effect is to cement the primary particles together enough so that they resist collapse upon drying. A silica made in this way is referred to as an *intermediate density* gel because the density of the dried silica structure is intermediate between that of the regular-(high-) density xerogel and the low-density aerogel.

The final category of silica gels of commercial importance is the *aerogel.* Aerogels, like xerogels, are dry gels, but they are made in such a way as to prevent pore collapse upon drying. One method is to replace the water in the hydrogel with a water-miscible liquid of much lower surface tension, such as alcohol or acetone. This liquid is then removed by heating the gel in an autoclave to above the critical point, then releasing the pressure. In this way a liquid–vapor interface never forms, so surface tension forces never have an opportunity to collapse the pore structure. Although such products do have large pore volumes, shrinkage will occur if the aerogel is brought into contact with water and dried again. If stability is necessary, the intermediate density gel with its reinforced pore structure is the better choice.

In summary, the processing parameters that have the greatest impact on gel properties, and consequently on suitability for various end uses, are the following:

- pH and method of gel formation
- pH and temperature of washing
- method of drying or milling

Precipitated Silicas. Figure 3 shows a typical manufacturing process for precipitated silicas. Precipitated silicas are formed by the acidification of sodium silicate solution under conditions that form primary particles that coagulate into clusters. In contrast to the conditions in a gel, the entire liquid phase is not enclosed by the solid silica phase.

Precipitation is carried out under alkaline conditions, generally at lower concentrations than are employed in gel-making. Properties are

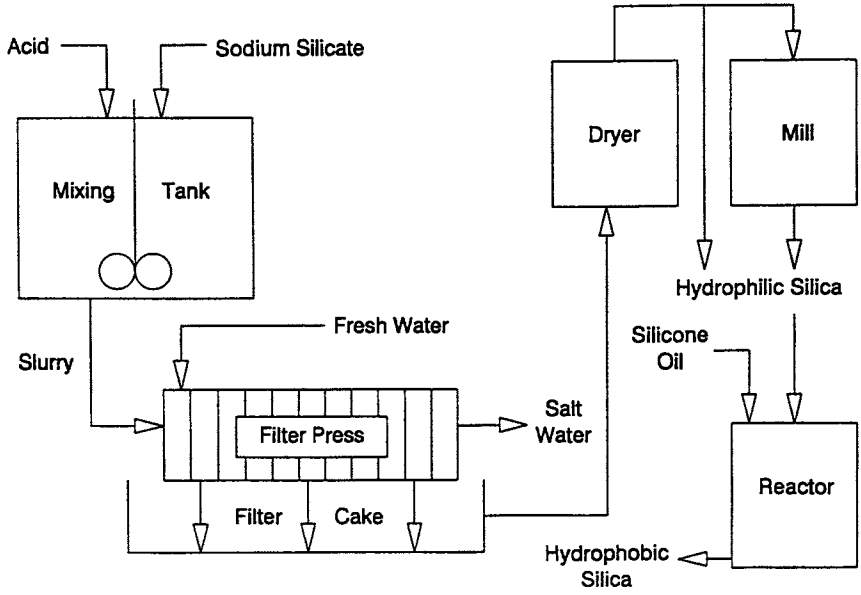

Figure 3. Typical manufacturing process for precipitated silicas.

varied by the choice of agitation, duration of precipitation, rate of addition of reactants, temperature, and concentration. Under typical conditions, the primary silica particles grow to sizes larger than 4–5 nm and are coagulated into aggregates by the sodium ion contributed by the sodium silicate raw material. In fact, this self-coagulation must be avoided if the objective is to produce a stable sol instead of a precipitate. The subject of silica sols is covered in detail in Chapter 29, by Payne; the practical means of achieving the objective is to use an ion-exchange resin rather than a mineral acid as a source of H^+, and at the same time Na^+ will be removed from the solution.

The precipitated silica slurry is next washed to remove soluble salts. The conditions of washing, although important, have less effect on the final product properties than for silica gels. Washing is typically conducted in filter presses. For applications requiring exceptionally low levels of soluble salt impurities, the extent of washing is critical.

The resultant filter cake is dried by one of several methods. Most common are spray drying and rotary drying, which give rise to different particle shapes, degrees of agglomeration, and (to a lesser extent) porosity. The dried silica may be subjected to milling and classifying steps to achieve specific particle-size distributions. Figure 3 shows an optional step in which the silica is reacted with a chemical, in this case silicone, to render it hydrophobic.

In summary, the processing parameters that have the greatest impact on precipitated silica properties, and consequently on suitability for various end uses, are the following:

- conditions during precipitation: time, temperature, concentration, agitation, and method of addition of reactants
- degree of washing
- method of drying or milling

Applications

Reinforcing Agent. The use of silica as a reinforcing agent is probably the largest single application. The chief end use is rubber reinforcement, primarily in the production of tires. This is a major market for precipitated silicas, but not for silica gels. A reinforcing filler may be defined as one that improves the modulus and failure properties (tensile strength, tear resistance, and abrasion resistance) of the final vulcanizate (*3*).

Historically, carbon black has been the first and foremost reinforcing agent for natural and synthetic rubbers. The degree of reinforcement increases roughly with decreasing particle size (*4*). Silica can be used to replace or complement carbon black; an advantage of silica is that it permits the production of durable rubber goods in colors other than black (an aspect important in the manufacture of shoe soles, for example). The degree of reinforcement by silica increases with the quantity of "bound rubber" (rubber that cannot be extracted by solvents), which forms by a free-radical mechanism during milling (*5*).

Another important reinforcement application is in silicone rubber. Historically, fumed silicas have played the major role here, but recently precipitated silicas have been developed that possess the characteristics required for this application (*6*). Compared to conventional precipitated silicas, a product designed for this end use must have higher purity (to impart acceptable electrical properties, because silicone rubbers are often used as insulating materials) and lower water adsorption (to prevent bubbles from forming during extrusion and to impart resistance against moisture pickup). Good dispersibility is also important.

Carrier. The ability to manufacture precipitated silicas and silica gels having large pore volumes gives rise to their use as carriers of numerous liquids; a silica can be made to absorb up to 3 times its weight of many liquids (*7*).

Because silicas can be manufactured to conform to food-grade regulations, they can be used to absorb essential oils, flavors, and feed supplements such as choline chloride. The absorption of pesticides is also a

major application. Often the liquid is released when the powder comes into contact with water, owing to the higher affinity of the silica surface for water than for the absorbed liquid. Potential benefits include more convenient dispensing and improved stability when sensitive materials are handled.

Anticaking and Free-Flow Agent. Many powdered products of commercial importance must be treated to prevent the individual particles from sticking together. Such products include fire extinguisher powders, whey solids, urea used in animal feeds, milk substitutes, cocoa, powdered coffee creamers, spices, citric acid, and many others. The mechanism of interparticle attachment varies with the powder in question, but can include moisture pickup, fusing in materials of low melting point, static charge buildup, or simple agglomeration as a result of surface forces. Both precipitated silicas and silica gels are used as anticaking and free-flow agents. These silicas generally perform the desired function by coating and separating the powder particles and by adsorbing moisture within their pore structures.

Thickener. Silicas are widely employed as thickeners in liquid systems. Fumed silicas are often the cost-effective choice despite their higher price per unit weight. However, precipitated silicas and silica gels also find wide application in this end use. A noteworthy example is the use of wet-process silicas to thicken toothpaste.

The mechanism of thickening depends greatly on the polarity of the liquid and the degree of hydrophilic or hydrophobic character of the silica. Iler (*8*) provided an excellent summary of the principles involved. The best thickening occurs when silica particles are able to interact with each other in such a way as to produce an open network throughout the liquid. This situation is favored when there are portions of the silica surface that have low forces of attraction to the liquid; these areas are free to bond to each other on neighboring particles. On the other hand, if the entire silica surface has low forces of attraction to the liquid, the particles clump together in dense aggregates, reducing the thickening effectiveness. At the other extreme, if the entire surface has strong forces of attraction to the liquid, so that the particles are completely disaggregated, the thickening effect is minimized.

Thus, the characteristics of a silica surface that affect the energy of particle–particle versus particle–liquid contacts, as well as the particle size and degree of dispersion, determine the potential of that silica to thicken. The thickening behavior of a silica can be altered by modification of its surface, such as by the partial attachment of hydrophobic groups.

Adsorbent. A familiar adsorbent application of silica is its use as a desiccant. The small packets of powder included with most electronic products usually contain a desiccant-grade silica gel. For this purpose, a regular-density xerogel is most effective, owing to its high surface area on which water can be adsorbed. The small average pore size of such a gel, a result of unimpeded shrinkage upon drying of the regular-density hydrogel, is not a disadvantage because water molecules are small enough to penetrate these pores.

An adsorbent application of major commercial importance is the adsorption of potentially haze-forming proteins from beer. This process is called *chillproofing* because the haze forms when the beer is cooled after a period of aging subsequent to bottling. Silica hydrogels and intermediate-density xerogels are employed, because both have pores of sufficient size (>10-nm average diameter) to admit the proteins in question.

Silicas gels are also used as selective adsorbents in column chromatography. An exceptionally narrow particle-size distribution is necessary to prevent excessive back-pressure and to produce sharp peaks; precipitated silicas are not generally suitable because their agglomerates break down much more easily than do the stronger particles found in gels. High purity is also important to prevent contamination of the product being separated. The pore-size distribution must be matched to the separation being attempted. The surface of the silica is often reacted with a silane to create a *reverse-phase* packing, so-called because the elution sequence of solutes is the reverse of that for a normal-phase packing (i.e., an untreated silica). The definitive reference is Unger (*9*).

Defoamer. Silicas are the most widely used active particles in defoamer formulations. Precipitated silicas are used almost exclusively. To be effective, the silica must be reacted with an agent, typically polydimethylsiloxane, to render the surface hydrophobic. The mechanism of bubble breaking is the dewetting of the silica particle by the foam lamella, which creates a defect in the film that leads to its rupture. The criterion for dewetting is a three-phase contact angle of 90° or more (the three phases are the aqueous foam lamella, the silica particle, and the carrier oil in which the particle is dispersed). Patterson has identified the properties of silica that optimize performance in the largest U.S. end use, pulp and paper defoaming, for the two common methods of hydrophobing: dry-roast (*10*) and in situ (*11*). Other major defoaming applications include paint and coatings, textile dye baths, and (in Europe) laundry detergents.

Substrate. Silica gel is used as a catalyst substrate because of its resistance to high temperature and the availability of gels of controlled pore and particle size. A catalytically active coating is applied to the gel, often in the form of a precious metal compound.

Abrasive–Polishing Agent. Both silica gels and precipitates are found as abrasives (as well as thickeners) in toothpaste. Silicas are especially useful in the production of clear gel-type toothpastes, because it is possible to match the index of refraction of the liquid components of the formulation to that of the silica to provide the desired level of abrasivity while retaining the transparency of the toothpaste. This cannot be done with conventional abrasive agents, such as calcium carbonate.

Alkaline slurries of precipitated silicas are used as polishing agents for semiconductor silicon wafers. The mechanism of polishing is generally believed to be chemical–mechanical; the high pH of the slurry leads to oxidation of the silicon surface, followed by mechanical removal of the oxidized layer under the action of the silica particles and the polishing pad. In recent years the use of precipitated silicas in this application has largely been supplanted by the use of silica sols.

Antiblock Agent. *Antiblocking* is the prevention of the adhesion of two plastic films in contact with one another. This effect can be achieved by incorporating fine silica particles in the surface of the film. The relatively low refractive index of silica makes the particles less easy to see.

Flatting Agent. Silica xerogels and precipitated silicas are used extensively as flatting agents in paint and coatings. The silica particles protrude from the surface, and the resulting increase in roughness reduces the gloss of the coating. Particle size and degree of dispersion are obviously of importance. Some commercially available silica flatting agents are coated with wax to improve the redispersibility of silica that settles in the can during storage and to improve the scratch resistance of the dry coating.

Other Uses. Numerous other uses of silica gels and precipitated silicas are found in the literature. Two relatively new applications that are expected to be significant in the future are battery separators, in which the silica pore structure provides a path for the migration of conductive ions, and low-temperature insulation, in which the low thermal conductivity of dry silica powders makes them useful in consumer products such as refrigerators (Chapter 24).

References

1. Iler, R. K. *The Chemistry of Silica*; Wiley: New York, 1979; pp 462–464.
2. Adamson, A. W. *Physical Chemistry of Surfaces*; Wiley: New York, 1976; p 566.
3. Boonstra, B. B. In *Rubber Technology*; Morton, M., Ed.; Van Nostrand Reinhold: New York, 1973; p 55.
4. Billmeyer, F. W. *Textbook of Polymer Science*; Wiley: New York, 1971; p 546.

5. Iler, R. K. *The Chemistry of Silica*; Wiley: New York, 1979; p 582.
6. *Degussa Silicas for Silicone Rubber*; Technical Bulletin, Pigments No. 12; Degussa AG: Frankfurt, Germany, 1982.
7. *SYLOID Multifunctional Silicas for the Food Industry*; Davison Chemical Division, W. R. Grace: Baltimore, MD.
8. Iler, R. K. *The Chemistry of Silica*; Wiley: New York, 1979; pp 588–590.
9. Unger, K. K. *Porous Silica: Its Properties and Use as Support in Column Liquid Chromatography*; Elsevier: New York, 1979.
10. Patterson, R. E. In *1988 Nonwoven Conference*; TAPPI Press: Atlanta, GA, 1988; pp 39–48.
11. Patterson, R. E. *Colloids Surf. A*, in press.

Additional Reading

Alexander, G. *Silica and Me: The Career of an Industrial Chemist*; American Chemical Society: Washington, DC, 1973.
Barby, D. In *Characterization of Powder Surfaces*; Parfitt, G. D.; Sing, K. S. W., Eds.; Academic Press: New York, 1976; pp 353–425.
Gregg, S. J.; Sing, K. S. W. *Adsorption, Surface Area, and Porosity*; Academic Press: New York, 1967.
Soluble Silicates; Falcone, J. S., Jr., Ed.; ACS Symposium Series 194; American Chemical Society: Washington, DC, 1982.
Vail, J. G. *Soluble Silicates in Industry*; American Chemical Society Monograph Series 46; The Chemical Catalog Co.: New York, 1928.
Vail, J. G. *Soluble Silicates: Their Properties and Uses*; American Chemical Society Monograph Series 116; Reinhold: New York, 1952; Vols. 1 and 2.

RECEIVED for review April 23, 1991. ACCEPTED revised manuscript April 1, 1992.

33

Colloid Chemistry of Silica: Research in the Former Soviet Union

L. T. Zhuravlev

Institute of Physical Chemistry, Russian Academy of Sciences, Leninsky Prospect 31, Moscow 117915, Russia

Research of Soviet scientists is surveyed. Contributions to various aspects of the colloid chemistry of silica are examined: preparation and stabilization of silica hydrosols; preparation of silica gels; structural characterization of silicas; surface chemistry elucidation; adsorption and ion-exchange property examination; and geometric and chemical modification of silicas, silica coatings, and so forth.

SILICA IS ONE OF THE MOST WIDESPREAD SUBSTANCES on earth. The content of SiO_2 in the lithosphere is thought to be 58.3%, and the percentage of SiO_2 in independent rocks (quartz, opal, and chalcedony) is approximately 12%. Earth is apparently the most siliceous part of the universe: the content of SiO_2 in lunar soil is 41% and in rocky meteorites is 21% on average. Silica occurs not only as minerals and dissolved in water, but also is contained, in small quantities, in many organisms, in which it plays an important and not yet completely understood part in the living process. Traditional building and other materials based on silica, such as cement, concrete, firebrick, silicate glasses, rough and fine ceramics, and enamels, occupy a significant place in human life.

The past two decades saw a rapid growth in those fields of science and technology that deal with production and utilization of various colloid and microheterogeneous forms of silica with developed surfaces, such as sols, gels, and powders. The colloid chemistry of silica embraces a wide range of diverse scientific and applied problems. It is an important, independent, and progressive field of colloid chemistry that is closely interwoven with a number of physicochemical and other sciences. Research has led to the

0065–2393/94/0234–0629$13.04/0

creation of production technology for new materials containing silica and having valuable properties.

Various fields use efficient silica adsorbents and selective adsorbents, silica carriers of the active phase in catalysis, silica fillers for polymeric systems, silica thickeners for dispersion mediums, silica binding agents for molding materials, silica adsorbents and carriers for gas chromatography, and so forth. Chemical modification of the surface of dispersion silica has received a large amount of interest; this process allows researchers to change adsorption properties and performance data when synthesizing composite materials.

To understand the mechanisms of adsorption, adhesion, chromatographic separation of mixtures, filling of polymeric systems, and so forth, the nature of interaction of different substances with the surface of silica must be understood. In all such phenomena, the porous structure and the chemistry of the surface silica particles are important.

Colloid chemistry of silica has been researched on a large scale in the former Soviet Union. This chapter discusses not only recent scientific advances there, but also the most important trends in the chemistry of amorphous silica during the last 30–40 years. The most active study in the former Soviet Union of different aspects of colloid chemistry of silica is carried out in numerous scientific organizations in Moscow, Leningrad, and Kiev. Research in this field is also conducted in Minsk, Novosibirsk, Gorki, Kazan, Saratov, Vladivostok, Irkutsk, Tashkent, Vilnius, Baku, Yerevan, Tbilisi, Kishinev, and other cities. Large- and small-capacity industrial production of different kinds of sols, gels, and powders of amorphous silica is realized in a number of chemical plants in the area.

This chapter constitutes a brief review of research carried out in the former Soviet Union on the colloid chemistry of silica. A comprehensive survey of this field would involve an analysis of several thousand publications by Soviet scientists and lies outside the scope of this review. The main trends of research in the former Soviet Union are discussed and illustrated with appropriate examples.

Currently, the definitive book on the chemistry of silica is the monograph by Ralph K. Iler (*1*). This book contains 350 references to publications by Soviet researchers. The books by A. V. Kiselev and coworkers (*2, 3*), also published in the United States, are noteworthy for their description of Soviet research on silica surface chemistry and the adsorption properties of oxide adsorbents such as silica. Somewhat more attention is devoted in this chapter to the surface chemistry of amorphous silica, because this field is of special interest to me (*4, 5*).

Historical Sketch

The earliest reference to colloidal systems in Russia appeared in 1763, when Lomonosow described the properties of natural colloidal solutions. Even then he distinguished between the coagulation and crystallization processes. In 1785 Lovits investigated the process of adsorption from solutions. The phenomena that later became known as electroosmosis and electrophoresis were discovered in 1809 by Reiss. The concept of the colloidal state as a highly dispersed state of a given phase in a dispersion medium was developed by Borshchov (1869). Mendeleev suggested in 1871 that the general colloidal state of a substance depends on the complexity of its composition and the size of the particle. The works of Shvedov on structure formation in solutions of gelatin and the works of Sabaneev and Lyubavin on the determination of the molecular weight of colloids by the cryoscopic method appeared at the end of the 19th century. Veimarn, the author of one of the first textbooks on colloid chemistry (1904) showed that any substance can be converted into the colloidal state by sharply decreasing its solubility with the right solvent. In 1908 Gedroits studied the colloidal properties of soil, and Zelinsky reported in 1914 the results of investigations into the colloidal structure of proteins.

Large-scale, systematic research in colloid chemistry began in the Soviet Union in the 1920s. Among the prominent chemists in this field are Dumansky (lyophilic colloids), Peskov (stable disperse systems), Rebinder (surface-active substances, physicochemical mechanics), Zhukov (electrosurface phenomena), and Deryagin (surface forces). Fundamental interdisciplinary research was carried out by Frumkin, Balandin, Boreskov, Chmutov, Laskorin, and others. The outstanding schools in the former Soviet Union in the field of adsorption developed under the leadership of Dubinin, A. V. Kiselev, and Neimark.

Dubinin (Institute of Physical Chemistry, the U.S.S.R. Academy of Sciences, Moscow) and colleagues (Zaverina, Radushkevich, Timofeev, Bering, Serpinsky, Zhukovskaya, Nikolaev, Sarakhov, Isirikyan, Zolotarev, Yakubov, Bakaev, Onusaitis, Voloshchuk, and others) conducted a theoretical analysis of the sorption phenomena in porous substances, including silica, and applied these phenomena in practice (*6–11*).

A. V. Kiselev (Institute of Physical Chemistry, the U.S.S.R. Academy of Sciences, Moscow; Moscow State University) and colleagues (Avgul, Shcherbakova, Dreving, Dzhigit, Lygin, Muttik, Nikitin, Lopatkin, Davydov, Kuznetsov, Belyakova, Berezin, Eltekov, Zhuravlev, and others) studied the dependence of adsorption and the energy of adsorption on the structure and the chemical nature of the adsorbent surface and on the properties of the adsorbed substances. In their investigations, oxide-type adsorbents such as amorphous silica (silica gels, porous glasses, aerosils,

and aerosilogels) were widely used (*12–17*). A. Kiselev made notable contributions to the study of amorphous silica, quartz, diatomite, silicates, and zeolites. The number of publications in the field of silica chemistry written by A. Kiselev or in collaboration with colleagues exceeds 600 and includes several monographs and textbooks (*2, 3, 17, 18*), reviews (*12, 19–25*), and patents (*26, 27*).

Neimark (Institute of Physical Chemistry, the Ukrainian S.S.R. Academy of Sciences, Kiev) and colleagues (Slinyakova, Sheinfain, Piontkovskaya, Vysotsky, Chertov, Khatset, Rastenko, Il'in, Chuiko, Tertykh, and others) studied the synthesis and control of porous structures and the modification of the silica surface and other mineral sorbents. The theoretical principles for the formation of a porous structure were worked out (*28, 29*). Numerous silica gels were prepared that had pores ranging from very wide to very fine; the latter had molecular-sieve properties (*28–32*).

Preparation and Stabilization of Silica Hydrosols

The preparation and stabilization of silica hydrosols were investigated by Deryagin, Churaev, and co-workers (Institute of Physical Chemistry, the U.S.S.R. Academy of Sciences, Moscow) (*33–36*); Frolov, Shabanova, and co-workers (Mendeleev Chemico-Technological Institute, Moscow) (*37–41*); Rebinder, Shchukin, Kontorovich, and co-workers (Institute of Physical Chemistry, the U.S.S.R. Academy of Sciences, Moscow) (*42–48*); Strazhesko, Strelko, Vysotsky, and co-workers (Institute of Physical Chemistry, the Ukrainian S.S.R. Academy of Sciences, Kiev) (*49–55*); Neimark, Sheifain, and co-workers (Institute of Physical Chemistry, the Ukrainian S.S.R. Academy of Sciences, Kiev) (*28–32*); Belotserkovsky, Kolosentsev, and co-workers (Technological Institute, Leningrad) (*59–64*); Kazantseva et al. (Institute of Geology and Geophysics, Siberian Division of the U.S.S.R. Academy of Sciences, Novosibirsk) (*65*); Ryabenko et al. (All-Union Research Institute of Chemical Reagents and High-Purity Substances, Moscow) (*66*); and others.

In 1940 Derjaguin (*34*) studied the subject of coagulation of lyophobic colloids in the presence of an electrolyte. Later Derjaguin and Landau (*35*) and Verwey and Overbeek (*67*) developed a theory describing the stabilization of sols (the theory of DLVO). Such stabilization is due to the electrostatic repulsion of diffusion components in the double electrolytic layer formed during the adsorption of the electrolyte ions on the particle surface. The research carried out by Derjaguin into the aggregate stability of colloidal systems (*36*) showed that solvation shells consisting of solvent molecules hindered the conglomeration of particles because of the elasticity and higher viscosity; cleavage and separation of the particles resulted.

Rebinder (*48*) investigated the effect of the surface (adsorption) layers on the properties of colloidal systems. When the lyophobic dispersion systems are stable, the structural–mechanical stabilization occurs where the protecting layers of the micelle-forming surface-active agents or high-molecular compounds are formed at the interface boundary.

Research of the problems of the formation of disperse systems and the physicochemical mechanics of disperse structures was conducted by Rebinder, Shchukin, Kontorovich, and co-workers (*42–47*) particularly of the problems of structure formation in silica hydrosols. The properties of silica sols (their aggregate stability, the nature of the contacts between the individual particles, and so on) depend on many factors. Estimates of the diameter of globules in hydrogels of silicic acid were made by using narrow angle X-ray scattering. Within a wide range of time and temperature of aging, concentration of the solid phase, and pH of the sols (i.e., the conditions for the formation of gels), the radius of the globules varied from 15 to 37 Å. Light-scattering methods were used to study the regularities of the solid-phase aggregations. The scattering centers that were formed (of the order of magnitude of several hundred angstroms) belong to loose aggregates made up of primary particles. The rate of formation of solid-phase particles increased with an increase in the concentration of SiO_2 in sols and with an increase in pH. In supersaturated solutions of silica, the strength of contact scattered between the real particles in silica sols is of several orders of magnitude. Thus, the contacts could be subdivided into two main types: contacts of the coagulation type with strength $p \leq 10^{-2}$ dyne being due to the van der Waals interaction, and phase contacts with strength $p \geq 10^{-1}$ dyne being due to the coalescence of particles via the polycondensation mechanism. The effect of temperature on the syneresis kinetics of acid and alkaline hydrogels of polysilicic acids was studied. Above and below the isoelectric point spontaneous shrinkage took place at the same effective activation energy despite the different reaction mechanism of polycondensation within the pH range under consideration. The activation energy in this case was similar to the energy of the hydrogen bonds. The authors concluded that the rate of spontaneous shrinkage of the hydrogels of polysilicic acids is determined mainly by the interaction of particles through the surface forces that lead to the formation of easily mobile coagulative contacts.

Frolov, Shabanova, and co-workers (*37–39*) studied the transition of a sol into a gel and the aggregate stability of colloidal silica. Their aim was to develop a technology for the production of highly-concentrated silica sols and to use them as binders, catalyst supports, polymer fillers, adsorbents, and so forth. Kinetic studies were made of polycondensation and gel formation in aqueous solutions of silicic acids. At the stage of particle growth, polycondensation proceeds in the diffusion–kinetic region. With changes in pH, temperature, concentration, and the nature of electrolytes,

the properties of the surface layers have a decisive effect on heterogeneous polycondensation, gel formation, and aggregate stability. The maximum rate of gel formation at pH 5.5–6.5 corresponds to the transition in the gels' properties from a condensational type to a coagulational thixotropic type capable of undergoing subsequent peptization. The aggregate stability and kinetics of gel formation are limiting processes during the formation of the porous structure in the final product (silica gel). The results were analyzed from the point of view of the DLVO stability theory; the splitting pressure was taken into account.

Kolosentsev and Belotserkovsky (*59–61*) used the ion-exchange methods proposed by Bird (*68*) and Bechtold and Snyder (*69*) in preparing stable aqueous silica sols containing ~50 wt% SiO_2, with particle size ranging from 65 to 380 nm.

Frolov, Khorkin, Shabanova, and co-workers (Mendeleev Chemico-Technological Institute, Moscow; Branch of the Polymer Research Institute, Saratov) carried out the experimental production (*41*) of highly concentrated silica sol by using the same ion-exchange methods (*68, 69*). The concentration of SiO_2 sols obtained was ~40% by weight or more.

Lipkind et al (Experimental Plant of the All-Union Oil Processing Research Institute, Gorky; Research Institute of the Chemical Industry, Kemerovo) set up the industrial production of sols made from silicic acid by the electrodialysis method (*70*). The capacity of the experimental pilot plant is 100 L of sol per hour.

Frolov, et al (*40*) used the ion-exchange method in conjunction with electrodialysis for preparing SiO_2 hydrosols. The process consisted of the following: ion-exchange, electromigration of H+ and Na+ ions in an ion-exchange resin that involved the regeneration of the ionite, and electrodialysis of the starting solutions. The cationic resins were in the strongly acidic H+ form. The efficiency of the process was raised when ion exchange was carried out in a direct current electric field. The process makes possible the continuous production of highly concentrated hydrosols.

Ryabenko et al. (*66*) developed a method for synthesizing highly pure silica by heterogeneous hydrolysis of tetraethoxysilane followed by the concentration of the sol of polysilicic acid and thermal treatment.

Strazhesko, Strelko, Vysotsky, and co-workers (*49–51*) investigated the polymerization of monosilicic acid. Polysilicic acid is more acidic than monosilicic acid, and the dissociation constant of the acidic centers on the surface of polysilicic acid is 2 to 3 orders of magnitude greater than that of the monomer (*49–51*). Strazhesko, Vysotsky, and co-workers (*52–55*) showed that the isoelectric point represents not only the minimal rate of the gel formation process but also its syneresis. As a result, mechanically strong silica gels were obtained that had a maximum specific surface area.

Strelko and co-workers (*71–73*) investigated the properties of the siloxane bond and the polymerization mechanism for silicic acid on the basis of the difference in the electronic structure of the Si–O bonds in silanol and the siloxane groups of silica. A kinetic equation was proposed to describe the polymerization of silicic acid throughout the entire pH range. The authors believe that the molecular mechanisms for the formation of globular skeletons in silica gels are based on the polymerization and depolymerization of silicic acids.

Kazantseva et al. (*65*) synthesized monodisperse silica sols by hydrolysis of a mixture of tetraethoxysilane and C_2H_5OH–H_2O–NH_3 at room temperatures. The degree of monodispersion of the silica sols increased with time and corresponded to an increase in the diameter of the spherical particles. When hydrolysis had proceeded for 3.5–4 h, the same uniform size of the particles reached ~300 nm.

Churaev, Nikologorodskaya, and co-workers (*33*) investigated the Brownian and electrophoretic motion of silica hydrosol particles in aqueous solutions of an electrolyte at different concentrations of poly(ethylene oxide) (PEO) in the disperse medium. The adsorption isotherms of PEO on the surface of silica particles were obtained. The thickness of the adsorption layers of PEO was determined as a function of the electrolyte concentration and the pH of the dispersed medium. The results can be used in an analysis of the flocculation and stabilization conditions for colloidal dispersions of silica (with non-ionogenic water-soluble polymers of the PEO type).

Preparation of Silica Gels and Powders, Geometric Modification of Silicas, and Studies of Structural Characteristics

Silica gels, porous glasses, and silica powders were prepared by A. Kiselev, Nikitin, and co-workers (Moscow State University, Moscow) (*2, 3, 26, 27, 74–81*); Dzisko, Fenelonov, and co-workers (Institute of Catalysis, Siberian Division of the U.S.S.R. Academy of Sciences, Novosibirsk) (*82, 83*); Zhdanov and co-workers (Institute of Silicate Chemistry, the U.S.S.R. Academy of Sciences, Leningrad) (*84–87*); Belotserkovsky, Kolosentsev, and co-workers (Technological Institute, Leningrad) (*59–61*); Neimark, Sheinfain, and co-workers (Institute of Physical Chemistry, the Ukrainian S.S.R. Academy of Sciences, Kiev) (*28, 29*); Chuiko (Institute of Surface Chemistry, the Ukrainian S.S.R. Academy of Sciences, Kiev) (*88*); and others.

Porous glasses were first prepared and described by Grebenshchikov and co-workers (State Optical Institute, Leningrad) (*89, 90*). This research was continued by Zhdanov and co-workers (*85–87*). Usually, porous glasses are prepared by treating sodium-boron silicate glasses with inorganic acids.

The skeleton of porous glasses consists of an acid-resistant sponge network of the silica phase and of the secondary structure formed from highly dispersed hydroxylated silica having a globular structure. The latter precipitated inside the network cavities during the extraction of B_2O_3 and Na_2O. The specific surface area and porosity of such glasses depend on the leaching conditions: the concentration of the acid, the temperature of the solution, and so forth, as well as on the conditions of the thermal treatment of the initial glasses. A very valuable property of porous glasses is that their structure can be regulated within a wide range of porosity. In addition, they are mechanically and chemically stable. Such glasses are made at the Experimental Plant of the All-Union Research Institute of Oil Processing in Gorky (*91*).

Dobychin and co-workers (State Optical Institute, Leningrad) (*92, 93*) carried out a systematic investigation of the structure and adsorption properties of porous glasses and of the structural changes in them.

Plachenov and co-workers (Technological Institute, Leningrad) (*94, 95*) developed methods of synthesizing active metal oxides, including silicas. A systematic study of the secondary structure of porous substances was carried out (*96, 97*).

Belotserkovsky, Kolosentsev, and co-workers (Technological Institute, Leningrad) (*59–64*) worked on the synthesis and application of various silica gels. They were able to vary within certain limits the porous structure of the sorbents by compressing them into a powder form. They proposed that silicas could be obtained by ion-exchange, peptization, and other methods.

Sychev and co-workers (*98*) (Technological Institute, Leningrad) investigated SiO_2–P_2O_5 xerogels, which are of practical interest in the field of optical systems and other areas. The optimal conditions were established for preparing solutions containing the necessary oxides and for converting them into gels. Following thermal treatment at 800 °C, the average pore size of the xerogel was ~50 nm.

Komarov, Kuznetsova, and co-workers (Institute of General and Inorganic Chemistry, the Byelorussian S.S.R. Academy of Sciences, Minsk) (*99–102*) examined the possibility of forming and controlling the porous structure of xerogel during the gelling syneresis and the drying of the gel. The effects of different surface-active agents on the structure formation, the pH dependence of the micellar solutions, the temperature, the presence of electrolytes, and the solubilizing water-soluble organic substances were investigated. The surface-active agents were alkyl-substituted quaternary salts of pyridinium and ammonia (cation- and anion-type surface-active agents), and the solubilizers were decyl alcohol, capric acid, and others. A mechanism describing the gel formation in the presence of surface-active agents and solubilizers was proposed.

Lipkind et al. (Experimental Plant of the All-Union Research Institute of Oil Processing, Gorky) (*103*) worked out ways of setting up the industrial production of mineral adsorbents, including silica gels.

The most important adsorbents in gas-adsorption chromatography are macroporous silica (*26, 27, 74*). Silica carriers used in chromatography were described by Gavrilova, Bryzgalova, and co-workers (Moscow State University) (*104–106*).

Khotimchenko, Vasiloi, Demskaya, and co-workers (The Scientific Industrial Association Quartz, Leningrad) (*107, 108*) used sol–gel technology for making quartz glass. A heat-resistant composite was obtained from tetraethoxysilane by using quartz fibers (diameter $d = 5–10$ μm) as the filler. The activation of quartz glass with organic pigments was investigated.

Pryanishnikov, Chepizhnyi, and co-workers (State Research Institute of Glass, Moscow) (*109*) developed superfine silica fibers (Sivol) by thermochemical treatment of a natural mineral, chrysotile asbestos, in the presence of inorganic acids. The physicochemical properties of these fibers and the starting material were investigated by Pryanishnikov, Osipov, Guy, and co-workers (State Research Institute of Glass, and the Institute of Physical Chemistry, the U.S.S.R. Academy of Sciences; both in Moscow) (*110–112*) These superfine fibers have much greater porosity than the starting material. The pores were distributed according to their diameter within a broad range, with a maximum at 5–6 nm. The specific surface areas as measured by Kr and water adsorption was $S_{Kr} << S_{H2O}$. These measurements, as well as the data obtained by low-angle X-ray scattering, show that these superfine fibers contain fine ultramicropores comparable in diameter with the size of water molecules. Electron microscopic investigations show the fibers to be characterized by a multilayered fibril structure with a well-defined internal channel in the center.

Il'in, Turutina, and co-workers (Institute of Physical Chemistry, the Ukrainian S.S.R. Academy of Sciences, Kiev) (*113–115*) investigated the cation processes for obtaining crystalline porous silicas. The nature of the cation and the composition of the systems $M_2O–SiO_2–H_2O$ (where M is Li+, Na+, or K+) affect the rate of crystallization, the structure, and the adsorption properties of silica sorbents of a new class of microporous hydrated polysilicates (Siolit). These polysilicates are intermediate metastable products of the transformation of amorphous silica into a dense crystalline modification. The ion-exchange adsorption of alkali and alkaline earth metals by these polysilicates under acidic conditions increases with an increase in the crystallographic radius and the basicity of the cations; under alkaline conditions, the selectivity has a reverse order. The polysilicates exhibit preferential sorption of alkali cations in the presence of which the hydrothermal synthesis of silica was carried out. This phenomenon is known as the memory effect.

Korneev, Agafonov, and co-workers (Technological Institute and Pigment Science Industrial Association, both in Leningrad) (*116, 117*) synthesized aqueous solutions of systems that have high modulus and low alkalinity and are based on silicates of quaternary ammonia (SQA). The decomposition of SQA took place at ~190 °C. The calcined product of SQA has amorphous and crystalline phases. Aqueous solutions of quaternary ammonium silicates can be used as binders; they are not flammable, explosive, or toxic.

In 1961 Stishov and Popova (Moscow State University, Chair of Geochemistry, and Institute of High-Pressure Physics, the U.S.S.R. Academy of Sciences, respectively; both in Moscow) (*118*) for the first time synthesized modified crystalline silica having a very dense octahedral structure, which they named Stishovite.

The geometrical modification of the structure of silica adsorbents (by hydrothermal treatment in autoclave, by calcining in air and in an atmosphere of water vapor, by treatment at the hydrogel stage, etc.) was carried out by Nikitin, A. Kiselev, Bebris, Akshinskaya, and co-workers (Moscow State University) (*26, 27, 74–81, 119*); Chertov, Neimark, and co-workers (Institute of Physical Chemistry, the Ukrainian S.S.R. Academy of Sciences, Kiev) (*56–58*); Zhuravlev, Gorelik, and co-workers (Institute of Physical Chemistry, the U.S.S.R. Academy of Sciences, Moscow) (*4, 77, 80, 120–122*); Lipkind and co-workers (Experimental Plant of the All-Union Research Institute of Oil Processing, Gorky) (*26, 123*); and others.

Nikitin, A. Kiselev, and co-workers (*74, 124, 125*) developed the method of geometric modification of the adsorbent structure. This advance led to the industrial production in the Soviet Union of a new class of adsorbents—macroporous silica, in the form of silica gels and silochroms (the latter is the technical name for homogeneous large-pore aerosilogels (*26, 27*); the diameters of the pores vary from hundreds to thousands of angstroms. These silica gels have found wide application in gas and liquid chromatography, in the immobilization of ferments, and so forth (*74, 75, 119*). Different methods of geometric modification were studied (i.e., predetermined changes in the structure of the pores and the silica skeleton): hydrothermal treatment inside the autoclave; calcining in air and in the atmosphere of water vapor; and calcining in the presence of alkaline additives (*74, 76–78*). An investigation was carried out of the mechanism of the changes in the structure of silica during hydrothermal treatment: an increase in the diameter of the pores (a decrease in the specific surface area) was due to the dissolution of small silica particles and to the precipitation of this silica on the larger particles, primarily at the point of contact of the particles. In the course of hydrothermal treatment of silica gels ultrapores, in addition to very wide pores (macropores), are produced that are accessible mainly to water molecules but inaccessible to krypton and benzene molecules (*76, 77*). The thermal treatment of silica

gels in air and in water vapor atmosphere prevents the formation at microheterogeneities of the surface of the sample and enhances the geometric uniformity of macroporous silica gels (*74, 75*). The mechanism of the sintering of silica gels under different conditions of thermal treatment was studied (*79–81*).

The hydrothermal modification of SiO_2 was investigated by Chertov, Neimark, and co-workers at the hydrogel and xerogel stages (*56–58*). The hydrothermal treatment of hydrogels makes it possible to vary the structure of silica gels within a wide range (e.g., specific surface area from 800 to 20 m^2/g, and volume of pores from 0.20 to 2.20 cm^3/g).

Lazarev, Panasyuk, Danchevskaya, and co-workers (Institute of General and Inorganic Chemistry; the U.S.S.R. Academy of Sciences, Moscow State University, Moscow) (*126*) investigated the phase structural transformations occurring at an elevated temperature in amorphous silica under the influence of an active medium such as water. Such investigations have been carried out to meet the requirements of industry, because fine-grain quartz obtained in such processes serves as a raw material in the production of quartz glass. The starting silica gel was subjected to drastic hydrothermal treatment in an autoclave (300–400 °C at pressures of several tens of atmospheres). A thermodynamic analysis was made of the processes, and the enthalpy and energy of the activation were determined. A stepwise mechanism was proposed to describe the water-induced transformation of amorphous silica into a crystalline form (quartz). The high activity of water at elevated temperatures leads to the breaking of the siloxane bonds and the formation of intraskeletal silanol groups. The latter again interact with each other and form new, and thermodynamically more stable, siloxane bonds. This process is accompanied by the removal of interglobular water. Thus, hydrothermal treatment causes crystallization that yields quartz without transforming SiO_2 into a soluble state.

Dubinin, A. Kiselev, Deryagin, Chmutov, Zhdanov, Neimark, Serpinsky, Bering, Radushkevich, Karnaukhov, Plachenov, Nikitin, Dzisko, Keltsev, Torocheshnikov, Dobychin, and others made a significant contribution to elucidating the geometrical structure of dispersed and porous substances, in particular for silica. The structural characteristics of silica were investigated by theoretical analysis, adsorption methods, measurement of apparent density, mercury porosimetry, kinetic methods, narrow-angle X-ray scattering, electron microscopy, and other methods.

The classification of pores according to their size, proposed by Dubinin, has been adopted by IUPAC (*127, 128*): the classifications are macropores ($d >$ 2000–4000 Å), mesopores (30–32 Å $< d <$ 2000–4000 Å), supermicropores (12–14 Å $< d <$ 30–32 Å), and micropores ($d <$ 12–14 Å). This classification system has proved useful and is used in the study of amorphous silica having different structural characteristics (*4*).

A. Kiselev developed the adsorption–structural method of investigation (*129*), which made possible a rational classification of adsorbents (*130–132*). Dubinin, Radushkevitch, Bering, Serpinsky, and others have developed on the basis of their experimental results a theory on the physical adsorption of gases and vapors in microporous adsorbents that they call the theory of volume filling of micropores. The theory is applicable to almost all the adsorption systems, including microporous silica gels and porous glasses (*133, 134*).

Plachenov (*96, 97*) estimated the limiting dimensions of the equivalent radii of mesopores. The distribution of the volume of the mesopores calculated from their equivalent radii was compared with capillary condensation measurements. The macroporous and the intermediate mesoporous structure were determined, as were the volume of the micropores and the constant in the equation of the isotherm adsorption theory describing the volume filling of micropores (*133, 134*).

Karnaukhov, A. Kiselev, and co-workers (*12, 14, 135–142*) investigated the hypothetical geometrical structure describes by a corpuscular model in the form of a system of particles (globules) of uniform size in contact with one another. The diameter of the particles and the number of contacts between particles were taken as the main parameters of the model. An approximate theory of polymolecular adsorption and capillary condensation was developed. The simultaneous process of polymolecular adsorption and capillary condensation was analyzed for porous systems with a globular structure. It was shown that the contribution of both processes determines the form of the adsorption isotherm. The theoretical results obtained were compared with experimental data for different silica adsorbents by using different methods.

Zhuravlev, Gorelik, and co-workers (*77, 80, 120–122, 143*) carried out kinetic studies of water vapor adsorption and isotopic exchange (D_2O + ≡Si–OH) for different types of amorphous silica. A relationship was established between the nature of the porosity and the shape of the kinetic curve. For example, for bidispersed silica gels containing both wide mesopores and very fine ultramicropores, the kinetic plot consists of two sections: a very short period due to the mass transfer of water vapors through transport mesopores, and a very long period (tens of hours) due to the diffusion of water molecules inside very fine pores that have diameters comparable with that of the water molecule. Thus, such plots provide information on the type of pores present in the silica sample.

With the aid of a kinetic model for a biporous sorbent (*144*), Zolotarev et al. (*143*) described the diffusion and kinetics of sorption for water–silica gel systems. On the basis of this theoretical model, an explanation was given for the differences in the experimental kinetic curves for water-vapor sorption on biporous silica gels (*143*). The coefficients for the mass

transfer of water in the mesopores and ultramicropores were also determined.

Surface Chemistry of Amorphous Silica

In the 1930s, studies of the condensation processes of silicic acids showed that hydroxyl (silanol) groups, ≡Si–OH, should be present on the surface of silicates and silicas (*145–147*). On the basis of measurements of the heat of wetting and a comparison of the adsorption data with the date from chemical analysis and the corresponding results reported in the literature, A. Kiselev (*147*) suggested (1936) that the water evolved during calcination from silica gel is not physically adsorbed water but is formed from OH groups that are chemically held on the silica surface. This suggestion led to an understanding of the dehydroxylation mechanism (*147*).

Yaroslavsky and Terenin (Leningrad State University) (*148*), by using an infrared spectroscopy method, proved for the first time (1949) the existence of hydroxyl groups on the silica surface (porous glass). This fact was soon confirmed by other researchers (*149–153*).

Zhdanov (Institute of Silicate Chemistry, the U.S.S.R. Academy of Sciences, Leningrad) (*154*) showed (1949) that the adsorption of water vapor by SiO_2 (porous glasses, silica gels) strongly depends on the temperature of the preliminary thermal treatment of the adsorbent. Calcination of 300–500 °C resulted in a sharp decrease in the adsorption of H_2O at low values of pressure over initial pressure p/p_o (<0.3), and the adsorption isotherms were found to be irreversible. On the other hand, the adsorption isotherms of water on silica subjected to calcination in vacuo at <500 °C (but after the sample was kept in contact with water vapor or liquid water at room temperature) again became reversible; that is, the adsorption activity of SiO_2 was restored.

In the 1950s, A. Kiselev, Zhdanov, and co-workers (*12, 84, 155–159*) showed that when the adsorption isotherms of water are expressed as absolute isotherms (referred to as the unit surface of the SiO_2 sample), widely different forms of amorphous silica having a completely hydroxylated state adsorb the same amount of water at the same relative pressure ($p/p_0 < 0.3$). Thus the plots of absolute adsorption isotherms for different samples showed that the surfaces of these samples are of a similar nature. The adsorption properties of nonporous silica and silica having large pores (i.e., an absence of micropores) depend above all on the presence of OH groups and on the degree of hydroxylation of the surface.

On the basis of the concept of the "absolute" adsorption properties of SiO_2, an attempt was made by A. Kiselev, Zhdanov, and co-workers (*12, 158, 160*) to establish a value for the concentration of OH groups (or the silanol number, α_{OH}) on the surface of amorphous completely hydroxylated silica. The most probable value was $\alpha_{OH} = 6.9–7.5$ OH groups per square

nanometer. However, the possible presence of structurally bound water inside the silica was not taken into account (*161–163*), so a somewhat higher calculated value for α_{OH} resulted.

Other workers in this field were critical of the concept put forward by A. Kiselev and Zhdanov. Sidorov (Leningrad State University) (*151, 153*), in infrared spectroscopic studies of water adsorption at a low degree of coverage, had observed that the intensity of the absorption band due to the free surface OH groups ($\nu_{OH} = 3750$ cm^{-1}) remained unchanged. Similar experiments were carried out by other researchers. It was concluded by Sidorov and by V. Kiselev and co-workers (Moscow State University, Physics Department) (*164–166*) that the initially free H_2O molecules are adsorbed not on OH group sites but on more active centers that they called centers of the II-type.

The main ideas put forward by V. Kiselev and co-workers (*164–166*) are as follows:

1. The extent of hydration and hydroxylation of silica surface, and also the adsorption properties (per unit of silica surface), are different for samples having different specific surface area under the same conditions of preliminary treatment. The extent decreases with an increase in the specific surface area.
2. Coordinately bound water firmly held in the form of H_2O molecules exists on nonhydroxyl centers of the II-type; these centers are coordinately unsaturated Si atoms on the surface of the sample. The concentration of the II-type centers is small: $\alpha_{Si} = 0.1–0.3$ Si atoms per square nanometer.
3. Coordinately bound water is removed in vacuo at ~400 °C. Above this temperature there remains on the surface of silica a hydroxylated layer that has a heterogeneous composition. The NMR data (*164–166*) point to the presence of siloxane groups; single, isolated OH groups; paired vicinal and paired geminal OH groups; and probably triple $-Si(OH)_3$ groups.

The presence of coordinated water was confirmed by Chuiko and coworkers (Institute of Surface Chemistry, the Ukrainian S.S.R. Academy of Sciences, Kiev) (*88, 167*). Experiments were carried out on pyrogenic silica (aerosil) with different methods. The main conclusions of these studies are as follows:

1. The topography of SiO_2 is determined by the index of face (111) and face (100) in β-cristobalite; the silanol number of

the starting aerosil is $\alpha_{OH} \cong 1.7$ OH groups per square nanometer.

2. The adsorption centers of the coordinated water are coordinately unsaturated Si atoms on the silica surface to which OH groups are attached. The adsorbed water molecule (with the coordinate bond) near the adsorption center can be located either over the face of the silicon–oxygen tetrahedron

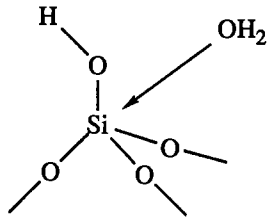

or under the Si atom of the silanol group

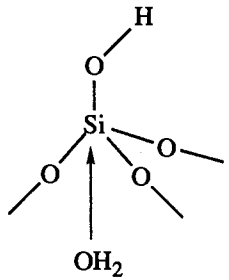

3. The concentration of the II-type centers is high, $\alpha_{Si} \cong 1.7$ Si atoms per square nanometer; that is, all the surface Si atoms with attached OH groups belong to these centers.
4. The centers of the II-type ensure a strong retention of coordinated (molecular) water on the SiO_2 surface up to ~650 °C, with the energy of the interaction of H_2O molecule with such a center being up to 62 kcal/mol (259 kJ/mol) (*167*).

On the other hand, some investigations confirm the main conclusions of A. Kiselev and Zhdanov. Galkin, Lygin, and co-workers (Moscow State University) (*3, 168–170*) investigated the changes in absorption band intensity due to valence vibrations of free OH groups ($\nu_{OH} = 3750$ cm^{-1}) during the adsorption of water under conditions in which the infrared

heating of the sample was excluded. When water was gradually introduced to a system originally at a low degree of coverage, the intensity of the absorption band decreased. Thus, the surface OH groups act as the water adsorption centers. Other investigations (*171–173*) also indicate the important role played by silanol groups as the centers of molecular adsorption of water.

Zhuravlev (Institute of Physical Chemistry, the U.S.S.R. Academy of Sciences, Moscow) (*4, 5*) carried out a systematic investigation of the hydroxylated surface of amorphous silicas by using the deutero-exchange method and the programmed-temperature method. The main conclusions are as follows:

1. The temperature threshold corresponding to the removal of physically adsorbed water from the hydroxylated SiO_2 surface lies at 190 °C.
2. The maximum hydroxylated state of the surface of SiO_2 samples (the degree of surface coverage with OH groups, $\theta_{OH} = 1$) is obtained after preliminary treatment of the samples in vacuo at 180–200 °C, when for each Si atom there is approximately one OH group. The average value of the silanol number for such a state, $\alpha_{OH} = 4.6$ OH groups per square nanometer, is a physicochemical constant (it is independent of the type of the amorphous silica used, the method of preparing it, and the structural characteristics, that is, the specific surface area, the type of pores, the distribution of the pores according to their diameter, the packing density of the particles, and the skeleton structure of SiO_2).
3. The kinetic order of the thermal desorption of water in the range 200–1100 °C is $n = 2$. Thus, the removal of water from the surface (associative desorption) takes place owing to the interaction of pairs of hydroxyl groups that leads to the formation of siloxane bonds. The degree of coverage with silanol groups, θ_{OH}, in this temperature range varies from 1 to ~0.
4. With the degree of coverage of OH groups in the range $1 \geq \theta_{OH} > 0.5$, the activation energy of desorption, E_d, changes from 16.5 to ~25 kcal/mol (~105 kJ/mol). Lateral interaction (hydrogen bonding) occurs between the OH groups. The chemisorption of water (dissociative adsorption) involving the breaking of the siloxane bridges and the formation of new silanol groups is a rapid nonactivated (or weakly activated) process.

5. At the degree of coverage $\theta_{OH} < 0.5$, the energy of activation, E_d, increases substantially [from ~25 to 50 kcal/mol (~105 to 210 kJ/mol) and probably higher] owing to the fact that there exist on the surface of SiO_2 only isolated OH groups, and for the condensation reaction to take place, there must be an activated process involving the migration of protons and the evolution, during the final stage, of H_2O molecules due to the accidental interaction in pairs of OH groups (which draw close to one another to a distance of ~0.3 nm). The chemisorption of water is a slow and strongly activated process.
6. In addition to surface OH groups, there may exist OH groups inside the silica skeleton and inside the very fine ultramicropores (*143*) that have diameters comparable to that of the water molecule. The relationship between the amount of surface OH groups and the intraskeleton OH groups depends on the method of preparation and subsequent treatment of silica (*162*).

Investigations of Silica Surface Processes by Physical and Physicochemical Methods

Infrared and ultraviolet spectral methods—electron paramagnetic resonance (EPR) and NMR spectroscopy, luminescent probing, mass spectrometric methods, calorimetric methods, and other procedures—were used in investigating surface processes of SiO_2 by Terenin, Yaroslavsky, Sidorov, and co-workers (Leningrad State University) (*148, 150–153*); Kurbatov and Neuymin (Naval Medical Academy, Leningrad) (*149*); Lygin, Galkin, Davydov, and co-workers (Moscow State University) (*168–171, 174–183*); Titova, Arutyunyan, Kosheleva, and co-workers (Institute of Physical Chemistry, the U.S.S.R. Academy of Sciences, Moscow) (*3, 172, 173, 184*); Vedeneeva and Musatov (Institute of Crystallography, the U.S.S.R. Academy of Sciences, Moscow) (*185, 186*); Zhdanov et al. (Institute of Silicate Chemistry, the U.S.S.R. Academy of Sciences, Leningrad) (*173*); Kvlividze, Egorow, V. Kiselev, Chukin, and co-workers (Moscow State University; All-Union Research Institute of Oil Processing, Moscow) (*164–166, 187–190*); Bakaev, Pribylov, and co-workers (Institute of Physical Chemistry, the U.S.S.R. Academy of Sciences, Moscow) (*191, 192*); Butyagin, Radtsig, and co-workers (Institute of Chemical Physics, the U.S.S.R. Academy of Sciences, Moscow) (*193–197*); Kotov, Pshezhetskii, and co-workers (Physico-Chemical Institute, Moscow) (*198, 199*); Chuiko, Sobolev, Tertykh, Eremenko, and co-workers (Institute of Surface Chemistry, the Ukrainian S.S.R. Academy of Sciences, Kiev) (*88, 200–207*); Zhuravlev,

Agzamkhodzhaev, Gorelik, Shengeliya, and co-workers (Institute of Physical Chemistry, the U.S.S.R. Academy of Sciences, Moscow) (*77, 120–122, 176, 208–210*); Kazansky, Kustov, and co-workers (Institute of Organic Chemistry, the U.S.S.R. Academy of Sciences, Moscow) (*211–214*); Mastikhin et al. (Institute of Catalysis, Siberian Division of the U.S.S.R. Academy of Sciences, Novosibirsk) (*215*); and others.

Bondarenko, V. Kiselev, and co-workers (*216*) carried out a mass spectroscopic analysis of the gaseous products formed during the thermal treatment (300–1000 °C) of various crystalline and amorphous silicas. The only product formed was water.

Lygin, Galkin, Davydov, Shchepalin, and co-workers (*3, 168–171, 174, 183, 217*) carried out a series of infrared spectroscopic investigations of silica. The problems they studied include hydroxyl coverage, surface chemical reactions, and the adsorption mechanism of molecules having different structures. They established that high-temperature dehydroxylation of the SiO_2 surface changed the properties of the OH groups. Research has been conducted into the behavior of hydroxyl groups and electron-acceptor centers of silica surface in samples modified with admixtures, Al_2O_3, and B_2O_3. The reaction of surface OH groups with different chemical reagents was examined, in particular, with $ClSi(CH_3)_3$ and $Cl_2Si(CH_3)_2$. The behavior of intraskeletal hydroxyl groups (absorption band with a maximum of 3650 cm^{-1}) in relation to the conditions of the preliminary treatment of silica sample was investigated. The surface silanol groups were divided into free, isolated, and perturbed groups that were linked by a hydrogen bond. Spectral and energy evidence of the interaction of OH groups with molecules having different electronic structures in the process of physical adsorption was established. Before complete coverage of the silica surface with a monolayer of water, a number of associated H_2O molecules were formed. On the dehydroxylated sections of the SiO_2 surface, chemisorption of water takes place in addition to molecular adsorption.

Analogous infrared spectroscopic investigations were carried out by Titova, Arutyunyan, Kosheleva, and co-workers (*3, 172, 173, 184*). The structure of associates silanol groups on hydroxylated silica surface was examined: in addition to free, isolated OH groups, associations with intramolecular hydrogen bond both by hydrogen atom and by oxygen atom, in the form of mutually perturbed silanol pairs, were found. With a change in the temperature, reversible transitions take place between the free and associated silanol groups. Molecularly adsorbed water on the surface of highly pure silica is held owing to the formation of hydrogen bonds with the surface hydroxyl groups.

Using ^{19}F NMR spectroscopy, Bakaev and Pribylov (*191*) determined the location of $CFCL_3$ molecules with respect to one another in an adsorbed state on silica gel at 77.4 K. In adsorption of $CFCL_3$, the OH

groups being first removed from the surface of the silica gel and under the conditions of a low degree of coverage, there is an increase of the second moment M_2 line with an increase in adsorption. Such a dependence is due to the nonuniform nature of the SiO_2 surface, that is, to the presence of surface adsorption centers that differ in their adsorption activity.

Krasilnikov, V. Kiselev, and co-workers (*218*) investigated the oxidizing properties of the SiO_2 surface in the process of its dehydroxylation by thermal treatment (300–900 °C) in air. The oxidizing capacity was very low: for the same surface the number of oxidizing equivalents was smaller by 3 orders of magnitude than the number of OH groups. The amount of adsorbed oxygen increases with an increase in the calcination temperature. It was concluded that oxygen is adsorbed by the surface radicals produced during the dehydroxylation of the surface. Surface radicals of the ≡Si–O• type are centers of high activity.

Kuznetsov, Dzhigit, Muttik, and co-workers (Moscow State University) (*15, 217, 219–226*) carried out calorimetric investigations and obtained the characteristics of adsorbed substances having different geometrical and electronic structures. They also measured the energy of adsorption for hydroxylated and dehydroxylated surfaces of silica. The difference in the heat of adsorption, ΔQ_{OH}, for a fully hydroxylated and strongly dehydroxylated silica surface (degree of coverage $\theta \cong 0.5$) was determined. The difference represents the contribution due to the energy of the specific interaction of the surface hydroxyl groups with the linkages and the bonds of different organic molecules having locally concentrated electron density. The differential heat of adsorption of water vapor as a function of the degree of coverage on a hydroxylated silica surface was measured (*15*).

The dependence of the differential heat of adsorption of *n*-alkanes, alcohols, and other substances was investigated by Isirikyan and coworkers (*227–229*), who used the calorimetric method for silica gels possessing different degrees of porosity and hydroxylation. The heat of adsorption was always sharply lower at a low degree of coverage owing to the nonuniform surface of silica. The adsorption isotherms and the differential heats of adsorption for benzene vapor are higher than those of hexane. The greater value for the adsorption energy of benzene is due to the additional specific dispersion interaction of the molecule with the OH groups on silica (due to the local concentration of electron density on the periphery of the benzene ring attributable to π electrons). The heat of adsorption of benzene increases with an increase in the concentration of the silanol groups, whereas the differential heat of adsorption of hexane remains the same for SiO_2 with different degrees of hydroxylation of the surface. For *n*-alkanes in the region of high relative pressures, p/p_o, there appears a sharp maximum in the differential heat of adsorption. This effect is explained by capillary condensation theory (*135*).

Egorov, Murina, V. Kiselev, and co-workers (*230*) measured the heat of wetting of silica for water and other liquids in relation to the degree of hydroxylation. The plot of the heat of wetting versus the calcination temperature showed a maximum corresponding to 200–300 °C. The heat of wetting decreased at higher calcination temperatures, that is, with a decrease in the degree of hydroxylation of the SiO_2 surface.

Berezin and co-workers (Institute of Physical Chemistry, the U.S.S.R. Academy of Sciences, Moscow) (*231–237*) measured by the calorimetric method the heat capacity of benzene, water, and other substances adsorbed on silica gel at low temperatures and different degrees of adsorption. In monlayered coverage, the adsorbate does not undergo phase transition. But in polymolecular coverage, there is a range of temperatures (below the normal melting temperature of a given substance) within which the adsorbate undergoes phase transition corresponding to the volume melting of the substance. These results are of practical interest in solving problems related to the freezing of water in different porous substances.

Gusev and co-workers (State University, Kazan) (*238, 239*) investigated the dielectric relaxation of adsorbed water in silica gel, aerosil, and quartz. Characteristic of these systems is the presence of two disperse regions of dielectric permeability, the position of the amplitude of which depends on temperature, humidity, specific surface area, and porosity. The relaxation time of these regions increases with an increase in the diameter of the pores. The distribution parameters of these time periods are much greater than the corresponding relaxation periods for free water and ice. Disperse region I appears only when the humidity corresponds to a monolayer. Disperse region II is due to the reorientation of water molecules caused by the nonuniform surface of the sample. On a silica surface the phase transition temperature of water–ice is lowered.

Zhilenkov, Glazun, and co-workers (Agricultural Institute, Voronezh) (*240–243*) measured the dielectric permeability ϵ of water and other substances adsorbed on a silica surface. At a low degree of coverage, the permeability was proportional to the concentration of the adsorbed substance (benzene, chloroform, acetone, and water). In this case, the ϵ of the adsorbate did not differ from that of liquid. When the degree of coverage with water was high, there was a notable decrease in growth of the dielectric permeability in comparison with that of an ordinary liquid. The decrease in ϵ was explained as being due to electrostatic attraction on the silica surface inside the narrow pores; this attraction decreases the ability of the dipole moment of water molecule to orient itself in the external electrical field, a situation that causes a decrease in the polarization. In the adsorbed structural water at low temperatures, the dielectric relaxation is 5–6 orders of magnitude greater than that of ordinary ice.

This observation illustrates the nonuniform nature of the silica surface, with active centers having different adsorption potentials.

Physical and Chemical Adsorption

A great number of physical adsorption investigations of different substances on surfaces of silica have been conducted. For example, Shcherbakova, Belyakova, Aristov, and co-workers (Moscow State University; Institute of Physical Chemistry, the U.S.S.R. Academy of Sciences, Moscow) (*13, 244–253*) investigated the physical adsorption of different substances on silica gels as a function of the degree of coverage of the silica surface with hydroxyl groups. A quantitative dependence was established for the physical adsorption of nitrogen, hexane, benzene, water, methanol, and other substances in the vapor phase on the concentration of the OH groups on the surface of silica. Adsorption due mainly to the dispersion interaction (e.g., hexane) is only slightly dependent on the concentration of OH groups. Adsorption of benzene vapor, on the other hand, is very sensitive to the presence of silanol groups on the silica surface. Adsorption of methanol vapor on SiO_2 depends on the concentration of OH groups on the surface of the adsorbent, too. A decrease in the degree of the surface hydroxylation of silica gel leads to an increase in the chemisorption of water and methanol.

The physical modification of silica surfaces by various regents was investigated too. For example, Bugnina and Serpinsky (*254*) investigated the adsorption of N_2 and H_2O vapors at two different temperature intervals on macroporous silica gel that was physically modified with dibutyl phthalate (DBPh). When DBPh in the sorption state on SiO_2 surface loses its lateral mobility (at −194 °C), it in fact modifies the starting silica gel. It changes the gel's porous structure, specific surface area, and nature of the surface. But when DBPh retains its surface mobility (adsorption at room temperature) during the subsequent adsorption of the second adsorbate (H_2O), it acts as one of the components of the binary mixture; these components are simultaneously adsorbed on SiO_2.

Chemical modification of the silica surface was the subject of investigations carried out by Lisichkin, Kudryavtsev, Staroverov, and coworkers (Moscow State University) (*255–257*); A. Kiselev, Nikitin, Shcherbakova, and co-workers (Moscow State University) (*258–264*); Chuiko, Tertykh, and co-workers (Institute of Surface Chemistry, the Ukrainian S.S.R. Academy of Sciences, Kiev) (*88, 200–203, 265–269*); Neimark, Sheinfain, and co-workers (Institute of Physical Chemistry, the Ukrainian S.S.R. Academy of Sciences, Kiev) (*270–273*); Aleskovsky, Kolstov, and coworkers (Technological Institute, Leningrad; Leningrad State University) (*274–281*); Yuffa and co-workers (State University, Tyumen) (*279, 282*); Trofimchuk and co-workers (State University, Kiev) (*283*); Fillipov (Insti-

tute of Physical Chemistry, the Ukrainian S.S.R. Academy of Sciences, Kiev) (*284*); Reikhsfeld and Skvortsov (Technological Institute, Leningrad) (*285*); Ermakov et al. (Institute of Catalysis, Siberian Division of the U.S.S.R. Academy of Sciences, Novosibirsk) (*286*); Smit et al. (Institute of Organic Chemistry, the U.S.S.R. Academy of Sciences, Moscow) (*287*); and others.

The grafting of organic and inorganic compounds and of metalloorganic complexes onto the surface of amorphous silica is a subject of intense research in the former Soviet Union. As is well known, modified silicas are widely used in sorption, catalysis, and chromatography, as fillers for polymers, and as thickening agents in dispersed media.

The first mention of chemical modification of silica in the former Soviet Union goes back to 1950, when A. Kiselev, Dzhigit, and co-workers (*248*) observed the irreversible adsorption of methanol vapors on silica gel. The mechanism of the chemisorption of methanol on dehydroxylated SiO_2, which involves the breaking of the siloxane bond, was described by Belyakova et al. (*251*).

Shcherbakova, Petrova, and co-workers (*258–263*) studied the chemical modification of silica for applications in gas chromatography (for example, in the adsorption separation of hydrocarbons by gas chromatographic methods). The adsorption properties are investigated as a function of the degree of surface modification with $ClSi(CH_3)_3$. A number of silica samples were chemically modified so that they would have the desired adsorption properties (*17*). Chemical modification is an effective means of changing the shape of adsorption isotherms.

Fundamental research into adsorption and chemical modification has helped to elucidate chromatographic processes. This research has led to new developments in gas adsorption chromatography by A. Kiselev, Yashin (Experimental Design Office, Dzerzhinsk), Poshkus (Institute of Chemistry and Chemical Technology, the Lithuanian Academy of Sciences, Vilnius) and co-workers (*2, 17, 288–290*). Together with theoretical investigations and molecular statistical calculations, this method can be used to determine the structural parameters of the adsorbate molecule (this direction of research is referred to as chromatoscopy).

Lisichkin, Kudryavtsev, Staroverov, and co-workers (*255–257*) investigated the chemical modification of mineral sorbents, in particular, of amorphous silica. The structure of a grafted organic layer depends on the structure of the modifying agent, the structural characteristics of the carrier (SiO_2), the conditions of modification, and so forth. Modified silicas are classified according to two groups: those containing a monomolecular organic layer on the surface of the sample and those containing high-molecular-weight compounds.

The most widely used method of synthesizing modified silicas of the first type is reaction between the silanol groups of SiO_2 surface and

organosilicon compounds. Zhuravlev and co-workers (*209*) showed that, owing to the steric limitations in the modification reactions, not all surface silanol groups enter into the reaction. In a majority of cases, the distribution of the modifying agent on the silica surface during surface coverage is of an island nature. The same is true of modification with chlorosilanes and of reactions of amines and amino acids and with alkyl halides. In practice, there is a range of pore size, and consequently there may be cases in which the grafted layer has a mixed structure: inside the wide pores the grafted molecular chains will be highly mobile (labile structure), whereas inside the narrow pores, owing to steric hindrance, the grafted layer will have a rigid structure.

The introduction of functional groups into a grafted molecule can affect the structure of the grafted layer because of the possible interaction of the functional groups with the residual silanol groups on the silica surface. In this respect, the most often investigated are silicas modified by γ-aminopropyltriethoxysilane. These systems show the presence of hydrogen bonds between the amino groups and the residual OH groups.

When the surface of silica contains high-molecular-weight compounds, the simplest way to make such samples is by the adsorption of organic polymers from solutions. The best results were obtained by using heterochain nitrogen-containing oligomers derived from polyethyleneimine because they are firmly adsorbed on the hydroxylated surface of silica. In general, such silicas are obtained by polymerizing monomers on the surface of unmodified silica or on the surface of silica-containing, chemically grafted initiators of radical polymerization (peroxides, unsaturated compounds of the vinyltrichlorosilane type, etc.).

Radiation can also be used to initiate the polymerization. The modification in such reactions mainly results in island-type surface coverage. In polymerization reactions, often no covalent bond is formed between the polymer and the silica carrier. As a result, the modifying layer is held on the surface by adsorption forces or by geometric factors. With regard to the state of the macromolecules on the silica surface, two cases should be analyzed: the conformation of the adsorbed polymer and the conformation of the polymer chain firmly held by one end of the silica surface. At present, investigations are being carried out on the adsorption on the surface of silica of various types of polymers, in particular polystyrene, polymethylmethacrylate, and so forth. In the general case, the surface of the polymer-coated silica is less uniform compared with analogous silica modified with grafted compounds (*255–257*).

Surface chemical reactions were employed by Neimark, Sheinfain, and co-workers (*270–272*) to synthesize a large number of chemically modified

silica gels. Approximately 40 types of organosylyl groups on silica surface were obtained, and their adsorption properties were investigated (*273*).

Chuiko, Tertykh, and co-workers (*88, 200–203, 265–269, 291*) studied chemical reactions on the silica surface. As a result, practical applications were found (*88, 291*) for methylaerosils; butoxyaerosils; aerosils modified with monoethanolamine, ethylene glycol, and α-oxypropionic acid; and other highly dispersed organosilicas. To classify reactions on the silica surfaces, use was made of the electrophilic and nucleophilic mechanisms developed by Ingold (*292*).

Tarasevich and co-workers (*293, 294*) (Institute of Colloid Chemistry and the Chemistry of Water, the Ukrainian S.S.R. Academy of Sciences, Kiev) investigated the formation of a modified polyorganohydridesiloxane layer on the surface of amorphous silica (aerosil, silochrom, etc.). The modifying agents used were polyalkylhydridesiloxanes $(RSiHO)_n$, where $n = 10–15$ and R is CH_3 and C_2H_5. The degree of polymerization was controlled by thermal treatment. The adsorption isotherms of water vapors, benzene, and *n*-hexane were investigated for the modified and unmodified silicas. The modified samples had a hydrophobic surface with a specific heat of wetting of $\leq 20–30$ mJ/m^2. On the basis of the results of this study, inert, heat-stable (up to ~450 °C) chromatographic carriers were developed.

Ganichenko, V. Kiselev, and co-workers (Moscow State University) (*295*) investigated the adsorption of vapors of water, benzene, and cyclohexane on the chemically modified (methylated) surface of large-pore silica gels. The partial substitution of the surface hydroxyl groups by methyl groups caused a decrease in the adsorption capacity.

The differential heat of adsorption of different vapors on SiO_2 samples subjected to chemical modification (esterification, etc.) was measured by Kuznetsov and co-workers (Moscow State University) (*224, 225*).

Aleskovsky, Kolstov, Volkova, and co-workers investigated the chemical modification of silica surfaces by inorganic compounds (*274–281*). The materials obtained are useful in heterogeneous catalysis, electronics, and so forth. The method for molecular lamination was developed (*276–278*) by interacting volatile and readily hydrolyzing halides of transitional metals with the surface of hydroxylated silica. This method makes it possible to modify the silica surface with mono- and polymolecular layers of V, Cr, Ti, Fe, Al, B, and so forth.

To prepare highly dispersed metallic adsorbents, S. Kiselev and Sokolova (Institute of Physical Chemistry, the U.S.S.R. Academy of Sciences, Moscow) (*296*) coated the surface of SiO_2 samples with platinum by reacting platinochloric acid with the amino groups of modified aerosils. Subsequent thermal treatment (250 °C) resulted in a reduction to platinum by the hydrogen of the amino groups.

Adsorption from Solutions

Eltekov, Pavlova, Shikalova, Bogacheva and co-workers (Moscow State University; Institute of Physical Chemistry, the U.S.S.R. Academy of Sciences, Moscow) (*17, 290, 297–307*) investigated the effect of the chemical nature and the dimensions of the pores in silica adsorbents on the adsorption from solutions. The adsorption of benzene from *n*-hexane solutions on silica gels with a hydroxylated and a dehydroxylated surface was studied. Dehydroxylation sharply lowered the heat of adsorption of benzene. A comparison was made of the adsorption isotherms for a series of *n*-hexane solutions of aromatic hydrocarbons on hydroxylated silica gel. The intermolecular interaction of aromatic hydrocarbons with this adsorbent is stronger than the interaction of saturated hydrocarbons because aromatic hydrocarbons form hydrogen bonds with the silanol groups on the SiO_2 surface.

The adsorption from three-component solutions (*n*-hexane, benzene, and dioxane) on the hydroxylated silica surface was studied. The effect of the chemical properties of the SiO_2 surface and the nature of the solvent on the adsorption of polymers was investigated. The adsorption of macromolecules on nonporous and fairly large-pore silica is determined by their conformational transformations. The adsorption equilibrium is often established very slowly: the process may take up to several months.

The adsorption isotherms of polystyrene of different molecular weights were determined with CCl_4, toluene, and other solvents for silica gels with different porosity and different degrees of hydroxylation and surface modification. Adsorption of polystyrene from toluene on the hydroxylated surface of SiO_2 was negative, because the solvent molecules enter into a specific interaction with the surface OH groups. The accessibility of the porous silica gel surface to the macromolecules of polystyrene depends on the size of the pores, the molecular mass distribution in the starting polystyrene, and the temperature. Many different high-molecular-weight compositions were investigated, including oligomers, polymers, proteins, and viruses.

Larionov and co-workers (Institute of Physical Chemistry, the U.S.S.R. Academy of Sciences, Moscow) (*308–312*) carried out systematic theoretical and experimental investigations of the adsorption from liquid solutions of nonelectrolytes on silica adsorbents. They studied the adsorption of individual substances and binary liquid solutions (benzene/carbon tetrachloride, carbon tetrachloride/isooctane, benzene/isooctane, etc.) on SiO_2 samples with different degrees of porosity but identical surface chemical properties. The experimental results were compared with the theoretical calculations carried out by the Gibbs' method. This procedure made it possible to calculate the dependence of the enthalpy, entropy, and free energy of wetting on the concentration and to obtain expressions describ-

ing the chemical potential of the components of adsorption solutions. The considerable difference between the activity coefficients of the volume and the adsorption solutions was explained on the basis of the compression of the adsorption solution in the adsorption field. It was shown that the adsorption equilibrium of solutions can be calculated from the adsorption properties of individual substances. For the adsorption of solutions on hydroxylated, nonporous and large-pore SiO_2 samples, the proposed theoretical method for calculating the adsorption equilibrium of solutions gave results in agreement with experimental data.

V. Kiselev, Ganichenko, and co-workers (*313, 314*) investigated the adsorption of different substances from solutions on the surface of silicas with different degrees of hydroxylation. They studied adsorption of phenol from heptane solutions and the adsorption of aliphatic alcohols from solutions of CCl_4. The extent of the hydroxylation has a marked effect on the magnitude of the maximum absorption. This effect was especially noticeable in the adsorption of methanol. The maximum adsorption decreases with an increase in the calcination temperature of SiO_2.

Nikitin, Khokhlova, Voroshilova and co-workers (Moscow State University) (*119, 264*) studied the use of macroporous silica for adsorption from aqueous solutions, chromatographic retention, and covalent immobilization of biopolymers. The porous structures of SiO_2 were examined, including the surface chemistry of silica and the chemical nature of the biopolymers under the conditions necessary for the adsorption–desorption and gel chromatography of macromolecules. The effect of dehydroxylation and chemical modification of silica with organic and inorganic substances on the adsorption of proteins and some other problems were also studied. By using various proteins (urease, ferritin, hemoglobin, and others), they carried out an investigation to ascertain how the amount of covalently bound proteins depends on the geometric parameters of silica gels, with the hydrodynamic radii of the proteins taken into account.

Zuevsky, Kulaev, and co-workers (Physico-Chemical Medicine Research Institute of RSFSR Public Health Ministry, Moscow) (*315, 316*) carried out an investigation of specific silica hemosorbents for the treatment of blood. Such silica hemosorbents are capable of adsorbing cholesterol from the blood. Macroporous silicas were used for this purpose (*26, 27*). Their surface is accessible to proteins with a molecular mass up to 70,000 daltons. These adsorbents proved more effective than carbon hemosorbents.

Ion Exchange

Strazhesko, Vysotskii, Kirichenko, and co-workers (Kiev State University; Institute of Physical Chemistry, the Ukrainian S.S.R. Academy of Sciences, Kiev) (*49–55*) investigated the mechanism of ion exchange of Na+, Cs+,

Ca^{2+}, Sr^{2+}, Ba^{2+}, and other ions on silica surfaces. Changes in the magnitude of pK_a on the silica surface were determined as a function of surface neutralization. By using the method of ion-exchange sorption of rubidium ions on silica gels, it was found that the isoelectric point lay at pH ~1.5. On the basis of these investigations, methods for synthesizing highly selective sorbents and ion exchangers were developed.

Strelko, Kartel, and co-workers (Institute of General and Inorganic Chemistry, the Ukrainian S.S.R. Academy of Sciences, Kiev) investigated cation exchange on dispersed silicas (*71, 72*). Such a sorption takes place not only at pH > 9 but also in neutral and even acidic solutions.

Using the numerical experimental method, Ulberg and Churaev (Institute of Physical Chemistry, the U.S.S.R. Academy of Sciences, Moscow) (*317*) calculated the adsorption energy of ions on the molecularly smooth surface of fused quartz. For ions to be adsorbed, the presence of charged centers is essential. In the case of quartz for a silica–electrolyte system, the ionized OH groups (or the $\equiv SiO^-$ groups) with a negative charge act as such centers. The calculations were based on a model for the localized adsorption of hydrogen ions and electrolyte cations on the same charged centers. The experimental values of the cation and hydrogen ion adsorption potential accorded well with the theoretical values that took into account coulombic and other forces.

Bartenev (Institute of Physical Chemistry, the U.S.S.R. Academy of Sciences, Moscow) (*318*) carried out a systematic investigation of the relaxation and destruction processes in vitreous quartz. The rupture energy of the Si–O bond is less for alkalisilicate glasses than for vitreous quartz. Also, the strength of the Si–O bond is reduced under the influence of hydroxyl groups in the glass.

Action of Ionizing Radiation and Mechanical Activation

The effect of different types of ionizing radiation and mechanical activation on silicas was investigated by Krylova and Dolin (Institute of Electrochemistry, the U.S.S.R. Academy of Sciences, Moscow) (*319, 320*); Strelko et al. (Institute of Physical Chemistry, the Ukrainian S.S.R. Academy of Sciences, Kiev) (*321*); V. Kiselev and co-workers (Moscow State University) (*322, 323*); Garibov, Gezalov, and co-workers (Institute of Chemistry, Azerbaijan S.S.R. Academy of Sciences, Baku) (*324, 355*); Pshezhetskii, Kotov, and co-workers (Physico-Chemical Institute, Moscow) (*198, 199*); Kazansky, Pariisky, and co-workers (Institute of Organic Chemistry, the U.S.S.R. Academy of Sciences, Moscow) (*326–328*); Ermatov and co-workers (Institute of Nuclear Physics, the Kazakh S.S.R. Academy of Sciences, Alma-Ata) (*329–331*); Voevodsky (Institute of Chemical Physics, Siberian Division of the U.S.S.R. Academy of Sciences, Novosibirsk) (*332*); Krylov, Butyagin, Radtsig, and co-workers (Institute of

Chemical Physics, the U.S.S.R. Academy of Sciences, Moscow) (*193–197, 323, 333*); Khrustalev, Zhuravlev, and co-workers (Institute of Physical Chemistry, the U.S.S.R. Academy of Sciences, Moscow) (*208*); Boldyrev (Institute of Catalysis, Siberian Division of the U.S.S.R. Academy of Sciences, Novosibirsk) (*334*); Spitsyn, Pirogova, Ryabov, and co-workers (Institute of Physical Chemistry, the U.S.S.R. Academy of Sciences, Moscow) (*335–338*); Klevikov, Fenelonov, and co-workers (Institute of Catalysis, Siberian Division of the U.S.S.R. Academy of Sciences, Novosibirsk) (*339*); and others.

Krylova and Dolin (*319, 320*) investigated the radiolysis of water adsorbed on silica gel induced by γ-radiation (^{60}Co). The radiolysis products, H_2 and CO_2, formed as a result of the energy transfer from the solid adsorbent silica gel to the molecules of the adsorbed water. The oxidation component of radiolysis is spent on the oxidation of trace amounts of organic compounds present on the sample surface; carbon dioxide results. Radiolysis was investigated in relation to the conditions of the preliminary treatment of SiO_2, the amount of adsorbed water, and the intensity of the radiation. The formation of hydrogen from the surface OH groups of silica gel was also possible. A likely mechanism of radiolysis was described.

Tagieva and V. Kiselev (*322*) showed that when quartz and silica were exposed to γ-radiation (^{60}Co source), a strong dehydroxylation of the surface occurred. The adsorption of water vapor by SiO_2 following such an exposure decreased sharply.

Butyagin (*193*) and Radtsig and co-workers (*194–197*) investigated the tribochemical process leading to the formation of different types of structural defects on the silica surface (quartz glass and aerosil). The homolytic breaking of the siloxane bonds is the primary act of mechanical activation. In addition to the paramagnetic centers $\equiv Si\bullet$ and $\equiv SiO\bullet$ described earlier (*193, 340*), Ratsig and co-workers identified radicals of the type

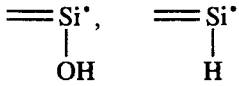

(paramagnetic centers), as well as the sililene (=Si:), silanone (=Si=O), and siladioxyrane

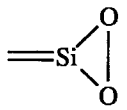

groups (dimagnetic centers). When the samples were heated in vacuo or in an inert atmosphere, the concentration of the defects decreased and the siloxane bonds were restored. Determinations were made of the conditions for stabilization of the defects and the nature of their transformations. The reactivity of the defects toward different substances in the gas phase was examined for O_2, CO, CO_2, N_2O, H_2, and others. The experimental results (obtained by the EPR spectroscopic method and infrared spectroscopic method) and theoretical calculations made it possible to determine the geometrical and electronic characteristics of different types of silica defects in the ground state and in the excited state and also to make thermochemical calculations for a number of processes.

V. Kiselev, Krasilnikov, and co-workers investigated the physicochemical properties of silica, including tribochemical coercion (*164–166, 187, 341–343*). They found (*344*) that during the dry grinding of crystalline and amorphous silicas, fine particles became aggregated and the aggregated particles had an ultraporous structure. When grinding was carried out in water, no aggregation took place. The presence of an amorphous layer on the surface of the quartz was established by the differential thermal analysis (DTA) method. The same effects were observed earlier by Khodakov, Rebinder, and co-workers (*345–347*).

Khrustalev, Zhuravlev, and co-workers (*208*) investigated the evolution of molecular hydrogen and CO_2 from mechanically activated silica (both crystalline and fused quartz). With the cleaving or scratching of the platelike samples, there was a reproducible effect of H_2 evolution. As shown earlier by Derjaguin, Krotova, Karasev and co-workers (*348, 349*), from a freshly formed solid surface mechanoelectrons having an energy up to 100 keV, which have a radiochemical effect, are emitted. Experiments were carried out (*208*) in which samples are subjected to preliminary thermal treatment in vacuo (from room temperature to ~200 °C). Thus (*4, 5*), the formation of gaseous H_2 is a result of the dissociative ionization by mechanoelectrons of the residual adsorbed water molecules and silanol groups on the silica surface that involve the breaking of the H–O bond. Such a surface mechanism of hydrogen evolution in the mechanical activation of silica is apparently predominant, as compared to hydrogen evolution from the bulk of a silica sample (from fine pores, inclusions, etc.).

Silica Coatings

Pashchenko, Voronkov, Svidersky, and co-workers (Polytechnical Institute, Kiev; Institute of Organic Chemistry, Siberian Division of the U.S.S.R. Academy of Sciences, Irkutsk (*350–352*) investigated silicon-organic coatings. New types of coatings were developed. The coatings consist of bilayered silicon–organic coatings based on the hydrolysis products of tetraethoxysilane and polyorganohydridesiloxane (*352*). The

product of hydrolysis of $Si(OC_2H_5)_4$, silicic acid, is strongly adsorbed on the surface of many different materials and interacts with organosilicon compounds containing ≡Si–OH, ≡Si–H, and other groups. The silica surface, which is the substrate, and the hydrophobic layer become chemically bound and form a hydrophobic film. The effect of seawater, organic solvents, and the adhesion of ice on such coatings, as well as thermal and biological stability, were investigated (*352*).

Properties of Water in Dispersed Silica

Derjaguin, Churaev, Zorin, Muller, Sobolev, and co-workers (Institute of Physical Chemistry, the U.S.S.R. Academy of Sciences, Moscow) (*33, 353–359*) investigated the properties of water in dispersed media and porous bodies, including silica systems. The physicochemical and mechanical properties of dispersed systems depend on the properties of the water present in them. The kinetics of mass-exchange processes is determined by the mobility and energy of the boundary between water and the solid phase. The authors studied the properties of thin layers of water in quartz capillaries (*354*) and fine-porous glasses (*355*). A quantitative investigation was made of the effect of water slipping in micrometer-size quartz capillaries with a smooth surface that was made hydrophobic by methylation.

Within the layers limited by hydrophobic walls, the water molecule dipoles are oriented parallel to the surface. The effect of ordered orientation spreads to a considerable distance; that is, it is of a long-range nature. Such an orientation of water molecules causes a decrease in density near the walls and an increase in the mobility of the molecules in the tangential direction. This situation is interpreted as a decrease in the viscosity of the boundary layers. From a macroscopic point of view, this effect can manifest itself as the slipping of water on the hydrophobic substrate.

In layers bound by the hydrophilic surfaces, the situation changes. Near such a surface, the water dipoles are oriented normal to the surface. This geometry results in an increase in the density of water and a decrease in the tangential mobility of water molecules within layers that are several nanometers thick. From a macroscopic point of view, there should be an increase in the viscosity of the boundary layers of water. With a decrease in the radius of the quartz hydrophilic capillary, the average viscosity of water increases.

Churaev, Zorin, Novikova, and co-workers (*356, 357*) investigated the evaporation of liquids from quartz capillaries ($0.05\ \mu m \leq R \leq 2\ \mu m$; R is the capillary radius), including the problem of the stability of metastable films on the SiO_2 surface. They also determined the critical pressure at which such films lose their stability, as well as the effect of the hydrophilic

nature (the presence of OH groups) of the quartz surface on the film flow. For a hydrophilic surface, there is some increase in the rate of evaporation of water, whereas a hydrophobic surface causes a decrease in the evaporation rate from the capillaries.

Sobolev, Churaev, and co-workers (*358*) studied the effect of the composition of aqueous electrolyte solutions (KOH, KCl, $BaCl_2$, and others) on the potential and the surface charge of fused quartz. The Shtern potential, ψ, and the charge, σ, of the molecularly smooth virgin surface were determined for solutions of different concentrations and at different pH values.

Gribanova, Chernoberezhsky, Friedrichsberg, and co-workers (Leningrad State University) (*360–363*) investigated the aggregative stability and electrical conductivity of quartz suspensions in aqueous electrolyte solutions, the dependence of contact angles on quartz and silica glass surfaces on the pH value of solutions, and so forth.

Rebinder (Institute of Physical Chemistry, the U.S.S.R. Academy of Sciences, Moscow) (*364*) examined how the water layer is bound to the dispersed materials in the course of drying. The isothermic free energy (or characteristic binding strength of water on the surface) of the free water equals zero:

$$-\Delta F = A = RT \ln (p_o/p) \qquad (\text{at } p = p_o)$$

R is the gas constant, and T is the temperature. In the region of physical adsorbed water, the magnitude of A increases continuously. In chemically bound water (OH groups for SiO_2), A will increase abruptly. Such a leapwise increase in A was predicted by Rebinder (*364*) and experimentally confirmed by Zhuravlev (*5*).

Theoretical Investigations

A. Kiselev, Avgul, Poshkus, and co-workers (Moscow State University) (*17, 20–22, 288, 365, 366*) carried out a theoretical investigation of the thermodynamics of adsorption processes. This work for the first time combined into one thermodynamic analysis the adsorption studies of vapors, gases, pure liquids, and solutions on the surface of solids (including SiO_2) and liquids. A. Kiselev, Poshkus, Lopatkin, and co-workers (*17, 288, 267–370*) developed a molecular-statistical theory of adsorption. A. Kiselev, Lopatkin, Bezus, Pham, and co-workers performed molecular-statistical calculations for gas adsorption on silicalite (*367, 368*) and zeolites (*369, 371, 372*). Berezin, A. Kiselev, and co-workers did a thermodynamic analysis of mono- and polymolecular layers on silica surfaces and developed a thermodynamic theory of phase transition of the adsorbate (*231–233*). A theory of intermolecular interaction on the surface

of solids was developed by A. Kiselev and co-workers (*17, 20–22, 288, 365*). Using the quasichemical equilibrium method, A. Kiselev developed a general equation for the adsorption isotherm that takes into account the adsorbate–adsorbent and adsorbate–adsorbate interactions. This equation provides a satisfactory description of all known cases of adsorption on adsorbents with a uniform surface (*17, 288, 365*).

Il'in (Moscow State University) (*373*) investigated the nature of the adsorption interactions on the assumption that the adsorbate molecule has a dipole structure and an electrical field is present owing to the charged surface of the adsorbent.

Poshkus (Institute of Physical Chemistry, the U.S.S.R. Academy of Sciences, Moscow) (*374*) calculated the energy of interaction between the hydroxyl groups of silica and the benzene molecule. The main contribution to the intermolecular interaction between the benzene molecule (locally concentrated electron density due to π-electrons on the periphery of the benzene ring) and the hydroxyl group (two-point model with dipole moment $\mu = 1.6$ D) in the case where the OH group was in a perpendicular direction with respect to the plane of the ring comes from coulomb attraction. Other types of interactions were also considered (induction, dispersion, and repulsion).

Babkin and A. Kiselev (Moscow State University) (*375*) calculated the dispersion component of the adsorption potential for molecules of benzene and *n*-hexane for a model of chemically modified ($ClSi(CH_3)_3$) silica. The model consisted of two parts: the silica skeleton and a modifying layer of trimethylsilyl groups. The energy of interaction of the molecules with the adsorbent consists of the energy of interaction with the silica lattice and the energy of interaction with the modifying layer.

Voronkov, Klyuchnikov, and co-workers (Institute of Organic Chemistry, Siberian Division of the U.S.S.R. Academy of Sciences, Irkutsk) (*376, 377*) developed a precise method of combusting organosilicon compounds in a calorimetric bomb to prepare hydrated amorphous silica and measure its standard heat of formation. For samples of SiO_2 that had specific surface areas varied from 140 to 300 m^2/g, the heat of formation was

$$\Delta H^\circ_{f,298.15}SiO_2 = (-0.1681125S - 888.96) \text{ kJ/mol}$$

Lygin and co-workers (Moscow State University) (*378–381*) used the methods of quantum chemistry in calculating cluster models of the surface structure of silica. The selection of cluster models was based on experimental infrared spectral data. Quantum chemical calculations were made of models describing the defects of the dehydroxylated silica surface that had been thermally treated. Calculations were carried out on models describing the surface structures of water molecules interacting with silanol groups on the silica surface.

Dyatkina, Shchegolev, and co-workers (Institute of General and Inorganic Chemistry, the U.S.S.R. Academy of Sciences, Moscow) (*382, 383*) carried out quantum chemical calculations by using the method of molecular orbits, and they analyzed the peculiarities of the electronic structure of the oxyanion SiO_4^{4-}, $Si(OH)_4$, and the fragment [Si–O–Si]. The results of the calculations were used in interpreting the X-ray spectra of amorphous silica, quartz, and stishovite on the basis of the covalent model of their structure. Calculations for the [Si–O–Si] fragment showed the possible angular mobility of this fragment (from 100° to 180°) to be due to the redistribution of electron density. An analysis of the effective charges on Si and O atoms pointed to the covalent nature of the Si–O bond.

Dikov, Dolin, and co-workers (Institute of Geology of Ore Deposits, Petrography, Mineralogy, and Geochemistry, the U.S.S.R. Academy of Sciences, Moscow) (*384*) carried out an X-ray analysis of the valence bands of the main silicate-forming elements for the most widely distributed types of silicate structures. The experimental data were interpreted on the basis of a structural analysis and with the aid of quantum chemical conceptions within the framework of the theory of molecular orbitals. In silicates, distortions of the silicon–oxygen tetrahedron were present. This distortion was manifested in changes in the Si–O distances and the O–Si–O and Si–O–Si angles.

Grivtsov, Zhuravlev, and co-workers (Institute of Physical Chemistry, the U.S.S.R. Academy of Sciences, Moscow) (*385, 386*) resorted to numerical modeling of molecular dynamics in investigating problems of water adsorption by the hydroxylated surface of the face (0001) in β-tridymite. β-tridymite was chosen as a model form of silica because such a crystalline modification is close in density to that of amorphous silica. The boundary layer in SiO_2 was considered when each surface Si atom held one OH group. The rotational mobility of the hydroxyl groups is an important factor in the adsorption of water.

The development of the theory of surface forces by Derjaguin, Churaev, and Muller (*353*) made it possible to carry out quantitative estimations of wetting in relation to the properties of the solid support (hydrophilic or hydrophobic surface of SiO_2, in particular) as well as of the effect of the interaction between the wetting substances and the surface.

Rusanov and co-workers (Leningrad State University) (*387, 388*) gave a thermodynamic description of adsorption phenomena for a multicomponent system.

Tovbin (Physico-Chemical Institute, Moscow) (*389*) gave a theoretical description of the physicochemical processes taking place at the atomic–molecular level on the surface at the gas–solid interface.

Pryanishnikov (State Research Institute of Glass, Moscow) (*390*) carried out a theoretical analysis of the silica structure and analyzed the

experimental data on the structure and properties of various modifications of silica.

Romankov, Lepilin, and co-workers (*391, 392*) investigated adsorption dynamics and developed a general equation describing such a process.

Natural Mineral Sorbents

Aripov and Agzamkhodzhaev (Institute of Chemistry, the Uzbek S.S.R. Academy of Sciences, Tashkent) (*393, 394*); Ovcharenko and Tarasevich (Institute of Colloid Chemistry and the Chemistry of Water, the Ukrainian S.S.R. Academy of Sciences, Kiev) (*395, 396*); Bykov and co-workers (Far-East State University, Vladivostok) (*397, 398*); Gryazev and co-workers (State University, Saratov) (*399, 400*); Komarov (Institute of General and Inorganic Chemistry, the Byelorussian S.S.R. Academy of Sciences, Minsk) (*401, 402*); Tsitsishvili and co-workers (Institute of Physical and Organic Chemistry, the Georgian S.S.R. Academy of Sciences, Tbilisi) (*403, 404*); Kerdivarenko, Russu, and co-workers (Chemical Institute, the Moldavian Academy of Sciences, Kishinev) (*405, 406*); and others investigated natural mineral sorbents that are high in silica content.

References

1. Iler, R. K. *The Chemistry of Silica: Solubility, Polymerization, Colloid and Surface Properties and Biochemistry;* Wiley: New York, 1979.
2. Kiselev, A. V.; Yashin Ya. I. *Gas-Adsorption Chromatography* (transl. from Russian; Plenum Press: New York, 1969.
3. Kiselev, A. V.; Lygin, V. I. *Infrared Spectra of Surface Compounds* (transl. from Russian); Wiley: New York, 1975.
4. Zhuravlev, L. T. *Langmuir* **1987,** *3,* 316.
5. Zhuravlev, L. T. *Pure Appl. Chem.* **1989,** *61,* 1969.
6. Dubinin, M. M. In *Main Problems of Physical Adsorption Theory;* Dubinin, M. M.; Serpinskii, V. V., Eds.; Nauka: Moscow, **1970;** p 251.
7. Bering, B. P.; Dubinin, M. M.; Serpinsky, V. V. *J. Colloid Interface Sci.* **1966,** *21,* 378.
8. Voloshchuk, A. M.; Dubinin, M. M.; Zolotarev, P. P. In *Adsorption and Porosity;* Dubinin, M. M.; Serpinskii, V. V., Eds.; Nauka: Moscow, 1976; p 285.
9. Dubinin, M. M.; Polstyanov, E. F. *Zh. Fiz. Khim.* **1966,** *40,* 1169.
10. Dubinin, M. M.; Bering, B. P.; Serpinskii, V. V. In *Recent Progress in Surface Science;* Danielli, J. F.; Pankhurst, K. G. A.; Riddeford, A. C., Eds.; Academic: New York, 1964; p 42.
11. Dubinin, M. M. *Zh. Fiz. Khim.* **1987,** *61,* 1301.
12. Kiselev, A. V. In *Surface Chemical Compounds and Their Role in Adsorption Phenomena;* Kiselev, A. V., Ed.; MGU Press: Moscow, 1957; p 90.
13. Belyakova, L. D.; Kiselev, A. V. *Dokl. Akad. Nauk SSSR* **1958,** *119,* 298.
14. Karnaukhov, A. P.; Kiselev, A. V. *Zh. Fiz. Khim.* **1960,** *34,* 2146.
15. Dzhigit, O. M.; Kiselev, A. V.; Muttik, G. G. *Kolloidn. Zh.* **1961,** *23,* 553.
16. Kiselev, A. V.; Petrova, R. S.; Shcherbakova, K. D. *Kinet. Katal.* **1964,** *5,* 526.

17. Kiselev, A. V. *Intermolecular Interactions in Adsorption and Chromatography*; Vysshaya Shkola: Moscow, 1986.
18. Kiselev, A. V. et al. *Experimental Methods in Adsorption and Molecular Chromatography*; Kiselev, A. V.; Dreving, V. P., Eds.; MGU Press: Moscow, 1973.
19. Kiselev, A. V. *Proc First All-Union Conf. Gas Chromatogr.*; Acad. Sci. Publishers: Moscow, 1960; p 45.
20. Kiselev, A. V. *Zh. Fiz. Khim.* **1961**, *35*, 233.
21. Kiselev, A. V. *Zh. Fiz. Khim.* **1964**, *38*, 2753.
22. Kiselev, A. V. *Discuss Faraday Soc., Intermolecular Forces* **1965**, *40*, 205.
23. Kiselev, A. V. Proc. Third All-Union Conf. Gas Chromatogr.; DF OKBA: Dzerzhinsk, 1966; p 15.
24. Kiselev, A. V. *Zh. Fiz. Khim.* **1967**, *41*, 2470.
25. Kiselev, A. V. *J. Chromatogr.* **1970**, *49*, 84.
26. Kiselev, A. V.; Kustova, G. L.; Lipkind, B. A.; Nikitin, Yu. S. U.S. Patent 3,888,972, 1975.
27. Bebris, N. K.; Kiselev, A. V.; Nikitin, Yu. S.; Yashin, Ya. I. U.S. Patent 3,869,409, 1975.
28. Neimark, I. E. In *Preparation, Structure and Characteristics of Sorbents*; Goskhimizdat: Leningrad, 1959; p 112.
29. Neimark, I. E.; Sheinfain, R. Yu. *Silica Gel, Its Preparation, Characteristics and Application*; Naukova Dumka: Kiev, 1973.
30. Sheinfain, R. Yu; Neimark, I. E. *Kinet. Kataliz* **1970**, *8*, 433.
31. Neimark, I. E.; Slinyakova, I. B. *Kolloidn. Zhur.* **1956**, *18*, 219.
32. Neimark, I. E. In *Adsorption and Porosity*; Dubinin, M. M.; Serpinsky, V. V., Eds.; Nauka: Moscow, 1976; p 57.
33. Nikologorskaya, E. A.; Kasaikin, V. A.; Churaev, N. V. *Kolloidn. Zhur.* **1990**, *52*, 489.
34. Deryagin, V. B. *Trans. Faraday Soc.* **1940**, *36*, 203.
35. Deryagin, B. V.; Landau, L. D. *Acta Physicochim. USSR* **1941**, *14*, 633.
36. Deryagin, B. V. *Theory of Colloid Stability and Thin Films*; Nauka: Moscow, 1986.
37. Frolov, Yu. G.; Shabanova, N. A. *Langmuir* **1987**, *3*, 640.
38. Frolov, Yu. G.; Shabanova, N. A.; Savochkina, T. V. *Kolloidn. Zhur.* **1980**, *42*, 1015.
39. Shabanova, N. A.; Frolov, Yu. G. *Izv. Vuzov. Khimiya i Khimich Tekhnologiya* **1985**, *28*, 1.
40. Frolov, Yu. G.; Grodsky, A. S.; Kleschevnikova, S. I.; Pashchenko, L. A.; Rastegina, L. L. In *Preparation and Application of Silica Hydrosols*; Frolov, Yu. G., Ed.; Proceed. of Mendeleev Chemico-Technological Institute: Moscow, 1979; Issue 107, p 31.
41. Frolov, Yu. G.; Khorkin, A. A.; Lebedev, E. N.; Shabanova, N. A.; Kuzmin, M. P.; Reshetnikova, L. V.; Khon, V. N. In *Preparation and Application of Silica Hydrosols*; Frolov, Yu. G., Ed.; Proceed. of Mendeleev Chemico-Technological Institute: Moscow, 1979; Issue 107, p 21.
42. Kontorovich, S. I.; Kononenko, V. G.; Shchukin, E. D. In *Preparation and Application of Silica Hydrosols*; Frolov, Yu. G., Ed.; Moscow, 1979; Issue 107, p 58.
43. Kontorovich, S. I.; Lavrova, K. A.; Plavnik, G. M.; Shchukin, E. D.; Rebinder, P. A. *Dokl. Akad. Nauk USSR* **1971**, *196*, 633.
44. Kontorovich, S. I.; Lavrova, K. A.; Kononenko, V. G.; Shchukin, E. D. *Kolloidn. Zhur.* **1973**, *35*, 1062.

45. Kontorovich, S. I.; Lankin, Ya. I.; Aleshinsky, V. V.; Amelina, E. A.; Shchukin, E. D. *Kolloidn. Zhur.* **1980,** *42,* 639.
46. Yaminsky, V. V.; Pchelin, V. A.; Amelina, E. A.; Shchukin, E. D. *Coagulative Contacts in Dispersed Systems*; Khimiya: Moscow, 1982.
47. Kontorovich, S. I.; Ponomareva, T. P.; Sokolova, L. N.; Sokolova, N. P.; Kochetkova, E. I.; Shchukin, E. D. *Kolloidn. Zhur.* **1988,** *50,* 1100.
48. Rebinder, P. A. *Surface Phenomena in Dispersed Systems: Colloidal Chemistry, Selected Works*; Moscow, 1978.
49. Belyakov, V. N.; Soltievsky, N. M.; Strazhesko, D. N.; Strelko, V. V. *Ukrain. Khimich. Zhur.* **1974,** *40,* 236.
50. Strazhesko, D. N.; Yankovskaya, G. F. *Ukrain. Khimich. Zhur.* **1959,** *25,* 471.
51. Strazhesko, D. N.; Strelko, V. V.; Belyakov, V. N.; Rubanik, S. C. *J. Chromatogr.* **1974,** *102,* 191.
52. Vysotskii, Z. Z.; Strazhesko, D. N. In *Adsorption and Adsorbents*; Strazhesko, D. N., Ed.; Wiley: New York, 1974; p 55.
53. Vysotskii, Z. Z.; Strazhesko, D. N. In *Adsorption and Adsorbents*. Strazhesko, D. N., Eds.; Wiley: New York, 1973; Vol. 1, p 63.
54. Kirichenko, L. F.; Vysotskii, Z. Z. *Dokl. Akad. Nauk USSR* **1967,** *175,* 635.
55. Klimentova, V. P.; Kirichenko, L. F.; Vysotskii, Z. Z. In *Research in Surface Forces*; Deryagin, B. V., Ed.; Consult. Bureau: New York, 1975; Vol. 4, p 77.
56. Chertov, V. M.; Dzhambaeva, D. V.; Plachinda, A. S.; Neimark, I. E. *Dokl. Akad. Nauk USSR* **1965,** *161,* 1149.
57. Chertov, V. M.; Dzhambaeva, D. B.; Neimark, I. E. *Kolloidn. Zhur.* **1965,** *27,* 279.
58. Chertov, V. M.; Neimark, I. E. *Ukrain. Khimich. Zhur.* **1969,** *35,* 499.
59. Kolosentsev, S. D.; Belotserkovsky, G. M. In *Preparation and Application of Silica Hydrosols*; Frolov, Yu. G., Ed.; Proceed. of Mendeleev Chemico-Technological Institute: Moscow, 1979; Issue 107, p 44.
60. Kolosentsev, S. D.; Belotserkovsky, G. M.; Plachenov, T. G. In *Preparation, Structure and Characteristics of Sorbents*; Plachenov, T.G.; Aleksandrov, N. S. Eds.; Proceed. of Leningrad Technological Institute: Leningrad, 1971; Issue 1, p 32.
61. Kolosentsev, S. D.; Belotserkovsky, G. M.; Plachenov, T. G. *Zhur. Prikl. Khim.* **1975,** *48,* 252.
62. Dobruskin, V. Kh.; Belotserkovsky, G. M.; Karelskaya, V. F.; Plachenov, T. G. *Zhur. Prikl. Khim.* **1967,** *40,* 2443.
63. Belotserkovsky, G. M.; Novgorodov, V. N.; Dobruskin, V. Kh.; Plachenov, T. G. *Zhur. Prikl. Khim.* **1969,** *42,* 2749.
64. Belotserkovsky, G. M.; Kolosentsev, S. D. *Preparation of Silica Gel*; Technological Institute: Leningrad, 1975.
65. Kazantseva, L. K.; Kalinin, D. V.; Deniskina, N. D. In *Physico-Chemical Investigations of Sulphuric and Silicate Systems*; Institute of Geology and Geophysics, Siberian Division of the USSR Academy of Sciences: Novosibirsk, 1984; p 59.
66. Ryabenko, E. A.; Kuznetsov, A. I.; Shalumov, B. Z.; Loginov, A. F.; D'yakova, V. V. In *Preparation and Application of Silica Hydrosols*; Frolov, Yu. G., Ed.; Proceed. of Mendeleev Chemico-Technological Institute: Moscow, 1979; Issue 107, p 39.
67. Verwey, E. J. W.; Overbeek, J. Th. *G. Theory of Stability of Lyophobic Colloids*; Elsevier: Amsterdam, 1948.
68. Bird, P. G. U.S. Patent 2,244,325, 1941.
69. Bechtold, M. F.; Snyder, O. E. U.S. Patent 2,574,902, 1951.

70. Lipkind, B. A.; Drozhzhennikov, S. V.; Burylov, V. A.; Tezikov, I. I. In *Preparation and Application of Silica Hydrosols*; Frolov, Yu. G., Ed.; Proceed. of Mendeleev Chemico-Technological Institute: Moscow, 1979; Issue 107, p 26.
71. Laskorin, B. N.; Strelko, V. V.; Strazhesko, D. N.; Denisov, V. I. *Sorbents on Basis of Silica Gels in Radiochemistry*; Atomizdat: Moscow, 1977.
72. Strelko, V. V.; Shvets, D. A.; Kartel, N. T.; Suprunenko, K. A.; Doroshenko, V. I.; Kabakchi, A. M. *Radiation-Chemical Processes in Heterogeneous Systems on Basis of Dispersed Oxides*; Energoizdat: Moscow, 1981.
73. Strelko, V. V. *Adsorption and Adsorbents* **1974,** Kiev: No. 2, p 65.
74. Kiselev, A. V.; Nikitin, Yu. S. In *Modern Problems of Physical Chemistry*; Gerasimov, Ya. I.; Akishin, P. A., Eds.; MGU Press: Moscow, 1968; Vol. 3, p 195.
75. Kiselev, A. V.; Nikitin, Yu. S. In *Chromatography (Itogi nauki i tekhniki)*; VINITI: Moscow, 1978; Vol 2, p 5.
76. Kiselev, A. V.; Nikitin, Yu. S.; Oganesyan, E. B. *Kolloidn. Zhur.* **1969,** *31*, 525.
77. Gorelik, R. L.; Davydov, V. Ya.; Zhuravlev, L. T.; Curthoys, G.; Kiselev, A. V.; Nikitin, Yu. S. *Kolloidn. Zhur.* **1973,** *35*, 456.
78. Bebris, N. K.; Bruk, A. I.; Vyakhirev, D. A.; Kiselev, A. V.; Nikitin, Yu. S. *Kolloidn, Zhur. 1972, 34*, 491.
79. Kiselev, A. V.; Nikitin, Yu. S.; Oganesyan, E. B. *Kolloidn. Zhur.* **1967,** *29*, 95.
80. Gorelik, R. L.; Zhuravlev, L. T.; Kiselev, A. V.; Nikitin, Yu. S.; Oganesyan, E. B.; Shengeliya, K. Ya. *Kolloidn. Zhur.* **1971,** *33*, 51.
81. Kiselev, A. V.; Nikitin, Yu. S.; Oganesyan, E. B. *Kolloidn. Zhur.* **1978,** *40*, 37.
82. Simonova, L. G.; Fenelonov, V. B.; Dzisko, V. A.; Kryukova, G. N.; Shmachkova, V. P. *Kinet. Kataliz* **1982,** *23*, 138.
83. Fenelonov, V. B.; Simonova, L. G.; Gavrilov, V. Yu.; Dzisko, V. A. *Kinet. Kataliz* **1982,** *23*, 44.
84. Zhdanov, S. P. In *Surface Chemical Compounds and Their Role in Adsorption Phenomena*; Kiselev, A. V., Eds.; MGU Press: Moscow, 1957; p 129.
85. Zhdanov, S. P. *Summary of Dissertation.* Leningrad, Institute of Silicate Chemistry, the USSR Academy of Sciences, 1952.
86. Zhdanov, S. P.; Koromaldi, E. V. *Izv. Akad. Nauk USSR, Ser. Khim.* **1959,** *4*, 626.
87. Zhdanov, S. P. *Zhur. Vsesoyuzn. Khimich. Obshchestva im. Mendeleeva* **1989,** *34*, 298.
88. Chuiko, A. A. *Teoret. Experim. Khimiya* **1987,** *23*, 597.
89. Grebenshchikov, I. V.; Favorskaya, T. C. *Proceed. of State Optical Institute Leningrad* **1931,** *7*, Issue 72, 1.
90. Grebenshchikov, I. V.; Molchanova, O. S. *Zhur. Obshchey Khim.* **1942,** *12*, 588.
91. Kolikov, V. M.; Mchedlishvili, B. V. In *Chromatography of Biopolymers on Macroporous Silica*; Nauka: Leningrad, 1986; p 189.
92. Ragulin, G. K.; Aleksandrova, N. E.; Dobychin, D. P. *Zhur. Neorganich. Khim.* **1976,** *21*, 2724.
93. Aleksandrova, N. E.; Ragulin, G. K.; Burkat, T. M.; Dobychin, D. P.; Zinyakov, V. M.; Krasii, B. V. In *Investigation of Adsorption Processes and Adsorbents*; Dubinin, M. M., Ed.; Fan: Tashkent, 1979; p 112.
94. Plachenov, T. F.; Filyanskaya, E. D. *Izv. Vuzov USSR* **1958,** *1*, 78.
95. Plachenov, T. G.; Belotserkovsky, G. M.; Karelskaya, V. F. In *Natural Mineral Sorbents*; The Ukrainian SSR Academy of Sci. Publishers: Kiev, 1960; p 43.

96. Plachenov, T. F. In *Main Problems of Physical Adsorption Theory*; Dubinin, M. M.; Serpinskii, V. V., Eds.; Nauka: Moscow, 1970; p 312.
97. Plachenov, T. G. In *Adsorption and Porosity*; Dubinin, M. M.; Serpinskii, V. V., Eds.; Nauka: Moscow, 1976; p 191.
98. Barvinok, G. M.; Sychev, M. M.; Kondratenko, N. E. *Zhur. Prikl. Khim.* **1989**, *4*, 721.
99. Komarov, V. S.; Kuznetsova, T. F. *Vestnik Akad. Nauk Byelorussiun SSR, Ser. Khim.* **1986**, *2*, 26.
100. Kuznetsova, T. F.; Komarov, V. S. *Vestnik Akad. Nauk Byelorussiun SSR, Ser. Khim.* **1986**, *3*, 18.
101. Kuznetsova, T. F.; Komarov, V. S.; Barkatina, E. N. *Vestnik Akad. Nauk Byelorussiun SSR, Ser. Khim.* **1986**, *5*, 24.
102. Kuznetsova, T. F.; Kryukova, E. P.; Barkatina, E. N.; Goryaeva, L. E. *Zhur. Prikl. Khim.* **1990**, *1*, 71.
103. Lipkind, B. A.; Kapatsinsky, S. V.; Kustova, G. L.; Maslova, A. A. In *Preparation, Structure and Characteristics of Sorbents*; Goskhimizdat: Leningrad, 1959; p 156.
104. Bryzgalova, N. I.; Gavrilova, T. B.; Kiselev, A. V.; Khokhlova, T. D. *Neftekhimiya* **1968**, *8*, 915.
105. Bryzgalova, N. I.; Wu Van Tyeu; Gavrilova, T. B.; Kiselev, A. V. *Neftekhimiya* **1969**, *9*, 463.
106. Bakunets, V. V.; Bryzgalova, N. I.; Gavrilova, T. B.; Kiselev, A. V.; Ter-Oganesyan, G. T. In *Analytical Applications of Chromatographic Processes*. NIFKHI Publishers: Moscow, 1976; Issue 26, p 9.
107. Vasiloy, Yu. V.; Demskaya, A. L.; Sokolova, A. P.; Khotimchenko V. S. *Chemistry and Practical Application of Silicon-Organic Compounds*. Theses of papers. Leningrad, 1989, 132.
108. Vasiloy, Yu. V.; Demskaya, A. L.; Kozlova, M. A.; Khotimchenko, V. S.; Khudobina, I. V.; Shkonda, P. A. *Chemistry and Practical Application of Silicon-Organic Compounds*. Theses of papers. Leningrad, 1989, 156.
109. Pryanishnikov, V. P.; Gusynin, V. F.; Sorokin, N. F.; Chepizhny, K. I. *Author. Certificate, Inventions and Discoveries, USSR*. No. 579246; Published in *Invent. Bulletin*, USSR, 1977, No. 41.
110. Guy, A. P.; Zhuravlev, L. T.; Osipov, A. N.; Pryanishnikov, V. P. *Second All-Union Conference on Composition Polymeric Materials*. Theses of papers. Tashkent, 1983 Part I, 90.
111. Belyakova, L. D.; Voloshchuk, A. M.; Guy, A. P.; Zhuravlev, L. T.; Pryanishnikov, V. P.; Shevchenko, T. I. *Izv. Akad. Nauk USSR, Ser. Khim.* **1988**, *4*, 731.
112. Plavnik, G. M.; Khrustaleva, G. N.; Troshkin, G. N.; Guy, A. P. *Izv. Akad. Nauk USSR, Ser. Khim.* **1990**, *5*, 978.
113. Belyakova, L. A.; Il'in, V. G. *Teoret. Experim. Khimiya* **1976**, *12*, 420.
114. Turutina, N. V.; Il'in, V. G.; Kurilenko, M. S. *Teoret. Experim. Khimiya* **1977**, *14*, 656.
115. Il'in, V. G.; Voloshinets, V. G.; Turutina, N. V.; Bobonich, F. M. *Dokl. Akad. Ukrain. Nauk Ukrain. SSR, Ser. B. Geol., Khim., Biolog. nauki*, **1988**, *2*, 43.
116. Danilov, V. V.; Blen, E. V.; Korneev, V. I.; Agafonov, G. I. *Zhur. Prikl. Khim.* **1987**, *7*, 1508.
117. Blen, E. V.; Korneev, V. I.; Danilov, V. V.; Lykov, A. D.; Agafonov, G. I. *Zhur. Prikl. Khim.* **1989**, *7*, 1471.
118. Stishov, S. M.; Popova, S. V. *Geokhimiya* **1961**, *10*, 837.

119. Khokhlova, T. D.; Nikitin, Yu. S.; Voroshilova, O. I. *Zhur. Vsesouzn, Khimich. Obshchestva im. Mendeleeva* **1989,** *34,* 363.
120. Gorelik, R. L.; Zhuravlev, L. T.; Kiselev, A. V. *Kinet. Kataliz* **1971,** *12,* 447.
121. Gorelik, R. L.; Zhdanov, S. P.; Zhuravlev, L. T.; Kiselev, A. V.; Luk'yanovich, V. M.; Nikitin, Yu. S. *Kolloidn. Zhur.* **1972,** *34,* 677.
122. Gorelik, R. L.; Zhdanov, S. P.; Zhuravlev, L. T.; Kiselev, A. V.; Luk'yanovich, V. M.; Malikova, I. Ya.; Nikitin, Yu. S.; Sheshenina, Z. E. *Kolloidn. Zhur.* **1973,** *35,* 911.
123. Burylov, V. A.; Dobruskin, V. Kh.; Belotserkovsky, G. M.; Drozhzhenikov, S. V.; Zolotov, V. T.; Kostina, N. D.; Lipkind, B. A.; Monetov, A. G.; Pishchaev, P. M.; Slepneva, A. T. *Khimich. Promyshlen. Ukrainy* **1969,** *6,* 19.
124. Nikitin, Yu. S. In *Main Problems of Physical Adsorption Theory*; Dubinin, M. M.; Serpinskii, V. V., Eds.; Nauka: Moscow, 1970; p 303.
125. Nikitin, Yu. S. *Summary of Dissertation*; Moscow State University: Moscow, 1975.
126. Lazarev, V. B.; Panasyuk, G. P.; Danchevskaya, M. N.; Budova, G. P. In *Advances in Inorganic Chemistry*; Spitsyn, V. I., Ed.; MIR Publishers: Moscow, 1983; p 196.
127. Dubinin, M. M. *J. Colloid Interface Sci.* **1967,** *23,* 487.
128. Dubinin, M. M. *J. Colloid Interface Sci.* **1974,** *46,* 351.
129. Kiselev, A. V. In *Problems of Kinetics and Catalysis*; Acad. Sci. Publishers: Moscow, 1948; Vol. 5, p 230.
130. Kiselev, A. V. *Zh. Fiz. Khim.* **1949,** *23,* 452.
131. Kiselev, A. V. *Vestn. MGU, Ser. Khim.* **1949,** *11,* 111.
132. Kiselev, A. V. In *Methods of Structure Investigation of High-Dispersed and Porous Solids*; Acad. Sci. Publishers: Moscow, 1953; p 86.
133. Dubinin, M. M.; Yakubov, T. S. *Izv. Akad. Nauk USSR, Ser. Khim.* **1977,** *10,* 2428.
134. Dubinin, M. M. *Prog. Surf. Membr. Sci.* **1975,** *9,* 1.
135. Karnaukhov, A. P.; Kiselev, A. V. *Zh. Fiz. Khim.* **1957,** *31,* 2635.
136. Karnaukhov, A. P. *Kinet. Kataliz* **1971,** *12,* 1235.
137. Karnaukhov, A. P. *Kinet. Kataliz* **1982,** *23,* 1439.
138. Karnaukhov, A. P. In *Adsorption and Porosity*; Dubinin, M. M.; Serpinsky, V. V., Eds.; Nauka: Moscow, 1976; p 7.
139. Dzisko, V. A.; Karnaukhov, A. P.; Tarasova, D. V. *Physico-Chemical Principles of Synthesis of Oxide Catalysts*; Nauka: Novosibirsk, 1978.
140. Gavrilov, V. Yu.; Karnaukhov, A. P.; Fenelonov, V. B. *Kinet. Kataliz* **1978,** *19,* 1549.
141. Aristov, B. G.; Karnaukhov, A. P.; Kiselev, A. V. *Zh. Fiz. Khim.* **1962,** *36,* 2153.
142. Aristov, B. G.; Davydov, V. Ya.; Karnaukhov, A. P.; Kiselev, A. V. *Zh. Fiz. Khim.* **1962,** *36,* 2758.
143. Zolotarev, P. P.; Zhuravlev, L. T.; Ugrozov, V. V. *Kolloidn. Z.* **1984,** *46,* 247.
144. Zolotarev, P. P.; Dubinin, M. M. *Dokl. Akad. Nauk SSSR* **1973,** *210,* 136.
145. Hofmann, U.; Endell, K.; Wilm, D. *Ang. Chem.* **1934,** *47,* 539.
146. Rideal, E. K. *Trans. Faraday Soc.* **1936,** *32,* 4.
147. Kiselev, A. V. *Kolloidn. Zhur.* **1936,** *2,* 17.
148. Yaroslavsky, N. G.; Terenin, A. N. *Dokl. Akad. Nauk USSR* **1949,** *66,* 885.
149. Kurbatov, L. N.; Neuymin, G. G. *Dokl. Akad. Nauk USSR* **1949,** *68,* 34.
150. Yaroslavsky, N. G. *Zhur. Fiz. Khim.* **1950,** *24,* 68.
151. Sidorov, A. N. *Dokl. Akad. Nauk USSR* **1954,** *95,* 1235.

152. Terenin, A. N. In *Surface Chemical Compounds and Their Role in Adsorption Phenomena*; Kiselev, A. V., Ed.; MGU Press: Moscow, 1957; p 206.
153. Nikitin, V. A.; Sidorov, A. N.; Karyakin, A. V. *Zh. Fiz. Khim.* **1956,** *30*, 117.
154. Zhdanov, S. P. *Dokl. Akad. Nauk USSR* **1949,** *68*, 99.
155. Zhdanov, S. P. In *Preparation, Structure and Characteristics of Sorbents*; Goskhimizdat: Leningrad, 1959; p 166.
156. Belyakova, L. D.; Kiselev, A. V. In *Preparation, Structure and Characteristics of Sorbents*; Goskhimizdat: Leningrad, 1959; p 180.
157. Muttik, G. G. In *Preparation, Structure and Characteristics of Sorbents*; Goskhimizdat: Leningrad, 1959; p 193.
158. Belyakova, L. D.; Dzhigit, O. M.; Kiselev, A. V.; Muttik, G. G.; Shcherbakova, K. D. *Zh. Fiz. Khim.* **1959,** *33*, 2624.
159. Zhdanov, S. P. *Zh. Fiz. Khim.* **1962,** *36*, 2098.
160. Zhdanov, S. P.; Kiselev, A. V. *Zh. Fiz. Khim.* **1957,** *31*, 2213.
161. Zhuravlev, L. T.; Kiselev, A. V. *Kolloidn. Zhur.* **1962,** *24*, 22.
162. Zhuravlev, L. T. In *Main Problems of Physical Adsorption Theory*; Dubinin, M. M.; Serpinskii, V. V., Eds.; Nauka: Moscow, 1970; p 309.
163. Zhuravlev, L. T.; Kiselev, A. V. In *Surface Area Determination*; Everett, D. H., Ed.; Butterworth: London, 1970; p 155.
164. Egorow, M. M.; Kvlividze, W. I.; Kiselev, V. F.; Krassilnikow, K. G.; Kolloid, Z. Z. *Polym.* **1966,** *B212*, 126.
165. Ignat'eva, L. A.; Kiselev, V. F.; Chukin, G. D. *Dokl. Akad. Nauk USSR* **1968,** *181*, 914.
166. Ignat'eva, L. A.; Kvlividze, V. I.; Kiselev, V. F. In *Bound Water in Dispersed Systems*; Kiselev, V. F., Kvlividze, V. I., Eds.; MGU Press: Moscow, 1970; Issue 1, p 56.
167. Gorlov, Yu. I.; Golovatyi, V. G.; Konoplya, M. M., Chuiko, A. A. *Teoret. Experim. Khimiya* **1980,** *16*, 202.
168. Galkin, G. A.; Kiselev, A. V.; Lygin, V. I. *Zhur. Fiz. Khim.* **1968,** *42*, 1470.
169. Galkin, G. A.; Kiselev, A. V.; Lygin, V. I. *Zhur. Fiz. Khim.* **1969,** *43*, 1992.
170. Galkin, G. A. *Zhur. Prikl. Spektroskop.* **1975,** *23*, 104.
171. Davydov, V. Ya.; Kiselev, A. V.; Lokutsievsky, V. A.; Lygin, V. I. *Zhur. Fiz. Khim.* **1973,** *47*, 809.
172. Arutyunyan, B. S.; Kiselev, A. V.; Titova, T. I. *Dokl. Akad. Nauk USSR* **1980,** *251*, 1148.
173. Zhdanov, S. P.; Kosheleva, L. A.; Titova, T. I. *Langmuir* **1987,** *3*, 960.
174. Kiselev, A. V.; Lygin, V. I. *Uspekhi Khimii* **1962,** *31*, 351.
175. Galkin, G. A. *Zhur. Prikl. Spektroskop.* **1976,** *24*, 53.
176. Agzamkhodzhaev, A. A.; Galkin, G. A.; Zhuravlev, L. T. In *Main Problems of Physical Adsorption Theory*; Dubinin, M. M., Serpinsky, V. V., Eds.; Nauka: Moscow; 1970; p 168.
177. Davydov, V. Ya.; Kiselev, A. V.; Lygin, V. I. *Kolloidn. Zhur.* **1963,** *25*, 152.
178. Davydov, V. Ya.; Kiselev, A. V.; Lygin, V. I. *Zh. Fiz. Khim.* **1963,** *37*, 469.
179. Davydov, V. Ya.; Kiselev, A. V. *Zh. Fiz. Khim.* **1963,** *37*, 2593.
180. Davydov, V. Ya.; Zhuravlev, L. T.; Kiselev, A. V. *Zh. Fiz. Khim.* **1964,** *38*, 2047.
181. Davydov, V. Ya.; Kiselev, A. V.; Zhuravlev, L. T. *Trans. Faraday Soc.* **1964,** *60*, 2254.
182. Volkov, A. V.; Kiselev, A. V.; Lygin, V. I.; Titova, T. I.; Shchepalin, K. L. *Kolloidn. Zhur.* **1976,** *38*, 32.
183. Kiselev, A. V.; Lygin, V. I.; Shchepalin, K. L. *Kolloidn. Zhur.* **1976,** *38*, 163.

184. Arutyunyan, B. S.; Volodin, V. Ya.; Kiselev, A. V.; Tarasov, N. N.; Titova, T. I. *Kolloidn. Zhur.* **1980,** *42,* 430.
185. Vedeneeva, N. E. In *Surface Chemical Compounds and Their Role in Adsorption Phenomena*; Kiselev, A. V., Ed.; MGU Press: Moscow, 1975; p 243.
186. Musatov, I. K. *Summary of Dissertation*; Institute of Crystallography, the USSR Academy of Sciences: Moscow, 1955.
187. Kiselev, V. F. *Surface Phenomena on Semiconductors and Dieletrics*; Nauka: Moscow, 1970.
188. Golovanova, G. F.; Ivanova, N. N.; Kvlividze, V. I.; Neimark, I. E.; Khrustaleva, S. V.; Chukin, G. D.; Sheinfain, R. Yu. *Teoret. Experim. Khimiya* **1973,** *9,* 383.
189. Chukin, G. D.; Malavich, V. I. *Zhur. Prikl. Spektroskop.* **1976,** *24,* 536.
190. Chukin, G. D.; Malavich, V. I. *Zhur. Struktur. Khim.* **1977,** *18,* 97.
191. Bakaev, V. A.; Pribylov, A. A. *Izv. Akad. Nauk USSR, Ser. Khim.* **1986,** *8,* 1756.
192. Pribylov, A. A.; Bakaev, V. A.; Thamm, H. *Zeolites* **1988,** *8,* 302.
193. Butyagin, P. Yu. *Uspekhi Khimii* **1984,** *53,* 1769.
194. Radtsig, V. A.; Bobyshev, A. A. *Phys. Stat. Sol. (B)* **1986,** *133,* 621.
195. Bobyshev, A. A.; Radtsig, V. A. *Kinet. Kataliz.* **1988,** *29,* 638.
196. Bobyshev, A. A.; Radtsig, V. A. *Khimich. Fizika* **1988,** *7,* 950.
197. Radtsig, V. A.; Senchenya, I. N.; Bobyshev, A. A.; Kazansky, V. B. *Kinet. Kataliz* **1989,** *30,* 1334.
198. Pshezhetskii, S. Ya.; Kotov, A. G.; Milinchuk, V. K.; Roginsky, V. A.; Tupikov, V. I. *EPR of Free Radicals in Radiochemistry*; Khimiya: Moscow, 1972.
199. Shamonina, N. F.; Kotov, A. G.; Pshezhetskii, S. Ya. *Khimiya Vysokikh Energ.* **1971,** *5,* 63.
200. Tertykh, V. A.; Belyakova, L. A. *Zhur. Vsesoyuzn. Khimich. Obshchestva im. Mendeleeva* **1989,** *34,* 395.
201. Tertykh, V. A.; Pavlov, V. V. *Adsorption and Adsorbents* **1978,** *6,* 67.
202. Tertykh, V. A.; Ogenko, V. M. *Teoret. Experim. Khimiya* **1975,** *11,* 827.
203. Yanishpolsky, V. V.; Tertykh, V. A.; Lyubinsky, G. V. *Ukrain. Biokhimich. Zhur.* **1979,** *51,* 324.
204. Sobolev, V. A.; Tertykh, V. A.; Chuiko, A. A. *Zhur. Prikl. Spectroskop.* **1970,** *13,* 646.
205. Sobolev, V. A.; Khoma, M. I.; Furman, V. I.; Ivanov, V. S.; Chebotarev, E. V.; Vatamanyuk, B. I. *Ukr. Khimich. Zhur.* **1976,** *42,* 142.
206. Eremenko, A. M.; Smirnova, N. P.; Tropinov, A. G. *Ukr. Fizich. Zhur.* **1982,** *27,* 1510.
207. Eremenko, A. M. In *Spectroscopy of Molecules and Crystals*; Naukova Dumka: Kiev 1981; Part II, p 137.
208. Guy, A. P.; Glazunov, M. P.; Zhuravlev, L. T.; Khrustalev, Yu. A.; Shengeliya K. Ya. *Dokl. Akad. Nauk USSR* **1984,** *277,* 388.
209. Belyakova, L. D.; Gerasimova, G. A.; Zhuravlev, L. T.; Kudryavtsev, G. V.; Lisichkin, G. V.; Ovchinnikova, N. S.; Platonova, N. P.; Shevchenko, T. I. *Izv. Akad. Nauk USSR, Ser. Khim.* **1989,** *5,* 983.
210. Agzamkhodzhaev, A. A.; Zhuravlev, L. T.; Kiselev, A. F.; Shengeliya, K. Ya. *Izv. Akad. Nauk USSR, Ser. Khim.* **1969,** *10,* 211.
211. Kazansky, V. B. *Kinet. Kataliz.* **1980,** *21,* 159.
212. Kustov, L. M.; Borovkov, V. Yu.; Kazansky, V. B. *J. Catalysis* **1981,** *72,* 149.
213. Kustov, L. M.; Alekseev, A. A.; Borovkov, V. Yu.; Kazansky, V. B. *Dokl. Akad. Nauk USSR* **1981,** *261,* 1374.

214. Kustov, L. M.; Borovkov, V. Yu.; Kazansky, V. B. *Zhur. Fiz. Khim.* **1985,** *59,* 2213.
215. Mastikhin, V. M.; Mudrakovskii, I. L.; Kotsarenko, N. S.; Karakchiev, L. G.; Pelmenshchikov, A. G.; Zamaraev, K. I. *React. Kinet. Catal. Lett.* **1985,** *27,* 447.
216. Bondarenko, A. V.; Kiselev, V. F.; Krasilnikov, K. G. *Kinet. Kataliz.* **1961,** *2,* 590.
217. Akshinskaya, N. V.; Davydov, V. Ya.; Zhuravlev, L. T.; Curthoys, G.; Kiselev, A. V.; Kuznetsov, B. V.; Nikitin, Yu. S.; Rybina, N. V. *Kolloidn. Zhur.* **1964,** *26,* 529.
218. Krasilnikov, K. G.; Kiselev, V. F.; Sysoev, E. A. *Dokl. Akad. Nauk USSR* **1957,** *116,* 990.
219. Dzhigit, O. M.; Kiselev, A. V.; Muttik, G. G. *Kolloidn. Zhur.* **1962,** *24,* 15.
220. Avgul, N. N.; Belyakova, L. D.; Vorob'eva, L. D.; Kiselev, A. V.; Muttik, G. G.; Chistozvonova, O. S.; Checherina, N. Yu. *Kolloidn. Zhur.* **1974,** *36,* 928.
221. Avgul, N. N.; Dzhigit, O. M.; Kiselev, A. V. In *Methods of Catalysts and Catalytic Reactions.* Acad. Sci. Publishers: Novosibirsk, 1965; Vol II, 21.
222. Davydov, V. Ya.; Kiselev, A. V.; Kuznetsov, B. V. *Zhur. Fiz. Khim.* **1965,** *39,* 2058.
223. Ekabson, Ya. Ya.; Kiselev, A. V.; Kuznetsov, B. V.; Nikitin, Yu. S.; *Kolloidn. Zhur.* **1970,** *32,* 41.
224. Kiselev, A. V.; Kuznetsov, B. V.; Lanin, S. N. *Kolloidn. Zhur.* **1976,** *38,* 158.
225. Kiselev, A. V.; Kuznetsov, B. V.; Lanin, S. N. *J. Colloid Interface Sci.* **1979,** *69,* 148.
226. Babkin, I. Yu; Kiselev, A. V. *Zh. Fiz. Khim.* **1963,** *37,* 228.
227. Isirikyan, A. A.; Kiselev, A. V. *Dokl. Akad. Nauk SSSR* **1957,** *115,* 343.
228. Isirikyan, A. A.; Kiselev, A. V.; Frolov, B. A. *Zh. Fiz. Khim.* **1959,** *33,* 389.
229. Nguen, Thi Min Hien; Isirikyan, A. A.; Serpinsky, V. V. *Izv. Akad. Nauk USSR, Ser. Khim.* **1986,** *6,* 1419.
230. Egorov, M. M.; Kiselev, V. F.; Krasilnikov, K. G.; Murina, V. V. *Zh. Fiz. Khim.* **1959,** *33,* 65.
231. Berezin, G. I.; Kiselev, A. V.; Kozlov, A. A.; Kuznetsova, L. V.; Firsova, A. A. *Zh. Fiz. Khim.* **1970,** *44,* 541.
232. Berezin, G. I.; Kiselev, A. V. *J. Colloid Interface Sci.* **1972,** *38,* 227.
233. Berezin, G. I.; Kiselev, A. V.; Sagatelyan, R. T.; Sinitsyn, V. A. *J. Colloid Interface Sci.* **1972,** *38,* 338.
234. Berezin, G. I.; Kiselev, A. V. *J. Chem. Soc. Faraday Trans. 1* **1962,** *78,* 1345.
235. Berezin, G. I.; Kozlov, A. A.; Kuznetsova, L. V. In *Main Problems of Physical Adsorption Theory*; Dubinin, M. M., Serpinsky, V. V., Eds.; Nauka: Moscow: 1970; p 425.
236. Berezin, G. I.; Kiselev, A. V.; Kozlov, A. A.; Kuznetsova, L. V. *Zh. Fiz. Khim.* **1970,** *44,* 1569.
237. Berezin, G. I. *Zh. Fiz. Khim.* **1968,** *42,* 563.
238. Gusev, A. A.; Borovkova, M. A.; Gusev, Yu. A. In *Collection of Post-Graduate Works: Precise Sci., Physics*; State University Press: Kazan, 1977; p 95.
239. Gusev, A. A. *Summary of Dissertation*; State University Press: Kazan, 1979.
240. Zhilenkov, I. V. *Izv. Akad. Nauk USSR, Ser. Khim.* **1957,** 232.
241. Zhilenkov, I. V. In *Main Problems of Physical Adsorption Theory*; Dubinin, M. M.; Serpinsky, V. V., Eds.; Nauka: Moscow, 1970; p 235.
242. Saushkin, V. V.; Zhilenkov, I. V. In *Adsorption in Micropores*; Dubinin, M. M.; Serpinsky, V. V., Eds; Nauka: Moscow, 1983; p 100.

243. Glazun, B. A.; Zhilenkov, I. V.; Rakityanskaya, M. F. *Zhur. Fiz. Khim.* **1969,** *43*, 2397.
244. Kiselev, A. V.; Mikos, N. N.; Romanchuk, M. A.; Shcherbakova, K. D. *Zh. Fiz. Khim.* **1947,** *21*, 1223.
245. Avgul, N. N.; Dzhigit, O. M.; Dreving, V. P.; Gur'ev, M. V.; Kiselev, A. V.; Likhacheva, O. A. *Dokl. Akad. Nauk USSR*, **1951,** *77*, 77.
246. Avgul, N. N.; Dzhigit, O. M.; Isirikyan, A. A.; Kiselev, A. V.; Shcherbakova, K. D. *Dokl. Akad. Nauk USSR* **1951,** *77*, 625.
247. Kiselev, A. V.; Krasilnikov, K. G.; Pokrovsky, N. L.; Avgul, N. N.; Dzhigit, O. M.; Shcherbakova, K. D. *Zh. Fiz. Khim.* **1952,** *26*, 986.
248. Dzhigit, O. M.; Kiselev, A. V.; Mikos-Avgul, N. N.; Shcherbakova, K. D. *Dokl. Akad. Nauk USSR* **1950,** *70*, 441.
249. Avgul, N. N.; Dzhigit, O. M.; Kiselev, A. V.; Shcherbakova, K. D. *Zh. Fiz. Khim.* **1952,** *26*, 977.
250. Belyakova, L. D.; Dzhigit, O. M.; Kiselev, A. V. *Zh. Fiz. Khim.* **1957,** *31*, 1577.
251. Belyakova, L. D.; Kiselev, A. V. *Zh. Fiz. Khim.* **1959,** *33*, 1534.
252. Aristov, B. G.; Kiselev, A. V. *Zh. Fiz. Khim.* **1963,** *37*, 2520.
253. Aristov, B. G.; Kiselev, A. V. *Zh. Fiz. Khim.* **1964,** *38*, 1984.
254. Bugnina, G. A.; Serpinskii, V. V. *Zh. Fiz. Khim.* **1966,** *40*, 887.
255. Lisichkin, G. V.; Kudryavtsev, G. V.; Serdan, A. A.; Staroverov, S. M.; Yuffa, A. Ya. *Modified Silicas in Sorption, Catalysis and Chromatography*; Khimiya: Moscow, 1986.
256. Lisichkin, G. V. *Zhur. Vsesoyuzn. Khimich. Obshchestva im. Mendeleeva* **1989,** *34*, 291.
257. Kudryavtsev, G. V.; Staroverov, S. M. *Zhur. Vsesoyuzn. Khimich. Obshchestva im. Mendeleeva* **1989,** *34*, 308.
258. Kiselev, A. V.; Kovaleva, N. V.; Korolev, A. Ya.; Shcherbakova, K. D. *Dokl. Akad. Nauk USSR* **1959,** *124*, 617.
259. Babkin, I. Yu.; Vasil'eva, V. S.; Drogaleva, I. V.; Kiselev, A. V.; Korolev, A. Ya.; Shcherbakova, K. D. *Dokl. Akad. Nauk USSR* **1959,** *129*, 131.
260. Kiselev, A. V.; Korolev, A. Ya.; Petrova, R. S.; Shcherbakova, K. D. *Kolloidn. Zhur.* **1960,** *22*, 671.
261. Vasil'eva, V. S.; Drogaleva, I. V.; Kiselev, A. V.; Korolev, A. Ya.; Shcherbakova, K. D. *Dokl. Akad. Nauk SSSR* **1961,** *136*, 852.
262. Akshinskaya, N. V.; Kiselev, A. V.; Nikitin, Yu. S.; Petrova, R. S.; Chuikina, V. K.; Shcherbakova, K. D. *Zh. Fiz. Khim.* **1962,** *36*, 1121.
263. Kiselev, A. V.; Petrova, R. S.; Shcherbakova, K. D. *Kinet. Kataliz.* **1964,** *5*, 526.
264. Khokhlova, T. D.; Skoraya, L. A.; Nikitin, Yu. S.; Zinov'eva, M. V. In *Chromatography in Biology and Medicine*; Moscow, 1986; p 186.
265. Brey, V. V.; Gorlov, Yu. I.; Chuiko, A. A. *Teoret. Experim. Khimiya* **1986,** *22*, 378.
266. Tertykh, V. A.; Pavlov, V. V.; Tkachenko, K. I.; Chuiko, A. A. *Teoret. Experim. Khimiya* **1975,** *11*, 174.
267. Tertykh, V. A.; Chuiko, A. A.; Neimark, I. E. *Teoret. Experim. Khimiya* **1965,** *1*, 400.
268. Chuiko, A. A., Guba, G. Ya.; Pavlov, V. V.; Voronin, E. F. *Ukrain. Khimich. Zhur.* **1986,** *52*, 605.
269. Burushkina, T. N.; Chuiko, A. A.; Khaber, N. V.; Manchenko, L. V. *Teoret. Experim. Khimiya* **1968,** *4*, 570.

270. Neimark, I. E.; Sheinfain, R. Yu.; Svintsova, L. G. *Dokl. Akad. Nauk USSR* **1956,** *108,* 87.
271. Neimark, I. E. *Neftekhimiya* **1963,** *3,* 149.
272. Neimark, I. E. In *Adsorption and Porosity*; Dubinin, M. M.; Serpinsky, V. V., Eds.; Nauka: Moscow, 1976; p 27.
273. Neimark, I. E. *Synthetic Mineral Adsorbents and Carriers of Catalysts*; Naukova Dumka: Kiev, 1982.
274. Kolstov, S. I.; Volkova, A. N.; Aleskovsky, V. B. *Zhur. Prikl. Khim.* **1969,** *42,* 73.
275. Kolstov, S. I.; Volkova, A. N.; Aleskovsky, V. B. *Zhur. Prikl. Khim.* **1969,** *42,* 2028.
276. Aleskovsky, V. B. *Zhur. Prikl. Khim.* **1974,** *47,* 2145.
277. Aleskovsky, V. B. *Vestnik Akad. Nauk USSR* **1975,** *6,* 45.
278. Aleskovsky, V. B. *Chemistry of Solids*; Vysshaya Shkola: Moscow, 1978.
279. Aleskovsky, V. B.; Yuffa, A. Ya.; *Zhur. Vsesoyuzn. Khimich. Obshchestva im. Mendeleeva* **1989,** *34,* 317.
280. Postnova, A. M.; Postnov, V. N.; Kolstov, S. I. *Zhur. Prikl. Khim.* **1984,** *57,* 1456.
281. Kovalkov, V. I.; Malygin, A. A.; Kolstov, S. I.; Aleskovsky, V. B. *Zhur. Prikl. Khimii* **1976,** *49,* 2355.
282. Yuffa, A. Ya. In *Chemistry of Heterogenized Compounds*; TGU Press: Tyumen, 1985; p 176.
283. Skopenko, V. V.; Trofimchuk, A. K.; Zaitsev, V. N. *Zhur. Neorganich, Khim.* **1982,** *27,* 2579.
284. Fillipov, A. P. *Teoret. Experim. Khimiya,* **1983,** *4,* 463.
285. Reikhsfeld, V. O.; Skvortsov, N. K. In *Chemistry of Heterogenized Compounds*; TGU Press: Tyumen, 1985; p 111.
286. Ermakov, Yu. I.; Zakharov, V. A.; Kuznetsov, B. N. *Grafted Complexes on Oxide Carriers in Catalysis*; Nauka: Novosibirsk, 1980.
287. Smit, V. A.; Simonyan, S. O.; Tarosov, V. A.; Shashkov, A. S.; Mamyan, S. S.; Gybin, A. S.; Ibragimov, I. I. *Izv. Akad. Nauk USSR, Ser. Khim.* **1988,** *12,* 2796.
288. Kiselev, A. V.; Poshkus, D. P.; Yashin, Ya. I. *Molecular Principles of Adsorption Chromatography*; Khimiya: Moscow 1986.
289. Kiselev, A. F.; Iogansen, A. V.; Sakodynsky, K. I.; Sakharov, V. M.; Yashin, Ya. I.; Karnaukhov, A. P.; Buyanova, N. E.; Kurkchi, G. A. *Physico-Chemical Application of Gas Chromatography*; Khimiya: Moscow, 1973.
290. Kiselev, A. V.; Yashin, Ya. I. *Gas- and Liquid-Adsorption Chromatography*; Khimiya: Moscow, 1975.
291. Pavlov, V. V.; Pavlik, G. E.; Khaber, N. V. *Chemistry and Practical Use of Chemical Modified Aerosils*; Znanie: Kiev, 1979.
292. Ingold, C. K. *Structure and Mechanism in Organic Chemistry,* 2nd ed.; Cornell University Press: Ithaca, NY, 1969.
293. Nazarenko, A. V.; Tarasevich, Yu. I.; Bondarenko, S. V., Lantukh, G. V. *Teoret. Experim. Khimiya* **1989,** *6,* 753.
294. Bondarenko, S. V.; Nazarenko, A. V.; Tarasevich, Yu. I. *Zhur. Prikl. Khim.* **1989,** *6,* 1252.
295. Ganichenko, L. G.; Dubinin, M. M.; Zaverina, E. D.; Kiselev, V. F.; Krasilnikov, K. G. *Izv. Akad. Nauk USSR, Ser. Khim.* **1960,** 9, 1535.
296. Kiselev, S. A.; Sokolova, N. P. *Kolloidn. Zhur.* **1981,** *43,* 165.
297. Kiselev, A. V.; Khopina, V. V.; Eltekov, Yu. A. *Izv. Akad. Nauk SSSR, Ser. Khim.* **1958,** *6,* 664.

298. Kiselev, A. V.; Pavlova, L. F. *Izv. Akad. Nauk SSSR, Ser. Khim.* **1962,** *12,* 2121.
299. Kiselev, A. V.; Pavlova, L. F. *Neftekhimiya* **1962,** *11,* 861.
300. Kiselev, A. V.; Shikalova, I. V. *Kolloidn. Zhur.* **1962,** *24,* 687.
301. Bogacheva, E. K.; Kiselev, A. V.; Nikitin, Yu. S.; Eltekov, Yu. A. *Zh. Fiz. Khim.* **1965,** *39,* 1777.
302. Bogacheva, E. K.; Kiselev, A. V.; Nikitin, Yu. S.; Eltekov, Yu. A. *Vysokomolekular. Soedin.* **1968,** *10A,* 574.
303. Kiselev, A. V.; Shikalova, I. V. *Kolloidn. Zhur.* **1970,** *32,* 702.
304. Zhdanov, S. P.; Kiselev, A. V.; Koromaldi, E. V.; Nazansky, A. S.; Eltekov, Yu. A. *Kolloidn. Zhur.* **1977,** *39,* 354.
305. Eltekov, Yu. A.; Kiselev, A. V. *J. Polymer. Sci., Polymer Symposium* **1977,** *61,* 431.
306. Davydov, V. Ya.; Kiselev, A. V.; Sapozhnikov, Yu. M. *Kolloidn. Zhur.* **1979,** *41,* 333.
307. Chuduk, N. A.; Eltekov, Yu. A.; Kiselev, A. V. *J. Colloid Interface Sci.* **1981,** *84,* 149.
308. Larionov, O. G.; Kurbanbekov, E. In *Physical Adsorption from Multi-Component Phases*; Dubinin, M. M., Serpinsky, V. V., Eds.; Nauka: Moscow, 1972; p 85.
309. Larionov, O. G.; Popov, E. A.; Chmutov, K. V. *Zh. Fiz. Khim.* **1974,** *48,* 2348.
310. Larionov, O. G. In *Physical Adsorption: Proc. Second Czechoslovak Conference on Physical Adsorption, Liblice* **1975,** 43.
311. Kazaryan, S. A.; Larionov, O. G.; Chmutov, K. V.; Yudilevich, M. D. *Zh. Fiz. Khim.* **1973,** *47,* 1619.
312. Kazaryan, S. A.; Larionov, O. G.; Chmutov, K. V.; Yudilevich, M.D. *Zh. Fiz. Khim.* **1973,** *47,* 2170.
313. Kiselev, V. F.; Krasilnikov, K. G. *Zh. Fiz. Khim.* **1958,** *32,* 1435.
314. Ganichenko, L. G.; Kiselev, V. F.; Krasilnikov, K. G. *Dokl. Akad. Nauk USSR* **1959,** *125,* 1277.
315. Zuevsky, V. V.; Kulaev, D. V.; Rabovsky, A. B.; Shmatkov, B. A. *Zhur. Vsesoyuzn, Khimich. Obshchestva im. Mendeleeva* **1989,** *34,* 325.
316. Zuevsky, V. V.; Shmatkov, B. A.; Turaev, A. N. In *Chromatography in Biology and Medicine*; Proceed. of International Symposium: Moscow, 1986; p 107.
317. Ulberg, D. E.; Churaev, N. V. *Kolloidn. Zhur.* **1988,** *50,* 1158.
318. Bartenev, G. M. *Fizika Khimiya Stekla* **1984,** *10,* 41.
319. Krylova, Z. L.; Dolin, P. I. *Kinet. Kataliz.* **1966,** *7,* 977.
320. Krylova, Z. L.; Dolin, P. I. *Khimaya Vysokikh Energii* **1969,** *3,* 152.
321. Strelko, V. V.; Suprunenko, K. A. *Khimiya Vysokikh Energ.* **1968,** *2,* 258.
322. Tagieva, M. M.; Kiselev, V. F. *Zh. Fiz. Khim.* **1961,** *35,* 1381.
323. Kiselev, V. F.; Krylov, O. V. *Electronic Phenomena on Semiconductors and Dielectrics in Adsorption and Catalysis*; Nauka: Moscow, 1979.
324. Garibov, A. A.; Bakirov, M. Ya.; Velibekaro, G. Z.; Elchiev, Ya. M. *Khimiya Vysokikh Energ.* **1984,** *18,* 506.
325. Garibov, A. A.; Gezalov, Kh. B.; Velibekova, G. Z.; Khudiev, A. T.; Ramazanova, M. Kh.; Kasumov, R. D.; Agaev, T. N.; Gasanov, A. M. *Khimiya Vysokikh Energ.* **1987,** *21,* 505.
326. Pariiskii, G. B.; Kazanskii, V. B. *Kinet. Kataliz* **1964,** *5,* 96.
327. Pariiskii, G. B.; Mishchenko, Yu. A; Kazanskii, V. B. *Kinet. Kataliz* **1965,** *6,* 625.
328. Brotikovsky, O. I.; Zhidomirov, G. M.; Kazanskii, V. B.; Mashchenko, A. I.; Shelimov, B. N. *Kinet. Kataliz* **1971,** *12,* 700.

329. Ermatov, S. E. *Izv. Akad. Nauk Kazakh. USSR Ser. fiz.-mat. nauk* **1971,** *2*, 60.
330. Ermatov, S. E.; Vakhabov, M.; Tuseev, T. In *Applied Nuclear Physics, Part I*; Fan: Tashkent, 1973; p 145.
331. Ermatov, S. E. *Radiation Stimulated Adsorption*; Nauka: Alma-Ata, 1973.
332. Voevodsky, V. V. *Physics and Chemistry of Elementary Chemical Processes*; Nauka: Moscow, 1969.
333. Krylov, O. V. *Khimiya Vysokikh Energ.* **1971,** *5*, 179.
334. Boldyrev, V. V. *Experimental Methods in Mechanochemistry of Inorganic Substances*; Nauka: Novosibirsk, 1983.
335. Spitsyn, V. I.; Pirogova, G. N.; Ryabov, A. I.; Kritskaya, V. E.; Naselsky, S. P.; Klimashina, E. V. *Dokl. Akad. Nauk USSR* **1986,** *289*, 1434.
336. Spitsyn, V. I.; Pirogova, G. N.; Ryabov, A. I.; Kritskaya, V. E.; Glazunov, P. Ya.; Naselsky, S. P. *Dokl. Akad. Nauk USSR* **1987,** *293*, 1148.
337. Spitsyn, V. I.; Pirogova, G. N.; Kritskaya, V. E.; Ryabov, A. I. *Izv. Akad. Nauk USSR, Ser. Neorganich Mater.* **1982,** *18*, 74.
338. Pirogova, G. N.; Ryabov, A. I.; Kritskaya, V. E. *Khimiya Vysokikh Energ.* **1988,** *22*, 322.
339. Klevikov, D. P.; Fenelonov, V. B.; Gavrilov, V. Yu; Zolotarevsky, B. V.; Goldenberg, G. I.; Dovbii, Z. A. *Kolloidn. Zhur.* **1989,** *51*, 278.
340. Hochstrasser, G.; Antonini, I. E. *Surface Sci.* **1972,** *32*, 644.
341. Kiselev, V. F. *Zh. Fiz. Khim.* **1960,** *34*, 698.
342. Egorov, M. M.; Kiselev, V. F. *Zh. Fiz, Khim.* **1962,** *36*, 318.
343. K.vlividze, V. I.; Kiselev, V. F. In *Problems of Kinetics and Catalysis*; Nauka: Moscow, 1967; p 302.
344. Egorov, M. M.; Kiselev, V. F.; Krasilnikov, K. G. *Zh. Fiz. Khim.* **1961,** *35*, 2031.
345. Khodakov, G. S.; Rebinder, P. A. *Dokl. Akad. Nauk USSR* **1959,** *127*, 1070.
346. Khodakov, G. S. *Physics of Grinding*; Nauka: Moscow, 1972.
347. Kiselev, V. F.; Krasilnikov, K. G.; Khodakov, G. S. *Dokl. Akad. Nauk USSR* **1960,** *130*, 1273.
348. Krotova, N. A.; Karasev, V. V. *Dokl. Akad. Nauk USSR* **1953,** *92*, 607.
349. Deryagin, V. B.; Krotova, N. A.; Smilga, V. P. *Adhesion of Solids*; Nauka: Moscow, 1973.
350. Paschenko, A. A.; Voronkov, M. G. *Silicon-Organic Protective Coatings*; Tekhnika: Kiev, 1969.
351. Pashchenko, A. A.; Voronkov, M. G.; Mikhailenko, L. A. *Hydrophobic Coatings*; Naukova Dumka: Kiev, 1973.
352. Pashchenko, A. A. et al. *Polyfunctional Element-Organic Coatings*; Pashchenko, A. A., Ed.; Vyshcha Sckola: Kiev, 1987.
353. Deryagin, B. V.; Churaev, N. V.; Muller, V. M. *Surface Forces*; Nauka: Moscow, 1985.
354. Churaev, N. V.; Sobolev, V. D.; Somov, A. N. *J. Colloid Interface Sci.* **1984,** *97*, 574.
355. Deryagin, B. V.; Zheleznyi, B. V.; Zorin, Z. M. In *Surface Forces in Thin Films and Stability of Colloids*; Nauka: Moscow, 1974; p 90.
356. Zorin, Z. M.; Novikova, A. V.; Churaev, N. V. In *Questions of Form Production Physics and Phase Transitions*; Tula, 1973; p 42.
357. Zorin, Z. M.; Novikova, A. V.; Petrov, A. K.; Churaev, N. V. In *Surface Forces in Thin Films and Stability of Colloids*; Nauka: Moscow, 1974; p 94.
358. Nosenko, N. V.; Sergeeva, I. P.; Sobolev, V. D.; Churaev, N. V. *Kolloidn. Zhur.* **1989,** *51*, 786.
359. Deryagin, B. V.; Churaev, N. V. *Wetting Films*. Nauka: Moscow, 1984.

360. Chardymskaya, E. Yu.; Sidorova, M. P.; Friedrichsberg, D. A.; Kulepova, E. V. *Kolloidn. Zhur.* **1986,** *48,* 589.
361. Golikova, E. V.; Gimanova, I. M.; Chernoberezhsky, Yu. M. *Vestnik LGU, Ser. 4* **1986,** *1,* 69.
362. Gribanova, E. V.; Cherkashina, L. M. *Kolloidn. Zhur.* **1989,** *51,* 854.
363. Gribanova, E. V.; Cherkashina, L. M. *Kolloidn. Zhur.* **1989,** *51,* 1069.
364. Rebinder, P. A. In *All-Union Scientific Conference on the Intensification of the Drying Processes and Improving the Quality of Materials in Drying Processes*; Profizdat: Moscow, 1958; p 20.
365. Gerasimov, Ya. I.; Dreving, V. P.; Eremin, E. N.; Kiselev, A. V.; Lebedev, V. P.; Panchenkov, G. M.; Shlygin, A. I. *Course of Physical Chemistry,* 3rd ed.; Gerasimov, Ya. I, Ed.; Khimiya: Moscow, 1973; Vol. 1, Chapters 16–19.
366. Avgul, N. N.; Kiselev, A. V.; Poshkus, D. P. *Adsorption of Gases and Vapours on Homogeneous Surfaces.* Khimiya: Moscow, 1975.
367. Kiselev, A. V.; Lopatkin, A. A.; Shulga, A. A. *Dokl. Akad. Nauk USSR* **1984,** 275, 916.
368. Kiselev, A. V.; Lopatkin, A. A.; Shulga, A. A. *Zeolites* **1985,** *5,* 261.
369. Bezus, A. G.; Kiselev, A. V.; Lopatkin, A. A.; Quang Du, Pham *J. Chem. Soc. Faraday Trans. 2* **1978,** *74,* 367.
370. Lopatkin, A. A. *Theoretical Principles of Physical Adsorption*; MGU Press: Moscow, 1983.
371. Kiselev, A. V.; Quang Du, Pham. *J. Chem. Soc. Faraday Trans. 2* **1981,** *77,* 1.
372. Kiselev, A. V.; Quang Du, Pham. *J. Chem. Soc. Faraday Trans. 2* **1981,** *77,* 17.
373. Il'in, B. V. *Nature of Adsorption Strengths*; Gostekhizdat: Moscow, 1952.
374. Poshkus, D. P. In *Preparation, Structure and Characteristics of Sorbents*; Goskhimizdat: Leningrad, 1959; p 270.
375. Babkin, I. Yu; Kiselev, A. V. *Dokl. Akad. Nauk USSR* **1959,** *129,* 357.
376. Klyuchnikov, V. A. *Summary of Dissertation*; State University Press: Kalinin, 1979.
377. Klyuchnikov, V. A.; Voronkov, M. G.; Pepekin, V. I.; Popov, V. T.; Balykova, I. A.; Kuz'mina, E. S. *Dokl. Akad. Nauk USSR* **1988,** *298,* 398.
378. Dunken, H.; Lygin, V. I. *Quantenchemie der Adsorption an Festkörperoberflachen*; Verlag Chemie, Weinheim: New York, 1978.
379. Lygin, V. I.; Magomedbekov, G. Kh.; Lygina, I. A. *Zhur. Struktur. Khim.* **1981,** 22, 156.
380. Lygin, V. I.; Serazetdinov, A. D.; Khlopova, Z. G.; Shchepalin, K. L. In *Catalysis: Fundamental and Applied Researches*; MGU Press: Moscow, 1987; p 223.
381. Lygin, V. I.; Serazetdinov, A. D.; Ryabenko, E. A.; Chertikhina, O. I. *Phys. Stat. Sol. (B)* **1989,** *156,* 205.
382. Shchegolev, B. F.; Dyatkina, M. E. *Zhur. Struk. Khimii* **1974,** *15,* 323.
383. Shchegolev, B. F.; Dyatkina, M. D. *Zhur. Struk. Khimii* **1974,** *15,* 325.
384. Dikov, Yu. P.; Brytov, I. A.; Romashenko, Yu. N.; Dolin, S. P. *Peculiarity of Electronic Structure of Silicates*; Nauka: Moscow, 1979.
385. Grivtsov, A. G.; Zhuravlev, L. T.; Gerasimova, G. A.; Bulatova, I. V.; Khazin, L. G. *Preprint of the Institute of Applied Mathematics, USSR Academy of Sciences,* **1983,** *142.*
386. Grivtsov, A. G.; Zhuravlev, L. T.; Gerasimova, G. A.; Khazin, L. G. *J. Colloid Interface Sci.* **1988,** *126,* 397.
387. Rusanov, A. I. *Phase Equilibrium and Surface Phenomena*; Khimiya: Leningrad, 1967.

388. Rusanov, A. I.; Levichev, S. A.; Zharov, V. T. *Surface Division of Substances*; Khimiya: Leningrad, 1981.
389. Tovbin, Yu. K. *Theory of Physico-Chemical Processes on Boundary of Gas-Solid*; Nauka: Moscow, 1990.
390. Pryanishnikov, V. P. *System of Silica*. Stroyizdat: Leningrad, 1971.
391. Romankov, P. G.; Lepilin, V. N. *Uninterrupted Adsorption of Gases and Vapours*; Leningrad, 1968.
392. Serpionova, E. N. *Industrial Adsorption of Gases and Vapours*; Vysshaya Shkola: Moscow, 1969.
393. Aripov, E. A. *Natural Mineral Sorbents, Their Activation and Modification*; Fan: Tashkent, 1970.
394. Agzamkhodzhaev, A. A. In *Investigation of Adsorption Processes and Adsorbents*; Dubinin, M. M., Ed.; Fan: Tashkent, 1979; p 218.
395. Tarasevich, Yu. I.; Ovcharenko, F. D. *Adsorption on Clayey Minerals*; Naukova Dumka: Kiev, 1975.
396. Tarasevich, Yu. I. *Structure and Surface Chemistry of Schistose Silicates*; Naukova Dumka: Kiev, 1988.
397. Bykov, V. T.; Gerasimova, V. G.; Gritsyuk, A. A.; Iovenko, L. M.; Shcherbatyuk, N. E. In *Natural Sorbents*; Bykov, V. T., Ed.; Nauka: Moscow, 1967; p 104.
398. Bykov, V. T. *Sorbtion Characteristics and Structure of Bleach Soils*; Acad. Sci. Publishers: Vladivostok, 1953.
399. Gryazev, N. N. In *Surface Chemical Compounds and Their Role in Adsorption Phenomena*; Kiselev, A. V., Ed.; MGU Press: Moscow, 1957; p 196.
400. Kiselev, A. V.; Gryazev, N. N. In *Natural Mineral Sorbents*; The Ukrainian SSR Academy of Sci. Publishers: Kiev, 1960; p 24.
401. Komarov, V. S. *Adsorption–Structural, Physico-Chemical and Catalytic Characteristics of Clays of Byelorussia*; Nauka i Tekhnika: Minsk, 1970.
402. Komarov, V. S. In *Investigation of Adsorption Processes and Adsorbents*; Dubinin, M. M., Ed.; Fan: Tashkent, 1979; p 186.
403. Tsitsishvili, G. V.; Shuakrishvili, M. S.; Barnabishvili, D. N. In *Natural Sorbents*; Bykov, V. T., Ed.; Nauka: Moscow, 1967; p 45.
404. Tsitsishvili, G. V. In *Natural Zeolites*; Metsniereba: Tbilisi, 1978.
405. Kerdivarenko, M. A. *Moldavian Natural Adsorbents and Technology of Their Application*; Shteentsa: Kishinev, 1975.
406. Russu, V. I.; Okopnaya, N. T.; Stratulat, G. V.; Ropot, V. M. In *Investigation of Adsorption Processes and Adsorbents*; Dubinin, M. M., Ed.; Fan: Tashkent, 1979; p 257.

Portions of this paper were first published by the same author in *Colloids Surf.* **1993,** *74(1).*

RECEIVED for review February 15, 1991. ACCEPTED revised manuscript January 13, 1992.

Author Index

Affiliation Index

Nissan Chemical Industries, Ltd., 51
The Pennsylvania State University, 113
The PQ Corporation, 617
Russian Academy of Sciences, 629
Sandia National Laboratories, 361, 433
Unilever Research, 341
Universität des Saarlandes Gebäude, 419
Université de Nancy I, 199
University of Illinois, 451
The University of Melbourne, 147
University of New Mexico, 361
University of Notre Dame, 223
University of Ottawa, 183
University of Utah, 309
University of Utrecht, 83
West Chester University, 595

Subject Index

A

Nissan Chemical Industries, Ltd., 51
The Pennsylvania State University, 113
The PQ Corporation, 617
Russian Academy of Sciences, 629
Sandia National Laboratories, 361, 433
Unilever Research, 341
Universität des Saarlandes Gebäude, 419
Université de Nancy I, 199
University of Illinois, 451
The University of Melbourne, 147
University of New Mexico, 361
University of Notre Dame, 223
University of Ottawa, 183
University of Utah, 309
University of Utrecht, 83
West Chester University, 595

Subject Index

A

B

C

D

E

F

G

H

I

L

M

N

O

P

Q

R

S

T

U

V

W

Copy editing: Steven Powell
Indexing: Deborah H. Steiner
Production: C. Buzzell-Martin
Acquisition: Cheryl Shanks
Cover design: Ellen Cornett

Typeset by ATLIS Publishing Services Inc., Beltsville, MD
Printed and bound by Maple Press, York, PA